Study of the molecular bases underlying cerebellar defects with emphasis on protein N-glycosylation impairment

Daniel Medina-Cano

▶ **To cite this version:**

Daniel Medina-Cano. Study of the molecular bases underlying cerebellar defects with emphasis on protein N-glycosylation impairment. Medical Imaging. Université Sorbonne Paris Cité, 2018. English. NNT : 2018USPCB054 . tel-02493474

HAL Id: tel-02493474
https://theses.hal.science/tel-02493474

Submitted on 27 Feb 2020

HAL is a multi-disciplinary open access archive for the deposit and dissemination of scientific research documents, whether they are published or not. The documents may come from teaching and research institutions in France or abroad, or from public or private research centers.

L'archive ouverte pluridisciplinaire **HAL**, est destinée au dépôt et à la diffusion de documents scientifiques de niveau recherche, publiés ou non, émanant des établissements d'enseignement et de recherche français ou étrangers, des laboratoires publics ou privés.

*Study of the molecular bases underlying cerebellar defects with emphasis on protein **N-glycosylation** impairment.*

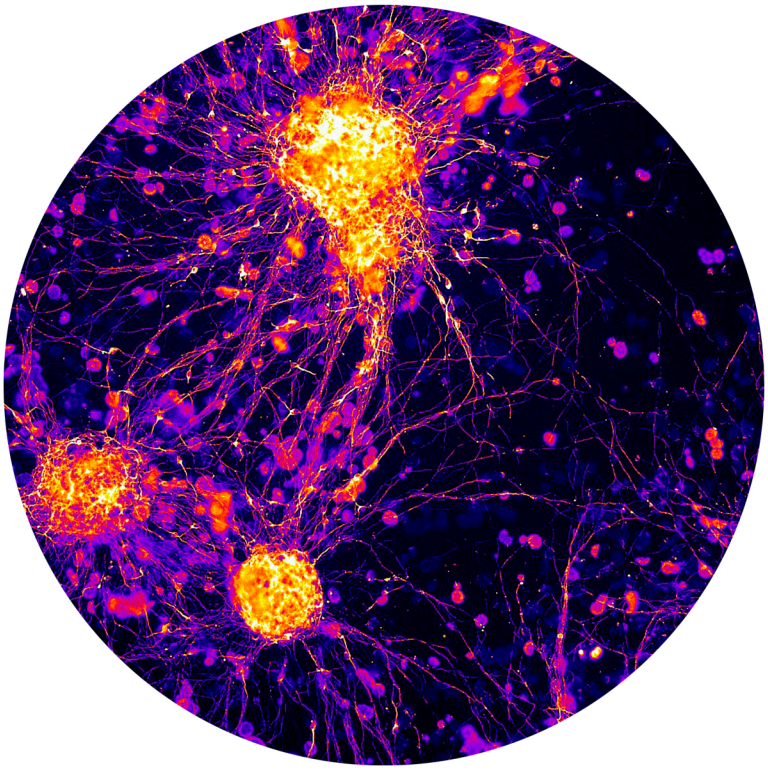

Daniel MEDINA-CANO

UNIVERSITE PARIS DESCARTES

FACULTE DE MEDECINE

ECOLE DOCTORALE BIO SORBONNE PARIS CITE

THESE pour obtenir le grade de

DOCTEUR DE L'UNIVERSITE PARIS DESCARTES

Study of the molecular bases underlying cerebellar defects with emphasis on protein N-glycosylation impairment

Présentée par

Daniel MEDINA-CANO

UMR163 - Molecular and pathophysiological bases of developmental brain disorders

Membres du jury:

Dr. Genevieve GOURDON	Présidente
Dr. Laurence GOUTEBROZE	Rapporteur
Pr. Gert MATTHIJS	Rapporteur
Dr. Cyril HANUS	Examinateur
Pr. Francesc PALAU	Examinateur
Dr. Vincent CANTAGREL	Codirecteur de thèse
Dr. Laurence COLLEAUX	Codirecteur de thèse

ACKNOWLEDGEMENTS

I would like to start by thanking the main supervisor of my thesis, Dr. Vincent Cantagrel. Thanks for guiding me through all of this process, encouraging me and for teaching me "how to science". I also thank Dr. Laurence Colleaux for her support, indispensable scientific input and motivation. Thank you very much to both of you for accepting me in your team, for all of the effort that you put into the PhD scholarship pursue so that I could stay and for revising this manuscript.

A special thanks to Dr. Laurence Goutebroze and Pr. Gert Matthijs for accepting being part of the jury and for reviewing the present work. To thank also Francesc Palau, Cyril Hanus and Geneviève Gourdon for being part of my thesis jury. I feel really honoured to have such a jury and I hope that you will enjoy the lecture of the manuscript.

I thank Michaël Nicouleau for his crucial help during the first years of my PhD. Thank you for teaching me so much and being such an amazing project partner. I also thank Maëva Langouet for being a PhD role model, counselling and helping me. Especial thanks also to Sonny Nguyen and Karine Siquier-Pernet for their constant help through all my PhD, for teaching me so much and being amazing lab mates. Thank you Kariiiiiine for your patience and guidance and thank you Sonny for all the technical as well as the personal advice. To the awesome PhD students of the lab, Ekin Ucuncu and Julien Fregeac, thank you very much for everything, the enriching discussions, funny moments, camaraderie, beers... Thank you Ekin for your kindness and all the help with the cells. I also thank Florine Verny and Matthieu Egloff for being great office "coloques" and well, basically, for teaching me French. I thank Nami Altin and Antoine Poli, the newbies, for helping to build the amazing group that we are nowadays. I would also like to thank to the other physicians of the team Anne, Valerie and Giulia for their support and their enriching lab meetings. Especial mention to Stéphanie Jaalouk and Emily Thorburn-Winsor for showing me how rewarding to mentor can be. Globally, I would like to thank to all of the members of the team for creating such an amazing work environment, full of laughs and amazing moments. This wouldn't have been the same (and maybe not even possible) without you. You will be missed.

I would also like to thank the Necker proteomic platform, especially Chiara Guerrera and Joanna Lipecka, not only for all of the 'OMICs work but for being so helpful, kind and teaching me how to deal with all of the data. I thank also Chistian Thiel and François Foulquier for crucial scientific input and enriching discussions, as well as Nicolas Cagnard and Olivier Pellé for helping me with all statistics and FACs experiments.

I also thank "de tout coeur très fuerte" Lucas Bianchi for his crucial moral support through all the PhD, as for the "neuneus" team, I'm not sure this would have been

possible without you. To thank also Caroline Besnard and Laura Barnabei for all of the time spend together, it's been a pleasure to share this experience with you. See you all out there. I also thank Daniel Darby, Sarah Issa, Kahina, Carmen Oleaga, together with Julien, Caro and Lucas, for all of the beers, afterworks, sport events and basically all of the stuff that we have done together these years, you're just awesome. I also thank the Imagine Sport Association (launched by Sonny and now leaded by Julien) for turning me into a sport addicted, it really help coping with all the PhD-related stress.

Thank you to all of the teams at the third floor and more globally to all the personal at the Imagine Institute for turning this institute into such a great place for science. I feel really lucky of having spent so many years here.

In a more personal field, I thank from the bottom of my heart to Pedro Antonio Pallás Monter. Sin ti sí que estoy seguro que nada de todo esto habría ocurrido (sin olvidar la aportación clave de Carolina Gandini!). Muchas gracias por tu comprensión, tu apoyo, por aguantarme cada día, por soportar los tres años separados, por ser mi mejor amigo, por todos los consejos, cuidarme cada día, por venirte a París, por aguantar mis findes en el laboratorio, por animarme siempre que lo necesito, por los viajes… (y un larguísimo etcétera). Un placer compartir la vida contigo! Un gràcies molt especial també a Ferran Gómez per haver sigut un company genial d'aquesta aventura parisienne i crear un "safe place" durant tots aquests anys. Muchas gracias también a Adrián Almoguera por ser el mejor coloque ever y junto a Pedrín formar una especie de mini-hogar en París. Especial thanks to Giulia, Federica, Mariangela, Stefania and Ángel (and Viola!) for all of the amazing time we have spend together (and that we will keep spending no matter where) and reminding me that science is not everything. Agradecer también a Helena, Jordi, Víctor, Alba, Anna, Alberto, María, Carolina y Melanie todo su apoyo durante estos años y hacer que cada vez que vuelvo a casa sea como si nunca me hubiera ido.

Por ultimo, muchas gracias a mi familia. Sin vosotros nada de todo esto sería posible. Muchas gracias por el apoyo, por ser mi válvula de escape todos estos años, por entenderme y en definitiva por ser la mejor familia que uno podría desear.

ABSTRACT

Cerebellar defects encompass a group of rare diseases affecting cerebellar functions. The prevalence of these defects is estimated to be at 26/10000 children in Europe. These diseases lead to movement disorders (ataxia) and are frequently associated with intellectual disability, life-threatening conditions that prevent patients from coping with normal daily life. For most of these conditions, only supportive treatments are available. Besides genetic diagnosis, which is essential for genetic counselling, an in-depth understanding of the physiopathology underlying the disorder is necessary for future therapeutic development. Thus, the objectives of my thesis project are to improve the genetic diagnosis of cerebellar defects and to explore the mechanism behind one of the most frequent causes of cerebellar defects: disruption of protein N-glycosylation. Disruption of protein N-glycosylation causes Congenital Disorders of Glycosylation (CDG), multisystemic disorders with severe neurological impairment. Early-onset cerebellar atrophy and hypoplasia are frequently observed, especially in CDG cases with *SRD5A3* mutations.

To understand how a general N-glycosylation defect affects cerebellar development, we generated a cerebellum-specific *Srd5a3* conditional KO mouse model. This model recapitulates the human defects with abnormal N-glycosylation, cerebellar hypoplasia and motor coordination impairment. Histological evaluation of the cerebellum identified a subset of granule cells unable to initiate their final migration during cerebellar development. By combining proteomic and glycoproteomic approaches, we showed that defect in N-glycosylation has variable impact depending on the number of N-glycosylation sites on each protein. The more N-glycosylation sites that a protein has, the more sensitive it is to hypoglycosylation and/or degradation. Our data suggest that the heavily N-glycosylated cell adhesion molecules with immunoglobulin domains (IgSF-CAMs) are highly sensitive to glycosylation defect.

Using *in vitro* live granule cell imaging, we identified an IgSF-CAM-dependant neurite extension defect. This defect is linked to impaired glycosylation and function of L1CAM and NrCAM. We next evaluated if the defect was conserved in human neurons. To investigate that possibility, we generated *SRD5A3*$^{-/-}$ hiPSCs that were further differentiated towards cortical neurons. Human neurons recapitulate the biochemical defect in mouse (e.g. L1CAM and NrCAM hypoglycosylation). This finding expands our conclusions to the whole human brain. Finally, using electron microscopy, we could identify disrupted organization of the cerebellar parallel fibers in the mouse mutant, consistent with the established role of numerous IgSF-CAMs in axon guidance.

Our results provide important evidence into the molecular mechanism underlying cerebellar sensitivity to N-glycosylation impairment. Moreover, we show how defect in N-glycosylation primarily affects cell adhesion. Finally, our work emphasizes the critical role of IgSF-CAM N-glycosylation for normal mammalian brain development and function.

RÉSUMÉ

Les anomalies cérébelleuses englobent un groupe de maladies rares affectant le fonctionnement du cervelet. La prévalence de ces défauts est estimée à 26 sur 10000 enfants en Europe. Ces maladies entraînent des troubles du mouvement (ataxie) et sont fréquemment associées à des déficiences intellectuelles, des défauts qui empêchent les patients touchés d'avoir une vie normale et qui peuvent entrainer une mortalité précoce. Pour la plupart de ces conditions, seul un traitement symptomatique est disponible. Outre le diagnostic génétique, indispensable pour pouvoir proposer un conseil génétique, une compréhension profonde de la physiopathologie sous-jacente à l'anomalie est nécessaire pour le développement potentiel des thérapies. Mon travail de thèse avait pour but l'amélioration du diagnostic génétique des défauts cérébelleux et la compréhension de la physiopathologie de l'une des causes les plus fréquentes d'anomalies cérébelleuses: les anomalies de la N-glycosylation.
Les anomalies de N-glycosylation sont responsables des syndromes CDG (troubles congénitaux de la glycosylation ou «congenital disorders of glycosylation»), maladies multisystémiques avec des troubles neurologiques sévères. Une atrophie et une hypoplasie cérébelleuses précoces sont fréquemment observées, en particulier dans les cas des CDG avec des mutations au gène *SRD5A3*.

Pour mieux comprendre comment un défaut général de N-glycosylation affecte le développement cérébelleux, nous avons généré une souris Srd5a3 KO conditionnelle au niveau du cervelet. Ce modèle récapitule le défaut humain avec une N-glycosylation anormale, une hypoplasie cérébelleuse et une altération de la coordination motrice. L'évaluation histologique précise du cervelet des souris mutantes a montré que certaines cellules granulaires étaient incapables d'initier leur migration finale lors du développement du cervelet. En combinant une approche protéomique et une approche glycoprotéomique, nous avons montré qu'un défaut de N-glycosylation a un impact variable en fonction du nombre de sites de N-glycosylation des protéines. Plus le nombre de sites de N-glycosylation d'une protéine est élevé, plus elle est sensible à l'hypoglycosylation et/ou à la dégradation dans un contexte de CDG. Nos données montrent en particulier que les protéines d'adhésion cellulaire de la super famille des immunoglobulines (IgSF-CAMs) sont hautement sensibles au défaut de N-glycosylation.

En utilisant de l'imagerie en temps réel de cellules granulaires en culture, nous avons identifié un défaut d'extension des neurites liée aux IgSF-CAMs. Ce défaut est lié à une altération de la glycosylation et du fonctionnement de L1CAM et NrCAM. Nous avons ensuite évalué si le défaut était conservé dans les neurones humains. Pour étudier cette possibilité, nous avons généré des cellules humaines pluripotentes (hiPCS) *SRD5A3*$^{-/-}$ qui ont été différenciés vers des neurones corticaux. Ces neurones récapitulent le défaut biochimique trouvé chez la souris (hypoglycosylation de NrCAM et L1CAM). Cette découverte étend nos conclusions à l'ensemble du cerveau humain. Enfin, en utilisant la microscopie électronique, nous avons pu identifier une organisation des fibres parallèles cérébelleuses perturbée chez le mutant, en accord avec le rôle établi de nombreuses IgSF-CAM dans le guidage axonal.

Nos résultats apportent des nouveaux éléments quant aux mécanismes responsables de la forte sensibilité du cervelet aux défauts de N-glycosylation. De plus, nous montrons comment les défauts de la N-glycosylation affectent principalement l'adhésion cellulaire. Notre travail fournit également de nouveaux arguments en faveur du rôle critique de la N-glycosylation des IgSF-CAM pour leur stabilité et leur fonctionnalité au cours du développement du cerveau des mammifères.

INDEX

INTRODUCTION

1 THE CEREBELLUM IN NORMAL AND PATHOLOGICAL CONDITIONS

1.1 Cerebellar generalities and structure

The human cerebellum ("little brain", Latin) contains more than half of the neurons of the brain (more than 10^{11} cells), even though it represents only 10% of total brain volume. Due to its relatively simple cytoarchitecture and connectivity, the cerebellum is widely used as a model to study neurodevelopment. Many discoveries arising from its study can be extended to other parts of the brain that have more complex organization such as the cerebral cortex.

Allometric studies show that, relative to other mammals and to the body weight, the human cerebellum is one of the biggest. Interestingly, apes have a higher ratio of cerebellum/neocortex than non-apes. These data is suggestive of an involvement of the cerebellum in complex functions, such as technical intelligence, associated with apes evolution[1,2]. The mammal cerebellum can be broadly subdivided into the anterior, posterior and flocculonodular lobe or into vermis (central zone) and lateral hemispheres (Figure 1).

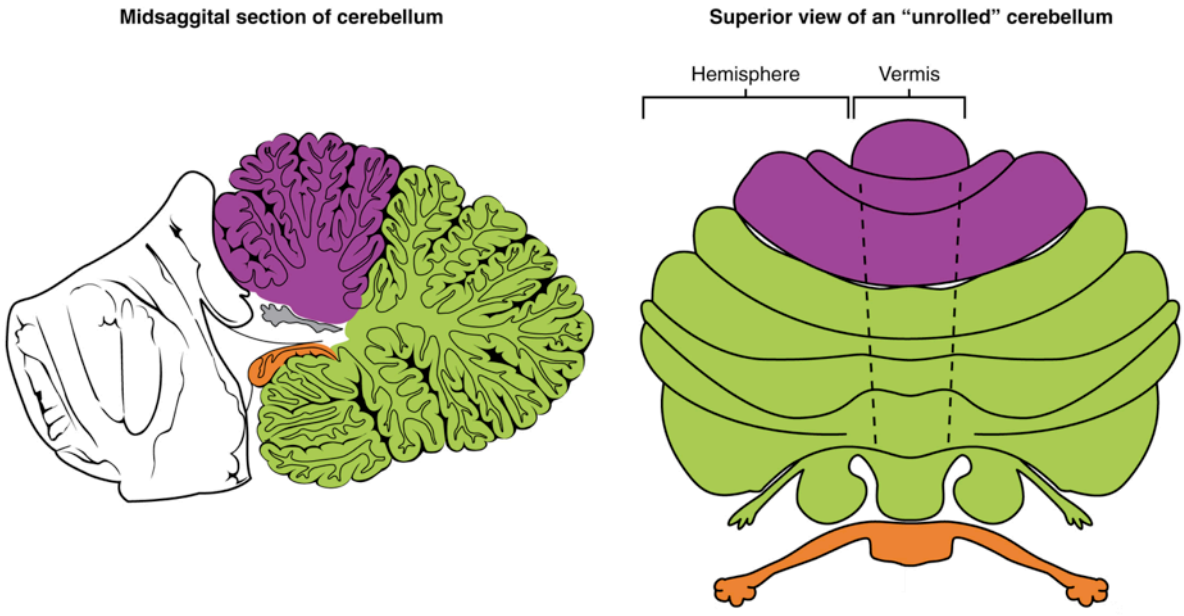

Figure 1. Regions of the human cerebellum. The anterior lobe is highlighted in purple, the posterior in green and the flocculonodular in orange. Image by Phil Schatz.

The cerebellar cortex has a relatively simple and regular organization and has its surface significantly increased by the high lobulation of the whole structure. Indeed, an un-rolled adult human cerebellum measures more than $1m^2$. One of the first accurate descriptions of the cerebellar cortex was given by Dr Santiago Ramón y Cajal (1852-1934), partially thanks to the advances in tissue staining by Dr Camillo Golgi (1843-1926)[3] (Figure 2a). Golgi developed a silver staining method that allows stochastic neuronal stain, where only a portion of all neurons is randomly labelled. This technique permits visualization of single neuron morphology by bypassing the excessive background that a whole tissue staining would generate. Ramón y Cajal used this technique to analyse, among others, the cerebellar Purkinje cells (PCs, discussed later on). Indeed, this work allowed Ramón y Cajal to postulate the neuron doctrine. This doctrine claims that the nervous system is composed of neurons, distinctive and individual elements, as opposed to Golgi's doctrine, where the nervous system was defined as a continuous tissue with a diffuse reticular network[4].

The cortex contains five main neuronal cell types, within three distinctive layers, including the GABAergic PCs, the only output of the cerebellar cortex. PCs form an intermediate monolayer from which they extend their tree-like dendrites to the upper part (molecular layer, ML). Those dendrites will receive most of the inputs from the other cell types present in the cerebellum and will integrate them. The PCs will then contact through their axons to the deep cerebellar nuclei (DCN) cells, located at the center of the cerebellum and that represent the actual output of the cerebellum towards other regions of the brain. The most numerous cell type of the cerebellum, and even the whole brain, is the glutamatergic granule cells (GCs). GCs form the lower layer of the cortex, the granule cell layer (GCL). The GCs extend their axons up until the external ML, where they bifurcate to form the excitatory parallel fibres (PFs) that will contact the PCs ramifications. The other three major cell types are all GABAergic and directly or indirectly modulate the PCs firing: basket, golgi and stellate cells[5] (Figure 2b). The cerebellar cortex receives also two different kinds of afferent neurons from outside the cerebellum, the climbing fibres and the mossy fibres. The climbing fibres arise from the inferior olive complex, located in the medulla, and directly contact with the PCs. Mossy

fibres arise from different places, such as the spinal cord and the vestibular nuclei, and will indirectly affect PCs firing by modulating the GCs' one. Each mossy fibre makes contact with 400-600 GCs (for review see[6]).

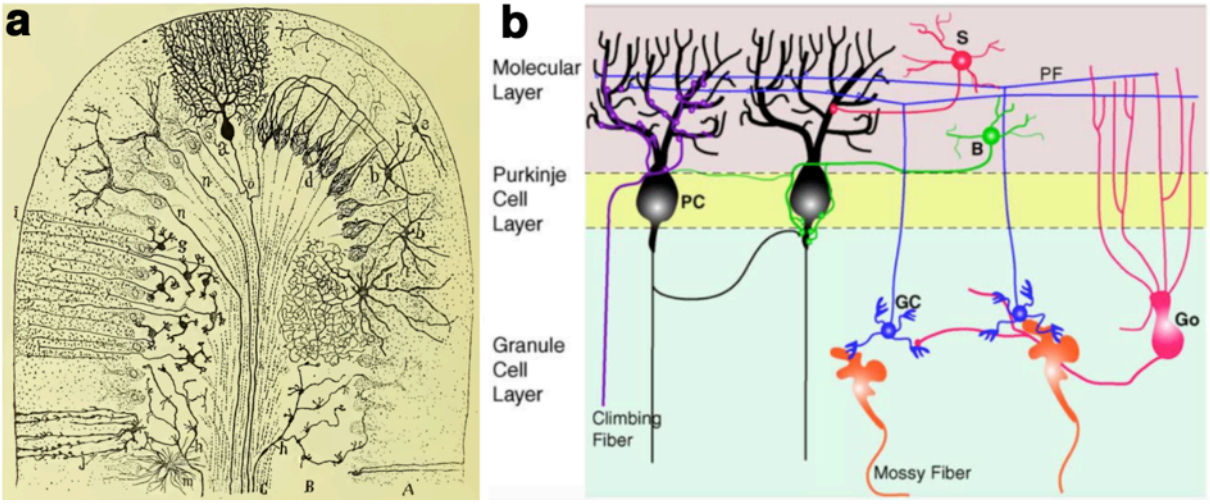

Figure 2. (a) Ramón y Cajal's drawing of the mammalian cerebellum and (b) current vision of the cerebellar cortex, from Chédotal et al, 2010. Abbreviations: Purkinje cell (PC), stellate cell (S), basket cell (B), parallel fibre (PF), granule cell (GC), Golgi cell (Go).

Different functional modules of the cerebellar cortex can be delimitated depending on the specific area in the DCN that the PCs contact. The DCN cells will spread their axons outside the cerebellum and will communicate with the rest of the brain through the cerebello-thalamo-cerebro-cortical circuits. Different DCN regions will be involved in specific circuits. The cerebello-thalamo-cerebro-cortical circuits connect the human cerebellum directly with different areas of the brain such as the thalamus, subcortical areas and the cerebral cortex itself, including cortical areas of a motor, sensory or associative nature[7]. Interestingly, this circuitry directly links the cerebellum to higher cognitive function-related areas.

1.2 Functions of the cerebellum

The cerebellum plays an important role in movement control and in cognitive processing. The first one has long been known whereas its involvement in higher cognitive function has emerged less than 30 years ago.

Dr Luigi Luciani (1840-1919) provided one of the first solid proofs of an involvement of the mammalian cerebellum in motor coordination. He performed a cerebellectomy to a dog and described three associated symptoms: asthenia (general weakness), atony (lost of strength in the muscles) and astasis (inability to stand)[8]. Nowadays the key role of the cerebellum in those functions has not only been confirmed but its importance for a broader range of motor-related functions has been described. One of the more widely reported motor-related functions of the cerebellum is gait or coordinated walking. Indeed, a gait disruption or ataxia is the more classic sign of cerebellar malfunction[9]. The cerebellum also plays an important role in oculomotor control. Inhibition by the PCs is necessary to reduce eye instability and to ensure a good fixation and calibration of the eyes movement. Another function is related to motor speech. To develop a rapid, coordinated and smooth bucco-labio-lingual movement, more than 80 muscles and 1,400 motor commands per second are needed, a process that partially relies on the cerebellum. Sir Gordon Holmes (1876-1965) described it for the first time in a paper about the cerebellar injuries' associated symptoms following gunshots during World War I: "*Speech is abnormal in most cases in which the lesions are recent and severe; it is usually slow, drawling and monotonous, but at the same time tends to be staccato and scanning*"[10]. Other important motor functions with a cerebellar involvement include timing, sensorimotor synchronization and grip forces (for review see[11]).

Besides its role in movement control, at the end of the 20th century several evidences pointed towards an involvement of the cerebellum in higher cognitive processing. The doctors Janet C. Sherman and Jeremy D. Schmahmann gave one of the first solid proofs when describing the behavioural abnormalities linked to a cerebellar defect and named it the cerebellar cognitive affective syndrome (CCAS)[12]. Their research started with a female patient, 23 years old, who just had gone through excision of a cerebellar ganglioglioma. The patient showed no consequent movement impairment. Nevertheless, they observed a behavioural change in the patient, towards a more childhood-like comportment. She was diagnosed as having altered executive function, spatial cognition and language processing. This observation led them to study this phenomenon in a larger cohort. Such cohort was composed of patients with isolated cerebellar injury, mostly strokes. The previous findings were confirmed, leading them to the description of the CCAS. The syndrome is characterized by disturbances in executive function, such

as working memory and verbal fluency, spatial cognition, altered behaviour and language difficulties. Importantly, these observations were done in adult patients, where the cerebellar development is complete and the renewal of neuronal connections is limited. It has been documented that, when a cerebellar defect arises during development, the brain plasticity can play a major role leading to a phenomena of functional compensation[13]. Therefore, congenital cerebellum disorders versus acute cerebellar defect (stroke, tumour resection, trauma…) can be more challenging to analyse in order to elucidate the physiological cerebellar function.

Recent work has divided functionally some regions of the cerebellum, depending on whether they are dedicated to motor-related tasks or cognitive ones. Stoodley and colleagues[14] studied a cohort of patients with isolated cerebellar stroke including patients with cerebellar motor symptoms only or CCAS. Anterior cerebellar disturbances were mostly associated with motor disturbance, while the posterior ones had a cognitive component (Figure 3).

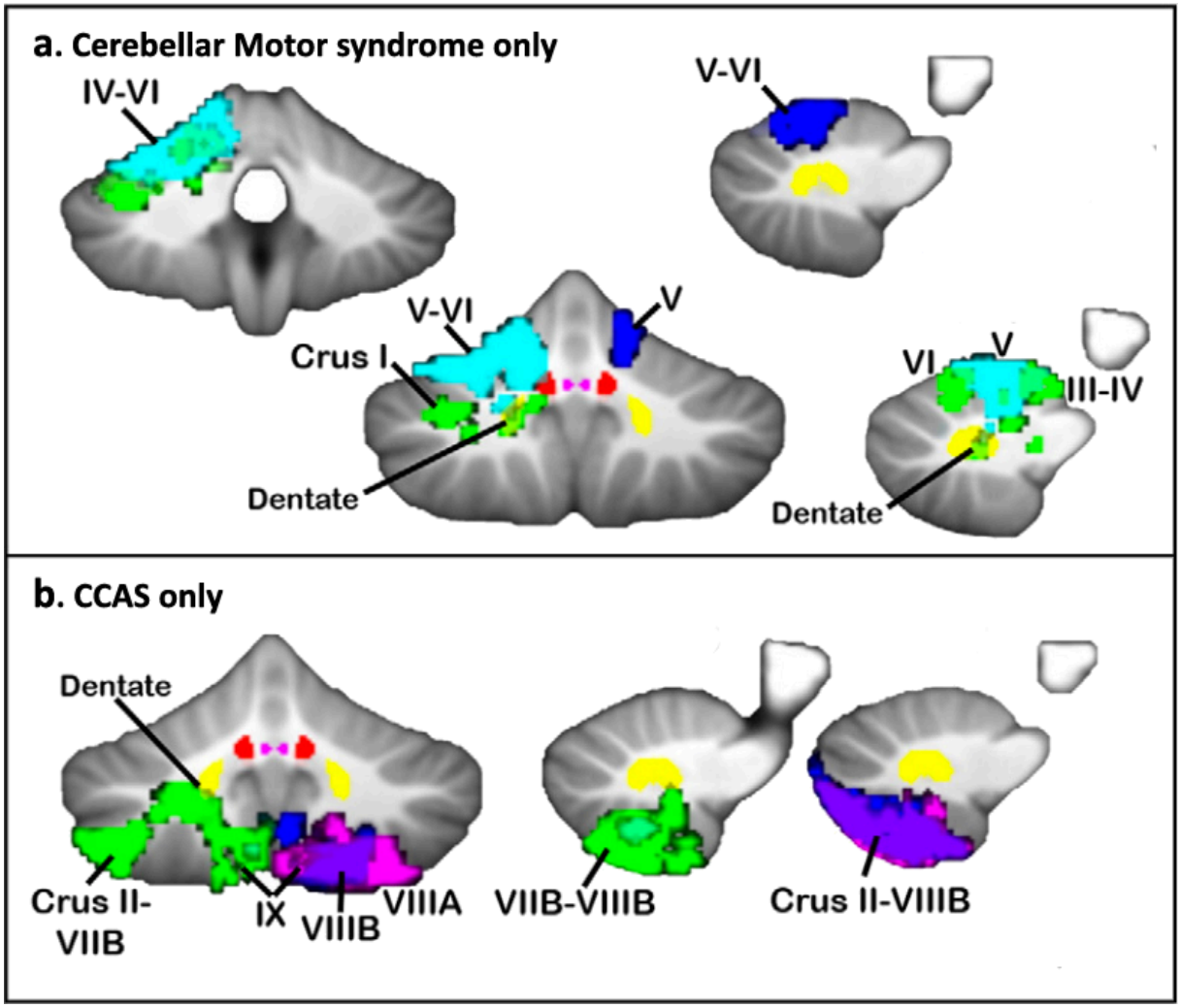

Figure 3. Map of the cerebellar lesions after stroke subdivided by clinical diagnosis. The names indicate the precise cerebellar regions affected by the cerebrovascular accident. Each colour represents a different patient. Simplified image from Stoodley at al, 2016.

All of those evidences lead to a division of the cerebellar functions into two main groups: motor-related and cognitive-related ones. Moreover, those functions can be delimitated to precise cerebellar regions, further proving that, even though the cerebellar cortex is relatively uniform, each module's connectivity will implicate a concrete function.

Even though the cerebellar role in human cognition is no longer questioned, many aspects about its precise contribution remain unknown[15]. In addition to that, the precise mechanisms that trigger the formation of functionally different cerebellar cortex modules, a process at the basis of the differential function, remain elusive. Understanding how the cerebellum develops and generates its complex connectivity can shed light on these questions.

1.3 Development of the cerebellum

The human cerebellum starts to develop during early stages, around embryonic day 32, and goes on until the second year of life, being one of the last structures to accomplish development[16–19]. Consistently, the cerebellum is one of the few places were neurogenesis if highly active after birth. It has been estimated that around 85% of the cerebellar GCs are generated during postnatal stages[20]. Interestingly, this trait seems to favour both, a high plasticity of the cerebellar tissue during early postnatal stages and a major sensitivity of the tissue to early postnatal stress[21,22].

The central nervous system (CNS) as a whole arises from the neural plate, an epithelial sheet developed from the dorsal embryonic ectoderm. The sheet will fold with itself giving rise to the neural tube, with marked anterior-posterior (AP) and dorsal-ventral (DV) axes. The anterior part of the neural tube will be further divided intro three different vesicles/regions that will generate the adult brain: the forebrain, the midbrain and the hindbrain (or rhombencephalon), from anterior to posterior. The posterior part of the neural tube will keep the cylindrical shape and give raise to the spinal cord. The hindbrain can be further subdivided into seven rhombomeres, being r0 the more anterior one (Figure 4a). Each rhombomere is defined at first by the expression of specific markers and later on by forming a distinguishable morphologic segment[23].

The boundary between the midbrain and the hindbrain is delimitated by molecular signals orchestrated by the isthmic organizer (r0), the earliest segmentation event of the developing CNS. The cerebellar vermis develops from the r0 and the r1 roof plate (the dorsal part), while the hemispheres arise from the alar r1, the area contiguous to the roof plate (Figure 4b). The homeobox genes of the engrailed family, *En1* and *En2*, are expressed early during development and are crucial for the development of the cerebellar neuroepithelium' boundaries. Lack of *En1* in mouse leads to almost complete absence of cerebellum and early-postnatal lethality[24]. The cerebellar identity acquisition also relies on the expression of certain genes by the r0, such as *Fgf8, Wnt1* and the homeobox gene *Gbx2*[25]. *Gbx2* is expressed at the posterior part of the r0 while the transcription factor *Otx2* is active in the anterior part. *Gbx2* delimitates the anterior hindbrain, the future cerebellum, and *Otx2* marks the future posterior midbrain. Indeed, it has been shown that ectopic expression of *Otx2* in the future anterior hindbrain (by

using a knock-in strategy into the *En1* promoter) will lead to an almost complete loss of the cerebellar vermis and enlarged midbrain structures[26].

Cerebellar neurons are generated in two major regions within the rhombomeres, the rhombic lip (RL) and the ventricular zone (VZ, Figure 4c). The rhombic lip is characterized by early expression of the *Atoh1* marker and gives rise to glutamatergic neurons, including the GCs. GABAergic cerebellar neurons, PCs and interneurons, are generated in the VZ and migrate radially towards a more dorsal location, beneath the future location of the GC progenitors. The GC progenitors exit the RL and position themselves above the GABAergic neurons, forming the external granule cell layer (EGL)[27].

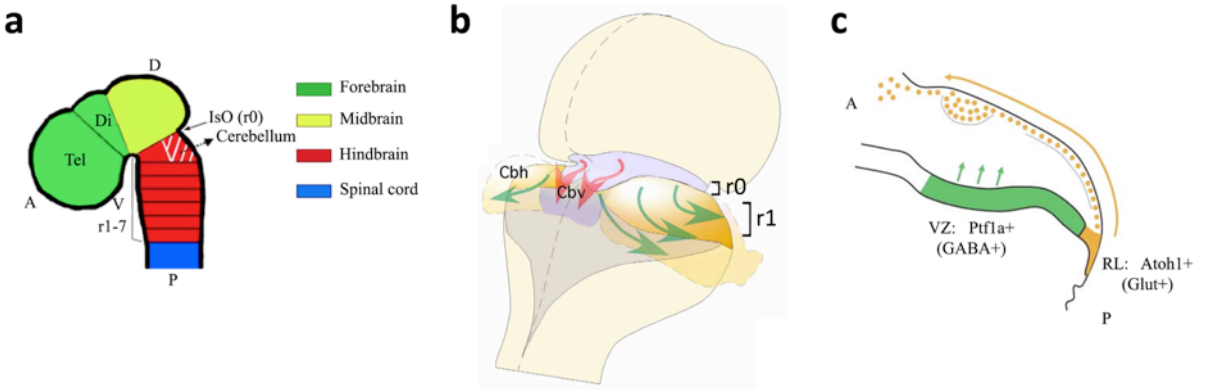

Figure 4. Early embryonic cerebellar development. (a) Modified images from Chizhikov et al, 2003, (b) Martinez et al, 2013 and (c) Aldinger et al, 2009. Tel = telencephalon; Di = diencephalon; Cbv = cerebellar vermis; Cbh = cerebellar hemispheres.

1.3.1 Migration, differentiation and proliferation of granule cells

GC progenitors go through two rounds of proliferation during their development before final maturation, the first round being at the RL itself and the second at the EGL. After proliferation, in the mouse, GCs precursors migrate towards the EGL around embryonic day 13 (E13). They acquire a unipolar morphology, with a leading growth cone, and migrate tangentially over the surface of the cerebellar primordium. The migratory process is mostly forward, with almost none medio-lateral dispersion of GCs precursors[28]. This fact goes in agreement with the early separation in the cerebellar primordium between the hemisphere cells that arise mostly from the lateral parts of the r0-r1, and the vermis, mostly medial. Several molecules have been characterized as playing a major role in the tangential migration of the GC precursors, including

attracting and repulsive guidance cues. For example, the upper meninges (a mesoderm derivative) secrete attractive cues, such as SDF-1[29]. At the same time, the RL will express Slit2, which through its receptor in GC precursors, Robo2, leads to a Ca^{2+} wave within the GC precursors that promotes the extension of the growth cone in the opposite direction to the signal source[30,31]. This repulsive signal contributes to the exit of the GC precursors from the RL to the EGL.

Once the neuronal precursors arrive to the EGL they lose the axonal projections used during migration and start differentiation towards mature neurons. Before differentiation, a second round of proliferation takes place at the EGL. Every single GC progenitor divides approximately every 20h, and can give up to 250 cells before stop dividing [32]. One of the signals that induce a high proliferative ratio of GCs comes from the underlying layer of PCs, the Purkinje cell layer (PCL). PCs will secrete sonic hedgehog (Shh) that will act as a strong mitogenic signal[33]. Little is known about how GCs stop diving and become post-mitotic. It has been proposed that Bmp2 could act as antagonist of the Shh signalling, supressing proliferation and leading to GCs maturation[34].

After becoming post-mitotic, the GCs will initiate their migration towards the inner part of the cerebellum, beneath the PCs and above the DCN, forming the inner granule cell layer (IGL, Figure 5c). The final migration of GCs takes place during post-natal stages in both human and mouse. Ramón y Cajal provided the first accurate description of this process (Figure 5a). As the image shows, when leaving the EGL, the GCs first extend parallel axons (the future PFs) in the ML and migrate tangentially. Once the PFs are extended, they initiate a radial migration process, going through the PCL, until the IGL, leaving behind a T-shaped fibre, the PF, key for its connectivity with PCs. All of these processes do not only rely on PC-GC communication, but also the GC-autonomous interactions act as a pacemaker to ensure correct synchrony[35,36].

After extension of the parallel fibres, the GCs will initiate radial migration until the IGL. Interestingly, isolated GC explants, extracted by the time that they are going through tangential migration, will spontaneously start a radial-like migration. These results suggest that the radial migration is part of an intrinsic GCs program that does not require signals from other cell types, such as the PCs or the glial cells of the cerebellum,

the Bergmann glia (BG)[37]. BG cells are located in the PCL and extend their processes trough the ML, until the external pial surface. These processes are used by the GCs to migrate inwards and are necessary for the them to reach their final position[38]. BG cells do not only act as a scaffold for migration but also express several factors that will induce GCs migration. It has been shown that BG cells-specific expression of Bicaudal-D2 is necessary for generation of a pertinent extra-cellular matrix environment for the GCs to migrate[39]. Other key factors are mostly involved in the generation of the glial processes *per se*. Alpha-dystroglycan expression from the BG is necessary for them to properly anchor their processes in the pial surface thus allowing migration initiation[40].

In summary, GCs development includes two rounds of cell proliferation (at the RL and at the EGL) and two different migration processes and a tight interaction with the other cerebellar cell types. Although many years of research have allowed a better understanding of this process, many aspects, such as how do GCs interact between themselves to synchronize their development and what kind of signals make them escape one phase to start the next one, remain unknown.

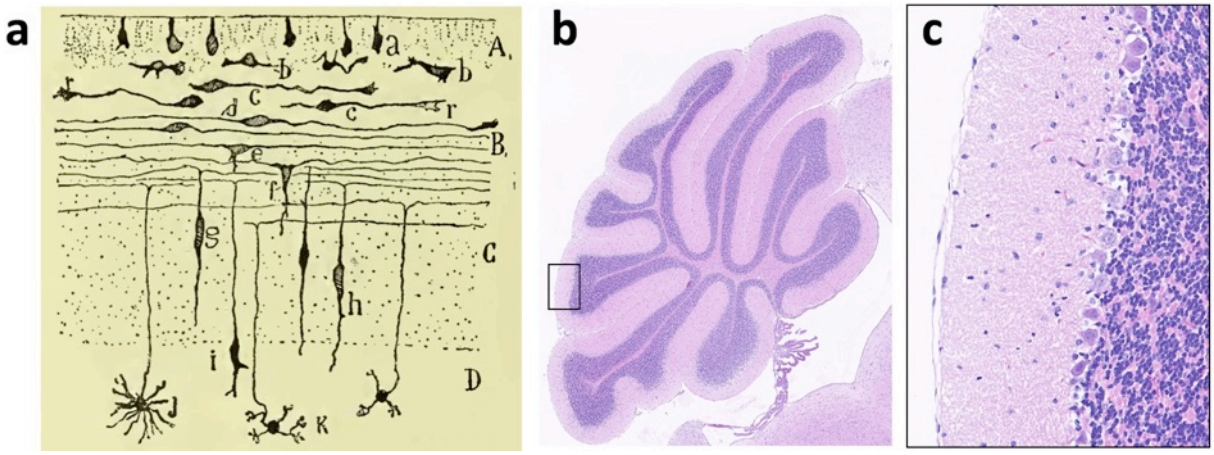

Figure 5. Ramón y Cajal drawing of GCs migration stages (a-k, A). P21 mid-sagittal cerebellum slice stained by hematoxylin-eosin (B). Detail of the three layers of the cerebellar cortex, note that by P21 all of the GCs are within the dense IGL, only the cerebellar interneurons remain in the ML (C).

In mouse, most of the GCs are located in the IGL by the third postnatal week. The ending of this process will mark the end of migration and cell differentiation in the cerebellum. After this, the cerebellum will keep on growing in size, but the organization will not further change (Figure 5b,c). One of the main triggers of the post-developmental cerebellar size increase is PCs myelination, important for action potential propagation[41,42].

Disruption of any of the steps necessaries to accomplish full cerebellar development may lead to a cerebellar malformation and consequent impairment of its function.

1.4 Cerebellar defects

Recent advances in brain neuroimaging have allowed a more precise classification of the different cerebellar defects arising in pediatric patients. These defects can be broadly subdivided into cerebellar hypoplasia (CBH, incomplete development with normal structure), atrophy (cellular degeneration) and dysgenesis (abnormal growth or development)[43]. These defects may affect specifically the cerebellum or be associated with other abnormalities, inside or outside the CNS, which can also contribute to the patient phenotype (Figure 6)[44]. In addition to cerebellar ataxia, intellectual disability (ID) is frequently associated with such defects, in agreement with the recognised roles of the cerebellum in cognitive processing[43].

The more precise epidemiological studies are based on the patients' ataxia as sign of cerebellar dysfunction. In children, ataxia has a prevalence of 26/100,000 births, most of them having a genetic component[45]. Dandy-Walker malformation (DWM) is one of the most prevalent forms of cerebellar defects associated with ataxia, with a prevalence of 1/3,000 to 1/30,000 depending on the cohort[46]. DWM-associated malformations include severe hypoplasia of the cerebellar vermis and an enlarged fourth ventricle, located beneath the cerebellum (Figure 6b)[47]. The cerebellar defects can be present alone or accompanied by other cerebral defects such as hydrocephaly.

A classical CBH does not imply an enlargement of the fourth ventricle. The hypoplasia can be generalised or more severe in the vermis/hemispheres. CBH usually leads to both, a cognitive and a motor impairment. As most of the cerebellar defects, it is commonly associated with other CNS malformations such as microcephaly and grey matter heterotopia, a defective migration and proliferation of neurons[46]. Mutations in the reelin (*RELN*) gene are one of the better-characterized causes of CBH associated with lissencephaly (Figure 6c)[48]. *RELN* codes for an extracellular protein with a crucial role during neuronal migration. Decrease or lack of Reelin, secreted by the cerebellar GCs,

will lead to defective migration of the PCs and other abnormalities in the cerebral cortex development, leading to aberrant neuron stratification[49].

PC death is at the basis of most forms of cerebellar atrophy, progressive conditions leading to cerebellar ataxia. It has been hypothesized that, due to the large PC length, starting from the dendritic trees at the ML until the contact with the DCNs through their axons, an altered energy supply (ex. mitochondrial dysfunction) will affect more severely the PCs than the rest of cerebellar populations (for review see [50]).

1.4.1 Genetic causes of cerebellar defects

Cerebellar defects may arise from an environmental factor such as an infection (cerebellitis) or mercury intoxication (Minamata disease) but most of them have a genetic component[51,52]. An accurate magnetic resonance imaging (MRI) together with a careful clinical evaluation is key to allow further genetic screening.

In a recent retrospective study of 300 patients with cerebellar ataxia Al-Maawali and collaborators diagnosed almost half of them (48%)[53]. In agreement with previous studies, they found a mitochondrial disorder as the most prevalent cause of cerebellar malformation within their cohort[43]. Other frequent diagnosis included neuronal ceroid lipofuscinoses (storage disorder), neuroaxonal dystrophy and congenital disorders of glycosylation (CDG) type I (Figure 6j, discussed in chapters 2 and 3).

Adequate genetic diagnosis is crucial for patients management, genetic counseling and potential treatment. Development of the next-generation sequencing (NGS) techniques, mostly whole-exome sequencing (WES), has allowed to accelerate the molecular diagnosis of the patients, overcoming the clinical heterogeneity of cerebellar malformations[54]. Recently, and in order to increase the speed of the genetic diagnosis, while diminishing its cost, specific gene panel approaches have also been developed.

1.4.1.1 Whole-exome sequencing (WES) and gene panel as a diagnostic tool

Before the NGS revolution in 2006-2009, the most widely used sequencing technique was the Sanger method. Through Sanger sequencing, a single genomic region is inquired at the time, making technically impossible whole sequencing of a patient by a single sequencing center. Actually, it was not until 2001 that a first, and incomplete, version of the human genome was published in a collaborative multicentre effort[55]. Prior to WES implantation, patients' genetic diagnosis was based on sequencing of known disease genes. Search for new genes was performed in consanguineous families using a combination of homozygosity mapping and Sanger sequencing of candidate genes. Homozygosity mapping is only useful when the affected individuals are likely to share the same identical-by-descendent allele in the homozygous state (recessive mutations). The regions in common between the affected individuals, and not present in the homozygous state in the healthy ones, would then be sequenced by Sanger sequencing[56]. Nevertheless, discovery of the disease-causing mutation was challenging for *de novo* mutations or in not inbreed populations.

WES allows sequencing of most of the exons (protein coding regions) of the human genome that, even though representing only 1% of the whole genome, are estimated to harbour around 85% of the disease-causing mutations[57]. Ever since the first report in 2009 using WES to decipher the genetic cause of a Mendelian disorder[58], the use of this technique has increased exponentially. This increase has been accompanied by an exponential decrease in its price[59]. In some scenarios, WES may even correct an inaccurate clinical diagnosis. Koenekoop and colleagues[60] reported a case of two patients primary diagnosed with Leber congenital amaurosis (LCA), an eye disorder, as carrying homozygous mutations in the *PEX1* gene. PEX1 is well known for playing a role in peroxisomes biogenesis. Such finding allowed to re-evaluate the clinical diagnosis and confirmed those patients as suffering of a peroxisome biogenesis disorder (PBD) that was secondarily leading to a visual impairment.

On the other hand, WES requires an important amount of work after the sequences are obtained. Such sequences need to be first aligned to the reference human genome and the single-nucleotide variants (SNVs) present in the patient need to be filtered. Filtering of the SNVs comprises, to analyse their prevalence in the general population and which

are their predicted consequences (for a more detailed description, see materials and methods). In addition to that, some exons might be poorly covered (low number of reads), complicating any interpretation, and insertions or deletions (indels) larger than 5 base pairs cannot be accurately recognised. Owing to this, and to the fact that it does not cover the non-coding regions, WES may not be a universal solution for patients' genetic diagnosis. To solve the coverage defect, whole-genome sequencing (WGS) may be used, even though the interpretation of variants in non-coding regions can be extremely challenging. Regarding the time consuming and relatively low coverage of some exons associated to WES, a more targeted approach has been developed: the gene panels.

Gene panels or targeted gene screening consist in a similar NGS technology as WES but instead of sequencing the entire exome, only genes associated with a certain pathology/malformation are captured and sequenced. Targeted sequencing leads to an increase in the coverage of the targeted genes of around 4-fold[61]. The increased number of reads leads to more reliable results and to a higher probability to detect small deletions or duplications and potential mosaicism. In 2015 Ortiz Brüchle and colleagues[62] published their results when using a gene panel approach for Joubert syndrome (JS), a ciliopathy that leads to a specific and unique cerebellar malformation (Figure 6k). Out of 35 patients, a genetic diagnosis was achieved for the 62%, proving the efficiency of the technique for a fast and precise genetic diagnosis. Nevertheless, WES allows the discovery of new causative mutations in new genes, something impossible by gene panel.

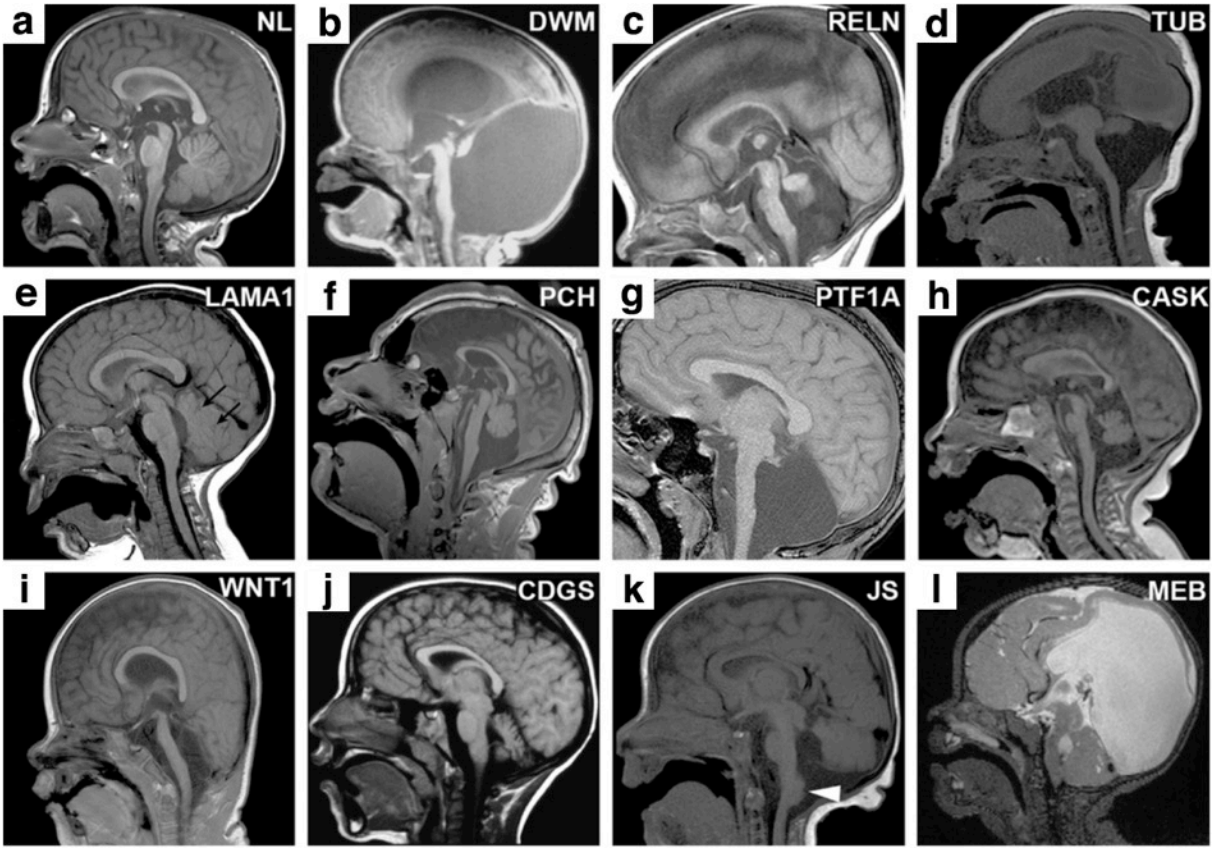

Figure 6. MRI images of cerebellar defects with known genetic etiology. (A) Control. (B) Dandy-Walker malformation. Note the huge enlargement of the 4th ventricle, beneath the cerebellum. (C) Patient with homozygous deleterious mutations in the *RELN* gene with CBH and a severe lissencephaly. (D) CBH in a patient with mutation in the *TUBA1A* gene, coding for an isoform of tubulin. (E) Mild CBH by *LAMA1* mutations. (F) Pontocerebellar hypoplasia (PCH), a combination of hypoplasia in both the cerebellum and the pons. (G) Mutations in the *PTF1A* gene lead, at least in mouse, to a defect of specification of the cerebellar VZ progenitors' identity, which die or do not properly migrate. In humans, it can lead to a complete absence of the cerebellum. (H) *CASK* mutations also lead to PCH. (I) Dysgenesis or agenesis of the cerebellum and the midbrain associated with a hypoplasia of the pons in a patient carrying *WNT1* homozygous mutations. (J) Patient carrying homozygous mutations in the *PMM2* gene, what leads to a defect in protein N-glycosylation/CDG type I. (K) JS patient. (L) CBH, abnormal tectum and hydrocephaly in a patient suffering of muscle-eye-brain disease (MEB) due to *POMGNT1* mutations. Image from Aldinger et al, 2016.

1.4.1.2 Diagnosis of cerebellar defects at the Necker hospital

Within the Necker hospital, a new paradigm for patients genetic diagnosis has been settled based on these two novel technologies. Gene panels have been generated for a variety of syndromes such as ID, inflammatory diseases, renal abnormalities and cerebellar atrophy[63,64]. The cerebellar atrophy panel contains 72 genes in which mutations have been previously proven to drive such malformation or CBH, since both phenotypes can overlap. Patients with cerebellar defects (proved by MRI and following physicians' advice) are examined by targeted gene screening. In a recent report[65], a

likely diagnosis was identified for 28% of the families (out of 25), which included heterozygous indels undetectable by WES. Families without genetic diagnosis by gene panel are then sequenced by WES. WES allowed further identification of 6 new variants likely causative of the defect (further details are discussed in the results section).

This study shows the pertinence of gene panel as a first choice for genetic screening, for fast and reliable results, followed by WES in the unresolved cases. However, these techniques do not cover most of the non-coding regions, thus masking the potential implication in the disease etiology of a variant within that region. It is likely that in the next years, with the improvement in WGS technologies, WES will be replaced by WGS, even though the interpretation of non-coding variants is still challenging[66].

In most of the cases, the identification of a likely pathogenic variant is not enough for correct patient management. Generation of an *in vivo/in vitro* model of a certain gene variant is first necessary for variant pathogenicity validation itself. The same models can be further used to understand the physiopathological mechanisms underlying the phenotype and as a last goal, for therapy testing. In the case of cerebellar defects, mouse models are a precious tool, due to the resemblance between mouse and human cerebellar development and cytoarchitecture. Nevertheless, to extrapolate the results to human pathology, an intermediate step of validation in a pertinent human cell model is necessary. This step is even more challenging when referring to brain-related disorders due to the impossibility to obtain human samples. In this aspect, development of human-induced pluripotent stem cells (hiPSCs) that can be further differentiated into human progenitor neurons, together with the implementation of accurate genome editing techniques, has open a whole new path of possibilities to model human brain diseases "in a dish".

1.5 *In vitro* human models of brain defects - hiPSCs

The main step to generate hiPSCs from differentiated cells, such as human fibroblasts, is the re-induction of pluripotency in order to restore their capacity to give rise to all of the cells that form the human body. Many years of research were required to demonstrate the capacity of the cells to be re-converted, and even more challenging, to learn how to

do it *in vitro*. The Nobel laureate, Dr John B. Gurdon, gave the first solid evidence in the 60s. He injected the nucleus of a differentiated epithelial cell into a *Xenopus laevis* egg, whose nucleus had previously been destroyed by UV light. These eggs survived and developed into tadpoles[67]. These experiments showed that during cell differentiation, the genetic material remained unchanged, broadly speaking, and that epigenetic events could most likely trigger the cells final fate acquisition. The next challenge was to re-induce cells pluripotency *in vitro*. *In vivo*, cell fate determination is orchestrated by transcription factors that drive a change in the transcriptional program of the cell, leading to the cells final identity acquisition. In agreement with this, it has been widely shown that ectopic expression of transcription factors will alter cell differentiation and may lead to a change in cell fate. In 2010 Dr. Marius Werning's lab infected mouse fibroblasts with lentiviruses containing various combinations of 19 neural tissue-specific transcriptional factors. They proved that three of them (*Ascl1*, *Brn2* and *Myt1l*) were sufficient to induce mesoderm-derived cells' (fibroblasts) conversion into ectoderm-derived cells (induced neuronal cells)[68]. Nevertheless, these induced neurons, in comparison to hiPSCs, are postmitotic neurons, do not proliferate and cannot model the development of the nervous system since a number of neurodevelopmental stages are skipped.

Diverse protocols are used to generate hiPSCs out of a wide range of human cell types, mostly by viral transfection of the so-called Yamanaka factors (*Oct4*, *Sox2*, *Klf4* and *c-Myc*) to induce cell pluripotency[69,70]. Early protocols included integration of the viral genome into the host chromosome, leading to a broad spectrum of associated consequences, such as insertional mutagenesis, residual expression of the reprogramming factors and immunogenicity. Those consequences would eliminate any potential therapeutic hope for hiPSCs. To overcome this issue, nowadays most of the hiPSCs are generated through Sendai virus vectors that do not integrate in the genome and whose presence diminishes by serial passaging of the cells, therefore eliminating any trace of the virus[71,72]. The resulting hiPSCs have been shown to mimic the expression and epigenetic profiles of human embryonic stem cells (hESCs), proving its research utility[73]. An important aspect to take into account when referring to the potential of the hiPSCs for cell transplantation is the associated genomic abnormalities that may occur during its derivation and culturing. The differentiation process can be

mutagenic and induce *de novo* events in the cells. The same events may also occur during serial passaging, which could potentially lead to some spontaneous single-cell variations increasing cell proliferation that could overcome the whole population[74]. To this concern, for tissues outside the nervous system, such as the liver, some authors defend the use of hESCs from the patient himself combined with genome editing technologies as a source for transplantation[75].

1.5.1 Induction of hiPSCs-derived neuronal cells

Pluripotent cells cultured *in vitro* spontaneously differentiate into neuronal cells in absence of growth factors in the media[76]. As a consequence, neural induction is based in the inhibition of other possible derivations of the cells rather than in the enhancement of a specific pathway. Indeed, most widely used protocols include inhibition of BMP and TGF-β pathways, which may lead to other cell lineages or maintain the stem cell state, by dual SMAD inhibition (Figure 7)[77]. This protocol will generate neural pluripotent cells (NPCs) that will retain the self-renewal capacity and can be further derived into specific mature neuronal cell types (for review see [78]). High hiPSCs concentration during dual SMAD inhibition will lead to anterior CNS-like neurons, also called late cortical progenitors – LCPs – or cortical neuronal precursors. Lower concentration of cells will generate neural crest-like progenitor cells, suitable for generation of the peripheral nervous system-like cells.

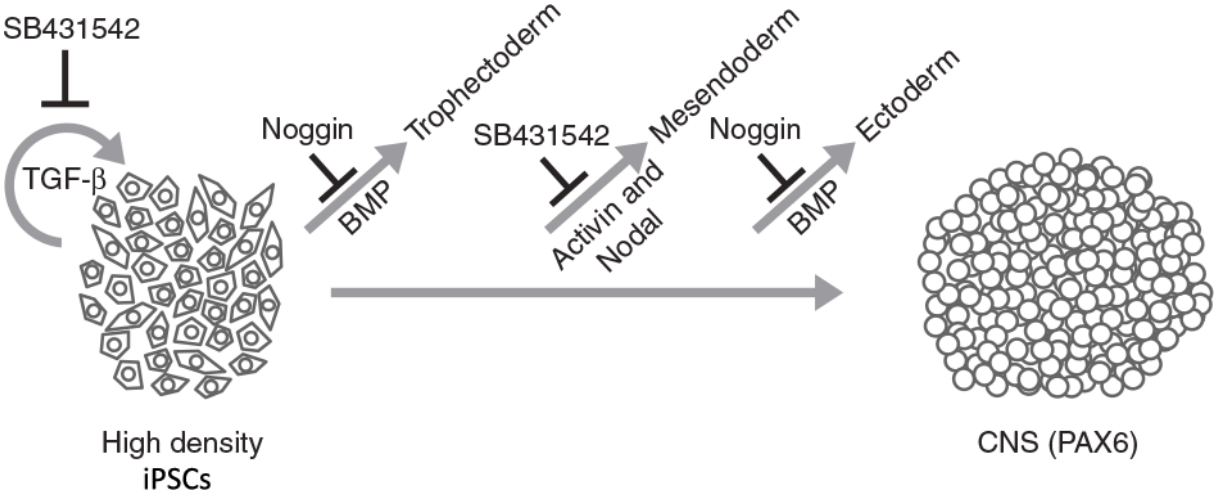

Figure 7. Double SMAD inhibition of hiPSCs induces differentiation into NPCs. Two different SMAD inhibitors, Noggin and SB431542 are used to block self-renewal of the cells and derivation into other cell fates than the neuronal one. Simplified image from Chambers et al, 2009.

The utility of patient-derived NPCs or LCPs for investigating disease physiopathology and drug screening has been widely reported. In 2011 Brüstle and colleagues[79] used such protocol to generate neuronal and glial cells from patients fibroblasts with spinocerebellar ataxia 3 (SCA3) due to pathogenic CAG expansions in the *MJD1* gene. They recapitulated the toxic protein aggregation found in human brains only in the neuronal cells, and not in the glial, hiPSCs or fibroblasts, what could explain the human brain-specific phenotype. Moreover, they show that the aggregates formation depends on the Ca^{2+}-dependent activation of calpain, since they were able to rescue the phenotype by calpain inhibitors. Interestingly, NPCs can also be used to study multigenic neurological diseases such as Parkinson's disease or Alzheimer's disease, even when the genetic cause remains unknown[80].

Two different kinds of cells source can be used as a starting material to generate hiPSCs-derived NPCs. On one hand, patient cells (blood cells, fibroblasts) can be used and compared to control donor cells. Another possible approach is to perform mutagenesis for the gene of interest by genome editing and compare the obtained cell line with its isogenic control. The last one will remove the genetic background bias found in patient/control cells and will allow the use of the same iPSCs line to model different diseases/mutations without having to come back to fibroblasts' transformation.

1.5.2 Gene editing by CRISPR/Cas9: origins and applications

Different genome editing technologies have arisen in the past two decades, such as TALENs (transcription activator-like effector nucleases), zinc-finger nucleases and CRISPR-Cas9 (clustered regularly interspaced short palindromic repeats-CRISPR-associated protein 9). CRISPR/Cas9 is the more widely used genomic editing technique nowadays (almost 10-fold more papers found in PubMed – 2016 - when searching for "CRISPR Cas9" compared to the other two methodologies) probably due to its versatility and low cost[81,82].

The CRISPR-Cas system was first described by Dr Francisco Mojica in bacteria and archaea as part of the adaptive immune system to protect against foreign nucleic acids (viruses and plasmids)[83,84]. This system consists of the insertion of foreign DNA into the bacterial genome (in the CRISPR locus) for its future expression. The expressed non-

coding RNA will attach to the DNA/RNA from the pathogen. After binding, Cas proteins will recognise the resulting complex and will splice the foreign genomic material leading to immunity against the invader[85]. This system has been replicated *in vitro* to accomplish accurate gene edition. Out of the many different CRIPR/Cas systems, which mostly differ in the Cas endonuclease properties, the most frequently used is the CRISPR/Cas9.

Currently used CRIPSR/Cas9 system consists basically of the Cas9 protein-coding sequence and a single-guide RNA (sgRNA), which includes the targeting RNA sequence and an auxiliary trans-activating RNA that facilitates processing. The major limiting step when designing the sgRNA is that the target DNA sequence needs to be next to a PAM (protospacer adjacent motif, 5'-NGG) sequence so Cas9 can slice. All of the three components can be assembled into the plasmid with which the cells will be transfected. Once transfected, the expressed sgRNA will bind to the target DNA sequence and the Cas9 protein will provoke a double strand break (DSB). DSBs lead to the activation of one of the two major pathways for DNA damage repair: non-homologous end joining (NHEJ) or homology directed repair (HDR), being the first one the most frequent. NHEJ can take place at any cell-cycle phase and is template-independent, what leads to a fast but imprecise DSBs repair. This mechanism will tend to lead to indels in the sgRNA-targeted region that will likely drive the apparition of an early stop codon, knocking-out the gene (Figure 8)[86].

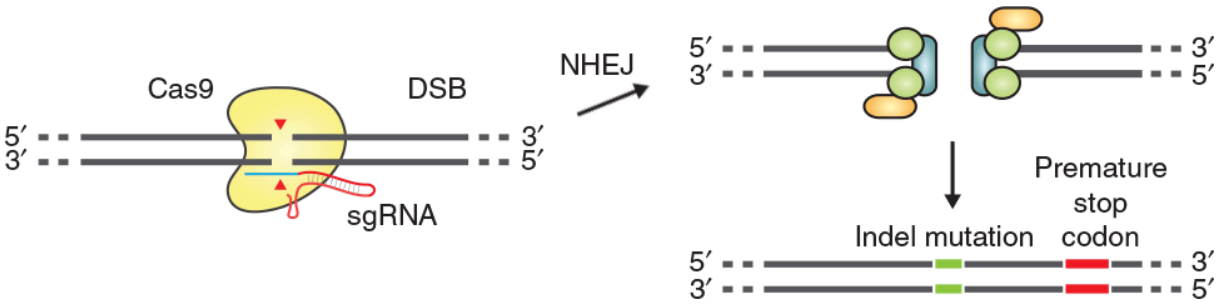

Figure 8. CRISPR/Cas9 plasmid mode of action. Modified image from Ran et al, 2013.

The major concern when using CRISPR/Cas9 is sgRNA design, to avoid any off-target binding[87]. This issue can be partially solved by careful design of the sgRNA using different software such as Crispor (http://crispor.tefor.net/) that calculates the off-target probabilities of a given sgRNA.

Many technique variations have been developed further beyond simple gene knockout (KO). For example, specific base substitutions (to study non-synonymous mutations), generation of in-frame proteins and correction of gene mutations can be achieved by CRISPR/Cas9-mediated DSB followed by DNA template-mediated HDR[88].

In conclusion, recent advances in genetic engineering (CRISPR/Cas9) and *in vitro* re-induction of cells pluripotency, together with differentiation into NPCs, have provided an extremely powerful tool to study neurodevelopmental and any brain-related disorder. They cannot only be used to gain insights into the disease physiopathology but also provide a unique model for drug testing.

2 PROTEIN N-GLYCOSYLATION

2.1 The N-glycosylation pathway

Protein N-glycosylation takes place in all three domains of life (archaeans, bacteria and eukaryotes) and consists in the attachment of sugar chains (oligosaccharides/glycans) to asparagine residues of the nascent proteins. More precisely, glycan attachment takes place mostly in N-X-S/T amino acid sequences – the canonical N-glycosylation sequence or sequon – where X can be any amino acid but proline. Some other sequons have been described such as NXC, but they represent only a small percentage of all N-glycosylation sites[89]. The glycan is attached predominantly while the proteins are being synthesized in the lumen of the endoplasmic reticulum (ER) and plays important roles in protein folding, assembly, trafficking and function. N-glycosylation is one of the most common protein post-translational modifications with a high incidence in secreted and membrane-anchored proteins[90,91]. According to some studies, up to 90% of the post-translationally modified proteins are indeed N-glycoproteins[92].

Some N-glycosylation sites are not always glycosylated (glycosylation macro heterogeneity) and the final glycan chain composition can differ between sequons/cell type/tissue/time[93]. These aspects add a new layer of complexity to the DNA-RNA-protein paradigm, where protein function can be further modulated by its N-glycan charge[94].

2.1.1 Early steps of protein N-glycosylation: synthesis of the lipid-linked oligosaccharide (LLO) and glycan transfer

The first step for N-glycosylation consists in the synthesis of a glycan chain that will be afterwards transferred to nascent proteins (Figure 9). The oligosaccharide is built on top of a polyisoprenoid lipid-carrier called dolichol (Dol), which together with the glycan chain form the lipid-linked oligosaccharide (LLO), the core unit for protein N-glycosylation. The core glycan is composed of three different types of sugars, N-acetylglucosamine (GlcNAc), mannose (Man) and glucose (Glc). Those sugars need to be previously converted into nucleotide-activated sugar when used in the cytoplasmic side or attached to another Dol molecule when used in the ER lumen (ex. GDP-Man in the cytoplasm, Dol-P-Man in the lumen). Since Dol is not only used as the anchor of the final glycan chain but also as a carrier of single monosaccharide units, to form a complete LLO, 8 Dol molecules are needed. Interestingly, the Dol-P-monosaccharide structures are not used in the ER lumen not because of a lack of the nucleotide-activated forms (they are indeed transported into the ER for a variety of processes) but it is rather hypothesized that it is reflective of the pathway origin in prokaryotes[95]. The transfer of the monosaccharides to Dol is triggered by several glycosyltransferases, starting with two GlcNAc and five Man units in the cytoplasm (nucleotide-activated form). The Dol-PP-($GlcNAc_2Man_5$) form will be afterwards translocated/flipped into the luminal face of the ER. Once in the ER, four Man and three Glc from Dol-P-Man and Dol-P-Glc will be added, generating the full LLO: Dol-PP-($GlcNAc_2Man_9Glc_3$)[96].

After, the oligosaccharyltransferase (OST) complex will transfer the glycan from the Dol carrier to the nascent protein. In mammals there are two different OST subunits (STT3A and STT3B) that will define two partially complementary OST protein complexes. Both complexes can transfer the glycan chain while the protein is still being synthesized by the ribosome (co-translational modification), the most common way of transfer, with a predominant role of STT3A. STT3B will mostly transfer the glycans to sequons that have been skipped by the STT3A complex, to ensure adequate protein N-glycosylation. In addition to that, STT3B can also transfer the glycans from the LLO post-translationally, once the full protein is located in the ER[97].

Once the glycan is transferred to the amide nitrogen (N, N-linked glycan) of the asparagine residues, it can still be further processed/modified both, in the ER and in the Golgi, leading to the wide range of different N-linked glycan chains present in eukaryotes.

2.1.2 Glycan processing in the ER and the Golgi apparatus

Right after the N-glycan is assembled on the protein, the top glucose will be removed by the enzyme glucosidase I, releasing the glycan from the OST complex. After, and consistent with the role of N-linked glycans in protein folding and stability, carbohydrate-binding/lectin chaperones (e.g. calnexin and calreticulin) will attach to the glycan while further oligosaccharide processing by glucosidase II takes place and the overall protein tertiary structure is achieved[98].

Once the Glc residues, and potentially one extra Man, are removed, the protein will leave the ER to enter the Golgi compartment. Once there, the glycan can be further processed in many possible ways, leading to the high diversity of glycan structures present in mammalian cells[99]. During its pass through the Golgi cisterns, the glycans can be further completed with different sugar residues such as fucose, galactose and sialic acid, leading to the three main kinds of N-linked glycan structures: high mannose (no extra residues are added), hybrid (only one of the two branches of the glycan is modified) or complex (both branches are modified)[100]. The type of N-glycan chain attached to the protein will change its intrinsic properties and potential interactions, thus playing an important role in protein function.

Disruption of any step of the N-glycosylation pathway in humans can lead to aberrant protein N-glycosylation, also called congenital disorders of glycosylation (CDG).

2.2 CDG: Classification and genetic etiology

CDG include different inborn metabolic disorders with aberrant glycan processing. In addition to N-linked glycosylation some other forms of glycosylation, such as protein O-glycosylation and glycosylphosphatidylinositol (GPI) anchored proteins synthesis, may also lead, when impaired, to CDG. CDG are rare multisystemic disorders with more than 2,500 patients diagnosed worldwide[101]. The discovery of CDG-associated mutations has experimented a significant amelioration with the implementation of NGS methodologies. Whereas before 2006 less than 50 genes had been associated with these disorders, more than 125 different genes are known nowadays (Dr. Hudson Freeze' webpage). Most CDG are caused by autosomal recessive mutations with some cases of X-linked inheritance[102]. In North America, it has been estimated that 20-26% of the population is carrier of a CDG-causing allele in the heterozygous state[103].

Regarding the defects in N-glycan processing, the most prevalent ones, they can be further subdivided into CDG type I, arising from defective oligosaccharide synthesis and/or transfer (Figure 9), or CDG type II, defects in N-glycan processing, once attached to the protein. In a recent report on 1450 clinically confirmed CDG patients, genetic diagnosis was achieved for 1350, an extremely high diagnosis rate when compared to other disorders. Out of the 1350 diagnosed CDG patients, 94% of them where diagnosed as type I, partially due to the high prevalence of PMM2-CDG, present in 62% of the patients[101]. PMM2-CDG is a CDG-Type I caused by mutations in the phosphomannosemutase-2 gene, involved in mannose activation prior its use in the LLO synthesis, and some reports estimate its prevalence in 1/20,000[103].

The primary consequence of defective synthesis and/or transfer of the glycan will be a stochastic loss of N-glycan chains in the nascent proteins (hypoglycosylation, CDG type I). When the defects concern the cropping and modification of the oligosaccharide, the proteins will not miss full chains but will contain incomplete N-linked glycans (CDG type II).

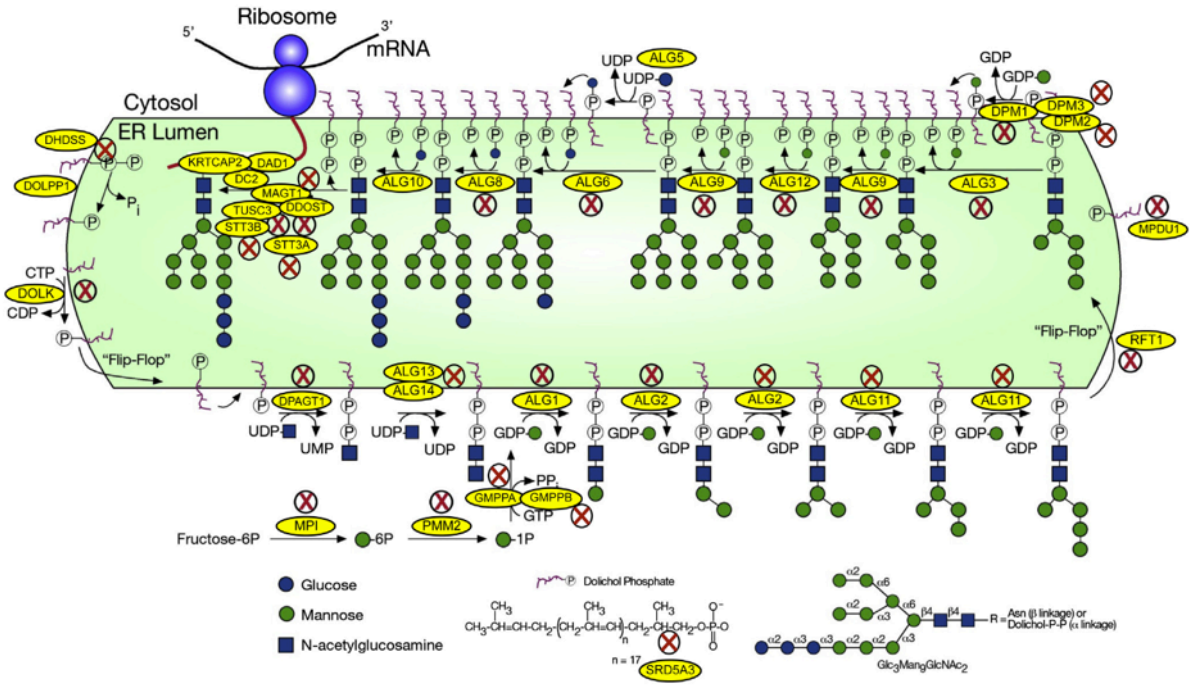

Figure 9. Early steps of the N-glycosylation pathway and known CDG type I-associated genes. When mutations in an enzyme-coding gene have been found as a cause of CDG, a cross is added on top. Image from Freeze et al, 2014.

2.2.1 Diagnosis of a CDG

CDG clinical diagnosis is based on the consequent aberrant glycan structures present in the patient proteins. The most widely used test in case of suspicious CDG is transferrin isoelectric focusing (TIEF), a technique developed by Dr Jaeken in 1984[104]. Transferrin is a plasma N-glycoprotein that contains two N-glycan chains and up till five branches ending in a sialic acid molecule. The sialic acids of the transferrin will add extra negative charges to the protein and its migration towards an electric field can shed light on the precise number of sialic acid molecules that the protein contains. This information is directly related not only to the number of sialic acid units itself but to the number of N-glycan chains that the protein has, allowing to discern between a type I and a type II CDG (Figure 10)[105,106].

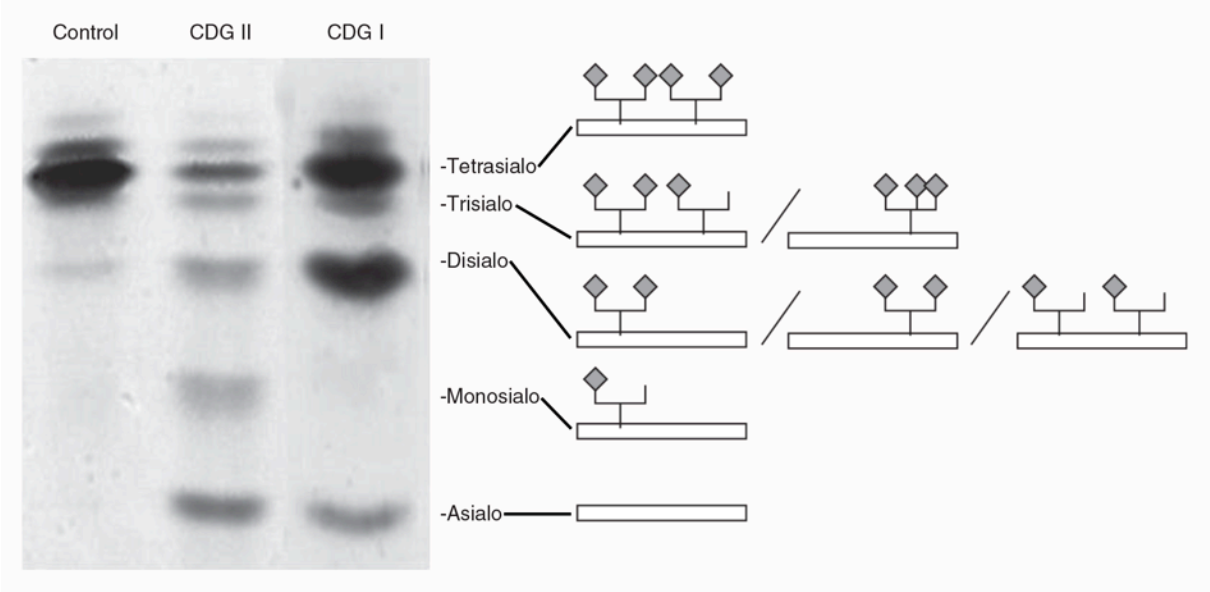

Figure 10. Examples of TIEF in control, CDG type I and type II patient samples. Each band represents a different isoform or glycoform of transferrin. In type I, there is a higher frequency of the disialo (only one N-glycan) and asialo (no N-glycan) form of the protein. Defects in the N-glycan processing (type II) lead, among others, to the appearance of the monosialo glycoform and a decrease in the physiological tetrasialo form. Images from Supraha-Goreta et al, 2011 and Denecke et al, 2009.

Nevertheless, TIEF may not always be accurate enough. It is known that the glycosylation profile in humans changes with age and a defect may not be detectable at all ages and neither not in all tissues/cells[107,108]. Consistent with this fact, current research strategy to diagnosis a suspicious CDG case does not only rely on TIEF. When there is a negative TIEF result but the symptomatology resembles to other CDG cases, NGS technologies (WES, WGS or gene panel) are applied before ruling-out CDG as the cause[101].

2.2.2 Clinical spectrum of CDG type I

CDG are multisystemic disorders, but display a specific associated-symptomatology that helps to the clinical diagnosis. They can appear at any age, but most cases arise during early infancy. Clinical features include skin abnormalities, liver dysfunction, bone and heart defects, endocrine de-regulations, coagulation abnormalities, ocular problems and neurological defects[109]. The overlap of several different defects such as abnormal fat distribution, liver cirrhosis and thrombosis is highly frequent in CDG type I, leading to the clinical suspicion[110].

Defective immunological system is also frequently observed: defects in coagulation, aberrant number of B an T cells, altered amounts of interleukins in blood, leucocytosis…[111] Indeed, the most frequent cause of death in CDG type I patients within the first year of life is the recurrent infections[112]. It has been hypothesized that this is caused by a lack of adequate immune system response after vaccination together with poor clearance mechanisms and the aberrant skin integrity.

2.2.2.1 Neurological abnormalities in CDG type I

Neurological impairment is the most common trait in CDG. Neurological presentations have even been found as the only clinical trait in some patients carrying homozygous mutations in the *DOLK* gene (DOLK-CDG), necessary for Dol biosynthesis, in PMM2-CDG and in TUSC3-CDG, which arises from defective OST function, among others[113–115]. Most of CDG patients present ID and psychomotor retardation. CBH and/or atrophy are also frequently observed, together with ataxia, abnormal eye movements, microcephaly, epilepsy and stroke episodes[116,117]. Indeed, in a recent report, out of 60 patients with major global cerebellar atrophy, 21 were diagnosed as PMM2-CDG[43].

Cerebellar defects are more frequent in CDG than any other brain malformation[118,119]. These defects are at the basis of the patients' ataxia and are likely to play a major role in patients ID (chapter 1). A recent medical report sustains that the cerebellar dysfunction is indeed "the main daily functional limitation" in CDG patients[120]. CBH is commonly detected in PMM2-CDG. Indeed, patients' cerebellum is usually small in newborns[119]. In contrast, when present, the cerebellar atrophy is progressive: it might not be easily detectable during the first months of life, but it becomes more obvious with aging[121,122]. There is only one clinicopathological study performed on a post-mortem PMM2-CDG brain. Histological evaluation showed a loss of both, PCs and GCs, and aberrant PCs arborization, consistent with a cerebellar atrophy[123]. Interestingly, a recent study in PMM2-CDG patients showed that through the course of live, even if there is a progressive reduction in the cerebellum size, the cerebellar-associated deficits actually stabilize or even improve[124]. As mentioned in the first chapter of the introduction, the large time developmental window of the cerebellum opens the possibility of high postnatal plasticity that could partially explain this finding.

All of these evidences point towards a major involvement of protein N-glycan charge during brain development and function, especially in the cerebellum. Nevertheless, little is know about how N-glycoproteins modulate central nervous system (CNS) development and how a defect in those can lead to the neurological findings in CDG type I.

2.3 Biological functions of protein N-glycosylation

2.3.1 N-glycosylation and protein folding

The primary and most widely studied role of protein glycosylation is to help the protein to achieve its native conformation both, while being synthetized and once it is released in the ER lumen. Addition of the glycan chain will increase protein stability, and together with the luminal chaperones, will induce correct protein folding[125]. As mention in chapter 2.1.2, the lectin-like chaperones calnexin and calreticulin will recognise the glycan chain after removal of two of the three terminal glucose residues. The chaperones will interact with the protein as long as the last glucose residue is not removed, providing a window of time to achieve correct protein folding. If the protein is yet not folded after chaperone release, the UDP-glucose glycoprotein:glucosyltransferase (UGGT) enzyme will add once again a glucose residue to the glycan chain, promoting a new chaperone interaction and further protein folding. If this situation persists, the ER-associated degradation (ERAD) pathway will be activated to induce protein degradation[126].

2.3.2 ER-associated degradation (ERAD) pathway and unfolded protein response (UPR)

To degrade a misfolded glycoprotein, it first needs to escape the cycles of re-glucosylation, then exist the ER through a dislocon towards the cytoplasm, a complete removal of the glycan chains and finally be degraded by the proteasome. To avoid further recognition by the lectin-like chaperones, several EDEM proteins, for ER degradation-enhancing α-mannosidase-like protein, will trim the terminal mannose residues, avoiding any further UGGT action[127]. The final $Man_7GlcNAc_2$ glycan moiety will be recognised by the protein OS-9 and transported to the HRD1 complex, which through

autoubiquitination allows the bypass of the unfolded protein to the cytosol and its further processing into small peptides[128].

Different situations, such as an accumulation of unfolded proteins, will affect the ER homeostasis and lead to an ER stress. The cell will react to such stress by activation of the unfolded protein response (UPR) pathway. The activation of the UPR pathway includes an increase in the chaperones synthesis (ex. BiP), a slow-down of protein synthesis, an increase in the ER size by increasing the lipid synthesis and an over activation of the ERAD. One of the key steps of UPR activation is IRE1 oligomerization and consequent activation. BiP usually sequesters IRE1 molecules, avoiding an excessive activation of the UPR pathway, physiologically active at low levels. When BiP is targeted to the unfolded proteins, IRE1 gets released, oligomerizes and induces an increase in the UPR response. This mechanism can modulate itself, since once the pathological accumulation of unfolded proteins is bypassed; BiP will bind once again IRE1 and will return the UPR to its basal levels[129,130].

If the UPR fails to restore normal ER function, and the protein accumulation persists, cell death-related mechanisms will be activated. For example, IRE1 constant activation will induce a kinase cascade through ASK1/JNK leading to an activation of the pro-apoptotic protein Bax, which will then activate Bim and inhibit anti-apoptotic members of the Bcl-2 family[131]. Indeed, a fully blocked N-glycosylation pathway, such as the one triggered by the drug tunicamycin (that inhibits the initial transfer of GlcNAc to Dol), will lead to IRE1 oligomerization and, if continued across time, cell death[132]. Nevertheless, in normal conditions, the correctly folded glycoprotein will scape the action of UGGT and will be transported to the Golgi apparatus.

2.3.3 N-glycan role in protein trafficking and function

Some glycan chains are also important for correct protein targeting, mostly to the plasma membrane or to the extracellular space. Many reports show how the lack of a specific glycan chain (empty N-glycosylation site) can lead to protein retention within the cell, without reaching the plasma membrane[133,134]. Interestingly, some other N-glycosylation sites do not play a major role in protein folding or trafficking[135,136] but

directly influence, between others, protein interaction (ex. adhesion molecules) or ion channels properties.

Most of the knowledge about the glycan-specific functions arises from protein N-glycosylation site-specific studies (e.g. directed mutagenesis against the N-glycosylated residue) and thus represent a small portion of all glycoproteins and N-glycosylation sites. Moreover, use of N-glycosylation blocking drugs such as tunicamycin will lead to a pathologic UPR activation that will mask the molecular consequences at the glycoprotein level. In this context, there is a lack of understanding about how a global N-glycosylation defect will affect the whole glyco/proteome.

In a recent report, Mann and colleagues performed an in-depth glycoproteome analysis in different mouse tissues (plasma, heart, kidney, liver and brain)[137]. The highest number of N-glycosylation sites (3162 sites within 1296 glycoproteins) was observed in the brain, with about 1/3 of them being brain-specific. Together with the major neurological disruption in CDG patients, these data suggest a crucial involvement of protein N-glycosylation during brain development and function that remains poorly investigated.

2.4 Protein N-glycosylation and brain development

Several evidences have pointed to a major involvement of N-glycosylation in synaptic transmission and cell adhesion/axonal growth dynamics, processes that rely on membrane-anchored N-glycoproteins[138]. Interestingly, many mRNAs coding for those membrane-anchored proteins are located and transcribed directly in the neuronal dendrites. This fact implies a local protein N-glycosylation machinery in the dendrites, and is supported by the presence of ER and ER-Golgi intermediate cisterns in the dendrites. Most of the dendrites though lack a complete Golgi apparatus. Consistent with this, Hanus and colleagues described in a recent paper[139] a major presence of core glycosylated ($Man_9GlcNAc_2$) membrane proteins in the brain, which lack any Golgi-related modifications. Such peculiarity is associated with a fast protein turnover in the dendrites of those core-glycosylated proteins, with a high incidence of neurotransmitter receptors and adhesion proteins.

2.4.1 Neural transmission and N-glycans

Neurotransmitter receptors are commonly N-glycosylated and such modification has been shown to play a major role not only for protein folding and trafficking but also for the receptor excitatory properties *per se* and its turnover. For example, cerebellar GCs contact the PCs through the glutamatergic PFs synapses, with variable proportions of AMPA, NMDA and mGluR receptors [140]. Most of these receptors are indeed N-glycosylated in different domains, including the ligand-binding ones, further supportive of a functional role of the glycan chain[141].

It is not only important to have a glycan chain, but the precise composition of the oligosaccharide will also impact the functional properties of the receptor. One of the possible modifications is the so-called HNK-1 epitope (a sulphated glucuronid acid attached to a terminal GlcNAc residue) that has been shown to play a major role in the glutamate receptor subunit GluR2 dynamics. Oka and colleagues[142] proved GluR2 to carry an HNK-1 epitope and demonstrated it to be necessary for adequate GluR2-N-cadherin interaction. Correct GluR2-N-cadherin interaction is key for the stabilization of the receptor in the plasma membrane.

Correct N-glycosylation of a receptor may also affect its ability to form homo/heterodimers. Such is the case of the δ subunit of the acetylcholine receptor (AChR): disruption of any of its two N-glycosylation sites will not affect protein stability but the binding dynamics[143]. As these examples show, glycan chains without any obvious role in folding, or trafficking can affect the protein interacting properties.

2.4.2 Role of the N-linked glycan chain in cell adhesion

In a similar manner to neurotransmitters, N-glycosylation of adhesion proteins is also crucial for their normal function not only in terms of folding, trafficking and stability but also to modulate, among others, their protein-protein interactions. Already in the early 70s, Warren and colleagues described an increase in the glycan charge of immortalized cells and proposed a pro-metastatic role of such increase[144,145]. Those studies provided

one of the first evidences of a major role of the oligosaccharide in cell-to-cell communication and further illustrate how N-glycoproteins activity is indeed greatly modulated by their glycan charge. More recent studies further confirm the N-glycosylation role in cancer progression. Abnormal protein N-glycosylation will alter cell-to-cell and cell-to-extracellular matrix adhesion through aberrant glycan structures, with increased frequency of sialylated and fucosylated glycans that will promote a increase in the cell metastatic potential[146] (for review see [147]).

In a recent report, J. Stevens and A. Spang described how in *C. elegans* an attenuation of protein N-glycosylation (hypoglycosylation) would affect cell-to-cell adhesion from early embryonic development (2-4 cells stage) with an obvious loss of interacting surface between cells[148] (Figure 11a). Similar results were obtained by deletion of an N-glycosylation site of the Drosophila adhesion protein Chp, which lead to a defective cell aggregation in culture[149] (Figure 11bB).

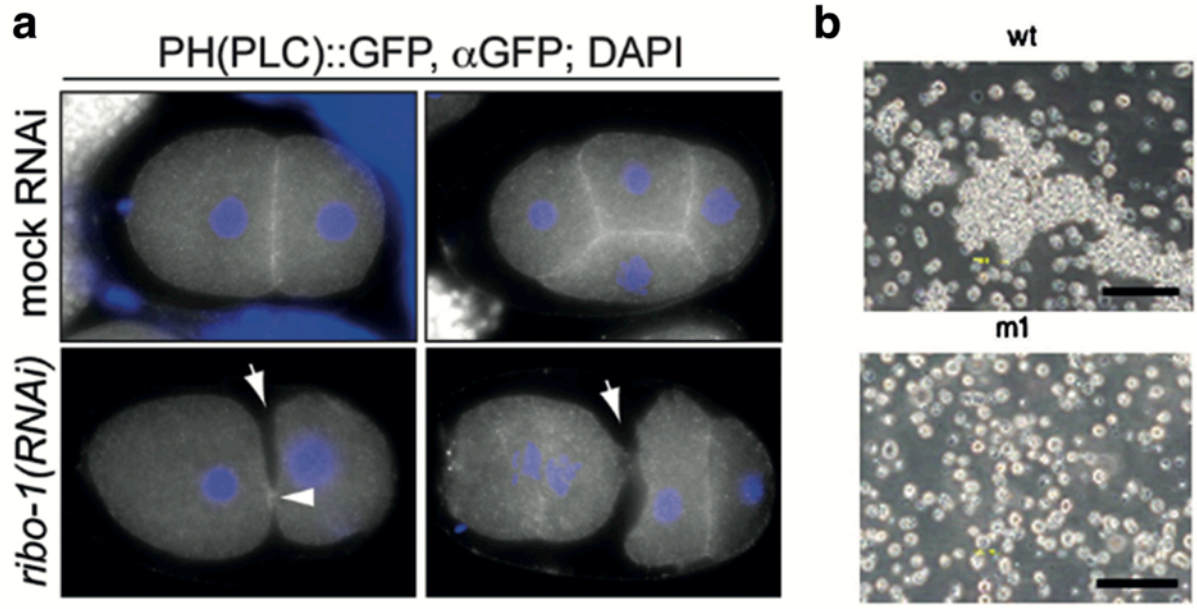

Figure 11. Major role of N-glycosylation in cell-to-cell adhesion. (a) C.Elegans embryos were injected with iRNA targeting and OST complex subunit (ribo-1), leading to impaired protein N-glycosylation. The 2 and 4-cell embryonic stages were analysed (nucleus in blue). Note the almost inexistent interaction between the cells' membrane (white arrows). (b) Aggregation assay of *Drosophila* S2 cells expressing the WT or hypoglycosylated (m1) form of Chp. Note the tendency of the control cells to form relatively big cell aggregates, which were not found in mutant cultures.

In agreement with the importance for cell-to-cell adhesion and communication, Mann and colleagues described an overrepresentation within the mouse N-glycoproteome for cell adhesion proteins[137].

In the context of brain development and function, cell-to-cell adhesion is important at many different levels, starting from cell migration and differentiation, to axonal growth, neuron-glia communication, synapse formation and maintenance, axonal fasciculation… Consequently, protein adhesion, together with adequate protein N-glycosylation, is important for virtually all of the brain-related functions. Indeed, evolutionary studies have pointed to a major diversification and increase in number of neural cell adhesion molecules (CAMs) together with the increased brain complexity in higher organisms[25,26]. There are three main kinds of neural CAMs: cadherins, integrins and immunoglobulin superfamily CAMs (IgSF-CAMs)[152].

Cadherins are transmembrane N-glycoproteins characterized by their cadherin repeats, which contain Ca^{2+}-binding domains and several N-glycosylation sites. Cadherins depend on the Ca^{2+} availability to form homo or heterodimers and contact with the neighbouring cell, forming adherent junctions. Their downstream pathways depend on the cytoskeletal and transmembrane proteins with which they interact[153]. Interestingly, hypoglycosylation of the extracellular domain of one of its members, E-cadherin, will not impact its abundance at the membrane but will change its interactome and thus disrupt its downstream effectors[154].

Integrins also contain Ca^{2+}-responding domains and can form dimers with other integrins or other CAMs such as the IgSF-CAMs. Time-restricted integrin expression and glycosylation are key for postnatal cerebellar development. Among others, β1 integrin has been shown to be necessary for Shh-dependant neuronal proliferation at the EGL. Integrins are also an important driving force to, through their interaction with extracellular matrix proteins, accelerate GCs movement across the ML (for review see [155]).

All integrins are predicted to carry N-glycan chains, which do also play major roles in integrin-mediated adhesion. *In vitro*, integrins react to fibronectin-coated surfaces.

Ablation of integrin N-glycosylation does not only impair the interaction with fibronectin but can potentially block any dimer formation[156,157]. In a recent paper[158], Zhu and colleagues performed site directed-mutagenesis against each N-glycosylation site of α2b, α5 and β3 integrins. Besides some N-glycosylation sites being essential for protein stability, they found that while loss of some N-glycosylation sites diminished the protein binding capacity and consequently its activity, some others enhanced it. Interestingly, aberrant α5 and β3 glycosylation (i.e. increased frequency of sialylated complex glycans) has already been linked to cancer prognosis, likely through changes in their adhesive properties[159]. This work further emphasizes the fact that each N-glycosylation site plays a different function depending not only on its localization within the protein but its composition.

2.4.3 Immunoglobulin superfamily cell adhesion molecules (IgSF-CAMs) and brain development

Most of the adhesion molecules in the CNS belong to the IgSF-CAM superfamily. They are characterized by the presence of one or several immunoglobulin-like (Ig) domains. Ig domains are "sandwiches" of two β-sheets, forming a fold, highly enriched in N-glycosylation sites[160,161]. Together with the Ig domains, IgSF-CAMs can have variable numbers of other domains, such as fibronectin domains, which also contain N-glycosylation sites.

Most of the members of this superfamily have transmembrane domains or are anchored to the membrane by a GPI anchor. The extracellular portion of the protein can interact with other molecules of the same IgSF-CAM (homophilic interaction) and with other CAMs (heterophilic interaction). The Ig domain itself is key for the adhesive properties of the protein. Indeed, loss of those multiple Ig domains avoids any homophilic interaction between IgSF-CAMs[162]. Furthermore, the N-glycans within the Ig domains play a major role in the interaction dynamics by modulating the distance between the different monomers and thus the strength and duration of the interaction (Figure 12a)[163,164].

IgSF-CAMs contact intracellularly with the cytoskeleton, which regulates and is regulated at the same time by their activity. IgSF-CAMs can directly interact with the cytoskeleton, actin or tubulin, or do it through an intermediate protein, such as ankyrin (linker protein). Importantly, IgSF-CAMs contain different intracellular binding domains that amplify the possible partners, favouring the assembly of multiple cytoskeleton components. Even the GPI-anchored proteins do interact with the cytoskeleton through its lipidic component. Interestingly, IgSF-CAMs overexpression leads to an increase in the transcription of cytoskeletal components, illustrating how IgSF-CAMs do not only modulate cytoskeletal organization but components' expression. At the same time, the cytoskeleton modulates IgSF-CAMs activity by clustering them, enhancing their membrane localization and favouring the interaction with other transmembrane proteins (for review see [165]).

The IgSF-CAMs superfamily can be further subdivided into smaller protein families, such as L1CAMs, contactins (CNTNs) and NCAMs. These protein families have long been known for their roles in axonal fasciculation and elongation, neuronal migration, myelination and synapse formation and maintenance[166]. Consistently with this role, L1CAM, CNTN2/TAG1 (a contactin member) and NCAM1 have higher expression in the cerebrum and the cerebellum than in the rest of the human tissues (Figure 12b).

One of the first *in vivo* evidence that supports the crucial neuronal function of IgSF-CAMs was given by Rutishauren and colleagues in 1988[167]. They studied L1CAM and NCAM1 roles in axon fasciculation and muscle neural innervation; these processes rely first on a strong axon-axon union (fasciculation) and after on the capacity of those axons to separate and make contact with different muscles. They showed that these processes rely on L1CAM and NCAM1 adhesive properties, L1CAM for axon-axon binding and NCAM1 for later axonal spreading and muscle-neuron contact (indeed, muscle cells also express NCAM1). Even more, they demonstrated that NCAM1 function fully relies on it being properly glycosylated with a terminal sialic acid (polysialic acid, PSA) and that this modification allows temporal control of the process.

NCAM1 contains different N-glycosylation sites, many of which are located at the Ig domains. One of these N-glycosylation sites gets further modified by addition of an

homopolymer composed by up to 90 sialic acid residues[168]. PSA addition will decrease the heterophilic and homophilic interactions of NCAM1 and thus will modulate its adhesive properties. Interestingly, in the previously mention study[167], during the period of axonal growth, the NCAM1 located at the muscle has a high PSA content, avoiding a major axon-muscle interaction and indirectly reinforcing the axonal bundling. Later on NCAM1 will have its PSA content reduced and will enhance axonal contact with the muscles, leading to muscle innervation.

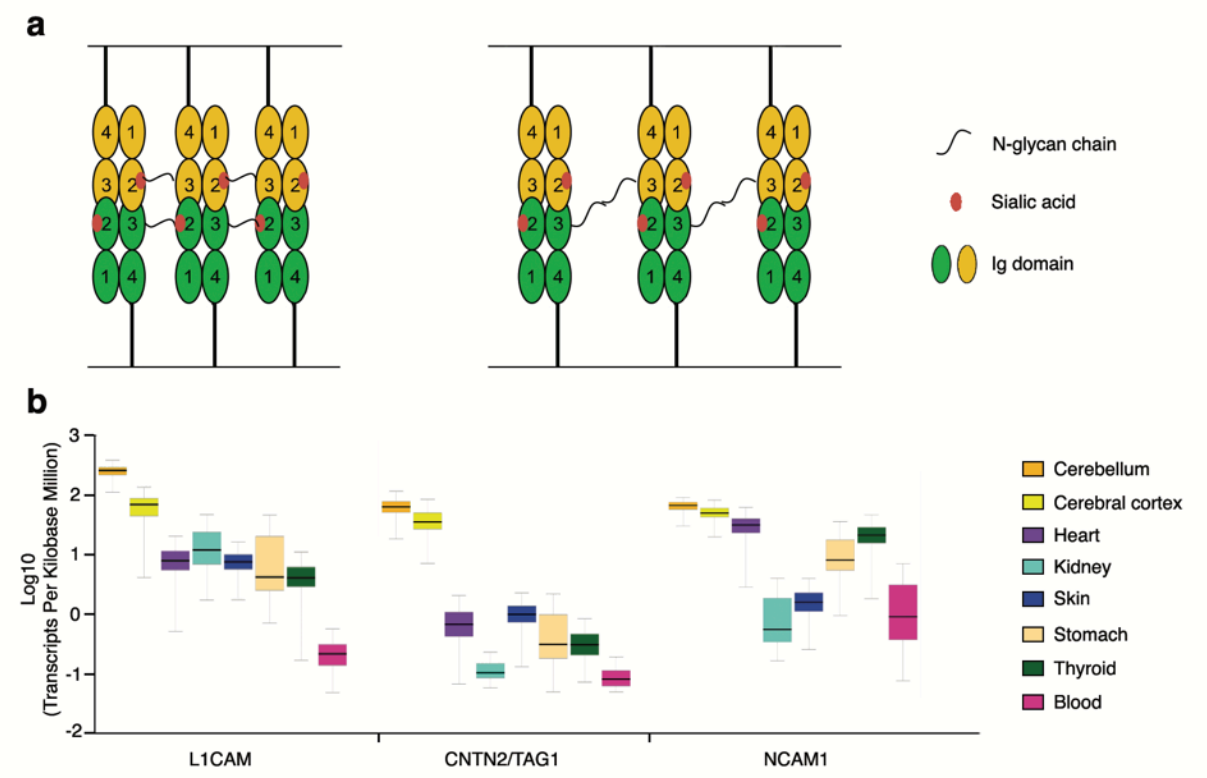

Figure 12. IgSF-CAMs homophilic interaction and expression. (a) Representation of the possible interaction between L1CAM (an IgSF-CAM member) molecules. The Ig domains in each molecule form a zipper-like structure and contact with the neighbour L1CAM through their glycan component. Modified image from CH. Wei at al, 2012. (b) mRNA expression levels of different IgSF-CAMs members with a known role in brain development and function in different human tissues (GTEx database). Most of the L1CAM/CNTN/NCAM families' members show higher mRNA expression in the brain, especially in the cerebellum.

As previously mentioned, the cerebellar cortex has a relatively simple cytoarchitecture comparable to the cerebral cortex organization. Due to this, many studies focus on IgSF-CAMs function during cerebellar development to understand their role during brain development. During postnatal cerebellar development four different CNTNs are highly expressed (CNTN1/2/3/5). Those proteins are key for GCs migration from the EGL to the IGL, a process that requires prior development of their axons that will become the

PFs. CNTNs are expressed in a sequential manner, with partial overlaps[169]. CNTN2 and CNTN1 are the first to be expressed at the EGL and are required for axon fasciculation and proper orientation of the fibres. As mentioned in the first chapter, the PFs are all parallel to the upper cerebellar pial surface. Indeed, mouse KO for *Cntn1* show an aberrant orientation of the PFs associated with an ataxic phenotype by P10 and early mortality (no mutant recovered after P18)[36]. In a similar manner, *ex ovo Cntn2* RNAi electroporation into the chick embryo lead to abnormal formation of the PFs[35]. Those evidences suggest a potential redundancy of CNTNs and thus IgSF-CAMs functions in the developing cerebellum.

Following CNTNs expression, two members of the L1CAM family start to be highly expressed in the developing GCs, NrCAM and L1CAM itself. Interestingly, whereas NrCAM or L1CAM KO mice show no major GCs underdevelopment, the double KO mouse presents a reduced IGL and early lethality (P8)[170,171]. Indeed, GCs from the different KO mice (L1CAM/NrCAM, Cntn1, Cntn2) show aberrant neurite dynamics *in vitro*, consistent with a predominant IgSF-CAMs role during PFs formation in the cerebellum.

As highlighted by Stoeckli in a review about IgSF-CAMs function during cerebellar development[169], all steps in GCs development from the EGL to the IGL, but the migration itself, are tightly controlled by IgSF-CAMs, expressed in a sequential and partially overlapping manner, with both, unique and concomitant roles. Together with the pivotal role of adequate N-glycosylation of IgSF-CAMs and other adhesion proteins such as integrins, it is likely that disruption of their glycosylation status will have an impact on their functions during development. Nevertheless, almost no study has addressed this question, and if so, it is based on a single N-glycosylation site loss[172], and thus do not provide a global and unbiased picture of the N-glycosylation importance during cerebrum and cerebellar development.

2.5 Model organisms for CDG Type I

To understand how N-glycosylation orchestrates CNS development and leads to the major neurological defects in CDG-Type I, one necessary step is to generate an adequate *in vivo* and/or *in vitro* model of the disease. Such a model could not only answer to the

previous questions but could also be used for therapy testing, inexistent nowadays for most CDG. So far, the more successful therapeutic approach is for PMI-CDG (phosphomannose isomerase) by oral treatment with mannose. Nevertheless, the treatment is not 100% effective and helps only to a minority of CDG type I patients[173].

The development of an *in vivo* mouse model for CDG has been shown to be more challenging than expected. Protein N-glycosylation is only partially impaired in CDG but the KO of the corresponding gene in mouse is in general embryonically lethal, such as the *Pmm2* KO mouse[174,175]. The more promising models existent nowadays for CDG type I can be subdivided into three categories, all related to the most frequent CDG-Type I, PMM2-CDG.

The first category consists on the use of morpholinos in Xenopus and zebrafish to reduce Pmm2 levels. Both models achieve a partial reduction in the Pmm2 activity comparable to the one observed in human patients[176]. In zebrafish, Pmm2 reduction leads to craniofacial and motility defects, resembling those found in human patients[177]. In Xenopus it also leads to developmental abnormalities such as a reduced head-to-tail size, eye dismorphisms and head malformations. The researchers also proved Pmm2 loss to drive an altered Wnt pathway signalling and hypothesized a contribution of Wnt hypoglycosylation to the physiopathology of PMM2-CDG[178]. Similar results were obtained with a CRISPR/Cas9-mediated *Pmm2* KO in Drosophila[179].

Regarding a mammal model for CDG-Type I, the more successful trials include the insertion of the human mutation (usually a missense mutation for PMM2-CDG[180]) into the mouse genome. Two different groups have generated a mouse model for the PMM2-CDG. In 2012 Körner and colleagues publish a hypomorphic *Pmm2* mouse mutant[181]. The homozygous mutant mice were not viable and died before E10.5. Nevertheless, they showed how a prenatal mannose treatment (mannose within the mice' drinking water) could rescue the embryonic mortality. The mutant mice became then viable and showed no major difference with their control littermates. Such results were really promising as a therapeutic approach. However, the mannose supplementation can only be given when the CDG diagnosis is done and is not effective by then in humans[182]. Four years later another group published a similar hypomorphic mouse model, carrying the most

common human mutations (composite heterozygous), but in this case, mannose supplementation did not rescue the partial lethality of their model. Similar to the human patients, they found a developmental delay in the surviving mutants and similar biochemical properties of the mouse embryonic fibroblasts (MEFs) and PMM2-CDG patients' fibroblasts. Nevertheless, they did not observe any major cerebellar defect, as usually found in patients[183].

The third major line of investigation includes the use of patient-induced iPSCs (section 1.5). Two years ago, Buettner and colleagues published the first report using PMM2-CDG patient fibroblasts and reconverting them into iPSCs by lentiviruses coding for the Yamanaka factors[184]. Those iPSCs show a 75% reduction in Pmm2 activity and a consistent reduction of high-mannose-containing glycan chains.

All those models are promising tools to better understand the physiopathology underlying CDG Type-I and so to gain insights into protein N-glycosylation role in CNS. Nevertheless, none of those studies relies on a global investigation of the transcriptome or proteome in the mutant, thus missing a great opportunity to understand the molecular consequences of the defect. Moreover, none of these models present *a priori* any cerebellar defect or can be easily used to address this question, which is indeed one of the main traits of the disease.

3 CELLULAR ROLE OF SRD5A3 AND CLINICAL SYMPTOMS ASOCIATED WITH ITS MUTATIONS

In a recent report, SRD5A3-CDG was highlighted as the third more frequent type of CDG-Type I in the European population[101]. SRD5A3-CDG was described for the first time by Vincent Cantagrel et al, in the group of Joseph G. Gleeson in 2010[175]. They identified STOP mutations in the *SRD5A3* gene in a large consanguineous family where all affected child had ocular colobomas, developmental delay and brain malformations including cerebellar vermis hypoplasia. Due to the high phenotypic resemblance with other CDG patients, they tested them by TIEF, where they observed a clear Type-I profile. Further biochemical analyses in the yeast *SRD5A3* ortholog (*DFG10*) demonstrated that SRD5A3 is the enzyme responsible of the conversion of polyprenol into Dol, which is later used

as a glycan carrier (chapter 2). Indeed, they found an increase in polyprenol levels in patients' cells, which usually cannot even be detected in control subjects. Surprisingly, they still found normal Dol levels in the patients, highly suggesting that Dol can also be synthesized through an alternative pathway that does not require polyprenol. Nevertheless, patients display a huge decrease in the LLO levels, illustrating that, even if Dol can be synthesized, the full Dol + core glycan chain (LLO) cannot be properly synthesized and thus leads to a defective protein N-glycosylation in mouse, yeast and human.

They consequently screened other patients with similar phenotype for *SRD5A3* mutations. The cohort enlargement showed a high recurrence of cerebellar defects characterized by atrophy and/or vermis hypoplasia (5/6 patients, 83%). Later on published reports further confirm the high prevalence of cerebellar defects, together with learning difficulties and psychomotor retardation, in SRD5A3-CDG, as observed in PMM2-CDG[109,185]. Indeed, together with PMM2-CDG and dystroglycanopathies, SRD5A3-CDG is within the CDG with higher occurrence of cerebellar malformations[119]. SRD5A3-CDG patients can also present abnormal coagulation, muscle hypotonia, liver fibrosis, dermatitis and abnormal fat distribution, among others[175,185,186]. Most SRD5A3-CDG patients present eye malformations characterized by a slowly progressive early-onset retinal dystrophy, visual loss, myopia and nystagmus[187].

This discovery expanded the number of known CDG caused by disruption in the mevalonate pathway, which has as a final product, between others, dolichol, cholesterol and ubiquinone (Figure 13)[188]. It is remarkable that, even if the primary defect happens in a lipid synthesis-related pathway, the major biochemical defect, and the only one proved in SRD5A3-CDG patients, is in terms of protein hypoglycosylation.

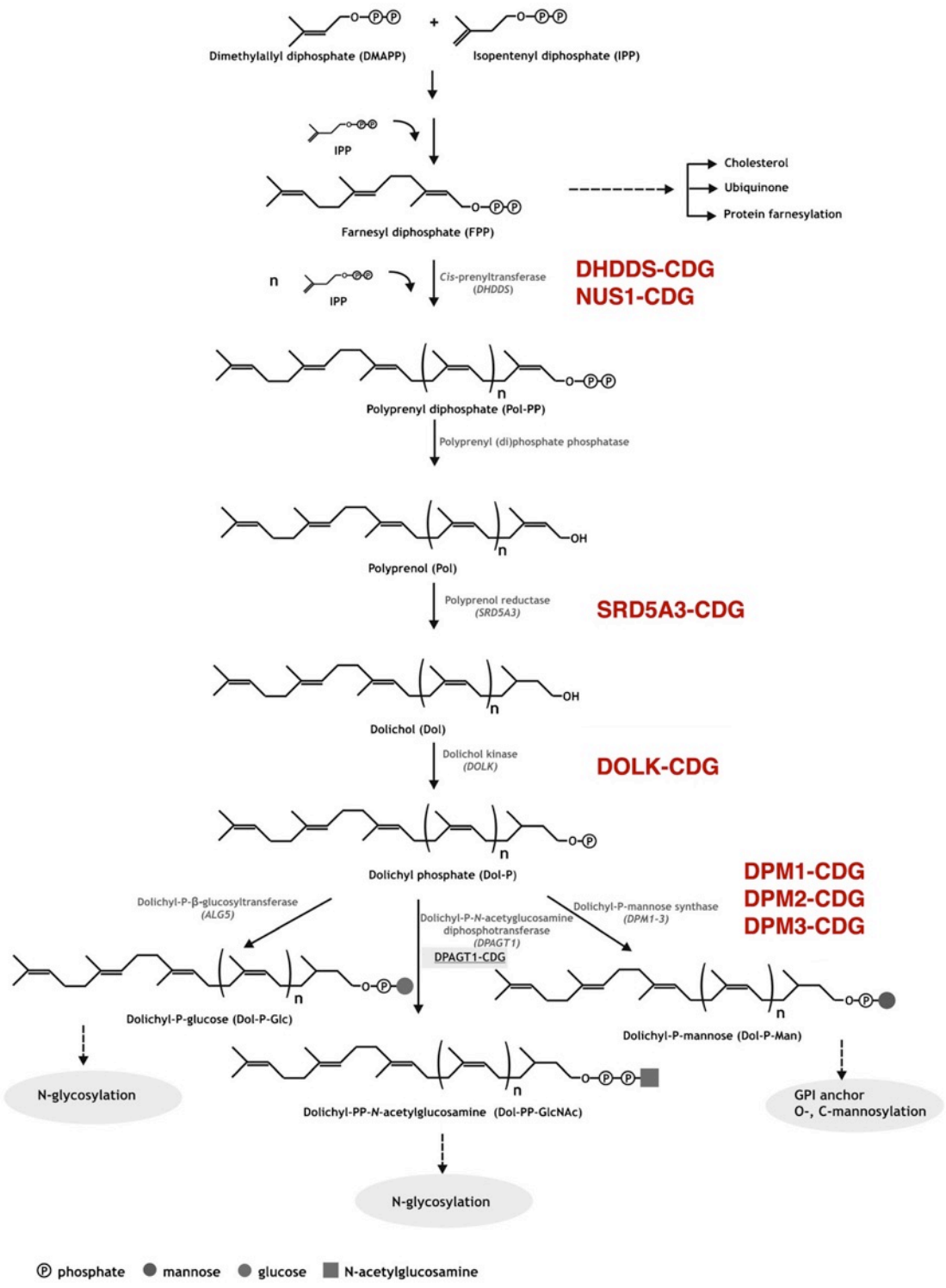

Figure 13. Simplified mevalonate pathway. All of the known CDG caused by disruption in a product of the pathway are highlighted in red. Modified image from Buczkowska et al, 2015.

The mouse KO for *Srd5a3* is not viable and no embryo can be recovered after E12.5. This observation is unexplained as patients also carry likely null homozygous alleles[175]. A tempting explanation is a different regulation of the alternative Dol biosynthetic pathway in mouse versus human. Embryos at that stage show, between others, defect in

tail rotation, dilated heart and open neural tube. Transcriptomic studies in the embryo showed an over activation of the UPR pathway, suggesting a major requirement of Srd5a3 activity for protein folding. This is consistent with a hypoglycosylation-driven accumulation of misfolded proteins in the ER that could over activate the UPR pathway.

In conclusion, to characterize SRD5A3-CDG underlying physiopathology, an alternative mouse model should be developed. Given the high prevalence of a cerebellar defect in this type of CDG, such model could help to understand its molecular origin. By doing so, we could also gain insights into the crucial role of protein N-glycosylation during CNS development and function, a largely under investigated function.

4 AIMS OF THE PROJECT

PART I

1 – Identification of the genetic basis of human cerebellar defects

For many patients with cerebellar malformations a molecular diagnosis is yet to be achieved. As a side project during my PhD, I used a combination of WES and validation of certain gene variants impact to improve the molecular diagnosis of syndromes with cerebellar defects.

PART II

1 – To characterize the histopathology associated with *Srd5a3* cerebellar deletion

A new mouse model for SRD5A3-CDG was developed by conditional *Srd5a3* deletion in the cerebellum (Cre/LoxP system) before my arrival to the laboratory. This model can potentially be used to understand the CDG-Type I physiopathology in other affected organs such as the skin, eyes and immune system. Our aim was to characterize the histopathology associated to cerebellar Srd5a3 loss. This study should highlight if there is any cerebellar population more sensitive to the N-glycosylation block and which is the histological consequence.

2 – Biochemical and molecular characterization of the physiopathological mechanisms underlying *Srd5a3*-loss associated defects

A full molecular study of the *Srd5a3* conditional KO (cKO) mouse should shed light on the precise impact of an N-glycosylation disruption in an *in vivo* and viable CDG model, something that has never been deeply analysed before. In addition to that, and taking into account the role that Dol plays as carrier of the oligosaccharides transferred in the ER (e.g. mannose and glucose), defective Dol synthesis may also impair the core glycan composition. This possibility was further evaluated.

3 – Impact assessment of the molecular findings

The potentially altered pathways in the mutant cerebellum have been validated as contributing or not to the mouse neurological phenotype. In addition to that, we have generated *SRD5A3* KO iPSCs to evaluate the relevance of our findings in an appropriate human model.

4 - Rescue of the defect

The final goal of developing a mouse model for CDG-Type I, besides its contribution for the glycobiology and neurobiology fields, is to set up a system for therapy testing. Even if a definitive therapeutic approach is out of the scope of the present work, a prove-of-concept rescue could prove the suitability of our model for further testing.

RESULTS

PART I

1 Unravelling the genetic basis of cerebellar malformations

Context: Cerebellar malformations are life-challenging conditions that affect patients' capacities to cope with a normal life and can be associated with reduced life expectancy. Cerebellar defects are often also associated with ID and ataxia. Identifying the genetic cause, when existent, will help to counsel the family when facing new pregnancies and can also lay the first stone towards therapy. In this context, WES and gene panel are important tools to help to elucidate the genetic component of the disease. Nevertheless, identification of a likely pathogenic variant is often not enough to prove causality and thus validation of its pathogenicity requires further functional work. Part of the work performed during my PhD included WES analysis and investigation of variant segregation by Sanger sequencing (case I), characterization of the candidate protein expression pattern during brain development (case II) and the establishment of a cell model KO for a novel disease-causing gene using genome editing techniques (case III).

1.1 A recurrent de novo mutation in the KIF1A gene

Thanks to collaboration between the National Research Center in Cairo (Egypt) and the Necker hospital, many Egyptian families with children suffering of a cerebellar defect were explored at the Imagine Institute Genomic and Bioinformatic platforms using WES and gene panel testing.

Once the WES/gene panel data is generated, the laboratory of development brain disorders, leaded by Laurence Colleaux and Vincent Cantagrel, interprets the resulting sequences.

As part of this collaboration, the Dr. Hisham Megahead diagnosed a 2 years old child (family CerID-Egy-21) suffering of cerebellar atrophy (diagnosed by MRI, Figura 14a). The patient, born from a consanguineous union, is the only reported affected individual. In addition to the cerebellar atrophy, she suffers of right temporal epileptogenic activity. These features are accompanied by delayed motor and social development.

Usually, when testing an inbred family by WES, where also the parents are sequenced, the first mode of inheritance tested is the autosomal recessive one. In this scenario, both parents are heterozygous for the same variant (common origin of the mutation) that is

transmitted and homozygous in the affected child. Nevertheless, when testing for that hypothesis no potentially pathogenic variant meeting this criteria was identified.

Surprisingly, a genetic diagnosis was only achieved when seeking for a *de novo* origin of the potentially pathogenic variant. I identified and validated a heterozygous *de novo* variant in the *KIF1A* gene (NM_001244008.1, c173C>T, p.S58L) in the affected individual CerID-Egy-21-ea (Figure 14b). The mutation is located within the ATP binding domain of KIF1A, a microtubule-dependent cargo protein, important for the transport of different components across the neurites[189]. ATP hydrolysis allows KIF1A movement. Indeed, the detected variant is predicted to alter the hydrogen bonds within the ATP domain and thus disrupt adequate ATP hydrolysis and consequently, disrupt protein function.

The c173C>T variant had already been identified as causing cerebellar atrophy in other patients[190]. These data prove the *KIF1A* variant as responsible of the observed cerebellar atrophy and highlights the importance of considering *de novo* variants in single-case consanguineous families.

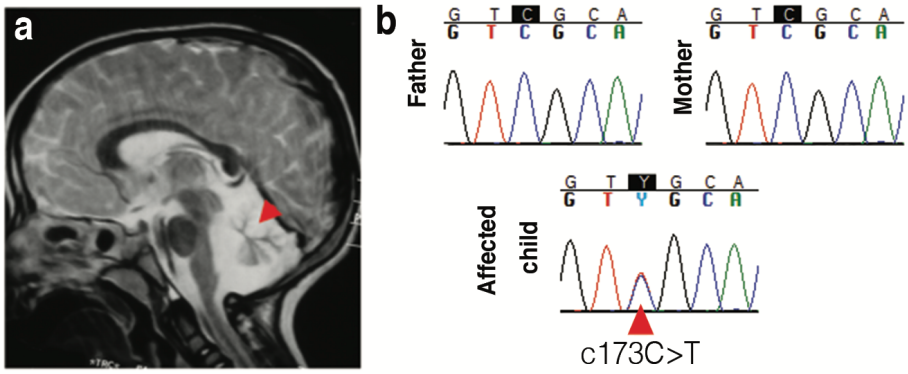

Figure 14. *KIF1A* c173C>T mutation leads to early-onset cerebellar atrophy. (A) MRI of the patient CerID-Egy-21-ea. The red arrowhead points to the atrophic cerebellum. (B) Sanger sequencing results of *KIF1A* in the healthy progenitors and the affected child. The red arrowhead indicates the nucleotide number 173 in the affected child, where two peaks, corresponding to a heterozygous C/T state, are detected.

1.2 Enlarging the phenotypic spectrum of CACNA1G mutations

More recently, a cohort of 47 patients followed at Necker Hospital was investigated by gene panel and/or WES. All patients presented with cognitive and motor dysfunction during paediatric age together with cerebellar ataxia and atrophy and/or hypoplasia. This study allowed the identification of the likely disease-causing variants in 62% of the families.

Part of the research was then focused on one potentially pathogenic variant detected in the *CACNA1G* gene (c2881G>A, pA961T). This variant was predicted to be deleterious by the PolyPhen, SIFT and Mutation Taster databases. Notably, this was the first *de novo* mutation in the Ca^{2+} channel CACNA1G linked to a congenital disorder. Other *CACNA1G* mutations were previously described but all were associated with late-onset cerebellar ataxias[191].

In search for additional patients presenting with a similar phenotype and a mutation in *CACNA1G* we contacted collaborators from other centres and used the online platform Gene Matcher. Gene Matcher is a tool to share worldwide potentially pathogenic variants with their associated phenotype. Through this collaboration, three additional patients with early-onset cerebellar ataxia were identified, two carrying the same variant (suggesting a hotspot mutation) and another carrying a new variant (c4591A>G, pM1531V). Interestingly, both mutations were demonstrated to be gain-of-function, opening possibility of a therapy with a sensitive channel inhibitor (TTA-P2)[192]. Surprisingly, half of the patients present also congenital microcephaly, suggesting a defect in the development of the cerebral cortex. The role and expression of CACNA1G is well characterized in the cerebellar PCs and DCNs[193] but not clearly reported during cortical development.

My contribution to this work consisted in testing for the expression of *CACNA1G* in other brain regions. To do so, wild-type (WT) E14.5 mouse embryos were OCT-embedded, sliced and stained with CACNA1G and Tuj1 (neuronal marker) antibodies (Figure 15, top). The results demonstrated that CACNA1G is expressed in the mouse post-mitotic neurons of the developing cerebral cortex. As a control, a developing mouse cerebellum (P7) was also stained and the localisation of CACNA1G in PCs and DCNs was confirmed (Figure 15, bottom).

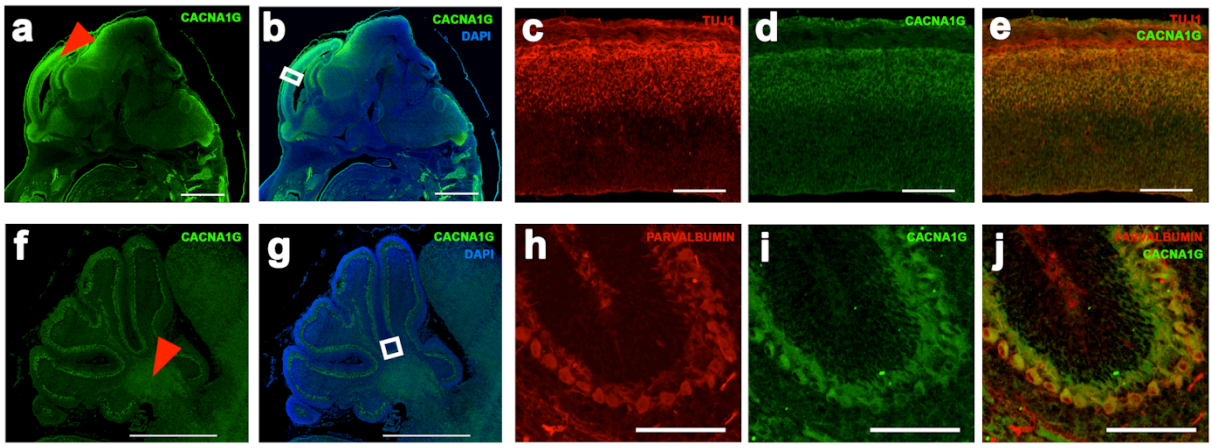

Figure 15. *CACNA1G* is expressed in the cerebral cortex and the cerebellum during development. (A) CACNA1G staining in the E14.5 mouse embryo. Note that the highest intensity is located within the cerebral cortex (red arrowhead). (B) Same image counterstained with DAPI. Scale bar 1mm. (C, D, E) Magnification of the E14.5 cerebral cortex stained against Tuj1 and CACNA1G. The CACNA1G-positive cells in the cortex are also Tuj1-positive, proving their neuronal fate. Scale bar 100µm. (F) P7 cerebellum stained with the CACNA1G antibody. Note the positive labelling of the DCNs (red arrowhead) as previously described. (G) Same image counterstained with DAPI. Scale bar 1mm. (H, I, J) Magnification of the PC layer stained against parvalbumin (PC marker) and CACNA1G. As expected, a robust expression of CACNA1G is detected in the developing PCs. Scale bar 100µm.

1.3 MINPP1 mutations as a new cause of pontocerebellar hypoplasia

A novel form of pontocerebellar hypoplasia (PCH), accompanied by an atrophy of the basal ganglia (the striatum), was recently identified in the lab. We identified biallelic mutations in the *MINPP1* gene in children presenting a unique neuroimaging phenotype combining PCH features with hyper-intensities in the basal ganglia. MINPP1 encodes the multiple inositol-polyphosphate phosphatase 1. The mutations include indels leading to early STOP codons and SNVs predicted by the software SIFT and/or Mutation Taster to be deleterious (Figure 16a). MINPP1 is an enzyme involved in inositol phosphate metabolism, important for cell migration, gene regulation and membrane dynamics[194,195]. Nevertheless, its precise role in inositol phosphate metabolism remains elusive. Previous studies had already highlighted the importance of inositol for cerebellar function, with disruption of its metabolism leading to neurodegeneration with major consequences for the PCs[196–198]. Nonetheless, this is the first time that *MINPP1* is directly linked with a congenital disorder.

We next focused the research in the patients for which primary fibroblasts were available (family CerID30, Figure 16b). The family CerID30 includes two affected children and no healthy siblings. Both affected individuals are homozygous for a frame-shift insertion (c.223_224insGGGGG; p.Glu75Glyfs*30).
I first evaluated the protein expression levels in those patients (Figure 16c). As shown, no protein was detected in none of the affected individuals.

We next aimed to generate a human *in vitro* model to understand the biochemical consequences of MINPP1 depletion. To do so, together with Michael Nicouleau, we generated CRISPR/Cas9 constructs targeting the first exon and used them to knockout the gene in HEK293T cells, a transformed human kidney cell line (Figure 16d). We further confirmed efficient MINPP1 depletion by WB (Figure 16e). The biochemical characterization of these cells and *MINPP1*$^{-/-}$ iPSCs is nowadays the main research activity of Ekin Ucuncu, PhD student under the supervision of Vincent Cantagrel.

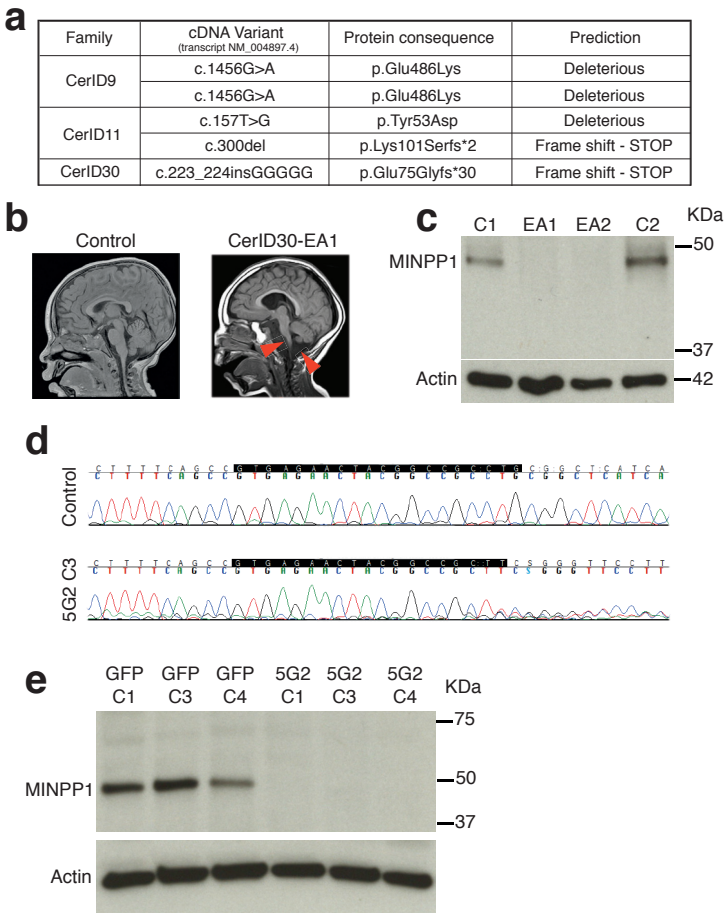

Figure 16. MINPP1 depletion leads to a novel form of PCH. (a) *MINPP1* variants in the patients. The software SIFT and Mutation Taster were used for prediction. (b) MRI of an affected individual (CerID30-EA1) showing the atrophy of the pons and the cerebellum (arrowheads). (c) WB against MINPP1 in patient (EA1/2) and control fibroblasts. (d) *MINPP1* sequence in control and *MINPP1*$^{-/-}$ HEK293T cells (guide 5G2 clone 3). The sgRNA-targeted region is highlighted in black. (e) WB against MINPP1 in *MINPP1*$^{-/-}$ and control HEK293T cells.

PART II

1 Characterization of the histopathology associated with *Srd5a3* cerebellar deletion

Context: The main goal of my PhD was to elucidate the physiopathology underlying the neurological symptoms in CDG type I and by doing so, to understand how protein N-glycosylation regulates brain development and function. To note, there is already a substantial amount of work published about the impact of a single N-glycan chain loss in a precise protein or about the phenotypic consequences of an N-glycosylation impairment. However, none of these works investigated in-depth the molecular consequences of an N-glycosylation impairment.

Before the investigation of the molecular defect, we aimed to elucidate the histological consequences of cerebellar N-glycosylation block, which could also help us to understand the molecular consequences. In CDG type I, most of the knowledge regarding the cerebellar pathology comes from patients' MRI, which doesn't allow investigation at the cellular level. Only one histopathological study has been performed in a PMM2-CDG cerebellum and none is available for SRD5A3-CDG[123]. The PMM2-CDG patient was 1-month-old at the age of examination, when the cerebellum is yet not fully developed. Histological evaluation showed an atrophy of some cerebellar folia, a reduction in PC and GC number and aberrant PC arborization. Importantly, the patient carried severe *PMM2* mutations (V231M/T237R), leading to a complete loss of enzymatic activity. This contrasts with most of *PMM2* pathogenic mutations, which keep some residual enzymatic activity. In this context, a precise histopathological analysis of the *Srd5a3* cKO mouse is necessary. Such analysis will allow evaluating if a specific cellular population is affected and potentially point towards a defect in cell proliferation, survival, differentiation or migration.

Conditional deletion of Srd5a3 in the whole developing cerebellum

Since we sought to examine the function of *SRD5A3* in brain disease pathogenesis, we generated targeted conditional and null alleles of mouse *Srd5a3*, flanking exons 2-4 with loxP sequences (Figure 17a,b). Homozygous germline mutants (*Srd5a3*$^{-/-}$) are embryonic lethal (data not shown) consistent with results from the *Srd5a3* gene-trap mutant[175]. So,

we used the Engrailed1-cre (En1-Cre) transgenic line to produce conditional knockouts En1-Cre; *Srd5a3*$^{fl/-}$ in the developing hindbrain[199] and confirmed the gene deletion at the transcript level (Figure 17c,d,e). En1-Cre; *Srd5a3*$^{fl/-}$ mice were fertile and showed nearly Mendelian ratios at weaning age (data not shown). We used far-western blotting with biotinylated Sambucus Nigra lectin (SNA) to investigate the abundance of complex sialylated N-glycans[200]. Total protein extracts from mutant cerebellums showed a non-significant 12% decrease in normalized signal intensity (Figure 17f,g). We obtained similar results with Concanavalin A (ConA) lectin that binds to core and immature mannosylated N-glycans (Figure 17h,i).

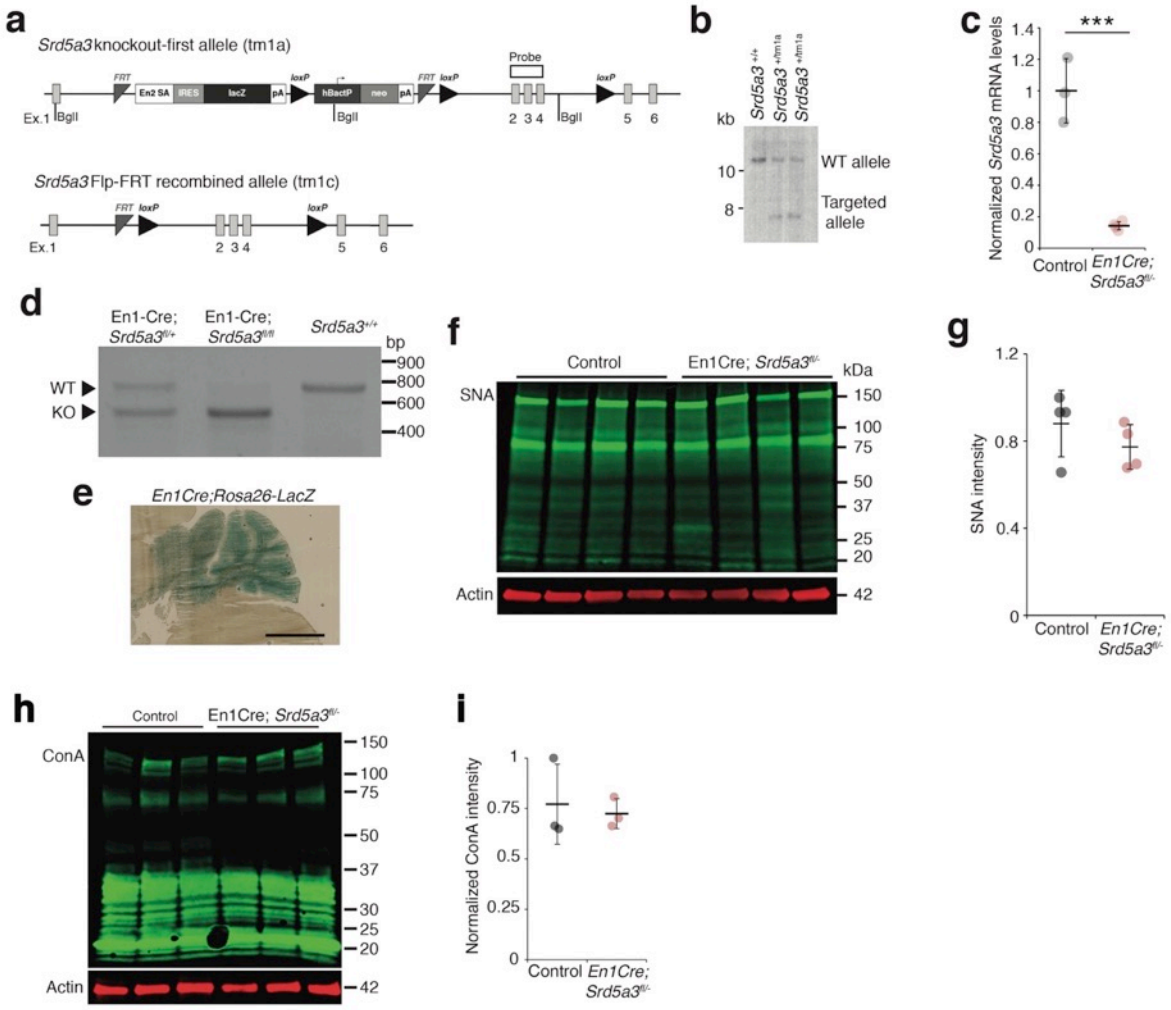

Figure 17. Generation of conditional *Srd5a3* knockout mice and first biochemical analyses. (a) Schematic of the *Srd5a3* knockout-first allele (tm1a), the same allele after Flp-mediated recombination (tm1c) and (b) validation of the tm1a allele insertion by southern blot. (c) RT-qPCR analysis of *Srd5a3* expression levels in the P7 cerebellum (Control, n=3; En1-Cre; *Srd5a3*$^{fl/-}$, n=4) (d) RT-PCR analysis of the recombined (KO) and wild-type (WT) *Srd5a3* mRNA in the cerebellum. (e) LacZ staining image of the En1Cre; Rosa26 mouse showing Cre expression within the entire cerebellum. Scale bar 2mm. (f) Far-western blot with

SNA lectin in P7 cerebellum and (g) quantification (n=4) for each genotype, p-value=0.29. (h) ConA far-WB and (i) quantification (t-test, p-value=0.7190; n=3 for each genotype). Two-tailed t-test was used for statistics. *** p<0.001. Results are presented as mean ± s.d.

These results indicate that cerebellar *Srd5a3* deletion does not cause a severe general glycosylation defect. However, Lamp1, a broadly used marker for N-glycosylation defects[201,202], indicated a severe decrease in protein levels across samples (Figure 18a,b,c). The remaining proteins showed a shift toward a lower molecular weight before PNGase treatment, which indicated impaired glycosylation (Figure 18d).

Next, we investigated the functional consequences of this cerebellar glycosylation defect on learning ability and motor behavior[15] in a cohort of control and mutant mice (n=30). In the Morris Water Maze (MWM), we exposed mice twice to the same hidden platform to test working memory. We found no significant difference on swimming speed between En1-Cre; *Srd5a3*$^{fl/-}$ and control mice (Figure 18e). The latency to reach the platform was significantly lower on the second trial than on the first one for control mice, but not for En1-Cre; *Srd5a3*$^{fl/-}$ mice (Figure 18f). This result suggests a mild impairment of working memory in the mutant mice. In contrast, En1-Cre; *Srd5a3*$^{fl/-}$ mice showed a severe and highly significant (p=0.0007) motor coordination defect assessed with the rotarod test (Figure 18g). These results suggest that in the absence of *Srd5a3,* the impaired cerebellum function arises from a mild and potentially selective hypoglycosylation of glycoproteins.

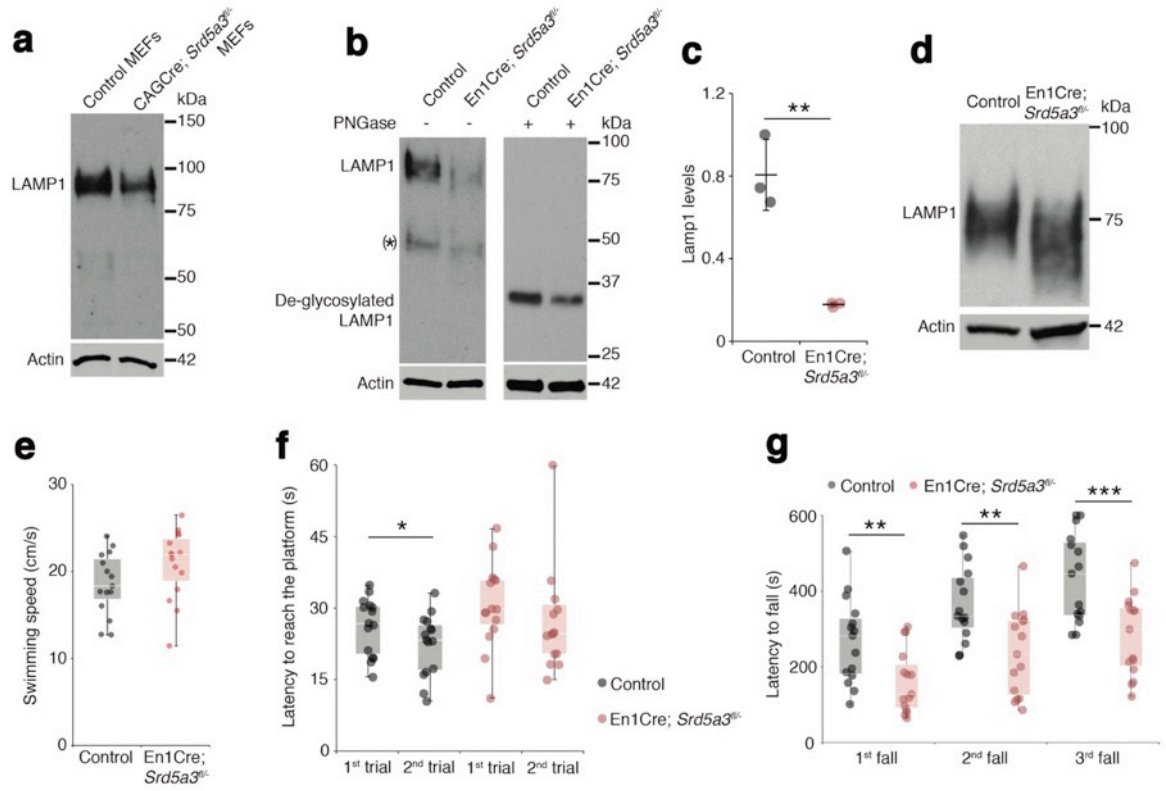

Figure 18. Deletion of *Srd5a3* in the cerebellum impairs protein N-glycosylation and motor function. (a) WB analysis of LAMP1 expression in mouse embryonic fibroblasts (MEFs). (b) WB analysis of LAMP1 level from P7 cerebellum and (c) quantification. * indicates a PNGase sensitive LAMP1 isoform; ** p-value=0.0032. (d) WB analysis as described in (b) but with increased electrophoretic migration and adjusted protein amounts to highlight LAMP1 hypoglycosylation in the mutant sample. (e) Average swimming speed during the Morris water maze test (MWM; n=15 for each genotype). (f) MWM results. After two trials to find the same hidden platform (average of a total of eight sessions), only control mice significantly reduced the time to find the platform on the second trial (t-test, type I, p=0.0329). (g) Box plot of the latency to fall during rotarod testing (n=15 for each condition). One-way ANOVA was used for MWM and rotarod statistics. For all others, two-tailed student t-test was used. * p<0.05; ** p<0.01; *** p<0.001. Results are presented as mean ± s.d.

Conditional deletion of Srd5a3 disrupts cerebellum granule cell development

Then, we wanted to examine cerebellar development after deletion of *Srd5a*3 by conducting a morphological and histological survey at P14, P21, 2 and 6 months. We observed a significant hypoplasia in the En1-Cre; *Srd5a3*$^{fl/-}$ mice (Figure 19a-d). Examining the mutant cerebellum cytoarchitecture revealed an accumulation of scattered ectopic cell clusters in the external part of the molecular layer (ML; Figure 19e). These clusters were NeuN-positive, post-mitotic granule cells (GCs) (Figure 19f) that failed to migrate to the internal granule cell layer (IGL). These cells remained in the external granule cell layer (EGL), a transient germinal zone. We observed this pattern at all our investigated timepoints.

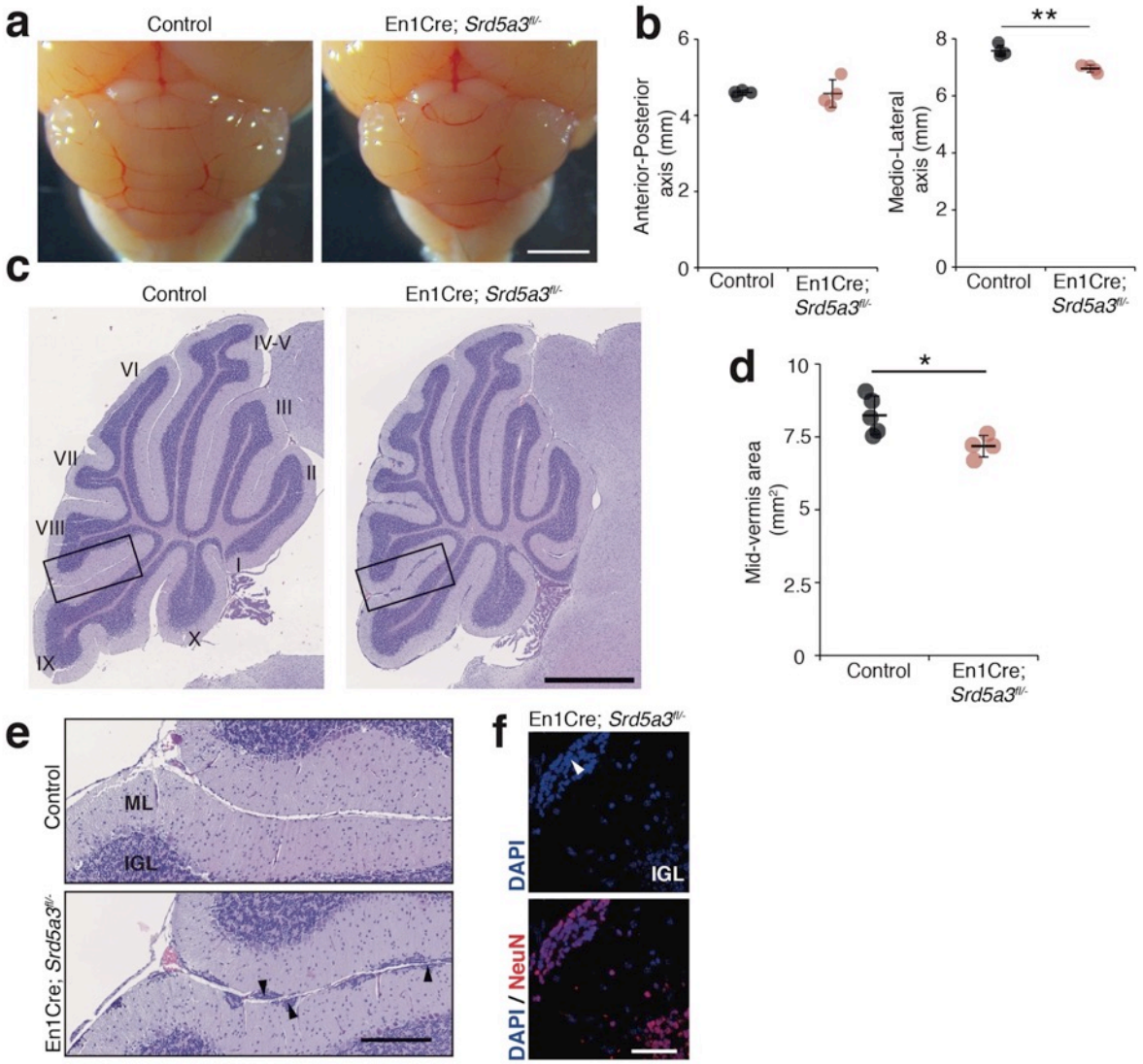

Figure 19. Reduced cerebellum size and ectopic granule neurons in the *Srd5a3* mutant. (a) Dorsal view of P21 posterior brains, scale bar 2mm. (b) Quantification of the cerebellar anterior-posterior and medio-lateral axes (n=4 for each genotype), ** p-value=0.0018. (c) Representative images of hematoxylin-eosin (HE) stained P21 sagittal slices of control and mutant cerebella, scale bar 1mm. Lobule numbers are indicated. (d) Quantification of the mid-vermis area in sagittal slices (Control, n=5; En1-Cre; *Srd5a3*$^{fl/-}$, n=4); *p-value=0.0245. (e) Magnification of HE-stained cerebellar cortex, scale bar 200µm. All examined mutants show ectopic cell clusters (arrow-head) in the outer part of the molecular layer (ML). (f) DAPI (blue) and NeuN (red) staining of P21 En1-Cre; *Srd5a3*$^{fl/-}$ cerebellum. Ectopic cells (arrow-head) are positive for the post-mitotic GCs marker NeuN, scale bar 50µm. Two-tailed student t-test was used for statistics. * $p<0.05$; ** $p<0.01$. Results are presented as mean ± s.d.

Our examination of the two other major cerebellar cell populations, Purkinje cells (PCs) and Bergman glia (BG), did not reveal major cellular defects (Figure 20a, b). Cerebellar development relies on key glycosylated proteins expressed and secreted by PC or BG cells, such as Shh[33] or dystroglycan[40]. So, we investigated the origin of the identified GCs

ectopia. We deleted *Srd5a3* using a GC-specific cre line (Atoh1-Cre)[203] (Figure 20c). Atoh1-Cre; *Srd5a3*$^{fl/fl}$ mice exhibit similar GC ectopia, which indicates that a GC-autonomous defect underlies the formation of these ectopic cell clusters (Figure 20d). Taken together, our results support a critical role for *Srd5a3* during cerebellar granule cells development likely through a GC-autonomous glycosylation impairment of specific, but undetermined, proteins.

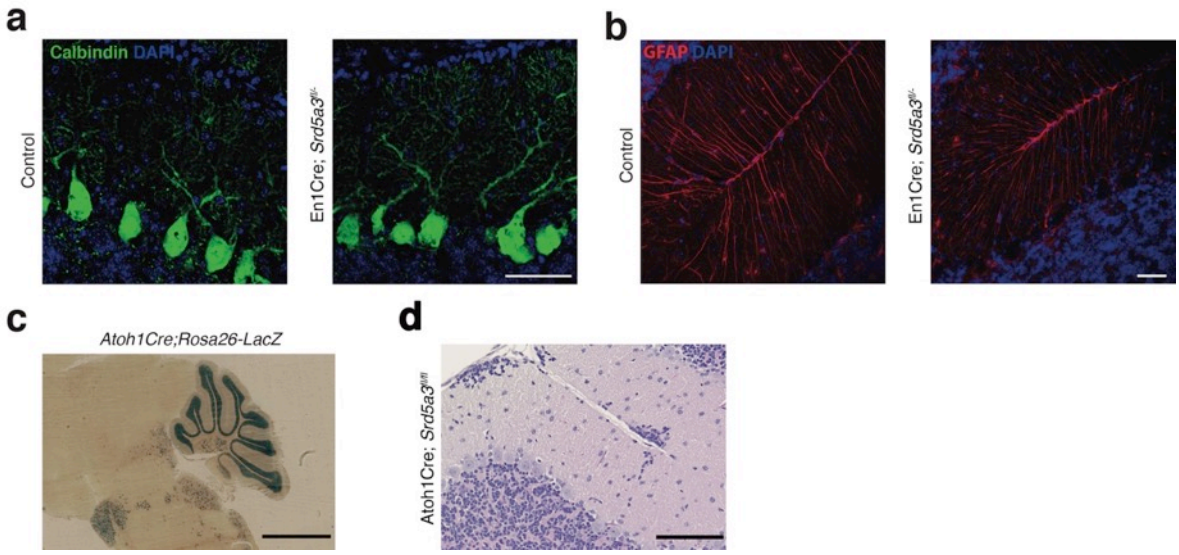

Figure 20. Histological analysis of Purkinje cells (PCs) and Bergmann glia (BG). (a) Representative immunohistochemical staining of control and mutant PCs (Calbindin, P14) and (b) BG (GFAP, P21). Scale bar 50µm. (c) LacZ staining image of the Atoh1Cre; Rosa26-LacZ. Scale bar 2mm. (d) Representative image of an HE-stained sagittal slice of Atoh1-Cre; *Srd5a3*$^{fl/fl}$ cerebellum showing similar ectopic cells in the outer ML under GC-specific *Srd5a3* deletion, scale bar 100µm (n=2).

2 Biochemical and molecular characterization of the mechanisms underlying the cerebellar defect

Context: No study has yet evaluated in-depth the molecular impact of partial protein N-glycan loss. In 2010, Mann and colleagues developed a novel technique to evaluate protein N-glycosylation site occupancy[204]. Relative to other published techniques[205,206], this approach detected the highest number of N-glycosylation sites together with a relatively simple design. Their approach could detect up to 3162 N-glycosylation sites within 1296 N-glycoproteins in the brain. Moreover, they showed how their technique also enriches in N-glycoproteins: 58% of the N-glycoproteins detected by glycoproteomics could not be detected by regular proteomics. Nevertheless, to our knowledge, such a promising technique has not yet been applied to a CDG model. The use of this technique, together with total proteomic and transcriptomic profiling should allow the first in-depth molecular analysis of the *in vivo* consequences of sub-optimal protein N-glycosylation.

Cerebellum-specific Srd5a3 deletion decreases the levels of highly glycosylated proteins

We investigated the molecular mechanisms underlying our observed cerebellar defect by conducting a total proteomic analysis on the developing P7 mouse cerebellum[207,208]. This approach quantified 1982 proteins, whose abundance profiles can cluster each sample by genotype (Figure 21a, Table S1). Our statistical analysis identified 97 differentially abundant proteins (DAP) (≈ 5% of the total; q-value < 0,05) in the En1-Cre; *Srd5a3*$^{fl/-}$ mice (Figure 21b). To determine the deregulated pathways among the highly active, neural development pathways at this stage, we performed an over-representation analysis of the 97 DAP using ConsensusPathDB. Our analysis indicated that different pathways involved in ion and amino acid transport, synapse function, cell adhesion-related signaling and cholesterol biosynthesis interplay to generate the mouse phenotype (Figure 21c). Aside from changes in cholesterol metabolism, all enriched pathways contained at least one deregulated N-glycoprotein. Protein N-glycosylation is critical for ER-protein folding, however we did not find any enrichment in the ER stress pathway.

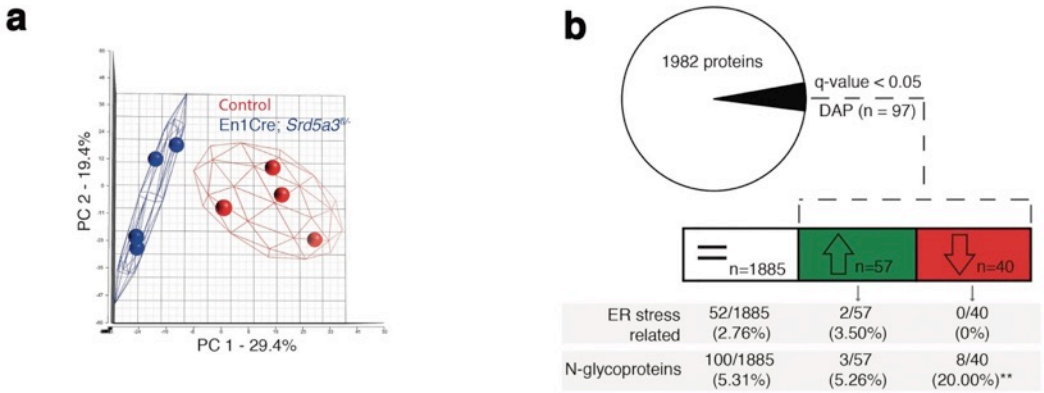

c

Pathway name	p-value	Deregulated proteins
Nicotine addiction	0.00233	SLC32A1 and GRIA2
Transport of inorganic cations/anions and amino acids/oligopeptides	0.00516	SLC32A1, SLC4A10 and SLC1A4
NCAM1 interactions	0.00677	NCAM1 and CNTN2
Superpathway of cholesterol biosynthesis	0.00748	ACAT2, PMVK and DHCR7
Glioma	0.00753	CALM1, PRKCG, NRAS and MTOR
Long-term potentiation	0.00820	CALM1, PRKCG, NRAS, GRIA2 and PPP1CA
Amphetamine addiction	0.00933	CALM1, PRKCG, GRIA2 and PPP1CA

Figure 21. Disrupted neural pathways in the *Srd5a3* mutant developing cerebellum. (a) Principal component analysis (PCA) based on the abundance profiles of the 1982 detected proteins. (b, upper

panel) Pie chart representing the total proteomics analysis in P7 cerebellum (n=4 for each genotype). 97 proteins were detected as differentially abundant proteins (DAP) in the mutant samples (q-value<0.05). (b, lower panel) Distribution of unchanged proteins (white box), increased DAP (green box) and decreased DAP (red box) into ER stress-related (GO:0034976) or N-glycoproteins (Reference glycoproteomic database, see method) categories. A significant enrichment was detected within the decreased DAP for N-glycoproteins (n=8, Fisher exact test, p-value=0.0012). (c) Over-representation analysis on DAP performed with ConsensusPathDB using the 1982 detected proteins as background. All pathways with p-value<0.01 are represented. N-glycoproteins are indicated in green.

Manual inspection of the 97 DAP revealed increased levels of only two ER-stress-related proteins, SDF2L1[209] and HYOU1[210], while BiP, the classical ER-stress marker[211], showed a 1.3 fold non-significant (q=0.08) increase (Table S1). We then performed a transcriptomic study on additional samples at the same stage, which confirmed the absence of any significant deregulation of the most widely used UPR markers (Figure 22a,b). In addition, we did not observe any change in BIP levels restricted to ectopic GC clusters (Figure 22c). Surprisingly, our results exclude a main effect of deregulated N-glycosylation processes on ER stress.

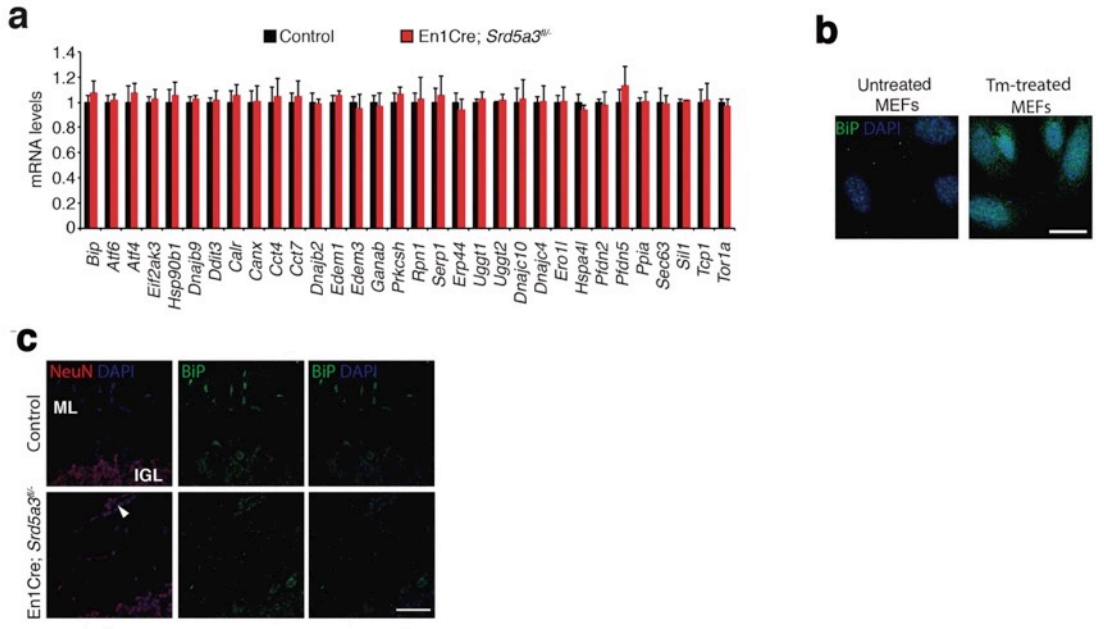

Figure 22. Extended total proteomic analysis of the unfolded protein response (UPR). (a) Transcriptomic analysis of UPR-related mRNAs in the control (n=4) and mutant (n=4) cerebellum. (b) Immunocytochemistry against BiP in MEFs treated with tunicamycin (Tm) for 24h to induce UPR activation and BiP expression (positive control) in mouse cells. Scale bar 25µm. (c) Immunohistochemistry against BiP and NeuN in the P21 mouse cerebellum. The arrowhead points to ectopic GCs. Scale bar 50µm. Two-tailed student t-test was used for statistics. Results are presented as mean ± s.d.

One possible consequence of defective protein N-glycosylation is decreased stability of hypoglycosylated proteins. We observed a significant, 4-fold enrichment of N-glycoproteins among the DAP with decreased levels (simplified as decreased N-glycoproteins; p=0.0012, Figure 21b). Examining this group of decreased N-glycoproteins revealed that they have more N-glycosylation sites (i.e. higher site multiplicity) with an average of 5.57 sites versus 3.24 in unchanged N-glycoproteins (Figure 23a). Indeed, N-glycoproteins with 4 or more N-glycosylation sites within the decreased N-glycoproteins show significant enrichment (Figure 23b). These data demonstrate that the mild glycosylation defect detected in the *Srd5a3* mutant cerebellum disrupts the levels of highly glycosylated proteins, but does not disrupt ER homeostasis.

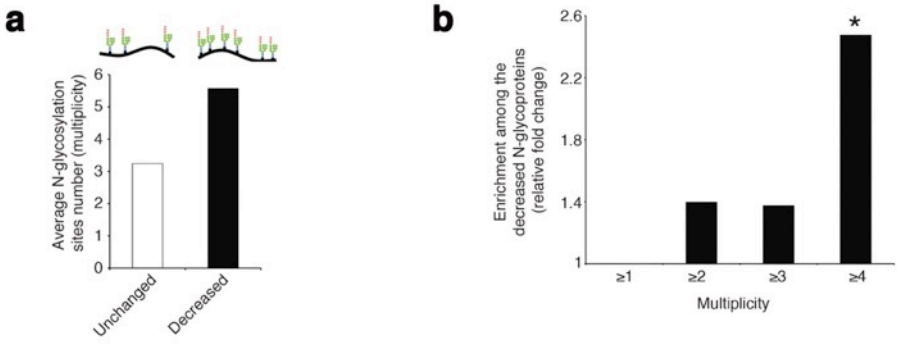

Figure 23. Highly N-glycosylated proteins are sensitive to an N-glycosylation impairment. (a) Average multiplicity in the unchanged and the decreased N-glycoproteins groups. (b) Enrichment for different glycoprotein categories among the decreased N-glycoproteins. Multiplicity represents groups of proteins with more than one (≥2), two (≥3) or three (≥4) N-glycosylation sites. Multiplicity of ≥1 represents all of the decreased N-glycoproteins and is set to one (no enrichment). There is a significant 2.4 fold-change enrichment for glycoproteins with 4 or more N-glycans among the decreased N-glycoproteins (Fischer exact test, p-value=0.0378).

N-glycosylation site multiplicity and primary sequence underlies the selective protein glycosylation defect

To further elucidate the N-glycosylation deficiency, we included a lectin-affinity based (ConA, WGA, RCA_{120}) enrichment step at the peptide level, followed by deglycosylation[204], prior proteomic analysis (Figure 24a). This enrichment can identify N-glycosylation sites and quantify the abundance of each site when they are glycosylated. Using this dataset, we identified 140 likely new glycosylation sites (≈8% of the total, see method, Table S2) with high recurrence of non-canonical sequons (≈40%

of the new sites, Table S2). Consistently, most proteins carrying these sites have been described as being part of the secretory pathway. Additionally, none is described as being located in the cytoplasm (Gene Ontology analysis in Table S2). In total, we identified 1404 glycopeptides detected in at least 3 out of 4 control samples (Figure 24b, Table S2). As we observed for the total proteome, we could cluster the expression levels of all the glycopeptides according to the genotype (see method, Figure 24c). Total proteomics and glycoproteomic analysis yielded complementary information. Total proteomics provides information of the protein abundance level but can only detect peptides containing an unoccupied N-glycosylation site. Glycoproteomics only allows detection of glycopeptides if the site is occupied. For 15% of the N-glycopeptides detected in glycoproteomics (n=206), we found decreased levels in the mutant samples. Of these, we only detected 24 N-glycopeptides in the previous total proteomic experimental settings, consistent with the high enrichment observed with the glycoproteomics analysis (Figure 24d, Table S3). Among these peptides 13 were never detected in control but only in mutant samples in total proteomics. These data indicate that they were not glycosylated in the mutant. We conclude that most differences we detected in the glycoproteomic experiment reflect reduced glycosylation site occupancy.

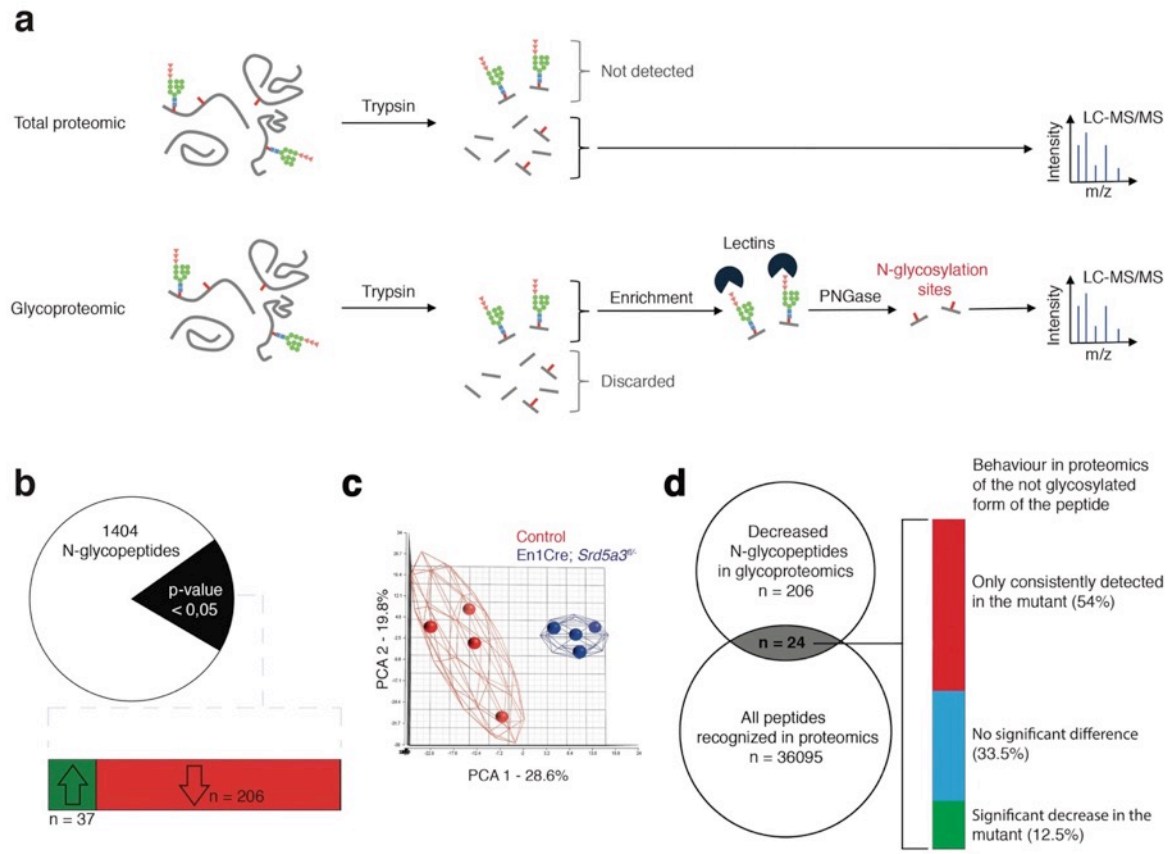

Figure 24. Glycoproteomic analysis results and validation. (a) Outline of the total proteomic and glycoproteomic techniques. In regular total proteomics, the proteins are digested into peptides by trypsin. Peptides containing an N-glycan chain cannot be recognized by LC-MS/MS due consequent changes in ion charge and mass. Only the not glycosylated form of the peptide is recognized, if it exists. In glycoproteomics, only the N-glycosylated peptides will be retained (lectin enrichment). After the glycopeptide is released by PNGase treatment, the resulting peptides are then analyzed by LC-MS/MS. (b) Pie chart representation of the glycoproteomic analysis in P7 cerebellum (n=4 for each genotype). The vast majority of the differentially abundant N-glycopeptides was decreased in the mutant samples (206/241, 85%). (c) PCA based on the MS intensities of the 1404 N-glycopeptides consistently detected in control samples. (d) Qualitative behavior of N-glycopeptides with lower abundance in mutant samples (glycoproteomics analysis) and also detected in the total proteomics analysis. Total proteomics analysis detected most of the peptides (54%) only in the mutant samples, a result consistent with constant glycosylation site occupancy in controls and hypoglycosylation in mutants.

We also detected an extremely significant correlation between N-glycan multiplicity and N-glycopeptide levels (Figure 25a, Mann-Whitney test, p-value<0.0001). This result is consistent with our larger glycoprotein dataset. To delineate the origin of reduced occupancy of individual N-glycosylation sites, we analysed their primary sequences (Figure 25b). We identified a mild effect of the presence of a non-aromatic amino-acid (other than Phe, Tyr, His or Trp) at position -2 and a more significant effect of the Serine at position +2 (Figure 25c), as previously described[212,213], with an increased impact in highly glycosylated proteins (Figure 25d). These findings demonstrate that N-glycan

multiplicity combined with sequon efficiency is a major parameter driving protein sensitivity to N-glycosylation defects.

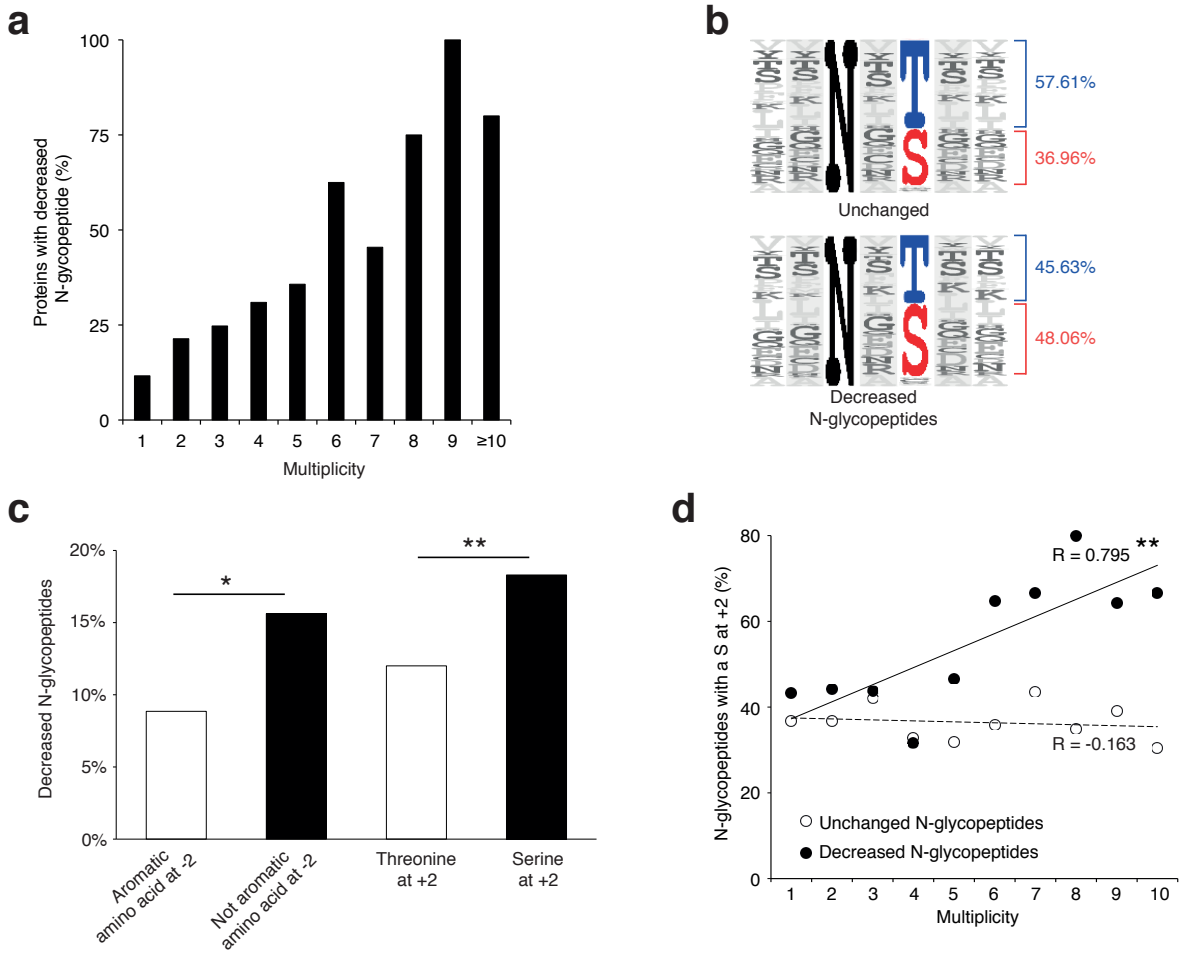

Figure 25. *Srd5a3* deletion impairs protein N-glycosylation in a sequon and multiplicity-dependent manner. (a) Percentage of proteins with decreased N-glycopeptide categorized according to their multiplicity (Mann-Whitney test, p-value<0.0001). Proteins with higher multiplicity are more likely to have decreased N-glycopeptide levels. (b) Motif analyses of the N-glycopeptides unchanged or decreased in the mutant. (c) Significant enrichment within the decreased N-glycopeptides for a non-aromatic amino acid (other than Phe, Tyr, His or Trp) in position -2 and a Ser in position +2 (NxS motif). (d) Correlation between protein multiplicity and their percentages of decreased (black) or unchanged (dashed line) glycopeptides with NxS sequon in the mutant samples. A significant positive correlation was found between the NxS-containing glycopeptides decreased occupancy in the mutant and their N-glycoprotein multiplicity (Pearson's coefficient, p-value=0.0062). NxS-containing N-glycopeptides are more likely to lack the glycan chain when located in a highly glycosylated protein. Unless indicated, two-tailed T student was used for statistics. * p<0.05; ** p<0.01.

IgSF-CAMs are highly sensitive to sub-optimal protein N-glycosylation

We next wanted to delineate the affected pathways based on our glycoproteomic results. We performed an over-representation analysis using proteins carrying at least one N-

glycopeptide significantly decreased in mutant samples (145 N-glycoproteins, 206 N-glycopeptides). This analysis revealed that the most significantly affected proteins (4 out of the top 10 deregulated pathways) derive directly from cell adhesion and axon guidance-related pathways involving adhesion proteins from the L1CAM family (Figure 26a, red circles). L1CAMs and the previously identified NCAM1 and CNTN2 (Figure 21c) belong to the immuno-globulin superfamily of cell adhesion proteins (IgSF-CAMs) with critical roles in brain development[214–216]. We speculated that this particular sensitivity of IgSF-CAMs to a N-glycosylation defect arises from their higher N-glycosylation site multiplicity with an average of 3.3 sites versus 2.3 in non IgSF-CAM proteins (Calculated based on the reference glycoproteomic dataset, Table S2, Mann Whitney test, p-value < 0.0001).

So, we next hypothesized that impaired IgSF-CAMs function derived from sub-optimal N-glycosylation and that defective IgSF-CAMs contributed to our observed histological defect. We confirmed our observed enrichment for IgSF-CAMs found in our over-representation analysis at the N-glycopeptide level (18.4% of the decreased N-glycopeptides belong to an IgSF-CAM protein, Fisher exact test, p-value=0.0058, Figure 26b). We selected two highly N-glycosylated IgSF-CAMs relevant for the granule cell histological phenotype for validation by WB. We did observe a clear hypoglycosylation defect for L1CAM and NrCAM with a detected shift to lower molecular weights and a significant decrease in the glycosylation-dependent cleavage of L1CAM[217] (Figure 26c,d).

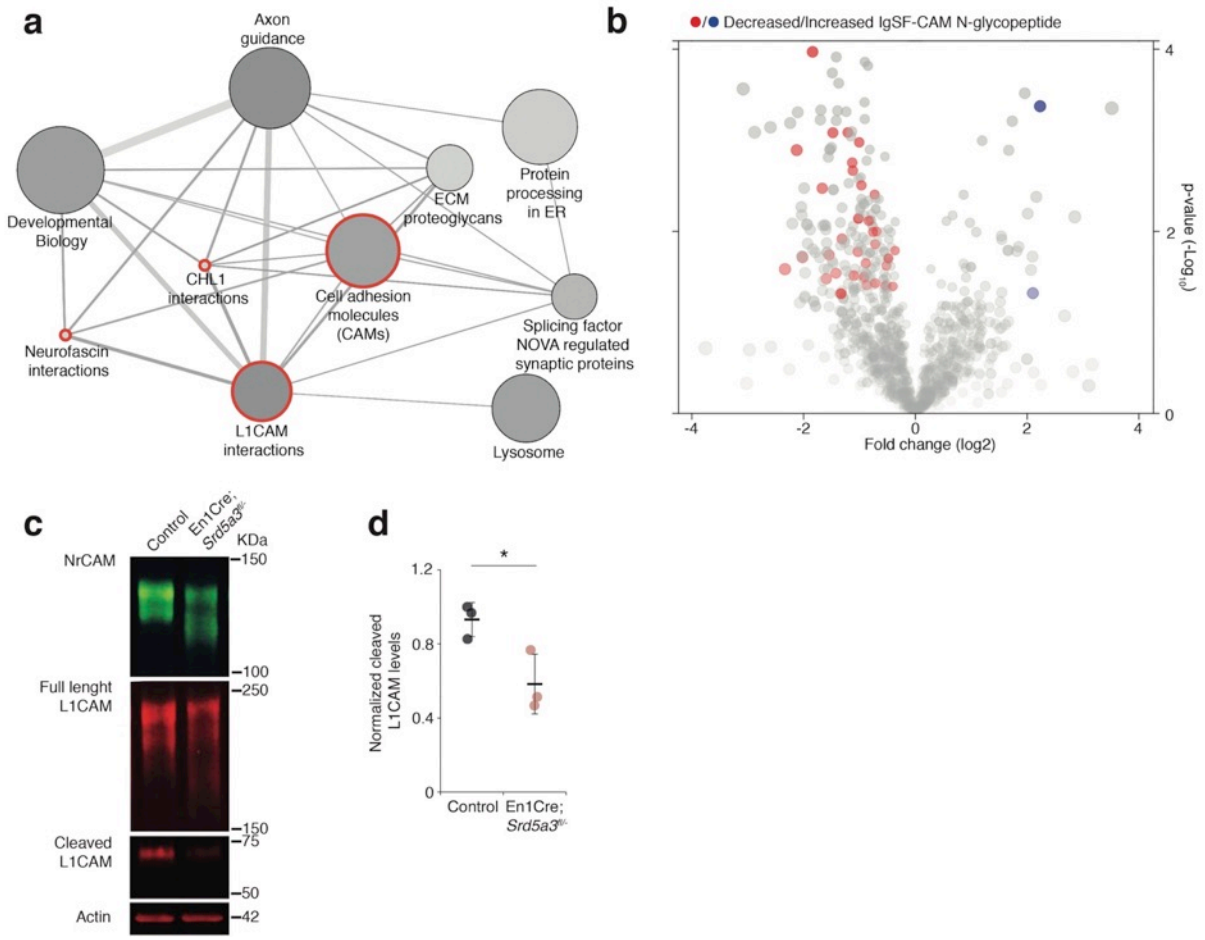

Figure 26. IgSF-CAMs are especially sensitive to a mild N-glycosylation impairment. (a) Graphical representation of enriched pathways and their interactions within proteins with reduced N-glycopeptide in the mutant (ConsensusPathDB). The nodes size indicates the number of proteins within the pathway, and their colour notes the significance (the darkest, the more significantly enriched). Red circles enclose the L1CAM family-related pathways. (b) Volcano plot against all N-glycopeptides. The decreased (red) or increased (blue) N-glycopeptides belonging to an IgSF-CAM protein are highlighted. There is enrichment for IgSF-CAMs glycopeptides within the decreased ones (Fisher exact test, p-value=0.0058). (c) WB against L1CAM and NrCAM in the P7 mouse cerebellum and (d) quantification of the 70KDa cleaved isoform of L1CAM (n=3 for each genotype, p-value=0.0312). Unless indicated, two-tailed T student was used for statistics. Results are presented as mean ± s.d. * p<0.05.

Srd5a3 loss likely impacts glycan composition

Besides the role of dolichol (Dol) in glycan anchoring and transfer, the glycan carbohydrate composition also relies in Dol function. Once the Dol-PP-($GlcNAc_2Man_5$) structure is translocated to the inner part of the ER, addition of 4 Man and 3 Glc is necessary to form the full core glycan, which will be after transferred in-block to the nascent proteins. Inside the ER, Dol also acts as a cargo for those activated sugars (Dol-P-Man and Dol-P-Glc). Indeed, out of the 8 Dol needed to build the LLO, only 1 is used as carrier of the full glycan whereas 7 are used to build the core glycan.

This suggests that defective Dol synthesis might also lead to aberrant core glycan synthesis. This possibility was evaluated in patient fibroblasts in the first SRD5A3-CDG report, but no aberrant glycan structures were found[175]. Further analysis of other SRD5A3-CDG patient fibroblasts by Dr. François Foulquier showed an increase in the $GlcNAc_2Man_5$ (Man5 for abbreviation) glycan amount in patient cells (unpublished data). These results are not conclusive enough and thus an evaluation of this trait in our model may help to understand the impact of *SRD5A3* mutations in the glycan composition.

To evaluate the possibility of an aberrant glycan configuration in addition to the partial glycan loss, the precise glycan composition was evaluated in MEFs (Figure 27a). François Foulquier and colleagues (glycobiology department of Lille university, UMR-8576) performed this work. The N-linked oligosaccharides (NLO, once attached to the proteins) were measured by metabolic labelling followed by high-performance liquid chromatography (HPLC). An accumulation of ≈30% of Man5 glycans was detected in the mutant cells. This result is consistent with the need of Dol-P-Man to convert the Man5 structures into Man9, prior to Glc addition.

We next investigated if this overrepresentation of Man5-type glycans was also present *in vivo*. To do so, we treated the mouse cerebellar protein extracts with EndoH. EndoH will only cleave the glycan when it is mannose-rich or contains at least one branch that ends in a Man (hybrid glycan). EndoH will have no effect when the attached glycan is complex (i.e. both terminal Man residues are further modified by the addition of other monosaccharides). We next evaluated the behaviour of LAMP1 under this treatment. LAMP1 has a mix of high-mannose, hybrid and complex glycans[218]. Consistently, in the EndoH-treated control samples treated we observed a mix of completely de-glycosylated LAMP1 (lower band, 2) and a more prominent band not fully de-glycosylated (1). The highest band is likely to belong to LAMP1 molecules with complex glycan chains that cannot be cleaved by EndoH (Figure 27b,c). We detected a relative increase in the fully de-glycosylated glycoform in the mutant samples treated with EndoH. This relative increase is likely to be caused by an increase in mannose-rich and/or hybrid glycan chains, such as Man5, in mutant LAMP1.

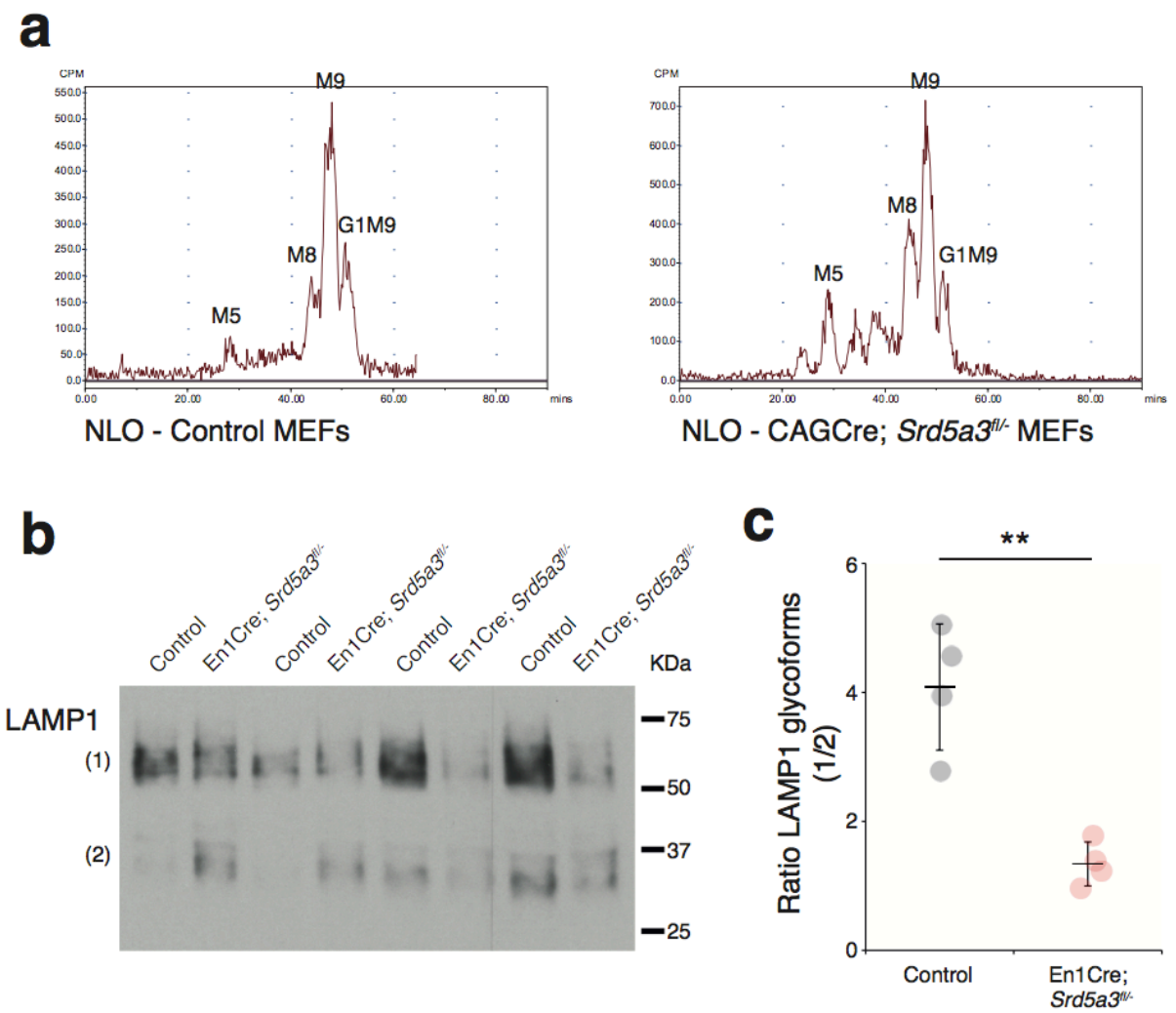

Figure 27. Defective Dol biosynthesis impacts the composition of the core oligosaccharide. (a) Quantification of the N-linked oligosaccharide (NLO) in control and mutant MEFs. (b) WB against LAMP1 in EndoH-treated samples. (1) indicates the partially de-glycosylated form of LAMP1 and (2) the fully de-glycosylated one. (c) Quantification of the LAMP1 glycoform 1 / glycoform 2 ratio in control and mutant samples (n=4 per genotype). ** p-value < 0,01

3 Impact assessment of the molecular findings

Context: Glyco/proteomic analyses point to the highly N-glycosylated IgSF-CAMs as being exquisitely sensitive to the metabolic defect. However, to extrapolate these results to the human physiopathology, further confirmation in human cells is necessary. Nowadays, the most frequently used protocol to produce human neurons "in a dish" goes trough generation of human induced pluripotent stem cells (hiPSCs). Those cells can be potentially differentiated into almost any cell type. Due to the difficulty to access to the affected tissue in neurological diseases, such possibility provides a unique opportunity to generate the desired neural cell type *in vitro*. This technology, together with CRISPR/Cas9 allows the generation of isogenic mutant and control neurons[219]. Such possibility eliminates any bias related to the patients' background thus allows precise evaluation of the impact of SRD5A3 loss in a consistent human cell model.

Even if we find IgSF-CAMs to be sensitive to N-glycosylation block also in human neurons, the consequences of the glycan loss are yet to be elucidated. Few reports have investigated the role of specific N-glycosylation sites in some IgSF-CAMs such as L1CAM[220]. However, in our case, L1CAM and NrCAM WB analyses suggest that loss of SRD5A3 does not always lead to the hypoglycosylation of the same N-glycosylation site. This point is illustrated by the observed smear including the fully glycosylated isoforms and other glycoforms with variable glycosylation status. To our knowledge, the functional implications of variable glycosylation status have never been reported. It is then necessary to functionally validate if IgSF-CAMs variable hypoglycosylation leads to a defect in neuronal cell adhesion or not.

IgSF-CAMs sensitivity to N-glycosylation defect is conserved in mammals

A major role for IgSF-CAMs in mammalian development is illustrated by the increased number of their encoding genes across evolution[221]. We also observed an increased in the N-glycan multiplicity for three IgSF-CAM families with critical roles in brain development (Figure 28a). To test if the IgSF-CAM sensitivity for glycosylation impairment is conserved, we generated *SRD5A3* knockout (KO) human induced pluripotent stem cells (hiPSCs). We then differentiated them toward cortical projection neurons (CPNs, Figure 28b,c,d). As previously observed in mouse, human L1CAM and NrCAM immuno-blotting profiles exhibit clear shifts in *SRD5A3*$^{-/-}$ CPNs (Figure 28e). These data demonstrated a similar exacerbated sensitivity of IgSF-CAMs to SRD5A3 loss in human neural progenitors. Our data suggest that the high multiplicity of N-glycosylation sites in IgSF-CAMs play a conserved and critical role for proper function during mammalian brain development.

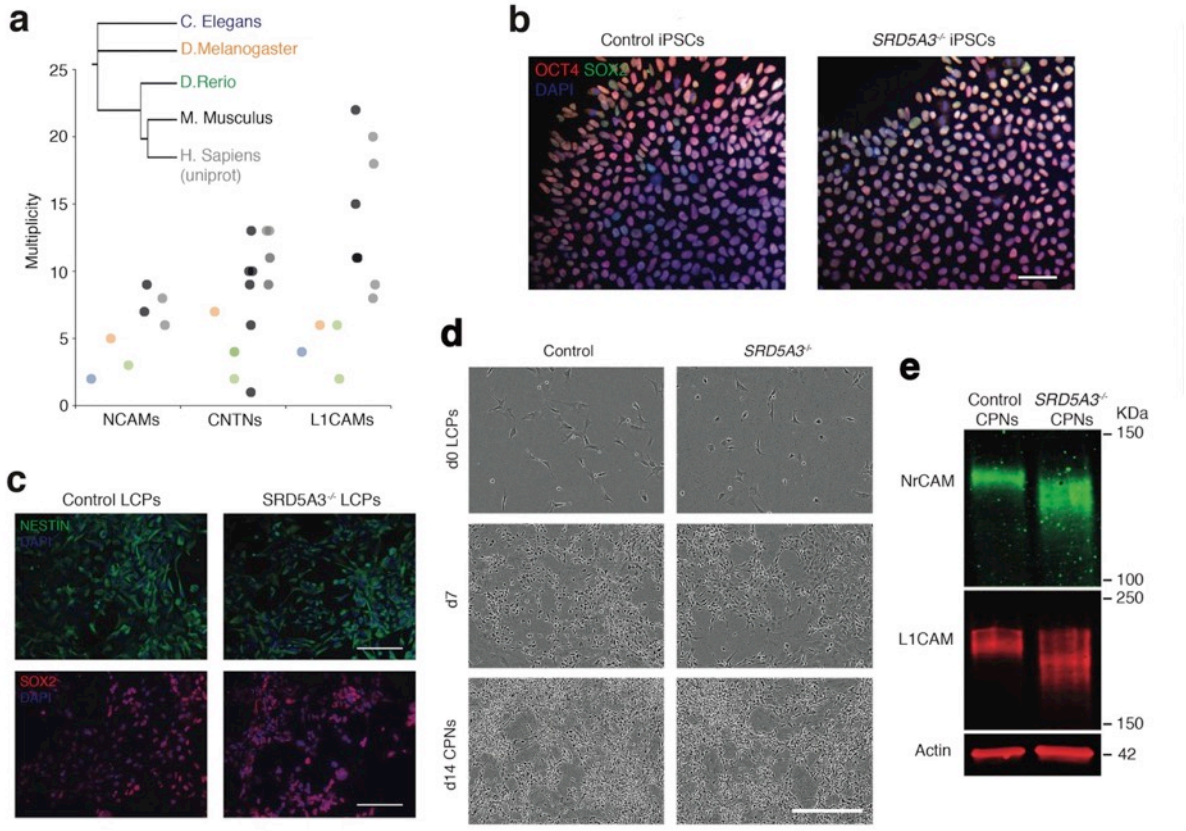

Figure 28. IgSF-CAMs sensitivity in a CDG type I context is conserved in human neurons (a) Multiplicity per protein of three IgSF-CAMs subfamilies (L1CAMs, CNTNs and NCAMs) in different species. Multiplicity information was collected from experimental datasets (Zielinska et al, 2010 and Zielinska et al, 2012) except for human information extracted from uniprot database (b) hiPSCs stained for the undifferentiation/pluripotency markers SOX2 and OCT4. (c) hiPSCs differentiated towards late cortical progenitors (LCPs, see method) and stained against Nestin and SOX2. Scale bar 100µm. (d) Representative images of control and *SRD5A3*$^{-/-}$ LCPs differentiation towards cortical projection neurons (CPNs, see method). Scale bar 300µm. (e) WB analysis of L1CAM and NrCAM levels in CPNs.

Srd5a3 is necessary for IgSF-CAM-dependent cerebellar granule cells adhesion and axon guidance

IgSF-CAMs rely on their glycan charge to interact with each other[222,223]. Proper IgSF-CAMs trans-interaction is essential for adequate nervous system connectivity for fasciculation and axonal guidance[216]. To demonstrate that IgSF-CAMs hypoglycosylation is directly involved in En1-Cre; *Srd5a3*$^{fl/-}$ mouse phenotype, we examined the neurite dynamics of GC re-aggregates on a coating with IgSF-CAM substrate (CNTN2, see method). We found a major defect in both neurite extension and number (Figure 29a). To quantify this defect, we used live cell imaging with isolated GCs cultured under different surface coating conditions. *En1-*

Cre; Srd5a3$^{fl/-}$ GCs did not show any major alterations that suggested differences in proliferation or cell death under any coating (Figure 29b). In contrast, GCs showed a 20% decrease in neurite sprouting under regular coating conditions (i.e. laminin with D-lysine) (Figure 29c,d). This phenotype is exacerbated in the presence of coatings that enhance IgSF-CAMs homophilic interactions (i.e. human recombinant L1CAM or NrCAM proteins)[224]. These results show a 37 and 52% decrease in neurite number compared to control GCs, respectively (Figure 29e). These results support our premise that IgSF-CAMs hypoglycosylation regulates cell adhesion. Given the prominent role of many IgSF-CAMs in axon guidance and the granule cells adhesion defect, we examined axon orientation in GCs. We analyzed the parallel fibres (PFs) organization in the cerebellar ML using electronic microscopy. In control samples, PFs are consistently oriented perpendicular to PCs branches. However, *Srd5a3* mutant mice exhibit an aberrant orientation of groups of PFs in the outer ML, likely due to defective axonal guidance (Figure 29f,g). Taken together, our data suggest that IgSF-CAMs hypoglycosylation may underlie many neurological defects in CDGs.

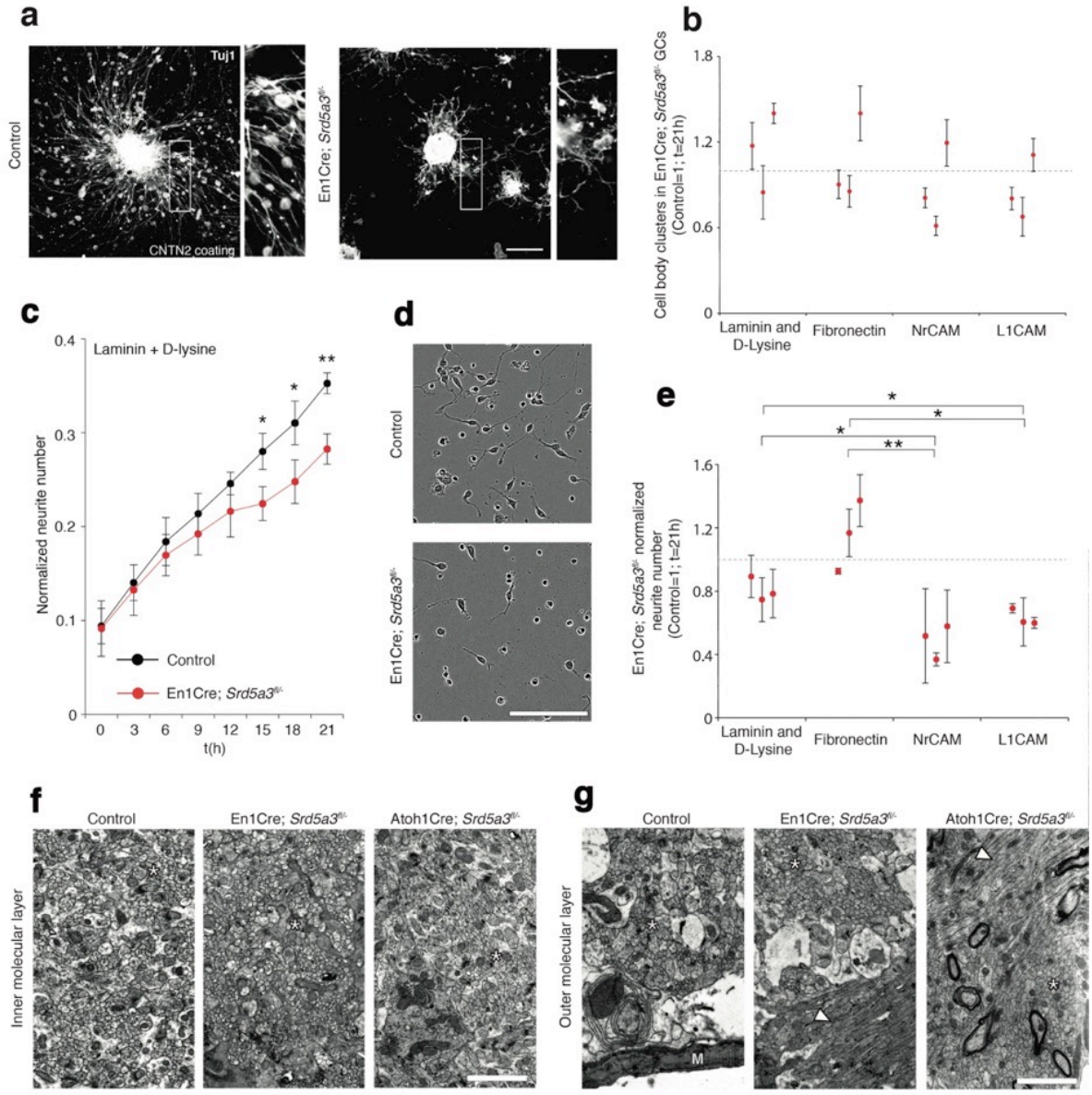

Figure 29. IgSF-CAM-dependent neurite dynamic and axon orientation defects in *Srd5a3* mutant cerebellum. (a) Representative images of GC re-aggregates seeded for 36h on an IgSF-CAM-coated surface (CNTN2) and stained for Tuj1 in control (n=2) and mutant (n=2). Scale bar 200µm. (b) GC body cluster number after 21h with laminin/D-lysine coatings, fibronectin or IgSF-CAMs-coated wells (NrCAM and L1CAM) and normalized to control littermates. Each dot per coating represents results from a single mutant mouse. All GC cultures were performed in technical triplicates (n=3 for each genotype). (c) Neurite number per GC body cluster across 21h in laminin and D-lysine coated wells as measured with Incucyte live cell imaging system (Control, n=3; En1-Cre; *Srd5a3*$^{fl/-}$, n=3). (d) Representative image of control and En1-Cre; *Srd5a3*$^{fl/-}$ GCs after 21h in laminin and D-lysine-coated wells. Scale bar 100µm. (e) Neurite number normalized to GC body clusters after 21h with laminin/D-lysine coatings, fibronectin or IgSF-CAMs-coated wells (NrCAM and L1CAM). Each dot per coating represents results a single mutant mouse (Control, n=3; En1-Cre; *Srd5a3*$^{fl/-}$, n=3). (f) Representative electron microscopy images of cerebellar middle ML or (g) outer ML Sagittal view at P21 taken from control (n=3) and *Srd5a3* mutant (En1-Cre; *Srd5a3*$^{fl/-}$ n=1; Atoh1-Cre; *Srd5a3*$^{fl/-}$ n=2) mice. Scale bar 2µm. Parallel fibres show a single orientation in control ML (asterisk in the mutant), whereas some exhibit an abnormal perpendicular orientation in the outer ML in the mutant mice (arrow-head). Two-tailed student t-test was used for statistics. * $p<0.05$; ** $p<0.01$. Results are presented as mean ± s.d.

4 Rescue of the defect

Context: My work provides evidence into the physiopathology underlying CDG type I and illustrates the importance for adequate neuronal adhesion of proteins with high N-glycan multiplicity. Additionally, our results demonstrate the cerebellar *Srd5a3* cKO as a valuable CDG type I model. This model, together with the *SRD5A3*$^{-/-}$ hiPSCs, could further be used for therapy testing. Regarding CDG type I caused by aberrant lipid synthesis or further Dol modification (ex. Dol-P-Man synthesis), it has been hypothesized that enhancement of Dol biosynthesis shall alleviate the molecular consequences[225,226]. As previously described[227], SRD5A3-CDG patients still synthesize Dol through an unknown alternative pathway. Stimulation of *de novo* lipid synthesis could potentially stimulate this alternative pathway and thus lead to an increased Dol synthesis, a consequent increase in LLO abundance and an improved protein N-glycosylation.

De novo lipid synthesis improves Srd5a3 loss-related protein hypoglycosylation

In order to try to ameliorate the defective dolichol biosynthesis in the *Srd5a3* cKO mouse, we next aimed to induce *de novo* lipid synthesis from mevalonate to dolichol. To do so, we removed the external source of lipids from the MEFs culturing media (FBS) and replace it with Ultroser G (UG), a lipoprotein-free serum[228,229]. Importantly, cell cultured with UG as the only source of lipids has already been proved to efficiently enhance *de novo* lipid synthesis[228]. Mutant and control MEFs were cultured for 2 and 6 days in FBS-free media and the efficacy of UG to induce *de novo* lipid synthesis was confirmed by qPCR against two enzymes of the mevalonate pathway, Hmgcr and Hmgcs1 (Figure 30a). Consistent with the proteomic results in the mouse cerebellum (Figure 21c), we detected increased steady-state Hmgcr and Hmgcs1 mRNA levels in the mutant MEFs. UG efficiently increased the expression levels but only for a short period of time. Indeed, after 6 days in FBS-free culture media, the enzymes were expressed at levels similar to the ones before treatment. We then used LAMP1 as a read-out to evaluate the treatment pertinence to ameliorate protein hypoglycosylation (Figure 30b,c). We found an apparent increase in LAMP1 N-glycosylation in the mutant MEFs after 2 days of treatment. Such increase disappeared after 6 days, as the enzymes' overexpression did.

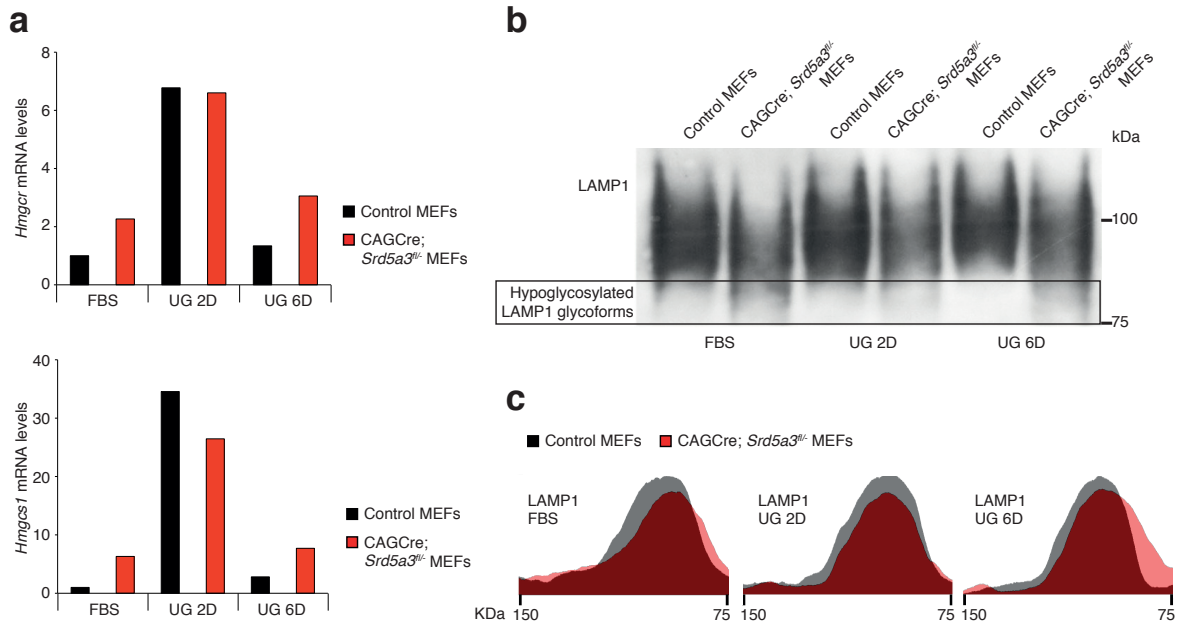

Figure 30. Increased lipid synthesis partially recovers LAMP1 hypoglycosylation in Srd5a3-deficient MEFs. (a) qPCR analysis of control and mutant (CAGCre; *Srd5a3*$^{fl/-}$) MEFs of the mevalonate pathway enzymes Hmgcr (top) and Hmgcs1 (bottom) under different culture media. UG treatment was performed for 2 (2D) or 6 days (6D). (b) LAMP1 WB in MEFs cultured with FBS or UG. (c) Lane plots of the above WB, generated with ImageJ, showing the hypoglycosylated form of LAMP1 in the mutant MEFs (arrows), almost inexistent after 2 days in culture with UG.

5 Retrospective analysis and future directions

Context: Collectively, our data pointed to protein hypoglycosylation as the main trigger of the CDG physiopathology. Moreover, by combination of glycoproteomics and total proteomics we prove highly N-glycosylated proteins to be more sensitive to the defect. Pathway analysis on the potentially hypoglycosylated proteins pinpointed to IgSF-CAMs as being the protein family the more affected in a cerebellar context. Additional functional work supported this hypothesis and proved their hypoglycosylation as a major trigger of the neurological defects. However, we did not observe major deregulation at the transcript level and neither not a major change in IgSF-CAM protein abundance. In light of these results, we decided to reanalyse the transcriptomic and total proteomics data to further characterize N-glycoprotein-coding mRNAs and IgSF-CAM protein abundance in the mutant cerebellum.

The finding of the more N-glycosylated proteins being one of the main triggers of the cerebellar-associated pathology suggests that a similar mechanism could also underlie CDG type I defects in other tissues. Investigation of other tissues physiopathology is out of the scope of my thesis. However, relatively simple preliminary results can be obtained combining Mann's mouse N-glycoproteome database[204] with our findings.

N-glycoprotein-coding mRNAs are deregulated under N-glycosylation blockage

No major deregulation in the En1Cre; *Srd5a3*$^{fl/-}$ mouse transcriptome was found, relative to the results obtained in total proteomics and glycoproteomics. While around 17.5% of the proteome and N-glycopeptides showed differential abundance in the mutant cerebellum, only 2.5% of the mRNAs did (p-value, Figure 31a). Yet, when we further analysed the differentially expressed mRNAs using our database for N-glycoproteins (reference N-glycoproteins database). Surprisingly, we observed a significant enrichment for N-glycoprotein-coding mRNAs within the upregulated mRNAs but not the downregulated ones (Figure 31b). Moreover, the upregulated N-glycoprotein-coding mRNAs are enriched for mRNA encoding high multiplicity N-glycoprotein mRNAs (Figure 31c). This result suggests a feedback regulation, where the hypoglycosylation-driven high-multiplicity proteins degradation leads to increase mRNA synthesis.

Next, we evaluated the IgSF-CAMs behaviour in total proteomics. We found a significant enrichment within the reduced DAP for IgSF-CAM proteins (Figure 31d). This data proves the IgSF-CAMs to be, not only more likely to lack the glycan chain, also more prone to show reduced abundance levels in the mutant cerebellum.

a

	Total detected	p-value < 0,05		p-value < 0,05 + FC > 1.2		p-value < 0,05 + FC > 2	
		Total	Percentage	Total	Percentage	Total	Percentage
Transcriptomics	23393	598	2.556%	68	0.291%	1	0.004%
Total proteomics	1982	352	17.760%	202	10.192%	70	3.532%
Glycoproteomics	1404	247	17.593%	247	17.593%	143	10.185%

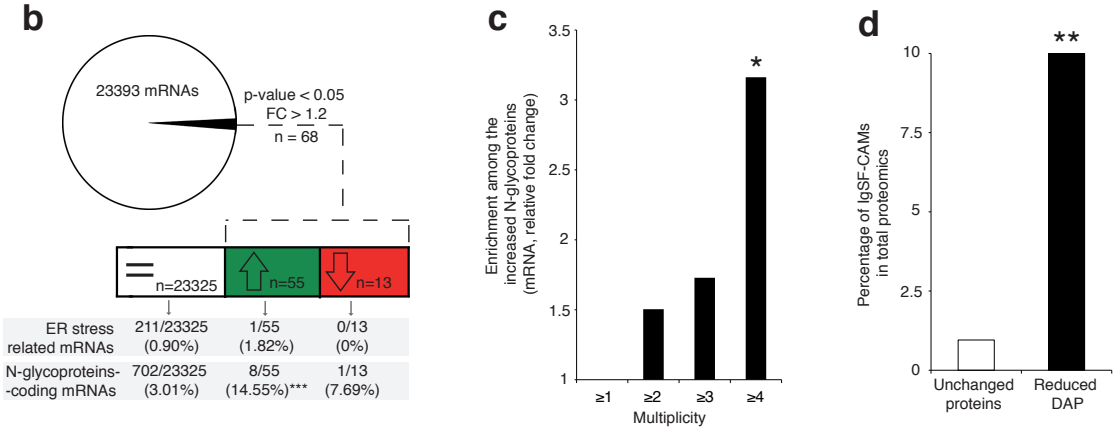

Figure 31. N-glycoprotein-coding mRNAs and IgSF-CAM proteins show altered abundance following *Srd5a3* deletion. (a) Comparative table of the results obtained in transcriptomics, total proteomics and glycoproteomics under different thresholds (n=4 per experiment and genotype). (b, upper panel) Pie chart representing the transcriptomic results in P7 cerebellum. (b, lower panel) Distribution of unchanged mRNAs (white box), upregulated mRNAs (green box) and downregulated mRNAs (red box) into ER stress-related (GO:0034976) or N-glycoprotein-coding mRNAs (Reference glycoproteomic database, see method) categories. A significant enrichment was detected within the upregulated mRNAs for N-glycoprotein-coding transcripts (Fisher exact test, p-value=0.0002). (c) Enrichment for different glycoprotein categories among the increased N-glycoprotein-coding mRNAs. Multiplicity represents groups of proteins with more than one (≥2), two (≥3) or three (≥4) N-glycosylation sites. Multiplicity of ≥1 represents all of the increased N-glycoprotein-coding mRNAs and is set to one (no enrichment). There is a significant 3.16 fold enrichment for N-glycoproteins with 4 or more N-glycans among the increased N-glycoprotein-coding mRNAs (Fischer exact test, p-value=0.027). (d) Enrichment for IgSF-CAMs in total proteomics within the reduced DAP (Fisher exact test, p-value=0.009). FC = fold-change

N-glycoproteins multiplicity can help to understand CDG type I physiopathology in other tissues than the CNS

As previously mentioned in the introduction (chapter 2.4.3) highly N-glycosylated IgSF-CAM subfamilies (i.e. L1CAMs, CNTNs and NCAMs) show higher abundance in the CNS than in the rest of the human body. It is therefore likely that hypoglycosylation of IgSF-CAMs is not involved in the defects observed in some other tissues. However, our results suggest that IgSF-CAMs sensitivity to an N-glycosylation block can be explained by their high multiplicity. Taking this into account, we used a previously published N-glycoproteins database[204] to analyse which are the proteins the more N-glycosylated and their function in another system affected in CDG type I.

One common trait in CDG type I is coagulopathies or bleeding disorders[230]. To investigate if our conclusions could help to decipher the underlying physiopathology, we performed enrichment analysis in the N-glycoproteins with multiplicity 4 or higher in the mouse plasma (Figure 32). Interestingly, out of the few enriched pathways, the more significantly enriched is “complement and coagulation cascades”. Manual inspection showed many coagulation factors (F2, F5, F8, F11 and F12) within the highly N-glycosylated proteins. Even more interesting, the activity of some of these proteins has already been linked by Eva Morava and colleagues[231] with the incidence of acute vascular events in PMM2-CDG. This preliminary result further emphasizes the importance of one of our main findings, the protein multiplicity-dependant sensitivity to N-glycosylation block, not only for the CNS physiopathology but for the whole organism.

Pathway name	p-value
Complement and Coagulation Cascades	0.000253
Hemostasis	0.000792
Intrinsic Pathway	0.0014
Formation of Fibrin Clot (Clotting Cascade)	0.00689

Figure 32. Overrepresentation analysis in plasma proteins with multiplicity ≥4. The database generated in Zielinska et al, 2010 of mouse plasma N-glycoproteome was used. Pathways enriched within the proteins with multiplicity 4 or higher were selected.

CONCLUSIONS

The genetic bases of cerebellar defects are known for approximately one third of the cases[232,65]. Nonetheless, the underlying physiopathology is yet poorly understood for most of the cases. My PhD aimed to gain insights into the molecular mechanisms behind one of the more prevalent cause of a cerebellar defect, partial block of the N-glycosylation pathway[233]. At the same time, we intended to understand the importance of this protein post-translational modification during brain development, a topic that, though well recognised, has largely been under investigated. Several conclusions can be inferred out of the present work:

- ➔ Congenital cerebellar disorders are highly genetically heterogeneous. These defects can arise from recessive (ex. *SRD5A3*) or *de novo* dominant mutations (ex. *CACNA1G*, *KIF1A*).

- ➔ By using the first conditional mouse model for a CDG type I, we recapitulated most of the cerebellar traits found in patients: protein hypoglycosylation, cerebellar hypoplasia and motor coordination defect.

- ➔ Cerebellar GCs are especially sensitive to a partial block in the ER-N-glycosylation machinery, with consequences for their cell adhesion-related functions, leading to defective migration and aberrant axonal guidance.

- ➔ Not all of the N-glycoproteins are equally sensitive to an N-glycosylation defect. Indeed, the proteins with the highest number of N-glycosylation sites are more prone to lack at least one N-glycan chain. This parameter has an additive effect with the sequon-related differential glycosylation efficacy.

- ➔ In the mouse cerebellum, the highly N-glycosylated members of the IgSF-CAM superfamily are especially sensitive to Srd5a3 loss.

➔ Partial and variable loss of N-glycan chains disrupts IgSF-CAMs adhesion-related functions. Aberrant IgSF-CAM-mediated cellular adhesion is a major trigger of the cerebellar defect observed in the En1Cre; *Srd5a3*$^{fl/-}$ mouse and likely in human patients.

➔ The pivotal role of highly N-glycosylated IgSF-CAM members during cerebellar development can explain the cerebellar sensitivity in CDG type I.

➔ We hypothesized that the increase in IgSF-CAM members and N-glycan multiplicity played a critical role during evolution to support the increased tissue complexity found in mammalian CNS.

DISCUSSION

1 Utility of NGS technologies for genetic diagnosis of cerebellar defects

WES allows almost full coverage (more than 95% nowadays) of all of the protein-coding regions, which are estimated to contain the majority of the disease-causing mutations (≈85%)[234]. Inquiring the exome allows what is called a "hypothesis-free approach"[235], where unexpected disease-causing gene variants can be found. For example, *CACNA1G* had never been associated before with a congenital form of cerebellar atrophy but with late-onset ataxia. This would have prevented *CACNA1G* from being included into any gene panel related to early-onset cerebellar malformations and thus the patients could not have been diagnosed by that technique.

The *CACNA1G* example illustrates how different mutations in the same gene can lead to different phenotypes. While 219 genes are associated with cerebellar malformations according to the Human Phenotype Ontology database (HP:0002438), they can lead to at least 269 phenotypically different entities. A similar situation occurs in SRD5A3-CDG, where patients carrying comparable likely null mutations can present a cerebellar hypoplasia, atrophy or normal morphology on MRI[119].

WES has several limitations, such as poor or absent coverage of most noncoding regions, inability to accurately detect large indels or to precisely evaluate an organ-specific mosaicism, among others. Other techniques can be applied to overcome some of these problems, such as WGS, gene panel and RNA sequencing of the affected tissue, when available[236,237].

Even when whole genome sequencing and transcriptomic analysis can be performed, the variant interpretation will keep on being challenging, mostly when located in a noncoding region. As recently highlighted by an international consortium for the molecular diagnosis of rare diseases (IRDiRC), a major investment needs to be done in variant impact evaluation. In this respect, transcriptomic, proteomic and metabolomics, among others, can help to understand the impact of a certain variant of unknown

significance, and thus help to increase the diagnosis rate for rare conditions such as cerebellar defects[235].

2 Generation of a mouse model for CDG type I

The starting point of my thesis, aiming to understand the neuronal physiopathology underlying CDG type I, was the generation of a relevant mouse model. Before this work began, at least three different research labs generated KO mice for CDG type I-related genes: *MPI*, *PMM2* and *SRD5A3*[227,238,239]. In the three cases the mutations lead to embryonic lethality, around E3.5 (*Pmm2*$^{-/-}$) or somewhere between E9.5 and E13.5 (*Mpi*$^{-/-}$ and *Srd5a3*$^{-/-}$). Interestingly, the *Srd5a3* KO mouse showed a defect in embryonic neural tube closure[175]. To overcome the mouse lethality, hypomorphic models for MPI-CDG and PMM2-CDG have been generated, both mimicking relatively frequent human mutations[240,241]. However, no neurological phenotype was reported for none of them and thus cannot be used to understand the neurological defects in CDG type I.

The present work describes the first conditional KO mouse model for SRD5A3-CDG, which, through cerebellar-specific deletion and late embryonic gene recombination (around E8.5, En1-Cre line[199]) overcomes the embryonic lethality and replicates some aspects of the human defect. Importantly, most of cerebellar development takes place after this stage and thus the possibility of missing an Srd5a3 loss-related defect during early cerebellum development are minor[25]. It could be speculated that the Dol pool generated by the cells prior to Cre-mediated *Srd5a3* recombination can alleviate the consequences of the later N-glycosylation partial block. However, the gene is deleted before any major cerebellar proliferation phase takes place[242], making this hypothesis quite unlikely. Consistently, our model recapitulates one of the more prevalent neurological phenotype of the CDG type I, the motor coordination defect, and thus provides an interesting tool to gain insights into the disease mechanisms.

3 Evaluation of an N-glycosylation defect

After the model generation, we focused our efforts on evaluating if it recapitulates or not the protein hypoglycosylation observed in patient' cells, as previously reported in Arabidopsis, yeast and the mouse gene trap mutants for the *SRD5A3* ortholog[227,243].

Transferrin isoelectric focusing (TIEF) does not always efficiently identify a CDG syndrome (introduction, chapter 2.2.1). CDG patients show variable transferrin profiles in an age-dependent manner[107,244]. Similarly, a high variability in N-glycosylation site occupancy and type of glycan chain has been described *in vitro*[245]. This variability can mask an N-glycosylation deficiency and thus the type of technique used is critical to minimize the risk of false negative. In the present work, a lectin far-western blotting, a technique frequently used to quantify the cellular glycosylation status[139,246], failed to identify any significant difference in cellular glycan amounts (Figure 17f-i). Similar results were obtained by cerebellar IHC with lectins and by quantification of MEFs' cell surface glycosylation status by lectin staining followed by FACs (data not shown). Indeed, we could only detect protein hypoglycosylation when using a sensitive marker, LAMP1 (Figure 18a-d)[247,248]. LAMP1 contains 11 N-glycosylation sites according to our glycosylation sites database (18 sites are predicted by uniprot); I-CAM1, another glycosylation marker frequently used[249], is predicted to have 10 N-glycosylation sites. However, the low ICAM-1 expression in the cerebellum did not allow us to characterize its glycosylation status by WB in our mutant[250]. Interestingly, our proteomic and glycoproteomic analysis show that the highly N-glycosylated proteins, containing 4 or more N-glycosylation sites, are more prone to lack the glycan chain under partial block of the ER glycosylation machinery. Whereas only 11% of the N-glycoproteins with 1 N-glycosylation site (multiplicity 1) showed reduced N-glycopeptide abundance in the mutant samples, up to 80% of the N-glycoproteins with 10 or more N-glycan chains did (Figure 25a).

Out of the whole cerebellar N-glycoproteome detected, proteins with 1 to 3 N-glycosylation sites represent 82.74% of the total. In contrast, proteins with 10 or more N-glycosylation sites account only for 1.49% of the detected N-glycoproteome. We hypothesize that the signal of lectin far-WB corresponding to low multiplicity proteins,

which are mildly affected in the mutant, mask the major deregulation of highly N-glycosylated proteins highlighted by glycoproteomics.

In a CDG type II context, where potentially only one type of sugar is missing from the glycan chain, lectin blots are relevant tools. Each lectin targets a different type of sugar (GlcNAc, fucose, sialic acid…) and thus a combination of different lectins can highlight a sugar-specific deficiency[251,252].

Based on these evidence, we can conclude that, at least in our hands, when trying to evaluate an *in vivo* defect in the transfer of the LLO, the use of sensitive (highly N-glycosylated) markers is much more reliable than a global approach (lectin-related techniques). The multiplicity-dependent N-glycoprotein sensitivity to an N-glycosylation defect, described here for the first time, provides solid evidence supporting this.

4 Cerebellar histopathology and underlying cellular mechanism in CDG type I

Our data suggest that in a CDG type I, not all the cerebellar cell populations are equally affected from a histological point of view. PCs develop normally (Figure 20a) and no major decrease in number was detected in the mutant cerebellum. The glial ascending fibres projected by the BG cells are used by the GCs during migration from the EGL to the IGL and an aberrant organization of these processes can lead to defective GC migration[40]. Nevertheless, the glial processes in the mutant cerebellum are normally oriented, perpendicular to the pial membrane (Figure 20b). Moreover, no gliosis was observed. In contrast, examination of the GCs proved a portion of them to be unable to initiate migration (Figure 19e,f). These GC clusters remain in the upper ML until adulthood (data not shown). Many different defects have been described as disrupting GCs migration[253–255], including loss of the IgSF-CAM member CNTN2/TAG1[256]. Interestingly, defects in GC migration from the EGL have already been associated with movement disorders[257–259]. To note, we did not analysed the different cerebellar cell populations at the functional level. Consequently, we cannot conclude that only GCs are affected. However, the Atoh1Cre; *Srd5a3*$^{fl/-}$ mouse histological evaluation (Figure 20d) proved that the mechanism underlying GC defective migration has a major GC-

autonomous component. Further experiments would be needed to address the sensitivity of the other cell populations to an N-glycosylation defect.

In the case of major cellular migration defects, such as grey matter heterotopia[260], regular MRI can detect it[261]. Unfortunately, the technique is not precise enough to detect isolated GC heterotopias in the cerebellum. Future patients' histopathological examination will be needed to better correlate our findings to the human defect. Cerebellar evaluation of CDG type I patients by MRI varies from normal cerebellum to hypoplasic, atrophic or a combination of both. Combined cerebellar atrophy/hypotrophy and hypoplasia are relatively common in both SRDA3-CDG and PMM2-CDG[119]. When present, the cerebellar atrophy can be progressive[122,262]. Surprisingly, in a recent report, a group of physicians described how the cerebellar associated-defects (such as gait, speech or oculomotor function) do not get worse with time even when there is a progressive atorphy[124]. It is tempting to speculate that most of the previously mentioned cerebellar-associated defects have their basis in events occurring during cerebellar development. Indeed, the En1Cre; *Srd5a3*$^{fl/-}$ mouse shows a reduction in the cerebellar size and defective GCs' development (Figure 19a-d) that is not accompanied by late neurodegeneration (data not shown).

To the best of my knowledge, there is only one histopathological study of a CDG type I cerebellum[123]. Precise examination of the tissue showed a lobule-specific atrophy and decrease in GC and PC numbers, together with defective PCs' arborization. The PMM2-CDG patient analysed had a very severe form of the disease and the cerebellum was not fully developed by the time of the death. For example, a defective GC migration initiation could not be accurately assessed since, even in healthy individuals, GC migration is not fully accomplished at 6 months (age of examination). Thus, this study is not conclusive enough and further histopathological studies are needed to fully understand the tissue pathology and to correlate our findings in mouse with the human pathology.

Cerebellar mouse GCs have already been shown to be more sensitive than other types of neurons to tunicamycin-induced N-glycosylation impairment both *in vitro* and *in vivo*[263,264]. *in vivo* experiments proved the developing GCs at the EGL (at P4) being more sensitive than at later stages or than the GCs at the IGL. These findings are highly

suggestive of a higher demand of adequate protein N-glycosylation during GCs development at the EGL than in the rest of the cerebellum. Interestingly, at P4 GC migration to the IGL is highly active and IgSF-CAMs with high number of N-glycosylation sites, such as CNTN1/2, are expressed[169]. This data further supports our finding of GCs' migration being highly sensitive to a partial N-glycosylation block.

The discovery of IgSF-CAMs hypoglycosylation together with their known role (mostly CNTNs) in cerebellar axonal guidance prompted us to analyse PFs disposition in the *Srd5a3*$^{fl/-}$ mouse. We found aberrant parallel fibre (PF) organization in both models (En1Cre and Atoh1Cre, Figure 29f,g). This finding further validates IgSF-CAM defective function under hypoglycosylation. Disrupted PFs were only found in the outer ML, the layer where the ectopic cells are located. As previously described (introduction, chapter 1), GCs first need to extend the PFs and then start to migrate towards the IGL. It is possible that the failure to migrate arises from incorrect fibre extension. Indeed, aberrant GCs' PF extension has already been associated with migration defects[265]. Nevertheless, more experiments should be performed to validate this hypothesis.

Here we present the first longitudinal histological survey of CDG type I-associated cerebellar histopathology. Our results point to the highly proliferative GCs as being especially sensitive to the partial N-glycosylation block with major consequences for their adhesion and axonal growth properties.

5 Proteomic consequences of a partial ER glycosylation machinery block

Even though several approaches have been developed to examine proteins N-glycosylation site occupancy[89,205,206], only few studies have used comparable methodologies to understand how an N-glycosylation impairment affects the whole proteome. One of these studies included proteomics on Chinese hamster ovary (CHO) cells defective for Dol biosynthesis (Lec9)[249,266]. Precise Lec9 CHO proteome investigation highlighted decreased ICAM-1 abundance under partial N-glycosylation blockage. These results were further validated in CDG type I patient fibroblasts, where 28/30 tested samples showed decreased ICAM1 levels. ICAM1 is a highly N-glycosylated

IgSF-CAM and thus its increased sensitivity in a CDG type I context matches with our glyco/proteomic results. Interestingly, the same group published two years later a study associating ICAM1 deregulation with defective leukocytes extravasation in a mouse carrying a hypomorphic *Mpi* variant, mimicking a MPI-CDG mutation. The authors correlate it with the defective immune system response observed in CDG type I[267,268]. These results support our hypothesis of IgSF-CAMs deregulation also triggering the defect observed in other organs.

This study also showed that the mouse defective for Mpi harbours only a mild reduction in ICAM1 abundance, less acute that the major decrease induced under *in vitro* tunicamycin treatment or by regular *in vitro* culture of the Lec9 cells. This fact further shows how acute tunicamycin treatment does not perfectly mimics an *in vivo* N-glycosylation impairment, but does lead to a more severe blocking. Tunicamycin is widely used as a UPR inducer and thus led to the hypothesis that a disrupted ER homeostasis is the main trigger of the CDG-related physiopathology[269,270]. Following this line of investigation, a mild UPR signature has been detected in CDG patients' fibroblasts[271]. Additionally, embryonically-lethal CDG mouse models also present an over activated UPR[227]. However, neither the first experiment reflects the *in vivo* situation nor the second recapitulates the human physiopathology. Indeed, Srd5a3-depleted immortalized MEFs do also present a significant *BiP* upregulation (data not shown).

Our proteomics, transcriptomics and IHC results did not highlight any significant upregulation of the UPR pathway in the En1Cre; *Srd5a3*$^{fl/-}$ cerebellum (Figures 21,22). Nonetheless, proteomic analysis highlighted a significant increase in HYOU1 and SDF2L1 abundance in the P7 cerebellum. Interestingly, HYOU1 overexpression has been shown as partially preventing UPR-related cerebellar neurodegeneration in a Marinesco-Sjögren syndrome mouse model, a disorder that, among others, leads to cerebellar ataxia[210]. SDF2L1 is a chaperone involved in clearance of protein aggregates generated under ER stress[209]. Additionally, we cannot underestimate the fact that BiP shows a not significant 1.3-fold increase in the mutant (q-value = 0.08). One possible explanation for this increase is that not all neurons are equally affected but only the ectopic GCs have a pathologic UPR activation. This UPR upregulation could potentially explain the failure in migration initiation. Two different results contradict this hypothesis. First, a constitutively overactive UPR pathway shall lead to apoptosis, but the ectopic clusters

are still present in the adult mouse. Second, IHC against BiP in the P21 cerebellum did not show any ectopia-specific BiP signature (Figure 22b,c). We hypothesize that these results reflect a physiological adaptation to an increase in misfolded proteins at the ER driven by protein hypoglycosylation. Indeed, the primary role of BiP is to facilitate protein folding. However, further experiments should be performed to characterize this potential ER-stress adaptive mechanism.

No major mRNA deregulation was detected in the *Srd5a3* mutant by transcriptomics when compared to the results coming from total proteomics or glycoproteomics (Figure 31a). The biological replicates did not even cluster together by genotype as they did based on their protein and N-glycoprotein abundance levels (data not shown, Figure 21a and 24c). This is consistent with N-glycosylation being a post-translational protein modification. Interestingly, we could still detect enrichment for highly N-glycosylated proteins within the relatively few upregulated mRNAs (Figure 31b,c). We hypothesize that this is the consequence of highly N-glycosylated protein degradation-driven upregulation of the mRNA levels.

Both total proteomic and glycoproteomic data show that the probability of a protein to be affected by the Srd5a3 loss correlated with its number of N-glycosylation sites. The highest the multiplicity, the highest the probability to have at least one decreased N-glycosylation site and/or being degraded. Moreover, both analyses highlighted a higher frequency of low multiplicity N-glycoproteins versus those with high multiplicity in the mouse cerebellum (Figure 33). This is consistent with other reports in different tissues and species where highly N-glycosylated proteins are a small fraction of the glycoproteome[137,272,273].

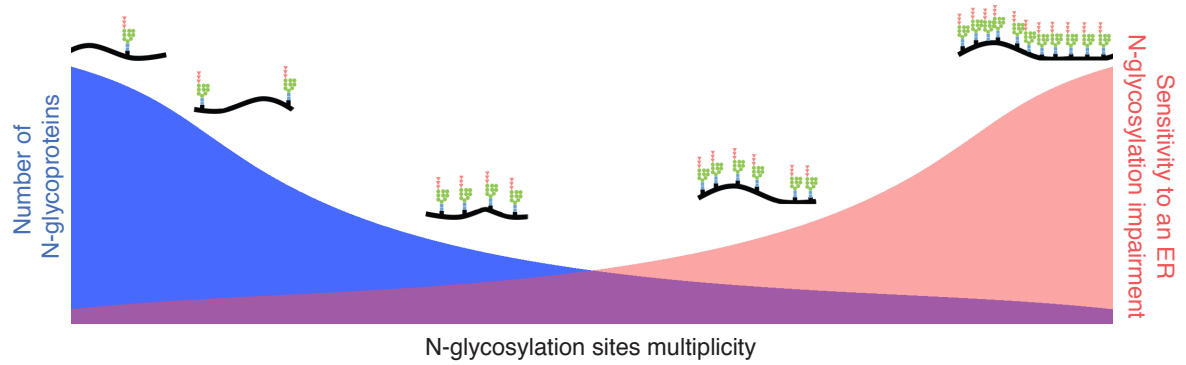

Figure 33. Proteomic consequences of a mild N-glycosylation defect. Our results in total proteomics and glycoproteomics show, first, that there is a higher frequency of proteins with low multiplicity than high in the cerebellar N-glycoproteome. Second, that the proteins with higher multiplicity are more likely to harbour empty N-glycosylation sites and/or be degraded in a CDG type I context.

To our knowledge, the present work is the first report showing the multiplicity-dependant sensitivity of N-glycoproteins to a partial block of the N-glycosylation pathway. The only previous work that focused on the importance of proteins N-glycan multiplicity was the one leaded by the Dr. James W. Dennis (Lunenfeld-Tanenbaum Research Institute, Ontario). His work shows how highly N-glycosylated membrane proteins are more prone to interact with extracellular galectins, forming a lattice that avoids protein internalization by endosomes. His research points to the highly N-glycosylation of growth factors helping to keep a proliferative cell status, while the less N-glycosylated and pro-differentiation proteins are subjected to a higher turnover[274,275]. No galectins-IgSF-CAM binding has been described in neurons to our knowledge and thus this mechanism would not play a major role in the SRD5A3-CDG neurological phenotype.

We also validated previous findings in terms of motif-dependent N-glycosylation efficacy. It has been reported that sequons with a Ser at +2 are less efficiently glycosylated than those carrying a Thr[276]. A similar situation happens at the position -2 of the N residue: sequons with a non-aromatic Aa at -2 are less efficiently glycosylated than the ones harbouring an aromatic one[277]. Within the decreased N-glycopeptides we detected enrichment for both, peptides with a Ser at +2 and peptides with a non-aromatic Aa at -2 (Figure 25c). This is consistent with a partial block of N-glycosylation affecting more the sites that are intrinsically less efficiently glycosylated under normal conditions. Moreover, we proved a cumulative effect between N-glycan multiplicity and a Ser at +2 (Figure 25d). We failed though to see any significant correlation between the

Aa at -2 and protein N-glycan number, possibly due to the low number of N-glycopeptides carrying an aromatic Aa at -2 (13.7% of the total).

Dol is also necessary for protein O-mannosylation, C-mannosylation and GPI-anchored protein biosynthesis. N-glycosylation is the most demanding process, with eight Dol molecules needed for N-glycosylation of a single site. GPI-anchored synthesis requires three Dol molecules and the other two just one (Figure 34). No study, to our knowledge, has yet highlighted an effect of SRD5A3-loss on other glycosylation pathway than N-glycosylation. Consistently, we did not observe any enrichment for C/O-mannosylated or GPI-anchored proteins within the DAP in total proteomics (data not shown).

Disruption of alpha-dystroglycan O-mannosylation leads to GC failure to initiate EGL-IGL migration[278]. We investigated O-mannosylation of alpha-dystroglycan in the mutant cerebellum by using a glyco-epitope specific antibody (IIH6)[279]. Consistent with the total proteomic results, we found no significant difference in alpha-dystroglycan glycosylation or MW in the En1Cre; *Srd5a3*$^{fl/-}$ cerebellum (data not shown). Interestingly, it has been shown that it is the alpha-dystroglycan secretion by the cerebellar glial cells, and not by the GCs, that is necessary to promote GCs migration[278]. GC-specific *Srd5a3* deletion leads to the same failure to initiate migration, further supporting that alpha-dystroglycan has no implication in the observed migratory defect.

SRD5A3 loss does not eliminate the intracellular Dol pool[227]. It is likely that a partial defect on Dol synthesis will only affect the most demanding glycosylation process, *i.e.* N-glycosylation, and have minor or no effect on the other Dol-mediated glycosylation processes.

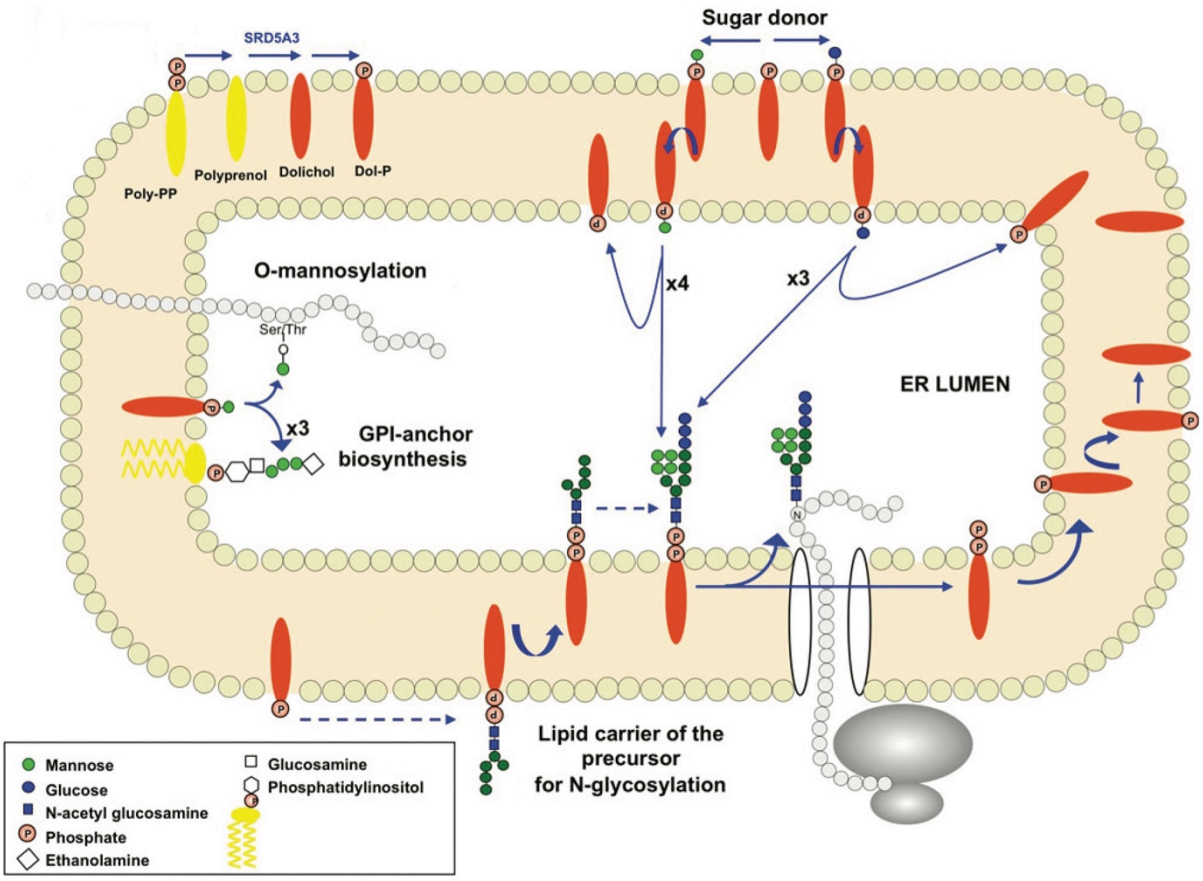

Figure 34. Dol function in protein and lipid glycosylation. Modified image form Cantagrel et al, 2011.

6 The high N-glycan multiplicity of IgSF-CAMs and its importance in CDG type I physiopathology

Overrepresentation analysis on the hypoglycosylated proteins pinpointed to the large super family of IgSF-CAMs as being significantly deregulated in the En1Cre; *Srd5a3*$^{fl/-}$ developing cerebellum (Figure 26a). This result was further validated at the N-glycopeptide level: there is enrichment for IgSF-CAM N-glycopeptides within the reduced N-glycopeptides (Figure 26b). Moreover, reanalysis of the data obtained in total proteomics also demonstrated enrichment for IgSF-CAMs within the proteins with reduced abundance (Figure 31d).

Using our own N-glycosylation site database (reference glycoproteomic dataset) we found that cerebellar IgSF-CAMs contain more N-glycosylation sites than the average N-glycoprotein (3.3 VS 2.3 in the rest, Mann Whitney test, p-value < 0.0001). If we focus on the IgSF-CAM subfamilies with well-known role in cerebellar development, we find an

even higher glycan multiplicity (e.g. L1CAMs 9.5, NCAMs 4.5 and CNTNs 5). Additionally, and thanks to the work of Matthias Mann and colleagues[137,151], we could also show an increase on these proteins' multiplicity across evolution (Figure 28a).

As pinpointed by Lebrilla and colleagues (PMID: 19700364) "a protein with three sites of glycosylation with 10 different glycans in each site can result in a 1000 different glycoforms of the protein". The high multiplicity of IgSF-CAMs can therefore lead, theoretically, to thousands of glycoforms. Differential glycan composition of IgSF-CAM members has already been proved to modulate their activity[168,280]. This observation, combined with the increased IgSF-CAM-coding genes and N-glycosylation site multiplicity in mammals[150] suggests that these proteins may contribute to the high complexity of the mammalian brain. Moreover, the high IgSF-CAM proteins multiplicity fully matches our total proteomics and glycoproteomics results, where the highly N-glycosylated proteins are more sensitive to an N-glycosylation impairment.

As previously discussed in the introduction (chapter 2.4.2.1), IgSF-CAMs role in brain development and synapse physiology has been widely reported[281]. Even more interesting, those proteins can act in partially redundant manners to ensure correct axonal navigation and cell migration. Single IgSF-CAM protein KO in *C.Elegans* does not lead to major neuronal defects but when crossed between them[282]. In other contexts, this overlap is less obvious[283]. Regarding the mouse cerebellum, it has already been proved that L1CAM and NrCAM play overlapping roles. Grumet and colleagues published few years ago a mouse KO for *NrCAM*[284]. *NrCAM*$^{-/-}$ mice developed normally with just few abnormalities in cerebellar foliation. They hypothesized that some other IgSF-CAMs could help to overpass the lack of NrCAM. To investigate that possibility, they crossed their model with *L1CAM*$^{-/-}$ mice. Double mutant mice did not survive beyond the 2nd postnatal week, show severe cerebellar hypoplasia and delayed cerebellar development. Interestingly, while the lethality of the double mutant did not allow histological analysis after normal GC migration, a significant decrease in the size of the IGL was detected at P8. Indeed, one of the authors' main hypotheses for the defect is an aberrant PF extension. Other IgSF-CAM mutant mice also show defects that overlap with the ones found in the En1Cre; *Srd5a3*$^{fl/-}$ mouse. As previously mentioned in the introduction, lack of Cntn1 leads to cerebellar ataxia and aberrant PF orientation in

mouse[36]. *Cntn2* KO mouse also shows ectopic GC clusters in the outer ML[35]. Collectively, these studies support that disruption of cerebellar IgSF-CAM primarily affects GCs postnatal development.

One interesting aspect of IgSF-CAMs is their dependence on homophilic interactions to function properly. *Cntn2* KO neurons lose their ability to fasciculate in Cntn2-coated surfaces *in vitro*[285]. In a similar manner, the Nfasc-coating induction of neurite outgrowth is lost when neurons lack Nfasc[286]. These examples illustrate the pivotal role of IgSF-CAM homophilic adhesion over heterophilic binding under certain circumstances.

Another important observation of IgSF-CAMs sensitivity to a partial N-glycosylation blocking is that not all of the proteins lack some glycan chain. As the L1CAM and NrCAM WB show (Figure 26c and 28e), not all of the proteins are hypoglycosylated in the absence of Srd5a3. The blot shows the coexistence in the mutant cerebellum of normal MW glycoforms (not hypoglycosylated form) and lower MW glycoforms (hypoglycosylated form). We consequently hypothesize that the partial hypoglycosylation has a more important output in highly IgSF-CAM demanding processes. One of the situations where different highly N-glycosylated IgSF-CAMs are necessary is the migration initiation and axonal projection of the GCs. This hypothesis is consistent with the *in vitro* data showing that more the cells depend on IgSF-CAM function (L1CAM and NrCAM-coating conditions) the more severe the defect is.

Partial N-glycosylation block likely does not always concern the same site but each site can potentially remain empty (stochastic glycan loss, with higher occurrence within NxS motifs and N-glycosylation sites with a non-aromatic Aa at -2). However, depending on the affected site, the consequences can vary: impaired folding, decreased protein stability, defective trafficking or abnormal function[287]. Our glycoproteomic data allowed however the identification of the sites most frequently lacking the glycan chain. One of those sites is the Cntn2 N-glycosylation site N206. This result is interesting for two reasons. First, using glycoproteomics, we identified two glycoforms of the N-glycopeptide, one containing two occupied N-glycosylation sites (N200 and N206) and another with only one occupied site (N200). While the N-glycopeptide with the two

occupied N-glycosylation sites is reduced in the mutant, the N-glycopeptide with only one occupied site shows a 21-fold increase in the mutant (Figure 35a). This evidence strongly suggests that the absence of Srd5a3 results in a specific hypoglycosylation of the N206 site without consequences on protein abundance. Lack of glycan chain at N206 seems to be compatible with adequate protein expression. Second, a team published few years ago the crystal structure of the N-terminal domain of CNTN2, the extracellular binding module[285]. Combination of the protein crystal structure with the software Glycoprot (http://www.glycosciences.de) allows generation of a 3D model of the N-terminal portion of CNTN2 and to visualize the position of the N-glycan chain (Figure 35b,c). As the image shows the glycan chain is located at the Cntn2 binding site (Ig domain number 2), and does not fall into any protein pocket. This position could expose the glycan and be compatible with a direct role in the regulation of affinity with its ligand and consequently cell adhesion.

Interestingly, we already found a Cntn2 adhesion-mediated defect in GC aggregates *in vitro* (Figure 29a).

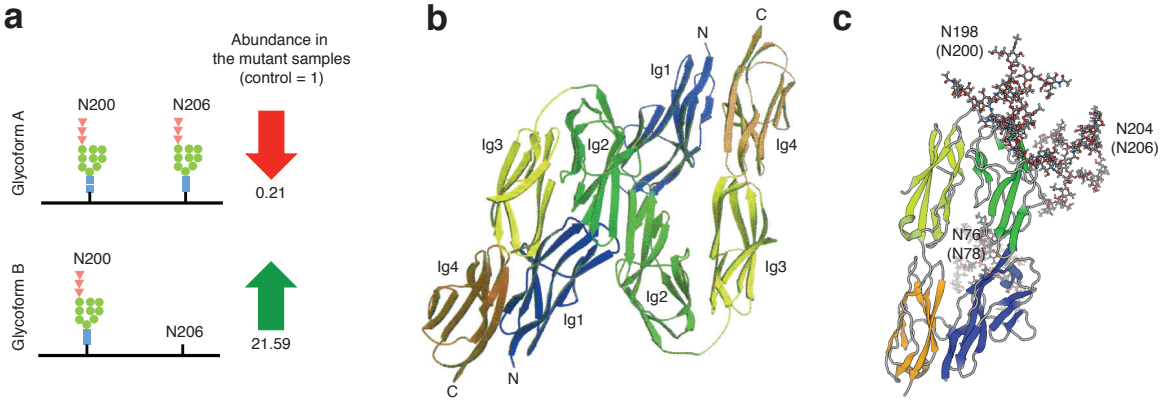

Figure 35. Hypoglycosylation of Cntn2 N206 is likely to alter protein interaction. (a) Descriptive diagram of the two glycoforms detected in glycoproteomics of the N-glycopeptide harbouring the N200 and N206 sites and their behaviour in the En1Cre; *Srd5a3*$^{fl/-}$ cerebellum. (b) Representative crystal structure of the ligand-binding module of two CNTN2 molecules. Modified image from Mörtl et al, 2007. (c) N-glycan emplacement in the N-terminal domain of CNTN2. The positions between brackets indicate the precise glycan position in the mouse protein, the rest represent the human CNTN2 N-glycosylation sites. This image was generated with the Glycoprot database.

IgSF-CAMs are not the only hypoglycosylated proteins in the mutant cerebellum. For example, several AMPA receptors (e.g. Gria1 and Gria3) show reduced N-glycopeptide abundance. Both receptor subunits are highly expressed in the PCs[288]. Other adhesion proteins such as cadherins (Pcdhga4), plexins (Plxnb2) or integrin ligands (Tnc) were

also found to be hypoglycosylated by both, glycoproteomics and total proteomics (Sup. Table 3). Nonetheless, the results from total proteomics, glycoproteomics and *in vitro* functional analysis demonstrate that the proteins of the IgSF-CAM superfamily are more sensitive to an N-glycosylation block. Their increased sensitivity leads to hypoglycosylation and/or protein degradation and impairs their adhesion-related functions, with a major impact on cerebellar development.

Highly N-glycosylated IgSF-CAMs, such as Chl1, L1CAM and NCAM1, are also important for other brains regions such as the cerebral cortex and the hippocampus, where they regulate, among others, cell death and synapse stability[289–292]. Our work shows that in cortical-like human neurons IgSF-CAMs are also sensitive to an N-glycosylation impairment (Figure 28). It is tempting to speculate that, together with their role in cerebellar function, an impairment of their activity in the cerebral cortex and hippocampus may contribute to the highly prevalent ID observed in CDG type I patients[101].

All together, our CDG type I model shows that protein sensitivity to an N-glycosylation impairment will depend on their glycan multiplicity with an influence of the Aas surrounding the asparagine residue. Proteins will stochastically lack their glycan chain and thus proteins with high glycan multiplicity are more prone to lack at least one N-linked oligosaccharide. The highly N-glycosylated cerebellar IgSF-CAMs are exquisitely sensitive to Srd5a3 loss and their hypoglycosylation during development is a major trigger of the cerebellar defect.

7 Other SRD5A3-loss related molecular defects

The more consistent finding in SRD5A3-CDG patients and mouse, Arabidopsis and yeast mutants for the corresponding ortholog gene is stochastic loss of N-glycan chains[227,243]. My work further emphasizes the major role of glycan loss in the neurological symptoms and likely other affected tissues symptomatology. However, defective Dol biosynthesis can potentially affect other physiological functions that could play a role in the resulting phenotype.

Thanks to collaboration with François Foulquier, we showed an accumulation of Man5-type N-glycans in the *Srd5a3* mutant MEF proteins (Figure 27a). We also provide

preliminary evidences of an *in vivo* increase of protein glycosylation with mannose-rich glycans (Figure 27b,c). Interestingly, François Foulquier' lab demonstrated a similar increase in Man5-glycosylated proteins in SRD5A3-CDG fibroblasts (data not shown). A comparable situation occurs in ALG3-CDG. ALG3 catalyses the transfer of the first Man in the ER, from Dol-P-Man, to form the intermediate glycan form Man6. Mutations that diminish ALG3 function lead to accumulation of Man5-containing glycoproteins[293]. The Lec9 CHO line, defective for dolichol synthesis, also shows an increase in Man5 species[266]. A similar defect occurs in PMM2-CDG, where one of the enzymes that participate in Man activation prior to its attachment to the oligosaccharide chain, PMM2, shows reduced activity[101]. Collectively, these evidences suggest a SRD5A3 deletion-driven defective mannose addition to the glycan, a relatively common trait in CDG type I. Considering the importance of Man9-glycan structures in the CNS[294], the accumulation of proteins with Man5 glycans observed in SRD5A3-CDG could potentially play a role in the physiopathology. However, CDG type I arising from a disruption of later ER-glycosylation steps, such as altered OST function, do also lead to classical neurological symptoms such as cerebellar atrophy and ID[295]. This observation further proves that the stochastic glycan loss is at the basis of the observed defect. Moreover, it highly suggests that, even though SRD5A3 loss is likely to lead to aberrant glycan composition, it might not play a major role in disease development. Additional investigation will be needed to further characterize the exact impact in LLO and N-glycan composition and its consequences during brain development.

Another important characteristic of SRD5A3-CDG is the polyprenol accumulation[227,296]. Dol is likely to be synthesized trough an SRD5A3-independent pathway, leading consequently to an accumulation of the enzyme substrate, polyprenol. Both polyprenol and Dol can modulate membrane fluidity[297]. Interestingly, the presence of Dol is not restricted to ER membranes[298]. Adequate membrane fluidity is important for cell growth, membrane-associated enzymes and molecules transport. Impaired membrane fluidity can disrupt these processes and lead to pathological situations[299]. Beyond the demonstrated effects on N-glycosylation, the absence of SRD5A3 could therefore also alter membrane fluidity in patients' cells. Nevertheless, as for the aberrant glycan composition, most of CDG type I patients do not show increased polyprenol abundance,

thus eliminating the possibility of polyprenol being a major player in CDG type I physiopathology.

Lastly, it has been hypothesized that the defective glycan transfer can be due to the use of polyprenol instead of Dol as glycan carrier[296]. Polyprenol is indeed the lipid carrier used in most eubacteria[300]. This hypothesis assumes that polyprenol is less efficient for N-glycan transfer in mammals and that enzymes such as ALG3 would not interact as efficiently with the un-reduced version of Dol[301]. Nonetheless, phosphorylation of either polyprenol or Dol is needed prior attachment of the first GlcNAc unit. The enzyme carrying this reaction has been shown to have almost 3-fold more affinity for Dol than polyprenol[302].
In any case, the possibility of polyprenol being used in presence of a defect in Dol synthesis remains under investigated and further research is needed to evaluate its implications in the SRD5A3 loss-driven protein hypoglycosylation.

8 Therapeutic approaches in SRD5A3-CDG

The Dol pool dedicated to N-glycosylation represents just a small portion of the total[298]. Accordingly, liposome-mediated polyisoprenol dietary supplement in rats leads to only a small increase in the amount of phosphorylated Dol, the form used during N-glycosylation[303]. Moreover, the biodistribution of Dol in the brain is very low[304]. As a consequence, current efforts to alleviate the defect focus on enhancing the alternative Dol biosynthetic pathway rather than increasing Dol pool through dietary supplement.

One of the most successful *in vitro* trials relies on the use of zaragozic acid in DPM1-CDG fibroblasts, where the defect arises from defective Dol-P-Man synthesis[305]. Zaragozic acid inhibits the conversion of farnesyl-PP into cholesterol. This inhibition enhances the conversion of farnesyl-PP into other metabolic products including Dol (Figure 36). Treatment of DPM1-CDG patient fibroblasts with zaragozic acid lead to an improved synthesis of the full LLO, likely through an increase in *de novo* Dol synthesis[306]. In agreement with this, we showed that enhanced *de novo* lipid synthesis in mutant MEFs tends to alleviate protein hypoglycosylation (Figure 30).

Another potential therapeutic approach consists in the supplementation with farnesyl-PP itself. Farnesyl-PP is much smaller than Dol and thus shall have a better dietary absorption and biodistribution than Dol. In a recent study, Dr. Melissa Westwood and colleagues[307] used statins, HMG-CoA reductase inhibitors, to partially block protein N-glycosylation in human cells. The consequent protein hypoglycosylation was partially ameliorated by combining the statins with farnesyl-PP.

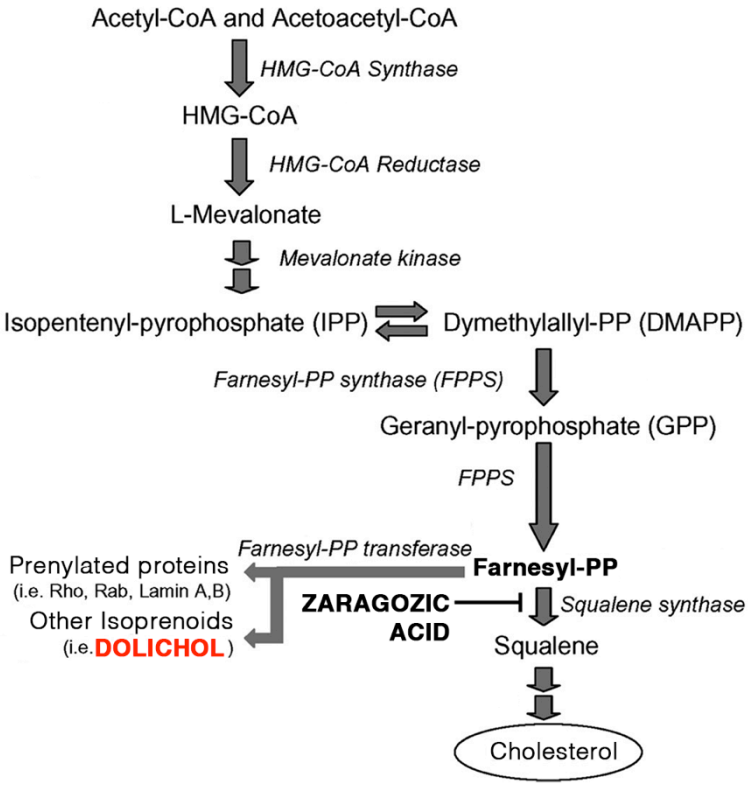

Figure 36. Simplified representation of the mevalonate pathway.

The above-discussed therapies are likely to be useful for Dol synthesis-related CDG, but potentially not for all CDG type I. In this regard, a recent review points to two other main strategies to try to restore proper protein N-glycosylation. One aims to enhance the residual enzymatic activity[101]. This aim can be achieved by dietary supplementation with the enzyme substrate, like Man for PMI-CDG, the only treatable CDG, or D-galactose in PGM1-CDG[308], which has been found recently as an effective therapy in a pilot study[309]. In PMM2-CDG, Man dietary supplementation is not effective[310]. In this case, and as long as some PMM2 mutations lead to aberrant enzyme folding, a chaperone therapy has been proposed[311].

9 Relevance of our findings for other CDG and affected tissues

SRD5A3-CDG shares many biochemical aspects with other CDG, such as ALG3-CDG, DPM1-CDG and PMM2-CDG. Indeed, the main consequence of the defect, the stochastic N-glycan chain-loss, is shared with CDG type I. The functional and molecular consequences of such defect are indeed the main finding of my PhD.

Our results show for the first time, a relatively simple but yet never described before, multiplicity-dependent sensitivity to partial N-glycosylation block. Consequently, we identified the highly N-glycosylated cerebellar IgSF-CAMs as being especially sensitive to the defect. Our work and the previously published works on IgSF-CAMs N-glycosylation (introduction, chapter 2.4.2.1 and discussion, part 6) show how an impairment of their normal glycosylation profile affects their adhesion-related functions. It is likely that the high demand of IgSF-CAMs during GCs development is at the basis of the cerebellar sensitivity to an N-glycosylation impairment.

The visual system is also frequently affected in CDG type I (retinitis pigmentosa, optic atrophy and iris colobomas, among others)[312]. Interestingly, NrCAM and Cntn2 are essential for adequate axonal disposition across the optic chiasm. The first one coordinates the ipsilateral/contralateral migration of the retinal ganglion cells' axons[313], while Cntn2 plays a role in axonal length and fasciculation[285]. Indeed, most of L1CAMs and CNTNs are highly expressed during eye development[313]. The main cause of early lethality in CDG type I is the high frequency of infections together with a defective immune system[268]. ICAM-1, a highly N-glycosylated IgSF-CAM, shows reduced abundance levels in a CDG type I context[249,267]. Interestingly, ICAM-1 plays important roles in viral pathogenicity, by avoiding viral replication[314,315]. These data further link impaired IgSF-CAMs N-glycosylation to other affected tissues in CDG type I. Even in tissues were IgSF-CAMs are not highly expressed, the multiplicity-dependent glycoprotein sensitivity should provide clues into the tissue-specific disease mechanism (Figure 32).

In conclusion, our work provides new evidences of the underlying molecular mechanism in CDG type I. We describe for the first time protein multiplicity-dependant sensitivity to an N-glycosylation impairment. The proteins with high number of N-glycosylation sites are more prone to lack at least one N-glycan chain in CDG type I-related conditions. The N-glycan loss can lead to a wide variety of consequences, from defective protein folding and consequent degradation to aberrant interaction with other proteins. Consequently, we demonstrated the key role played by the highly N-glycosylated IgSF-CAM members in the neurological signs, and provide important clues for the understanding of the impact of IgSF-CAM hypoglycosylation in the other affected organs.

Moreover, the mouse model that we have developed should, when crossed with relevant Cre lines, open multiple possibilities for the study of physiopathological mechanisms outside the CNS. Glycoproteome investigation of the tissues affected in CDG type I should identify the proteins with higher multiplicity in each tissue. These proteins could be used as starting point to understand the tissue-specific pathogenesis.

Last but not least, our work illustrates the importance of IgSF-CAMs N-glycan multiplicity for their function and how their increased multiplicity during evolution could support the complexity of the mammalian brain.

METHODS

Targeted gene panel and whole exome sequencing

The rational behind the genetic screening firstly involved exploring the subjects using gene panel unless the clinical presentation suggests a new syndromic entity that will be directly explored through WES. All patients negative with one approach were systematically tested using the other one.

A custom gene panel including 72 childhood-onset cerebellar atrophy-related genes was set up[65]. Cerebellar hypoplasia genes were included as this phenotype often overlaps with cerebellar atrophy at the pediatric age[316]. Genes such as *CASK*, *EXOSC3* or *WDR81* can be involved in cerebellar atrophy/hypoplasia without or with pons hypoplasia (i.e. pontocerebellar hypoplasia (PCH)) and consequently PCH genes are also included. Genomic DNA libraries were generated from 2 µg DNA sheared with a Covaris S2 Ultrasonicator using SureSelectXT Library PrepKit (Agilent, Garches, France) and the Ovation® Ultralow System V2 (NuGen) according to the suppliers' recommendations. 1459 regions of interest encompassing all exons and 25 base pairs intronic flanking sequences of the 72 selected genes were captured by hybridation with biotinylated complementary 120-pb RNA baits designed with SureSelect SureDesign software (hg19, GRCh37, February 2009). The 309.16 Kb targeted DNA region was pulled out with magnetic streptavidin beads, PCR-amplified using indexing primers and sequenced on an Illumina HiSeq2500 HT system. NGS data analysis was performed with Paris Descartes University / Institut IMAGINE's Bioinformatics core facilities. Paired-end sequences were mapped on the human genome reference (NCBI build37/hg19 version) using the Burrows-Wheeler Aligner. Downstream processing was carried out with the Genome Analysis Toolkit (GATK), SAMtools, and Picard, according to documented best practices (http://www.broadinstitute.org/gatk/guide/topic?name=best-practices).

WES was performed with DNA extracted from blood and processed at the Genomic core facility in the Imagine Institute as previously described[54]. Briefly, exome capture was performed with the SureSelect Human All Exon kit (Agilent technologies) and sequencing was carried out on a HiSeq2500 (Illumina). The mean depth of coverage obtained for each sample was > 150x with >97 % of the exome covered at least 30x.

All identified variants were validated using Sanger sequencing or multiplex ligation-dependent probe amplification (MLPA) for duplications or deletions.

Variant analysis, databases and bioinformatic tools

A variant filtering pipeline was systematically applied to narrow down the number of putative causative variants. All the possible inheritance patterns were tested. Briefly, variant calling was performed with the GATK Unified Genotyper (https://www.broadinstitute.org/ gatk/) based on the 72 version of ENSEMBL database. Common variants (i.e. minor allele frequency >1 %) were filtered out by using dbSNP, 1000 genomes databases and our In-house exome collection, which includes more than 10,000 exomes. Further, functional (protein-altering) alleles were prioritized versus non-functional. Potentially pathogenic variants in known disease genes were identified if flagged as damaging by polyphen2 (http://genetics.bwh. harvard.edu/pph2/), Sift (http://sift.jcvi.org/) or mutation taster (http://www.mutationtaster.org/). Remaining variants were compared with those in the public databases EXAC (http://exac.broadinstitute.org/) and EVS (http://evs.gs.washington.edu/EVS/) exome database. The presence of candidate recessive variants in homozygous intervals was checked by identifying predicted regions of SNP homozygosity from exome data with the UnifiedGenotyper tool from GATK (https://www.broadinstitute.org/gatk/). Additional filtering of de novo variants was done using the following criteria. Candidate de novo mutations were excluded if already reported in the EXAC database, if present more than 5 times in our In-house exome and genome database or if located in a gene already involved in a distinct developmental defect without neurological involvement.

Animal care

Animals were used in compliance with the French Animal Care and Use Committee from the Paris Descartes University (APAFIS#961-201506231137361). All behavioural analysis were performed in

compliance with the guidelines of the French Ministry of Agriculture for experiments with laboratory animals. The experimental protocol and euthanasia have been approved by the Ethical Committee 27, registered at the French ministry of research.

Generation of the *Srd5a3* conditional KO mouse

Embryonic stem (ES) cell clone EPD0575_2_F01 carrying the *Srd5a3*$^{tm1a(EUCOMM)Wtsi}$ allele was acquired from the International Mouse Phenotyping Consortium (IMPC; http://www.mousephenotype.org/). After additional QC validation based on Southern-blot, ES cells were injected into C57BL/6 at the University of California, San Diego Transgenic and Gene targeting Core yielding chimeric mice. Chimera were bred to C57Bl/6 until germline transmission was successful to produce knockout first allele. Then, the *Srd5a3*tm1a mice were bred with ACTB:FLPe B6J (JAX stock #005703) Flp recombinase expressing transgenic mice to produce mice expressing a functional *Srd5a3* allele that retained flox sites surrounding exon 2 to 4 (out of the 6 exons) and including part of the enzymatic domain (PFAM, *Steroid_dh*). After outbreeding the Flp recombinase transgene, *Srd5a3* floxed mice were crossed with hemizygous CMV-Cre line transgenic mice (Metzger, Clifford, Chiba, & Chambon, 1995) to generate *Srd5a3* KO allele. *Srd5a3* floxed mice were bred with hemizygous *En1*$^{tm2(cre)Wrst}$ transgenic mice (JAX stock #007916) expressing Engrailed1 promoter driven Cre to produce cerebellum-specific deletion (En1Cre; *Srd5a3*$^{fl/-}$) or with hemizygous Tg(Atoh1-cre)1Bfri (JAX stock #011104) expressing Atoh1 promoter driven Cre to produce cerebellum granule cell-specific deletion (Atoh1Cre; *Srd5a3*$^{fl/-}$). Specific Cre expression was confirmed by breeding with a LacZ reporter-carrier mouse line (R26R^{LacZ} mouse). Efficient *Srd5a3* recombination was assessed by RT-PCR and RT-qPCR in the absence of any specific antibody.

Mouse embryonic fibroblasts (MEFs) generation

For MEFs generation, *Srd5a3*$^{fl/-}$ mice were bred with CAGCre mice (B6.Cg-Tg(CAG-cre/Esr1*)5Amc/J; CAGCre; *Srd5a3*$^{fl/-}$). *CAGCre;Srd5a3*$^{fl/-}$ embryos fibroblasts were isolated at E14.5 and immortalized by serial passaging as described by Xu(Xu, 2005). For *Srd5a3* recombination primary MEFs were treated for 4 days with tamoxifen (1µM, H6278, Sigma) prior to immortalization. Efficient *Srd5a3* recombination was assessed by RT-qPCR after immortalization.

Behavioral studies

For behavioral analysis, 15 *En1Cre; Srd5a3*$^{fl/-}$ and 15 control littermates, gender-matched, 2-3 months old were used. The number of animals per group was chosen as the optimal number likely required for conclusion of statistical significance, established from prior experience using the same behavioral tests[317]. Morris water maze (MWM) test was used to assess working memory. Prior to the test, the mouse swimming speed was analyzed. No differences in the swimming speed were detected. For MWM, mice were exposed twice to the same hidden platform for a total of eight sessions. The improvement to find the platform on the second trial was evaluated. For motor coordination, classic accelerating rotarod testing was done for 10 minutes and for a total of three sessions, 24h apart. The first three falls from the rod during each session were annotated.

Histological analysis

Gross anatomical analyses and HE staining was performed as previously described[318]. The resulting slices were scanned with NanoZoomer-XR (Hamamatsu Photonics, Japan). For IHC, the cerebellum was embedded in OCT. 12µm-thick slices were generated with cryostat. The following antibodies were used for IHC: NeuN (1:200, MAB377; Millipore), Calbindin (1:10.000; CB-38A, Swant), GFAP (1:1.000; AB5804, Millipore), CACNA1G (1:1000, ACC-021, Alomone labs), Parvalbumin (1:1000, 235, Swant), Tuj1 (1:500, 801201, Biolegend) and BiP (1:50, ADI-SPA-826, Enzo). All samples were mounted with ProLong Gold Antifade Mountant with DAPI (Life Tech). Images were taken with confocal Leica SP8 STED and analyzed with ImageJ.

Protein extraction and western blotting

P7 mouse cerebellum samples and MEFs were isolated in RIPA buffer (1% SDS; 0,1% for cell extracts) supplemented with EDTA-free protease inhibitor (11836170001, Sigma) and phosphatase inhibitor cocktail (4906845001, Sigma), homogenized by sonication (Bioruptor Pico sonication device – 8 cycles 30''ON/30''OFF) and centrifuged at 12.000g at 4ºC for 20min. The supernatant was recovered and quantified with BCA (Life technologies). For cell extracts, RIPA was added directly to the flask and the cells were recovered with a cell scrapper followed by the same protocol. Equal amounts of protein were loaded from each sample in polyacrylamide gels. Gel transfer to nitrocellulose membranes was performed with the Trans-Blot Turbo Transfer System for 10min at 1.3A and 25V. Membranes were blocked with 5% dry milk and incubated O/N at 4ºC with the following antibodies: LAMP1 (1:2.000; AB24170, Abcam), MINPP1 (1:2000, sc-10399, Santa Cruz Biotechnologies), L1CAM (1:2.000; AB24345, Abcam), NrCAM (1:2.000; AB24344, Abcam) and β-actin (1:20.000; AM4302, Thermo Fisher). Depending on the antibody suitability, the membrane was developed by HRP system (LAMP1, ChemiDoc XRS+ System) or with fluorescent secondary antibodies (Odyssey CLx imaging system). All secondary antibodies were used at 1:10000. For far-western blotting, no blocking step was performed, and the membrane was directly incubated for 1h with biotinylated SNA (1:2.000; B-1305, Vector laboratories) or ConA (1:2000; C2272, Sigma) and posteriorly with IRDye 800CW-streptavidin for 1 extra hour (1:10.000; 926-32230, LI-COR). All WB results were replicated at least twice.

RNA extraction, RT-PCR, RT-qPCR and transcriptomic analysis

RNA was extracted with Trizol reagent (15596-026, Thermo Fisher) according to manufacturer's instructions. For transcriptomic studies, 4 *En1Cre;Srda5a3*$^{fl/-}$ P7 mice and 4 control littermates were used. RNA quality was validated with Bioanalyzer 2100 (using Agilent RNA6000 nano chip kit) and 180 ng of total RNA were reverse transcribed using the GeneChip WT Plus Reagent Kit (Affymetrix). The resulting double strand cDNA was used for *in vitro* transcription with T7 RNA polymerase (WT cDNA synthesis and amplification kit, Affymetrix). After purification according to Affymetrix protocol, 5.5 ug of the cDNA obtained were fragmented and biotin-labelled using Terminal Transferase (WT terminal labelling kit, Affymetrix). cDNA was then hybridized to GeneChip Mouse Transcriptome Array 1.0 (MTA 1.0., Affymetrix) at 45°C for 17 hours. After O/N hybridization, chips were washed on the fluidic station FS450 following specific protocols (Affymetrix) and scanned using the GCS3000 7G. The scanned images were then analyzed with Expression Console software (Affymetrix) to obtain raw data (cel files) and metrics for Quality Controls. The observations of these metrics and the study of the distribution of raw data showed no outlier experiment. Robust multi-array average (RMA) normalization was obtained using R, and normalized data were subjected to statistical tests. For RT-PCR/RT-qPCR 1µg of RNA was retrotranscribed into cDNA with SuperScript II reverse transcriptase (18064014, Thermo Fisher). qPCR was performed with PowerUp SYBR Green Master Mix (A25777, Thermo Fisher). The following primers were used: m*βActin* (F 5'-TACAGCTTCACCACCACAGC-3', R 5'-AAGGAAGGCTGGAAAAGAGC-3'), *Hmgcr* (F 5'-CTTGTGGAATGCCTTGTGATTG-3' , R 5'-AGCCGAAGCAGCACATGAT-3'), *Hmgcs1* (F 5'-TGGCACAGTACTCACCTC-3', R 5'- CCTTCATCCAAACTGTGG-3') and m*Srd5a3* (F 5'-CCGGGCTATGGCTGGGTGG-3' and R 5'-CTGTCTCAGTGCCTCTAGGAATGG-3').

Total proteomics and Glycoproteomics

Four P7 *En1Cre;Srd5a3*$^{fl/-}$ and four control littermates were used for cerebellar protein extraction as previously described. Two different batches, each from at least two different litters, were used for total proteomics and another for glycoproteomics. For total proteomics, 100µg of protein were processed by filter-aided sample preparation (FASP) protocol, as described previously[319]. Briefly, samples were applied to 30KDa MWCO centrifugal filter units (UFC503024, Amicon Ultra, Millipore) mixed with 200uL of urea (UA) buffer (8M urea, 100mM Tris-HCl pH 8.8) and centrifuged twice. The samples were incubated for 20min in the dark with UA buffer containing 50mM iodocetamide for alkylation. The filter units were subsequently washed twice with UA buffer and twice more with ABC buffer (50mM ammonium bicarbonate). Peptide digestion was carried by incubation with trypsin (1:50) O/N at 37ºC. The resulting peptides were collected by two washes with ABC buffer, vacuum dried and dissolved in 0.1% (v/v) trifluoroacetic acid with 10% acetonitrile.

Glycoproteome analysis was performed by FASP with an additional step of enrichment in N-glycopeptides by lectins, as described by M. Mann and colleagues[137]. Briefly, 100ug of trypsinized peptides were recovered in binding buffer (20mM Tris/HCl pH 7.6, 1mM $MnCl_2$, 1mM $CaCl_2$, 0.5; NaCl) and incubated with a lectin mixture (90ug ConA, 90ug WGA and 71.5 ug RCA_{120}) for 1h. To elute the non-glycosylated peptides, not attached to the lectins, the filter units were washed four times with binding buffer and after with ABC solution in H_2O_{18} (O188P, Eurositop). To release the N-glycopeptides from the lectins, the samples were incubated with PNGase diluted in H_2O_{18} (P0704L, New England BioLabs) for 3h at 37ºC. The N-glycopeptides were recovered by washing twice with ABC. All centrifugation steps were performed at 14.000g at RT.

LC-MS/MS analysis

For each run, estimated 0.5 µg were injected in a nanoRSLC-Q Exactive PLUS (Dionex RSLC Ultimate 3000, Thermo Scientific, Waltham, MA, USA). Peptides were separated on a 50cm reversed-phase liquid chromatographic column (Pepmap C18, Dionex). Chromatography solvents were (A) 0.1% formic acid in water and (B) 80% acetonitrile, 0.08% formic acid. Peptides were eluted from the column with a linear gradient of 120 minutes from 5% A to 80% B followed by 27 minutes of column re-equilibration in 5% A. Two blanks, each with two 25 min-linear gradient, were run between samples to prevent carryover. Peptides eluting from the column were analyzed by data dependent MS/MS, using top-10 acquisition method. Briefly, the instrument settings were as follows: resolution was set to 70,000 for MS scans and 17,500 for the data dependent MS/MS scans in order to increase speed. The MS AGC target was set to 3.10^6counts with 200ms for the injection time, while MS/MS AGC target was set to 1.10^5 with 120ms for the injection time. The MS scan range was from 400 to 2000 m/z. Dynamic exclusion was set to 30 sec. All analyses were performed in four biological replicates.

Total proteomics and glycoproteomics data analysis

The MS files were processed with MaxQuant software version 1.5.8.3 and searched with Andromeda search engine against the mouse subset from the UniProtKB/Swiss-Prot complete proteome database (release 2016_06). Statistical analysis and logo extractions were performed using Perseus version 1.5.5.3. Different thresholds were applied to total proteomics and glycoproteomics analysis given that the intensity of several peptides in total proteomics is used for determining protein intensity, while a single peptide in glycoproteomics is analysed at the time. For total proteomics, only proteins detected in all 8 samples (4 controls and 4 mutants) were retained for statistical analysis, avoiding all data imputation. For comparative glycoproteomics, we retained glycosites detected in at least 3 out of 4 control samples. Additionally, we selected proteins that were specifically detected in control or mutant samples by retaining proteins detected solely in at least 3 samples of one group. Both FDR and p-value (q-value < 0,05, paired student t-test) was used for total proteomics, whereas the p-value (< 0,05, unpaired student t-test) was used for N-glycopeptides. As a database for N-glycoproteins and number of N-glycosylation sites per protein (qualitative dataset, reference glycoproteomic dataset), the data obtained by glycoproteomics was used: any glycopeptide detected in at least 2 control samples was considered as potentially N-glycosylated (Table S2). Sites that were not previously described in Zielinska et al, 2010 or not predicted by uniprot were classified as likely novel N-glycosylation sites. Volcano plots were generated using the VolcanoShiny app (https://hardingnj.shinyapps.io/volcanoshiny/). PCA and variance analysis were done with the Partek Genomics Suite software. For homologous IgSF-CAM proteins (CNTNs, L1CAMs and NCAMs), HomoloGene and the study from Chen et al. 2010 were used.

Granule cells culture

Cerebellar granule cells were extracted from P7 cerebellum following the Manzini and colleagues protocol(Lee, Greene, Mason, & Manzini, 2009). Cells were kept at 37ºC in 48-well plates for at least 24h. For surface coating, 48-well plates were incubated at 4ºC O/N with the coating solution, followed by 3 PBS washes, blocking for 30 min with BSA to inhibit non-specific binding (10mg/mL) and three more PBS washes. The coatings used were: human recombinant L1CAM (10µg/mL; 777-NC, R&D), human recombinant NrCAM (5µg/mL; 2034-NR, R&D) human recombinant CNTN2 (10µg/mL; 1714-CN-025,

R&D), fibronectin (50µg/mL; F2006, Sigma) and Laminin D-Lysine (2µg/mL and 30µg/mL; 11243217001 and P6407, respectively, Sigma). Cell and neurite dynamics were measured every 3h by live cell imaging (Incucyte ZOOM with Neurotracker module). As long as GCs do not arborize, the neurite branching points parameter provided by the Incucyte software was translated as neurite number. For GCs re-aggregates, cells were isolated and seeded for 24h in un-coated surfaces ($1x10^6$ cells/cm^2) to promote aggregation. The aggregates were then collected and seeded in the coated surface for 36h.

Human induced pluripotent stem cells (hiPSCs) *SRD5A3*$^{-/-}$ generation and culture

iPSCs were derived from hPBMCs from a control male donor via Cyto-Tune Sendai virus reprogramming. Cells were cultured at 37ºC on vitronectin-coated (10µg/mL; 07180, Stem Cell) dishes with mTeSR media (Stem Cell). *SRD5A3* KO hiPSCs clones were generated by CRISPR/Cas9. sgRNA (inserted into a GFP-containing PX458 plasmid, Addgene) targeting the first exon of the gene were generated via the CRISPOR website and validated in T293 HEK cells by Sanger sequencing combined with tides analysis (https://tide-calculator.nki.nl/; data not shown). hiPSCs were transfected by nucleofection (Amaxa 4D, Lonza) and transfected cells (GFP+) were isolated by FACs (BD FACSAria II SORP, BD Biosciences) to generate single-cell-of-origin colonies. DNA was extracted from a piece of each colony by ZR-Duet DNA MiniPrep (D7003, Zymo) and sequenced. After selection, SOX2 (1:2000; AB5603, Millipore) and OCT4 (1:100; SC5279, Santa Cruz) immunostaining was used to confirm pluripotency. No major chromosomal abnormalities were detected by CGH array (60K, data not shown).

hiPSCs differentiation towards late cortical progenitors (LCPs)

Differentiation of hiPSCs towards LCPs and cortical projection neurons (CPNs) was carried as described by Benchoua and colleagues[320]. Briefly, iPSCs colonies were transferred to a non-coated dish with neural induction media (N2B27 with FGF2 and double SMAD inhibition by SB431542 and LDN193189, Stem Cell) for 6h and were afterwards transferred onto poly-ornithine and laminin coated dishes. Following neural rosette formation (12-15 days), the cells were passaged onto a geltrex-coated (A1413301, Life Tech) flask (LCPs P1) and were further cultured with N2B27 supplemented with FGF2, EGF and BDNF (Stem Cell). SOX2 and Nestin (1:250; N5413, Sigma) staining confirmed LCPs multipotency. Neuroectodermal origin of the emerging neural progenitor-like cells was assessed by HNK1/P75 FACs staining (data not shown). LCPs were further differentiated towards CPNs by growth factor withdrawal for 15 days. Neuronal identity was assessed with Tuj1 (1:2000; T2200, Sigma) staining (data not shown). WB results were replicated with two different clones of control and *SRD5A3* mutant hiPSCs.

Electronic microscopy experiments

P21 *En1Cre; Srd5a3*$^{fl/-}$ (n=1), *Atoh1Cre; Srd5a3*$^{fl/-}$ (n=2) and control littermates (n=3) were perfused with 4% PFA / 2% glutaraldehyde. The cerebellum was kept in the same solution for at least one week. Sagittal slices, less than 1mm thick, were post-fixed with 1% osmium tetroxide in 0.1 M phosphate buffer and then dehydrated in ethanol. After 10 min in a 1:2 mixture of epoxy propane and epoxy resin and 10 min in epon, samples were covered by upside down gelatin capsules filled with freshly prepared epoxy resin and polymerized at 60°C for 24 h. After heat separation, ultrathin sections of 90nm were cut with an ultra-microtome (Reichert ultracut S), stained with uranyl acetate and Reynold's lead and observed with a transmission electron microscope (JEOL 1011). Acquisition was performed with a Gatan Orius 1000 CCD camera.

Statistics

For mouse experiments, no statistical methods were used to predetermine sample size. No animals or samples were excluded from the analysis. All mouse experiments included at least two different litters. For mouse behavioral analysis, one way ANOVA was used. Regular enrichment analyses were performed by Fisher exact test (significance 0.05). For multiplicity and NxS motif correlation, the Pearson coefficient was used. For enrichment in highly N-glycosylated proteins, two-tailed Mann-Whitney test was performed. Statistical differences between groups were assessed by two-tailed student t-test. For all

statistical tests, confidence intervals were set at 95%. All results are presented in mean value and standard deviation was used to calculate the error bars.

BIBLIOGRAPHY

1. Barton, R. A. & Venditti, C. Rapid evolution of the cerebellum in humans and other great apes. *Curr Biol* **24,** 2440–2444 (2014).
2. Sultan, F. & Braitenberg, V. Shapes and sizes of different mammalian cerebella. A study in quantitative comparative neuroanatomy. *J. Hirnforsch.* **34,** 79–92 (1993).
3. Cajal, R. *Histologie du système nerveux de l'homme et des vertébrés*. **Tome II,** (1909).
4. Cajal, R. *Recuerdos de mi vida*. **Tomo II-,** (1917).
5. Apps, R. & Garwicz, M. Anatomical and physiological foundations of cerebellar information processing. *Nat Rev Neurosci* **6,** 297–311 (2005).
6. Rahimi-Balaei, M. *et al.* Embryonic stages in cerebellar afferent development. *Cerebellum & ataxias* **2,** 7 (2015).
7. D'Angelo, E. & Casali, S. Seeking a unified framework for cerebellar function and dysfunction: from circuit operations to cognition. *Front Neural Circuits* **6,** 116 (2012).
8. Coco, M. & Perciavalle, V. Where did the motor function of the cerebellum come from? *Cerebellum Ataxias* **2,** 10 (2015).
9. Buckley, E., Mazzà, C. & McNeill, A. A systematic review of the gait characteristics associated with Cerebellar Ataxia. *Gait Posture* **60,** 154–163 (2018).
10. Holmes, G. The symptoms of acute cerebellar injuries due to gunshot injuries. *Brain* **40,** (1917).
11. Manto, M., Bower, J. M. & Gerwig, M. HHS Public Access. **11,** 457–487 (2015).
12. Schmahmann, J. D. & Sherman, J. C. The cerebellar cognitive affective syndrome. *Brain* **121,** 561–579 (1998).
13. Yu, F., Jiang, Q. J., Sun, X. Y. & Zhang, R. W. A new case of complete primary cerebellar agenesis: Clinical and imaging findings in a living patient. *Brain* **138,** e353 (2015).
14. Stoodley, C. J., MacMore, J. P., Makris, N., Sherman, J. C. & Schmahmann, J. D. Location of lesion determines motor vs. cognitive consequences in patients with cerebellar stroke. *NeuroImage Clin.* **12,** 765–775 (2016).
15. Koziol, L. F. *et al.* Consensus paper: the cerebellum's role in movement and cognition. *Cerebellum* **13,** 151–77 (2014).
16. Bystron, I., Rakic, P., Molnár, Z. & Blakemore, C. The first neurons of the human cerebral cortex. *Nat. Neurosci.* **9,** 880–886 (2006).
17. de Graaf-Peters, V. B. & Hadders-Algra, M. Ontogeny of the human central nervous system: What is happening when? *Early Hum. Dev.* **82,** 257–266 (2006).
18. Bernal, J. Thyroid hormone receptors in brain development and function. *Nat. Clin. Pract. Endocrinol. Metab.* **3,** 249–259 (2007).
19. Friede, R. L. Dating the development of human cerebellum. *Acta Neuropathol* **23,** 48–58 (1973).
20. Walløe, S., Pakkenberg, B. & Fabricius, K. Stereological estimation of total cell numbers in the human cerebral and cerebellar cortex. *Front. Hum. Neurosci.* **8,** 508 (2014).
21. Wang, S. S.-H., Kloth, A. D. & Badura, A. The cerebellum, sensitive periods, and autism. *Neuron* **83,** 518–32 (2014).
22. Jaeger, B. N. & Jessberger, S. Unexpected help to repair the cerebellum. *Nat. Neurosci.* **20,** 1319–1321 (2017).
23. Chizhikov, V. & Millen, K. J. Development and malformations of the cerebellum in mice. *Mol. Genet. Metab.* **80,** 54–65 (2003).
24. Wurst, W., Auerbach, a B. & Joyner, a L. Multiple developmental defects in Engrailed-1 mutant mice: an early mid-hindbrain deletion and patterning defects in forelimbs and sternum. *Development* **120,** 2065–2075 (1994).
25. Martinez, S., Andreu, A., Mecklenburg, N. & Echevarria, D. Cellular and molecular basis of cerebellar development. *Front. Neuroanat.* **7,** 1–12 (2013).
26. Broccoli V Wurst W, B. E. The caudal limit of Otx2 expression positions the isthmic organizer. *Nature* **401,** 164–168 (1999).
27. Aldinger, K. A., Elsen, G. E., Prince, V. E. & Millen, K. J. Model organisms inform the search for the

genes and developmental pathology underlying malformations of the human hindbrain. *Semin Pediatr Neurol* **16,** 155–163 (2009).
28. Chedotal, A. Should I stay or should I go? Becoming a granule cell. *Trends Neurosci* **33,** 163–172 (2010).
29. Zhu, Y., Yu, T. & Rao, Y. Temporal regulation of cerebellar EGL migration through a switch in cellular responsiveness to the meninges. *Dev. Biol.* **267,** 153–164 (2004).
30. Guan, C. B., Xu, H. T., Jin, M., Yuan, X. B. & Poo, M. M. Long-range Ca2+ signaling from growth cone to soma mediates reversal of neuronal migration induced by slit-2. *Cell* **129,** 385–395 (2007).
31. Marillat, V. *et al.* Spatiotemporal expression patterns of slit and robo genes in the rat brain. *J. Comp. Neurol.* **442,** 130–155 (2002).
32. Espinosa, J. S. & Luo, L. Timing neurogenesis and differentiation: insights from quantitative clonal analyses of cerebellar granule cells. *J. Neurosci.* **28,** 2301–12 (2008).
33. Dahmane, N. & Ruiz, A. Sonic hedgehog and cerebellum development. *Development* **3100,** 3089–3100 (1999).
34. Rios, I., Alvarez-Rodríguez, R., Martí, E. & Pons, S. Bmp2 antagonizes sonic hedgehog-mediated proliferation of cerebellar granule neurones through Smad5 signalling. *Development* **131,** 3159–68 (2004).
35. Baeriswyl, T. & Stoeckli, E. T. Axonin-1/TAG-1 is required for pathfinding of granule cell axons in the developing cerebellum. *Neural Dev* **3,** 7 (2008).
36. Berglund EO Fredette B, Sekerková G, Marturano B, Weber L, Mugnaini E, Ranscht B, M. K. K. Ataxia and Abnormal Cerebellar Microorganization in Mice with Ablated Contactin Gene Expression. *Neuron* **24,** 739–750 (1999).
37. Kawaji, K., Umeshima, H., Eiraku, M., Hirano, T. & Kengaku, M. Dual phases of migration of cerebellar granule cells guided by axonal and dendritic leading processes. *Mol Cell Neurosci* **25,** 228–240 (2004).
38. Yue, Q. *et al.* PTEN deletion in Bergmann glia leads to premature differentiation and affects laminar organization. *Development* **132,** 3281–3291 (2005).
39. Jaarsma, D. *et al.* A role for Bicaudal-D2 in radial cerebellar granule cell migration. *Nat Commun* **5,** 3411 (2014).
40. Nguyen, H. *et al.* Glial scaffold required for cerebellar granule cell migration is dependent on dystroglycan function as a receptor for basement membrane proteins. *Acta Neuropathol. Commun.* **1,** 58 (2013).
41. Wu, K. H., Chen, C. Y. & Shen, E. Y. The cerebellar development in chinese children-a study by voxel-based volume measurement of reconstructed 3D MRI scan. *Pediatr. Res.* **69,** 80–83 (2011).
42. Barron, T., Saifetiarova, J., Bhat, M. A. & Kim, J. H. Myelination of Purkinje axons is critical for resilient synaptic transmission in the deep cerebellar nucleus. *Sci. Rep.* **8,** 1–12 (2018).
43. Boddaert, N. *et al.* Posterior fossa imaging in 158 children with ataxia. *J Neuroradiol* **37,** 220–230 (2010).
44. Bolduc, M. E. & Limperopoulos, C. Neurodevelopmental outcomes in children with cerebellar malformations: a systematic review. *Dev Med Child Neurol* **51,** 256–267 (2009).
45. Salman, M. S. Epidemiology of Cerebellar Diseases and Therapeutic Approaches. *Cerebellum* (2017). doi:10.1007/s12311-017-0885-2
46. Aldinger, K. A. & Doherty, D. The genetics of cerebellar malformations. *Semin. Fetal Neonatal Med.* **21,** 321–332 (2016).
47. Doherty, D., Millen, K. J. & Barkovich, A. J. Midbrain and hindbrain malformations: Advances in clinical diagnosis, imaging, and genetics. *Lancet Neurol.* **12,** 381–393 (2013).
48. Hong, S. E. *et al.* Autosomal recessive lissencephaly with cerebellar hypoplasia is associated with human RELN mutations. *Nat. Genet.* **26,** 93–96 (2000).
49. Honda, T., Kobayashi, K., Mikoshiba, K. & Nakajima, K. Regulation of cortical neuron migration by the reelin signaling pathway. *Neurochem. Res.* **36,** 1270–1279 (2011).
50. Huang, M. & Verbeek, D. S. Why do so many genetic insults lead to Purkinje Cell degeneration and spinocerebellar ataxia? *Neurosci. Lett.* (2018). doi:10.1016/j.neulet.2018.02.004
51. Lancella, L. *et al.* Acute cerebellitis in children: An eleven year retrospective multicentric study in Italy. *Ital. J. Pediatr.* **43,** 1–10 (2017).
52. Valk, J. & van der Knaap, M. S. Toxic encephalopathy. *AJNR Am J Neuroradiol* **13,** 747–60. (1992).
53. Al-Maawali, A., Blaser, S. & Yoon, G. Diagnostic Approach to Childhood-Onset Cerebellar Atrophy. *J. Child Neurol.* **27,** 1121–1132 (2012).
54. Megahed, H. *et al.* Utility of whole exome sequencing for the early diagnosis of pediatric-onset cerebellar atrophy associated with developmental delay in an inbred population. *Orphanet J. Rare*

Dis. **11,** 57 (2016).
55. Lander, E. S. *et al.* Initial sequencing and analysis of the human genome. *Nature* **409,** 860–921 (2001).
56. Alkuraya, F. S. Homozygosity mapping: One more tool in the clinical geneticist's toolbox. *Genet. Med.* **12,** 236–239 (2010).
57. Rabbani, B., Tekin, M. & Mahdieh, N. The promise of whole-exome sequencing in medical genetics. *J. Hum. Genet.* **59,** 5–15 (2014).
58. Ng, S. B. *et al.* Targeted capture and massively parallel sequencing of 12 human exomes. *Nature* **461,** 272–276 (2009).
59. Katsonis, P. *et al.* Single nucleotide variations: Biological impact and theoretical interpretation. *Protein Sci.* **23,** 1650–1666 (2014).
60. Majewski, J. *et al.* A new ocular phenotype associated with an unexpected but known systemic disorder and mutation: novel use of genomic diagnostics and exome sequencing. *J. Med. Genet.* **48,** 593–596 (2011).
61. Kammermeier, J. *et al.* Targeted gene panel sequencing in children with very early onset inflammatory bowel disease—evaluation and prospective analysis. *J. Med. Genet.* **51,** 748–755 (2014).
62. Knopp, C. *et al.* Syndromic ciliopathies: From single gene to multi gene analysis by SNP arrays and next generation sequencing. *Mol. Cell. Probes* **29,** 299–307 (2015).
63. Rice, G. I. *et al.* Assessment of Type I Interferon Signaling in Pediatric Inflammatory Disease. *J. Clin. Immunol.* **37,** 123–132 (2017).
64. Lerat, J. *et al.* An Application of NGS for Molecular Investigations in Perrault Syndrome: Study of 14 Families and Review of the Literature. *Hum. Mutat.* **37,** 1354–1362 (2016).
65. Jean Chemin, Karine Siquier-Pernet, Michaël Nicouleau, Giulia Barcia, Ali Ahmad, Daniel Medina-Cano, Sylvain Hanein, Nami Altin, Laurence Hubert, Christine Bole-Feysot, Cécile Fourage, Patrick Nitschké, Julien Thevenon, Marlène Rio, Pierre Blanc, Céline v, V. C. De novo mutations screening in childhood-onset cerebellar atrophy identifies gain of function mutations in the calcium channel CACNA1G. *Brain* (2018).
66. Carss, K. J. *et al.* Comprehensive Rare Variant Analysis via Whole-Genome Sequencing to Determine the Molecular Pathology of Inherited Retinal Disease. *Am. J. Hum. Genet.* **100,** 75–90 (2017).
67. Gurdon, J. B. Multiple genetically identical frogs. *J. Hered.* **53,** 9 (1962).
68. Kalani, M. Y. S. & Martirosyan, N. Direct conversion of fibroblasts to functional neurons. *World Neurosurg.* **77,** 7–8 (2012).
69. Takahashi, K. *et al.* Induction of Pluripotent Stem Cells from Adult Human Fibroblasts by Defined Factors. *Cell* **131,** 861–872 (2007).
70. Okita, K., Ichisaka, T. & Yamanaka, S. Generation of germline-competent induced pluripotent stem cells. *Nature* **448,** 313–317 (2007).
71. Hu, K. All Roads Lead to Induced Pluripotent Stem Cells: The Technologies of iPSC Generation. *Stem Cells Dev.* **23,** 1285–1300 (2014).
72. Ban, H. *et al.* Efficient generation of transgene-free human induced pluripotent stem cells (iPSCs) by temperature-sensitive Sendai virus vectors. *Proc. Natl. Acad. Sci.* **108,** 14234–14239 (2011).
73. Wernig, M. *et al.* In vitro reprogramming of fibroblasts into a pluripotent ES-cell-like state. *Nature* **448,** 318–324 (2007).
74. Liang, G. & Zhang, Y. Genetic and Epigenetic Variations in iPSCs: Potential Causes and Implications for Application. *Cell Stem Cell* **13,** 149–159 (2013).
75. Broutier, L. *et al.* Culture and establishment of self-renewing human and mouse adult liver and pancreas 3D organoids and their genetic manipulation. *Nat. Protoc.* **11,** 1724–1743 (2016).
76. Smukler, S. R., Runciman, S. B., Xu, S. & Van Der Kooy, D. Embryonic stem cells assume a primitive neural stem cell fate in the absence of extrinsic influences. *J. Cell Biol.* **172,** 79–90 (2006).
77. Chambers, S. M. *et al.* Highly efficient neural conversion of human ES and iPS cells by dual inhibition of SMAD signaling. *Nat. Biotechnol.* **27,** 275–280 (2009).
78. Suzuki, I. K. & Vanderhaeghen, P. Is this a brain which I see before me? Modeling human neural development with pluripotent stem cells. *Development* **142,** 3138–3150 (2015).
79. Koch, P. *et al.* Excitation-induced ataxin-3 aggregation in neurons from patients with Machado–Joseph disease. *Nature* 0–5 (2011). doi:10.1038/nature10671
80. Xu, X. & Zhong, Z. Disease modeling and drug screening for neurological diseases using human induced pluripotent stem cells. *Acta Pharmacol. Sin.* **34,** 755–764 (2013).
81. Gaj, T. ZFN, TALEN and CRISPR/Cas based methods for genome engineering. *2013* **31,** 397–405

(2014).
82. Joung, J. *et al.* Genome-scale CRISPR-Cas9 knockout and transcriptional activation screening. *Nat. Protoc.* **12,** 828–863 (2017).
83. Mojica, F. J. M., Díez-Villaseñor, C., Soria, E. & Juez, G. Biological significance of a family of regularly spaced repeats in the genomes of Archaea, Bacteria and mitochondria. *Mol. Microbiol.* **36,** 244–246 (2000).
84. Mojica, F. J. M., Díez-Villaseñor, C., García-Martínez, J. & Soria, E. Intervening sequences of regularly spaced prokaryotic repeats derive from foreign genetic elements. *J. Mol. Evol.* **60,** 174–182 (2005).
85. Makarova, K. S. *et al.* Evolution and classification of the CRISPR–Cas systems. *Nat. Rev. Microbiol.* **9,** 467–477 (2011).
86. Ran, F. A. *et al.* Genome engineering using the CRISPR-Cas9 system. *Nat. Protoc.* **8,** 2281–2308 (2013).
87. Duan, J. *et al.* Genome-wide identification of CRISPR/Cas9 off-targets in human genome. *Cell Res.* **24,** 1009–1012 (2014).
88. Hess, G. T., Tycko, J., Yao, D. & Bassik, M. C. Methods and Applications of CRISPR-Mediated Base Editing in Eukaryotic Genomes. *Mol. Cell* **68,** 26–43 (2017).
89. Mann, M. Resource Precision Mapping of an In Vivo N-Glycoproteome Reveals Rigid Topological and Sequence Constraints. *Cell* **141,** 897–907 (2010).
90. Apweiler, R., Hermjakob, H. & Sharon, N. On the frequency of protein glycosylation, as deduced from analysis of the SWISS-PROT database. *Biochim. Biophys. Acta - Gen. Subj.* **1473,** 4–8 (1999).
91. Khoury, G. A., Baliban, R. C. & Floudas, C. A. Proteome-wide post-translational modification statistics: Frequency analysis and curation of the swiss-prot database. *Sci. Rep.* **1,** 1–5 (2014).
92. Gahmberg, C. G. & Tolvanen, M. Why mammalian cell surface proteins are glycoproteins. *Trends Biochem. Sci.* **21,** 308–311 (1996).
93. Nettleship, J. E. *et al.* Analysis of variable N-glycosylation site occupancy in glycoproteins by liquid chromatography electrospray ionization mass spectrometry. *Anal. Biochem.* **361,** 149–151 (2007).
94. Varki, A. & Kornfeld, S. *Historical Background and Overview*. *Essentials of Glycobiology* (2015).
95. Oriol, R., Martinez-Duncker, I., Chantret, I., Mollicone, R. & Codogno, P. Common origin and evolution of glycosyltransferases using Dol-P-monosaccharides as donor substrate. *Mol. Biol. Evol.* **19,** 1451–63 (2002).
96. Aebi, M. N-linked protein glycosylation in the ER. *Biochim. Biophys. Acta - Mol. Cell Res.* **1833,** 2430–2437 (2013).
97. Shrimal, S., Cherepanova, N. A. & Gilmore, R. Cotranslational and posttranslocational N-glycosylation of proteins in the endoplasmic reticulum. *Semin. Cell Dev. Biol.* **41,** 71–78 (2015).
98. Hebert, D. N., Garman, S. C. & Molinari, M. The glycan code of the endoplasmic reticulum: Asparagine-linked carbohydrates as protein maturation and quality-control tags. *Trends Cell Biol.* **15,** 364–370 (2005).
99. E., J. in *Glycosylation* (InTech, 2012). doi:10.5772/48154
100. Varki, A., Cummings RD., E. J. *N-Glycans. Essentials of Glycobiology*. (2015).
101. Péanne, R. *et al.* Congenital disorders of glycosylation (CDG): Quo vadis? *Eur. J. Med. Genet.* (2017). doi:10.1016/j.ejmg.2017.10.012
102. Sparks, S. E. & Krasnewich, D. M. *Congenital Disorders of N-Linked Glycosylation and Multiple Pathway Overview*. *GeneReviews(®)* (2005).
103. Freeze, H. H., Chong, J. X., Bamshad, M. J. & Ng, B. G. Solving glycosylation disorders: Fundamental approaches reveal complicated pathways. *Am. J. Hum. Genet.* **94,** 161–175 (2014).
104. Jaeken, J. *et al.* Sialic acid-deficient serum and cerebrospinal fluid transferrin in a newly recognized genetic syndrome. *Clin. Chim. Acta.* **144,** 245–7 (1984).
105. Denecke, J. Biomarkers and diagnosis of congenital disorders of glycosylation. *Expert Opin. Med. Diagn.* **3,** 395–409 (2009).
106. Supraha Goreta, S., Dabelic, S. & Dumic, J. Insights into complexity of congenital disorders of glycosylation. *Biochem. Medica* **22,** 156–70 (2012).
107. Morava, E., Guillard, M., Lefeber, D. J. & Wevers, R. A. Autosomal recessive cutis laxa syndrome revisited. *Eur J Hum Genet* **17,** 1099–1110 (2009).
108. Vermeer, S. *et al.* Cerebellar ataxia and congenital disorder of glycosylation Ia (CDG-Ia) with normal routine CDG screening. *J. Neurol.* **254,** 1356–1358 (2007).
109. Pérez-Cerdá, C. *et al.* A Population-Based Study on Congenital Disorders of Protein N- and Combined with O-Glycosylation Experience in Clinical and Genetic Diagnosis. *J Pediatr* **183,** 170–7 (2016).
110. Scott, K., Gadomski, T., Kozicz, T. & Morava, E. Congenital disorders of glycosylation: New defects

and still counting. *J. Inherit. Metab. Dis.* **37,** 609–617 (2014).
111. Monticelli, M., Ferro, T., Jaeken, J., dos Reis Ferreira, V. & Videira, P. A. Immunological aspects of congenital disorders of glycosylation (CDG): a review. *J. Inherit. Metab. Dis.* **39,** 765–780 (2016).
112. Blank, C. *et al.* Recurrent infections and immunological dysfunction in congenital disorder of glycosylation Ia (CDG Ia). *J. Inherit. Metab. Dis.* **29,** 592 (2006).
113. Helander, A. *et al.* Dolichol kinase deficiency (DOLK-CDG) with a purely neurological presentation caused by a novel mutation. *Mol. Genet. Metab.* **110,** 342–344 (2013).
114. Molinari, F. *et al.* Oligosaccharyltransferase-Subunit Mutations in Nonsyndromic Mental Retardation. *Am. J. Hum. Genet.* **82,** 1150–1157 (2008).
115. Jaeken, J. in 1737–1743 (2013). doi:10.1016/B978-0-444-59565-2.00044-7
116. Freeze, H. H., Eklund, E. A., Ng, B. G. & Patterson, M. C. Neurology of inherited glycosylation disorders. *Lancet Neurol.* **11,** 453–466 (2012).
117. Wolfe, L. A. & Krasnewich, D. Congenital disorders of glycosylation and intellectual disability. *Dev. Disabil. Res. Rev.* **17,** 211–225 (2013).
118. Kjaergaard, S. Congenital disorders of glycosylation type Ia and Ib. Genetic, biochemical and clinical studies. *Dan. Med. Bull.* **51,** 350–63 (2004).
119. Barone, R., Fiumara, A. & Jaeken, J. Congenital disorders of glycosylation with emphasis on cerebellar involvement. *Semin. Neurol.* **34,** 357–66 (2014).
120. Serrano, M. *et al.* Phosphomannomutase deficiency (PMM2-CDG): ataxia and cerebellar assessment. *Orphanet J. Rare Dis.* **10,** 138 (2015).
121. Peters, V. *et al.* Congenital disorder of glycosylation IId (CDG-IId) -- a new entity: clinical presentation with Dandy-Walker malformation and myopathy. *Neuropediatrics* **33,** 27–32 (2002).
122. de Diego, V. *et al.* Erratum to: Longitudinal volumetric and 2D assessment of cerebellar atrophy in a large cohort of children with phosphomannomutase deficiency (PMM2-CDG) (J Inherit Metab Dis, 10.1007/s10545–017–0028-4). *J. Inherit. Metab. Dis.* **40,** 753–754 (2017).
123. Aronica, E. *et al.* Congenital disorder of glycosylation type Ia: A clinicopathological report of a newborn infant with cerebellar pathology. *Acta Neuropathol.* **109,** 433–442 (2005).
124. Serrano, N. L. *et al.* A quantitative assessment of the evolution of cerebellar syndrome in children with phosphomannomutase-deficiency (PMM2-CDG). *Orphanet J. Rare Dis.* **12,** 155 (2017).
125. Helenius, A. Intracellular Functions of N-Linked Glycans. *Science (80-.).* **291,** 2364–2369 (2001).
126. Xu, C. & Ng, D. T. W. Glycosylation-directed quality control of protein folding. *Nat. Rev. Mol. Cell Biol.* **16,** 742–752 (2015).
127. Roth, J. & Zuber, C. Quality control of glycoprotein folding and ERAD : the role of N -glycan handling , EDEM1 and OS-9. *Histochem. Cell Biol.* **147,** 269–284 (2017).
128. Baldridge, R. D. & Rapoport, T. A. Autoubiquitination of the Hrd1 Ligase Triggers Protein Retrotranslocation in ERAD. *Cell* **166,** 394–407 (2016).
129. Pincus, D., Chevalier, M. W., El-samad, H. & Walter, P. BiP Binding to the ER-Stress Sensor Ire1 Tunes the Homeostatic Behavior of the Unfolded Protein Response. **8,** (2010).
130. Bravo, R. *et al. Endoplasmic Reticulum and the Unfolded Protein Response: Dynamics and Metabolic Integration*. (2013). doi:10.1016/B978-0-12-407704-1.00005-1.Endoplasmic
131. Sano, R. & Reed, J. C. ER stress-induced cell death mechanisms . *BBAMCR* **1833,** 3460–3470 (2013).
132. Li, H., Korennykh, A. V, Behrman, S. L. & Walter, P. Mammalian endoplasmic reticulum stress sensor IRE1 signals by dynamic clustering. **2010,** (2010).
133. Karpa, K. D. *et al.* N -linked Glycosylation Is Required for Plasma Membrane Localization of D5 , but Not D1 , Dopamine Receptors in Transfected Mammalian Cells. **1078,** 1071–1078 (1999).
134. Fan, H., Meng, W., Kilian, C., Grams, S. & Reutter, W. Domain-specific N-glycosylation of the membrane glycoprotein dipeptidylpeptidase IV (CD26) influences its subcellular trafficking , biological stability , enzyme activity and protein folding. **251,** 243–251 (1997).
135. Vagin, O., Kraut, J. A. & Sachs, G. Role of N-glycosylation in trafficking of apical membrane proteins in epithelia. **90073,** 459–469 (2018).
136. Marada, S. *et al.* Functional Divergence in the Role of N-Linked Glycosylation in Smoothened Signaling. 1–27 (2015). doi:10.1371/journal.pgen.1005473
137. D. Zielinska, F. Gnad, J. Wisniewski, and M. M. Resource Precision Mapping of an In Vivo N-Glycoproteome Reveals Rigid Topological and Sequence Constraints. *Cell* **141,** 897–907 (2010).
138. Scott, H. & Panin, V. M. N-glycosylation in Regulation of the Nervous System. 367–394 (2015). doi:10.1007/978-1-4939-1154-7
139. Hanus, C. *et al.* Unconventional secretory processing diversifies neuronal ion channel properties. 1–27 (2016). doi:10.7554/eLife.20609

140. Isope, P. & Barbour, B. Properties of Unitary Granule Cell 3 Purkinje Cell Synapses in Adult Rat Cerebellar Slices. **22,** 9668–9678 (2002).
141. Traynelis, S. F. *et al.* Glutamate Receptor Ion Channels : Structure , Regulation , and Function. (2014). doi:10.1124/pr.109.002451.405
142. Surface, C. HNK-1 Glyco-epitope Regulates the Stability of the Glutamate Receptor Subunit GluR2 on the Neuronal. **284,** 30209–30217 (2009).
143. Ramanathan, V. K. & Hall, Z. W. Altered Glycosylation Sites of the delta Subunit of the Acetylcholine Receptor (AChR) Reduce alphadelta Association and Receptor Assembly *. **274,** 20513–20520 (1999).
144. Buck, C. A., Click, C. & Warren, L. A Comparative Study of Glycoproteins from the Surface of Control and Rous Sarcoma Virus Transformed Hamster Cells. **9,** 4567–4576 (1970).
145. L. WARREN, J. P. F. A. C. A. B. Surface Glycoproteins of Normal and Transformed Cells: A Difference Determined by Sialic Acid and a Growth-Dependent Sialyl Transferase. **516,** 97–127 (1978).
146. Agrawal, P. *et al.* A Systems Biology Approach Identifies FUT8 as a Driver of Melanoma Metastasis. *Cancer Cell* **31,** 804–819.e7 (2017).
147. A. Magalhaes, H. D. and C. R. Aberrant Glycosylation in Cancer : A Novel Molecular Mechanism. 733–735 (2017). doi:10.1016/j.ccell.2017.05.012
148. Stevens, J. & Spang, A. Attenuation of N-glycosylation causes polarity and adhesion defects in the C . elegans embryo. **1,** 1224–1231 (2017).
149. Hirai-fujita, Y., Yamamoto-hino, M., Kanie, O. & Goto, S. N -Glycosylation of the Drosophila neural protein Chaoptin is essential for its stability , cell surface transport and adhesive activity. **582,** 2572–2576 (2008).
150. Vogel, C. & Chothia, C. Protein Family Expansions and Biological Complexity. **2,** (2006).
151. DF. Zielinska, F. Gnad, K. Schropp, JR. Wiśniewski, M. M. Mapping N-Glycosylation Sites across Seven Evolutionarily Distant Species Reveals a Divergent Substrate Proteome Despite a Common Core Machinery. (2012). doi:10.1016/j.molcel.2012.04.031
152. Gulisano, W., Bizzoca, A., Gennarini, G., Palmeri, A. & Puzzo, D. Molecular and Cellular Neuroscience Role of the adhesion molecule F3 / Contactin in synaptic plasticity and memory. *Mol. Cell. Neurosci.* **81,** 64–71 (2017).
153. Seong, E. *et al.* Cadherins and catenins in dendrite and synapse morphogenesis Cadherins and catenins in dendrite and synapse morphogenesis. **6918,** (2015).
154. Jamal, B. T. N-glycosylation status of E-cadherin controls cytoskeletal dynamics through the organization of distinct β-catenin- and γ-catenin-containing AJs . (2009).
155. Tharmalingam, S. & Hampson, D. R. The calcium-sensing receptor and integrins in cellular differentiation and migration. *Front. Physiol.* **7,** 1–18 (2016).
156. Loss, C., Fibronectin, O. F. & Actmty, B. Functional Role of N-Glycosylation in a 5 p l Integrin Receptor. (1994).
157. Janik, M. E., Lity, A. & Vereecken, P. Biochimica et Biophysica Acta Cell migration — The role of integrin glycosylation. **1800,** 545–555 (2010).
158. Cai, X., Thinn, A. M. M., Wang, Z., Shan, H. & Zhu, J. The importance of N-glycosylation on β3integrin ligand binding and conformational regulation. *Sci. Rep.* **7,** 1–14 (2017).
159. Pocheć, E. *et al.* Aberrant glycosylation of αvβ3 integrin is associated with melanoma progression. *Anticancer Res.* **35,** 2093–103 (2015).
160. Williams, A. F. A year in the life of the immunoglobulin superfamily. **8,** (1987).
161. DM. Halaby, J. M. The Immunoglobulin Superfamily : An Insight on Its Tissular , Species , and Functional Diversity. 389–400 (1998).
162. Fitzli, D. *et al.* A Direct Interaction of Axonin-1 with NgCAM-related Cell Adhesion Molecule (NrCAM) Results in Guidance , but not Growth of Commissural Axons. **149,** 951–968 (2000).
163. Wei, C. H. & Ryu, S. E. Homophilic interaction of the L1 family of cell adhesion molecules. **44,** 413–423 (2012).
164. Jiang, N., Chen, W., Jothikumar, P., Patel, J. M. & Lippincott-schwartz, J. Effects of anchor structure and glycosylation of Fc γ receptor III on ligand binding affinity. **27,** (2016).
165. Leshchyns, I. & Sytnyk, V. Reciprocal Interactions between Cell Adhesion Molecules of the Immunoglobulin Superfamily and the Cytoskeleton in Neurons. **4,** 1–10 (2016).
166. Yoshihara, Y., Oka, S., Ikeda, J. & Mori, K. Immunoglobulin superfamily molecules in the nervous system. **10,** 83–105 (1991).
167. Landmesser, L; Dahm, L; Schultz, K. R. U. Distinct Roles for Adhesion Molecules during Innervation of Embryonic Chick Muscle. **670,** 645–670 (1988).
168. Mu, M., Oltmann-norden, I., Weinhold, B. & Hildebrandt, H. Brain development needs sugar : the

role of polysialic acid in controlling NCAM functions. **390,** 567–574 (2009).
169. Stoeckli, E. T. Neural circuit formation in the cerebellum is controlled by cell adhesion molecules of the Contactin family. *Cell Adhes. Migr.* **4,** 523–526 (2010).
170. Sakurai, T. *et al.* Overlapping functions of the cell adhesion molecules Nr-CAM and L1 in cerebellar granule cell development. **154,** 1259–1273 (2001).
171. Fransen, E. *et al.* L1 knockout mice show dilated ventricles , vermis hypoplasia and impaired exploration patterns. **7,** 999–1009 (1998).
172. Fogel, A. I. *et al.* N-Glycosylation at the SynCAM (Synaptic Cell Adhesion Molecule) Immunoglobulin Interface Modulates Synaptic Adhesion. **285,** 34864–34874 (2010).
173. Lonlay, P. De. The clinical spectrum of phosphomannose isomerase de fi ciency , with an evaluation of mannose treatment for CDG-Ib. *BBA - Mol. Basis Dis.* **1792,** 841–843 (2009).
174. Thiel, C. & Körner, C. Mouse models for congenital disorders of glycosylation. 879–889 (2011). doi:10.1007/s10545-011-9295-7
175. Cantagrel, V. *et al.* SRD5A3 Is Required for Converting Polyprenol to Dolichol and Is Mutated in a Congenital Glycosylation Disorder. 203–217 (2010). doi:10.1016/j.cell.2010.06.001
176. Schaftingen, E. Van & Jaeken, J. Phosphomannomutase deficiency is a cause of carbohydrate-deficient glycoprotein syndrome type I. **377,** 318–320 (1995).
177. Cline, A. *et al.* A zebrafish model of PMM2-CDG reveals altered neurogenesis and a substrate-accumulation mechanism for N-linked glycosylation deficiency. *Mol. Biol. Cell* **23,** 4175–87 (2012).
178. Himmelreich, N., Kaufmann, L. T., Steinbeisser, H., Körner, C. & Thiel, C. Lack of phosphomannomutase 2 affects Xenopus laevis morphogenesis and the non-canonical Wnt5a / Ror2 signalling. (2015). doi:10.1007/s10545-015-9874-0
179. Parkinson, W. M., Dookwah, M., Dear, M. L., Gatto, C. L. & Aoki, K. Synaptic roles for phosphomannomutase type 2 in a new Drosophila congenital disorder of glycosylation disease model. 513–527 (2016). doi:10.1242/dmm.022939
180. Matthijs, G. *et al.* Mutations in PMM2 That Cause Congenital Disorders of Glycosylation , Type Ia (CDG-Ia). **394,** 386–394 (2000).
181. Schneider, A. *et al.* Successful prenatal mannose treatment for congenital disorder of glycosylation-Ia in mice. **18,** 2011–2013 (2012).
182. Grünewald, S. The clinical spectrum of phosphomannomutase 2 deficiency (CDG-Ia). **1792,** 827–834 (2009).
183. Chan, B. *et al.* A mouse model of a human congenital disorder of glycosylation caused by loss of PMM2. *Hum. Mol. Genet.* **25,** 2182–2193 (2016).
184. Thiesler, C. T. *et al.* Glycomic Characterization of Induced Pluripotent Stem Cells Derived from a Patient Suffering from Phosphomannomutase 2 Congenital Disorder of Glycosylation. 1435–1452 (2016). doi:10.1074/mcp.M115.054122
185. Morava, E. *et al.* A novel cerebello-ocular syndrome with abnormal glycosylation due to abnormalities in dolichol metabolism. 3210–3220 (2010). doi:10.1093/brain/awq261
186. Kara, B., Ayhan, Ö., Gökçay, G. & Ba, N. Adult phenotype and further phenotypic variability in SRD5A3-CDG. (2014).
187. Taylor, R. L. *et al.* Association of steroid 5α-reductase type 3 congenital disorder of glycosylation with early-onset retinal dystrophy. *JAMA Ophthalmol.* **135,** 339–347 (2017).
188. Buczkowska, A., Swiezewska, E. & Lefeber, D. J. Genetic defects in dolichol metabolism. 157–169 (2015). doi:10.1007/s10545-014-9760-1
189. McVicker, D. P. *et al.* Transport of a kinesin-cargo pair along microtubules into dendritic spines undergoing synaptic plasticity. *Nat. Commun.* **7,** 1–13 (2016).
190. Lee, J. R. *et al.* De novo mutations in the motor domain of KIF1A cause cognitive impairment, spastic paraparesis, axonal neuropathy, and cerebellar atrophy. *Hum. Mutat.* **36,** 69–78 (2015).
191. Coutelier, M. *et al.* A recurrent mutation in CACNA1G alters Cav3.1 T-type calcium-channel conduction and causes autosomal-dominant cerebellar ataxia. *Am. J. Hum. Genet.* **97,** 726–737 (2015).
192. Dreyfus, F. M. *et al.* Selective T-Type Calcium Channel Block in Thalamic Neurons Reveals Channel Redundancy and Physiological Impact of ITwindow. *J. Neurosci.* **30,** 99–109 (2010).
193. Ly, R. *et al.* T-type channel blockade impairs long-term potentiation at the parallel fiber-Purkinje cell synapse and cerebellar learning. *Proc. Natl. Acad. Sci.* **110,** 20302–20307 (2013).
194. Irvine, R. F. & Schell, M. J. Back in the Water: the Return of the Inositol Phosphates. *J. Palliat. Med.* **2,** 971–972 (2011).
195. York, J. D. Regulation of nuclear processes by inositol polyphosphates. *Biochim. Biophys. Acta - Mol. Cell Biol. Lipids* **1761,** 552–559 (2006).

196. Fu, C. *et al.* Inositol Hexakisphosphate Kinase-3 Regulates the Morphology and Synapse Formation of Cerebellar Purkinje Cells via Spectrin/Adducin. *J Neurosci* **35,** 11056–67 (2015).
197. Dentici, M. L. *et al.* Identification of novel and hotspot mutations in the channel domain of ITPR1 in two patients with Gillespie syndrome. *Gene* **628,** 141–145 (2017).
198. Yang, A. W., Sachs, A. J. & Nystuen, A. M. Deletion of Inpp5a causes ataxia and cerebellar degeneration in mice. *Neurogenetics* **16,** 277–285 (2015).
199. Sgaier, S. K. *et al.* Genetic subdivision of the tectum and cerebellum into functionally related regions based on differential sensitivity to engrailed proteins. *Development* **134,** 2325–2335 (2007).
200. Cao, J., Guo, S., Arai, K., Lo, E. H. & Ning, M. Studying extracellular signaling utilizing a glycoproteomic approach: lectin blot surveys, a first and important step. *Methods Mol. Biol.* **1013,** 227–33 (2013).
201. Rujano, M. A. *et al.* Mutations in the X-linked ATP6AP2 cause a glycosylation disorder with autophagic defects. *J. Exp. Med.* **214,** 3707–3729 (2017).
202. Kretzer, N. M. *et al.* RAB43 facilitates cross-presentation of cell-associated antigens by CD8α+ dendritic cells. *J. Exp. Med.* **213,** 2871–2883 (2016).
203. Matei, V. *et al.* Smaller inner ear sensory epithelia in Neurog 1 null mice are related to earlier hair cell cycle exit. *Dev. Dyn.* **234,** 633–50 (2005).
204. Zielinska, D. F., Gnad, F., Wiśniewski, J. R. & Mann, M. Precision mapping of an in vivo N-glycoproteome reveals rigid topological and sequence constraints. *Cell* **141,** 897–907 (2010).
205. Hülsmeier, A. J., Paesold-Burda, P. & Hennet, T. N-Glycosylation Site Occupancy in Serum Glycoproteins Using Multiple Reaction Monitoring Liquid Chromatography-Mass Spectrometry. *Mol. Cell. Proteomics* **6,** 2132–2138 (2007).
206. Thomas, S. N. *et al.* Multiplexed Targeted Mass Spectrometry-Based Assays for the Quantification of N-Linked Glycosite-Containing Peptides in Serum. *Anal. Chem.* **87,** 10830–8 (2015).
207. Lipecka, J. *et al.* Sensitivity of mass spectrometry analysis depends on the shape of the filtration unit used for filter aided sample preparation (FASP). *Proteomics* **16,** 1852–7 (2016).
208. Wiśniewski, J. R., Zougman, A., Nagaraj, N. & Mann, M. Universal sample preparation method for proteome analysis. *Nat. Methods* **6,** 359–62 (2009).
209. Fujimori, T. *et al.* Endoplasmic reticulum proteins SDF2 and SDF2L1 act as components of the BiP chaperone cycle to prevent protein aggregation. *Genes to Cells* **22,** 684–698 (2017).
210. Zhao, L., Rosales, C., Seburn, K., Ron, D. & Ackerman, S. L. Alteration of the unfolded protein response modifies neurodegeneration in a mouse model of Marinesco-Sjögren syndrome. *Hum. Mol. Genet.* **19,** 25–35 (2009).
211. Ron, D. & Walter, P. Signal integration in the endoplasmic reticulum unfolded protein response. *Nat. Rev. Mol. Cell Biol.* **8,** 519–29 (2007).
212. Murray, A. N. *et al.* Enhanced Aromatic Sequons Increase Oligosaccharyltransferase Glycosylation Efficiency and Glycan Homogeneity. *Chem. Biol.* **22,** 1052–62 (2015).
213. Gavel, Y. & von Heijne, G. Sequence differences between glycosylated and non-glycosylated Asn-X-Thr/Ser acceptor sites: implications for protein engineering. *Protein Eng.* **3,** 433–42 (1990).
214. Maness, P. F. & Schachner, M. Neural recognition molecules of the immunoglobulin superfamily: signaling transducers of axon guidance and neuronal migration. *Nat. Neurosci.* **10,** 19–26 (2007).
215. Stoeckli, E. T. Neural circuit formation in the cerebellum is controlled by cell adhesion molecules of the Contactin family. *Cell Adh. Migr.* **4,** 523–6
216. Pollerberg, G. E., Thelen, K., Theiss, M. O. & Hochlehnert, B. C. The role of cell adhesion molecules for navigating axons: density matters. *Mech. Dev.* **130,** 359–72
217. Lutz, D. *et al.* Myelin basic protein cleaves cell adhesion molecule L1 and promotes neuritogenesis and cell survival. *J. Biol. Chem.* **289,** 13503–18 (2014).
218. Tan, K. P. *et al.* Fucosylation of LAMP-1 and LAMP-2 by FUT1 correlates with lysosomal positioning and autophagic flux of breast cancer cells. *Cell Death Dis.* **7,** e2347 (2016).
219. Hockemeyer, D. & Jaenisch, R. Cell Stem Cell Induced Pluripotent Stem Cells Meet Genome Editing. *Cell Stem Cell* **18,** 573–586 (2016).
220. Moulding, H. D., Martuza, R. L. & Rabkin, S. D. Clinical mutations in the L1 neural cell adhesion molecule affect cell-surface expression. *J. Neurosci.* **20,** 5696–702 (2000).
221. Hortsch, M. Structural and functional evolution of the L1 family: are four adhesion molecules better than one? *Mol. Cell. Neurosci.* **15,** 1–10 (2000).
222. Wei, C. H. & Ryu, S. E. Homophilic interaction of the L1 family of cell adhesion molecules. *Exp. Mol. Med.* **44,** 413–23 (2012).
223. Horstkorte, R., Schachner, M., Magyar, J. P., Vorherr, T. & Schmitz, B. The fourth immunoglobulin-

like domain of NCAM contains a carbohydrate recognition domain for oligomannosidic glycans implicated in association with L1 and neurite outgrowth. *J. Cell Biol.* **121,** 1409–21 (1993).
224. Dequidt, C. *et al.* Fast turnover of L1 adhesions in neuronal growth cones involving both surface diffusion and exo/endocytosis of L1 molecules. *Mol. Biol. Cell* **18,** 3131–43 (2007).
225. Haeuptle, M. A. *et al.* Improvement of dolichol-linked oligosaccharide biosynthesis by the squalene synthase inhibitor zaragozic acid. *J. Biol. Chem.* **286,** 6085–6091 (2011).
226. Forbes, K. *et al.* Statins inhibit insulin-like growth factor action in first trimester placenta by altering insulin-like growth factor 1 receptor glycosylation. *Mol. Hum. Reprod.* **21,** 105–14 (2015).
227. Cantagrel, V. *et al.* SRD5A3 Is Required for Converting Polyprenol to Dolichol and Is Mutated in a Congenital Glycosylation Disorder. *Cell* **142,** 203–217 (2010).
228. Sorrentino, G. *et al.* Metabolic control of YAP and TAZ by the mevalonate pathway. *Nat. Cell Biol.* **16,** 357–366 (2014).
229. Hilaire, N., Salvayre, R., Thiers, J. C., Bonnafe, M. J. & Negre-Salvayre, A. The turnover of cytoplasmic triacylglycerols in human fibroblasts involves two separate acyl chain length-dependent degradation pathways. *J. Biol. Chem.* **270,** 27027–27034 (1995).
230. Pérez-Dueñas, B. *et al.* Long-term evolution of eight Spanish patients with CDG type Ia: typical and atypical manifestations. *Eur. J. Paediatr. Neurol.* **13,** 444–51 (2009).
231. Linssen, M., Mohamed, M., Wevers, R. A., Lefeber, D. J. & Morava, E. Thrombotic complications in patients with PMM2-CDG. *Mol. Genet. Metab.* **109,** 107–11 (2013).
232. Coutelier, M. *et al.* Efficacy of Exome-Targeted Capture Sequencing to Detect Mutations in Known Cerebellar Ataxia Genes. *JAMA Neurol.* 1–9 (2018). doi:10.1001/jamaneurol.2017.5121
233. Boddaert, N. *et al.* Posterior fossa imaging in 158 children with ataxia. *J. Neuroradiol.* **37,** 220–230 (2010).
234. Botstein, D. & Risch, N. Discovering genotypes underlying human phenotypes: Past successes for mendelian disease, future approaches for complex disease. *Nat. Genet.* **33,** 228–237 (2003).
235. Boycott, K. M. *et al.* International Cooperation to Enable the Diagnosis of All Rare Genetic Diseases. *Am. J. Hum. Genet.* **100,** 695–705 (2017).
236. Dunn, P. *et al.* Next Generation Sequencing Methods for Diagnosis of Epilepsy Syndromes. *Front. Genet.* **9,** 1–11 (2018).
237. Cummings, B. B. *et al.* Improving genetic diagnosis in Mendelian disease with transcriptome sequencing. *bioRxiv* **5209,** 74153 (2017).
238. DeRossi, C. *et al.* Ablation of mouse phosphomannose isomerase (Mpi) causes mannose 6-phosphate accumulation, toxicity, and embryonic lethality. *J. Biol. Chem.* **281,** 5916–5927 (2006).
239. Thiel, C., Lubke, T., Matthijs, G., von Figura, K. & Korner, C. Targeted Disruption of the Mouse Phosphomannomutase 2 Gene Causes Early Embryonic Lethality. *Mol. Cell. Biol.* **26,** 5615–5620 (2006).
240. Chan, B. *et al.* A mouse model of a human congenital disorder of glycosylation caused by loss of PMM2. *Hum. Mol. Genet.* **25,** 2182–2193 (2016).
241. Sharma, V. *et al.* Mannose supplements induce embryonic lethality and blindness in phosphomannose isomerase hypomorphic mice. *FASEB J.* **28,** 1854–1869 (2014).
242. Butts, T., Green, M. J. & Wingate, R. J. T. Development of the cerebellum: simple steps to make a 'little brain'. *Development* **141,** 4031–4041 (2014).
243. Jozwiak, A. *et al.* POLYPRENOL REDUCTASE2 Deficiency Is Lethal in Arabidopsis Due to Male Sterility. *Plant Cell* **27,** 3336–3353 (2015).
244. Mohamed, M. *et al.* Normal glycosylation screening does not rule out SRD5A3-CDG. *Eur. J. Hum. Genet.* **19,** 1019 (2011).
245. Galleguillos, S. N. *et al.* What can mathematical modelling say about CHO metabolism and protein glycosylation? *Comput. Struct. Biotechnol. J.* **15,** 212–221 (2017).
246. Castillo-Acosta, V. íM, Ruiz-Pérez, L. M., Van Damme, E. J. M., Balzarini, J. & González-Pacanowska, D. Exposure of Trypanosoma brucei to an N-acetylglucosamine-Binding Lectin Induces VSG Switching and Glycosylation Defects Resulting in Reduced Infectivity. *PLoS Negl. Trop. Dis.* **9,** 1–21 (2015).
247. Rujano, M. A. *et al.* Mutations in the X-linked *ATP6AP2* cause a glycosylation disorder with autophagic defects. *J. Exp. Med.* **214,** 3707–3729 (2017).
248. Park, E. J. *et al.* Mutation of Nogo-B receptor, a subunit of cis-prenyltransferase, causes a congenital disorder of glycosylation. *Cell Metab.* **20,** 448–457 (2014).
249. He, P., Ng, B. G., Losfeld, M. E., Zhu, W. & Freeze, H. H. Identification of intercellular cell adhesion molecule 1 (ICAM-1) as a hypoglycosylation marker in congenital disorders of glycosylation cells. *J. Biol. Chem.* **287,** 18210–18217 (2012).

250. Wu, H. *et al.* Caveolin-1 Is Critical for Lymphocyte Trafficking into Central Nervous System during Experimental Autoimmune Encephalomyelitis. *J. Neurosci.* **36,** 5193–5199 (2016).
251. Zhou, Y. *et al.* Inhibition of fucosylation by 2-fluorofucose suppresses human liver cancer HepG2 cell proliferation and migration as well as tumor formation. *Sci. Rep.* **7,** 1–12 (2017).
252. Fukuda, T. *et al.* 1,6-fucosyltransferase-deficient mice exhibit multiple behavioral abnormalities associated with a schizophrenia-like phenotype: Importance of the balance between the dopamine and serotonin systems. *J. Biol. Chem.* **286,** 18434–18443 (2011).
253. Kerjan, G. *et al.* The transmembrane semaphorin Sema6A controls cerebellar granule cell migration. *Nat. Neurosci.* **8,** 1516–1524 (2005).
254. Driver, A., Shumrick, C. & Stottmann, R. Ttc21b Is Required in Bergmann Glia for Proper Granule Cell Radial Migration. *J. Dev. Biol.* **5,** 18 (2017).
255. Oliver, T. G. Loss of patched and disruption of granule cell development in a pre-neoplastic stage of medulloblastoma. *Development* **132,** 2425–2439 (2005).
256. Xenaki, D. *et al.* F3/contactin and TAG1 play antagonistic roles in the regulation of sonic hedgehog-induced cerebellar granule neuron progenitor proliferation. *Development* **138,** 519–529 (2011).
257. Lorenz, A. *et al.* Severe Alterations of Cerebellar Cortical Development after Constitutive Activation of Wnt Signaling in Granule Neuron Precursors. *Mol. Cell. Biol.* **31,** 3326–3338 (2011).
258. McNeill, E. M. *et al.* Nav2 hypomorphic mutant mice are ataxic and exhibit abnormalities in cerebellar development. *Dev. Biol.* **353,** 331–343 (2011).
259. Men, Y. *et al.* LKB1 Regulates Cerebellar Development by Controlling Sonic Hedgehog-mediated Granule Cell Precursor Proliferation and Granule Cell Migration. *Sci. Rep.* **5,** 1–16 (2015).
260. Takano, T., Akahori, S., Takeuchi, Y. & Ohno, M. Neuronal apoptosis and gray matter heterotopia in microcephaly produced by cytosine arabinoside in mice. *Brain Res.* **1089,** 55–66 (2006).
261. Donkol, R. H. Assessment of gray matter heterotopia by magnetic resonance imaging. *World J. Radiol.* **4,** 90 (2012).
262. Monin, M.-L. *et al.* 29 French adult patients with PMM2-congenital disorder of glycosylation: outcome of the classical pediatric phenotype and depiction of a late-onset phenotype. *Orphanet J. Rare Dis.* **9,** 207 (2014).
263. Sun, L. *et al.* Insufficient ER-stress response causes selective mouse cerebellar granule cell degeneration resembling that seen in congenital disorders of glycosylation. *Mol. Brain* **6,** 2–9 (2013).
264. Wang, H. *et al.* Tunicamycin-induced unfolded protein response in the developing mouse brain. *Toxicol. Appl. Pharmacol.* **283,** 157–167 (2015).
265. Govek, E.-E. *et al.* Cdc42 Regulates Neuronal Polarity during Cerebellar Axon Formation and Glial-Guided Migration. *iScience* **1,** 35–48 (2018).
266. Rosenwald, a G. & Krag, S. S. Lec9 CHO glycosylation mutants are defective in the synthesis of dolichol. *J. Lipid Res.* **31,** 523–33 (1990).
267. He, P., Srikrishna, G. & Freeze, H. H. N-glycosylation deficiency reduces ICAM-1 induction and impairs inflammatory response. *Glycobiology* **24,** 392–398 (2014).
268. Blank, C. *et al.* Recurrent infections and immunological dysfunction in congenital disorder of glycosylation Ia (CDG Ia). *J. Inherit. Metab. Dis.* **29,** 592–592 (2006).
269. SHINJO, S., MIZOTANI, Y., TASHIRO, E. & IMOTO, M. Comparative Analysis of the Expression Patterns of UPR-Target Genes Caused by UPR-Inducing Compounds. *Biosci. Biotechnol. Biochem.* **77,** 729–735 (2013).
270. Shang, J., Körner, C., Freeze, H. & Lehrman, M. A. Extension of lipid-linked oligosaccharides is a high-priority aspect of the unfolded protein response: Endoplasmic reticulum stress in Type I congenital disorder of glycosylation fibroblasts. *Glycobiology* **12,** 307–317 (2002).
271. Lecca, M. R., Wagner, U., Patrignani, A., Berger, E. G. & Hennet, T. Genome-wide analysis of the unfolded protein response in fibroblasts from congenital disorders of glycosylation type-I patients. *FASEB J.* **19,** 240–242 (2005).
272. Pan, S. *et al.* Large-scale quantitative glycoproteomics analysis of site-specific glycosylation occupancy. *Mol. Biosyst.* **8,** 2850 (2012).
273. Fang, P. *et al.* In-depth mapping of the mouse brain *N*-glycoproteome reveals widespread *N*-glycosylation of diverse brain proteins. *Oncotarget* **7,** (2016).
274. Lau, K. S. *et al.* Complex N-Glycan Number and Degree of Branching Cooperate to Regulate Cell Proliferation and Differentiation. *Cell* **129,** 123–134 (2007).
275. Boscher, C., Dennis, J. W. & Nabi, I. R. Glycosylation, galectins and cellular signaling. *Curr. Opin. Cell Biol.* **23,** 383–392 (2011).
276. Gavel, Y. & Heyne, G. Von. Sequence differences between glycosylated and non-glycosylated Asn-X-

Thr / Ser acceptor sites : implications for protein engineering. **3,** 433–442 (1990).
277. Murray, A. N. *et al.* Enhanced Aromatic Sequons Increase Oligosaccharyltransferase Glycosylation Efficiency and Glycan Homogeneity. *Chem. Biol.* **22,** 1052–1062 (2015).
278. Michele, D. E. *et al.* Post-translational disruption of dystroglycan – ligand interactions in congenital muscular dystrophies. **418,** 417–422 (2002).
279. Ervasti, J. M. & Campbell, K. P. Membrane Organization of the Dystrophin-Glycoprotein Complex. *Cell* **66,** (1991).
280. Weinhold, B. *et al.* Genetic ablation of polysialic acid causes severe neurodevelopmental defects rescued by deletion of the neural cell adhesion molecule. *J. Biol. Chem.* **280,** 42971–7 (2005).
281. Pollerberg, G. E., Thelen, K., Theiss, M. O. & Hochlehnert, B. C. The role of cell adhesion molecules for navigating axons: Density matters. *Mech. Dev.* **130,** 359–372 (2013).
282. Schwarz, V., Pan, J., Voltmer-irsch, S. & Hutter, H. IgCAMs redundantly control axon navigation in Caenorhabditis elegans. **15,** 1–15 (2009).
283. Stoeckli, E. T., Sonderegger, P., Pollerberg, G. E. & Landmesser, L. T. Interference with Axonin-1 and NrCAM Interactions Unmasks a Floor-Plate Activity Inhibitory for Commissural Axons. **18,** 209–221 (1997).
284. Sakurai, T. *et al.* Overlapping functions of the cell adhesion molecules Nr-CAM and L1 in cerebellar granule cell development. **154,** 1259–1273 (2001).
285. Chatzopoulou, E. *et al.* Structural requirement of TAG-1 for retinal ganglion cell axons and myelin in the mouse optic nerve. *J. Neurosci.* **28,** 7624–36 (2008).
286. Pruss, T., Niere, M., Kranz, E. U. & Volkmer, H. Homophilic interactions of chick neurofascin in trans are important for neurite induction. *Eur. J. Neurosci.* **20,** 3184–8 (2004).
287. Takeuchi, Y., Morise, J., Morita, I., Takematsu, H. & Oka, S. Role of Site-Specific N-Glycans Expressed on GluA2 in the Regulation of Cell Surface Expression of AMPA-Type Glutamate Receptors. *PLoS One* **10,** e0135644 (2015).
288. Yamasaki, M. *et al.* Glutamate receptor δ2 is essential for input pathway-dependent regulation of synaptic AMPAR contents in cerebellar Purkinje cells. *J. Neurosci.* **31,** 3362–74 (2011).
289. Zhou, L. *et al.* The Neural Cell Adhesion Molecules L1 and CHL1 Are Cleaved by BACE1 Protease in Vivo. *J. Biol. Chem.* **287,** 25927–25940 (2012).
290. Katic, J., Loers, G., Tosic, J., Schachner, M. & Kleene, R. The cell adhesion molecule CHL1 interacts with patched-1 to regulate apoptosis during postnatal cerebellar development. *J. Cell Sci.* **130,** 2606–2619 (2017).
291. Perlson, E. *et al.* Dynein Interacts with the Neural Cell Adhesion Molecule (NCAM180) to Tether Dynamic Microtubules and Maintain Synaptic Density in Cortical Neurons. *J. Biol. Chem.* **288,** 27812–27824 (2013).
292. Sytnyk, V., Leshchyns'ka, I., Nikonenko, A. G. & Schachner, M. NCAM promotes assembly and activity-dependent remodeling of the postsynaptic signaling complex. *J. Cell Biol.* **174,** 1071–1085 (2006).
293. Körner, C. *et al.* Carbohydrate deficient glycoprotein syndrome type IV: deficiency of dolichyl-P-Man:Man(5)GlcNAc(2)-PP-dolichyl mannosyltransferase. *EMBO J.* **18,** 6816–22 (1999).
294. Hanus, C. *et al.* Unconventional secretory processing diversifies neuronal ion channel properties. *Elife* **5,** (2016).
295. Shrimal, S., Ng, B. G., Losfeld, M.-E., Gilmore, R. & Freeze, H. H. Mutations in STT3A and STT3B cause two congenital disorders of glycosylation. *Hum. Mol. Genet.* **22,** 4638–45 (2013).
296. Gründahl, J. E. H. *et al.* Life with too much polyprenol: polyprenol reductase deficiency. *Mol. Genet. Metab.* **105,** 642–51 (2012).
297. Valtersson, C. *et al.* The influence of dolichol, dolichol esters, and dolichyl phosphate on phospholipid polymorphism and fluidity in model membranes. *J. Biol. Chem.* **260,** 2742–51 (1985).
298. Hemming, F. W. in 261–305 (1985). doi:10.1016/S0167-7306(08)60023-X
299. Garcia, J. J. *et al.* Effects of trace elements on membrane fluidity. *J. Trace Elem. Med. Biol.* **19,** 19–22 (2005).
300. Taguchi, Y., Fujinami, D. & Kohda, D. Comparative Analysis of Archaeal Lipid-linked Oligosaccharides That Serve as Oligosaccharide Donors for Asn Glycosylation. *J. Biol. Chem.* **291,** 11042–54 (2016).
301. Szkopińska, A., Swiezewska, E. & Chojnacki, T. On the specificity of dolichol kinase and DolPMan synthase towards isoprenoid alcohols of different chain length in rat liver microsomal membrane. *Int. J. Biochem.* **24,** 1151–7 (1992).
302. Keller, R. K., Rottler, G. D., Cafmeyer, N. & Adair, W. L. Subcellular localization and substrate specificity of dolichol kinase from rat liver. *Biochim. Biophys. Acta* **719,** 118–25 (1982).

303. Jakobsson, A., Swiezewska, E., Chojnacki, T. & Dallner, G. Uptake and modification of dietary polyprenols and dolichols in rat liver. *FEBS Lett.* **255,** 32–6 (1989).
304. Chojnacki, T. & Dallner, G. The uptake of dietary polyprenols and their modification to active dolichols by the rat liver. *J. Biol. Chem.* **258,** 916–22 (1983).
305. Dancourt, J. *et al.* A new intronic mutation in the DPM1 gene is associated with a milder form of CDG Ie in two French siblings. *Pediatr. Res.* **59,** 835–9 (2006).
306. Haeuptle, M. A. *et al.* Improvement of dolichol-linked oligosaccharide biosynthesis by the squalene synthase inhibitor zaragozic acid. *J. Biol. Chem.* **286,** 6085–91 (2011).
307. Forbes, K. *et al.* Statins inhibit insulin-like growth factor action in first trimester placenta by altering insulin-like growth factor 1 receptor glycosylation. *Mol. Hum. Reprod.* **21,** 105–14 (2015).
308. Sciamanna, C. N. *et al.* Nutrition counseling in the promoting cancer prevention in primary care study. *Prev. Med. (Baltim).* **35,** 437–46 (2002).
309. Wong, S. Y.-W. *et al.* Oral D-galactose supplementation in PGM1-CDG. *Genet. Med.* **19,** 1226–1235 (2017).
310. Freeze, H. H. Towards a therapy for phosphomannomutase 2 deficiency, the defect in CDG-Ia patients. *Biochim. Biophys. Acta* **1792,** 835–40 (2009).
311. Yuste-Checa, P. *et al.* Pharmacological Chaperoning: A Potential Treatment for PMM2-CDG. *Hum. Mutat.* **38,** 160–168 (2017).
312. Sparks, S. E. & Krasnewich, D. M. *Congenital Disorders of N-Linked Glycosylation and Multiple Pathway Overview*. *GeneReviews*® (1993).
313. Williams, S. E. *et al.* A role for Nr-CAM in the patterning of binocular visual pathways. *Neuron* **50,** 535–47 (2006).
314. Othumpangat, S., Noti, J. D., McMillen, C. M. & Beezhold, D. H. ICAM-1 regulates the survival of influenza virus in lung epithelial cells during the early stages of infection. *Virology* **487,** 85–94 (2016).
315. Sugden, S. M., Pham, T. N. Q. & Cohen, É. A. HIV-1 Vpu Downmodulates ICAM-1 Expression, Resulting in Decreased Killing of Infected CD4+ T Cells by NK Cells. *J. Virol.* **91,** (2017).
316. Poretti, A., Boltshauser, E. & Doherty, D. Cerebellar hypoplasia: Differential diagnosis and diagnostic approach. *Am. J. Med. Genet. Part C Semin. Med. Genet.* **166,** 211–226 (2014).
317. Pereira, P. L. *et al.* A new mouse model for the trisomy of the Abcg1-U2af1 region reveals the complexity of the combinatorial genetic code of down syndrome. *Hum. Mol. Genet.* **18,** 4756–69 (2009).
318. Akizu, N. *et al.* AMPD2 regulates GTP synthesis and is mutated in a potentially treatable neurodegenerative brainstem disorder. *Cell* **154,** 505–17 (2013).
319. Lipecka, J. *et al.* Sensitivity of mass spectrometry analysis depends on the shape of the filtration unit used for filter aided sample preparation (FASP). *Proteomics* **16,** 1852–7 (2016).
320. Boissart, C. *et al.* Differentiation from human pluripotent stem cells of cortical neurons of the superficial layers amenable to psychiatric disease modeling and high-throughput drug screening. *Transl. Psychiatry* **3,** e294 (2013).

ANNEX 1 – SUPPLEMENTARY TABLES

Supplementary table 1. Total proteomics

Gene name	Protein uniprot IDs	Levels in the Mutant (log2 difference)	p-value	q-value
Aak1	Q3UHJ0-2	-0,043	0,6399109	0,79594264
Aars	Q8BGQ7	0,157	0,08541151	0,28878383
Aarsd1	Q3THG9	0,196	0,30677703	0,38700565
Abat	P61922	-0,170	0,00206158	0,16265292
Abcd3	P55096	0,974	0,00424813	0
Abce1	P61222	-0,091	0,33887449	0,56286678
Abcf1	Q6P542	0,003	0,97947579	0,98217551
Abcf2	Q99LE6	-0,127	0,33051899	0,49204558
Abr	Q5SSL4-4	-0,341	0,24597899	0,27730248
Acaa1a	Q921H8	0,046	0,87627846	0,89491614
Acaa2	Q8BWT1	0,013	0,94502095	0,95323804
Acaca	Q5SWU9	0,004	0,96883512	0,97640106
Acad9	Q8JZN5	-0,200	0,18378806	0,31104234
Acadl	P51174	-0,272	0,06003964	0,1695619
Acadm	P45952	-0,167	0,02577922	0,21690435
Acads	Q07417	-0,525	0,03522001	0,11657732
Acadsb	Q9DBL1	-0,035	0,74519847	0,85166786
Acadvl	P50544	0,264	0,01432699	0,12163043
Acat1	Q8QZT1	0,025	0,87023098	0,9093266
Acat2	Q8CAY6	0,787	0,0091924	0,027
Acbd3	Q8BMP6	-0,244	0,23576247	0,31274674
Acin1	Q9JIX8-4	-0,315	0,07544568	0,16445638
Acly	Q91V92	-0,148	0,09394635	0,31420432
Aco1	P28271	0,045	0,60719001	0,78021883
Aco2	Q99KI0	-0,145	0,15144545	0,36347848
Acot1	O55137	-0,134	0,17038332	0,38658362
Acot7	Q91V12-2	-0,196	0,0048271	0,15623045
Acox1	Q9R0H0-2	0,118	0,30250664	0,49246591
Acp1	Q9D358	0,128	0,71605596	0,74469648
Acsbg1	Q99PU5	-0,279	0,0090026	0,10755245
Acsf2	Q8VCW8	0,431	0,03312658	0,11550413
Acsl3	Q9CZW4	-0,114	0,68342571	0,72545555
Acsl6	Q91WC3	0,592	0,01432967	0,06730435
Acss2	Q9QXG4	-0,170	0,44209106	0,50641252
Actb	P60710	-0,254	0,02166243	0,15422222
Actl6a	Q9Z2N8	-0,168	0,10030299	0,28578481
Actl6b	Q99MR0	0,363	0,01253355	0,11903158
Actn1	Q7TPR4	0,068	0,64437431	0,75946524
Actn4	P57780	0,196	0,29060842	0,38142026
Actr10	Q9QZB7	0,178	0,04746609	0,22665314
Actr1a	P61164	0,212	0,28159475	0,36981953
Actr1b	Q8R5C5	0,164	0,00937306	0,19382741
Actr2	P61161	-0,301	0,05265792	0,15892913
Actr3	Q99JY9	-0,058	0,14297079	0,61378127
Acyp1	P56376	-0,011	0,85264732	0,9340241
Add1	Q9QYC0-2	-0,153	0,30662488	0,43202064
Add2	Q9QYB8-2	0,223	0,61023938	0,61037213
Add3	Q9QYB5-2	-0,050	0,5222123	0,7543807
Adh5	P28474	-0,184	0,12659613	0,2864139
Adk	P55264	-0,294	0,14023288	0,2171441
Adnp	Q9Z103	0,237	0,22492776	0,30801175
Ado	Q6PDY2	0,024	0,94667962	0,94314563
Adprh	P54923	0,509	0,03588371	0,11634951
Adrm1	Q9JKV1	0,203	0,22294912	0,33829499
Adsl	P54822	0,154	0,13438518	0,336
Adss	P46664	0,018	0,88509472	0,92187389
Afp	P02772	-0,150	0,77219056	0,77487918
Agap3	Q8VHH5	-0,112	0,54544955	0,62484195
Agfg1	Q8K2K6-3	-0,207	0,28057022	0,36935287
Agk	Q9ESW4	0,256	0,46876132	0,47736187
Agrn	A2ASQ1-3	22,303	ND	ND
Ahcy	P50247	-0,192	0,32807727	0,40689836
Ahcyl1	Q80SW1	-0,193	0,20230377	0,33493664
Ahcyl2	Q68FL4	-0,265	0,06145907	0,16890476
Ahsa1	Q8BK64	0,054	0,36224815	0,68211966
Aifm1	Q9Z0X1	-0,119	0,15497528	0,40316575
Aimp1	P31230	-0,235	0,0066276	0,12229508
Aimp2	Q8R010	-0,145	0,03481061	0,26962735
Aip	O08915	-0,044	0,7259197	0,82572266
Ak1	Q9R0Y5	0,055	0,40654598	0,6951281
Ak2	Q9WTP6-2	-0,052	0,67342309	0,78655164
Ak3	Q9WTP7	0,033	0,6262568	0,82546055
Akap12	Q9WTQ5-2	-0,176	0,0262685	0,21217882
Akr1a1	Q9JII6	0,103	0,10695529	0,40976358
Akr1b1	P45376	-0,259	0,08979663	0,19717647
Akr7a2	Q8CG76	-0,099	0,38139992	0,56432242
Akt1	P31750	-0,185	0,32949125	0,40920472
Akt3	Q9WUA6-2	-0,022	0,79170449	0,89330206
Alad	P10518	-0,002	0,98987234	0,99022549
Alb	P07724	-0,222	0,12790875	0,25798192
Alcam	Q61490	0,084	0,76021632	0,79161379
Aldh16a1	Q571I9	-0,187	0,17327421	0,31638068
Aldh18a1	Q9Z110-2	0,033	0,82129452	0,88377468
Aldh1l1	Q8R0Y6	-0,069	0,23377918	0,59122654
Aldh2	P47738	-0,046	0,11190261	0,6653927
Aldh5a1	Q8BWF0	-0,167	0,35038633	0,44476016
Aldh6a1	Q9EQ20	-0,106	0,46732789	0,60001289
Aldh7a1	Q9DBF1-2	0,107	0,38579953	0,53373139
Aldh9a1	Q9JLI2	-0,156	0,15406245	0,3412859
Aldoa	P05064	-0,128	0,37531005	0,51455404
Aldoc	P05063	0,104	0,03154745	0,36693134
Alg2	Q9DBE8	-0,055	0,25598786	0,65126736
Alyref	O08583	-0,410	0,02462691	0,11722222
Amph	Q7TQF7	-0,119	0,02666182	0,3132
Anapc1	P53995	0,398	0,10570541	0,16441096
Anapc5	Q8BTZ4	0,076	0,58752599	0,71049267
Ank2	Q8C8R3-2	-0,266	0,00404833	0,11270968
Ank3	G5E8K5-2	-0,308	0,05671493	0,15772093
Ankfy1	Q810B6	-0,369	0,22270369	0,25237956
Anp32a	O35381	-0,371	0,28755342	0,29203681
Anp32b	Q9EST5	0,277	0,34627436	0,37284439
Anp32e	P97822-2	-0,007	0,95588408	0,96852581
Anxa2	P07356	0,228	0,37380665	0,40979785
Anxa5	P48036	0,098	0,81393362	0,83015741
Anxa6	P14824	0,058	0,81677004	0,85156299
Ap1b1	O35643	-0,230	0,22353485	0,31282421
Ap1g1	P22892	0,096	0,75820803	0,78419494
Ap1m1	P35585	0,446	0,1764742	0,19700488
Ap2a1	P17426-2	0,064	0,61041333	0,74673769
Ap2a2	P17427	-0,143	0,10551153	0,33590137
Ap2b1	Q9DBG3	0,000	0,99370549	0,99648694
Ap2m1	P84091	-0,175	0,28595334	0,39244643
Ap3b2	Q9JME5	0,075	0,57644002	0,70494892
Ap3d1	O54774	-0,026	0,8519666	0,90057175
Ap3m1	Q9JKC8	-0,254	0,07475247	0,19237209

Gene name	Protein uniprot IDs	Levels in the Mutant (log2 difference)	p-value	q-value
Apba1	B2RUJ5-3	0,130	0,51163361	0,59005686
Apeh	Q8R146-2	0,596	0,44436626	0,38613825
Apex1	P28352	0,213	0,3250889	0,38673016
Api5	O35841	0,217	0,135474	0,26731034
Apmap	Q9D7N9	-0,094	0,59050038	0,67842867
Apoa1	Q00623	-0,430	0,03945113	0,10989781
Apoa1bp	Q8K4Z3	-0,434	0,01028219	0,08870968
Apoa4	P06728	-1,116	0,15946857	0,15776991
Apoe	P08226	-0,345	0,06640949	0,15501215
Apoo	Q9DCZ4-2	-0,331	0,09342933	0,1684893
Apool	Q78IK4	0,135	0,16237227	0,38238869
App	P12023-2	-0,221	0,00803798	0,14276498
Appl1	Q8K3H0	-0,223	0,16599446	0,27814984
Aprt	P08030	-0,004	0,97982221	0,97846688
Aqp4	P55088	0,306	0,53152327	0,51362103
Arcn1	Q5XJY5	-0,144	0,10256406	0,32881328
Arf3;Arf1	P61205	0,196	0,622053	0,62130687
Arf5	P84084	0,074	0,43183928	0,64220721
Arf6	P62331	-0,103	0,50388721	0,61794127
Arfgap1	Q9EPJ9-2	-0,193	0,04252732	0,21129858
Arhgap1	Q5FWK3	-0,105	0,49979382	0,61688194
Arhgap35	Q91YM2	-0,083	0,64151591	0,73114227
Arhgdia	Q99PT1	-0,081	0,51594998	0,66058901
Arhgef7	Q9ES28	-0,283	0,04719011	0,15654962
Arid1a	A2BH40	-0,202	0,23547282	0,34209449
Arl3	Q9WUL7	0,201	0,29352403	0,38172845
Arl8b	Q9CQW2	0,671	0,05990873	0,11186207
Armc1	Q9D7A8	0,191	0,4818203	0,52019048
Armc10	Q9D0L7-2	-0,050	0,66798535	0,78711643
Armc6	Q8BNU0	-0,211	0,09660812	0,23644015
Arpc1a	Q9R0Q6	-0,179	0,26357074	0,38159813
Arpc2	Q9CVB6	-0,763	0,00991704	0,0456
Arpc3	Q9JM76	-0,211	0,28879324	0,37017697
Arpc4	P59999	-0,303	0,13767565	0,2130991
Arpp19	P56212	-0,140	0,34463478	0,47950484
Arrb1	Q8BWG8	-0,291	0,18800926	0,25905925
Asah1	Q9WV54	0,068	0,88750899	0,89248686
Ash2l	Q91X20	-0,250	0,16944039	0,26864716
Asna1	O54984	0,110	0,07692881	0,38167485
Asph	Q8BSY0	-0,159	0,73971735	0,75260362
Asrgl1	Q8C0M9	-0,163	0,46997909	0,53033068
Atad1	Q9D5T0	0,001	0,99385999	0,99361088
Atad3	Q925I1	-0,206	0,29449188	0,37773603
Atg3	Q9CPX6	-0,246	0,07470584	0,19326952
Atic	Q9CWJ9	-0,193	0,04773697	0,21601826
Atp1a1	Q8VDN2	-0,217	0,11302647	0,24318959
Atp1a2	Q6PIE5	-0,120	0,40926763	0,53985069
Atp1a3	Q6PIC6	-0,224	0,10021244	0,22837751
Atp1b1	P14094	-0,075	0,63737389	0,74140054
Atp1b2	P14231	-0,018	0,92981811	0,93913449
Atp1b3	P97370	-0,209	0,17513239	0,29193846
Atp2a2	O55143	-0,033	0,66603277	0,83512864
Atp2b1	G5E829	-0,132	0,17079389	0,38676712
Atp2b2	Q9R0K7	-0,190	0,07821137	0,24330697
Atp2c1	Q80XR2	0,120	0,71023864	0,74520136
Atp5a1	Q03265	-0,238	0,02193767	0,15750794
Atp5b	P56480	-0,210	0,02356004	0,16596296
Atp5c1	Q91VR2	-0,167	0,40773623	0,48819791
Atp5f1	Q9CQQ7	-0,203	0,56026723	0,5738206
Atp5h	Q9DCX2	0,403	0,07769459	0,15638596
Atp5l	Q9CPQ8	0,021	0,82076408	0,90050564
Atp5o	Q9DB20	0,157	0,03065253	0,23829559
Atp6v0a1	Q9Z1G4-3	-0,132	0,08421344	0,33961828
Atp6v0d1	P51863	0,030	0,77996292	0,87569591
Atp6v1a	P50516	-0,169	0,17323887	0,34004278
Atp6v1b2	P62814	0,163	0,14349717	0,3274349
Atp6v1c1	Q9Z1G3	0,342	0,1823927	0,22839596
Atp6v1d	P57746	0,183	0,31827502	0,40768662
Atp6v1g1	Q9CR51	-0,044	0,7355968	0,83106829
Atp6v1h	Q8BVE3	0,218	0,06164406	0,2033619
Atp9a	O70228	0,117	0,71382854	0,74784906
Atrx	Q61687	-0,104	0,32293233	0,52892609
Atxn10	P28658	0,512	0,00833285	0,0774
Atxn2	O70305-2	-0,297	0,23245571	0,28354341
Atxn2l	Q7TQH0-3	-0,083	0,66810029	0,74678003
Bag6	Q9Z1R2	-0,101	0,40871758	0,57404474
Baiap2	Q8BKX1-4	-0,030	0,75476354	0,86666824
Banf1	O54962	0,990	0,07562566	0,11869231
Basp1	Q91XV3	-0,009	0,93387897	0,95471099
Bax	Q07813	-0,028	0,84676485	0,89560887
Baz1b	Q9Z277	-0,132	0,39539328	0,51853597
Bcan	Q61361	0,281	0,18391382	0,25976512
Bcas1	Q80YN3	0,224	0,14727072	0,26870869
Bcas2	Q9D287	0,121	0,44679527	0,56262722
Bckdha	P50136	0,197	0,1127238	0,26937907
Bckdhb	Q6P3A8	0,627	0,29979472	0,27008904
Bclaf1	Q8K019-2	-0,221	0,09122406	0,22108489
Bdh1	Q80XN0	-0,198	0,11343768	0,26874227
Bin1	O08539	0,027	0,61902918	0,84946914
Birc6	O88738-3	0,049	0,68567042	0,79654081
Blmh	Q8R016	-0,160	0,19331237	0,36529161
Blvrb	Q923D2	-0,380	0,14054003	0,19123316
Bop1	P97452	0,086	0,80985024	0,83075929
Bpnt1	Q9ZDS1	-0,394	0,02747627	0,11377778
Brd3	Q8K2F0	-22,336	ND	ND
Bri3bp	Q8BXV2	-0,115	0,51738787	0,61334066
Brsk2	Q69Z98-4	0,053	0,82343112	0,85970195
Bsg	P18572-2	-0,363	0,02755575	0,10680556
Btf3	Q64152-2	0,401	0,02424134	0,1120354
Btf3l4	Q9CQH7	0,584	0,06423788	0,10754286
Bub3	Q9WVA3	-0,101	0,31482562	0,52771631
Bud31	Q6PGH1	-0,048	0,84139324	0,87849679
Bzw2	Q91VK1	-0,284	0,10110538	0,19278392
C1qbp	O35658	0,070	0,65693114	0,75996013
Ca2	P00920	0,908	0,07671126	0,11382456
Ca8	P28651	-0,109	0,44065449	0,57533223
Cab39	Q06138	0,030	0,80416056	0,8835491
Cacna2d1	O08532-2	0,187	0,03198122	0,20139423
Cacna2d2	Q6PHS9-4	-0,047	0,93197621	0,93033572
Cacybp	Q9CXW3	-0,205	0,23287492	0,33910519
Cad	B2RQC6	0,123	0,02214856	0,29188906
Cadm1	Q8R5M8-4	-0,041	0,75184195	0,84064617
Cadm2	Q8BLQ9-2	-0,293	0,02133237	0,1156648
Cadm3	Q99N28	-0,924	0,1668577	0,15714943
Cadm4	Q8R464	-0,159	0,06448699	0,27701843

Gene name	Protein uniprot IDs	Levels in the Mutant (log2 difference)	p-value	q-value
Cadps	Q80TJ1-2	-0,023	0,81461461	0,89456118
Calb1	P12658	-0,398	0,18009627	0,21503636
Calb2	Q08331	0,076	0,66047881	0,7543282
Calm1	P62204	-0,494	0,00185213	0,02492308
Calr	P14211	-0,010	0,87089068	0,93905486
Calu	O35887	0,006	0,94481051	0,96523962
Camk2b	P28652	-0,169	0,08962293	0,27860359
Camk2d	Q6PHZ2	0,160	0,24912577	0,38744344
Camk2g	Q923T9-3	0,334	0,2239663	0,26777202
Camk4	P08414	-0,413	0,18380558	0,21700917
Camsap2	Q8C1B1	0,005	0,97977355	0,97644421
Cand1	Q6ZQ38	0,016	0,81815058	0,91384237
Cand2	Q6ZQ73	0,292	0,15703545	0,23045908
Canx	P35564	-0,004	0,9715601	0,97608856
Cap1	P40124	-0,227	0,03751499	0,16594152
Cap2	Q9CYT6	-0,236	0,28451131	0,35908808
Capn2	O08529	-0,232	0,17574306	0,27925203
Capns1	O88456	-0,008	0,98072436	0,97660338
Caprin1	Q60865	0,037	0,62102141	0,80788119
Capza1	P47753	-0,055	0,2390075	0,64472375
Capza2	P47754	-0,038	0,39260388	0,76902685
Capzb	P47757-2	-0,184	0,07935638	0,25528857
Carkd	Q9CZ42-3	-0,517	0,13203405	0,16018375
Carm1	Q9WVG6-2	-0,017	0,83335419	0,91407598
Cars	Q9ER72	0,403	0,04557976	0,1054269
Cask	O70589	-0,064	0,71626777	0,78645902
Caskin1	Q6P9K8-2	-0,550	0,10552169	0,14805381
Casp3	P70677	-0,055	0,39763344	0,69352516
Cat	P24270	-0,133	0,17078742	0,38743578
Cbr1	P48758	-0,004	0,97280814	0,97557429
Cbs	Q91WT9-2	-0,339	0,03312726	0,11099429
Cbx1	P83917	0,151	0,44514161	0,52937857
Cbx3	P23198	-0,204	0,28526148	0,37272989
Cbx5	Q61686	-0,153	0,02462086	0,23598459
Ccar1	Q8CH18-3	-0,195	0,26015521	0,37027723
Ccar2	Q8VDP4	-0,042	0,46408216	0,76349769
Ccdc22	Q9JIG7	0,442	0,07447373	0,13898077
Ccdc88a	Q5SNZ0-2	-0,221	0,03268068	0,16991617
Cct2	P80314	-0,066	0,45175054	0,67282839
Cct3	P80318	-0,158	0,1446258	0,33785617
Cct4	P80315	-0,119	0,1707305	0,40935768
Cct5	P80316	0,140	0,37317443	0,49745865
Cct6a	P80317	0,255	0,14310371	0,24053232
Cct7	P80313	-0,055	0,14600815	0,62184287
Cct8	P42932	-0,153	0,08768498	0,29762671
Cd200	O54901	-0,140	0,40240895	0,51472727
Cd2bp2	Q9CWK3	21,377	ND	ND
Cd47	Q61735-2	-0,060	0,46773626	0,69826676
Cd81	P35762	-0,154	0,23008442	0,38729062
Cd9	P40240	0,124	0,48334385	0,5774659
Cdc23	Q8BGZ4	-0,076	0,57212829	0,69835162
Cdc37	Q61081	0,312	0,08714749	0,16840356
Cdc42	P60766-1	0,089	0,54378267	0,65833358
Cdc42	P60766	0,490	0,11250437	0,15830588
Cdc42bpb	Q7TT50	-0,048	0,3428861	0,71090934
Cdc5l	Q6A068	0,078	0,4761887	0,64556909
Cdh2	P15116	-0,100	0,43848236	0,59127007
Cdk5	P49615	0,166	0,21968571	0,36998054
Cdkn1b	P46414	-0,060	0,59516225	0,74973773
Cdkn2aip	Q8BI72	-0,425	0,2090943	0,22498144
Cdv3	Q4VAA2-2	0,064	0,67850655	0,77071327
Celf2	Q9Z0H4	0,086	0,51625411	0,64782531
Cend1	Q9JKC6	0,140	0,4103667	0,51614414
Cenpv	Q9CXS4	-0,197	0,02168091	0,17533894
Cep170	Q6A065	-0,136	0,05304033	0,29743158
Cfdp1	O88271	0,013	0,94504993	0,95357634
Cfl1	P18760	0,014	0,87761747	0,93037844
Cfl2	P45591	0,247	0,16982906	0,26916724
Chchd2	Q9D1L0	-0,428	0,01113703	0,08333333
Chchd3	Q9CRB9	-0,258	0,18122477	0,27067119
Chchd6	Q91VN4	-0,090	0,47150109	0,62151988
Chd4	Q6PDQ2	0,018	0,89262545	0,92727775
Cherp	Q8CGZ0	-0,135	0,21918264	0,40862975
Chl1	P70232	-0,249	0,00352735	0,10602817
Chmp4b	Q9D8B3	-0,104	0,11643082	0,41004641
Chmp5	Q9D7S9	0,158	0,09515706	0,29232268
Chordc1	Q9D1P4	-0,276	0,07497999	0,17439335
Chtop	Q9CY57-5	-0,266	0,12013146	0,21691028
Ciapin1	Q8WTY4	-0,046	0,86068344	0,88476399
Cirbp	P60824	0,033	0,74681433	0,85666469
Ckap4	Q8BMK4	-0,099	0,03900065	0,3814965
Ckap5	A2AGT5-3	-0,054	0,68846705	0,78785157
Ckb	Q04447	-0,104	0,38245731	0,55750468
Ckm	P07310	0,082	0,84195674	0,85670826
Ckmt1	P30275	0,139	0,24515429	0,41009362
Clasp1	Q80TV8-2	0,089	0,57425116	0,67608046
Clasp2	Q8BRT1	-0,056	0,34933447	0,67159827
Clic1	Q9Z1Q5	0,016	0,83239012	0,91372575
Clic4	Q9QYB1	-0,184	0,00920436	0,16545231
Clip2	Q9Z0H8	-0,137	0,48057797	0,56276456
Clpp	O88696	-0,006	0,89483305	0,95634328
Clptm1	Q8VBZ3	-0,050	0,59779258	0,76890708
Cltb	Q6IRU5	-0,078	0,42385956	0,6243675
Cltc	Q68FD5	-0,178	0,13614275	0,29766667
Cmas	Q99KK2	0,245	0,49561691	0,50234726
Cmpk1	Q9DBP5	-0,071	0,42260984	0,64481798
Cnbp	P53996	-0,216	0,24468398	0,33958879
Cndp2	Q9D1A2	0,135	0,16461276	0,38212178
Cnn3	Q9DAW9	0,270	0,00034446	0,09851429
Cnot1	Q6ZQ08	-0,449	0,00131018	0,04023529
Cnp	P16330-2	-0,114	0,53607367	0,62062558
Cnpy2	Q9QXT0	0,273	0,39996415	0,40813434
Cnrip1	Q5M8N0	-0,195	0,14788832	0,28720126
Cntfr	O88507	0,250	0,23397085	0,30779852
Cntn1	P12960	-0,149	0,35066952	0,46927326
Cntn2	Q61330	-0,762	0,00783723	0,0324
Commd5	Q8R395	-20,639	ND	ND
Comt	O88587-2	0,163	0,38734163	0,48039612
Comtd1	Q8BIG7	0,510	0,11153723	0,15627755
Copa	Q8CIE6	0,064	0,13556943	0,57834483
Copb1	Q9JIF7	-0,105	0,1692743	0,44778182
Copb2	O55029	-0,048	0,36801508	0,71754489
Cope	O89079	-0,088	0,75443893	0,78585471
Copg1	Q9QZE5	0,424	0,06763619	0,12857143
Copg2	Q9QXK3-4	0,257	0,04650276	0,16628571

Gene name	Protein uniprot IDs	Levels in the Mutant (log2 difference)	p-value	q-value
Cops2	P61202	0,034	0,91348691	0,91867627
Cops3	O88543	0,072	0,40372425	0,63410415
Cops4	O88544	-0,183	0,00496237	0,16075177
Cops5	O35864	-0,050	0,85647724	0,88384678
Cops6	O88545	-0,067	0,25689301	0,60972196
Cops7a	Q9CZ04	-0,179	0,15660442	0,31435193
Cops7b	Q8BV13	0,452	0,33057243	0,31409607
Cops8	Q8VBV7	-0,082	0,41981714	0,61817479
Copz1	P61924	0,355	0,28723977	0,29825113
Coro1a	O89053	-0,539	0,00857227	0,05643243
Coro1b	Q9WUM3	-0,102	0,60813928	0,67891535
Coro1c	Q9WUM4	-0,134	0,23085111	0,41068225
Coro7	Q9D2V7	0,569	0,13119121	0,15715589
Cotl1	Q9CQI6	-0,071	0,67390972	0,76407662
Cox4i1	P19783	-0,013	0,78994802	0,91617788
Cox5a	P12787	-0,280	0,13270669	0,21650862
Cox6a1	P43024	-0,161	0,51010765	0,56239119
Cox6b1	P56391	-0,122	0,34831991	0,50705515
Cpe	Q00493	-0,443	0,09795206	0,1567012
Cplx2	P84086	0,430	0,1495134	0,18058667
Cpne3	Q8BT60	-0,272	0,07143952	0,17682486
Cpsf1	Q9EPU4	0,935	0,02009857	0,03866667
Cpsf6	Q6NVF9	0,223	0,18618093	0,28917941
Crip2	Q9DCT8	-0,023	0,89026528	0,91566889
Crk	Q64010	-0,257	0,12760152	0,22601633
Crkl	P47941	-0,131	0,274852	0,44853065
Crmp1	P97427	-0,031	0,6437521	0,83486267
Crot	Q9DC50	0,175	0,61643873	0,62437936
Crtc1	Q68ED7	21,875	ND	ND
Cryz	P47199	0,190	0,38193482	0,44563895
Cryzl1	Q921W4	0,056	0,7282347	0,804933
Cs	Q9CZU6	0,275	0,23338652	0,28932919
Csde1	Q91W50	-0,112	0,14947031	0,41005508
Cse1l	Q9ERK4	0,087	0,23080937	0,52848142
Csk	P41241	0,471	0,22656343	0,22883702
Csnk1a1	Q8BK63-2	21,916	ND	ND
Csnk1e	Q9JMK2	-0,373	0,02831716	0,10831655
Csnk2a1	Q60737	-0,041	0,65572628	0,80803965
Csnk2a2	O54833	0,136	0,69530123	0,72256944
Csrp1	P97315	-0,508	0,18541318	0,1922394
Cst3	P21460	-0,274	0,09620663	0,19256716
Cstf2	Q8BIQ5-2	-0,117	0,4179283	0,55361986
Ctbp1	O88712-2	-0,020	0,62975476	0,88185873
Ctbp2	P56546	-0,152	0,40754773	0,50264558
Ctcf	Q61164	-0,094	0,71121952	0,76185043
Ctif	Q6PEE2	-20,501	ND	ND
Ctnna1	P26231	-0,140	0,49644767	0,57118599
Ctnna2	Q61301	0,088	0,17689526	0,50125185
Ctnnb1	Q02248	-0,164	0,22977118	0,37863647
Ctnnd1	P30999	-0,200	0,00970405	0,15886347
Ctnnd2	O35927-2	0,100	0,46950464	0,61014557
Ctps1	P70698	0,232	0,58196102	0,57812016
Ctps2	P70303	-0,084	0,05180421	0,44801211
Ctsb	P10605	0,230	0,26623469	0,34211827
Ctsd	P18242	0,384	0,03031899	0,10910145
Ctsz	Q9WUU7	-0,142	0,37462681	0,4972389
Cttn	Q60598	0,178	0,30953151	0,40670011
Cul2	Q9D4H8	-0,152	0,09769429	0,30792342
Cul3	Q9JLV5	0,018	0,85306381	0,91398661
Cul4a	Q3TCH7	-0,267	0,6180606	0,60568505
Cul4b	A2A432	0,010	0,93378899	0,95323523
Cul5	Q9D5V5	-0,075	0,70972388	0,77193544
Cuta	Q9CQ89	-0,169	0,56795905	0,60077751
Cxadr	P97792	-0,206	0,03047885	0,17856522
Cyb5b	Q9CQX2	-0,355	0,02652466	0,10609272
Cyb5r3	Q9DCN2-2	-0,078	0,03871988	0,46357438
Cyc1	Q9D0M3-2	-0,387	0,225536	0,24561922
Cycs	P62897	0,472	0,01994284	0,11008
Cyfip1	Q7TMB8	-0,074	0,60407965	0,72416575
Cyfip2	Q5SQX6	-0,150	0,0788755	0,29321527
Cyp51a1	Q8K0C4	-0,168	0,39924839	0,48161464
Cyth2;Cyth3	P63034-3	-0,024	0,89945686	0,91925097
D10Jhu81e	Q9D172	0,331	0,1266531	0,19375758
Dak	Q8VC30	-0,442	0,01468257	0,09472464
Dars	Q922B2	-0,118	0,0471756	0,34008054
Dazap1	Q9JII5-2	-0,140	0,21449611	0,39669778
Dbi	P31786	-0,746	0,00785302	0,02945455
Dbn1	Q9QXS6-3	-0,102	0,62620761	0,69266099
Dbnl	Q62418-3	-0,019	0,79478708	0,90060757
Dcakd	Q8BHC4	-0,197	0,24323281	0,35935385
Dclk1	Q9JLM8	-0,124	0,21889486	0,42932636
Dclk2	Q6PGN3-2	0,579	0,01564628	0,07116981
Dcps	Q9DAR7	0,221	0,0651934	0,20448456
Dctn1	O08788	-0,159	0,03204181	0,23627079
Dctn2	Q99KJ8	0,038	0,68386251	0,82464911
Dctn3	Q9Z0Y1	0,648	0,12119551	0,15330357
Dctn4	Q8CBY8	-0,236	0,00113722	0,112
Dctn5	Q9QZB9	0,493	0,35345194	0,32564575
Dcx	O88809	-0,028	0,74538195	0,86956481
Ddah1	Q9CWS0	-0,375	0,12521286	0,17618733
Ddah2	Q99LD8	-0,227	0,03977887	0,17046154
Ddb1	Q3U1J4	-0,142	0,20110477	0,38624601
Ddost	O54734	-0,220	0,17320871	0,28614308
Ddx1	Q91VR5	0,052	0,59726665	0,76672084
Ddx17	Q501J6	-0,142	0,03774355	0,27914809
Ddx19a	Q61655	-0,362	0,00017137	0,0453913
Ddx21	Q9JIK5	-0,031	0,8946779	0,91195973
Ddx39a	Q8VDW0	0,139	0,46357284	0,55213047
Ddx39b	Q9Z1N5	-0,219	0,03213987	0,16642815
Ddx3x;D1Pas1	Q62167	-0,182	0,00583693	0,16391919
Ddx42	Q810A7	0,119	0,21044062	0,43246694
Ddx46	Q569Z5	-0,504	0,00597637	0,054
Ddx5	Q61656	-0,174	0,11328411	0,28657638
Ddx6	P54823	-0,295	0,06737527	0,16863366
Dek	Q7TNV0	-0,134	0,20359322	0,40011441
Denr	Q9CQJ6	-0,310	0,20683465	0,26351832
Dhcr7	O88455	-0,495	0,00136406	0,036
Dhx15	O35286	-0,181	0,03526503	0,21406335
Dhx29	Q6PGC1	-0,027	0,90634672	0,91930011
Dhx30	Q99PU8-2	-0,076	0,76283575	0,79903671
Dhx9	O70133-2	-0,047	0,42667864	0,73676451
Dip2b	Q3UH60	0,013	0,91267585	0,94007154
Diras2	Q5PR73	0,182	0,08432994	0,26270194
Dis3	Q9CSH3	-0,217	0,20313953	0,30793529
Dkc1	Q9ESX5	0,203	0,353942	0,4098698

Gene name	Protein uniprot IDs	Levels in the Mutant (log2 difference)	p-value	q-value
Dlat	Q8BMF4	0,149	0,40108791	0,50218994
Dld	O08749	0,192	0,27728857	0,37967221
Dlg2	Q91XM9-3	0,190	0,04073479	0,21138605
Dlgap4	B1AZP2-2	-0,074	0,67565192	0,76235497
Dlst	Q9D2G2	0,316	0,25890119	0,28843344
Dmxl2	Q8BPN8-2	0,029	0,92091996	0,92867438
Dnaja1	P63037	-0,231	0,10372509	0,22583231
Dnaja2	Q9QYJ0	-0,008	0,97277017	0,97425027
Dnaja3	Q99M87-3	-0,206	0,07137206	0,2180766
Dnajb11	Q99KV1	-0,015	0,90836912	0,93780131
Dnajc11	Q5U458	-0,002	0,99284109	0,9916651
Dnajc2	P54103	0,405	0,12391281	0,16945345
Dnajc5	P60904	-0,153	0,32945616	0,44811682
Dnajc6	Q80TZ3-2	-0,027	0,79647698	0,88326389
Dnajc7	Q9QYI3	0,009	0,94336819	0,95813704
Dnajc8	Q6NZB0	-0,157	0,41977666	0,50149815
Dnm1	P39053-3	-0,036	0,5261724	0,79087829
Dnm1l	Q8K1M6	-0,110	0,24638184	0,47946512
Dnm2	P39054-2	-0,114	0,6368998	0,68302203
Dnm3	Q8BZ98-2	0,282	0,27612528	0,31837746
Dnmt1	P13864	-0,022	0,88340099	0,91557262
Dnmt3a	O88508	-0,145	0,37530993	0,49202654
Dnpep	Q9Z2W0	-0,059	0,5772152	0,74640811
Dnph1	Q80VJ3	0,416	0,34320754	0,33358345
Dock7	Q8R1A4-2	0,038	0,74757603	0,84529094
Dpf2	Q61103	-0,069	0,55442848	0,70843885
Dpp3	Q99KK7	0,084	0,51499868	0,65149225
Dpp6	Q9Z218	-0,477	0,00479021	0,05236364
Dpy30	Q99LT0	0,199	0,85966098	0,85212165
Dpysl2	O08553	-0,147	0,01149585	0,22470248
Dpysl3	Q62188	-0,097	0,23199763	0,50078816
Dpysl4	O35098	-0,195	0,02690644	0,18289764
Dpysl5	Q9EQF6	-0,183	0,05185517	0,22405749
Drg1	P32233	0,812	0,18959105	0,16954407
Drg2	Q9QXB9	-0,410	0,08301915	0,15183264
Dstn	Q9R0P5	-0,157	0,31474496	0,43291417
Dtd1	Q9DD18	-0,122	0,68919765	0,72388406
Dus3l	Q91XI1	0,046	0,85342568	0,88351564
Dusp3	Q9D7X3	0,028	0,83443728	0,8919107
Dync1h1	Q9JHU4	-0,057	0,01383518	0,55739693
Dync1i2	O88487	0,120	0,39094401	0,53331095
Dync1li1	Q8R1Q8	-0,080	0,69178195	0,76177513
Dync1li2	Q6PDL0	-0,066	0,63988235	0,75954072
Dynll1	P63168	-0,084	0,74079475	0,77972282
Dynll2	Q9D0M5	-0,374	0,09456012	0,16019649
Dynlrb1	P62627	-0,306	0,27602865	0,30901466
Ebf3	O08791-2	-0,081	0,53798663	0,67185539
Ech1	O35459	0,096	0,2511557	0,51313201
Echs1	Q8BH95	0,013	0,92544154	0,94248216
Eci1	P42125	0,254	0,16235316	0,25958645
Eci2	Q9WUR2-2	-0,184	0,22202316	0,35816021
Ecm29	Q6PDI5-2	-0,104	0,76845731	0,7870202
Edc4	Q3UJB9	-0,152	0,22762122	0,3858066
Eea1	Q8BL66	-0,372	0,10042676	0,1657351
Eef1a1	P10126	-0,294	0,02508512	0,1274555
Eef1a2	P62631	0,285	0,10048284	0,19432061
Eef1b	O70251	-0,080	0,34504133	0,59939355
Eef1d	P57776-3	0,014	0,90423691	0,93800327
Eef1g	Q9D8N0	-0,211	0,30110863	0,37922183
Eef2	P58252	-0,182	0,00558929	0,16329252
Eftud2	O08810	0,071	0,36581773	0,62160976
Egfr	Q01279	-0,197	0,21545412	0,33915789
Ehd1	Q9WVK4	0,195	0,21203054	0,3378374
Eif1	P48024	0,334	0,29601678	0,31480229
Eif1ax	Q8BMJ3	0,508	0,29059115	0,27781145
Eif2a	Q8BJW6	-0,129	0,46113889	0,56259322
Eif2b4	Q61749	-0,014	0,93708962	0,94656819
Eif2s1	Q6ZWX6	0,032	0,44856182	0,79868244
Eif2s2	Q99L45	0,038	0,52177768	0,78398478
Eif2s3x	Q9Z0N1	-0,173	0,14333228	0,31363953
Eif3a	P23116	0,062	0,66115385	0,76859974
Eif3b	Q8JZQ9	-0,017	0,67563436	0,89505708
Eif3c	Q8R1B4	-0,026	0,72913414	0,87206792
Eif3d	O70194	-0,116	0,43795658	0,56419512
Eif3e	P60229	0,357	0,19832025	0,2342846
Eif3f	Q9DCH4	-0,103	0,42232907	0,57474031
Eif3g	Q9Z1D1	-0,049	0,69654	0,80067122
Eif3h	Q91WK2	0,124	0,39502569	0,52807815
Eif3i	Q9QZD9	-0,057	0,43916785	0,69846934
Eif3j1;Eif3j2	Q3UGC7	0,068	0,72596237	0,78675079
Eif3k	Q9DBZ5	-0,304	0,08172579	0,17001212
Eif3l	Q8QZY1	-0,128	0,27545968	0,458468
Eif3m	Q99JX4	0,172	0,10547573	0,28523613
Eif4a1	P60843	-0,073	0,69776163	0,76882857
Eif4a2	P10630	-0,148	0,65037519	0,67195643
Eif4a3	Q91VC3	0,000	0,99726363	0,99738277
Eif4b	Q8BGD9	0,014	0,93216315	0,94310367
Eif4e	P63073	-0,247	0,0735426	0,19318367
Eif4g1	Q6NZJ6	-0,031	0,73884717	0,85793128
Eif4g2	Q62448	-0,025	0,82267054	0,89476625
Eif4g3	Q80XI3-2	-0,199	0,27826557	0,37317788
Eif4h	Q9WUK2	-0,074	0,47078039	0,65460677
Eif5	P59325	0,022	0,84798713	0,90662395
Eif5a	P63242	-0,253	0,15910867	0,25867148
Eif5b	Q05D44	0,061	0,54331059	0,72584848
Eif6	O55135	0,073	0,78619861	0,81887431
Elavl1	P70372	-0,517	0,22122284	0,21643384
Elavl2	Q60899	-0,191	0,03358233	0,19652555
Elavl3	Q60900	-0,419	0,06703496	0,13082927
Elavl4	Q61701	-0,035	0,74504817	0,85182339
Elp2	Q91WG4	-0,137	0,13174838	0,36340126
Emc1	Q8C7X2	0,427	0,01637428	0,09828571
Emc2	Q9CRD2	-0,400	0,01617149	0,11004444
Emc3	Q99KI3	0,175	0,14180785	0,30784661
Emc8	O70378	0,081	0,37059222	0,60603352
Emd	O08579	-0,292	0,15608614	0,228832
Eml1	Q05BC3-2	-0,249	0,27843527	0,33820452
Eml4	Q3UMY5-2	-0,296	0,01836978	0,10604706
Enah	Q03173-6	-0,152	0,18641798	0,36942962
Eno1	P17182	-0,114	0,23435108	0,46302982
Eno2	P17183	0,059	0,3883341	0,67440807
Enoph1	Q8BGB7	0,236	0,0071936	0,12483422
Ensa	P60840-2	0,251	0,08773992	0,2010988
Epb41	P48193-2	-0,216	0,0350469	0,17487778
Epb41l1	Q9Z2H5	-0,075	0,54455199	0,68449432

Gene name	Protein uniprot IDs	Levels in the Mutant (log2 difference)	p-value	q-value
Epb41l2	O70318	0,193	0,26584951	0,36972881
Epb41l3	Q9WV92-3	-0,106	0,2758884	0,50424322
Ephb2	P54763	-0,337	0,02191296	0,10534247
Epm2aip1	Q8VEH5	0,188	0,03903665	0,21337089
Eprs	Q8CGC7	-0,038	0,49840371	0,77969604
Eps15	P42567	-0,224	0,2738674	0,35904639
Eps15l1	Q60902-2	0,234	0,2368437	0,31836953
Ept1	Q80TA1	21,615	ND	ND
Erc1	Q99MI1	-0,039	0,87183661	0,89527955
Ergic1	Q9DC16	-0,198	0,04891487	0,21187879
Erh	P84089	-0,260	0,07135466	0,17993531
Erlin2	Q8BFZ9	0,036	0,79677578	0,86874178
Erp29	P57759	-0,161	0,38391998	0,47993016
Erp44	Q9D1Q6	0,000	0,99812817	0,99742589
Esd	Q9R0P3	-0,073	0,22112919	0,57310483
Etf1	Q8BWY3	0,046	0,65537654	0,79404005
Etfa	Q99LC5	0,147	0,18326181	0,37324669
Etfb	Q9DCW4	-0,091	0,4750597	0,62082028
Etfdh	Q921G7	0,208	0,25721272	0,35981491
Evl	P70429-2	-0,227	0,06705062	0,19810169
Ewsr1	Q61545	-0,176	0,0464859	0,22929058
Exoc2	Q9D4H1	-0,015	0,96542725	0,96466951
Exoc4	O35382	0,018	0,69718619	0,89279131
Exoc8	Q6PGF7	-0,124	0,4010892	0,53284025
Ezr	P26040	-0,105	0,04242119	0,36991495
Fabp5	Q05816	-0,121	0,55303477	0,62317114
Fabp7	P51880	-0,146	0,27471983	0,41828391
Faf2	Q3TDN2	0,042	0,60439933	0,78908475
FAM120A	Q6A0A9	-0,330	0,02039266	0,10391892
Fam123a	Q8CCJ4	20,662	ND	ND
Fam125b	Q6KAU4	21,564	ND	ND
Fam129b	Q8R1F1	-0,062	0,44092133	0,67934478
Fam192a	Q91WE2	21,703	ND	ND
Fam40a	Q8C079-4	22,477	ND	ND
Fam49a	Q8BHZ0	-0,067	0,15081556	0,57402826
Fam49b	Q921M7	-0,376	0,11630818	0,16844058
Fam63a	Q76LS9-2	-21,376	ND	ND
Fam96b	Q9D187	22,785	ND	ND
Fam98a	Q3TJZ6	-0,010	0,8757874	0,93971926
Fam98b	Q80VD1	-0,005	0,96301632	0,9763411
Farp1	F8VPU2	-0,089	0,28600597	0,54517647
Farsa	Q8C0C7	-0,118	0,29443742	0,48866286
Farsb	Q9WUA2	-0,214	0,47734145	0,50188126
Fasn	P19096	-0,078	0,02726593	0,45701301
Fbl	P35550	-0,131	0,4591056	0,55787212
Fdft1	P53798	0,120	0,50344998	0,60097506
Fdps	Q920E5	-0,133	0,53862601	0,60886804
Fen1	P39749	0,368	0,1550379	0,20194258
Fermt2	Q8CIB5	0,069	0,08336124	0,5344127
Fh	P97807-2	0,097	0,07840428	0,40908976
Fhl1	P97447	0,077	0,71469717	0,77242811
Fip1l1	Q9D824-3	0,099	0,56417259	0,65391304
Fis1	Q9CQ92	0,194	0,05937586	0,2187563
Fkbp1a	P26883	0,055	0,62938122	0,76790594
Fkbp3	Q62446	-0,007	0,84146461	0,94605819
Fkbp4	P30416	-0,087	0,40331543	0,60612271
Fkbp8	O35465	0,048	0,72870051	0,81528098
Flna	Q8BTM8	-0,118	0,19314658	0,42460314
Flnb	Q80X90	-0,083	0,68697492	0,75981079
Flot1	O08917	0,199	0,3226735	0,39602673
Flot2	Q60634	0,230	0,01474392	0,15376271
Fmr1	P35922-3	-0,159	0,20228158	0,36890244
Fscn1	Q61553	-0,149	0,16513733	0,36334171
Fsd1	Q7TPM6	0,053	0,64682314	0,7744251
Fto	Q8BGW1-2	-0,127	0,35637003	0,50091682
Fubp1	Q91WJ8	-0,101	0,55302653	0,64508601
Fus	P56959	-0,108	0,4376639	0,57521452
Fxr1	Q61584-3	0,192	0,03720128	0,20242686
Fxr2	Q9WVR4	-0,255	0,04295535	0,16273898
Fxyd6	Q9D164-2	-0,095	0,74301704	0,77414103
G3bp1	P97855	-0,226	0,03709862	0,16545773
G3bp2	P97379	-0,366	0,04608803	0,12522751
G6pdx	Q00612	-0,136	0,17219857	0,38249013
Gaa	P70699	-18,992	ND	ND
Gab1	Q9QYY0	-0,179	0,07598098	0,25871199
Galk1	Q9R0N0	-0,336	0,04542901	0,13982775
Gamt	O35969	0,309	0,06105944	0,1573633
Ganab	Q8BHN3	-0,003	0,9701598	0,97662559
Gap43	P06837	0,029	0,80670455	0,88337803
Gapdh	P16858	0,195	0,45187539	0,49698589
Gapvd1	Q6PAR5	-0,023	0,82783153	0,89773824
Gars	Q9CZD3	0,104	0,07178002	0,38788222
Gart	Q64737	0,140	0,11419623	0,34083377
Gatad2b	Q8VHR5	-0,312	0,03009656	0,12456842
Gbe1	Q9D6Y9	21,343	ND	ND
Gcn1l1	E9PVA8	0,091	0,09262785	0,44834608
Gdap1	O88741	-0,164	0,39315485	0,48184942
Gdap1l1	Q8VE33	0,047	0,62380459	0,78075414
Gdi1	P50396	-0,193	0,04846074	0,21247427
Gdi2	Q61598	-0,139	0,12700399	0,36027799
Gdpd1	Q9CRY7	-0,413	0,20088257	0,21872234
Get4	Q9D1H7	-0,086	0,83120268	0,84643029
Gfap	P03995	-0,360	0,0852158	0,15959124
Gfpt1	P47856-2	-0,109	0,48744463	0,60609569
Ggt7	Q99JP7	0,429	0,35206139	0,33877551
Git1	Q68FF6	-0,011	0,95388175	0,9606549
Gldc	Q91W43	1,368	0,0037428	0
Glg1	Q61543	-0,123	0,55359271	0,62117321
Glo1	Q9CPU0	0,743	0,07451106	0,10860606
Glod4	Q9CPV4	-0,004	0,96660939	0,97760762
Glrx3	Q9CQM9	-0,098	0,33482712	0,54605004
Glrx5	Q80Y14	-0,135	0,73311458	0,75775518
Gls	D3Z7P3	0,075	0,22984254	0,56761905
Glud1	P26443	-0,053	0,19984879	0,64578141
Glul	P15105	0,040	0,65826552	0,80900928
Glyr1	Q922P9	-0,180	0,18278709	0,33401648
Gmfb	Q9CQI3	-0,214	0,02347789	0,1673955
Gmps	Q3THK7	-0,013	0,88232973	0,93398795
Gna13	P27601	0,087	0,19029073	0,51377778
Gnai1	B2RSH2	-0,296	0,17471149	0,24422684
Gnai2	P08752	-0,121	0,31995344	0,49711488
Gnai3	Q9DC51	0,056	0,50291278	0,72548414
Gnao1	P18872	-0,583	0,04928288	0,11405405
Gnao1	P18872-2	0,209	0,09034116	0,23298039
Gnaq	P21279	-0,014	0,55534616	0,89884611

Gene name	Protein uniprot IDs	Levels in the Mutant (log2 difference)	p-value	q-value
Gnas	P63094	0,271	0,31722586	0,36089682
Gnaz	O70443	0,101	0,73643104	0,76902277
Gnb1	P62874	-0,153	0,08359731	0,2921896
Gnb2	P62880	0,110	0,52914255	0,62129746
Gnb2l1	P68040	0,003	0,97214794	0,97593056
Gnb4	P29387	-0,286	0,48562225	0,48
Gng2	P63213	-0,202	0,18101442	0,30581009
Gng3	P63216	-0,071	0,7992051	0,83314495
Gng4	P50153	21,850	ND	ND
Gorasp2	Q99JX3-2	0,063	0,27585623	0,62270038
Got1	P05201	0,548	0,24849478	0,2337357
Got2	P05202	-0,074	0,28752232	0,59159256
Gpc1	Q9QZF2	-0,151	0,2220286	0,38632611
Gpd1l	Q3UJ0	-0,106	0,65124875	0,70544258
Gpd2	Q64521	0,088	0,26371275	0,5368377
Gphn	Q8BUV3	0,018	0,8675515	0,91556024
Gpi	P06745	-0,295	0,07743422	0,16996386
Gpm6a	P35802	-0,361	0,03499016	0,10667456
Gpm6b	P35803-8	-0,582	0,0310985	0,11156757
Gprin1	Q3UNH4	-0,269	0,05654462	0,16632588
Gps1	Q99LD4	-0,235	0,02237526	0,1576875
Gpsm1	Q6IR34	-0,096	0,36775337	0,56426555
Grb2	Q60631	-0,651	0,09675426	0,12296703
Gria2	P23819-4	0,666	0,00787289	0,038
Grm3	Q9QYS2	-0,192	0,17614897	0,31236364
Grwd1	Q810D6	-18,222	ND	ND
Gsk3b	Q9WV60	0,088	0,26318208	0,53796325
Gspt1	Q8R050-2	0,092	0,48131043	0,62178151
Gsr	P47791-2	-0,061	0,60066742	0,75049832
Gstk1	Q9DCM2	0,023	0,93537289	0,94039434
Gstm1	P10649	0,213	0,22188638	0,32700139
Gstm5	P48774	-0,082	0,36074816	0,60049196
Gsto1	O09131	-0,462	0,26230547	0,26177856
Gstp1	P19157	0,091	0,4563225	0,61758879
Gtf2e2	Q9D902	0,160	0,57278047	0,61034231
Gtf2i	Q9ESZ8-5	-0,147	0,02500587	0,25107353
Gtpbp1	O08582	-0,091	0,68744705	0,74945161
H2afy	Q9QZQ8	-0,195	0,13413302	0,28233548
H2afy2	Q8CCK0	-0,140	0,33071047	0,47041879
H3f3a;H3f3c	P84244	-0,542	0,0356309	0,11772043
Hacd3	Q8K2C9	0,417	0,19376883	0,21637802
Hadh	Q61425	0,529	0,01361895	0,07512727
Hadha	Q8BMS1	0,139	0,31922746	0,463357
Hadhb	Q99JY0	-0,110	0,50172995	0,61233465
Hars	Q61035	0,060	0,65549531	0,76852276
Hat1	Q8BY71	-0,180	0,03077656	0,21287119
Hba	P01942	-0,305	0,1553805	0,22036667
Hbb-b1;Hbb-b	P02088	-0,324	0,10771055	0,17944865
Hccs	P53702	-0,670	0,08492229	0,1057561
Hcfc1	Q61191	-0,095	0,58340314	0,67299567
Hdac2	P70288	-0,024	0,75774501	0,88333411
Hdac6	Q9Z2V5	-0,163	0,29438444	0,40964378
Hdgf	P51859	-0,010	0,93686319	0,95344421
Hdgfrp2	Q3UMU9	-0,140	0,55796449	0,61356795
Hdgfrp3	Q9JMG7	0,094	0,37563261	0,57473527
Hdhd2	Q3UGR5	0,383	0,09583397	0,16248029
Hdlbp	Q8VDJ3	-0,103	0,19889306	0,47047656
Hepacam	Q640R3	0,529	0,05250023	0,10778947
Hexb	P20060	-0,049	0,66335366	0,7870603
Hibadh	Q99L13	-0,052	0,61642355	0,76977173
Hibch	Q8QZS1	-0,089	0,48734236	0,63025152
Hid1	Q8R1F6-2	-20,973	ND	ND
Hint1	P70349	-0,067	0,71403156	0,78072081
Hip1	Q8VD75	-0,151	0,26665054	0,41023897
Hist1h1a	P43275	-0,387	0,25972037	0,27748322
Hist1h1b	P43276	-0,251	0,00866521	0,11163218
Hist1h1c	P15864	0,076	0,53857241	0,68163143
Hist1h1e	P43274	-0,062	0,38586859	0,66107331
;Hist1h2bh;H	Q8CGP2	0,110	0,7686892	0,78390386
Hist1h4a	P62806	-0,145	0,54804807	0,6031936
Hk1	P17710-3	-0,045	0,4414549	0,74801886
Hm13	Q9D8V0-4	0,127	0,35099474	0,50283209
Hmgb1	P63158	-0,972	0,09638364	0,10678014
Hmgb2	P30681	-1,099	0,06297886	0,10192593
Hmgb3	O54879	-0,338	0,05024548	0,14342593
Hmgcl	P38060	-0,076	0,81721381	0,84107069
Hmgcs1	Q8JZK9	0,041	0,67421465	0,81251295
Hmgn5	Q9JL35	-0,313	0,19826228	0,25482609
Hmox2	O70252	-0,243	0,09248692	0,21510805
Hn1	P97825	-0,028	0,73365208	0,86676778
Hnrnpa0	Q9CX86	0,065	0,58827624	0,73535934
Hnrnpa1	P49312	-0,451	0,02528108	0,11779167
Hnrnpa2b1	O88569	-0,072	0,55826168	0,69807303
Hnrnpa3	Q8BG05	0,036	0,77108815	0,85894849
Hnrnpab	Q99020	0,201	0,14891564	0,2863616
Hnrnpc	Q9Z204-2	-0,046	0,77807294	0,84479375
Hnrnpd	Q60668-3	-0,096	0,39133372	0,57542197
Hnrnpdl	Q9Z130	0,807	0,08818355	0,10322148
Hnrnpf	Q9Z2X1	-0,242	0,04278758	0,1669125
Hnrnph1	O35737	-0,113	0,41013891	0,55642393
Hnrnph2	P70333	-0,148	0,15264992	0,36016389
Hnrnpk	P61979-2	0,201	0,19226148	0,31436805
Hnrnpl	Q8R081	-0,018	0,84722617	0,91449693
Hnrnpll	Q921F4	-0,060	0,553625	0,7345634
Hnrnpm	Q9D0E1	-0,046	0,48881164	0,75938544
Hnrnpu	Q8VEK3	-0,140	0,1771118	0,38203302
Hnrnpul1	Q8VDM6	-0,212	0,04297732	0,19187629
Hnrnpul2	Q00PI9	-0,245	0,00544202	0,10579641
Homer3	Q99JP6	-0,479	0,23651747	0,23456751
Hook3	Q8BUK6	-0,122	0,30801192	0,48929389
Hp1bp3	Q3TEA8	-0,046	0,68375666	0,80234637
Hpca	P84075	0,064	0,79231975	0,83386001
Hpcal1	P62748	-0,168	0,31445421	0,41237053
Hprt1	P00493	0,152	0,40860055	0,50217844
Hsd17b10	O08756	-0,137	0,39286859	0,51038462
Hsd17b12	O70503	-0,059	0,1523104	0,60994783
Hsd17b4	P51660	-0,196	0,12274574	0,27794958
Hsdl1	Q8BTX9	-0,506	0,0001161	0
Hsdl2	Q2TPA8	-0,168	0,34606323	0,4402444
Hsp90aa1	P07901	-0,449	0,02731048	0,11439216
Hsp90ab1	P11499	-0,179	0,07067896	0,25264469
Hsp90b1	P08113	0,212	0,18454043	0,29758663
Hspa12a	Q8K0U4	-0,056	0,32405885	0,67024419
Hspa14	Q99M31	0,096	0,21992631	0,50471536
Hspa2	P17156	-0,138	0,31484046	0,46333003

Gene name	Protein uniprot IDs	Levels in the Mutant (log2 difference)	p-value	q-value
Hspa4	Q61316	0,042	0,31257695	0,73556498
Hspa4l	P48722	0,098	0,09040252	0,41032666
Hspa5	P20029	0,381	0,00616607	0,0859375
Hspa8	P63017	-0,191	0,17693283	0,31436571
Hspa9	P38647	-0,053	0,49051655	0,73064011
Hspbp1	Q99P31	0,817	0,14334821	0,15574249
Hspd1	P63038	0,029	0,73946642	0,86445203
Hspe1	Q64433	-0,107	0,36561773	0,53935652
Hsph1	Q61699	-0,167	0,04670269	0,24376604
Htatsf1	Q8BGC0	0,050	0,76472574	0,83445593
Huwe1	Q7TMY8	-0,157	0,15128169	0,33775597
Hyou1	Q9JKR6	0,618	0,00181172	0
Iah1	Q9DB29	0,076	0,71620091	0,7743815
Iars	Q8BU30	0,190	0,01189721	0,16639252
Iars2	Q8BIJ6	0,379	0,02125015	0,10904202
Ide	Q9JHR7	0,057	0,67959817	0,78026938
Idh1	O88844	0,201	0,2247302	0,34010724
Idh2	P54071	-0,104	0,29054158	0,51519563
Idh3a	Q9D6R2	-0,177	0,00274847	0,16018909
Idh3g	P70404	-0,218	0,01888722	0,1596087
Idi1	P58044	-0,034	0,81555203	0,88176587
Igsf21	Q7TNR6	-0,131	0,11438396	0,36392424
Igsf3	Q6ZQA6	-0,954	0,01801189	0,04745455
Ik	Q921M8	-0,071	0,77228355	0,81157064
Ikbkap	Q7TT37	-0,035	0,77046125	0,85924497
Ilf2	Q9CXY6	-0,067	0,12825322	0,56310321
Ilf3	Q9Z1X4	-0,174	0,0179583	0,19754455
Ilk	O55222	0,178	0,42055636	0,48943923
Immt	Q8CAQ8-2	-0,195	0,27962503	0,37801195
Impa1	O55023	-0,670	0,32022929	0,27654516
Impdh2	P24547	-0,220	0,30337289	0,37222515
Ina	P46660	0,181	0,38829689	0,46099203
Inpp1	P49442	0,315	0,02480008	0,11293023
Inpp4a	Q9EPW0	-0,170	0,56962642	0,60167763
Ints3	Q7TPD0	-0,142	0,54225961	0,60170833
Ipo11	Q8K2V6	0,703	0,13372473	0,15311392
Ipo4	Q8VI75	-0,236	0,09371583	0,21447577
Ipo5	Q8BKC5	0,455	0,00170385	0,0522
Ipo7	Q9EPL8	-0,047	0,62852964	0,78385814
Ipo9	Q91YE6	0,145	0,08460685	0,31149708
Iqgap1	Q9JKF1	0,110	0,51617044	0,61735409
Irgq	Q8VIM9	0,845	0,0510827	0,10450633
Isoc1	Q91V64	-0,126	0,23115319	0,43265213
Isoc2a	P85094	0,019	0,75602894	0,89468565
Isyna1	Q9JHU9	-0,111	0,79333485	0,8024472
Itch	Q8C863-2	20,073	ND	ND
Itgb1	P09055	-0,075	0,38813041	0,62269325
Itpa	Q9D892	-0,062	0,35578746	0,64977219
Itpr1	P11881-7	-0,186	0,14271026	0,29248541
Itsn1	Q9Z0R4	-0,216	0,39206997	0,43351452
Ivd	Q9JHI5	-0,110	0,45459437	0,58294754
Iws1	Q8C1D8	21,243	ND	ND
Kars	Q99MN1	0,087	0,72449382	0,77027125
Kcnj6	P48542-2	-0,420	0,31425911	0,30175334
Kctd12	Q6WVG3	0,149	0,30961428	0,44004077
Kdm1a	Q6ZQ88	-0,127	0,85288563	0,85178359
Khdrbs1	Q60749	0,672	0,16734497	0,16749186
Khsrp	Q3U0V1	0,076	0,38275693	0,61860263
Kiaa1468	Q148V7	0,055	0,21669512	0,64187829
Kif1a	P33173	-0,089	0,19830182	0,51055545
Kif21a	Q9QXL2-3	-0,318	0,01764138	0,10462585
Kif21b	Q9QXL1	0,040	0,73065571	0,83567777
Kif2a	P28740	0,074	0,715241	0,7736451
Kif5b	Q61768	-0,058	0,50736125	0,72314068
Kif5c	P28738	-0,147	0,10940064	0,32835912
Kifap3	P70188-2	0,237	0,46777274	0,48562991
Klc1	O88447	-0,097	0,5475423	0,64511869
Klc2	O88448	-0,115	0,28340118	0,48990805
Kpna1	Q60960	-0,147	0,41305823	0,51146569
Kpna2	P52293	0,435	0,01664901	0,1032
Kpna3	O35344	-0,053	0,61892096	0,76908333
Kpna4	O35343	-0,300	0,38858725	0,38725141
Kpna6	O35345	-0,129	0,40742225	0,52818456
Kpnb1	P70168	0,533	0,01728275	0,08626667
Kras	P32883-2	0,010	0,97311778	0,97373036
Ktn1	Q61595-16	0,085	0,52975837	0,65881645
L1cam	P11627	-0,610	0,01167015	0,048
Lamp1	P11438	-0,541	0,01824835	0,08485246
Lamtor1	Q9CQ22	0,526	0,02509075	0,10876712
Lamtor3	O88653	22,538	ND	ND
Lancl1	O89112	-0,092	0,38919854	0,58137796
Lancl2	Q9JJK2	-0,065	0,27658533	0,61923292
Lap3	Q9CPY7-2	0,028	0,3907517	0,81376355
Larp7	Q05CL8	-0,245	0,31358757	0,36936296
Lars	Q8BMJ2	0,063	0,35566342	0,64447917
Lasp1	Q61792	-0,058	0,50292689	0,72149374
Lbr	Q3U9G9	0,138	0,28207354	0,43967689
Ldha	P06151	-0,273	0,05907168	0,16685897
Ldhb	P16125	0,027	0,90316775	0,9172919
Letm1	Q9Z2I0	-0,051	0,86635123	0,88503345
Lgmn	O89017	-0,031	0,94690298	0,94220563
Lig1	P37913	0,021	0,81028802	0,89839365
Limch1	Q3UH68-3	0,025	0,87447729	0,91181839
Lin7c	O88952	0,045	0,79546181	0,85239524
Lman1	Q9D0F3	-0,073	0,69562077	0,76916743
Lman2	Q9DBH5	-0,309	0,67440267	0,6447946
Lmnb1	P14733	-0,020	0,71200223	0,88758089
Lmnb2	P21619	-0,090	0,44981689	0,61756006
Lonp1	Q8CGK3	-0,080	0,7302671	0,77674121
Lonp2	Q9DBN5	-0,187	0,21566813	0,34395294
Lpcat1	Q3TFD2-2	-0,088	0,8559256	0,86527991
Lppr3	Q7TPB0	-0,011	0,89084465	0,94007613
Lrp1	Q91ZX7	-0,189	0,304413	0,39088018
Lrpap1	P55302	0,061	0,5488645	0,72774673
Lrpprc	Q6PB66	-0,094	0,18046871	0,48937643
Lrrc40	Q9CRC8	-0,636	0,03150323	0,09611765
Lrrc47	Q505F5	-0,230	0,09620154	0,2187907
Lrrc57	Q9D1G5	0,414	0,15540509	0,19206138
Lrrc59	Q922Q8	0,014	0,89994467	0,93712411
Lsamp	Q8BLK3	0,320	0,2548565	0,28702839
Lsm12	Q9D0R8	-0,015	0,86860298	0,92779006
Lsm14a	Q8K2F8	0,121	0,7233844	0,75607229
Lsm14b	Q8CGC4	-0,165	0,35039922	0,44856855
Lsm2	O35900	0,147	0,07921495	0,30018507
Lta4h	P24527	-0,242	0,03586584	0,16384983

Gene name	Protein uniprot IDs	Levels in the Mutant (log2 difference)	p-value	q-value
Luc7l2	Q7TNC4-2	-0,057	0,11586614	0,60838443
Luc7l3	Q5SUF2	-0,101	0,33446992	0,53749301
Lxn	P70202	-0,425	0,11069972	0,16076056
Ly6h	Q9WUC3	-0,280	0,17669203	0,25450909
Lyar	Q08288	21,417	ND	ND
Lypla2	Q9WTL7	0,634	0,09113313	0,11514124
Lzic	Q8K3C3	0,079	0,86698544	0,88218925
Lztfl1	Q9JHQ5	-0,103	0,45051029	0,59170526
Macf1	Q9QXZ0	-0,145	0,02305439	0,25284095
Madd	Q80U28-3	-0,527	0,00605352	0,0348
Maoa	Q64133	-0,236	0,23263704	0,31533333
Map1a	Q9QYR6	0,081	0,22703929	0,54770026
Map1b	P14873	0,041	0,39082427	0,75927418
Map1s	Q8C052	-0,101	0,51093995	0,62199541
Map2	P20357	-0,091	0,14935412	0,48115111
Map2k2	Q63932	-0,132	0,61899401	0,65435762
Map2k4	P47809	-0,523	0,38144498	0,34256842
Map2k6	P70236	-0,318	0,03125236	0,12618378
Map4	P27546-2	-0,039	0,44010492	0,7686985
Map4	P27546-4	0,024	0,79415156	0,89108893
Map4k4	P97820	0,060	0,61541087	0,76075582
Map6	Q7TSJ2	-0,028	0,78841966	0,88385349
Mapk1	P63085	0,298	0,04294253	0,15507692
Mapk10	Q61831-2	0,698	0,05242976	0,11538776
Mapk3	Q63844	0,195	0,18988364	0,31837288
Mapk8ip3	Q9ESN9-2	-0,184	0,33486357	0,4095222
Mapre1	Q61166	-0,046	0,58913185	0,77436724
Mapre2	Q8R001-2	0,232	0,45342653	0,4755443
Mapre3	Q6PER3	0,084	0,41684941	0,61552702
Mapt	P10637-5	-0,170	0,05369432	0,24540741
Marc2	Q922Q1	0,198	0,52636256	0,54953184
Marcks	P26645	0,223	0,34226709	0,39051121
Marcksl1	P28667	-0,009	0,70810585	0,93065275
Mark3	Q03141-2	-0,376	0,01823275	0,11943396
Mars	Q68FL6	0,119	0,45719882	0,57124333
Mat2a	Q3TH56	-0,083	0,19255143	0,52732021
Mat2b	Q99LB6-2	0,054	0,67271305	0,78414956
Matr3	Q8K310	-0,063	0,66193875	0,76875916
Maz	P56671	-0,363	0,11565009	0,17578409
Mbd3	Q9Z2D8-2	0,174	0,27887063	0,3886382
Mbp	P04370-4	0,059	0,71361258	0,7923985
Mccc1	Q99MR8	-0,173	0,60173173	0,61819614
Mccc2	Q3ULD5	-0,196	0,23826236	0,35825681
Mcm2	P97310	0,082	0,31351282	0,57554012
Mcm3	P25206	-0,001	0,98790854	0,990066
Mcm4	P49717	-0,054	0,14491861	0,62192536
Mcm5	P49718	-0,088	0,52016495	0,64533036
Mcm6	P97311	-0,420	0,11704386	0,16807895
Mcm7	Q61881	0,000	0,99879474	0,99725822
Mdh1	P14152	-0,521	0,05321461	0,10805882
Mdh2	P08249	-0,118	0,25140069	0,46284577
Mdk	P12025	-21,787	ND	ND
Me1	P06801	0,172	0,05574725	0,24288806
Me2	Q99KE1	0,681	0,10951725	0,12934673
Mecp2	Q9Z2D6-2	-0,173	0,31817917	0,40962116
Memo1	Q91VH6	-0,162	0,20874067	0,368838
Mesdc2	Q9ERE7	0,162	0,22233141	0,37732057
Metap1	Q8BP48	0,165	0,37789898	0,46938039
Metap2	O08663	0,477	0,0515317	0,10539474
Mettl26	Q9DCS2	-20,885	ND	ND
Mfap1	Q9CQU1	-0,086	0,57496437	0,68091583
Mff	Q6PCP5	0,077	0,69518263	0,76472178
Mgea5	Q9EQQ9	0,190	0,01435957	0,16691765
Mgll	O35678	0,269	0,38616652	0,40121239
Mia3	Q8BI84	0,080	0,45586082	0,63414017
Mif	P34884	0,852	0,38682557	0,31792968
Mlec	Q6ZQI3	-0,058	0,62909415	0,76610554
Mllt4	Q9QZQ1	-0,108	0,48338166	0,60625879
Mms19	Q9D071-3	1,076	0,03280429	0,07036364
Mogs	Q80UM7	0,242	0,23068586	0,30948755
Mpc2	Q9D023	-0,567	0,113633	0,15572294
Mpi	Q924M7	-0,005	0,97391828	0,97693185
Mpst	Q99J99	-0,064	0,84583999	0,86647004
Mrpl39	Q9JKF7	21,227	ND	ND
Mrps23	Q8VE22	23,371	ND	ND
Msh2	P43247	-0,302	0,41523958	0,40863568
Msh6	P54276	-0,196	0,15914234	0,29158959
Msi1	Q61474	0,120	0,30301174	0,49022945
Msi2	Q920Q6-3	0,088	0,28366787	0,54758276
Msn	P26041	0,277	0,20929728	0,27776159
Mta1	Q8K4B0	0,064	0,64019657	0,76132891
Mta2	Q9R190	-0,138	0,31624275	0,46318416
Mtap	Q9CQ65	0,270	0,43672999	0,43991828
Mtap7d1	A2AJI0	21,918	ND	ND
Mtch2	Q791V5	-0,153	0,02002737	0,23
Mtco1	P00397	-0,301	0,11451655	0,19705679
Mtco2	P00405	0,413	0,19676812	0,21625751
Mtdh	Q80WJ7	-0,226	0,15039168	0,2682517
Mtfr1l	Q9CWE0	-0,058	0,68053777	0,77983663
Mthfd1	Q922D8	-0,275	0,03620993	0,15557025
Mthfd1l	Q3V3R1	0,392	0,4333018	0,40055507
Mtor	Q9JLN9	0,592	0,00285644	0,04628571
Mtpn	P62774	-0,484	0,05129754	0,10606897
Mtx1	P47802	-0,140	0,22191594	0,40099669
Mut	P16332	-0,350	0,13481898	0,1942481
Mvd	Q99JF5	0,068	0,61785864	0,74429076
Mybbp1a	Q7TPV4	-0,068	0,56176656	0,71779387
Myef2	Q8C854	0,010	0,83558888	0,9358358
Myg1	Q9JK81	-0,230	0,02032834	0,15711197
Myh10	Q61879	-0,019	0,9577934	0,95475884
Myh9	Q8VDD5	0,092	0,2170364	0,50723091
Myl12b;Myl9	Q3THE2	0,190	0,28847295	0,38591445
Myl6	Q60605-2	-0,117	0,61145027	0,66583516
Myo18a	Q9JMH9-4	-0,026	0,81802623	0,89099083
Myo1b	P46735	0,131	0,24916682	0,43306528
Myo5a	Q99104	-0,032	0,70370182	0,84630631
Myo6	Q64331	0,020	0,90814969	0,93026278
Naa15	Q80UM3	-0,279	0,13648514	0,21829769
Naca	Q60817	-0,178	0,06292811	0,24320599
Nacad	Q5SWP3	-0,222	0,52569886	0,53723944
Nae1	Q8VBW6	0,019	0,81975171	0,9039685
Nampt	Q99KQ4	-0,059	0,46830536	0,69861506
Nap1l1	P28656	0,252	0,0743102	0,19172308
Nap1l4	Q78ZA7	-0,151	0,18018491	0,36923985
Napa	Q9DB05	-0,251	0,06379823	0,1780813

Gene name	Protein uniprot IDs	Levels in the Mutant (log2 difference)	p-value	q-value
Napb	P28663	-0,378	0,02421911	0,114688
Napg	Q9CWZ7	-0,001	0,98632092	0,9897065
Nars	Q8BP47	0,079	0,09441973	0,50213133
Nasp	Q99MD9	0,060	0,62379611	0,76183411
Nbea	Q9EPN1-4	-0,326	0,00708489	0,119
Ncald	Q91X97	0,661	0,06888019	0,10698507
Ncam1	P13595-2	-23,986	ND	ND
Ncam2	O35136	-0,123	0,47133492	0,57452073
Ncan	P55066	-0,040	0,85593718	0,88628145
Ncapd2	Q8K2Z4	0,121	0,4576114	0,56658745
Ncbp1	Q3UYV9	-0,238	0,04546046	0,16893023
Ncdn	Q9Z0E0-2	0,115	0,41659371	0,55605802
Nceh1	Q8BLF1	-0,089	0,79213035	0,81201232
Nckap1	P28660	0,043	0,53700653	0,77108926
Ncl	P09405	0,263	0,09814696	0,20223389
Ncoa5	Q91W39	0,222	0,31195109	0,37818571
Ndel1	Q9ERR1-2	-0,391	0,36450134	0,35862354
Ndrg1	Q62433	20,060	ND	ND
Ndrg2	Q9QYG0-2	-0,176	0,09295352	0,27655518
Ndrg3	Q9QYF9	-0,157	0,48416643	0,54557649
Ndrg4	Q8BTG7-2	-0,203	0,45571831	0,49679773
Ndufa10	Q99LC3	-0,109	0,17385047	0,43905133
Ndufa13	Q9ERS2	-0,077	0,54262593	0,68166215
Ndufa4	Q62425	-0,112	0,2870566	0,4963016
Ndufa5	Q9CPP6	-0,059	0,47757379	0,70493427
Ndufa6	Q9CQZ5	-0,231	0,40483495	0,43261698
Ndufa7	Q9Z1P6	0,117	0,54668912	0,62247167
Ndufa8	Q9DCJ5	0,305	0,30427589	0,33544186
Ndufa9	Q9DC69	0,835	0,03971915	0,08730159
Ndufb10	Q9DCS9	-0,028	0,80342566	0,88286771
Ndufb11	O09111	0,016	0,9095731	0,93698579
Ndufb4	Q9CQC7	-0,045	0,51315099	0,76601714
Ndufb7	Q9CR61	-0,205	0,52048372	0,53630635
Ndufb8	Q9D6J5	0,026	0,82660446	0,89369503
Ndufb9	Q9CQJ8	0,200	0,3751204	0,43210811
Ndufs1	Q91VD9	0,175	0,10822283	0,28579487
Ndufs2	Q91WD5	0,027	0,38445104	0,81556047
Ndufs3	Q9DCT2	0,226	0,00760815	0,13965217
Ndufs8	Q8K3J1	-0,272	0,66275229	0,63767946
Ndufv1	Q91YT0	0,579	0,03258377	0,10068293
Ndufv2	Q9D6J6	0,207	0,26887904	0,36580176
Necap1	Q9CR95	0,075	0,70589657	0,77036423
Nedd4	P46935	0,219	0,02618578	0,16640777
Nefh	P19246	-0,486	0,16377711	0,18155496
Nefl	P08551	0,367	0,30036668	0,3073432
Nefm	P08553	0,141	0,57276855	0,61865325
Neo1	P97798-5	0,136	0,29032241	0,44839759
Nes	Q6P5H2	-0,063	0,46239138	0,68302703
Nf1	Q04690-2	0,106	0,74947035	0,77363144
Nfasc	Q810U3	-0,211	0,26264169	0,36011765
Nfia	Q02780-3	0,032	0,90424342	0,91532071
Nfib	P97863-2	-0,207	0,03556914	0,18337895
Nfix	P70257-1	-0,296	0,08908157	0,17669231
Nfu1	Q9QZ23	-0,320	0,00331387	0,11027778
Nhp2l1	Q9D0T1	-0,148	0,06723491	0,288575
Nipsnap1	O55125	-0,003	0,98495853	0,98552231
Nipsnap3b	Q9CQE1	0,494	0,15122852	0,16698851
Nit2	Q9JHW2	-0,100	0,26878273	0,51331142
Nln	Q91YP2	0,121	0,51602308	0,60668576
Nme1	P15532	0,819	0,10970744	0,11449438
Nme2	Q01768	-0,134	0,39121817	0,5131558
Nmral1	Q8K2T1	0,594	0,05058263	0,11303571
Nmt1	O70310	0,013	0,90511728	0,9397361
Nmt2	O70311	-0,761	0,02538673	0,06646154
Nomo1	Q6GQT9	0,137	0,13159249	0,36346532
Nono	Q99K48	-0,098	0,22568043	0,50009765
Nop56	Q9D6Z1	-0,117	0,06358262	0,36057727
Nop58	Q6DFW4	-0,318	0,08091379	0,16694805
Nova1	Q9JKN6	-0,240	0,01979982	0,15551667
Npepps	Q11011	-0,199	0,06259533	0,21579443
Nploc4	P60670	-0,276	0,40293079	0,40872727
Npm1	Q61937	0,254	0,10261113	0,21651259
Npm3	Q9CPP0	-0,182	0,23559523	0,36641096
Nptn	P97300-3	-0,244	0,45167535	0,46571709
Nras	P08556	-0,518	0,00554441	0,036
Nrbp1	Q99J45	0,017	0,8959728	0,92944714
Nrcam	Q810U4-2	-0,202	0,12471851	0,27190525
Nrd1	Q8BHG1	-0,026	0,84950098	0,89868174
Nrxn1	Q9CS84-4	0,174	0,47487028	0,52891868
Nsdhl	Q9R1J0	0,027	0,85205399	0,89846154
Nsf	P46460	-0,213	0,03964921	0,18300792
Nsfl1c	Q9CZ44	-0,145	0,03572274	0,27058065
Nsun2	Q1HFZ0	0,019	0,8987934	0,9282624
Nt5dc3	Q3UHB1	-0,100	0,77740467	0,7945175
Ntm	Q99PJ0	-0,068	0,69004721	0,77121244
Nucb1	Q02819	-0,121	0,5213954	0,60977637
Nudc	O35685	-0,218	0,21193004	0,31473745
Nudcd1	Q6PIP5	-0,093	0,57788523	0,67331594
Nudcd2	Q9CQ48	-0,238	0,33058865	0,38179669
Nudt21	Q9CQF3	0,104	0,40527703	0,56706198
Nudt3	Q9JI46	-0,064	0,53131613	0,71098883
Nup133	Q8R0G9	0,254	0,15301959	0,24853039
Nup155	Q99P88	-0,381	0,17699927	0,21105778
Nup160	Q9Z0W3	0,152	0,46561876	0,53877895
Nup210	Q9QY81	-0,057	0,78343524	0,83524712
Nup214	Q80U93	0,574	0,01781817	0,08021429
Nup35	Q8R4R6	-0,191	0,34321213	0,41014634
Nup93	Q8BJ71	-0,247	0,0634577	0,18010638
Nup98	Q6PFD9	0,101	0,37504548	0,56093197
Nutf2	P61971	0,032	0,8639232	0,89824717
Oat	P29758	0,143	0,2832867	0,43194639
Ociad1	Q9CRD0	0,527	0,35146506	0,31639149
Ogdh	Q60597-3	-0,185	0,07267272	0,2427514
Ogfr	Q99PG2	-0,381	0,238293	0,2625193
Ogt	Q8CGY8	-0,139	0,30209372	0,45422668
Ola1	Q9CZ30	0,151	0,37167999	0,48207907
Opa1	P58281-2	-0,079	0,29565437	0,57812961
Optn	Q8K3K8	-0,153	0,39704866	0,49676981
Osbp	Q3B7Z2	-0,317	0,20385513	0,25952518
Osbpl1a	Q91XL9-3	0,512	0,04869492	0,10943511
Osbpl8	B9EJ86	0,006	0,96016563	0,97158789
Ostf1	Q62422	0,285	0,12676375	0,21262022
Otub1	Q7TQI3	-0,145	0,1984315	0,38476477
Otud6b	Q8K2H2	-0,021	0,93478122	0,9394354
Oxct1	Q9D0K2	0,031	0,71719506	0,8522903

Gene name	Protein uniprot IDs	Levels in the Mutant (log2 difference)	p-value	q-value
Oxr1	Q4KMM3-4	0,127	0,4634475	0,56375063
Oxsr1	Q6P9R2	0,112	0,46052781	0,58276495
P4hb	P09103	0,014	0,74135598	0,91130756
Pa2g4	P50580	-0,064	0,44763458	0,67558879
Pabpc1	P29341	-0,173	0,07178613	0,26205954
Pabpn1	Q8CCS6-2	-0,165	0,18052603	0,34882705
Pacs1	Q8K212	0,211	0,07192502	0,21590351
Pacsin1	Q61644	-0,305	0,10379458	0,18455352
Pacsin2	Q9WVE8	-0,105	0,60773316	0,67584173
Paf1	Q8K2T8	20,936	ND	ND
Pafah1b1	P63005	-0,126	0,12086127	0,37267146
Pafah1b2	Q61206	0,048	0,71500373	0,81020247
Pafah1b3	Q61205	0,106	0,35809562	0,53621603
Paics	Q9DCL9	-0,091	0,45672662	0,61781761
Pak1	O88643	-0,257	0,1671719	0,26186195
Pak2	Q8CIN4	-0,075	0,64817024	0,74612289
Palm	Q9Z0P4-2	-0,149	0,08614083	0,30173214
Papola	Q61183-2	21,815	ND	ND
Papss1	Q60967	-0,003	0,98810882	0,98849948
Park7	Q99LX0	-0,009	0,95016899	0,96021772
Parp1	P11103	-0,169	0,12222839	0,29764671
Parva	Q9EPC1	0,118	0,76346564	0,77723785
Pax6	P63015	0,029	0,85835004	0,8984086
Pbdc1	Q9D0B6	-0,243	0,35410274	0,38733183
Pbx1	P41778-2	-0,205	0,34396387	0,40679913
Pc	Q05920	-0,146	0,04509604	0,27868439
Pcbp1	P60335	-0,146	0,13382727	0,3435
Pcbp2	Q61990	0,047	0,83575673	0,87330837
Pcbp3	P57722-2	0,134	0,59140572	0,63458308
Pcbp4	P57724	-0,079	0,5064211	0,65833309
Pcca	Q91ZA3	-0,232	0,09284999	0,21737691
Pccb	Q99MN9	0,263	0,02060812	0,14170616
Pck2	Q8BH04	0,274	0,04924077	0,1619
Pcmt1	P23506	0,082	0,46008207	0,6312829
Pcna	P17918	0,123	0,21739542	0,42962083
Pcp2	P12660	-0,486	0,14652622	0,16940896
Pcsk1n	Q9QXV0	-0,645	0,08358227	0,10730952
Pcyox1	Q9CQF9	0,284	0,16898351	0,2441203
Pcyox1l	Q8C7K6	0,025	0,85557363	0,90254648
Pdap1	Q3UHX2	-0,315	0,04180989	0,14409302
Pdcd11	Q6NS46	-0,098	0,8051761	0,81837255
Pdcd4	Q61823	-0,202	0,22198097	0,33783784
Pdcd5	P56812	-0,010	0,95107584	0,96013896
Pdcd6	P12815	-0,121	0,13016446	0,38626866
Pdcd6ip	Q9WU78	0,170	0,21475322	0,36686783
Pde12	Q3TIU4	0,030	0,60684236	0,83481868
Pde1c	Q64338-2	0,066	0,59710221	0,73660383
Pdha1	P35486	0,152	0,20978002	0,38214771
Pdhb	Q9D051	-0,144	0,18256535	0,37794749
Pdia3	P27773	0,245	0,05823383	0,17819074
Pdia4	P08003	0,291	0,07271309	0,1670184
Pdia6	Q922R8	0,155	0,16380838	0,35831169
Pdlim3	O70209	0,215	0,31889194	0,38594444
Pdlim5	Q8CI51	0,272	0,40213724	0,40848328
Pds5a	Q6A026	-0,335	0,15484692	0,21358014
Pds5b	Q4VA53	-0,083	0,63266891	0,72516736
Pdxdc1	Q99K01-2	-0,161	0,46516502	0,52866253
Pdxk	Q8K183	0,226	0,26339707	0,34348624
Pdxp	P60487	-0,372	0,08558553	0,15795489
Pea15	Q62048	-0,154	0,63287773	0,65005765
Pebp1	P70296	-0,150	0,43557617	0,52267504
Pelp1	Q9DBD5	-0,160	0,05308201	0,26487805
Pex19	Q8VCI5	0,015	0,87423491	0,92698069
Pfas	Q5SUR0	-0,262	0,26247002	0,3193427
Pfdn5	Q9WU28	0,002	0,99200814	0,99025969
Pfkl	P12382	0,157	0,22334925	0,38115286
Pfkm	P47857-3	-0,174	0,03732833	0,21851883
Pfkp	Q9WUA3	0,775	0,02198489	0,0755122
Pfn1	P62962	-0,164	0,16664154	0,33730861
Pfn2	Q9JJV2	0,049	0,70478753	0,80443397
Pgam1	Q9DBJ1	-0,258	0,11146084	0,21415453
Pgap1	Q3UUQ7	0,432	0,48348831	0,4399959
Pgd	Q9DCD0	0,058	0,58487356	0,75264966
Pgk1	P09411	0,066	0,17446403	0,5832339
Pgls	Q9CQ60	0,031	0,64234723	0,83472727
Pgm1	Q9D0F9	-0,166	0,10420376	0,28809877
Pgm2	Q7TSV4	-0,241	0,22619388	0,30688922
Pgm2l1	Q8CAA7	-0,147	0,23296111	0,3967386
Pgm3	Q9CYR6	-0,042	0,84745438	0,88300405
Pgp	Q8CHP8	0,136	0,47780071	0,56242568
Pgrmc1	O55022	0,212	0,15069427	0,27617021
Pgrmc2	Q80UU9	0,202	0,38260706	0,43542035
Phb	P67778	0,151	0,57328219	0,61632864
Phb2	O35129	-0,140	0,56835636	0,61812753
Phgdh	Q61753	0,084	0,37527751	0,60216051
Phpt1	Q9DAK9	1,182	0,03980176	0,06776471
Phyhipl	Q8BGT8	-0,053	0,79824768	0,84579832
Picalm	Q7M6Y3-2	-0,492	0,20687472	0,21454875
Pigs	Q6PD26	0,586	0,22732312	0,21152784
Pigu	Q8K358	-0,340	0,49492952	0,47099317
Pih1d1	Q9CQJ2	-0,253	0,32387864	0,368978
Pik3r4	Q8VD65	-20,730	ND	ND
Pin1	Q9QUR7	-0,081	0,42193947	0,62149846
Pin4	Q9CWW6	-0,074	0,28181597	0,58971707
Pitpna	P53810	-0,066	0,4124922	0,65439528
Pitrm1	Q8K411-2	0,102	0,36012745	0,55233333
Pkm	P52480	-0,039	0,61824598	0,7999204
Plaa	P27612	0,024	0,79275285	0,89006889
Plcb1	Q9Z1B3-3	-0,023	0,82796032	0,89759683
Plcg1	Q62077	0,029	0,82138973	0,88730075
Plcxd3	Q8BLJ3	-0,010	0,90518441	0,94365461
Plec	Q9QXS1-12	-0,047	0,22175834	0,68257082
Plekho2	Q8K124	-0,008	0,96293174	0,96995853
Plin3	Q9DBG5	0,568	0,05391741	0,11362602
Plp1	P60202	0,275	0,34063691	0,36984951
Plrg1	Q922V4	-0,129	0,35300596	0,50357638
Plxnb1	Q8CJH3	-22,441	ND	ND
Plxnb2	B2RXS4	-0,097	0,01407815	0,36534336
Pmpcb	Q9CXT8	0,290	0,38387196	0,38681532
Pmyk	Q9D1G2	21,599	ND	ND
Pnn	O35691	0,598	0,07051803	0,10335484
Pogz	Q8BZH4	0,188	0,25370609	0,36988235
Pold1	P52431	0,334	0,15022943	0,21428704
Poldip3	Q8BG81	-0,166	0,14759945	0,32563231
Polr2a	P08775	0,012	0,95796317	0,96036946

Gene name	Protein uniprot IDs	Levels in the Mutant (log2 difference)	p-value	q-value
Polr2b	Q8CFI7	-0,070	0,62432768	0,74482768
Por	P37040	0,273	0,01860457	0,128
Ppa1	Q9D819	0,045	0,69272894	0,80850927
Ppa2	Q91VM9	23,643	ND	ND
Ppap2b	Q99JY8	-0,092	0,52911704	0,64535922
Ppfia2	Q8BSS9	-0,024	0,90401178	0,92218484
Ppia	P17742	-0,151	0,68319269	0,69802821
Ppib	P24369	-0,583	0,01394586	0,06587234
Ppid	Q9CR16	0,493	0,00285539	0,04971429
Ppil1	Q9D0W5	-0,234	0,11402437	0,23114286
Ppm1a	P49443	-0,211	0,27060041	0,36340554
Ppm1e	Q80TL0	-0,076	0,35557639	0,61210726
Ppm1g	Q61074	-0,071	0,11140583	0,53925198
Ppm1h	Q3UYC0	-0,091	0,64148199	0,72099236
Ppme1	Q8BVQ5	-0,010	0,87789222	0,93956522
Ppp1ca	P62137	-0,433	0,00155172	0,0435
Ppp1cb	P62141	-0,328	0,53706657	0,51408711
Ppp1cc	P63087	0,114	0,61125316	0,67050182
Ppp1r12a	Q9DBR7-2	-0,108	0,49734996	0,6121576
Ppp1r14b	Q62084	0,432	0,25946418	0,26768858
Ppp1r14c	Q8R4S0	-0,354	0,08210343	0,15827941
Ppp1r18	Q8BQ30	-0,239	0,02768305	0,1575316
Ppp1r21	Q3TDD9	-0,170	0,18021575	0,34128402
Ppp1r7	Q3UM45	-0,104	0,46357395	0,59978422
Ppp1r8	Q8R3G1	-0,368	0,09447179	0,16321379
Ppp1r9b	Q6R891	-0,103	0,26481785	0,5017164
Ppp2ca	P63330	-0,028	0,73158059	0,86541745
Ppp2r1a	Q76MZ3	-0,097	0,34204939	0,55278559
Ppp2r2a	Q6P1F6	-0,142	0,23232773	0,4045614
Ppp2r4	P58389	-0,181	0,05698236	0,23327559
Ppp2r5c	Q60996-2	0,173	0,49663947	0,53888792
Ppp2r5e	Q61151	-0,517	0,02103661	0,09755224
Ppp3ca	P63328	-0,087	0,21234678	0,5255914
Ppp3cb	P48453-2	-0,071	0,36819605	0,6232481
Ppp3r1	Q63810-2	0,117	0,68456795	0,72466621
Ppp4r2	Q0VGB7	0,050	0,57478189	0,76492632
Ppp5c	Q60676	0,192	0,28570286	0,38097674
Ppp6c	Q9CQR6	-0,017	0,91664823	0,93703987
Ppp6r3	Q922D4-2	-0,104	0,15532681	0,43946939
Prcp	Q7TMR0	-21,462	ND	ND
Prdx1	P35700	-0,142	0,53484864	0,59545763
Prdx2	Q61171	-0,198	0,27653641	0,37282892
Prdx3	P20108	-0,034	0,79803601	0,87182894
Prdx4	O08807	0,033	0,37847711	0,77997968
Prdx5	P99029-2	-0,071	0,59182926	0,72332687
Prdx6	O08709	0,127	0,20503919	0,40971551
Prep	Q9QUR6	0,050	0,5407668	0,76081225
Prex1	Q69ZK0	0,779	0,00395034	0
Prkaa1	Q5EG47	0,564	0,16514791	0,1674384
Prkaca	P05132-2	-0,277	0,14061762	0,22451852
Prkacb	P68181	0,155	0,06655895	0,27983766
Prkar1a	Q9DBC7	-0,221	0,22028194	0,31600566
Prkar2a	P12367	0,287	0,2382362	0,2873605
Prkar2b	P31324	0,166	0,12915998	0,31365457
Prkcb	P68404-2	-0,169	0,03995372	0,23097416
Prkce	P16054	-0,416	0,0749519	0,14355963
Prkcg	P63318	-0,520	0,00485334	0,04015385
Prkcsh	O08795	0,005	0,94788244	0,97159192
Prmt1	Q9JIF0-2	-0,066	0,22196411	0,60151481
Prmt5	Q8CIG8	0,280	0,15363491	0,23343811
Prpf19	Q99KP6	-0,126	0,28719694	0,46363815
Prpf31	Q8CCF0-2	0,312	0,0940977	0,17632676
Prpf4	Q9DAW6	-0,208	0,09146669	0,23461748
Prpf40a	Q9R1C7	-0,422	0,03002699	0,11076667
Prpf4b	Q61136	0,032	0,92781209	0,93182867
Prpf6	Q91YR7	-0,122	0,12087774	0,38270118
Prpf8	Q99PV0	0,042	0,25799524	0,72542007
Prps1	Q9D7G0	-0,243	0,01220391	0,13019417
Prps2	Q9CS42	-0,253	0,11600347	0,21855158
Prpsap1	Q9D0M1	-0,178	0,45854599	0,51284307
Prpsap2	Q8R574	0,766	0,04867352	0,09862069
Prrc1	Q3UPH1	0,205	0,61208329	0,61723341
Prrc2c	Q3TLH4-5	-0,180	0,29604224	0,39576366
Prune	Q8BIW1	-0,031	0,76630171	0,86749031
Psap	Q61207	-0,833	0,0130489	0,036
Psat1	Q99K85	0,101	0,46489839	0,60716879
Psd3	Q2PFD7-5	-0,280	0,13428342	0,21687179
Psip1	Q99JF8	-0,124	0,49282055	0,58275896
Psma1	Q9R1P4	-0,028	0,68932572	0,8571734
Psma2	P49722	0,349	0,02591089	0,10402597
Psma3	O70435	-0,403	0,08605223	0,15521285
Psma4	Q9R1P0	0,493	0,00658432	0,07015385
Psma5	Q9Z2U1	0,171	0,01210732	0,19138303
Psma6	Q9QUM9	-0,028	0,7966733	0,88361043
Psma7	Q9Z2U0	0,112	0,35304071	0,52907665
Psmb1	O09061	-0,121	0,09412828	0,36996069
Psmb2	Q9R1P3	0,350	0,13973803	0,19688452
Psmb3	Q9R1P1	-0,004	0,96623725	0,97742434
Psmb4	P99026	-0,164	0,29954684	0,41020043
Psmb5	O55234	-0,312	0,06161311	0,15915152
Psmb6	Q60692	-0,149	0,72548327	0,74458192
Psmb7	P70195	0,101	0,58680685	0,66778717
Psmc1	P62192	0,084	0,08562501	0,47366472
Psmc2	P46471	-0,040	0,42713671	0,76528252
Psmc3	O88685	0,214	0,00065134	0,10410191
Psmc4	P54775	-0,144	0,52274536	0,58185294
Psmc5	P62196	0,125	0,31832867	0,48912869
Psmc6	P62334	0,069	0,52246463	0,69328895
Psmd1	Q3TXS7	-0,143	0,26890793	0,42124239
Psmd11	Q8BG32	0,146	0,13207494	0,34393194
Psmd12	Q9D8W5	0,261	0,10663648	0,21487558
Psmd13	Q9WVJ2	0,040	0,79527444	0,86002835
Psmd14	O35593	-0,199	0,08395421	0,23738432
Psmd2	Q8VDM4	-0,072	0,35167983	0,61852469
Psmd3	P14685	-0,077	0,01458722	0,44147304
Psmd4	O35226-2	-0,128	0,4971086	0,58228805
Psmd5	Q8BJY1	-0,102	0,68445205	0,73781719
Psmd6	Q99JI4	-0,404	0,00364817	0,06318367
Psmd7	P26516	0,169	0,03073737	0,21837792
Psmd8	Q9CX56	0,261	0,02312147	0,14696364
Psmd9	Q9CR00	-0,219	0,10945036	0,24129032
Psme1	P97371	0,114	0,03207425	0,33596721
Psme2	P97372	-0,798	0,03220285	0,08449123
Pspc1	Q8R326	-0,149	0,31778273	0,44606883
Ptbp1	P17225	0,455	0,23179725	0,23382879

Gene name	Protein uniprot IDs	Levels in the Mutant (log2 difference)	p-value	q-value
Ptbp2	Q91Z31	0,041	0,67852301	0,81348431
Ptges2	Q8BWM0	0,169	0,7331786	0,74508844
Ptges3	Q9R0Q7	-0,129	0,24733852	0,43553498
Ptk7	Q8BKG3	-0,223	0,38745639	0,42114046
Ptma	P26350	-0,307	0,03024621	0,12919588
Ptms	Q9D0J8	-0,315	0,0695375	0,16132384
Ptn	P63089	-0,038	0,85997385	0,89165158
Ptpn1	P35821	-0,047	0,7411223	0,82828816
Ptpn11	P35235	-0,059	0,46477793	0,69887887
Ptprs	B0V2N1-4	-0,113	0,60231545	0,66326901
Ptprz1	B9EKR1	-0,605	0,05019692	0,11831776
Puf60	Q3UEB3-3	0,027	0,79195065	0,88275304
Pum1	Q80U78-3	0,097	0,58603025	0,67234153
Pura	P42669	0,329	0,31848893	0,33874659
Purb	O35295	0,127	0,37139799	0,51267092
Pycr2	Q922Q4	-0,015	0,83957454	0,91827177
Pygb	Q8CI94	0,283	0,06275891	0,16803922
Qdpr	Q8BVI4	-0,294	0,34798021	0,3703362
Qki	Q9QYS9-8	0,023	0,75285415	0,88235797
Rab10	P61027	-0,194	0,28124384	0,37950769
Rab11b	P46638	-0,087	0,24761691	0,53736148
Rab12	P35283	-0,115	0,09523757	0,38259624
Rab14	Q91V41	-0,370	0,01955543	0,11090598
Rab18	P35293	0,088	0,16873604	0,50265797
Rab1A	P62821	0,961	0,07992714	0,11283478
Rab1b	Q9D1G1	0,854	0,02315286	0,06347368
Rab2a	P53994	-0,127	0,18857949	0,40659519
Rab35	Q6PHN9	-0,082	0,49263306	0,64496274
Rab3a	P63011	-0,064	0,65667094	0,76531229
Rab3c	P62823	0,200	0,50949499	0,53422026
Rab5a	Q9CQD1	-0,014	0,64110592	0,90224099
Rab5b	P61021	-0,285	0,13637123	0,21604301
Rab5c	P35278	0,191	0,0737303	0,23813077
Rab6b	P61294	-0,050	0,46011986	0,7356411
Rab7a	P51150	-0,141	0,19073324	0,38583372
Rab8a	P55258	-0,263	0,04607849	0,16434722
Rabgap1	A2AWA9	-0,077	0,4931856	0,65858529
Rac1;Rac2	P63001	-0,331	0,11761962	0,18763542
Rad21	Q61550	-0,156	0,35427758	0,46360675
Rad23b	P54728	0,077	0,67908138	0,76165206
Rala	P63321	0,049	0,91758176	0,91577086
Raly	Q64012-2	-0,155	0,21205844	0,37877251
Ran	P62827	-0,100	0,35497618	0,55323736
Ranbp1	P34022	-0,021	0,77610549	0,89205956
Ranbp2	Q9ERU9	-0,307	0,01138211	0,11027692
Ranbp3	Q9CT10	-0,238	0,10990124	0,22490984
Rangap1	P46061	0,254	0,02058178	0,14629864
Rap1a	P62835	0,362	0,17687314	0,21697624
Rap1b	Q99JI6	0,248	0,07714254	0,19272
Rap2a	Q80ZJ1	0,056	0,90474775	0,90668389
Rars	Q9D0I9	-0,068	0,48587537	0,67727495
Raver1	Q9CW46	-0,112	0,4652341	0,58306916
Rbbp4	Q60972	-0,111	0,01785964	0,32415105
Rbbp7	Q60973	-0,352	0,09951072	0,16743574
Rbbp9	O88851	-0,089	0,49460674	0,63506274
Rbm12	Q8R4X3	-0,062	0,68391783	0,77443489
Rbm14	Q8C2Q3	-0,069	0,60760381	0,73710731
Rbm22	Q8BHS3	-0,118	0,0816611	0,36969458
Rbm25	B2RY56	0,615	0,00363174	0,0405
Rbm3	O89086	-0,321	0,0856554	0,16849211
Rbm39	Q8VH51-2	-0,200	0,09159614	0,24366229
Rbm8a	Q9CWZ3-2	-0,088	0,41685764	0,60975238
Rbmxl1	Q91VM5	-0,149	0,13100474	0,33865426
Rcc1	Q8VE37	0,073	0,47729857	0,66127965
Rcc2	Q8BK67	-0,375	0,01360442	0,12030769
Rcn1	Q05186	-0,137	0,56739738	0,61908217
Rcn2	Q8BP92	0,074	0,61575342	0,73096286
Rcor2	Q8C796	21,373	ND	ND
Rdx	P26043	-0,072	0,48364626	0,66882156
Rer1	Q9CQU3	0,026	0,87909778	0,91105104
Rfc3	Q8R323	0,970	0,02544724	0,04937143
Rfc4	Q99J62	1,451	0,13686365	0,114
Rhoa	Q9QUI0	-0,275	0,22285679	0,2860828
Rlbp1	Q9Z275	-0,009	0,92426455	0,95356643
Rnaseh2b	Q80ZV0	0,364	0,16207268	0,21237383
Rnaseh2c	Q9CQ18	-22,403	ND	ND
Rnf14	Q9JI90	-0,064	0,68340627	0,77228129
Rnf2	Q9CQJ4	-0,355	0,01945101	0,11455738
Rnf214	Q8BFU3	0,046	0,79628727	0,85180691
Rnh1	Q91VI7	-0,105	0,06640632	0,38715765
Rnmt	Q9D0L8	-0,116	0,53275297	0,61875252
Rnpep	Q8VCT3	-0,396	0,00319443	0,06192
Rnps1	Q99M28	-0,190	0,03978646	0,21233097
Rpa1	Q8VEE4	-0,190	0,25309309	0,37085217
Rpa2	Q62193	-0,067	0,82880557	0,85208815
Rpa3	Q9CQ71	1,989	0,10382534	0,11614679
Rpf2	Q9JI80	-0,154	0,26698528	0,40907391
Rph3a	P47708	-0,060	0,59332717	0,75024226
Rpl10;Rpl10l	Q6ZWV3	0,149	0,49555812	0,56245971
Rpl10a	P53026	-0,242	0,18160065	0,27646711
Rpl11	Q9CXW4	-0,130	0,19053992	0,40152486
Rpl12	P35979	-0,163	0,01203586	0,19849275
Rpl13	P47963	-0,221	0,07734438	0,212
Rpl13a	P19253	-0,113	0,12329939	0,39913873
Rpl14	Q9CR57	-0,124	0,10964416	0,3705006
Rpl15	Q9CZM2	-0,084	0,56330105	0,6777151
Rpl17	Q9CPR4	-0,325	0,00978168	0,12057143
Rpl18	P35980	-0,006	0,94656658	0,96575386
Rpl18a	P62717	-0,016	0,76959089	0,90629663
Rpl21	O09167	-0,919	0,05367965	0,10722078
Rpl22	P67984	-0,093	0,79830481	0,81452735
Rpl22l1	Q9D7S7-2	-0,279	0,11913521	0,21537182
Rpl23	P62830	0,126	0,23632597	0,43363543
Rpl23a	P62751	-0,127	0,02779281	0,28798764
Rpl27	P61358	-0,321	0,18457487	0,23783908
Rpl27a	P14115	-0,196	0,01523547	0,16699379
Rpl28	P41105	26,112	ND	ND
Rpl3	P27659	-0,040	0,2563082	0,74026721
Rpl30	P62889	-0,037	0,75548457	0,85069378
Rpl32	P62911	-0,443	0,08851258	0,15708297
Rpl37a	P61514	-0,041	0,79774883	0,85959338
Rpl38	Q9JJI8	-0,576	0,01957225	0,08162712
Rpl4	Q9D8E6	-0,018	0,79750919	0,90247833
Rpl5	P47962	-0,426	0,08624727	0,15247059
Rpl6	P47911	0,567	0,46780641	0,40704139

Gene name	Protein uniprot IDs	Levels in the Mutant (log2 difference)	p-value	q-value
Rpl7	P14148	0,074	0,73443036	0,78526928
Rpl7a	P12970	-0,135	0,50246783	0,57794079
Rpl8	P62918	0,117	0,44585099	0,56672925
Rpl9	P51410	-0,446	0,02429741	0,12029787
Rplp0	P14869	-0,138	0,04062739	0,28596491
Rplp1	P47955	0,340	0,1173515	0,17962865
Rplp2	P99027	-0,189	0,09805514	0,26696707
Rpn1	Q91YQ5	-0,233	0,04802053	0,17667403
Rpn2	Q9DBG6	-0,049	0,76595447	0,83575456
Rprd1b	Q9CSU0-2	-0,077	0,45181136	0,64035489
Rps10	P63325	-0,031	0,69792323	0,84896048
Rps11	P62281	-0,363	0,12749611	0,17998942
Rps12	P63323	-0,398	0,03754481	0,10269231
Rps13	P62301	-0,104	0,49443742	0,61546039
Rps14	P62264	-0,177	0,17681109	0,33447593
Rps15	P62843	-0,233	0,35194254	0,39036872
Rps17	P63276	0,756	0,10517248	0,1161768
Rps2	P25444	0,062	0,47929064	0,6960424
Rps23	P62267	-0,113	0,75180152	0,77097158
Rps24	P62849-2	0,951	0,20461157	0,16746974
Rps26	P62855	-0,887	0,04927814	0,10219718
Rps27	Q6ZWU9	-0,279	0,02848921	0,14476636
Rps27a;Ubb;U	P62983	-0,493	0,03334594	0,11552475
Rps28	P62858	25,065	ND	ND
Rps3	P62908	-0,105	0,36624671	0,5462487
Rps3a	P97351	0,032	0,83471202	0,8867908
Rps4x	P62702	-0,440	0,14250306	0,17583146
Rps5	P97461	-0,654	0,18278125	0,17630595
Rps6	P62754	-0,058	0,7199793	0,7937043
Rps6ka3	P18654	-0,053	0,78125582	0,83537122
Rps6ka5	Q8C050-2	0,237	0,10060261	0,21640938
Rps7	P62082	-0,390	0,07379196	0,15707489
Rps8	P62242	-0,281	0,02171075	0,12853333
Rps9	Q6ZWN5	-0,140	0,29706846	0,44662892
Rpsa	P14206	-0,044	0,51279395	0,76505967
Rraga	Q80X95	-21,476	ND	ND
Rrbp1	Q99PL5	0,386	0,00060279	0,04176
Rrm1	P07742	0,345	0,12267173	0,18241885
Rsl1d1	Q8BVY0	-0,257	0,13440204	0,23268119
Rsu1	Q01730	0,750	0,0466813	0,09946988
Rtcb	Q99LF4	-0,129	0,09925388	0,35935302
Rtn1	Q8K0T0	0,086	0,47418899	0,63004693
Rtn3	Q9ES97-3	-0,055	0,17510853	0,62669295
Rtn4	Q99P72	-0,011	0,82398794	0,93149067
Rufy3	Q9D394	-0,208	0,02631154	0,16889143
Ruvbl1	P60122	0,057	0,71430878	0,79501438
Ruvbl2	Q9WTM5	-0,084	0,11705511	0,49264711
Saal1	Q9D2C2	0,188	0,15617296	0,30063378
Sae1	Q9R1T2	0,117	0,35086555	0,51603968
Safb	D3YXK2	-0,093	0,30707877	0,54359099
Samm50	Q8BGH2	-0,204	0,00020662	0,10279245
Sap18	O55128	1,372	0,04735459	0,07651852
Sar1a	P36536	0,273	0,40688732	0,41030769
Sar1b	Q9CQC9	-0,089	0,69523448	0,75944
Sarm1	Q6PDS3	0,012	0,94336159	0,95326033
Sarnp	Q9D1J3	-0,716	0,11185392	0,1294898
Sars	P26638	-0,177	0,341187	0,42925392
Sart1	Q9Z315	-0,173	0,0414167	0,22619959
Sart3	Q9JLI8	0,041	0,70781042	0,82581418
Sbds	P70122	0,139	0,22230128	0,40290549
Sbf1	Q6ZPE2	0,085	0,83301175	0,84718705
Scamp1	Q8K021	-0,386	0,11678507	0,16949849
Scarb2	O35114	-0,494	0,10781405	0,15691803
Sccpdh	Q8R127	0,226	0,55669147	0,56103653
Scfd1	Q8BRF7-3	-0,185	0,62087432	0,62476958
Scp2	P32020-2	0,812	0,04797718	0,10863158
Scrib	Q80U72	0,192	0,65127426	0,64623111
Scrn1	Q9CZC8	-0,080	0,27327916	0,56529866
Scrn2	Q8VCA8	0,120	0,70923645	0,74511337
Sdf2l1	Q9ESP1	21,381	ND	ND
Sdha	Q8K2B3	-0,012	0,79597764	0,92246987
Sdhb	Q9CQA3	-0,150	0,51240605	0,57189342
Sdhc	Q9CZB0	-0,021	0,74137699	0,88673272
Sec13	Q9D1M0	0,751	0,0150375	0,03728571
Sec22b	O08547	0,074	0,64386801	0,74705755
Sec23a	Q01405	-0,214	0,07629354	0,21596537
Sec23b	Q9D662	-0,261	0,19612259	0,27961333
Sec23ip	Q6NZC7	-0,057	0,6947478	0,78616761
Sec31a	Q3UPL0-2	0,032	0,81096613	0,8822548
Sec61g	P60060	0,917	0,02915772	0,0688
Sec62	Q8BU14	20,193	ND	ND
Seh1l	Q8R2U0-2	-0,251	0,27452089	0,33961186
Sel1l	Q9Z2G6	-0,123	0,3844129	0,52747001
Selenbp1;Selenb	P17563	-0,294	0,0560313	0,15945185
Sephs1	Q8BH69	0,097	0,54523288	0,64538806
Sept10	Q8C1B7-3	-0,065	0,13374146	0,57439073
Sept2	P42208	0,255	0,06814336	0,18117204
Sept3	Q9Z1S5	-0,181	0,11440495	0,2827916
Sept5	Q9Z2Q6	-0,136	0,45578964	0,55191058
Sept6	Q9R1T4-2	0,132	0,22489854	0,41058174
Sept7	O55131	-0,372	0,04769115	0,12417021
Sept8	Q8CHH9	0,079	0,48313959	0,64567532
Sept9	Q80UG5-3	0,575	0,12322562	0,15564228
Serbp1	Q9CY58	-0,411	0,03349581	0,10619259
Serpina1c;Serpin	Q00896	-0,031	0,91993521	0,9272936
Serpine2	Q07235	-0,427	0,2129402	0,22711382
Serpinh1	P19324	-0,369	0,03550999	0,10707879
Set	Q9EQU5-2	-0,196	0,03573871	0,19657143
Sf1	Q64213-2	-0,192	0,12894957	0,28040843
Sf3a1	Q8K425	-0,175	0,06633003	0,25191985
Sf3a2	Q62203	-0,382	0,05628043	0,12985075
Sf3a3	Q9D554	-0,134	0,19998531	0,39905543
Sf3b1	Q99NB9	-0,140	0,05774029	0,29276829
Sf3b3	Q921M3	-0,075	0,19540439	0,55625619
Sf3b4	Q8QZY9	-0,106	0,4348542	0,57721582
Sf3b6	P59708	-0,058	0,56858029	0,74677131
Sfpq	Q8VIJ6	-0,289	0,02958586	0,14066667
Sfxn1	Q99JR1	0,358	0,10133262	0,16902532
Sfxn3	Q91V61-2	0,153	0,17008713	0,36120152
Sfxn5	Q925N0	-0,211	0,00060545	0,10375155
Sgip1	Q8VD37-2	-0,065	0,42271886	0,66494375
Sgta	Q8BJU0-2	-0,107	0,03573632	0,36125888
Sh3bgrl	Q9JJU8	-0,013	0,95835334	0,96017949
Sh3gl1	Q62419	-0,239	0,33271119	0,38304583
Sh3gl2	Q62420	-0,264	0,19721819	0,27774958

Gene name	Protein uniprot IDs	Levels in the Mutant (log2 difference)	p-value	q-value
Shmt1	P50431	0,272	0,07223858	0,1753649
Sirt2	Q8VDQ8-2	-0,010	0,78320874	0,93064254
Skiv2l2	Q9CZU3	-0,260	0,06770983	0,17818082
Skp1	Q9WTX5	0,246	0,23515095	0,31209913
Slc12a5	Q91V14-2	0,171	0,52570762	0,56382155
Slc16a1	P53986	-0,083	0,08352148	0,47786978
Slc1a2	P43006	-0,055	0,62599101	0,76819608
Slc1a3	P56564	-0,005	0,97538585	0,97691658
Slc1a4	O35874	1,312	0,00820038	0
Slc25a11	Q9CR62	-0,238	0,08743699	0,21394896
Slc25a12	Q8BH59	-0,114	0,11377847	0,38831496
Slc25a18	Q9DB41	0,142	0,40047437	0,50658953
Slc25a22	Q9D6M3	-0,087	0,74372063	0,7801963
Slc25a3	Q8VEM8	0,395	0,3276032	0,32119495
Slc25a4	P48962	-0,101	0,05103997	0,38671264
Slc25a5	P51881	-0,101	0,19083237	0,47058456
Slc29a1	Q9JIM1-2	-0,101	0,72373549	0,7646363
Slc2a3	P32037	0,030	0,79723975	0,88227972
Slc32a1	O35633-2	-23,443	ND	ND
Slc3a2	P10852	0,237	0,10525136	0,21990852
Slc4a10	Q5DTL9-2	20,782	ND	ND
Slc4a4	O88343	0,425	0,19375896	0,21462832
Slc6a1	P31648	-0,511	0,08622177	0,12920792
Slc7a5	Q9Z127	0,035	0,81872794	0,88162515
Slc9a3r1	P70441	0,096	0,64597735	0,71829408
Sltm	Q8CH25-2	-0,189	0,0933966	0,26139929
Smad2;Smad3;Sn	Q62432-2	-0,148	0,34038445	0,46427273
Smarca4	Q3TKT4	0,016	0,63578353	0,89405233
Smarca5	Q91ZW3	-0,037	0,30262138	0,76046543
Smarcb1	Q9ZOH3-2	-0,204	0,15302099	0,28590415
Smarcc1	P97496-2	-0,142	0,44944216	0,53830675
Smarcc2	Q6PDG5-2	-0,174	0,3112365	0,40994397
Smarcd1	Q61466	-0,080	0,68943151	0,76265076
Smarce1	O54941	0,244	0,07410457	0,19320301
Smc1a	Q9CU62	-0,182	0,07313401	0,24898893
Smc2	Q8CG48	-0,223	0,03462469	0,16741003
Smc3	Q9CW03	-0,243	0,07413106	0,19298263
Smc4	Q8CG47	-0,163	0,25315064	0,38716913
Smchd1	Q6P5D8	0,383	0,26684308	0,27852941
Smek1	Q6P2K6	0,099	0,4322241	0,59079092
Smndc1	Q8BGT7	-0,003	0,98594334	0,98460294
Smpd3	Q9JJY3	0,075	0,5029187	0,67026201
Sms	P97355	0,462	0,05220886	0,10344304
Smu1	Q3UKJ7	-0,118	0,18856091	0,42066387
Snap25	P60879	-0,137	0,30411079	0,45859481
Snap47	Q8R570	-0,165	0,15896515	0,33831522
Snap91	Q61548-3	0,085	0,41594051	0,61405031
Snca	O55042-2	-0,243	0,27510641	0,3403545
Snd1	Q78PY7	-0,006	0,92159455	0,96047914
Snrnp200	Q6P4T2	0,040	0,53555865	0,77933929
Snrnp40	Q6PE01	-0,053	0,19788159	0,6454437
Snrnp70	Q62376	-0,264	0,23739018	0,29832881
Snrpa	Q62189	-0,015	0,89333376	0,93115304
Snrpa1	P57784	0,316	0,25420758	0,28675039
Snrpb2	Q9CQI7	0,101	0,81228663	0,82538556
Snrpd1	P62315	-0,932	0,07615518	0,11509091
Snrpd2	P62317	0,092	0,59304757	0,6811449
Snrpd3	P62320	-0,102	0,31852354	0,52901779
Snrpe	P62305	-0,128	0,32128073	0,48544722
Snw1	Q9CSN1	0,384	0,20895158	0,23474219
Snx2	Q9CWK8	-0,184	0,11735662	0,28053722
Snx27	Q3UHD6-2	-0,256	0,03500677	0,15855094
Snx6	Q6P8X1	-0,368	0,12815291	0,18106952
Sod2	P09671	-0,024	0,8856643	0,91385388
Soga3	Q6NZL0	-0,436	0,0161593	0,10584615
Son	Q9QX47-3	-0,054	0,79415276	0,84322938
Sorbs1	Q62417-5	-0,308	0,06774963	0,15963636
Spag7	Q7TNE3	-0,295	0,05958597	0,16306475
Sparcl1	P70663	0,223	0,15450631	0,27598651
Spast	Q9QYY8-2	-0,314	0,08267858	0,16796226
Spats2	Q8K1N4	-0,208	0,24538663	0,34394785
Spcs2	Q9CYN2	22,527	ND	ND
Spr	Q64105	-0,126	0,22684566	0,42973931
Sptan1	P16546	-0,113	0,22271227	0,45872927
Sptbn1	Q62261	-0,128	0,11625343	0,36930703
Srcin1	Q9QWI6	-0,175	0,0545646	0,23945802
Srek1	Q8BZX4-2	21,486	ND	ND
Srgap2	Q91Z67	0,130	0,42701302	0,53668352
Srgap3	Q812A2	0,085	0,56009047	0,67560231
Sri	Q6P069-2	-0,267	0,00457327	0,11288189
Srm	Q64674	-0,042	0,78008762	0,85037896
Srp54	P14576	0,674	0,11000544	0,12794118
Srp68	Q8BMA6	-0,206	0,1202846	0,26670609
Srprb	P47758	-0,215	0,11144123	0,2452616
Srr	Q9QZX7-2	-0,542	0,07608524	0,11227746
Srrm2	Q8BTI8	-0,238	0,03226313	0,16377855
Srrt	Q99MR6-3	-0,063	0,42210187	0,67193324
Srsf1	Q6PDM2	0,112	0,22220007	0,45881954
Srsf10	Q9R0U0-3	-0,011	0,93465253	0,95302691
Srsf2	Q62093	-0,148	0,30521155	0,43987705
Srsf3	P84104-2	-0,310	0,17989122	0,2390019
Srsf4	Q8VE97	-0,020	0,92198187	0,93639387
Srsf5	O35326	0,084	0,59417388	0,69875989
Ssb	P32067	0,201	0,39421124	0,44467411
Ssbp1	Q9CYR0	0,273	0,5101769	0,50196122
Ssr4	Q62186	-0,370	0,08195086	0,15775385
Ssrp1	Q08943	-0,210	0,21342643	0,32219608
St13	Q99L47	-0,272	0,09936104	0,19669438
Stag2	O35638	0,460	0,30016672	0,28568889
Stam	P70297	0,228	0,32882003	0,3847935
Stip1	Q60864	-0,057	0,62278654	0,76542989
Stk24	Q99KH8	-0,689	0,02682454	0,08303448
Stk39	Q9Z1W9	0,317	0,05042532	0,15441702
Stmn1	P54227	-0,226	0,13421273	0,25917563
Stmn2	P55821	0,076	0,30011035	0,59016234
Stoml2	Q99JB2	0,274	0,37231405	0,38760909
Strap	Q9Z1Z2	-0,144	0,20375802	0,386848
Strbp	Q91WM1	0,044	0,88976089	0,90112126
Strn4	P58404-2	-0,004	0,94264803	0,97459947
Stub1	Q9WUD1	0,011	0,91244993	0,9427315
Stx12	Q9ER00	0,102	0,4495694	0,59541519
Stx1b	P61264	-0,042	0,76424041	0,8446787
Stx7	O70439	-0,108	0,01430485	0,32606954
Stxbp1	O08599	-0,068	0,27688522	0,61426457
Sub1	P11031	0,124	0,54170023	0,61668125

Gene name	Protein uniprot IDs	Levels in the Mutant (log2 difference)	p-value	q-value
Sucla2	Q9Z2I9	-0,139	0,0508404	0,28923364
Suclg1	Q9WUM5	-0,217	0,33776602	0,39044295
Suclg2	Q9Z2I8-2	0,120	0,57566135	0,63637651
Sugt1	Q9CX34	-0,130	0,10373011	0,36053061
Sun2	Q8BJS4-3	-0,292	0,0392867	0,1564
Supt16h	Q920B9	-0,181	0,12735934	0,28803756
Supt5h	O55201	0,133	0,07158593	0,32561667
Surf4	Q64310	0,260	0,27451006	0,33449657
Sv2a	Q9JIS5	-0,045	0,81505868	0,86458289
Syap1	Q9D5V6	-0,127	0,64317629	0,67820057
Sympk	Q80X82	0,177	0,62674607	0,63434691
Syn1	O88935	0,000	0,99999006	0,99983525
Syn2	Q64332	0,155	0,26502723	0,40630011
Syn3	Q8JZP2	0,465	0,11767622	0,15903249
Syncrip	Q7TMK9-2	-0,008	0,79954985	0,94005444
Syne2	Q6ZWQ0	-0,289	0,1860653	0,25934414
Synj1	Q8CHC4	0,149	0,05789899	0,28291143
Synrg	Q5SV85-2	-0,078	0,57184383	0,69628006
Syt1	P46096	0,022	0,75548217	0,88725662
Syt2	P46097	-23,084	ND	ND
Tagln2	Q9WVA4	-0,125	0,09487067	0,36438432
Tagln3	Q9R1Q8	-0,080	0,20137848	0,53702358
Taldo1	Q93092	-0,175	0,07474156	0,26223944
Taok1	Q5F2E8	-0,144	0,39085002	0,50377196
Tardbp	Q921F2	0,058	0,28499705	0,64505689
Tars	Q9D0R2	0,311	0,15613151	0,21901266
Tbc1d10b	Q8BHL3	-21,358	ND	ND
Tbc1d24	Q3UUG6-2	-0,193	0,36516279	0,42983975
Tbca	P48428	0,319	0,21327735	0,26624306
Tbcb	Q9D1E6	-0,207	0,05664033	0,21267925
Tbcd	Q8BYA0	-0,066	0,61410316	0,74669371
Tbl1xr1	Q8BHJ5	-0,423	0,0601455	0,12550538
Tbl2	Q9R099	-0,395	0,03600382	0,10470588
Tcea1	P10711	-0,262	0,18829546	0,27363514
Tceb1	P83940	-0,168	0,13557543	0,31375287
Tceb2	P62869	-0,495	0,00471835	0,03367742
Tcerg1	Q8CGF7-2	-0,106	0,61973126	0,68166119
Tcp1	P11983	-0,145	0,46613644	0,54340087
Tdrkh	Q80VL1	-0,331	0,02469536	0,10311111
Tecpr1	Q80VP0	20,854	ND	ND
Tf	Q921I1	-0,328	0,03858425	0,13
Tfrc	Q62351	-0,144	0,27946044	0,42981211
Thoc2	B1AZI6	0,039	0,79779204	0,86219835
Thoc6	Q5U4D9	21,923	ND	ND
Thop1	Q8C1A5	-0,036	0,60385776	0,80887214
Thrap3	Q569Z6	-0,379	0,07826112	0,15583871
Thy1	P01831	-0,351	0,27508264	0,28888062
Tia1	P52912	-0,156	0,01251518	0,2121435
Timm13	P62075	-0,236	0,58933472	0,58200653
Timm50	Q9D880	-0,074	0,44281164	0,6451151
Tiprl	Q8BH58	-0,220	0,46032715	0,48976122
Tjp1	P39447	-0,134	0,36945455	0,50330159
Tjp2	Q9Z0U1	0,250	0,16365611	0,26286014
Tkt	P40142	-0,203	0,04562405	0,19779612
Tln1	P26039	-0,030	0,85732972	0,89871964
Tln2	Q71LX4	0,063	0,54617585	0,7229792
Tm9sf2	P58021	-0,236	0,0912226	0,21210643
Tma7	Q8K003	23,588	ND	ND
Tmed10	Q9D1D4	0,160	0,34978255	0,45650501
Tmed2	Q9R0Q3	-0,132	0,30196154	0,46335114
Tmed9	Q99KF1	0,088	0,43534062	0,61547962
Tmem33	Q9CR67	-0,004	0,96870999	0,97725793
Tmem35	Q9D328	0,421	0,35466574	0,34007497
Tmem43	Q9DBS1	-0,292	0,15422471	0,2288583
Tmod2	Q9JKK7	0,824	0,05666419	0,10764045
Tmpo	Q61033	-0,313	0,07522604	0,16739799
Tmpo	Q61029	-0,270	0,02011625	0,1305
Tmx2	Q9D710	-0,080	0,53346994	0,67241189
Tnc	Q80YX1	-0,415	0,01569345	0,10109091
Tnfaip8	Q921Z5	0,617	0,31478406	0,27662295
Tnik	P83510	-0,050	0,44835442	0,73491558
Tnpo1	Q8BFY9-2	-0,040	0,67317831	0,81480689
Tnpo2	Q99LG2	0,097	0,25174882	0,5116234
Tnpo3	Q6P2B1	0,194	0,33771943	0,40892441
Tomm22	Q9CPQ3	0,438	0,01830737	0,09976744
Tomm40	Q9QYA2	0,108	0,20906848	0,46346825
Tomm70a	Q9CZW5	-0,029	0,66597455	0,84845242
Top1	Q04750	-0,255	0,12808652	0,22929839
Top2a	Q01320	0,136	0,5693302	0,61910254
Top2b	Q64511	0,125	0,45052732	0,56114092
Tp53bp1	P70399	0,005	0,96695543	0,97669243
Tpi1	P17751	-0,343	0,00085582	0,0645
Tpm3	P21107-2	-0,254	0,05470438	0,16790533
Tpm4	Q6IRU2	-0,160	0,44411714	0,5159712
Tpp2	Q64514-2	-0,067	0,59512185	0,73506722
Tpr	F6ZDS4	-0,353	0,07427298	0,15833463
Tpt1	P63028	-0,453	0,02723007	0,11308
Tra2b	P62996	-0,622	0,00561218	0,02314286
Trap1	Q9CQN1	-0,194	0,3216956	0,40046069
Trappc3	O55013	0,028	0,81126812	0,88512046
Trim2	Q9ESN6	-0,143	0,15656271	0,37047264
Trim28	Q62318	-0,005	0,93002203	0,96837021
Trim3	Q9R1R2	0,046	0,84483759	0,88202216
Trio	Q0KL02-3	-0,333	0,35769375	0,365285
Trip12	G5E870	-0,240	0,10428723	0,21858475
Trmt112	Q9DCG9	0,210	0,49082921	0,51266847
Trmt2a	Q8BNV1	21,313	ND	ND
Trnt1	Q8K1J6	-0,196	0,08301017	0,24083333
Trove2	O08848	0,503	0,43564444	0,38736312
Trrap	Q80YV3	-20,703	ND	ND
Tsfm	Q9CZR8	0,128	0,31237793	0,47996902
Tsg101	Q61187	0,030	0,88998371	0,91133707
Tsn	Q62348	-0,149	0,02753559	0,25120734
Tsnax	Q9QZE7	-0,043	0,7979731	0,85735231
Tst	P52196	-0,150	0,05197155	0,27822222
Ttll12	Q3UDE2	0,230	0,62596102	0,61813831
Tuba1a	P68369	-0,421	0,00357953	0,07371429
Tuba1b	P05213	1,505	0,16634486	0,1476347
Tubal3	Q3UX10	26,234	ND	ND
Tubb2b	Q9CWF2	0,142	0,32678673	0,46381441
Tubb3	Q9ERD7	-0,005	0,96353728	0,97373397
Tubb4a	Q9D6F9	-0,484	0,0590505	0,10247853
Tubb4b	P68372	0,034	0,69964091	0,84116184
Tubb5	P99024	0,188	0,09065266	0,2604405
Tubg1;Tubg2	P83887	0,121	0,1571716	0,40108168
Tufm	Q8BFR5	-0,237	0,14610379	0,25947143
Twf1	Q91YR1	-0,171	0,00702916	0,17585475
Twf2	Q9Z0P5	0,504	0,3934455	0,35997967
Txlna	Q6PAM1	-0,417	0,02163921	0,11422222
Txn	P10639	-0,277	0,29799499	0,33955733
Txndc12	Q9CQU0	-0,505	0,06094085	0,1044
Txndc5	Q91W90	-0,037	0,53877625	0,787555
Txnl1	Q8CDN6	0,031	0,61371893	0,83454745
Txnl4a	P83877	21,103	ND	ND
Txnrd1	Q9JMH6-2	0,029	0,74079223	0,86496113
U2af1	Q9D883	-0,073	0,86557115	0,88173862
U2af2	P26369	0,138	0,31866064	0,46378346
U2surp	Q6NV83-2	0,279	0,40268487	0,40857701
Uba1	Q02053	-0,091	0,21020907	0,50976881
Uba2	Q9Z1F9	0,010	0,89954028	0,94279719
Uba3	Q8C878	0,057	0,4610361	0,70316468
Uba5	Q8VE47	-0,264	0,0221034	0,14375587
Uba6	Q8C7R4	0,059	0,80026541	0,84127942
Ubap2	Q91VX2	0,054	0,74478327	0,81462408
Ubap2l	Q80X50	-0,137	0,43999128	0,53944112
Ube2i	P63280	-0,386	0,07374961	0,15641379
Ube2k	P61087	-0,068	0,53287565	0,69834153
Ube2l3	P68037	0,389	0,32778702	0,32464246
Ube2m	P61082	-0,049	0,61099683	0,77516913
Ube2n	P61089	0,007	0,94262183	0,96340053
Ube2o	Q6ZPJ3	-0,035	0,69158492	0,83536804
Ube2v2	Q9D2M8	0,607	0,06965022	0,10469333
Ube3a	O08759	-0,146	0,02917285	0,26053901
Ube4a	E9Q735	-0,776	0,21342627	0,18901818
Ube4b	Q9ES00	-0,399	0,05615799	0,12679167
Ubqln1	Q8R317-2	0,088	0,74503222	0,78048631
Ubqln2	Q9QZM0	0,054	0,60555272	0,76572596
Ubqln4	Q99NB8	0,446	0,28225961	0,27684488
Ubr4	A2AN08-3	0,012	0,9322304	0,94682391
Ubtf	P25976-2	-0,440	0,00469156	0,072
Ubxn1	Q922Y1	0,125	0,41427402	0,53843433
Ubxn4	Q8VCH8	0,015	0,92552702	0,94064572
Ubxn6	Q99PL6-2	0,660	0,03068225	0,08461538
Ubxn7	Q6P5G6	-0,188	0,15308869	0,29787952
Uchl1	Q9R0P9	-0,258	0,33229744	0,37044444
Uchl3;Uchl4	Q9JKB1	-0,155	0,45255323	0,52954862
Uchl5	Q9WUP7-2	-0,295	0,04711671	0,156032
Ufd1l	P70362	-0,047	0,57933071	0,77059082
Uggt1	Q6P5E4	-0,064	0,68840861	0,77493196
Ugp2	Q91ZJ5-2	0,672	0,09668045	0,11502222
Uhrf1	Q8VDF2-2	-0,505	0,20942141	0,2155262
Unc119b	Q8C4B4	-0,278	0,16623181	0,24303911
Upf1	Q9EPU0-2	-0,023	0,88378304	0,91413036
Uqcr10	Q8R1I1	-0,388	0,01184168	0,10094118
Uqcrb	Q9D880	-0,538	0,0690849	0,10643373
Uqcrc1	Q9CZ13	0,042	0,32324948	0,74295711
Uqcrc2	Q9DB77	-0,232	0,03856375	0,17006098
Uqcrfs1	Q9CR68	0,074	0,59997273	0,72325607
Urod	P70697	0,156	0,62325935	0,64374494
Uso1	Q9Z1Z0	0,118	0,0177727	0,29829003
Usp10	P52479	0,217	0,21429305	0,31636984
Usp14	Q9JMA1	-0,028	0,75004108	0,87081829
Usp24	B1AY13	0,151	0,37310218	0,48401153
Usp39	Q3TIX9	0,016	0,92019759	0,93996948
Usp4	P35123	0,374	0,44379612	0,41015418
Usp47	Q8BY87-2	-0,239	0,05389441	0,17769399
Usp5	P56399	-0,031	0,37634858	0,79402124
Usp7	Q6A4J8	0,241	0,04273563	0,16647678
Usp9x	P70398	-0,081	0,28627246	0,56828047
Vac14	Q80WQ2	-0,133	0,5055212	0,5823287
Vamp2	P63044	0,060	0,65169566	0,7674047
Vapa	Q9WV55	-0,719	0,00883156	0,04275
Vapb	Q9QY76	-0,387	0,30033286	0,29698498
Vars	Q9Z1Q9	-0,194	0,00152639	0,14273585
Vasp	P70460	-0,025	0,87977696	0,91192613
Vat1	Q62465	-0,144	0,08471501	0,31281503
Vat1l	Q80TB8	0,732	0,01648242	0,05082353
Vbp1	P61759	-0,044	0,68168363	0,80753932
Vcan	Q62059-2	-0,093	0,27055819	0,52854756
Vcl	Q64727	0,065	0,51829282	0,69758316
Vcp	Q01853	0,104	0,20340071	0,46885967
Vcpip1	Q8CDG3	-0,345	0,06469988	0,15621577
Vdac1	Q60932-2	-0,206	0,00480381	0,1470991
Vdac2	Q60930	0,000	0,97926965	0,99343021
Vdac3	Q60931	-0,207	0,01949667	0,16689032
Vim	P20152	-0,044	0,56621898	0,77313329
Vps26b	Q8C0E2	-0,545	0,04645687	0,1099661
Vps28	Q9D1C8	-0,133	0,04877845	0,30069151
Vps29	Q9QZ88	-0,077	0,56072001	0,69244287
Vps35	Q9EQH3	-0,150	0,0204901	0,23416279
Vps37b	Q8R0J7	-0,014	0,91717248	0,9392968
Vps4a	Q8VEJ9	22,296	ND	ND
Vps51	Q3UVL4	21,418	ND	ND
Vsnl1	P62761	-0,357	0,0209537	0,11113178
Vta1	Q9CR26	0,243	0,18281738	0,27692257
Vwa5a	Q99KC8	-22,431	ND	ND
Wars	P32921-2	-0,057	0,70925369	0,79270883
Wasf1	Q8R5H6	0,351	0,10730318	0,16795376
Wasl	Q91YD9	-0,097	0,74266582	0,77391763
Wdr1	O88342	-0,227	0,20522885	0,29701349
Wdr11	Q8K1X1	-21,385	ND	ND
Wdr13	Q91V09	20,826	ND	ND
Wdr37	Q8CBE3	-0,402	0,32422676	0,31594334
Wdr43	Q6ZQL4	21,193	ND	ND
Wdr47	Q8CGF6	-0,054	0,61812247	0,76711546
Wdr48	Q8BH57	-0,106	0,36324983	0,53993755
Wdr5	P61965	-0,294	0,06721273	0,16752787
Wdr6	Q99ME2	0,314	0,17336409	0,23222134
Wdr61	Q9ERF3	0,195	0,47746701	0,51327059
Wdr7	Q920I9-2	0,325	0,32016891	0,33915478
Wdr77	Q99J09	-0,035	0,8798425	0,90081623
Wdr82	Q8BFQ4	-0,585	0,15724606	0,16579618
Whsc1	Q8BVE8	-0,229	0,28366304	0,36043766
Wibg	Q8CHP5-2	0,297	0,05862239	0,16017582
Wnk2	Q3UH66-6	-0,143	0,302566	0,44620061
Xkr7	Q5GH64	-0,331	0,17044351	0,22154357
Xpnpep1	Q6P1B1	0,610	0,14985092	0,16146341
Xpo1	Q6P5F9	0,080	0,1229509	0,5019576
Xpo5	Q924C1	-0,052	0,59832868	0,76478004
Xpo7	Q9EPK7	-0,052	0,69642094	0,79352559
Xrcc5	P27641	-0,168	0,19405823	0,35950968
Xrn2	Q9DBR1-2	-0,032	0,68563045	0,84013976
Yars	Q91WQ3	0,092	0,2457958	0,52520538
Ybx1	P62960	0,139	0,36182445	0,49249336
Ybx3	Q9JKB3-2	-0,150	0,31072766	0,44012692
Ylpm1	Q9R0I7	-22,185	ND	ND
Ythdf3	Q8BYK6	-0,403	0,09622407	0,15677612
Ywhab	Q9CQV8-2	0,063	0,43002372	0,67203755
Ywhae	P62259	-0,027	0,5889864	0,84096261
Ywhag	P61982	0,619	0,10079372	0,1306599
Ywhah	P68510	-0,118	0,35416755	0,51618051
Ywhaq	P68254	0,079	0,50994429	0,66223263
Ywhaz	P63101	0,089	0,33441206	0,56694983
Zbtb18	Q9WUK6	-0,350	0,07055293	0,15688538
Zc3h15	Q3TIV5	-0,154	0,24177727	0,39058586
Zc3h18	Q0P678	0,043	0,79913367	0,8568441
Zcchc8	Q9CYA6	21,420	ND	ND
Zfr	O88532	-0,094	0,58389425	0,67560259
Zic2	Q62520	-0,270	0,30167183	0,34439687
Znf22	Q9ERU3	-0,269	0,05316668	0,16684
Znf326	O88291	-0,238	0,30692581	0,37039206
Znf428	Q8C1M2	-0,019	0,93525158	0,94013644
Znf512	Q69Z99	-0,211	0,1578671	0,28360835
Znf638	Q61464-4	-0,024	0,81474601	0,89464615
Zranb2	Q9R020	-0,232	0,03060548	0,16340541
	Q9D882	-0,197	0,26275467	0,37073606
	Q9CQE8	0,224	0,45644933	0,48317692

Supplementary table 1. Total proteomics. Normalized intensities of the 1982 proteins detected by total proteomics and their relative abundance levels in the En1-Cre; *Srd5a3*$^{fl/-}$ mutant cerebellum.

Supplementary table 2. Glycoproteomics

Spread sheet 1. Reference glycoproteomic dataset (Qualitative dataset)

Gene names	Leading proteins	Positions within proteins	Also found in Zielinska et al, 2010 or predicted by uniprot (release 31/01/2018)
A2m	Q61838	1385	YES
A2m	Q61838	568	YES
A2m	Q61838	881	YES
Abca1	P41233	96	YES
Abca1	P41233	1637	NO
Abca1	P41233	98	YES
Abca1	P41233	196	YES
Abca1	P41233	400	YES
Abca2	P41234	432	YES
Abca2	P41234	1549	YES
Abca2	P41234	1557	YES
Abca2	P41234	1678	YES
Abca3	Q8R420	228	YES
Abca5	Q8K448	190	YES
Abca7	Q91V24	299	YES
Ace	P09470	719	YES
Ace	P09470	116	YES
Ace	P09470	514	YES
Ace	P09470	700	YES
Ache	P21836	296	NO
Acp2	P24638	267	YES
Acp2	P24638	167	YES
Acp2	P24638	177	YES
Adam10	O35598	552	YES
Adam10	O35598	279	YES
Adam10	O35598	440	YES
Adam17	Q9Z0F8-2	264	YES
Adam17	Q9Z0F8-2	606	YES
Adam22	Q9R1V6-19	517	YES
Adam22	Q9R1V6-19	632	YES
Adam23	Q9R1V7-4	661	YES
Adam23	Q9R1V7-4	97	YES
Adam9	Q61072	381	YES
Adcy3	Q8VHH7	828	NO
Adcy9	P51830	964	YES
Adgrf5	G5E8Q8	665	YES
Adgrf5	G5E8Q8	648	YES
Adgrf5	G5E8Q8	254	YES
Adgrf5	G5E8Q8	270	YES
Aebp1	Q640N1-2	533	NO
Afp	P02772	503	YES
Afp	P02772	498	YES
Afp	P02772	247	YES
Ahsg	P29699	156	YES
Ahsg	P29699	176	YES
Ahsg	P29699	99	YES
Alcam	Q61490	265	NO
Alcam	Q61490	499	YES
Alcam	Q61490	361	YES
Alk	P97793	328	YES
Alpl	P09242	140	NO
Alpl	P09242	430	YES
Anpep	P97449	114	YES
Anpep	P97449	606	YES
Anpep	P97449	817	YES
Antxr2	Q6DFX2	260	YES
Aplp2	Q06335-2	485	YES
Apmap	Q9D7N9	159	YES
Apod	P51910	98	YES
Apoe	P08226	130	YES
Apoh	Q01339	162	YES
Apoh	Q01339	105	YES
Apoh	Q01339	117	YES
Arsb	P50429	292	YES
Arsb	P50429	280	YES
Arsb	P50429	189	YES
Asah1	Q9WV54	258	YES
Asah1	Q9WV54	341	YES
Asah1	Q9WV54	347	YES
Astn1	Q61137-2	975	YES
Astn1	Q61137-2	733	NO
Astn1	Q61137-2	734	YES
Astn1	Q61137-2	976	YES
Astn1	Q61137-2	721	YES
Astn2	Q80Z10-2	792	YES
Astn2	Q80Z10-2	791	YES
Astn2	Q80Z10-2	1029	YES
Astn2	Q80Z10-2	779	YES
Atf6	F6VAN0	570	YES
Atf6b	O35451	673	YES
Atf6b	O35451	607	YES
Atp13a3	Q5XF89	1046	YES
Atp13a3	Q5XF89	1052	YES
Atp13a3	Q5XF89	1038	YES
Atp1b1	P14094	158	YES
Atp1b1	P14094	163	YES
Atp1b1	P14094	158	YES
Atp1b1	P14094	193	YES
Atp1b1	P14094	266	YES
Atp1b2	P14231	250	YES
Atp1b2	P14231	96	YES
Atp1b2	P14231	118	YES
Atp1b2	P14231	193	YES
Atp1b2	P14231	197	YES
Atp1b2	P14231	197	YES
Atp1b2	P14231	238	YES
Atp1b3	P97370	124	YES
Atp1b3	P97370	197	YES
Atp6ap1	Q9R1Q9	255	YES
Atp6ap1	Q9R1Q9	164	YES
Atp6ap1	Q9R1Q9	267	YES
Atp6ap1	Q9R1Q9	344	YES
Atp6ap1	Q9R1Q9	351	YES
Atp6v0a2	P15920	484	YES
Atp6v0e1	Q9CQD8	70	YES
Atp6v0e2	Q91XE7	70	YES
Atp8b1	Q148W0	174	YES
Atp8b1	Q148W0	175	YES
Atraid	Q6PGD0	73	YES
Atraid	Q6PGD0	133	YES
Atrn	Q9WU60	382	NO
Atrn	Q9WU60	913	YES
Atrn	Q9WU60	263	YES
Atrn	Q9WU60	415	YES
Atrn	Q9WU60	1042	YES
Atrn	Q9WU60	1197	YES
Atrn	Q9WU60	299	YES
Atrn	Q9WU60	913	YES
Atrn	Q9WU60	922	YES
Atrnl1	Q6A051-3	151	YES
B3galnt1	Q920V1	154	NO
B3galnt1	Q920V1	153	YES
B3galnt1	Q920V1	198	YES
B3galt6	Q91Z92	127	YES
B3galtl	Q8BHT6	327	YES
B3galtl	Q8BHT6	78	NO
B4galnt1	Q09200	78	NO
B4galnt1	Q09200	79	YES
Bai3;Bai2	Q80ZF8	625	YES
Bcan	Q61361	129	YES
Bcan	Q61361	336	YES
Bgn	P28653	271	NO
Bmpr2	O35607	55	YES
Bpi	Q67E05-2	320	YES
Brinp1	Q920P3	630	YES
Brinp1	Q920P3	599	NO
Brinp1	Q920P3	156	YES
Brinp2	Q6DFY8	626	YES
Brwd1	Q921C3-2	57	YES
Brwd1	Q921C3-2	60	YES
Bscl2	Q9Z2E9	88	NO
Bsg	P18572-2	190	YES
Bsg	P18572-2	154	YES
Btbd17	Q9DB72	61	YES
Btd	Q8CIF4	326	YES
Btd	Q8CIF4	180	YES
Btd	Q8CIF4	96	YES
C1qa	P98086	146	YES
C4b	P01029	224	YES
Ca4	Q64444	214	YES
Cabs1	Q8C633	102	YES
Cachd1	Q6PDJ1-2	601	YES
Cachd1	Q6PDJ1-2	913	YES
Cacna2d1	O08532-2	656	NO
Cacna2d1	O08532-2	657	NO
Cacna2d1	O08532-2	979	YES
Cacna2d1	O08532-2	324	YES
Cacna2d1	O08532-2	136	YES
Cacna2d1	O08532-2	762	YES
Cacna2d1	O08532-2	805	YES
Cacna2d1	O08532-2	869	YES
Cacna2d1	O08532-2	876	YES
Cacna2d2	Q6PHS9-4	1022	YES
Cacna2d2	Q6PHS9-4	696	YES
Cacna2d2	Q6PHS9-4	1033	YES
Cacna2d2	Q6PHS9-4	692	YES
Cacna2d2	Q6PHS9-4	205	YES
Cacna2d2	Q6PHS9-4	627	YES
Cacna2d2	Q6PHS9-4	692	YES
Cacng8	Q8VHW2	53	YES
Cacng8	Q8VHW2	56	YES
Cadm1	Q8R5M8-5	311	YES
Cadm1	Q8R5M8-5	104	YES
Cadm1	Q8R5M8-5	168	YES
Cadm1	Q8R5M8-5	307	YES
Cadm1	Q8R5M8-5	116	YES
Cadm1	Q8R5M8-5	70	YES
Cadm2	Q8BLQ9-2	58	NO
Cadm2	Q8BLQ9-2	220	YES
Cadm2	Q8BLQ9-2	296	YES
Cadm2	Q8BLQ9-2	300	YES
Cadm2	Q8BLQ9-2	60	YES
Cadm2	Q8BLQ9-2	296	YES
Cadm3	Q99N28	288	YES
Cadm4	Q8R464	67	YES
Cadm4	Q8R464	262	YES
Cadm4	Q8R464	286	YES
Calcrl	Q9R1W5	122	YES
Calcrl	Q9R1W5	127	YES
Calcrl	Q9R1W5	128	YES
Calcrl	Q9R1W5	122	YES
Calcrl	Q9R1W5	65	YES
Calm1	P62204	98	YES
Calu	O35887	131	YES
Carkd	Q9CZ42-3	220	YES
Casc4	Q6P2L7-3	151	NO
Casc4	Q6P2L7-3	114	YES
Casc4	Q6P2L7-3	115	YES
Casc4	Q6P2L7-3	150	YES
Casd1	Q7TN73	241	YES
Casd1	Q7TN73	141	YES
Casd1	Q7TN73	175	YES
Casd1	Q7TN73	187	YES
Cbln1;Cbln2	Q9R171	79	YES
Cd163	Q2VLH6	122	YES
Cd163	Q2VLH6	872	YES
Cd164	Q9R0L9	103	YES
Cd164	Q9R0L9	98	YES
Cd180	Q62192	78	YES
Cd180	Q62192	394	YES
Cd180	Q62192	402	YES
Cd1d1	P11609	183	YES
Cd1d1	P11609	38	YES
Cd200	O54901	181	YES
Cd200	O54901	190	YES
Cd276	Q8VE98	104	YES
Cd320	Q9Z1P5-2	159	YES
Cd38	P56528	124	YES
Cd38	P56528	223	YES
Cd44	P15379-2	59	YES
Cd47	Q61735-2	71	YES
Cd47	Q61735-2	73	YES
Cd47	Q61735-2	80	YES
Cd63	P41731	172	YES
Cd68	P31996-2	251	YES
Cd86	P42082-2	148	NO
Cd86	P42082-2	140	YES
Cd93	O89103	102	YES
Cd97	Q9Z0M6-2	205	YES
Cd97	Q9Z0M6-2	301	YES
Cd97	Q9Z0M6-2	367	YES
Cdh10	P70408	532	YES
Cdh10	P70408	534	YES
Cdh10	P70408	438	YES
Cdh10	P70408	456	YES
Cdh11	P55288	538	YES
Cdh13	Q9WTR5	639	YES
Cdh13	Q9WTR5	638	YES
Cdh13	Q9WTR5	489	YES
Cdh13	Q9WTR5	500	YES
Cdh13	Q9WTR5	530	YES
Cdh13	Q9WTR5	598	YES
Cdh13	Q9WTR5	671	YES
Cdh2	P15116	402	YES
Cdh2	P15116	692	YES
Cdh20	Q9Z0M3	420	YES
Cdh4	P39038	554	NO
Cdh5	P55284	59	YES
Cdh5	P55284	523	YES
Cdh6	P97326	536	YES
Cdh6	P97326	399	YES
Cdh6	P97326	437	YES
Cdh6	P97326	455	YES
Cdh7	Q8BM92	449	NO
Cdh8	P97291	463	YES
Celsr1	O35161	2160	YES
Celsr1	O35161	2155	YES
Celsr2	Q9R0M0-2	1077	NO
Celsr2	Q9R0M0-2	1502	YES
Celsr2	Q9R0M0-2	1566	YES
Celsr2	Q9R0M0-2	1037	YES
Celsr2	Q9R0M0-2	2062	YES
Celsr3	Q91ZI0	2465	YES
Celsr3	Q91ZI0	2042	YES
Celsr3	Q91ZI0	1213	YES
Celsr3	Q91ZI0	2185	YES
Cemip	Q8BII06	889	YES
Cemip	Q8BII06	165	YES
Cers2	Q924Z4	19	YES
Cers6	Q8C172	18	YES
Cfh	P06909	1225	YES
Cfh	P06909	676	YES
Cfh	P06909	773	YES
Cfi	Q61129	514	YES
Chadl	E9Q7T7	424	YES
Chd9	Q8BYH8-2	198	YES
Chd9	Q8BYH8-2	203	YES
Chl1	P70232	580	YES
Chl1	P70232	767	YES
Chl1	P70232	984	YES
Chl1	P70232	87	YES
Chl1	P70232	196	YES
Chl1	P70232	299	YES
Chl1	P70232	476	YES
Chl1	P70232	562	YES
Chl1	P70232	822	YES
Chrna3	Q8R4G9	166	YES
Chst12	Q99LL3	139	YES
Chst15	Q91XQ5	142	YES
Chst2	Q80WV3	152	YES
Chst2	Q80WV3	243	YES
Clcn2	Q9R0A1	411	YES
Clcn5	Q9WVD4	408	YES
Cldnd1	Q9CQX5	42	YES
Cldnd1	Q9CQX5	72	YES
Clec10a	P49300	74	YES
Clmp	Q8R373	72	YES
Clmp	Q8R373	73	YES
Clmp	Q8R373	196	YES
Clptm1	Q8VBZ3	295	YES
Clptm1l	Q8BXA5	91	YES
Clptm1l	Q8BXA5	230	YES
Clu	Q06890	102	YES
Cnn3	Q9DAW9	240	YES
Cnnm3	Q32NY4-2	73	YES
Cnpy3	Q9DAU1	153	YES
Cnr1	P47746	78	YES
Cnr1	P47746	84	YES
Cntn1	P12960	472	YES
Cntn1	P12960	593	NO
Cntn1	P12960	457	YES
Cntn1	P12960	208	YES
Cntn1	P12960	494	YES
Cntn1	P12960	935	YES
Cntn2	Q61330	500	YES
Cntn2	Q61330	777	YES
Cntn2	Q61330	78	NO
Cntn2	Q61330	463	YES
Cntn2	Q61330	200	YES
Cntn2	Q61330	200	YES
Cntn2	Q61330	206	YES
Cntn2	Q61330	942	YES
Cntn4	Q69Z26	65	YES
Cntn4	Q69Z26	191	YES
Cntn4	Q69Z26	954	YES
Cntn6	Q9JMB8-2	748	YES
Cntn6	Q9JMB8-2	878	YES
Cntn6	Q9JMB8-2	914	YES
Cntnap1	O54991	277	YES
Cntnap1	O54991	290	NO
Cntnap1	O54991	277	NO
Cntnap1	O54991	127	YES
Cntnap1	O54991	1148	YES
Cntnap1	O54991	598	YES
Cntnap1	O54991	764	YES
Cntnap1	O54991	129	YES
Cntnap1	O54991	121	YES
Cntnap1	O54991	844	YES
Cntnap2	Q9CPW0	1117	YES
Cntnap2	Q9CPW0	437	YES
Cntnap2	Q9CPW0	436	YES
Cntnap2	Q9CPW0	289	YES
Cntnap2	Q9CPW0	630	YES
Cntnap4	Q99P47	540	NO
Cntnap4	Q99P47	708	YES

Gene names	Leading proteins	Positions within proteins	Also found in Zielinska et al, 2010 or predicted by uniprot (release 31/01/2018)
Cntnap4	Q99P47	287	YES
Cntnap5a	Q0V8T9	496	YES
Cntnap5a	Q0V8T9	768	YES
Cntnap5a	Q0V8T9	1021	YES
Col11a1	Q61245-2	1553	YES
Col12a1	Q60847-4	1519	YES
Col2a1	P28481-2	1291	YES
Col6a1	Q04857	801	YES
Col6a2	Q02788	155	YES
Col6a2	Q02788	800	YES
Colec12	Q8K4Q8	271	YES
Colec12	Q8K4Q8	416	NO
Colec12	Q8K4Q8	159	YES
Colec12	Q8K4Q8	386	YES
Colec12	Q8K4Q8	168	YES
Colgalt1	Q8K297	91	NO
Cp	Q61147	757	NO
Cpd	O89001	975	YES
Cpd	O89001	866	NO
Cpd	O89001	625	YES
Cpd	O89001	626	YES
Cpd	O89001	409	YES
Cpd	O89001	1067	YES
Cpd	O89001	398	YES
Cpd	O89001	810	YES
Cpe	Q00493	139	NO
Cpe	Q00493	390	YES
Cpq	Q9WVJ3-2	382	YES
Cr1l	Q64735-2	252	YES
Creld2	Q9CYA0	188	YES
Crhr1	P35347	98	YES
Csmd1	Q923L3-2	2795	NO
Cspg4	Q8VHY0	349	YES
Cspg4	Q8VHY0	1454	YES
Cspg4	Q8VHY0	2080	YES
Cspg5	Q71M36-2	57	YES
Ctbs	Q8R242	283	YES
Ctsa	P16675	239	YES
Ctsa	P16675	140	YES
Ctsb	P10605	38	YES
Ctsc	P97821	275	NO
Ctsc	P97821	276	YES
Ctsc	P97821	53	YES
Ctsd	P18242	134	YES
Ctsd	P18242	261	YES
Ctsf	Q9R013	138	YES
Ctsl	P06797	221	YES
Ctso	Q8BM88	96	YES
Cxadr	P97792	201	NO
Cxadr	P97792	106	YES
Cyp26a1	O55127	96	YES
Dag1	Q62165	639	YES
Dag1	Q62165	647	YES
Dbh	Q64237	476	YES
Dcc	P70211-2	478	NO
Dcc	P70211-2	60	YES
Dchs1	E9PVD3	250	YES
Dchs1	E9PVD3	1989	YES
Dchs1	E9PVD3	1514	YES
Dchs1	E9PVD3	2754	YES
Dcn	P28654	206	YES
Dcp1b	Q3U564-2	129	YES
Dgcr2	P98154	147	YES
Dkk3	Q9QUN9	120	NO
Dkk3	Q9QUN9	121	NO
Dkk3	Q9QUN9	106	YES
Dner	Q8JZM4	208	YES
Dner	Q8JZM4	204	YES
Dner	Q8JZM4	223	YES
Dpp10	Q6NXK7	112	YES
Dpp10	Q6NXK7	120	YES
Dpp10	Q6NXK7	749	YES
Dpp4	P28843	144	YES
Dpp4	P28843	145	YES
Dpp6	Q9Z218	112	YES
Dpp6	Q9Z218	113	YES
Dpp6	Q9Z218	410	YES
Dpp6	Q9Z218	258	YES
Dpp6	Q9Z218	343	YES
Dpp6	Q9Z218	505	YES
Dpp6	Q9Z218	752	YES
Dpp7	Q9ET22	325	NO
Dpy19l3	Q71B07	118	YES
Dpy19l4	A2AJQ3-2	121	YES
Dpy19l4	A2AJQ3-2	122	YES
Dscam	Q9ERC8	748	YES
ε1c;Dsg1a;Ds	Q7TSF0-2	110	YES
Ece1	Q4PZA2-3	193	YES
Ece1	Q4PZA2-3	232	YES
Ece1	Q4PZA2-3	234	YES
Ece1	Q4PZA2-3	366	YES
Ece1	Q4PZA2-3	149	YES
Ednrb	P48302	60	YES
Efna5	O08543-2	162	YES
Efnb1	P52795	139	YES
Efnb3	O35393	210	YES
Egfr	Q01279	124	NO
Egfr	Q01279	603	YES
Egfr	Q01279	128	YES
Egfr	Q01279	352	YES
Eif3a	P23116	586	YES
Eif4h	Q9WUK2	223	YES
Eif4h	Q9WUK2	227	YES
Eif4h	Q9WUK2	229	YES
Elfn2	Q68FM6	80	YES
Elfn2	Q68FM6	85	YES
Elovl6	Q920L5	2	YES
Eltd1	Q923X1	298	YES
Emb	P21995	101	YES
Emb	P21995	70	YES
Emb	P21995	118	YES
Emb	P21995	216	YES
Emb	P21995	221	YES
Emb	P21995	62	YES
Emc1	Q8C7X2-2	914	YES
Emilin1	Q99K41	456	YES
Emilin1	Q99K41	795	YES
Emp1	P47801	43	YES
Eng	Q63961	307	YES
Eng	Q63961	322	NO
Eng	Q63961	135	YES
Enpep	P16406	754	YES
Enpp1	P06802-2	323	YES
Enpp2	Q9R1E6	410	YES
Enpp3	Q6DYE8	594	NO
Enpp4	Q8BTJ4-2	246	YES
Enpp5	Q9EQG7	158	YES
Enpp5	Q9EQG7	329	YES
Entpd1	P55772	73	YES
Entpd1	P55772	291	YES
Entpd2	O55026	129	YES
Entpd5	Q9WUZ9	231	YES
Eogt	Q8BYW9	354	YES
Epdr1	Q99M71	182	YES
Epha4	Q03137-2	235	YES
Ephb2	P54763	265	YES
Ephb2	P54763	482	YES
Ephb2	P54763-4	483	YES
Erap1	Q9EQH2	403	YES
Erbb2	P70424	125	YES
Erbb4	Q61527-3	576	YES
Erbb4	Q61527-3	138	YES
Erbb4	Q61527-3	548	YES
Ergic2	Q9CR89-2	212	NO
Erlin2;Erlin1	Q8BFZ9	106	YES
Ero1l	Q8R180	276	YES
Ero1lb	Q8R2E9	140	YES
Ero1lb	Q8R2E9	145	YES
Ero1lb	Q8R2E9	140	YES
Esam	Q925F2	239	NO
Extl2	Q9ES89	75	YES
Extl3	Q9WVL6	591	YES
F3	P20352	37	YES
Fam171a2	A2A699	66	YES
Fam20c	Q5MJS3	465	YES
Fat2	Q5F226	2597	YES
Fat2	Q5F226	996	YES
Fat2	Q5F226	3770	YES
Fat2	Q5F226	3774	YES
Fat2	Q5F226	3432	YES
Fat2	Q5F226	568	YES
Fat2	Q5F226	2470	YES
Fat2	Q5F226	3278	YES
Fat2	Q5F226	2387	YES
Fat2	Q5F226	3127	YES
Fat2	Q5F226	39	YES
Fat4	Q2PZL6	1828	YES
Fat4	Q2PZL6	2923	YES
Fcgr3;Fcgr2	P08508	91	YES
Fetub	Q9QXC1	139	YES
Fgb	Q8K0E8	384	YES
Fgfr1	P16092-6	77	YES
Fgfr1	P16092-6	262	YES
Fgfr2	P21803	318	YES
Fkbp10	Q61576	390	NO
Fkbp10	Q61576	392	YES
Fkbp10	Q61576	406	YES
Fkbp10	Q61576	69	YES
Fkbp7	O54998	41	YES
Fkbp9	Q9Z247	174	YES
Fkbp9	Q9Z247	397	YES
Flt1	P35969	197	YES
Flt1	P35969	165	YES
Fn1	P11276	542	NO
Fn1	P11276	528	YES
Fn1	P11276	430	YES
Fn1	P11276	1006	YES
Fras1	Q80T14	2684	YES
Fras1	Q80T14	2666	YES
Frem2	Q6NVD0	2225	NO
Frem2	Q6NVD0	2110	YES
Fstl1	Q62356	221	NO
Fstl1	Q62356	225	NO
Fstl1	Q62356	178	YES
Fstl1	Q62356	173	YES
Fstl1	Q62356	142	YES
Fstl5	Q8BFR2	318	YES
Fuca2	Q99KR8	371	YES
Fut10	Q5F2L2-2	110	YES
Fut11	Q8BHC9	162	YES
Fut11	Q8BHC9	313	YES
Fut11	Q8BHC9	314	YES
Fut11	Q8BHC9	439	YES
Gaa	P70699	926	YES
Gaa	P70699	470	YES
Gabbr1	Q9WV18	501	NO
Gabbr1	Q9WV18	513	YES
Gabbr1	Q9WV18	439	YES
Gabbr1	Q9WV18	83	YES
Gabbr2	Q80T41	388	YES
Gabra2;Gabra	P26048	138	YES
Gabra3	P26049	163	YES
Gabra6;Gabra	P16305-4	117	YES
Gabrb1	P50571	105	YES
Gabrb2	P63137-2	104	YES
Gabrb3	P63080	105	YES
Galnt1	O08912	552	YES
Gba	P17439	165	YES
Gba	P17439	289	YES
Gba	P17439	78	YES
Gde1	Q9JL56	168	YES
Gdpd2	Q9ESM6	416	NO
Gdpd5	Q640M6	336	YES
Gfra1	P97785-2	401	YES
Gfra2	O08842	357	NO
Gfra2	O08842	52	YES
Ggcx	Q9QYC7	570	YES
Ggh	Q9Z0L8-2	160	YES
Ggh	Q9Z0L8-2	186	YES
Ggt7	Q99JP7	198	YES
Ggt7	Q99JP7	523	YES
Gla	P51569	139	YES
Gla	P51569	192	YES
Glce	Q9EPS3	225	YES
Glce	Q9EPS3	304	YES
Glg1	Q61543	782	YES
Glg1	Q61543	161	YES
Glg1	Q61543	206	YES
Glt8d1	Q6NSU3	257	YES
Glt8d1	Q6NSU3	249	YES
Gnptab	Q69ZN6-2	1062	YES
Gnptg	Q6S5C2	88	YES
Gns	Q8BFR4	379	YES
Gns	Q8BFR4	175	YES
Gns	Q8BFR4	103	YES
Gns	Q8BFR4	109	YES
Gns	Q8BFR4	271	YES
Gns	Q8BFR4	354	YES
Golm1	Q91XA2	108	YES
Golm1	Q91XA2	109	YES
Gpc1	Q9QZF2	116	NO
Gpc5	Q8CAL5	527	YES
Gpm6a	P35802	164	YES
Gpnmb	Q99P91	246	NO
Gpnmb	Q99P91	249	YES
Gpnmb	Q99P91	275	YES
Gpr107	Q8BUV8	64	NO
Gpr125	Q7TT36	676	YES
Gpr126	Q6F3F9	720	YES
Gpr56	Q8K209	303	NO
Gpr56	Q8K209	234	NO
Gria1	P23818	363	YES
Gria1	P23818	406	YES
Gria1	P23818	249	YES
Gria1	P23818	257	YES
Gria1	P23818	401	YES
Gria1	P23818	406	YES
Gria2	P23819-4	256	YES
Gria2	P23819-4	370	YES
Gria2	P23819-4	406	YES
Gria2	P23819-4	413	YES
Gria3	Q9Z2W9	374	YES
Gria3	Q9Z2W9	409	YES
Gria3	Q9Z2W9	416	YES
Gria4	Q9Z2W8	258	YES
Gria4	Q9Z2W8	371	YES
Gria4	Q9Z2W8	407	YES
Gria4	Q9Z2W8	414	YES
Grid2	Q61625	716	YES
Grid2	Q61625	426	YES
Grik2	P39087-2	430	YES
Grik2	P39087-2	423	YES
Grik2	P39087-2	430	YES
Grik2	P39087-2	412	YES
Grik2	P39087-2	73	YES
Grik2;Grik1	P39087-2	275	YES
Grik3	B1AS29	415	NO
Grik3	B1AS29	278	YES
Grik3	B1AS29	426	YES
Grik3	B1AS29	433	YES
Grik3;Grik2	B1AS29	752	YES
Grin1	P35438-2	440	YES
Grin1	P35438-2	350	YES
Grin1	P35438-2	276	YES
Grin1	P35438-2	368	YES
Grin1	P35438-2	771	YES
Grin2b	Q01097	348	YES
Grin2b	Q01097	341	YES
Grin2b	Q01097	444	YES
Grin2b	Q01097	74	YES
Grin2b;Grin2c;Gr	Q01097	688	YES
Grin2d	Q03391	712	YES
Grm1	P97772	223	YES
Grm1	P97772	397	YES
Grm3	Q9QYS2	238	YES
Grm3	Q9QYS2	414	YES
Grm3	Q9QYS2	439	YES
Grm4	Q68EF4-2	569	YES
Grm5	Q3UVX5-2	88	YES
Grm5	Q3UVX5-2	209	YES
Grm7	Q68ED2	458	YES
Grn	P28798	263	YES
Gusb	P12265	416	YES
Gusb	P12265	627	YES
Gxylt1	Q3UHH8	242	YES
Gxylt1	Q3UHH8	201	YES
Gxylt1	Q3UHH8	351	YES
H2-D1	P01899	110	YES
H2-K1	P01901	107	YES
Heg1	E9Q7X6-2	996	YES
Hepacam	Q640R3	189	YES
Heph	Q9ZQZ4-2	53	YES
Heph	Q9ZQZ4-2	54	YES
Heph	Q9ZQZ4-2	49	YES
Hexa	P29416	157	YES
Hfe	P70387	166	YES
Hgsnat	Q3UDW8-2	105	YES
Hgsnat	Q3UDW8-2	125	YES
Hgsnat	Q3UDW8-2	77	YES
Hpx	Q91X72	186	YES
Hs2st1	Q8R3H7	108	YES
Hs6st3	Q9QYK4	379	YES
Hsd11b1	P50172	162	YES
Hsp90b1	P08113	445	YES
Hsp90b1	P08113	62	YES
Hsp90b1;Hsp90	P08113	107	YES
Hspg2	Q05793	358	YES
Hspg2	Q05793	2336	YES
Hspg2	Q05793	89	YES
Hspg2	Q05793	3098	YES
Hyal2	O35632	103	YES
Hyal2	O35632	74	YES
Hyou1	Q9JKR6	222	YES
Hyou1	Q9JKR6	869	YES
Hyou1	Q9JKR6	515	YES

Gene names	Leading proteins	Positions within proteins	Also found in Zielinska et al, 2010 or predicted by uniprot (release 31/01/2018)
Hyou1	Q9JKR6	596	YES
Hyou1	Q9JKR6	830	YES
Hyou1	Q9JKR6	862	YES
Hyou1	Q9JKR6	931	YES
Icam1	P13597	47	YES
Icam2	P35330	158	YES
Icam2	P35330	176	YES
Icam2	P35330	82	YES
Icam2	P35330	49	YES
Ids	Q08890	117	YES
Igdcc4	Q9EQS9	156	NO
Igf1r	Q60751	748	NO
Igf1r	Q60751	608	YES
Igf1r	Q60751	623	YES
Igf1r	Q60751	914	YES
Igf2r	Q07113	740	YES
Igf2r	Q07113	2129	YES
Igf2r	Q07113	1532	YES
Igf2r	Q07113	1649	YES
Igf2r	Q07113	107	YES
Igf2r	Q07113	944	YES
Igf2r	Q07113	430	YES
Igf2r	Q07113	1809	YES
Igf2r	Q07113	1305	YES
Igf2r	Q07113	575	YES
Igfbp7	Q61581	170	YES
Igfbpl1	Q80W15	158	YES
Iglon5	Q8HW98	288	YES
Igsf1	Q7TQA1-5	662	YES
Igsf21	Q7TNR6	407	YES
Igsf21	Q7TNR6	165	YES
Igsf3	Q6ZQA6	655	YES
Igsf3	Q6ZQA6	1077	YES
Igsf3	Q6ZQA6	700	YES
Igsf3	Q6ZQA6	842	YES
Igsf3	Q6ZQA6	961	YES
Igsf8	Q8R366	137	NO
Igsf8	Q8R366	461	YES
Igsf8	Q8R366	325	YES
Ikbip	Q9DBZ1	151	YES
Ikbip	Q9DBZ1-2	325	YES
Il17rd	Q8JZL1	62	YES
Il6st	Q00560	83	YES
Il6st	Q00560	225	YES
Il6st	Q00560	157	YES
Il6st	Q00560	43	YES
Impad1	Q80V26	257	YES
Insr	P15208	910	YES
Insr	P15208	138	YES
Insr	P15208	242	YES
Insr	P15208	445	YES
Islr2	Q5RKR3	338	YES
Islr2	Q5RKR3	121	YES
Islr2	Q5RKR3	365	YES
Islr2	Q5RKR3	52	YES
Itfg1	Q99KW9	356	YES
Itfg1	Q99KW9	368	YES
Itfg1	Q99KW9	369	YES
Itfg1	Q99KW9	351	YES
Itfg1	Q99KW9	145	YES
Itfg1	Q99KW9	150	YES
Itfg3	Q8C0Z1	120	YES
Itfg3	Q8C0Z1	116	YES
Itga1	Q3V3R4	882	YES
Itga1	Q3V3R4	531	YES
Itga1	Q3V3R4	459	YES
Itga1	Q3V3R4	418	YES
Itga1	Q3V3R4	217	YES
Itga1	Q3V3R4	100	YES
Itga1	Q3V3R4	100	YES
Itga1	Q3V3R4	105	YES
Itga1	Q3V3R4	1113	YES
Itga1	Q3V3R4	112	YES
Itga2	Q62469	109	YES
Itga2	Q62469	1054	YES
Itga2	Q62469	1071	YES
Itga2	Q62469	102	YES
Itga2	Q62469	457	YES
Itga3	Q62470-3	575	YES
Itga3	Q62470-3	906	YES
Itga4	Q00651	487	YES
Itga5	P11688	715	YES
Itga5	P11688	727	YES
Itga5	P11688	185	NO
Itga5	P11688	678	YES
Itga6	Q61739-2	927	YES
Itga6	Q61739-2	731	YES
Itga6	Q61739-2	284	YES
Itga7	Q61738-4	740	YES
Itga7	Q61738-4	979	YES
Itga8	A2ARA8-2	176	YES
Itgam	P05555-2	58	YES
Itgam	P05555-2	617	YES
Itgam	P05555-2	905	YES
Itgav	P43406	615	YES
Itgav	P43406	869	NO
Itgav	P43406	835	NO
Itgav	P43406	941	YES
Itgav	P43406	851	YES
Itgav	P43406	74	YES
Itgb1	P09055	212	YES
Itgb1	P09055	481	YES
Itgb1	P09055	669	YES
Itgb5	O70309	705	YES
Itih3	Q61704	580	YES
Itih4	A6X935-2	835	YES
Itih4	A6X935-2	577	YES
Itih5	Q8BJD1	231	YES
Itih5	Q8BJD1	508	YES
Itm2b	O89051	170	YES
Itpr1	P11881-8	2420	NO
Itpr1	P11881-8	2448	YES
Itpr1	P11881-8	2655	YES
Itprip	Q3TNL8-2	27	YES
Jam2	Q9JI59	186	YES

Gene names	Leading proteins	Positions within proteins	Also found in Zielinska et al, 2010 or predicted by uniprot (release 31/01/2018)
Jam3	Q9D8B7	192	YES
Kdelc1	Q9JHP7-2	152	YES
Kdr	P35918-2	98	YES
Kiaa0319l	Q8K135	889	YES
Kiaa1161	Q69ZQ1	239	YES
Kiaa1161	Q69ZQ1	249	YES
Kiaa1161	Q69ZQ1	455	YES
Kiaa1324	A2AFS3-3	497	YES
Kiaa1467	Q8BYI8	398	YES
Kiaa1467	Q8BYI8	239	YES
Kiaa1549	Q68FD9	1113	NO
Kiaa1549	Q68FD9	1215	YES
Kirrel3	Q8BR86-3	167	YES
Kit	P05532-2	466	YES
Kit	P05532-2	146	YES
Kng1	O08677-2	242	YES
Kng1	O08677-2	82	YES
Krt28	A6BLY7	92	YES
Krt28	A6BLY7	93	YES
L1cam	P11627	432	YES
L1cam	P11627	978	YES
L1cam	P11627	670	YES
L1cam	P11627	848	YES
L1cam	P11627	246	YES
L1cam	P11627	478	YES
L1cam	P11627	968	YES
L1cam	P11627	293	YES
L1cam	P11627	725	YES
L1cam	P11627	1073	YES
L1cam	P11627	1107	YES
L1cam	P11627	489	YES
L1cam	P11627	875	YES
Lama1	P19137	1344	YES
Lama1	P19137	1812	YES
Lama1	P19137	2046	YES
Lama1	P19137	1659	YES
Lama1	P19137	2027	YES
Lama1	P19137	2526	YES
Lama2	Q60675	1696	YES
Lama2	Q60675	919	YES
Lama2	Q60675	1897	YES
Lama2	Q60675	2013	YES
Lama2	Q60675	1610	YES
Lama2	Q60675	1806	YES
Lama2	Q60675	2024	YES
Lama4	P97927	803	YES
Lama4	P97927	550	YES
Lama4	P97927	735	YES
Lama4	P97927	780	YES
Lama5	Q61001	2395	NO
Lamb1	P02469	1643	YES
Lamb1	P02469	1336	YES
Lamb1	P02469	1343	YES
Lamb1	P02469	1279	YES
Lamb1	P02469	1542	YES
Lamb1	P02469	677	YES
Lamb2	Q61292	1309	YES
Lamc1	P02468	1203	YES
Lamc1	P02468	648	YES
Lamc1	P02468	1020	YES
Lamc1	P02468	1105	YES
Lamc1	P02468	1221	YES
Lamc3	Q9R0B6	1514	YES
Lamc3	Q9R0B6	1196	YES
Lamp1	P11438	78	YES
Lamp1	P11438	248	YES
Lamp1	P11438	252	YES
Lamp1	P11438	115	YES
Lamp1	P11438	159	YES
Lamp1	P11438	177	YES
Lamp1	P11438	252	YES
Lamp1	P11438	296	YES
Lamp1	P11438	296	YES
Lamp1	P11438	311	YES
Lamp1	P11438	97	YES
Lamp2	P17047-3	234	YES
Lamp2	P17047-3	232	NO
Lamp2	P17047-3	247	YES
Lamp2	P17047-3	156	YES
Lamp2	P17047-3	322	YES
Lamp2	P17047-3	361	YES
Large	Q9Z1M7	122	YES
Lcat	P16301	44	YES
Leprel4	Q8K2B0	79	NO
Leprel4	Q8K2B0	367	YES
Lgals3bp	Q07797	69	YES
Lgals3bp	Q07797	543	YES
Lgi1	Q9JIA1	277	YES
Lgi1	Q9JIA1	422	YES
Lgi2	Q8K4Z0-2	268	YES
Lgmn	O89017	265	YES
Lgmn	O89017	265	YES
Lgmn	O89017	274	YES
Lifr	P42703-2	385	YES
Lingo1	Q9D1T0	138	YES
Lingo1	Q9D1T0	536	YES
Lingo2	Q3URE9	130	YES
Lingo3	Q6GQU6	509	YES
Lipa	Q9Z0M5	159	YES
Lman2	Q9DBH5	185	YES
Lnpep	Q8C129	256	YES
Lnpep	Q8C129	525	YES
Lnpep	Q8C129	145	YES
Lnpep	Q8C129	215	YES
Lnpep	Q8C129	447	YES
Lnpep	Q8C129	682	YES
Lphn1	Q80TR1-2	624	NO
Lphn1	Q80TR1-2	629	YES
Lphn1	Q80TR1-2	355	YES
Lphn2	Q8JZZ7	524	YES
Lphn2	Q8JZZ7	735	YES
Lphn3	Q80TS3-4	646	YES
Lphn3	Q80TS3-4	601	YES
Lppr1	Q8BFZ2-2	148	YES
Lppr1	Q8BFZ2-2	150	YES

Gene names	Leading proteins	Positions within proteins	Also found in Zielinska et al, 2010 or predicted by uniprot (release 31/01/2018)
Lrfn4	Q80XU8	376	YES
Lrfn5	Q8BXA0	339	YES
Lrig1	P70193	76	YES
Lrig2	Q52KR2	172	YES
Lrp1	Q91ZX7	1557	YES
Lrp1	Q91ZX7	2503	NO
Lrp1	Q91ZX7	2906	YES
Lrp1	Q91ZX7	3664	YES
Lrp1	Q91ZX7	1559	YES
Lrp1	Q91ZX7	2473	YES
Lrp1	Q91ZX7	3663	NO
Lrp1	Q91ZX7	1734	NO
Lrp1	Q91ZX7	1734	NO
Lrp1	Q91ZX7	1724	YES
Lrp1	Q91ZX7	1826	YES
Lrp1	Q91ZX7	2621	YES
Lrp1	Q91ZX7	4126	YES
Lrp1	Q91ZX7	3058	YES
Lrp1	Q91ZX7	3840	YES
Lrp1	Q91ZX7	1764	YES
Lrp1	Q91ZX7	2118	YES
Lrp1	Q91ZX7	3789	YES
Lrp1	Q91ZX7	3954	YES
Lrp1	Q91ZX7	4365	YES
Lrp1	Q91ZX7	447	YES
Lrp1	Q91ZX7	137	YES
Lrp1	Q91ZX7	1576	YES
Lrp1	Q91ZX7	2128	YES
Lrp1	Q91ZX7	240	YES
Lrp1	Q91ZX7	3049	YES
Lrp1	Q91ZX7	3334	YES
Lrp1	Q91ZX7	4076	YES
Lrp1	Q91ZX7	730	YES
Lrp1b	Q9JI18	1636	YES
Lrp1b	Q9JI18	3316	YES
Lrp1b	Q9JI18	3310	YES
Lrp1b	Q9JI18	1145	YES
Lrp1b	Q9JI18	3164	YES
Lrp4	Q8VI56-2	498	YES
Lrp4	Q8VI56-2	501	YES
Lrpap1	P55302	271	YES
Lrrc25	Q8K1T1	133	YES
Lrrc36	Q3V0M2-2	334	YES
Lrrc4	Q99PH1	409	YES
Lrrc4	Q99PH1	362	YES
Lrrc4b	P0C192	376	NO
Lrrc4b	P0C192	226	YES
Lrrc8a	Q80WG5	66	YES
Lrrc8a	Q80WG5	83	YES
Lrrc8b	Q5DU41-2	78	YES
Lrrd1	Q8C0R9	211	YES
Lrrn1	Q61809	69	NO
Lrrn1	Q61809	517	YES
Lrrn3	Q8CBC6	579	YES
Lrrtm2	Q8BGA3	57	YES
Lsamp	Q8BLK3	40	YES
Lsamp	Q8BLK3	279	YES
Lsamp	Q8BLK3	287	YES
Lsamp	Q8BLK3	287	YES
Ly75	Q60767	529	NO
Ly75	Q60767	1393	YES
Ly75	Q60767	1077	YES
Ly75	Q60767	1594	YES
Ly75	Q60767	1104	YES
Ly75	Q60767	135	YES
Ly75	Q60767	865	YES
Lyve1	Q8BHC0	52	YES
M6pr	P24668	117	YES
M6pr	P24668	114	YES
M6pr	P24668	108	YES
M6pr	P24668	84	YES
Mag	P20917-2	450	YES
Mag	P20917-2	454	YES
Mag	P20917-2	99	YES
Man2a2	Q8BRK9	1095	YES
Man2b1	O09159	693	YES
Man2b1	O09159	497	YES
Man2b1	O09159	367	YES
Manba	Q8K2I4	89	YES
Manba	Q8K2I4	77	NO
Mbtps1	Q9WTZ2	148	YES
Mcam	Q8R2Y2-2	58	YES
Mdga1	Q0PMG2	811	YES
Mdga1	Q0PMG2	235	YES
Mdga1	Q0PMG2	307	YES
Mdga1	Q0PMG2	331	YES
Mdga1	Q0PMG2	90	YES
Mdga2	P60755	610	YES
Mdga2	P60755	92	YES
Megf8	P60882	1271	YES
Megf8	P60882	810	YES
Megf9	Q8BH27	302	YES
Megf9	Q8BH27	303	YES
Megf9	Q8BH27	426	YES
Megf9	Q8BH27	357	YES
Mertk	Q60805	165	YES
Mertk	Q60805	202	YES
Mettl9	Q9EPL4	35	YES
Mfap4	Q9D1H9	89	NO
Mfap4	Q9D1H9	139	YES
Mfge8	P21956-2	279	YES
Mfge8	P21956-2	280	YES
Mgat3	Q10470	263	YES
Mgat5b	Q765H6	236	YES
Mgat5b	Q765H6	127	YES
Mgat5b	Q765H6	93	YES
Mia3	Q8BI84	631	YES
Mia3	Q8BI84	252	YES
Mif	P34884	54	YES
Minpp1	Q9Z2L6	236	YES
Mmrn2	A6H6E2	249	NO
Mpzl1	Q3TEW6-2	50	YES
Mrc1	Q61830	1204	YES
Mrc1	Q61830	104	YES
Mrc2	Q64449	1133	YES

Gene names	Leading proteins	Positions within proteins	Also found in Zielinska et al, 2010 or predicted by uniprot (release 31/01/2018)
Mrc2	Q64449	68	YES
Mrc2	Q64449	363	YES
Naga	Q9QWR8	201	YES
Naga	Q9QWR8	177	YES
Ncam1	P13595	479	NO
Ncam1	P13595	222	NO
Ncam1	P13595	450	YES
Ncam1	P13595	453	YES
Ncam2	O35136	168	NO
Ncam2	O35136	177	YES
Ncam2	O35136	474	YES
Ncam2	O35136	177	YES
Ncam2	O35136	219	YES
Ncan	P55066	1175	YES
Ncan	P55066	121	YES
Ncln	Q8VCM8	428	YES
Ncstn	P57716	611	YES
Ncstn	P57716	128	NO
Ncstn	P57716	529	YES
Ncstn	P57716	386	YES
Ncstn	P57716	434	YES
Ncstn	P57716	54	YES
Ncstn	P57716	561	YES
Ncstn	P57716	572	YES
Negr1	Q80Z24	260	YES
Negr1	Q80Z24	269	YES
Negr1	Q80Z24	269	YES
Negr1	Q80Z24	280	YES
Negr1	Q80Z24	288	YES
Nell2	Q61220	56	YES
Neo1	P97798-5	221	YES
Neo1	P97798-5	501	YES
Neo1	P97798-5	84	YES
Neo1	P97798-5	520	YES
Neo1	P97798-5	746	YES
Nfasc	Q810U3	778	YES
Nfasc	Q810U3	483	YES
Nfasc	Q810U3	881	YES
Nfasc	Q810U3	1015	YES
Nfasc	Q810U3	305	YES
Nfasc	Q810U3	866	YES
Nid1	P10493	415	NO
Nid2	O88322	681	YES
Nkain1	Q9D035	100	YES
Nlgn1	Q99K10	109	NO
Nomo1	Q6GQT9	210	NO
Nomo1	Q6GQT9	42	YES
Nomo1	Q6GQT9	361	YES
Notch1	Q01705-2	1404	NO
Npc1	O35604	598	YES
Npc1	O35604	1063	YES
Npc1	O35604	868	YES
Npc1	O35604	185	YES
Npc1	O35604	414	YES
Nptn	P97300-1	80	YES
Nptn	P97300-1	112	YES
Nptn	P97300-1	167	YES
Nptx2	O70340	146	YES
Nptxr	Q99J85	42	YES
Nrap	Q80XB4-3	403	YES
Nrcam	Q810U4-2	700	YES
Nrcam	Q810U4-2	786	YES
Nrcam	Q810U4-2	427	YES
Nrcam	Q810U4-2	217	YES
Nrcam	Q810U4-2	77	YES
Nrcam	Q810U4-2	1003	YES
Nrcam	Q810U4-2	270	YES
Nrcam	Q810U4-2	308	YES
Nrcam	Q810U4-2	501	YES
Nrcam	Q810U4-2	842	YES
Nrp1	P97333	522	YES
Nrp1	P97333	150	YES
Nrp1	P97333	261	YES
Nrp2	O35375-5	152	YES
Nrp2	O35375-5	157	YES
Nrxn1	Q9CS84-4	125	YES
Nrxn1	Q9CS84-4	190	YES
Nrxn3	Q6P9K9-2	825	YES
Ntm	Q99PJ0	44	YES
Ntm	Q99PJ0	284	YES
Ntm	Q99PJ0	292	YES
Ntn3;Ntn1	Q9R1A3	387	YES
Ntng1	Q8R4G0-6	320	YES
Ntrk2	P15209-2	178	YES
Ntrk2	P15209-2	325	YES
Ntrk2	P15209-2	205	YES
Ntrk2	P15209-2	241	YES
Ntrk2	P15209-2	254	YES
Ntrk2	P15209-2	67	YES
Ntrk2	P15209-2	95	YES
Ntrk3	Q6VNS1-3	163	YES
Ntrk3	Q6VNS1-3	388	YES
Nudcd2	Q9CQ48	144	YES
Nup210	Q9QY81	405	YES
Nup210	Q9QY81	1441	YES
Nup210	Q9QY81	44	YES
Nup210	Q9QY81	1135	YES
Ogfod3	Q9D136	263	YES
Olfm1	O88998-3	260	YES
Olfm1	O88998-3	279	YES
Olfm1	O88998-3	75	YES
Omg	Q63912	152	YES
Omg	Q63912	103	YES
Omg	Q63912	234	YES
Os9	Q8K2C7-2	177	YES
Ostm1	Q8BGT0	234	YES
Ostm1	Q8BGT0	139	YES
P2rx4	Q9JJX6-3	131	NO
P2rx4	Q9JJX6-3	75	YES
P2rx4	Q9JJX6-3	208	YES
P2rx7	Q9Z1M0	187	YES
P2rx7	Q9Z1M0	213	YES
P2rx7	Q9Z1M0	74	YES
P4ha1	Q60715-2	113	YES
P4htm	Q8BG58	349	YES

Gene names	Leading proteins	Positions within proteins	Also found in Zielinska et al, 2010 or predicted by uniprot (release 31/01/2018)
Panx1	Q9JIP4	254	YES
Pbxip1	Q3TVI8	455	YES
Pcdh19	Q80TF3	546	NO
Pcdh8	Q7TSK3-3	616	NO
Pcdhga4	O88689-3	893	NO
Pcsk2	P21661	374	YES
Pcsk2	P21661	523	YES
Pcyox1	Q9CQF9	353	YES
Pcyox1	Q9CQF9	196	YES
Pcyox1	Q9CQF9	323	YES
Pdgfrb	P05622	467	YES
Pdia3	P27773	90	YES
Pecam1	Q08481-2	141	YES
Pecam1	Q08481-2	360	YES
Pecam1	Q08481-2	74	YES
Pgap1	Q3UUQ7	234	YES
Pgap1	Q3UUQ7	363	YES
Pgap1	Q3UUQ7	558	YES
Piezo1	E2JF22	2310	YES
Pign	Q9R1S3-2	191	YES
Pign	Q9R1S3-2	192	YES
Pign	Q9R1S3-2	128	YES
Pigo	Q9JJI6	37	YES
Pigs	Q6PD26	370	YES
Pigt	Q8BXQ2	168	YES
Piwil1	Q9JMB7	857	YES
Pkd2	O35245-2	360	YES
Pla2g15	Q8VEB4	289	YES
Pla2g15	Q8VEB4	398	YES
Pld4	Q8BG07-2	239	YES
Plod1	Q9R0E2	539	YES
Plod2	Q9R0B9	696	YES
Plod3	Q9R0E1	66	NO
Pltp	P55065	245	YES
Pltp	P55065	398	YES
Pltp	P55065	143	YES
Pltp	P55065	64	YES
Plxdc1	Q91ZV7	81	YES
Plxna2	P70207	163	YES
Plxna3	P70208	1074	YES
Plxna3	P70208	60	YES
Plxna4	Q80UG2	1006	YES
Plxna4	Q80UG2	441	YES
Plxnb1	Q8CJH3	543	YES
Plxnb1	Q8CJH3	1251	YES
Plxnb2	B2RXS4	735	NO
Plxnb2	B2RXS4	1005	YES
Plxnb2	B2RXS4	1053	YES
Plxnb2	B2RXS4	1103	YES
Plxnb2	B2RXS4	127	YES
Plxnb2	B2RXS4	393	YES
Plxnb2	B2RXS4	451	YES
Plxnb2	B2RXS4	761	YES
Plxnb2	B2RXS4	919	YES
Plxnb3	Q9QY40	889	YES
Plxnc1	Q9QZC2	587	YES
Plxnc1	Q9QZC2	86	YES
Plxnc1	Q9QZC2	141	YES
Plxnc1	Q9QZC2	143	YES
Plxnc1	Q9QZC2	407	YES
Plxnc1	Q9QZC2	717	YES
Plxnc1	Q9QZC2	896	YES
Plxnc1	Q9QZC2	901	YES
Plxnd1	Q3UH93	1134	YES
Plxnd1	Q3UH93	1120	YES
Plxnd1	Q3UH93	585	YES
Podxl2	Q8CAE9-3	330	YES
Pofut1	Q91ZW2	165	YES
Pofut2	Q8VHI3	259	YES
Poglut1	Q8BYB9	373	NO
Poglut1	Q8BYB9	53	YES
Pomt1	Q8R2R1	471	YES
Pomt2	Q8BGQ4-2	583	YES
Pomt2	Q8BGQ4-2	98	YES
Pon2	Q62086	322	YES
Pon2	Q62086	254	YES
Pon2	Q62086	323	YES
Postn	Q62009-5	601	YES
Ppib	P24369	148	YES
Ppm1l	Q8BHN0	117	YES
Ppt1	O88531	197	YES
Ppt1	O88531	212	YES
Ppt2	O35448	289	YES
Ppt2	O35448	60	YES
Prkcsh	O08795	72	YES
Prnp	P04925	196	YES
Prom1	O54990-6	323	YES
Prom1	O54990-6	282	YES
Prom1	O54990-6	264	YES
Psap	Q61207	333	NO
Psap	Q61207	334	YES
Psap	Q61207	214	YES
Psap	Q61207	459	YES
Psap	Q61207	80	YES
Ptchd1	Q14B62	77	YES
Ptdss2	Q9Z1X2-2	159	YES
Ptgfrn	Q9WV91	618	YES
Ptgfrn	Q9WV91	300	YES
Ptgfrn	Q9WV91	600	YES
Ptk7	Q8BKG3	397	NO
Ptk7	Q8BKG3	108	YES
Ptk7	Q8BKG3	559	YES
Ptk7	Q8BKG3	98	YES
Ptma	P26350	29	YES
Ptprc	P06800-3	287	YES
Ptprc	P06800-3	288	YES
Ptprd	Q64487-1	714	YES
Ptprf	A2A8L5	957	NO
Ptprf	A2A8L5	941	NO
Ptprf	A2A8L5	721	YES
Ptprg	Q05909	113	YES
Ptprg	Q05909	444	YES
Ptprj	Q64455	662	YES
Ptprj	Q64455	78	YES
Ptprj	Q64455	267	YES

Gene names	Leading proteins	Positions within proteins	Also found in Zielinska et al, 2010 or predicted by uniprot (release 31/01/2018)
Ptprj	Q64455	313	YES
Ptprj	Q64455	317	YES
Ptprj	Q64455	437	YES
Ptprj	Q64455	572	YES
Ptprj	Q64455	576	YES
Ptprj	Q64455	668	YES
Ptprk	P35822	139	YES
Ptprm	P28828	249	YES
Ptprm	P28828	131	YES
Ptprn	Q60673	524	YES
Ptprn2	P80560	550	YES
Ptpro	E9Q612	154	YES
Ptprs	B0V2N1-6	674	YES
Ptprz1	B9EKR1	501	YES
Ptprz1	B9EKR1	317	YES
Ptprz1	B9EKR1	324	YES
Ptprz1	B9EKR1	232	YES
Ptprz1	B9EKR1	105	YES
Ptprz1	B9EKR1	552	YES
Ptprz1	B9EKR1	223	YES
Ptprz1	B9EKR1	1058	YES
Ptprz1	B9EKR1	134	YES
Ptprz1	B9EKR1	685	YES
Pttg1ip	Q8R143	42	YES
Pttg1ip	Q8R143	51	YES
Pvrl1	Q9JKF6	202	YES
Pvrl2	P32507-2	315	YES
Pvrl2	P32507-2	128	YES
Pvrl2	P32507-2	138	YES
Pvrl3	Q9JLB9	186	YES
Pvrl3	Q9JLB9	83	YES
Pxdn	Q3UQ28	1277	YES
Pxdn	Q3UQ28	1175	YES
Ramp2	Q9WUP0	99	YES
Rcn1	Q05186	47	YES
Rcn3	Q8BH97	140	NO
Reln	Q60841-3	1267	NO
Reln	Q60841-3	290	YES
Reln	Q60841-3	291	YES
Reln	Q60841-3	1600	YES
Reln	Q60841-3	3016	YES
Reln	Q60841-3	306	YES
Rfx4	Q7TNK1-4	89	YES
Rgma	Q6PCX7-2	99	YES
Rnaset2	Q9CQ01	80	YES
Rnf13	O54965-2	88	YES
Rnf13	O54965-2	75	YES
Rnf130	Q8VEM1	135	YES
Robo1	O89026	781	YES
Robo2	Q7TPD3-2	123	YES
Robo2	Q7TPD3-2	786	YES
Ror2	Q9Z138	318	YES
Rpn2	Q9DBG6	106	YES
Rtn4r	Q99PI8	179	YES
Rufy3	Q9D394	303	YES
Rufy3	Q9D394	304	YES
S1pr3	Q9Z0U9	15	YES
Scap	Q6GQT6	590	YES
Scara3	Q8C850	430	YES
Scarb1	Q61009	383	YES
Scarb2	O35114	304	NO
Scarb2	O35114	308	NO
Scarb2	O35114	325	YES
Scarb2	O35114	122	YES
Scarb2	O35114	209	YES
Scarb2	O35114	206	YES
Scarb2	O35114	224	YES
Scarb2	O35114	249	YES
Scarb2	O35114	105	YES
Scarb2	O35114	412	YES
Scarb2	O35114	45	YES
Scn1b	P97952	135	YES
Scn1b	P97952	93	YES
Scn3b	Q8BHK2	95	YES
Scube2	Q9JJS0	788	YES
Scube2	Q9JJS0	798	YES
Scube2	Q9JJS0	759	YES
Scube2	Q9JJS0	529	YES
Sdk2	Q6V4S5	1579	YES
Sdk2	Q6V4S5	581	YES
Sdk2	Q6V4S5	1260	YES
Sel1l	Q9Z2G6-2	218	YES
Sel1l	Q9Z2G6-2	554	YES
Sel1l	Q9Z2G6-2	377	YES
Sel1l3	Q80TS8-2	665	YES
Sema4b	Q62179	56	YES
Sema4c	Q64151	522	YES
Sema4c	Q64151	419	YES
Sema4c	Q64151	106	YES
Sema4d	O09126	77	YES
Sema4d	O09126	379	YES
Sema4d	O09126	419	YES
Sema4g	Q9WUH7	386	YES
Sema4g	Q9WUH7	55	YES
Sema4g	Q9WUH7	596	YES
Sema6a	O35464-3	434	NO
Sema6a	O35464-3	461	YES
Sema6d	Q76KF0-3	461	YES
Sema7a	Q9QUR8	328	YES
Sema7a	Q9QUR8	256	YES
Sepp1	P70274	83	YES
Serinc5	Q8BHJ6	295	NO
Serpina1c;Serpina1b;Serpin	Q00896	101	YES
Serpinc1	P32261	225	YES
Serpinh1	P19324	119	YES
Serpini1	O35684	157	YES
Serpini1	O35684	321	YES
Sez6l	Q6P1D5-2	375	YES
Sez6l	Q6P1D5-2	398	YES
Sez6l	Q6P1D5-2	558	YES
Sez6l	Q6P1D5-2	454	YES
Sez6l	Q6P1D5-2	268	YES
Sez6l	Q6P1D5-2	414	YES
Sfrp1	Q8C4U3	173	YES
Sgcb	P82349	213	YES

Gene names	Leading proteins	Positions within proteins	Also found in Zielinska et al, 2010 or predicted by uniprot (release 31/01/2018)
Sgce	O70258	200	YES
Sgtb	Q8VD33	167	YES
Shisa7	Q8C3Q5-2	62	YES
Shisa9	Q9CZN4-4	45	YES
Sidt1	Q6AXF6	67	YES
Sidt1	Q6AXF6	83	NO
Sidt2	Q8CIF6	165	YES
Sil1	Q9EPK6	197	YES
Sirpa	P97797-2	271	NO
Sirpa	P97797-2	312	NO
Sirpa	P97797-2	246	NO
Sirpa	P97797-2	205	YES
Sirpa	P97797-2	209	YES
Slc12a2	P55012	546	NO
Slc12a2	P55012	555	YES
Slc12a4	Q9JIS8	331	YES
Slc12a4	Q9JIS8	312	YES
Slc12a5	Q91V14-2	338	YES
Slc12a5	Q91V14-2	339	NO
Slc12a5	Q91V14-2	328	NO
Slc12a5	Q91V14-2	310	YES
Slc12a5	Q91V14-2	291	YES
Slc12a6	Q924N4-2	328	YES
Slc12a6	Q924N4-2	347	YES
Slc12a7	Q9WVL3-2	312	NO
Slc12a9	Q99MR3	243	YES
Slc13a5	Q67BT3	566	YES
Slc17a6	Q8BLE7	100	YES
Slc17a6	Q8BLE7	101	YES
Slc1a1	P51906	178	YES
Slc1a1	P51906	194	NO
Slc1a2	P43006	205	YES
Slc1a2	P43006	215	YES
Slc1a4	O35874	201	YES
Slc1a4	O35874	201	YES
Slc1a4	O35874	206	YES
Slc22a5	Q9Z0E8	91	YES
Slc22a5	Q9Z0E8	64	YES
Slc25a21	Q8BZ09	182	YES
Slc26a6	Q8CIW6-3	151	NO
Slc29a1	Q9JIM1-2	48	YES
Slc2a1	P17809	45	NO
Slc2a13	Q3UHK1	447	YES
Slc2a3	P32037	43	YES
Slc30a1	Q60738	294	YES
Slc39a10	Q6P5F6	341	NO
Slc39a14	Q75N73-2	52	YES
Slc39a14	Q75N73-2	100	YES
Slc39a14	Q75N73-2	85	YES
Slc39a6	Q8C145	275	YES
Slc39a6	Q8C145	68	YES
Slc3a2	P10852	385	YES
Slc3a2	P10852	166	YES
Slc3a2	P10852	259	YES
Slc3a2	P10852	385	YES
Slc3a2	P10852	399	YES
Slc3a2	P10852	399	YES
Slc44a1	Q6X893	134	YES
Slc44a2	Q8BY89-2	185	NO
Slc44a2	Q8BY89-2	198	YES
Slc46a1	Q6PEM8	58	YES
Slc4a8	Q8JZR6-2	591	YES
Slc6a15	Q8BG16	424	YES
Slc6a17	Q8BJI1	186	YES
Slc6a17	Q8BJI1	393	YES
Slc6a2	O55192	192	YES
Slc7a1	Q09143	229	NO
Slc7a1	Q09143	229	YES
Slc7a1	Q09143	223	YES
Slc9a7	Q8BLV3-2	145	YES
Slitrk1	Q810C1	253	YES
Slitrk2	Q810C0	422	YES
Smchd1	Q6P5D8	1701	YES
Smpd1	Q04519	518	YES
Smpd1	Q04519	333	YES
Sod3	O09164	121	YES
Sorcs1	Q9JLC4-2	774	YES
Sorcs1	Q9JLC4-2	775	YES
Sorcs3	Q8VI51	786	YES
Sorl1	O88307	2011	NO
Sorl1	O88307	1164	YES
Sorl1	O88307	871	YES
Sorl1	O88307	1895	YES
Sorl1	O88307	1733	YES
Sorl1	O88307	1855	YES
Sorl1	O88307	1987	YES
Sort1	Q6PHU5	160	NO
Sort1	Q6PHU5	161	YES
Sort1	Q6PHU5	272	YES
Sort1	Q6PHU5	404	YES
Sparcl1	P70663	462	YES
Spock2	Q9ER58	225	YES
Spock2	Q9ER58	286	YES
Spock3	Q8BKV0-2	287	YES
Spon1	Q8VCC9	214	YES
Sppl2a	Q9JJF9	119	YES
Sppl2a	Q9JJF9	61	YES
Sppl2a	Q9JJF9	69	YES
Sppl2b	Q3TD49-2	379	YES
Ssr1	Q9CY50	191	YES
Ssr1	Q9CY50	136	YES
Ssr2	Q9CPW5	88	YES
St3gal5	O88829-2	224	YES
St8sia2	O35696	219	NO
St8sia2	O35696	60	YES
St8sia3	Q64689	206	YES
Stab1	Q8R4Y4-2	674	NO
Stab1	Q8R4Y4-2	1398	YES
Stab1	Q8R4Y4-2	1180	YES
Stab1	Q8R4Y4-2	1179	YES
Stab1	Q8R4Y4-2	1171	YES
Stab1	Q8R4Y4-2	1011	YES
Stab1	Q8R4Y4-2	713	YES
Stim1	P70302	171	YES
Stt3a	P46978	549	YES
Stt3a	P46978	544	YES
Stt3a	P46978	548	YES
Stt3a	P46978	537	YES
Stt3b	Q3TDQ1	613	YES
Stt3b	Q3TDQ1	624	YES
Stt3b	Q3TDQ1	638	YES
Suco	Q8C341	529	YES
Suco	Q8C341	523	YES
Sulf2	Q8CFG0	149	NO
Sulf2	Q8CFG0	171	NO
Sulf2	Q8CFG0	241	YES
Sumf1	Q8R0F3	139	YES
Sun1	Q9D666-2	711	YES
Sun2	Q8BJS4-3	618	YES
Susd2	Q9DBX3-2	580	NO
Susd2	Q9DBX3-2	39	YES
Sv2a	Q9JIS5	498	NO
Sv2a	Q9JIS5	548	YES
Sv2a	Q9JIS5	573	YES
Sv2b	Q8BG39	491	YES
Sv2b	Q8BG39	516	YES
Sv2c	Q69ZS6	534	YES
Sv2c	Q69ZS6	559	YES
Sv2c	Q69ZS6	565	YES
Synpr	Q8BGN8-2	53	YES
Synpr	Q8BGN8-2	58	YES
Syp	Q62277	59	YES
Sypl1	O09117-2	52	NO
Sypl1	O09117-2	77	YES
Sypl1	O09117-2	54	YES
Tapbpl	Q8VD31	270	YES
Tctn2	Q2MV57-2	512	YES
Tenm2	Q9WTS5	1702	NO
Tenm2	Q9WTS5	1762	YES
Tenm2	Q9WTS5	1763	YES
Tenm2	Q9WTS5	1983	YES
Tenm2	Q9WTS5	1257	YES
Tenm2	Q9WTS5	443	YES
Tenm2	Q9WTS5	938	YES
Tenm3	Q9WTS6	1211	YES
Tenm3	Q9WTS6	380	YES
Tenm3	Q9WTS6	869	YES
Tenm3	Q9WTS6	1656	YES
Tenm4	Q3UHK6	1811	YES
Tenm4	Q3UHK6	1801	YES
Tenm4	Q3UHK6	2190	YES
Tf	Q921I1	513	YES
Tfrc	Q62351	730	YES
Tfrc	Q62351	725	YES
Tfrc	Q62351	730	YES
Tgfbr3	O88393	570	YES
Tgoln1	Q62313	110	YES
Thsd7a	Q69ZU6	957	NO
Thsd7a	Q69ZU6	1354	YES
Thsd7a	Q69ZU6	1488	YES
Thy1	P01831	118	YES
Thy1	P01831	94	YES
Tlr2	Q9QUN7	442	YES
Tm2d1	Q99MB3	73	NO
Tm2d1	Q99MB3	76	YES
Tm2d1	Q99MB3	198	YES
Tm2d3	Q8BJ83-2	140	YES
Tm2d3	Q8BJ83-2	105	YES
Tm2d3	Q8BJ83-2	152	YES
Tm2d3	Q8BJ83-2	70	YES
Tm9sf1	Q9DBU0	178	YES
Tm9sf3	Q9ET30	172	YES
Tmed4	Q8R1V4	117	YES
Tmed9	Q99KF1	125	YES
Tmeff1	Q6PFE7-3	55	YES
Tmem106b	Q8OX71	184	YES
Tmem106c	Q8OVP8	184	YES
Tmem131	O70472	1057	YES
Tmem132a	Q922P8	276	YES
Tmem132a	Q922P8	67	YES
Tmem145	Q8C4U2	109	YES
Tmem2	Q5FWI3	636	NO
Tmem2	Q5FWI3	362	YES
Tmem2	Q5FWI3	980	YES
Tmem2	Q5FWI3	1234	YES
Tmem2	Q5FWI3	525	YES
Tmem206	Q9D771	155	YES
Tmem206	Q9D771	162	YES
Tmem245	B1AZA5	549	YES
Tmem259	Q8CIV2	180	YES
Tmem30a	Q8VEK0	297	YES
Tmem30a	Q8VEK0	98	YES
Tmem30a	Q8VEK0	107	YES
Tmem30a	Q8VEK0	98	YES
Tmem62	Q8BXJ9	384	YES
Tmem87a	Q8BXN9-3	127	YES
Tmem87a	Q8BXN9-3	79	YES
Tmem87a	Q8BXN9-3	157	YES
Tmem87a	Q8BXN9-3	160	YES
Tmem87a	Q8BXN9-3	62	YES
Tmem9	Q9CR23	47	YES
Tmem9	Q9CR23	38	YES
Tmem9	Q9CR23	38	YES
Tmpo	Q61029	289	YES
Tmtc4	Q8BG19	609	NO
Tmtc4	Q8BG19	497	YES
Tmx3	Q8BXZ1	261	YES
Tnc	Q80YX1	184	NO
Tnc	Q80YX1	1018	NO
Tnc	Q80YX1	1301	YES
Tnc	Q80YX1	1394	YES
Tnc	Q80YX1	166	YES
Tnr	Q8BYI9	470	YES
Tnr	Q8BYI9	55	YES
Tnr	Q8BYI9	581	YES
Tnr	Q8BYI9	869	YES
Tnr	Q8BYI9	874	YES
Tor1aip1	Q921T2	411	YES
Tor1b	Q9ER41	165	YES
Tor1b	Q9ER41	64	YES
Tor2a	P0C7W3	149	YES
Tor3a	Q9ER38	110	YES
Tpbg	Q9Z0L0	124	YES
Tpbg	Q9Z0L0	281	YES
Tpbg	Q9Z0L0	262	YES
Tpbgl	Q8C013	66	NO
Tpbgl	Q8C013	73	NO
Tpcn1	Q9EQJ0	600	YES
Tpcn1	Q9EQJ0	612	YES
Tpcn1	Q9EQJ0	617	YES
Tpp1	O89023	442	YES
Tril	Q9DBY4	209	YES
Tspan13	Q9D8C2	114	YES
Tspan13	Q9D8C2	137	YES
Tspan2	Q922J6	139	YES
Tspan3	Q9QY33	167	YES
Tspan3	Q9QY33	152	YES
Tspan3	Q9QY33	183	YES
Tspan31	Q9CQ88	117	NO
Tspan31	Q9CQ88	134	YES
Tspan31	Q9CQ88	109	YES
Tspan31	Q9CQ88	117	YES
Tspan6	O70401	134	YES
Ttc17	E9PVB5-2	184	YES
Ttc17	E9PVB5-2	704	YES
Ttyh1	Q9D3A9	355	YES
Ttyh3	Q6P5F7-2	351	NO
Ttyh3	Q6P5F7-2	144	YES
Txndc11	Q8K2W3	306	YES
Txndc11	Q8K2W3	443	YES
Txndc15	Q6P6J9	165	YES
Txndc15	Q6P6J9	277	YES
Txndc15	Q6P6J9	165	YES
Txndc15	Q6P6J9	171	YES
Txndc16	Q7TN22-2	461	YES
Uggt1	Q6P5E4	269	YES
Ugt8	Q64676	442	YES
Ugt8	Q64676	78	YES
Unc5c	O08747	236	YES
Vcam1	P29533	225	YES
Vcan	Q62059-2	330	YES
Vtn	P29788	241	YES
Wbscr17	Q7TT15-2	459	YES
Wbscr17	Q7TT15-2	50	YES
Wfs1	P56695	748	YES
Wnt5a	P22725-2	292	YES
	Q8CE72	3061	YES
	Q8CE72	3070	YES
	P10404	58	NO
	Q32M26	26	YES
	Q3UZV7-3	577	YES
	Q3UZV7-3	619	YES
	P03987-2	179	YES
	P10404	297	YES
	P10404	369	YES

Spread sheet 2. Sequon analysis in the reference glycoproteomic dataset (Qualitative dataset)

	Raw number	% of total	% NxS/T
ALL	1665	100	93,63
Found in Zielinska et al, 2010	1223	73,45	96,08
Not found in Zielinska et al, 2010	442	26,55	86,88
Not found in Zielinska et al, 2010 but predicted by uniprot	302	18,14	99,01
NOVEL SITES - Not in uniprot neither no described in Zielinska et al, 2010	140	8,41	60,71

91,6% of the N-glycosylation sites were previously recognised in Zielinska et al, 2010 or are predicted by uniprot

Spread sheet 3. Gene ontology of the reference glycoproteomic dataset (Qualitative dataset)

GO analyses based on the glycoproteins not recognised in Zielinska et al, 2010 neither no predicted by uniprot (NOVEL sites)

91 genes (95.8%) from the input list are present in at least one GO category.

Gene ontology term	Category, level	Set size	Candidates contained	p-value	q-value
GO:0031224 intrinsic to membrane	CC 2	6194	66 (1.1%)	7.08e-15	2.34e-13
GO:0016021 integral to membrane	CC 3	6055	65 (1.1%)	1.12e-14	4.15e-13
GO:0031997 N-terminal myristoylation domain binding	MF 4	3	3 (100.0%)	1.09e-07	2.84e-06
GO:0072542 protein phosphatase activator activity	MF 4	6	3 (50.0%)	2.16e-06	2.81e-05
GO:0019211 phosphatase activator activity	MF 3	8	3 (37.5%)	6,00E-06	0.000174
GO:0005513 detection of calcium ion	BP 4	8	3 (37.5%)	6,00E-06	0.000978
GO:0031432 titin binding	MF 4	10	3 (30.0%)	1.28e-05	0.000111
GO:0014075 response to amine stimulus	BP 4	32	4 (12.5%)	1.65e-05	0.00135
GO:0043274 phospholipase binding	MF 4	12	3 (25.0%)	2.33e-05	0.000151
GO:0031996 thioesterase binding	MF 4	13	3 (23.1%)	3.01e-05	0.000157
GO:0007155 cell adhesion	BP 2	842	14 (1.7%)	4.71e-05	0.00273
GO:0034704 calcium channel complex	CC 4	42	4 (9.5%)	4.96e-05	0.00139
GO:0070296 sarcoplasmic reticulum calcium ion transport	BP 4	19	3 (15.8%)	9.99e-05	0.00543
GO:0043548 phosphatidylinositol 3-kinase binding	MF 3	21	3 (14.3%)	0.000136	0.00198
GO:0006812 cation transport	BP 4	605	11 (1.8%)	0.000147	0.00584

GO analyses in all of the reference glycoproteomic dataset

694 genes (98.6%) from the input list are present in at least one GO category.

Gene ontology term	Category, level	Set size	Candidates contained	p-value	q-value
GO:0031224 intrinsic to membrane	CC 2	6194	518 (8.4%)	4.44e-118	2.98e-116
GO:0016021 integral to membrane	CC 3	6055	497 (8.3%)	6.62e-106	6.02e-104
GO:0007155 cell adhesion	BP 2	842	147 (17.5%)	6.38e-60	5.68e-58
GO:0009986 cell surface	CC 2	526	92 (17.6%)	5.37e-37	1.8e-35
GO:0005886 plasma membrane	CC 2	4673	318 (6.8%)	3.9e-35	8.72e-34
GO:0071944 cell periphery	CC 2	4783	319 (6.7%)	1.66e-33	2.78e-32
GO:0044459 plasma membrane part	CC 2	1558	152 (9.8%)	5.35e-30	7.16e-29
GO:0007399 nervous system development	BP 4	1486	147 (9.9%)	1.54e-29	1.16e-26
GO:0005773 vacuole	CC 4	342	66 (19.4%)	2.74e-29	2.44e-27
GO:0005783 endoplasmic reticulum	CC 4	1177	126 (10.7%)	2.3e-28	1.02e-26
GO:0016337 cell-cell adhesion	BP 3	374	67 (18.0%)	1.04e-27	3.88e-25
GO:0048731 system development	BP 3	3298	237 (7.2%)	2.73e-27	5.08e-25
GO:0044432 endoplasmic reticulum part	CC 3	792	96 (12.1%)	1.76e-25	7.99e-24
GO:0031226 intrinsic to plasma membrane	CC 3	759	91 (12.0%)	8,00E-24	2.43e-22
GO:0031175 neuron projection development	BP 4	529	74 (14.0%)	1.73e-23	6.53e-21

Spread sheet 4. Comparative glycoproteomic dataset (Quantitative dataset)

Gene names	Protein Uniprot ID	Position within protein	Levels in the mutant (log2)	p-value
A2m	Q61838	568	-0,40	0,3347
A2m	Q61838	881	0,06	0,8509
A2m	Q61838	1385	0,01	0,9940
Abca1	P41233	96	ND	ND
Abca1	P41233	196	0,06	0,9416
Abca1	P41233	400	0,50	0,3116
Abca1	P41233	98	-0,46	0,4201
Abca1	P41233	1637	0,30	0,5684
Abca2	P41234	1678	0,26	0,5710
Abca2	P41234	1549	0,20	0,7000
Abca2	P41234	1557	0,20	0,7000
Abca3	Q8R420	228	-0,53	0,1183
Abca5	Q8K448	190	ND	ND
Abca7	Q91V24	299	ND	ND
Ace	P09470	700	0,80	0,0837
Ace	P09470	116	0,68	0,1651
Ace	P09470	514	-0,11	0,8249
Ace	P09470	719	-0,07	0,8893
Acp2	P24638	267	-1,34	0,0142
Acp2	P24638	167	-0,75	0,0387
Acp2	P24638	177	-2,59	0,1852
Adam10	O35598	279	-0,21	0,2707
Adam10	O35598	552	-0,25	0,4719
Adam10	O35598	440	-0,18	0,5920
Adam17	Q9Z0F8-2	264	ND	ND
Adam17	Q9Z0F8-2	606	0,11	0,8250
Adam22	Q9R1V6-19	517	-0,60	0,0693
Adam22	Q9R1V6-19	632	-0,16	0,6884
Adam23	Q9R1V7-4	97	0,37	0,3377
Adam9	Q61072	381	0,19	0,4764
Adcy9	P51830	964	-0,01	0,9905
Adgrf5	G5E8Q8	254	0,64	0,1616
Adgrf5	G5E8Q8	648	0,73	0,1817
Adgrf5	G5E8Q8	270	0,61	0,2490
Afp	P02772	503	-0,95	0,0735
Afp	P02772	247	0,30	0,2101
Afp	P02772	498	0,12	0,7867
Ahsg	P29699	176	ND	ND
Ahsg	P29699	99	1,82	0,0165
Alcam	Q61490	361	0,65	0,1956
Alcam	Q61490	499	0,08	0,8708
Alk	P97793	328	0,11	0,9079
Alpl	P09242	430	-0,03	0,9117
Anpep	P97449	114	1,31	0,2889
Anpep	P97449	817	0,57	0,1202
Anpep	P97449	606	0,47	0,2447
Antxr2	Q6DFX2	260	0,59	0,4213
Aplp2	Q06335-2	485	-0,97	0,2869
Apmap	Q9D7N9	159	-0,55	0,0167
Apod	P51910	98	-0,39	0,6788
Apoe	P08226	130	-0,77	0,3342
Apoh	Q01339	162	-0,26	0,3431
Apoh	Q01339	105	-0,01	0,9804
Apoh	Q01339	117	-0,01	0,9804
Arsb	P50429	280	-0,44	0,0102
Arsb	P50429	292	0,92	0,1638
Arsb	P50429	189	0,28	0,6338
Asah1	Q9WV54	341	-0,87	0,1769
Asah1	Q9WV54	347	-0,08	0,8471
Asah1	Q9WV54	258	0,03	0,8974
Astn1	Q61137-2	976	1,85	0,0148
Astn1	Q61137-2	975	1,55	0,0468
Astn1	Q61137-2	734	0,18	0,7559
Astn1	Q61137-2	721	0,21	0,7973
Astn1	Q61137-2	733	-0,01	0,9911
Astn2	Q80Z10-2	1029	-1,50	0,0012
Astn2	Q80Z10-2	779	-0,51	0,0380
Astn2	Q80Z10-2	791	-0,51	0,0380
Astn2	Q80Z10-2	792	-0,55	0,2057
Atf6	F6VAN0	570	-0,10	0,6632
Atf6b	O35451	607	-0,82	0,1850
Atf6b	O35451	673	0,50	0,2904
Atp13a3	Q5XF89	1046	-0,93	0,1418
Atp13a3	Q5XF89	1052	-0,93	0,1418
Atp13a3	Q5XF89	1038	-0,11	0,8150
Atp1b1	P14094	266	-0,03	0,9696
Atp1b1	P14094	193	-0,01	0,9892
Atp1b2	P14231	250	ND	ND
Atp1b2	P14231	96	1,30	0,4823
Atp1b2	P14231	197	0,94	0,0030
Atp1b2	P14231	193	-1,33	0,0483
Atp1b2	P14231	197	-1,33	0,0483
Atp1b2	P14231	118	0,18	0,5842
Atp1b2	P14231	238	0,06	0,8606
Atp1b3	P97370	124	2,25	0,4851
Atp1b3	P97370	197	0,52	0,3988
Atp6ap1	Q9R1Q9	164	-1,34	0,0080
Atp6ap1	Q9R1Q9	344	1,00	0,0246
Atp6ap1	Q9R1Q9	351	1,00	0,0246
Atp6ap1	Q9R1Q9	267	1,09	0,4979
Atp6v0a2	P15920	484	0,88	0,0454
Atp6v0e1	Q9CQD8	70	-0,43	0,4970
Atp6v0e2	Q91XE7	70	0,52	0,5110
Atp8b1	Q148W0	174	0,58	0,3864
Atp8b1	Q148W0	175	0,58	0,3864
Atraid	Q6PGD0	133	-1,26	0,0235
Atraid	Q6PGD0	73	-1,09	0,1261
Atrn	Q9WU60	913	ND	ND
Atrn	Q9WU60	299	-1,56	0,0015
Atrn	Q9WU60	1197	-1,99	0,0034
Atrn	Q9WU60	913	-1,47	0,0035
Atrn	Q9WU60	922	-1,47	0,0035
Atrn	Q9WU60	415	-0,50	0,1398
Atrn	Q9WU60	263	0,63	0,2614
Atrn	Q9WU60	1042	0,19	0,6353
Atrnl1	Q6A051-3	151	-0,08	0,9096
B3galnt1	Q920V1	153	-1,31	0,0055
B3galnt1	Q920V1	198	-1,63	0,0258
B3galnt1	Q920V1	154	-0,88	0,2213
B3galt6	Q91Z92	127	-0,76	0,2427
Bai3;Bai2	Q80ZF8	625	ND	ND
Bcan	Q61361	336	0,25	0,4060
Bcan	Q61361	129	-0,27	0,6872
Bpi	Q67E05-2	320	-0,62	0,2233
Brinp1	Q920P3	599	-0,15	0,7901
Brinp1	Q920P3	156	-0,03	0,8350
Brinp2	Q6DFY8	626	ND	ND
Brwd1	Q921C3-2	57	-0,48	0,5423
Brwd1	Q921C3-2	60	-0,48	0,5423
Bsg	P18572-2	190	0,35	0,7461
Bsg	P18572-2	154	-0,87	0,0296
Btbd17	Q9DB72	61	0,65	0,1858
Btd	Q8CIF4	180	-0,66	0,1866
Btd	Q8CIF4	326	0,66	0,2245
Btd	Q8CIF4	96	0,55	0,3858
C1qa	P98086	146	0,14	0,8019
Ca4	Q64444	214	-0,34	0,3915
Cabs1	Q8C633	102	-2,26	0,3270
Cachd1	Q6PDJ1-2	601	ND	ND
Cachd1	Q6PDJ1-2	913	0,15	0,6795
Cacna2d1	O08532-2	136	-0,91	0,3085
Cacna2d1	O08532-2	324	0,32	0,4911
Cacna2d1	O08532-2	762	-1,13	0,0008
Cacna2d1	O08532-2	805	-1,31	0,0751
Cacna2d1	O08532-2	869	-0,63	0,3266
Cacna2d1	O08532-2	876	-0,63	0,3266
Cacna2d2	Q6PHS9-4	692	ND	ND
Cacna2d2	Q6PHS9-4	696	ND	ND
Cacna2d2	Q6PHS9-4	1022	0,29	0,4687
Cacna2d2	Q6PHS9-4	1033	0,29	0,4687
Cacna2d2	Q6PHS9-4	627	0,19	0,5471
Cacna2d2	Q6PHS9-4	205	-0,10	0,7687
Cacna2d2	Q6PHS9-4	692	-0,05	0,8811
Cacng8	Q8VHW2	53	-0,44	0,6103
Cacng8	Q8VHW2	56	-0,44	0,6103
Cadm1	Q8R5M8-5	104	-1,10	0,0306
Cadm1	Q8R5M8-5	307	-0,39	0,2395
Cadm1	Q8R5M8-5	311	-0,54	0,2399
Cadm1	Q8R5M8-5	168	-0,52	0,5629
Cadm1	Q8R5M8-5	116	0,33	0,5656
Cadm1	Q8R5M8-5	70	-0,13	0,6429
Cadm2	Q8BLQ9-2	58	ND	ND
Cadm2	Q8BLQ9-2	296	-0,97	0,0031
Cadm2	Q8BLQ9-2	60	-1,03	0,0168
Cadm2	Q8BLQ9-2	296	-1,25	0,0996
Cadm2	Q8BLQ9-2	300	-1,25	0,0996
Cadm2	Q8BLQ9-2	220	-0,73	0,3193
Cadm3	Q99N28	288	-1,67	0,0034
Cadm4	Q8R464	286	-0,34	0,1453
Cadm4	Q8R464	67	0,03	0,8610
Cadm4	Q8R464	262	-0,01	0,9752
Calcrl	Q9R1W5	127	-1,65	0,0348
Calcrl	Q9R1W5	128	-1,10	0,0916
Calcrl	Q9R1W5	122	-1,37	0,0002
Calcrl	Q9R1W5	122	2,85	0,0069
Calcrl	Q9R1W5	65	-0,83	0,2165
Calm1	P62204	98	-0,45	0,6659
Calu	O35887	131	-0,28	0,3155
Carkd	Q9CZ42-3	220	-0,11	0,6729
Casc4	Q6P2L7-3	151	0,54	0,0654
Casc4	Q6P2L7-3	150	1,32	0,0684
Casc4	Q6P2L7-3	114	-0,43	0,4833
Casc4	Q6P2L7-3	115	0,36	0,5037
Casd1	Q7TN73	141	-0,37	0,4602
Casd1	Q7TN73	175	-0,65	0,1365
Casd1	Q7TN73	241	-1,02	0,1706
Casd1	Q7TN73	187	-0,21	0,6543
Cbln1	Q9R171	79	-0,58	0,3380
Cd163	Q2VLH6	122	0,49	0,2214
Cd163	Q2VLH6	872	-0,64	0,2670
Cd164	Q9R0L9	98	-0,26	0,2037
Cd164	Q9R0L9	103	-0,26	0,2037
Cd180	Q62192	394	-0,88	0,0881
Cd180	Q62192	402	-0,88	0,0881
Cd1d1	P11609	38	-0,97	0,0401
Cd1d1	P11609	183	0,49	0,4743
Cd200	O54901	181	3,10	0,4946
Cd200	O54901	190	3,10	0,4946
Cd276	Q8VE98	104	0,00	0,9958
Cd320	Q9Z1P5-2	159	ND	ND
Cd38	P56528	124	ND	ND
Cd38	P56528	223	-0,51	0,2168
Cd44	P15379-2	59	-0,04	0,9170
Cd47	Q61735-2	71	-27,66	ND
Cd47	Q61735-2	73	-1,33	0,0482
Cd47	Q61735-2	80	-1,33	0,0482
Cd63	P41731	172	-0,46	0,2309
Cd97	Q9Z0M6-2	301	0,45	0,4935
Cd97	Q9Z0M6-2	367	0,14	0,5990
Cd97	Q9Z0M6-2	205	-0,17	0,6210
Cdh10	P70408	532	-1,26	0,2176
Cdh10	P70408	534	-1,26	0,2176
Cdh10	P70408	438	0,81	0,1710
Cdh10	P70408	456	0,06	0,8093
Cdh11	P55288	538	ND	ND
Cdh13	Q9WTR5	639	1,09	0,2341
Cdh13	Q9WTR5	489	2,00	0,2525
Cdh13	Q9WTR5	500	2,00	0,2525
Cdh13	Q9WTR5	598	-0,22	0,3568
Cdh13	Q9WTR5	530	-0,25	0,5861
Cdh13	Q9WTR5	638	0,20	0,6328
Cdh13	Q9WTR5	671	0,03	0,9128
Cdh2	P15116	692	-0,64	0,2456
Cdh2	P15116	402	0,09	0,8019
Cdh20	Q9Z0M3	420	-2,88	0,0008
Cdh4	P39038	554	1,03	0,1596
Cdh5	P55284	523	-0,01	0,9784
Cdh6	P97326	455	1,16	0,1327
Cdh6	P97326	437	-0,19	0,5855
Cdh8	P97291	463	0,26	0,5775
Celsr1	O35161	2155	ND	ND
Celsr1	O35161	2160	ND	ND
Celsr2	Q9R0M0-2	1502	0,44	0,2776
Celsr2	Q9R0M0-2	1037	-1,36	0,1879
Celsr2	Q9R0M0-2	1566	-0,26	0,2721
Celsr2	Q9R0M0-2	2062	0,38	0,4460
Celsr3	Q91ZI0	1213	-0,91	0,0067
Celsr3	Q91ZI0	2185	-1,17	0,0303
Celsr3	Q91ZI0	2042	-0,82	0,0889
Cemip	Q8BIO6	165	ND	ND
Cers2	Q924Z4	19	-0,24	0,5218
Cers6	Q8C172	18	-0,72	0,0246
Cfh	P06909	1225	-0,33	0,6228
Cfh	P06909	676	0,28	0,6479
Cfh	P06909	773	0,05	0,9356
Cfi	Q61129	514	-19,79	ND
Chd9	Q8BYH8-2	198	0,14	0,8685
Chd9	Q8BYH8-2	203	0,14	0,8685
Chl1	P70232	984	ND	ND
Chl1	P70232	196	ND	ND
Chl1	P70232	562	-1,84	0,0001
Chl1	P70232	299	-1,48	0,0008
Chl1	P70232	87	-0,52	0,0239
Chl1	P70232	822	-0,43	0,0939
Chl1	P70232	476	0,55	0,2034
Chrna3	Q8R4G9	166	-0,60	0,1708
Chst12	Q99L3	139	0,19	0,5048
Chst15	Q91XQ5	142	-0,15	0,8444
Chst2	Q80WV3	152	0,89	0,1058
Chst2	Q80WV3	243	0,45	0,2525
Clcn2	Q9R0A1	411	-0,08	0,5689
Clcn5	Q9WVD4	408	-0,65	0,1986
Cldnd1	Q9CQX5	42	-1,71	0,0194
Cldnd1	Q9CQX5	72	0,15	0,7841
Clec10a	P49300	74	ND	ND
Clmp	Q8R373	72	-1,15	0,0795
Clmp	Q8R373	73	-1,15	0,0795
Clmp	Q8R373	196	0,10	0,6672
Clptm1	Q8VBZ3	295	-0,47	0,3790
Clptm1l	Q8BXA5	230	-0,47	0,0123
Clptm1l	Q8BXA5	91	1,51	0,0770
Clu	Q06890	102	-0,82	0,2780
Cnn3	Q9DAW9	240	-1,42	0,0001
Cnnm3	Q32NY4-2	73	-0,30	0,3084
Cnpy3	Q9DAU1	153	0,27	0,5170
Cnr1	P47746	78	-0,38	0,2560
Cnr1	P47746	84	-0,38	0,2560
Cntn1	P12960	935	-0,73	0,0039
Cntn1	P12960	457	-0,48	0,0199
Cntn1	P12960	494	0,15	0,2189
Cntn1	P12960	208	0,16	0,5011
Cntn2	Q61330	200	-2,25	0,0000
Cntn2	Q61330	206	-2,25	0,0000
Cntn2	Q61330	200	4,43	0,0001
Cntn2	Q61330	942	-0,92	0,1525
Cntn2	Q61330	463	-0,47	0,3019
Cntn4	Q69Z26	191	0,37	0,5048
Cntn4	Q69Z26	954	-0,24	0,6129
Cntn6	Q9JMB8-2	878	ND	ND
Cntn6	Q9JMB8-2	914	-1,20	0,0926
Cntnap1	O54991	127	ND	ND
Cntnap1	O54991	1148	-0,76	0,2118
Cntnap1	O54991	598	0,98	0,2346
Cntnap1	O54991	844	-0,65	0,3414
Cntnap1	O54991	121	-0,21	0,5608
Cntnap1	O54991	764	0,20	0,7032
Cntnap1	O54991	129	-0,03	0,9532
Cntnap2	Q9CPW0	437	0,19	0,5462
Cntnap2	Q9CPW0	289	-0,42	0,1070
Cntnap2	Q9CPW0	630	-0,10	0,5698
Cntnap2	Q9CPW0	436	0,03	0,8165
Cntnap4	Q99P47	287	1,11	0,1027
Cntnap5a	Q0V8T9	1021	0,67	0,4352
Cntnap5a	Q0V8T9	768	-0,14	0,5958
Col11a1	Q61245-2	1553	-0,95	0,1339
Col12a1	Q60847-4	1519	0,73	0,2413
Col2a1	P28481-2	1291	0,23	0,7033
Col6a1	Q04857	801	0,41	0,5314
Col6a2	Q02788	800	0,29	0,1334
Colec12	Q8K4Q8	159	-0,25	0,2762
Colec12	Q8K4Q8	168	-0,25	0,2762
Colec12	Q8K4Q8	386	0,50	0,4952
Cp	Q61147	757	1,61	0,1055
Cpd	O89001	625	ND	ND
Cpd	O89001	626	ND	ND
Cpd	O89001	1067	-0,87	0,0017
Cpd	O89001	409	0,42	0,3546
Cpd	O89001	398	0,18	0,4152
Cpd	O89001	810	0,00	0,9920
Cpe	Q00493	390	0,85	0,5877
Cpq	Q9WVJ3-2	382	-1,19	0,0030
Cr1l	Q64735-2	252	0,73	0,2043
Creld2	Q9CYA0	188	0,00	0,9945
Crhr1	P35347	98	-0,57	0,0495
Cspg4	Q8VHY0	349	0,88	0,4072
Cspg4	Q8VHY0	2080	-0,97	0,1718
Cspg4	Q8VHY0	1454	-0,12	0,7627
Cspg5	Q71M36-2	57	ND	ND
Ctbs	Q8R242	283	-0,42	0,3092
Ctsa	P16675	239	-1,88	0,0096
Ctsa	P16675	140	-0,38	0,0308
Ctsc	P97821	275	0,42	0,4905
Ctsc	P97821	276	0,42	0,4905
Ctsc	P97821	53	0,31	0,2094
Ctsd	P18242	134	0,40	0,2784
Ctsd	P18242	261	1,12	0,7560
Ctsf	Q9R013	138	-0,49	0,3183
Ctsl	P06797	221	-0,30	0,1800
Ctso	Q8BM88	96	-2,07	0,0607
Cxadr	P97792	201	ND	ND
Cxadr	P97792	106	-0,30	0,4524
Cyp26a1	O55127	96	-0,25	0,5021
Dag1	Q62165	639	0,19	0,6949
Dag1	Q62165	647	0,19	0,6949
Dcc	P70211-2	60	-0,34	0,2853
Dchs1	E9PVD3	1989	ND	ND
Dchs1	E9PVD3	250	0,66	0,4495
Dchs1	E9PVD3	2754	-1,24	0,0005
Dchs1	E9PVD3	1514	-0,56	0,1354
Dcn	P28654	206	-0,36	0,0079
Dcp1b	Q3U564-2	129	0,56	0,3837
Dgcr2	P98154	147	0,10	0,6237
Dner	Q8JZM4	204	-0,76	0,2365
Dner	Q8JZM4	208	-0,76	0,2365
Dner	Q8JZM4	223	0,12	0,4933

Gene names	Protein Uniprot ID	Position within protein	Levels in the mutant (log2)	p-value
Dpp10	Q6NXK7	749	-0,31	0,3326
Dpp10	Q6NXK7	112	1,35	0,3652
Dpp10	Q6NXK7	120	1,35	0,3652
Dpp4	P28843	144	ND	ND
Dpp4	P28843	145	ND	ND
Dpp6	Q9Z218	410	-1,24	0,0272
Dpp6	Q9Z218	258	-0,91	0,0004
Dpp6	Q9Z218	505	-1,11	0,0087
Dpp6	Q9Z218	343	-0,57	0,0421
Dpp6	Q9Z218	113	-0,45	0,3391
Dpp6	Q9Z218	752	0,66	0,4281
Dpy19l3	Q71B07	118	0,10	0,8869
Dpy19l4	A2AJQ3-2	121	0,55	0,0657
Dpy19l4	A2AJQ3-2	122	-0,21	0,6832
Dscam	Q9ERC8	748	-1,28	0,0527
Dsg1c	Q7TSF0-2	110	ND	ND
Ece1	Q4PZA2-3	149	ND	ND
Ece1	Q4PZA2-3	234	-0,85	0,1575
Ece1	Q4PZA2-3	366	-0,48	0,2670
Ece1	Q4PZA2-3	232	-0,51	0,3639
Ednrb	P48302	60	0,14	0,8375
Efna5	O08543-2	162	0,13	0,6156
Efnb1	P52795	139	0,63	0,7260
Efnb3	O35393	210	ND	ND
Egfr	Q01279	124	-21,83	ND
Egfr	Q01279	128	-22,77	ND
Egfr	Q01279	352	0,16	0,1896
Egfr	Q01279	603	0,72	0,3688
Eif3a	P23116	586	-1,63	0,2395
Eif4h	Q9WUK2	223	0,14	0,3895
Eif4h	Q9WUK2	227	0,14	0,3895
Eif4h	Q9WUK2	229	0,14	0,3895
Elfn2	Q68FM6	80	0,27	0,6417
Elfn2	Q68FM6	85	0,27	0,6417
Elovl6	Q920L5	2	0,42	0,4683
Eltd1	Q923X1	298	0,65	0,0665
Emb	P21995	216	-1,02	0,0072
Emb	P21995	221	-1,02	0,0072
Emb	P21995	62	-1,54	0,0181
Emb	P21995	118	-0,29	0,0706
Emb	P21995	101	1,80	0,3130
Emb	P21995	70	0,22	0,7267
Emc1	Q8C7X2-2	914	-3,02	0,4661
Emilin1	Q99K41	795	0,09	0,8450
Emp1	P47801	43	-0,48	0,3304
Eng	Q63961	135	0,17	0,8491
Enpep	P16406	754	0,47	0,4475
Enpp2	Q9R1E6	410	-0,20	0,5609
Enpp3	Q6DYE8	594	ND	ND
Enpp4	Q8BTJ4-2	246	-0,02	0,9081
Enpp5	Q9EQG7	329	0,59	0,1170
Enpp5	Q9EQG7	158	-0,34	0,1422
Entpd1	P55772	291	0,60	0,2378
Entpd2	O55026	129	-0,87	0,0185
Entpd5	Q9WUZ9	231	0,90	0,0777
Eogt	Q8BYW9	354	0,66	0,1623
Epdr1	Q99M71	182	0,48	0,6481
Epha4	Q03137-2	235	-1,10	0,0432
Ephb2	P54763-4	265	ND	ND
Ephb2	P54763-4	483	-1,07	0,0688
Ephb2	P54763	482	0,24	0,4994
Erap1	Q9EQH2	403	0,15	0,5808
Erbb2	P70424	125	0,32	0,3924
Erbb4	Q61527-3	576	ND	ND
Erbb4	Q61527-3	548	-2,20	0,0082
Erbb4	Q61527-3	138	-0,37	0,5034
Erlin2	Q8BFZ9	106	0,06	0,8794
Ero1l	Q8R180	276	0,16	0,7551
Ero1lb	Q8R2E9	140	1,73	0,0006
Ero1lb	Q8R2E9	140	-2,03	0,0188
Ero1lb	Q8R2E9	145	-2,03	0,0188
Extl2	Q9ES89	75	-0,23	0,6632
Extl3	Q9WVL6	591	1,46	0,2012
F3	P20352	37	0,89	0,0616
Fam171a2	A2A699	66	-0,52	0,0845
Fam20c	Q5MJS3	465	ND	ND
Fat2	Q5F226	3278	ND	ND
Fat2	Q5F226	996	ND	ND
Fat2	Q5F226	3770	-0,74	0,2421
Fat2	Q5F226	3774	-0,74	0,2421
Fat2	Q5F226	2387	-2,59	0,0007
Fat2	Q5F226	39	-0,79	0,0309
Fat2	Q5F226	3432	-1,98	0,0515
Fat2	Q5F226	3127	-0,65	0,0709
Fat2	Q5F226	2470	-1,20	0,1103
Fat2	Q5F226	568	0,31	0,7211
Fat4	Q2PZL6	2923	-0,26	0,3245
Fat4	Q2PZL6	1828	0,13	0,8275
Fcgr3	P08508	91	0,04	0,9224
Fetub	Q9QXC1	139	0,02	0,9697
Fgb	Q8K0E8	384	-0,23	0,4615
Fgfr1	P16092-6	77	ND	ND
Fgfr1	P16092-6	262	0,00	0,9952
Fgfr2	P21803	318	ND	ND
Fkbp10	Q61576	390	ND	ND
Fkbp10	Q61576	392	-0,34	0,3410
Fkbp10	Q61576	69	0,24	0,5589
Fkbp10	Q61576	406	-0,04	0,9215
Fkbp7	O54998	41	-1,27	0,2656
Fkbp9	Q9Z247	397	-0,12	0,8436
Flt1	P35969	197	0,56	0,3354
Flt1	P35969	165	-0,22	0,5615
Fn1	P11276	430	-0,26	0,6144
Fn1	P11276	528	-0,12	0,7793
Fn1	P11276	1006	-0,03	0,9133
Fras1	Q80T14	2684	-0,64	0,4297
Fras1	Q80T14	2666	-0,81	0,1447
Frem2	Q6NVD0	2225	-21,75	ND
Frem2	Q6NVD0	2110	-1,49	0,0002
Fstl1	Q62356	173	-0,73	0,2809
Fstl1	Q62356	178	-0,73	0,2809
Fstl1	Q62356	142	-0,11	0,5828
Fstl5	Q8BFR2	318	-0,04	0,9422
Fuca2	Q99KR8	371	-0,08	0,7777
Fut10	Q5F2L2-2	110	0,23	0,6954

Gene names	Protein Uniprot ID	Position within protein	Levels in the mutant (log2)	p-value
Fut11	Q8BHC9	439	-1,26	0,0124
Fut11	Q8BHC9	313	-0,30	0,1709
Fut11	Q8BHC9	314	-0,30	0,1709
Gaa	P70699	926	-1,56	0,0258
Gaa	P70699	470	-0,55	0,0558
Gabbr1	Q9WV18	83	-1,15	0,0009
Gabbr1	Q9WV18	439	0,25	0,2922
Gabbr1	Q9WV18	513	0,56	0,4931
Gabbr2	Q80T41	388	ND	ND
Gabra2	P62812	137	-0,16	0,7341
Gabra3	P26049	163	-0,07	0,8947
Gabra6	P16305-4	117	-0,54	0,1600
Gabrb1	P50571	105	-0,46	0,4040
Gabrb2	P63137-2	104	-0,27	0,2691
Gabrb3	P63080	105	-0,60	0,1139
Galnt1	O08912	552	0,87	0,0964
Gba	P17439	78	0,90	0,0251
Gba	P17439	289	0,18	0,5980
Gba	P17439	165	-0,22	0,7988
Gde1	Q9JL56	168	1,96	0,0003
Gfra1	P97785-2	401	-0,01	0,9741
Ggcx	Q9QYC7	570	0,08	0,8585
Ggh	Q9Z0L8-2	160	-1,35	0,1354
Ggh	Q9Z0L8-2	186	-0,97	0,1777
Ggt7	Q99JP7	198	-0,40	0,5493
Ggt7	Q99JP7	523	-0,47	0,0196
Gla	P51569	192	-0,28	0,0906
Gla	P51569	139	0,46	0,4035
Glce	Q9EPS3	304	0,48	0,1195
Glce	Q9EPS3	225	0,07	0,7955
Glg1	Q61543	782	0,82	0,1482
Glg1	Q61543	161	-0,22	0,6733
Glg1	Q61543	206	0,03	0,9644
Glt8d1	Q6NSU3	257	-0,18	0,6622
Glt8d1	Q6NSU3	249	0,06	0,8883
Gnptab	Q69ZN6-2	1062	-0,42	0,3347
Gnptg	Q6S5C2	88	0,99	0,1757
Gns	Q8BFR4	103	-0,56	0,3728
Gns	Q8BFR4	109	-0,56	0,3728
Gns	Q8BFR4	271	-0,59	0,0103
Gns	Q8BFR4	354	-0,76	0,0532
Gns	Q8BFR4	175	0,21	0,7693
Golm1	Q91XA2	108	-19,26	ND
Golm1	Q91XA2	109	-0,53	0,1154
Gpc5	Q8CAL5	527	ND	ND
Gpm6a	P35802	164	0,29	0,8865
Gpnmb	Q99P91	275	1,14	0,1872
Gpnmb	Q99P91	246	0,57	0,2894
Gpnmb	Q99P91	249	0,57	0,2894
Gpr107	Q8BUV8	64	1,54	0,1149
Gpr125	Q7TT36	676	0,75	0,1987
Gpr126	Q6F3F9	720	ND	ND
Gria1	P23818	249	ND	ND
Gria1	P23818	257	ND	ND
Gria1	P23818	401	-1,92	0,0000
Gria1	P23818	406	-1,92	0,0000
Gria1	P23818	406	1,19	0,0010
Gria1	P23818	363	-0,22	0,6829
Gria2	P23819-4	370	-0,49	0,0537
Gria2	P23819-4	406	-0,60	0,0741
Gria2	P23819-4	413	-0,60	0,0741
Gria2	P23819-4	256	0,63	0,1046
Gria3	Q9Z2W9	409	-0,71	0,0057
Gria3	Q9Z2W9	416	-0,71	0,0057
Gria3	Q9Z2W9	374	0,17	0,7720
Gria4	Q9Z2W8	407	-0,19	0,1785
Gria4	Q9Z2W8	414	-0,19	0,1785
Gria4	Q9Z2W8	258	0,49	0,2628
Gria4	Q9Z2W8	371	-0,19	0,6279
Grid2	Q61625	426	-1,10	0,0441
Grid2	Q61625	716	0,51	0,1022
Grik2	P39087-2	430	ND	ND
Grik2	P39087-2	423	-1,94	0,0084
Grik2	P39087-2	430	-1,94	0,0084
Grik2	P39087-2	73	-0,16	0,5455
Grik2	P39087-2	412	0,09	0,8564
Grik3	B1AS29	278	0,68	0,4578
Grik3	B1AS29	426	-0,15	0,4270
Grik3	B1AS29	433	-0,15	0,4270
Grik3	P39087-2	751	-0,71	0,0217
Grin1	P35438-2	276	2,07	0,0265
Grin1	P35438-2	368	-1,09	0,1215
Grin1	P35438-2	771	-0,29	0,1916
Grin2b	Q01097	74	-0,51	0,0418
Grin2b	Q01097	444	0,15	0,8033
Grin2b	Q01097	341	-0,01	0,9953
Grin2d	Q03391	712	-0,16	0,8606
Grm1	P97772	397	-0,91	0,0051
Grm1	P97772	223	-0,07	0,7253
Grm3	Q9QYS2	414	-0,71	0,0043
Grm3	Q9QYS2	238	-0,98	0,1475
Grm3	Q9QYS2	439	-0,01	0,9542
Grm4	Q68EF4-2	569	-1,06	0,1038
Grm5	Q3UVX5-2	209	-0,01	0,9804
Grm7	Q68ED2	458	0,25	0,3363
Grn	P28798	263	-0,47	0,2435
Gusb	P12265	627	1,19	0,1235
Gxylt1	Q3UHH8	242	-20,26	ND
Gxylt1	Q3UHH8	201	-0,10	0,8979
Gxylt1	Q3UHH8	351	-0,78	0,0370
H2-K1	P01901	107	0,57	0,0897
Heg1	E9Q7X6-2	996	1,14	0,1147
Hepacam	Q640R3	189	0,30	0,6056
Heph	Q9Z0Z4-2	49	-0,75	0,1799
Heph	Q9Z0Z4-2	54	-0,48	0,4117
Hexa	P29416	157	-0,30	0,1529
Hfe	P70387	166	0,41	0,4818
Hgsnat	Q3UDW8-2	105	-0,37	0,6638
Hgsnat	Q3UDW8-2	125	0,35	0,0892
Hgsnat	Q3UDW8-2	77	-0,49	0,4128
Hpx	Q91X72	186	-0,47	0,3649
Hs2st1	Q8R3H7	108	-0,05	0,8546
Hs6st3	Q9QYK4	379	0,24	0,7217
Hsd11b1	P50172	162	-0,88	0,0283
Hsp90b1	P08113	62	-0,99	0,0057

Gene names	Protein Uniprot ID	Position within protein	Levels in the mutant (log2)	p-value
Hsp90b1	P11499	46	ND	ND
Hspg2	Q05793	358	-0,39	0,4479
Hspg2	Q05793	3098	0,67	0,0067
Hspg2	Q05793	2336	-0,34	0,3341
Hspg2	Q05793	89	-0,15	0,7581
Hyal2	O35632	74	0,98	0,0081
Hyou1	Q9JKR6	596	-0,82	0,0013
Hyou1	Q9JKR6	931	-0,61	0,0067
Hyou1	Q9JKR6	830	-0,36	0,2632
Hyou1	Q9JKR6	869	-0,15	0,4477
Hyou1	Q9JKR6	862	-0,34	0,5411
Hyou1	Q9JKR6	222	-0,28	0,6562
Hyou1	Q9JKR6	515	-0,07	0,6835
Icam1	P13597	47	2,23	0,0004
Icam2	P35330	158	-0,41	0,5822
Icam2	P35330	176	-0,41	0,5822
Icam2	P35330	49	-0,46	0,4950
Icam2	P35330	82	-0,15	0,5560
Ids	Q08890	117	0,18	0,5793
Igdcc4	Q9EQS9	156	ND	ND
Igf1r	Q60751	608	-0,33	0,6244
Igf1r	Q60751	623	-0,33	0,6244
Igf1r	Q60751	914	-0,08	0,8791
Igf2r	Q07113	1532	ND	ND
Igf2r	Q07113	1649	ND	ND
Igf2r	Q07113	1809	1,56	0,1843
Igf2r	Q07113	740	-1,01	0,0069
Igf2r	Q07113	1305	0,45	0,0751
Igf2r	Q07113	2129	-0,49	0,1396
Igf2r	Q07113	430	-0,43	0,2348
Igf2r	Q07113	944	-0,52	0,5001
Igf2r	Q07113	107	0,49	0,5371
Igf2r	Q07113	575	0,14	0,7113
Igfbp7	Q61581	170	-0,39	0,5138
Igfbpl1	Q80W15	158	-0,17	0,4743
Igsf21	Q7TNR6	407	0,47	0,5956
Igsf21	Q7TNR6	165	-1,08	0,0258
Igsf3	Q6ZQA6	655	ND	ND
Igsf3	Q6ZQA6	842	-1,13	0,0018
Igsf3	Q6ZQA6	700	-0,87	0,0389
Igsf3	Q6ZQA6	961	-0,96	0,2073
Igsf3	Q6ZQA6	1077	-0,01	0,9702
Igsf8	Q8R366	461	ND	ND
Igsf8	Q8R366	325	0,20	0,6805
Ikbip	Q9DBZ1	151	0,68	0,1501
Ikbip	Q9DBZ1-2	325	-0,33	0,5936
Il17rd	Q8JZL1	62	0,53	0,5685
Il6st	Q00560	225	0,91	0,0320
Il6st	Q00560	157	-0,08	0,6222
Il6st	Q00560	43	0,00	0,9999
Impad1	Q80V26	257	0,05	0,7970
Insr	P15208	242	0,28	0,4323
Insr	P15208	138	-0,51	0,5773
Insr	P15208	445	0,13	0,6829
Islr2	Q5RKR3	338	0,73	0,3361
Islr2	Q5RKR3	121	0,73	0,3135
Islr2	Q5RKR3	365	0,18	0,4165
Islr2	Q5RKR3	52	0,14	0,6112
Itfg1	Q99KW9	369	-24,69	ND
Itfg1	Q99KW9	351	ND	ND
Itfg1	Q99KW9	368	-0,05	0,8626
Itfg1	Q99KW9	145	-0,57	0,0335
Itfg1	Q99KW9	150	-0,57	0,0335
Itfg3	Q8C0Z1	120	ND	ND
Itfg3	Q8C0Z1	116	ND	ND
Itga1	Q3V3R4	459	0,81	0,2430
Itga1	Q3V3R4	217	0,18	0,4981
Itga1	Q3V3R4	112	0,40	0,5343
Itga1	Q3V3R4	1113	-0,08	0,7209
Itga1	Q3V3R4	418	0,37	0,7276
Itga1	Q3V3R4	100	-0,06	0,8288
Itga1	Q3V3R4	100	-0,01	0,9822
Itga1	Q3V3R4	105	-0,01	0,9822
Itga2	Q62469	1054	-0,98	0,0148
Itga2	Q62469	1071	1,16	0,1081
Itga2	Q62469	102	0,67	0,1172
Itga2	Q62469	457	-0,05	0,8982
Itga3	Q62470-3	575	-0,41	0,6387
Itga3	Q62470-3	906	-0,05	0,7507
Itga4	Q00651	487	0,18	0,6857
Itga5	P11688	678	1,12	0,1930
Itga6	Q61739-2	927	ND	ND
Itga6	Q61739-2	284	ND	ND
Itga6	Q61739-2	731	-0,57	0,3200
Itga7	Q61738-4	740	-1,47	0,0225
Itga7	Q61738-4	979	0,28	0,6500
Itga8	A2ARA8-2	176	0,59	0,3546
Itgam	P05555-2	58	0,72	0,3593
Itgam	P05555-2	905	0,86	0,0001
Itgam	P05555-2	617	-0,18	0,3766
Itgav	P43406	835	-0,30	0,7912
Itgav	P43406	851	-0,20	0,8812
Itgav	P43406	941	-0,71	0,2677
Itgav	P43406	74	0,37	0,3422
Itgb1	P09055	212	-0,69	0,3815
Itgb1	P09055	481	-0,24	0,6049
Itgb1	P09055	669	0,11	0,8574
Itgb5	O70309	705	-0,64	0,5650
Itih3	Q61704	580	-0,98	0,0054
Itih4	A6X935-2	835	0,53	0,5006
Itih4	A6X935-2	577	-0,06	0,9191
Itih5	Q8BJD1	231	ND	ND
Itih5	Q8BJD1	508	0,05	0,8635
Itm2b	O89051	170	-0,12	0,4330
Itpr1	P11881-8	2448	-0,25	0,1214
Itpr1	P11881-8	2655	0,26	0,6961
Itprip	Q3TNL8-2	27	0,89	0,2292
Jam2	Q9JI59	186	0,59	0,2735
Kdelc1	Q9JHP7-2	152	-0,47	0,0918
Kdr	P35918-2	98	0,22	0,3449
Kiaa0319l	Q8K135	889	-1,39	0,1435
Kiaa1161	Q69ZQ1	455	-0,26	0,1331
Kiaa1161	Q69ZQ1	239	0,38	0,4214
Kiaa1161	Q69ZQ1	249	0,38	0,4214
Kiaa1324	A2AFS3-3	497	-0,39	0,2785

Gene names	Protein Uniprot ID	Position within protein	Levels in the mutant (log2)	p-value
Kiaa1467	Q8BYI8	398	ND	ND
Kiaa1467	Q8BYI8	239	-0,56	0,0285
Kiaa1549	Q68FD9	1215	0,05	0,9162
Kirrel3	Q8BR86-3	167	-0,45	0,4171
Kit	P05532-2	146	-1,42	0,0288
Kng1	O08677-2	242	0,83	0,1322
Kng1	O08677-2	82	0,60	0,3888
L1cam	P11627	478	-0,20	0,4953
L1cam	P11627	246	-0,19	0,8213
L1cam	P11627	489	-1,31	0,0121
L1cam	P11627	725	-0,31	0,2086
L1cam	P11627	1107	-0,60	0,2333
L1cam	P11627	293	0,35	0,3255
L1cam	P11627	1073	0,07	0,7099
L1cam	P11627	875	0,03	0,9441
L1cam	P11627	968	0,01	0,9630
Lama1	P19137	2046	1,33	0,0990
Lama1	P19137	1344	0,82	0,0869
Lama1	P19137	1659	-0,31	0,1156
Lama1	P19137	2526	1,14	0,1694
Lama1	P19137	1812	0,63	0,3814
Lama1	P19137	2027	-0,13	0,6542
Lama2	Q60675	2024	0,38	0,1891
Lama2	Q60675	1610	0,18	0,4377
Lama2	Q60675	1806	0,07	0,6854
Lama2	Q60675	2013	0,02	0,9695
Lama2	Q60675	1897	-0,03	0,9744
Lama4	P97927	780	0,94	0,3299
Lama4	P97927	550	-0,20	0,3526
Lama4	P97927	735	0,15	0,5382
Lamb1	P02469	1279	-0,87	0,2635
Lamb1	P02469	1643	0,10	0,8895
Lamb1	P02469	1336	1,35	0,1705
Lamb1	P02469	1343	1,35	0,1705
Lamb1	P02469	677	0,45	0,4725
Lamb1	P02469	1542	0,08	0,8527
Lamb2	Q61292	1309	1,55	0,0123
Lamc1	P02468	1105	ND	ND
Lamc1	P02468	1221	-0,43	0,0149
Lamc1	P02468	648	-0,23	0,0663
Lamc1	P02468	1020	-0,19	0,6098
Lamc3	Q9R0B6	1514	-0,76	0,4099
Lamc3	Q9R0B6	1196	0,18	0,5127
Lamp1	P11438	248	-1,58	0,0169
Lamp1	P11438	252	-1,58	0,0169
Lamp1	P11438	296	2,16	0,0042
Lamp1	P11438	97	-0,92	0,0333
Lamp1	P11438	296	-0,65	0,1140
Lamp1	P11438	311	-0,65	0,1140
Lamp1	P11438	115	1,21	0,1981
Lamp1	P11438	177	-0,18	0,3509
Lamp1	P11438	252	-0,04	0,6234
Lamp1	P11438	159	0,42	0,6245
Lamp2	P17047-3	156	-0,74	0,1791
Lamp2	P17047-3	361	-0,11	0,5241
Lamp2	P17047-3	322	0,14	0,7300
Large	Q9Z1M7	122	0,06	0,8135
Lcat	P16301	44	0,66	0,4998
Leprel4	Q8K2B0	367	-0,01	0,9872
Lgals3bp	Q07797	543	-0,52	0,2952
Lgi1	Q9JIA1	277	-0,73	0,2414
Lgi1	Q9JIA1	422	-0,03	0,9573
Lgi2	Q8K4Z0-2	268	-0,12	0,8470
Lgmn	O89017	265	5,97	0,0000
Lgmn	O89017	265	-0,17	0,3825
Lgmn	O89017	274	-0,17	0,3825
Lifr	P42703-2	385	-0,17	0,7856
Lingo1	Q9D1T0	138	-0,51	0,1307
Lingo1	Q9D1T0	536	-0,08	0,8428
Lingo2	Q3URE9	130	1,14	0,0774
Lipa	Q9Z0M5	159	0,26	0,6896
Lman2	Q9DBH5	185	-0,62	0,1470
Lnpep	Q8C129	256	ND	ND
Lnpep	Q8C129	215	1,67	0,0013
Lnpep	Q8C129	682	-1,93	0,0136
Lnpep	Q8C129	447	-0,35	0,1583
Lnpep	Q8C129	525	0,75	0,3102
Lnpep	Q8C129	145	-0,13	0,4474
Lphn1	Q80TR1-2	355	0,12	0,5706
Lphn1	Q80TR1-2	624	0,13	0,8155
Lphn1	Q80TR1-2	629	0,13	0,8155
Lphn2	Q8JZZ7	524	0,25	0,6176
Lphn2	Q8JZZ7	735	-0,07	0,8434
Lphn3	Q80TS3-4	601	0,14	0,3352
Lphn3	Q80TS3-4	646	-0,07	0,9360
Lppr1	Q8BFZ2-2	150	-23,67	ND
Lrfn4	Q80XU8	376	-0,56	0,2657
Lrig1	P70193	76	-0,77	0,1756
Lrig2	Q52KR2	172	-1,09	0,0557
Lrp1	Q91ZX7	3058	-20,80	ND
Lrp1	Q91ZX7	1826	ND	ND
Lrp1	Q91ZX7	2118	ND	ND
Lrp1	Q91ZX7	3789	ND	ND
Lrp1	Q91ZX7	3664	ND	ND
Lrp1	Q91ZX7	3954	-0,81	0,1553
Lrp1	Q91ZX7	4365	-2,97	0,1996
Lrp1	Q91ZX7	447	0,20	0,8061
Lrp1	Q91ZX7	730	-0,85	0,0002
Lrp1	Q91ZX7	1734	2,01	0,0064
Lrp1	Q91ZX7	3049	-0,87	0,0124
Lrp1	Q91ZX7	3840	-0,69	0,0127
Lrp1	Q91ZX7	2128	-0,52	0,0315
Lrp1	Q91ZX7	1724	-1,78	0,0665
Lrp1	Q91ZX7	1734	-1,78	0,0665
Lrp1	Q91ZX7	4076	-0,34	0,2289
Lrp1	Q91ZX7	1559	-0,29	0,3345
Lrp1	Q91ZX7	2473	0,31	0,5488
Lrp1	Q91ZX7	1576	0,10	0,6416
Lrp1	Q91ZX7	137	-0,21	0,6804
Lrp1	Q91ZX7	3663	-0,34	0,6922
Lrp1	Q91ZX7	4126	-0,29	0,7163
Lrp1	Q91ZX7	240	-0,20	0,7936
Lrp1	Q91ZX7	1764	0,04	0,8578
Lrp1	Q91ZX7	3334	0,06	0,8781
Lrp1	Q91ZX7	2621	0,01	0,9899

Gene names	Protein Uniprot ID	Position within protein	Levels in the mutant (log2)	p-value
Lrp1b	Q9JI18	3310	-1,98	0,0536
Lrp1b	Q9JI18	1145	-0,71	0,0746
Lrp1b	Q9JI18	3164	-0,01	0,9680
Lrp4	Q8VI56-2	501	ND	ND
Lrpap1	P55302	271	-0,04	0,8407
Lrrc25	Q8K1T1	133	0,60	0,3910
Lrrc36	Q3V0M2-2	334	-0,54	0,0434
Lrrc4	Q99PH1	409	-1,59	0,0331
Lrrc4	Q99PH1	362	-0,40	0,0401
Lrrc4b	P0C192	226	ND	ND
Lrrc8a	Q80WG5	83	-1,39	0,0005
Lrrc8a	Q80WG5	66	-0,08	0,5564
Lrrc8b	Q5DU41-2	78	0,26	0,1467
Lrrd1	Q8C0R9	211	1,06	0,0859
Lrrn1	Q61809	517	-0,72	0,0138
Lrrtm2	Q8BGA3	57	-0,85	0,2552
Lsamp	Q8BLK3	40	0,28	0,6858
Lsamp	Q8BLK3	287	3,20	0,0000
Lsamp	Q8BLK3	279	-0,52	0,2005
Lsamp	Q8BLK3	287	-0,52	0,2005
Ly75	Q60767	1594	ND	ND
Ly75	Q60767	135	0,19	0,7873
Ly75	Q60767	1104	-0,12	0,8267
Ly75	Q60767	865	0,25	0,4086
Lyve1	Q8BHC0	52	0,53	0,5867
M6pr	P24668	117	ND	ND
M6pr	P24668	108	-1,36	0,0742
M6pr	P24668	114	-0,70	0,4462
M6pr	P24668	84	-0,23	0,4639
Mag	P20917-2	450	-0,25	0,5921
Mag	P20917-2	454	-0,25	0,5921
Mag	P20917-2	99	-0,37	0,6128
Man2a2	Q8BRK9	1095	0,25	0,2195
Man2b1	O09159	693	1,15	0,3767
Man2b1	O09159	367	0,17	0,4162
Man2b1	O09159	497	-0,09	0,7417
Manba	Q8K2I4	77	-22,15	ND
Mbtps1	Q9WTZ2	148	0,29	0,5645
Mcam	Q8R2Y2-2	58	-0,11	0,3383
Mdga1	Q0PMG2	811	ND	ND
Mdga1	Q0PMG2	235	-0,24	0,3121
Mdga1	Q0PMG2	307	0,09	0,5590
Mdga1	Q0PMG2	90	0,16	0,7169
Mdga1	Q0PMG2	331	0,13	0,7780
Mdga2	P60755	92	-0,89	0,0224
Mdga2	P60755	610	-0,33	0,3354
Megf8	P60882	1271	0,28	0,7646
Megf8	P60882	810	-0,52	0,2017
Megf9	Q8BH27	302	ND	ND
Megf9	Q8BH27	303	ND	ND
Megf9	Q8BH27	357	-0,23	0,5649
Megf9	Q8BH27	426	0,20	0,7612
Mettl9	Q9EPL4	35	0,22	0,5789
Mfap4	Q9D1H9	139	-0,58	0,1138
Mfge8	P21956-2	279	-0,20	0,6690
Mfge8	P21956-2	280	-0,20	0,6690
Mgat3	Q10470	263	0,56	0,4157
Mgat5b	Q765H6	236	-3,08	0,0003
Mgat5b	Q765H6	93	1,52	0,0595
Mgat5b	Q765H6	127	0,39	0,1845
Mia3	Q8BI84	252	ND	ND
Minpp1	Q9Z2L6	236	0,47	0,1742
Mpzl1	Q3TEW6-2	50	-0,36	0,0163
Mrc1	Q61830	1204	0,77	0,2219
Mrc1	Q61830	104	0,23	0,6037
Mrc2	Q64449	68	ND	ND
Mrc2	Q64449	363	0,11	0,4174
Naga	Q9QWR8	201	2,82	0,3469
Naga	Q9QWR8	177	0,71	0,0736
Ncam1	P13595	450	-3,76	0,1917
Ncam1	P13595	453	1,15	0,3604
Ncam2	O35136	168	-1,54	0,0669
Ncam2	O35136	177	-1,19	0,0671
Ncam2	O35136	177	-0,92	0,0315
Ncam2	O35136	219	0,61	0,0997
Ncam2	O35136	474	-0,24	0,6645
Ncan	P55066	121	-0,33	0,0761
Ncan	P55066	1175	-1,36	0,2248
Ncln	Q8VCM8	428	-0,02	0,8982
Ncstn	P57716	529	-0,82	0,0908
Ncstn	P57716	434	1,16	0,1918
Ncstn	P57716	611	-0,71	0,2745
Ncstn	P57716	386	-0,71	0,3580
Ncstn	P57716	561	0,67	0,4202
Ncstn	P57716	572	0,67	0,4202
Ncstn	P57716	128	-0,15	0,8223
Ncstn	P57716	54	0,11	0,8248
Negr1	Q80Z24	280	0,21	0,3242
Negr1	Q80Z24	288	0,21	0,3242
Nell2	Q61220	56	-0,44	0,1713
Neo1	P97798-5	501	-2,12	0,0013
Neo1	P97798-5	520	-2,33	0,0260
Neo1	P97798-5	746	-0,63	0,1107
Neo1	P97798-5	84	0,71	0,1107
Nfasc	Q810U3	305	-0,69	0,0100
Nfasc	Q810U3	866	-0,31	0,1788
Nfasc	Q810U3	881	-0,22	0,2384
Nfasc	Q810U3	1015	0,06	0,8617
Nfasc	Q810U3	483	0,03	0,9544
Nid2	O88322	681	0,86	0,0040
Nkain1	Q9D035	100	1,35	0,2497
Nomo1	Q6GQT9	42	-21,14	ND
Nomo1	Q6GQT9	361	-0,57	0,0166
Npc1	O35604	185	-0,53	0,0614
Npc1	O35604	1063	0,92	0,2201
Npc1	O35604	868	-0,42	0,5332
Npc1	O35604	414	0,18	0,7267
Nptn	P97300-3	80	ND	ND
Nptn	P97300-3	167	2,67	0,0847
Nptn	P97300-3	112	0,14	0,6904
Nptx2	O70340	146	ND	ND
Nrap	Q80XB4-3	403	0,13	0,7914
Nrcam	Q810U4-2	700	ND	ND
Nrcam	Q810U4-2	217	3,16	0,2899
Nrcam	Q810U4-2	77	0,98	0,3599

Gene names	Protein Uniprot ID	Position within protein	Levels in the mutant (log2)	p-value
Nrcam	Q810U4-2	427	-1,12	0,0022
Nrcam	Q810U4-2	786	-0,83	0,0077
Nrcam	Q810U4-2	501	-0,76	0,0102
Nrcam	Q810U4-2	270	-0,72	0,0371
Nrcam	Q810U4-2	308	-0,34	0,0822
Nrcam	Q810U4-2	842	0,27	0,2373
Nrcam	Q810U4-2	1003	-0,36	0,5413
Nrp1	P97333	522	-0,44	0,0240
Nrp1	P97333	150	0,66	0,0410
Nrp1	P97333	261	0,28	0,3276
Nrp2	O35375-5	152	-0,48	0,1612
Nrp2	O35375-5	157	-0,48	0,1612
Nrxn1	Q9CS84-4	190	-0,30	0,4143
Nrxn1	Q9CS84-4	125	-0,28	0,5793
Ntm	Q99PJ0	44	0,41	0,6876
Ntm	Q99PJ0	284	0,26	0,7219
Ntm	Q99PJ0	292	0,26	0,7219
Ntn3	Q9R1A3	387	ND	ND
Ntng1	Q8R4G0-6	320	-0,05	0,9173
Ntrk2	P15209-2	325	-2,02	0,0192
Ntrk2	P15209-2	178	-1,08	0,1914
Ntrk2	P15209-2	254	-1,21	0,0008
Ntrk2	P15209-2	205	-1,00	0,0011
Ntrk2	P15209-2	241	-1,11	0,1454
Ntrk2	P15209-2	95	-0,39	0,2074
Ntrk2	P15209-2	67	0,09	0,8578
Ntrk3	Q6VNS1-3	388	0,67	0,1986
Ntrk3	Q6VNS1-3	163	0,73	0,2288
Nudcd2	Q9CQ48	144	-1,60	0,0087
Nup210	Q9QY81	1135	-1,11	0,0399
Nup210	Q9QY81	44	1,51	0,1174
Nup210	Q9QY81	1441	0,96	0,2645
Ogfod3	Q9D136	263	-0,14	0,5776
Olfm1	O88998-3	260	-1,10	0,0465
Olfm1	O88998-3	279	-0,68	0,3599
Olfm1	O88998-3	75	0,08	0,7067
Omg	Q63912	103	-1,32	0,0449
Omg	Q63912	152	-0,99	0,0983
Omg	Q63912	234	0,20	0,7974
Os9	Q8K2C7-2	177	ND	ND
Ostm1	Q8BGT0	234	-0,46	0,6628
Ostm1	Q8BGT0	139	-0,83	0,2657
P2rx4	Q9JJX6-3	75	ND	ND
P2rx4	Q9JJX6-3	208	0,03	0,9060
P2rx7	Q9Z1M0	187	-0,26	0,1895
P2rx7	Q9Z1M0	74	-0,47	0,3184
P2rx7	Q9Z1M0	213	-0,14	0,5795
P4ha1	Q60715-2	113	1,62	0,1804
Panx1	Q9JIP4	254	-1,06	0,0112
Pbxip1	Q3TVI8	455	-0,20	0,6422
Pcdhga4	O88689-3	893	-20,40	ND
Pcsk2	P21661	374	1,25	0,0400
Pcsk2	P21661	523	-0,23	0,6073
Pcyox1	Q9CQF9	353	ND	ND
Pcyox1	Q9CQF9	323	0,38	0,6636
Pcyox1	Q9CQF9	196	-0,07	0,8652
Pdgfrb	P05622	467	-0,45	0,1303
Pdia3	P27773	90	-1,79	0,0170
Pecam1	Q08481-2	141	1,54	0,0112
Pecam1	Q08481-2	74	0,78	0,2932
Pecam1	Q08481-2	360	0,14	0,8270
Pgap1	Q3UUQ7	363	-0,93	0,0049
Pgap1	Q3UUQ7	558	-0,44	0,1886
Pgap1	Q3UUQ7	234	0,03	0,9457
Pign	Q9R1S3-2	128	ND	ND
Pign	Q9R1S3-2	191	-0,78	0,2316
Pign	Q9R1S3-2	192	-0,78	0,2316
Pigs	Q6PD26	370	0,07	0,6932
Pigt	Q8BXQ2	168	ND	ND
Piwil1	Q9JMB7	857	ND	ND
Pla2g15	Q8VEB4	398	0,82	0,2184
Pla2g15	Q8VEB4	289	-0,16	0,5820
Pld4	Q8BG07-2	239	1,09	0,0102
Plod1	Q9R0E2	539	-0,03	0,8405
Plod2	Q9R0B9	696	0,26	0,6457
Pltp	P55065	398	-0,47	0,2447
Pltp	P55065	245	-0,32	0,1125
Pltp	P55065	143	-0,22	0,4270
Pltp	P55065	64	0,28	0,5599
Plxdc1	Q91ZV7	81	-1,46	0,1176
Plxna2	P70207	163	-0,43	0,0413
Plxna3	P70208	60	-0,30	0,0768
Plxna3	P70208	1074	-0,13	0,7151
Plxna4	Q80UG2	1006	0,49	0,1405
Plxna4	Q80UG2	441	-0,35	0,2489
Plxnb1	Q8CJH3	543	ND	ND
Plxnb1	Q8CJH3	1251	0,26	0,1096
Plxnb2	B2RXS4	1103	-2,24	0,0006
Plxnb2	B2RXS4	451	-1,26	0,0133
Plxnb2	B2RXS4	1005	-0,55	0,1590
Plxnb2	B2RXS4	127	-0,69	0,3567
Plxnb2	B2RXS4	393	-0,68	0,3586
Plxnb2	B2RXS4	761	0,59	0,4098
Plxnb2	B2RXS4	919	0,18	0,6240
Plxnb2	B2RXS4	1053	0,01	0,9638
Plxnb3	Q9QY40	889	0,18	0,5577
Plxnc1	Q9QZC2	141	-1,84	0,0157
Plxnc1	Q9QZC2	143	-1,84	0,0157
Plxnc1	Q9QZC2	407	-0,63	0,0205
Plxnc1	Q9QZC2	717	-1,17	0,2006
Plxnc1	Q9QZC2	896	-0,21	0,6405
Plxnc1	Q9QZC2	901	-0,21	0,6405
Plxnd1	Q3UH93	1120	ND	ND
Plxnd1	Q3UH93	1134	ND	ND
Plxnd1	Q3UH93	585	0,85	0,2840
Podxl2	Q8CAE9-3	330	0,67	0,4501
Pofut1	Q91ZW2	165	-0,74	0,0759
Pofut2	Q8VHI3	259	-0,47	0,2475
Poglut1	Q8BYB9	53	-0,12	0,7935
Pomt1	Q8R2R1	471	-0,52	0,3075
Pomt2	Q8BGQ4-2	98	-0,48	0,0194
Pomt2	Q8BGQ4-2	583	0,13	0,6660
Pon2	Q62086	254	-1,15	0,0101
Pon2	Q62086	323	0,37	0,5098
Postn	Q62009-5	601	-0,01	0,9594

Gene names	Protein Uniprot ID	Position within protein	Levels in the mutant (log2)	p-value
Ppib	P24369	148	-20,79	ND
Ppm1l	Q8BHN0	117	0,49	0,1629
Ppt1	O88531	197	0,98	0,0921
Ppt1	O88531	212	-1,05	0,1028
Ppt2	O35448	289	-0,36	0,5121
Ppt2	O35448	60	-0,12	0,9335
Prkcsh	O08795	72	-1,66	0,0087
Prnp	P04925	196	-0,90	0,0001
Prom1	O54990-6	323	-0,73	0,1905
Prom1	O54990-6	282	-0,84	0,3646
Prom1	O54990-6	264	0,35	0,5542
Psap	Q61207	333	ND	ND
Psap	Q61207	214	0,56	0,0077
Psap	Q61207	334	0,46	0,0378
Psap	Q61207	80	-0,33	0,1198
Psap	Q61207	459	-0,01	0,9761
Ptchd1	Q14B62	77	-1,28	0,0922
Ptdss2	Q9Z1X2-2	159	-0,54	0,0015
Ptgfrn	Q9WV91	600	-1,02	0,0139
Ptgfrn	Q9WV91	618	0,36	0,5726
Ptgfrn	Q9WV91	300	0,15	0,7438
Ptk7	Q8BKG3	98	ND	ND
Ptk7	Q8BKG3	108	-0,54	0,0395
Ptk7	Q8BKG3	559	-0,78	0,2155
Ptma	P26350	29	-0,36	0,2144
Ptprc	P06800-3	287	1,66	0,0162
Ptprc	P06800-3	288	1,66	0,0162
Ptprd	Q64487-1	714	0,29	0,6178
Ptprf	A2A8L5	941	0,53	0,5823
Ptprf	A2A8L5	721	0,02	0,9552
Ptprg	Q05909	444	1,18	0,0716
Ptprg	Q05909	113	0,26	0,3106
Ptprj	Q64455	78	ND	ND
Ptprj	Q64455	267	-0,91	0,0006
Ptprj	Q64455	437	-1,63	0,0084
Ptprj	Q64455	313	-0,76	0,0088
Ptprj	Q64455	317	-0,76	0,0088
Ptprj	Q64455	668	-0,39	0,1396
Ptprj	Q64455	572	-0,61	0,2124
Ptprj	Q64455	576	-0,61	0,2124
Ptprm	P28828	249	ND	ND
Ptprm	P28828	131	-0,44	0,1253
Ptprn	Q60673	524	-0,24	0,5936
Ptprn2	P80560	550	ND	ND
Ptpro	E9Q612	154	-0,06	0,7223
Ptprs	B0V2N1-6	674	0,20	0,5891
Ptprz1	B9EKR1	317	ND	ND
Ptprz1	B9EKR1	324	ND	ND
Ptprz1	B9EKR1	105	ND	ND
Ptprz1	B9EKR1	223	-0,84	0,0046
Ptprz1	B9EKR1	552	-1,49	0,0212
Ptprz1	B9EKR1	232	-1,52	0,0478
Ptprz1	B9EKR1	134	-1,35	0,0486
Ptprz1	B9EKR1	685	0,43	0,2339
Ptprz1	B9EKR1	1058	-0,23	0,3055
Ptprz1	B9EKR1	501	0,16	0,8352
Pttg1ip	Q8R143	42	-0,49	0,0215
Pttg1ip	Q8R143	51	-0,03	0,9347
Pvrl1	Q9JKF6	202	2,10	0,0477
Pvrl2	P32507-2	315	0,99	0,3391
Pvrl2	P32507-2	128	0,30	0,6181
Pvrl2	P32507-2	138	0,30	0,6181
Pvrl3	Q9JLB9	186	0,82	0,1030
Pvrl3	Q9JLB9	83	0,54	0,3941
Pxdn	Q3UQ28	1277	ND	ND
Pxdn	Q3UQ28	1175	0,00	0,9932
Ramp2	Q9WUP0	99	ND	ND
Rcn1	Q05186	47	-0,93	0,0161
Reln	Q60841-3	1600	-1,97	0,0285
Reln	Q60841-3	290	0,42	0,0974
Reln	Q60841-3	291	0,42	0,0974
Reln	Q60841-3	3016	-0,22	0,2578
Reln	Q60841-3	306	-0,25	0,3236
Rfx4	Q7TNK1-4	89	ND	ND
Rgma	Q6PCX7-2	99	-0,81	0,1002
Rnaset2	Q9CQ01	80	-1,42	0,0006
Rnf13	O54965-2	88	ND	ND
Rnf13	O54965-2	75	-0,70	0,2058
Rnf130	Q8VEM1	135	-0,59	0,2152
Robo1	O89026	781	0,23	0,3516
Robo2	Q7TPD3-2	123	0,91	0,3458
Robo2	Q7TPD3-2	786	-0,37	0,4270
Ror2	Q9Z138	318	ND	ND
Rpn2	Q9DBG6	106	-1,69	0,0005
Rtn4r	Q99PI8	179	-0,14	0,8451
Rufy3	Q9D394	303	-27,82	ND
Rufy3	Q9D394	304	-27,82	ND
S1pr3	Q9Z0U9	15	0,04	0,9658
Scap	Q6GQT6	590	-0,81	0,0542
Scara3	Q8C850	430	-0,57	0,3169
Scarb1	Q61009	383	-0,65	0,3721
Scarb2	O35114	224	-1,18	0,0160
Scarb2	O35114	209	-0,74	0,0605
Scarb2	O35114	412	-0,91	0,1526
Scarb2	O35114	206	-0,66	0,2144
Scarb2	O35114	249	0,50	0,2816
Scarb2	O35114	105	0,06	0,7730
Scarb2	O35114	45	-0,05	0,9261
Scn1b	P97952	93	ND	ND
Scn1b	P97952	135	0,47	0,0651
Scn3b	Q8BHK2	95	-0,56	0,1339
Scube2	Q9JJS0	759	ND	ND
Scube2	Q9JJS0	788	ND	ND
Scube2	Q9JJS0	798	ND	ND
Scube2	Q9JJS0	529	0,16	0,5781
Sdk2	Q6V4S5	581	-0,39	0,6548
Sdk2	Q6V4S5	1579	1,04	0,1449
Sdk2	Q6V4S5	1260	-0,63	0,1690
Sel1l	Q9Z2G6-2	218	-1,59	0,0134
Sel1l	Q9Z2G6-2	554	-1,06	0,1550
Sel1l	Q9Z2G6-2	377	-0,24	0,2746
Sel1l3	Q80TS8-2	665	-0,38	0,4794
Sema4b	Q62179	56	ND	ND
Sema4c	Q64151	419	-0,44	0,2415
Sema4c	Q64151	106	0,26	0,1528

Gene names	Protein Uniprot ID	Position within protein	Levels in the mutant (log2)	p-value
Sema4d	O09126	419	-1,03	0,0308
Sema4d	O09126	379	-0,18	0,3760
Sema4g	Q9WUH7	55	0,18	0,3478
Sema4g	Q9WUH7	386	0,56	0,4473
Sema4g	Q9WUH7	596	0,00	0,9968
Sema6a	O35464-3	461	-0,64	0,1192
Sema6a	O35464-3	434	-0,85	0,1433
Sema6d	Q76KF0-3	461	ND	ND
Sema7a	Q9QUR8	328	-0,60	0,4657
Sema7a	Q9QUR8	256	0,00	0,9908
Sepp1	P70274	83	0,41	0,1165
Serpina1c	Q00896	101	0,86	0,0226
Serpinc1	P32261	225	-0,22	0,2070
Serpinh1	P19324	119	1,14	0,0503
Serpini1	O35684	157	-1,60	0,0096
Serpini1	O35684	321	1,03	0,1782
Sez6l	Q6P1D5-2	414	-0,87	0,1172
Sez6l	Q6P1D5-2	268	-0,78	0,3425
Sez6l	Q6P1D5-2	454	-0,10	0,8975
Sfrp1	Q8C4U3	173	-0,68	0,3166
Sgcb	P82349	213	0,24	0,3293
Sgce	O70258	200	0,02	0,9630
Sgtb	Q8VD33	167	-0,22	0,8739
Shisa7	Q8C3Q5-2	62	0,29	0,3111
Shisa9	Q9CZN4-4	45	-0,10	0,8100
Sidt2	Q8CIF6	165	0,02	0,9765
Sil1	Q9EPK6	197	0,17	0,8017
Sirpa	P97797-2	205	ND	ND
Sirpa	P97797-2	209	ND	ND
Sirpa	P97797-2	246	-0,24	0,6858
Slc12a4	Q9JIS8	312	-1,20	0,0375
Slc12a4	Q9JIS8	331	0,59	0,4642
Slc12a5	Q91V14-2	328	ND	ND
Slc12a5	Q91V14-2	310	ND	ND
Slc12a5	Q91V14-2	338	-0,21	0,4328
Slc12a5	Q91V14-2	339	-0,21	0,4328
Slc12a5	Q91V14-2	291	-0,43	0,4372
Slc12a6	Q924N4-2	328	ND	ND
Slc12a6	Q924N4-2	347	-0,26	0,2920
Slc12a9	Q99MR3	243	0,75	0,4242
Slc13a5	Q67BT3	566	-0,37	0,2738
Slc17a6	Q8BLE7	100	ND	ND
Slc17a6	Q8BLE7	101	ND	ND
Slc1a2	P43006	205	0,31	0,2721
Slc1a2	P43006	215	-0,07	0,8207
Slc1a4	O35874	201	3,51	0,0004
Slc1a4	O35874	201	-0,72	0,3348
Slc1a4	O35874	206	-0,72	0,3348
Slc22a5	Q9Z0E8	91	0,33	0,2987
Slc22a5	Q9Z0E8	64	0,45	0,6475
Slc25a21	Q8BZ09	182	-0,36	0,6953
Slc29a1	Q9JIM1-2	48	-0,25	0,2467
Slc2a1	P17809	45	0,66	0,4887
Slc2a13	Q3UHK1	447	0,10	0,6688
Slc2a3	P32037	43	-0,55	0,2007
Slc30a1	Q60738	294	0,23	0,7283
Slc39a14	Q75N73-2	85	0,69	0,2963
Slc39a14	Q75N73-2	100	0,69	0,2963
Slc39a14	Q75N73-2	52	0,07	0,9119
Slc39a6	Q8C145	275	0,18	0,3210
Slc39a6	Q8C145	68	0,25	0,6068
Slc3a2	P10852-2	424	0,94	0,0593
Slc3a2	P10852-2	438	0,94	0,0593
Slc3a2	P10852-2	205	-1,05	0,1105
Slc3a2	P10852-2	438	-0,04	0,9601
Slc3a2	P10852-2	298	0,02	0,9810
Slc44a1	Q6X893	134	0,41	0,6023
Slc44a2	Q8BY89-2	198	2,12	0,3540
Slc46a1	Q6PEM8	58	-0,52	0,4647
Slc6a17	Q8BJI1	186	-0,17	0,1045
Slc6a17	Q8BJI1	393	0,89	0,2442
Slc6a2	O55192	192	-0,94	0,0116
Slc7a1	Q09143	223	-0,61	0,0151
Slc7a1	Q09143	229	-0,93	0,0260
Slc9a7	Q8BLV3-2	145	0,26	0,1935
Slitrk2	Q810C0	422	-0,26	0,1344
Smpd1	Q04519	333	ND	ND
Smpd1	Q04519	518	0,53	0,3251
Sod3	O09164	121	1,18	0,0919
Sorcs1	Q9JLC4-2	775	0,91	0,0985
Sorcs1	Q9JLC4-2	774	0,37	0,3960
Sorcs3	Q8VI51	786	ND	ND
Sorl1	O88307	1164	ND	ND
Sorl1	O88307	871	1,67	0,0977
Sorl1	O88307	1895	-1,92	0,1770
Sorl1	O88307	1733	-0,65	0,0044
Sorl1	O88307	1855	-0,15	0,6168
Sorl1	O88307	1987	-0,09	0,8909
Sort1	Q6PHU5	160	ND	ND
Sort1	Q6PHU5	161	ND	ND
Sort1	Q6PHU5	272	-0,60	0,3347
Sort1	Q6PHU5	404	-0,25	0,5873
Sparcl1	P70663	462	-0,27	0,1802
Spock2	Q9ER58	286	ND	ND
Spock2	Q9ER58	225	2,10	0,0189
Spock3	Q8BKV0-2	287	-1,02	0,0027
Spon1	Q8VCC9	214	-25,09	ND
Sppl2a	Q9JJF9	119	ND	ND
Sppl2a	Q9JJF9	61	-0,87	0,4560
Sppl2a	Q9JJF9	69	-0,87	0,4560
Sppl2b	Q3TD49-2	379	0,26	0,7245
Ssr1	Q9CY50	191	-0,99	0,4937
Ssr1	Q9CY50	136	0,55	0,3637
Ssr2	Q9CPW5	88	-0,22	0,3065
St3gal5	O88829-2	224	-0,24	0,7122
St8sia2	O35696	60	0,04	0,9053
St8sia3	Q64689	206	0,43	0,4337
Stab1	Q8R4Y4-2	1011	1,17	0,0646
Stab1	Q8R4Y4-2	1171	-0,29	0,1299
Stab1	Q8R4Y4-2	1180	-0,55	0,2359
Stab1	Q8R4Y4-2	713	0,15	0,7509
Stab1	Q8R4Y4-2	1179	-0,07	0,7770
Stim1	P70302	171	0,03	0,8578
Stt3a	P46978	544	ND	ND
Stt3a	P46978	549	ND	ND

Gene names	Protein Uniprot ID	Position within protein	Levels in the mutant (log2)	p-value
Stt3a	P46978	537	-0,67	0,3217
Stt3a	P46978	548	0,52	0,5862
Stt3b	Q3TDQ1	638	-0,48	0,0095
Stt3b	Q3TDQ1	624	-0,40	0,2357
Suco	Q8C341	529	-0,57	0,3653
Suco	Q8C341	523	-0,78	0,0255
Sulf2	Q8CFG0	241	0,06	0,8658
Sumf1	Q8R0F3	139	0,28	0,0259
Sun1	Q9D666-2	711	-1,70	0,0006
Sun2	Q8BJS4-3	618	-0,28	0,2192
Susd2	Q9DBX3-2	39	0,73	0,1184
Sv2a	Q9JIS5	573	0,76	0,3176
Sv2a	Q9JIS5	548	-0,20	0,5759
Sv2a	Q9JIS5	498	0,43	0,8335
Sv2b	Q8BG39	516	0,38	0,4956
Sv2b	Q8BG39	491	-0,05	0,7840
Sv2c	Q69ZS6	534	ND	ND
Sv2c	Q69ZS6	559	0,03	0,9454
Sv2c	Q69ZS6	565	0,03	0,9454
Synpr	Q8BGN8-2	53	-0,46	0,1543
Synpr	Q8BGN8-2	58	-0,95	0,4516
Syp	Q62277	59	-0,10	0,5035
Sypl1	O09117-2	77	-1,32	0,1091
Sypl1	O09117-2	54	0,47	0,3664
Tapbpl	Q8VD31	270	0,46	0,5915
Tctn2	Q2MV57-2	512	0,50	0,3817
Tenm2	Q9WTS5	1983	ND	ND
Tenm2	Q9WTS5	1257	ND	ND
Tenm2	Q9WTS5	1762	0,14	0,8274
Tenm2	Q9WTS5	938	1,08	0,0644
Tenm2	Q9WTS5	1763	0,62	0,2281
Tenm2	Q9WTS5	443	0,29	0,6244
Tenm3	Q9WTS6	869	-2,03	0,0066
Tenm3	Q9WTS6	380	0,86	0,0932
Tenm3	Q9WTS6	1656	-0,02	0,9306
Tenm4	Q3UHK6	2190	0,99	0,1076
Tf	Q921I1	513	-0,61	0,3925
Tfrc	Q62351	730	ND	ND
Tfrc	Q62351	725	1,31	0,6080
Tfrc	Q62351	730	1,31	0,6080
Tgfbr3	O88393	570	0,18	0,7615
Thsd7a	Q69ZU6	1354	-0,51	0,0487
Thsd7a	Q69ZU6	1488	-0,09	0,7005
Thy1	P01831	94	-0,11	0,5835
Thy1	P01831	118	0,07	0,9137
Tlr2	Q9QUN7	442	0,59	0,2745
Tm2d1	Q99MB3	198	0,02	0,9648
Tm2d3	Q8BJ83-2	140	ND	ND
Tm2d3	Q8BJ83-2	152	-1,66	0,0447
Tm2d3	Q8BJ83-2	70	-0,38	0,0748
Tm2d3	Q8BJ83-2	105	-1,46	0,4228
Tm9sf1	Q9DBU0	178	ND	ND
Tm9sf3	Q9ET30	172	-0,76	0,0173
Tmed4	Q8R1V4	117	0,76	0,3790
Tmed9	Q99KF1	125	-0,40	0,0796
Tmeff1	Q6PFE7-3	55	ND	ND
Tmem106b	Q80X71	184	-0,25	0,6423
Tmem106c	Q80VP8	184	0,01	0,9943
Tmem131	O70472	1057	ND	ND
Tmem132a	Q922P8	67	ND	ND
Tmem145	Q8C4U2	109	0,40	0,4909
Tmem2	Q5FWI3	980	ND	ND
Tmem2	Q5FWI3	525	-0,42	0,1082
Tmem2	Q5FWI3	1234	-0,24	0,3336
Tmem206	Q9D771	155	-1,31	0,0776
Tmem206	Q9D771	162	-1,31	0,0776
Tmem245	B1AZA5	549	-1,27	0,1296
Tmem259	Q8CIV2	180	0,07	0,8922
Tmem30a	Q8VEK0	98	-0,81	0,0171
Tmem30a	Q8VEK0	107	-0,81	0,0171
Tmem30a	Q8VEK0	98	0,13	0,8141
Tmem62	Q8BXJ9	384	0,22	0,1222
Tmem87a	Q8BXN9-3	157	-0,79	0,0076
Tmem87a	Q8BXN9-3	160	-0,79	0,0076
Tmem87a	Q8BXN9-3	127	-0,18	0,4607
Tmem87a	Q8BXN9-3	79	0,46	0,4813
Tmem87a	Q8BXN9-3	62	-0,20	0,5072
Tmem9	Q9CR23	38	-1,82	0,0585
Tmem9	Q9CR23	47	-1,82	0,0585
Tmem9	Q9CR23	38	0,96	0,1226
Tmpo	Q61029	289	-2,10	0,0005
Tmtc4	Q8BG19	497	0,43	0,1944
Tmx3	Q8BXZ1	261	-0,37	0,2942
Tnc	Q80YX1	1394	1,54	0,5819
Tnc	Q80YX1	166	-0,97	0,0044
Tnc	Q80YX1	1301	1,43	0,1037
Tnr	Q8BYI9	55	-0,45	0,5048
Tnr	Q8BYI9	581	-0,42	0,5218
Tnr	Q8BYI9	470	0,21	0,6957
Tnr	Q8BYI9	869	0,07	0,8304
Tnr	Q8BYI9	874	0,07	0,8304
Tor1aip1	Q921T2	411	1,46	0,1636
Tor1b	Q9ER41	165	-0,98	0,0026
Tor1b	Q9ER41	64	-0,35	0,1757
Tor3a	Q9ER38	110	ND	ND
Tpbg	Q9Z0L0	124	-2,04	0,0054
Tpbg	Q9Z0L0	262	-0,52	0,2382
Tpbg	Q9Z0L0	281	0,51	0,5664
Tpcn1	Q9EQJ0	600	0,90	0,3531
Tpcn1	Q9EQJ0	612	-0,23	0,1881
Tpcn1	Q9EQJ0	617	-0,23	0,1881
Tpp1	O89023	442	0,09	0,7660
Tril	Q9DBY4	209	-0,87	0,1498
Tspan13	Q9D8C2	137	ND	ND
Tspan2	Q922J6	139	0,05	0,9481
Tspan3	Q9QY33	167	ND	ND
Tspan3	Q9QY33	152	0,82	0,0681
Tspan3	Q9QY33	183	0,30	0,4083
Tspan31	Q9CQ88	134	0,47	0,6088
Tspan31	Q9CQ88	109	-1,29	0,0547
Tspan31	Q9CQ88	117	-1,29	0,0547
Tspan6	O70401	134	-1,05	0,0423
Ttc17	E9PVB5-2	184	0,81	0,2078
Ttc17	E9PVB5-2	704	0,03	0,9691
Ttyh3	Q6P5F7-2	351	1,65	0,4717

Gene names	Protein Uniprot ID	Position within protein	Levels in the mutant (log2)	p-value
Ttyh3	Q6P5F7-2	144	0,73	0,0664
Txndc11	Q8K2W3	306	-0,86	0,0454
Txndc11	Q8K2W3	443	-0,32	0,3490
Txndc15	Q6P6J9	277	1,15	0,1827
Txndc15	Q6P6J9	165	-1,53	0,0013
Txndc15	Q6P6J9	171	-1,53	0,0013
Txndc15	Q6P6J9	165	1,14	0,1455
Txndc16	Q7TN22-2	461	-0,78	0,0064
Uggt1	Q6P5E4	269	ND	ND
Ugt8	Q64676	442	-0,54	0,6130
Ugt8	Q64676	78	0,10	0,9265
Unc5c	O08747	236	ND	ND
Vcam1	P29533	225	1,38	0,2356
Wbscr17	Q7TT15-2	50	-0,36	0,2130
Wbscr17	Q7TT15-2	459	-0,08	0,7281
Wfs1	P56695	748	-0,82	0,0323
Wnt5a	P22725-2	292	ND	ND
	P10404	58	-1,20	0,3237
	P10404	297	-1,12	0,1670
	Q3UZV7-3	619	-0,41	0,1881
	P03987-2	179	0,96	0,2010
	Q32M26	26	0,45	0,3052
	P10404	369	0,18	0,7423
	Q3UZV7-3	577	0,21	0,7550

Spread sheet 5. Sequon analysis in the comparative glycoproteomic dataset (Quantitative dataset)

	Total	NxS	NxT	NxS/NxT
Raw number	1404	541	783	1324
Percentage		38,53	55,77	94,30

Supplementary table 2. Glycoproteomics. All of the N-glycosylation sites detected in at least 2 out of 4 control samples are included and classified based on their presence in PMID: 20510933 or if they are predicted by uniprot (reference glycoproteomic dataset, spread sheet 1). Sequon analyses on the 1665 N-glycopeptides within the glycoproteomic dataset (spread sheet 2). Gene ontology analyses on the N-glycosylation sites within the reference glycoproteomic dataset predicted by uniprot and/or found in PMID: 20510933 and on the N-glycosylation sites not present in none of them (novel sites, spread sheet 3). 1404 N-glycopeptides detected in at least 3 out of 4 control samples and their corresponding abundance levels in the mutant samples (comparative glycoproteomics, spread sheet 4). Sequon analyses on the comparative glycoproteomics dataset (spread sheet 5).

Supplementary table 3. Total proteomics and glycoproteomics

N-glycosylated peptide in glycoproteomics					Not glycosylated peptide in total proteomics					
		Log2 glycopeptide intensity								
N-glycosylation site	Gene names	AV Control samples	AV Mutant samples	Levels of the glycosylated form of the peptide in the mutant samples (log2)	Not glycosylated peptide starting and ending position		Detected in x out of 4 control samples	Detected in x out of 4 mutant samples	Levels of the not glycosylated form of the peptide in the mutant samples (log2)	Not glycosylated form of the peptide T-test (two-tailed)
1103	Plxnb2	24,93	22,69	-2,24	1088	1109	0	4		
288	Cadm3	23,15	21,48	-1,67	276	289	2	4		
134	Ptprz1	26,46	25,11	-1,35	133	148	0	4		
427	Nrcam	25,34	24,22	-1,12	405	431	0	4		
205	Ntrk2	25,53	24,52	-1,00	201	212	0	4		
47	Rcn1	27,67	26,74	-0,93	32	60	2	4		
166	Tnc	26,02	25,05	-0,97	165	181	0	4		
232	Ptprz1	26,87	25,35	-1,52	228	250	1	4		
248	Lamp1	21,81	20,23	-1,58	246	267	0	4		
505	Dpp6	25,10	23,99	-1,11	399	428	0	4		
106	Rpn2	27,35	25,66	-1,69	77	109	0	4		
893	Pcdhga4	N-glycopeptide not detected in the mutant		-20,40	891	908	0	4		
150	Lppr1			-23,67	141	161	1	4		
148	Ppib			-20,79	146	158	4	4	-0,57	0,1691532
240	Cnn3	23,33	21,92	-1,42	233	251	4	4	-0,93	0,080150827
62	Hsp90b1	26,31	25,32	-0,99	44/52	67	4	4	0,09	0,777698548
270	Nrcam	21,90	21,18	-0,72	259	278	4	4	-1,78	0,066863331
305	Nfasc	23,69	23,00	-0,69	303	321	4	4	-0,16	0,776068856
104	Cadm1	26,39	25,29	-1,10	100	111	4	3	0,05	0,947542674
72	Prkcsh	20,87	19,21	-1,66	60	91	4	4	-0,15	0,762202098
90	Pdia3	20,87	19,08	-1,79	83	94	4	4	-1,10	0,158241079
289	Tmpo	21,84	19,73	-2,10	286	296	4	4	-0,75	0,044150347
299	Chl1	22,14	20,66	-1,48	297	305	4	4	-1,40	0,008432416
144	Nudcd2	21,89	20,29	-1,60	130	147	4	4	-1,20	0,001163364

The not glycosylated form of the peptide is only consistently detected (n≥3) in the mutant samples

Significant decrease of the not glycosylated form of the peptide in the mutant

Supplementary table 3. Total proteomics and glycoproteomics. List, normalized intensities and relative abundance of the 24 peptides detected in total proteomics and with decreased abundance in glycoproteomics in the mutant.

ANNEX 2 – PUBLICATIONS

1 – *Utility of whole exome sequencing for the early diagnosis of pediatric-onset cerebellar atrophy associated with developmental delay in an inbred population.* Orphanet Journal of Rare Diseases, 2016. Published, fourth author.

2 – *WDR81 mutations cause extreme microcephaly and impair mitotic progression in human fibroblasts and Drosophila neural stem cells.* Brain, a journal of neurology, 2017. Published, fourth author.

3 – *De novo mutation screening in childhood-onset cerebellar atrophy identifies gain of function mutations in the calcium channel CACNA1G .* Brain, a journal of neurology, 2018. Accepted, sixth author.

4 - *High N-glycan multiplicity is critical for neuronal adhesion and sensitizes the developing cerebellum to N-glycosylation defect*. eLife, 2018. Under revision, first author.

Megahed et al. Orphanet Journal of Rare Diseases (2016) 11:57
DOI 10.1186/s13023-016-0436-9

Orphanet Journal of Rare Diseases

RESEARCH Open Access

Utility of whole exome sequencing for the early diagnosis of pediatric-onset cerebellar atrophy associated with developmental delay in an inbred population

Hisham Megahed[1†], Michaël Nicouleau[2,3†], Giulia Barcia[2,3,9], Daniel Medina-Cano[2,3], Karine Siquier-Pernet[2,3], Christine Bole-Feysot[4], Mélanie Parisot[4], Cécile Masson[5], Patrick Nitschké[5], Marlène Rio[3,6,9], Nadia Bahi-Buisson[3,7], Isabelle Desguerre[3,8], Arnold Munnich[3,9], Nathalie Boddaert[3,10], Laurence Colleaux[2,3] and Vincent Cantagrel[2,3*]

Abstract

Background: Cerebellar atrophy and developmental delay are commonly associated features in large numbers of genetic diseases that frequently also include epilepsy. These defects are highly heterogeneous on both the genetic and clinical levels. Patients with these signs also typically present with non-specific neuroimaging results that can help prioritize further investigation but don't suggest a specific molecular diagnosis.

Methods: To genetically explore a cohort of 18 Egyptian families with undiagnosed cerebellar atrophy identified on MRI, we sequenced probands and some non-affected family members via high-coverage whole exome sequencing (WES; >97 % of the exome covered at least by 30x). Patients were mostly from consanguineous families, either sporadic or multiplex. We analyzed WES data and filtered variants according to dominant and recessive inheritance models.

Results: We successfully identified disease-causing mutations in half of the families screened (9/18). These mutations are located in seven different genes, *PLA2G6* being the gene most frequently mutated ($n = 3$). We also identified a recurrent de novo mutation in the *KIF1A* gene and a molybdenum cofactor deficiency caused by the loss of the start codon in the MOCS2A open-reading frame in a mildly affected subject.

Conclusions: This study illustrates the necessity of screening for dominant mutations in WES data from consanguineous families. Our identification of a patient with a mild and improving phenotype carrying a previously characterized severe loss of function mutation also broadens the clinical spectrum associated with molybdenum cofactor deficiency.

Keywords: Cerebellum atrophy, Intellectual disability, Exome sequencing, Molybdenum cofactor deficiency, MOCS2, KIF1A

* Correspondence: vincent.cantagrel@inserm.fr
†Equal contributors
[2]INSERM UMR 1163, Laboratory of Molecular and Pathophysiological Bases of Cognitive Disorders, Paris, France
[3]Paris Descartes – Sorbonne Paris Cité University, Imagine Institute, Paris, France
Full list of author information is available at the end of the article

BioMed Central

© 2016 Megahed et al. **Open Access** This article is distributed under the terms of the Creative Commons Attribution 4.0 International License (http://creativecommons.org/licenses/by/4.0/), which permits unrestricted use, distribution, and reproduction in any medium, provided you give appropriate credit to the original author(s) and the source, provide a link to the Creative Commons license, and indicate if changes were made. The Creative Commons Public Domain Dedication waiver (http://creativecommons.org/publicdomain/zero/1.0/) applies to the data made available in this article, unless otherwise stated.

Background

Atrophy and hypoplasia of the cerebellum are neuroradiological findings identified in pediatric-onset cerebellar ataxias and generally associated with imbalance, poor coordination and developmental delay. Hereditary cerebellar atrophy in childhood is a clinically and genetically heterogeneous group of conditions. They include a vast number of differential diagnoses with overlapping clinical findings such as intellectual disability and epilepsy [1, 2].

The specificity of cerebellar atrophy as a neuroradiological finding has been formerly discussed [2]. In association with a careful initial clinical evaluation, the characterization of cerebellar atrophy and/or hypoplasia by MRI is currently used to prioritize specialized investigations and potential diagnosis [1, 3].

The most frequent causes of early-onset cerebellar atrophy include mitochondrial disorders, neuronal ceroid lipofuscinosis, congenital disorders of glycosylation, ataxia telangiectasia and infantile neuroaxonal dystrophy [1]. The reason for the exquisite sensitivity of the cerebellum to defects in general cellular processes involving mitochondria, protein glycosylation or lysosomes is not known. The loss of Purkinje cells could play a central role in the pathology of many cerebellar ataxias as they are highly metabolic cells and these cells are the only out-put of the cerebellum.

This group of disorders includes an ever-increasing number of very rare conditions and currently over 169 OMIM clinical synopses are associated with cerebellar atrophy (OMIM December 2015). The overlapping clinical features of these numerous conditions often prevent a rapid and accurate clinical and genetic diagnosis and for more than half of the patients with childhood-onset cerebellar atrophy, a molecular diagnosis is not available [3].

Additionally, many of these conditions start with motor and cognitive delay or deterioration but some diagnostic criteria appear later during the developmental course of the disease. For example, in the case of *PLA2G6*-associated neurodegeneration (PLAN), brain iron accumulation is generally not detected in the early stages of the disease [4, 5].

In such situations whole exome sequencing (WES) has been able to accelerate molecular diagnosis, better delineate the clinical spectrum associated with specific genetic defects and improve patient management [6, 7].

In this study, we assessed a cohort of 18 families of Egyptian origin with childhood-onset cerebellar atrophy and developmental delay. We analyzed them for both recessive and dominant variants and successfully identified disease-causing mutations in half of the families (9/18). This study highlights the importance of searching for dominant mutations in consanguineous families and broadens the clinical spectrum associated with some cerebellar conditions, including molybdenum cofactor deficiency.

Methods

Subject information

We studied 18 families including 12 sporadic cases (67 %) and 16 families with reported consanguinity (89 %). For half of these families only the proband was exome sequenced and for the other half we performed trio exome sequencing. The mean age was 4.6 years (Standard deviation 3.2 years) at the time of the study. Patients had various degrees of cerebellar atrophy identified on MRI, involving mainly the vermis or the entire cerebellum. Both static and progressive conditions were included. Written informed consent was obtained from all families, and the study was approved by the ethics committee of the National Research Center in Cairo.

Whole exome sequencing

DNA was extracted from blood and the sequencing core facility at the Imagine Institute performed WES. Briefly, WES libraries were prepared from 3 μg of genomic DNA sheared by ultrasonication (Covaris S220 Ultrasonicator). Exome capture was performed with the 51 Mb SureSelect Human All Exon kit V5 (Agilent technologies). Sequencing of the WES libraries was carried out on a HiSeq2500 (Illumina). Paired-end reads were generated and mapped on the human genome reference using Burrows-Wheeler Aligner (BWA) [8]. The mean depth of coverage obtained for each sample was > 160x with >97 % of the exome covered at least 30x. SNP and indel calling was made using GATK tools. Families CIE3, 4, 5, 8, 11, 12, 13, 18 and 19 ($n = 9$; 50 %) were investigated by trio WES and for families CIE1, 2, 7, 9, 14, 16, 17, 21, 29 ($n = 9$; 50 %) WES was only performed for the proband.

Bioinformatics, databases

A variant filtering pipeline was systematically applied to narrow down the number of putative causative variants. All the possible inheritance patterns were tested. Briefly, common (>1 % minor allele frequency) variants were filtered out by using dbSNP, 1000 genomes databases and our in house exome collection, which includes more than 7000 exomes. Functional (protein-altering) alleles were prioritized versus non-functional. Potentially pathogenic variants in known disease genes were identified if flagged as damaging by polyphen2 (http://genetics.bwh.harvard.edu/pph2/), Sift (http://sift.jcvi.org/) or mutation taster (http://www.mutationtaster.org/). Remaining variants were compared with those in the public databases EXAC (http://exac.broadinstitute.org/) and EVS (http://evs.gs.washington.edu/EVS/) exome database. The presence

of candidate recessive variants in homozygous intervals was checked by identifying predicted regions of SNP homozygosity from exome data with the unifiedgenotyper tool from GATK (https://www.broadinstitute.org/gatk/). In order to identify fully penetrant dominant mutation in singleton WES data we used the following method. We filtered out variants that were present in control individuals from our in house exome database and not predicted to be pathogenic by at least two prediction programs: PolyPhen, SIFT or Mutation-Taster. When a single rare variant predicted to be deleterious was observed in a single known cerebellar atrophy gene and associated with a dominant mode of inheritance, it was considered as potential candidate. When the same rare variant has been previously associated with disease, this was considered strong evidence that it was likely to be pathogenic. We validated potential de novo mutations by using Sanger sequencing on patients and parents DNA. However considering the large number of variants generated by this method, it is considered efficient only for the identification of mutations in known disease genes.

Results

Homozygous, compound heterozygous and potential de novo mutations were investigated in all families. We identified pathological mutations in 7 genes within nine families (9/18; 50 %): a homozygous *TPP1* mutation c.790C > T (NM_000391.3) p.Gln264* in family CIE7; a homozygous *EXOSC3* mutation c.395A > C (NM_016042.3) p.Asp132Ala in CIE9; a homozygous *PLA2G6* c.2070_2072del (NM_003560.2) p.Val691del mutation in families CIE11 and CIE13; a homozygous *MOCS2* c.3G > A (NM_176806.3) p.Met1? mutation in CIE12; a homozygous *SURF1* mutation c.237G > A (NM_003172.3) p.Trp79* in CIE16; a homozygous *MFSD8* c.1213C > T (NM_152778.2) p.Gln405* mutation in family CIE17; a de novo *KIF1A* mutation c.173C > T (NM_001244008.1) p.Ser58Leu in family CIE21 and a homozygous *PLA2G6* mutation c.1613G > A (NM_003560.2) p.Arg538His in family CIE29. Mutation segregation was checked by Sanger sequencing in all available samples (indicated by a star on Fig. 1).

Clinical findings in the affected individuals with molecular diagnosis are summarized in Table 1. Previously described mutations were identified in six genes *TPP1*, *EXOSC3*, *PLA2G6*, *MOCS2* and *SURF1* and *KIF1A*. The *PLA2G6* gene was the most frequently mutated gene and the c.2070_2072del mutation was identified in two families in our WES data. The identification of this recurrent mutation during the course of the project, led us to implement Sanger sequencing of this specific allele and only samples negative for this prescreen where submitted to WES. Using this method, we could identify a third family with the same c.2070_2072del mutation. In total, this 3 bp deletions accounts for 15 % of all the families tested in this study. The identification of *MFSD8* mutations in family CIE17 was consistent with an early onset of ceroid lipofuscinosis, neuronal 7 (CLN7) associated with cortical and cerebellar atrophy and an enlargement of the cerebral ventricles in the proband (Fig. 2a-c), a phenotype that usually manifests between 2 and 6 years old [9]. In family CIE21, we identified a recurrent de novo mutation in the *KIF1A* gene. This mutation is predicted to disrupt some hydrogen bonds in the ATP binding domain (Additional file 1: Figure S1) and results in cerebellar atrophy (Fig. 2d-f) and epilepsy (Table 1). In family CIE12, we found biallelic mutations in the initiation codon of the MOCS2A open reading frame of the bicistronic *MOCS2* gene. Mutations in this gene cause Molybdenum Cofactor (MoCo) deficiency, a severe neonatal inborn error of metabolism usually associated with subcortical multicystic lesions and death during early childhood stage [10]. Patient CIE12-A2 was born to consanguineous parents and was affected since birth. At 3.8 years, she presented with delayed speech and delayed walking. She had wide based gait, hyperreflexia and hypertonia with the left side of her body being more affected than the right. The mother had

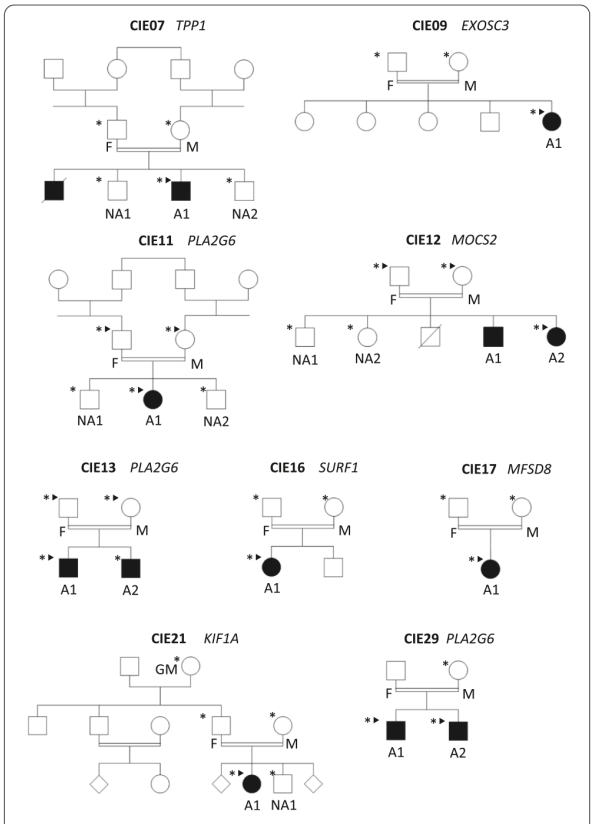

Fig. 1 Pedigrees of families with identified disease-causing genes. A *star* indicates individuals with DNA available for segregation test and *arrowheads* point to the samples sequenced by WES

Table 1 Clinical presentation, laboratory investigation and exome sequencing result for 10 patients with undiagnosed cerebellar atrophy

	CIE7-A1	CIE9-A1	CIE11-A1	CIE12-A2	CIE13-A1/A2	CIE16-A1	CIE17-A1	CIE-21-A1	CIE-29-A1
Gender	M	F	F	F	M	F	F	F	M
Gene mutated	*TPP1*	*EXOSC3*	*PLA2G6*	*MOCS2*	*PLA2G6*	*SURF1*	*MFSD8*	*KIF1A*	*PLA2G6*
Genbank reference	NM_000391.3	NM_016042.3	NM_003560.2	NM_176806.3	NM_003560.2	NM_003172.3	NM_152778.2	NM_001244008.1	NM_003560.2
Mutation cDNA level	c.790C > T	c.395A > C	c.2070_2072del	c.3G > A	c.2070_2072del	c.237G > A	c.1213C > T	c.173C > T	c.1613G > A
Mutation protein level	p.Q264*	p.D132A	p.V691del	p.M1?	p.V691del	p.W79*	p.Q405*	p.S58L	p.R538H
Final diagnosis	CLN2 Late infantile	Mild PCH type 1B	PLAN/INAD	Mild MoCo deficiency	PLAN/INAD	LEIGH SYNDROME	CLN7	AD ID	PLAN/INAD
Age of onset (years.months)	3.1	1	0.9	Neonatal	1.6/1.0	1	0.6	2.0	1.5
Last follow-up (years.months)	4.6	1.9	3.0	6.0	4.0/2.0	4.7	3.6	5.0	3.6
Initial symptom	Convulsions	Developmental delay	Convulsions	Developmental delay	Convulsions	Gait disturbance	Developmental delay	Gait disturbance	Developmental regression
Development									
Developmental delay	+	+	+	+	+	+	+	+	+
Motor developmental delay	+	+	+	+	+/++	+	+	+	+
Social development delay	+	+	+	+	+/++	+	++ (autistic features)	+	+
Progressive condition	+	-	Mildy progressive	-	+	+	+	-	+
Seizures									
Description	Focal epileptic activity	GTC	Focal Right-temporal discharges, GTC	Left fronto-temporal epileptogenic dysfunction	Focal, GTC	GTC	Right frontal epileptogenic focus, Akinetic fits	Right-temporal activity, intractable epilepsy	GTC
Neurological Findings									
Hypotonia	+	+	+	- (Hypertonia)	+	+	+	+	+
Nystagmus	-	+	+	-	+	+	-	-	+
Wide-based, staggering gait	+	+	Enable to walk	Wide based gait	+	Tetubation, ataxia	+	Wide-based, staggering gait	Tetubation,ataxia
Peripheral neuropathy	-	+	+	-	+	+	-	+	+

Table 1 Clinical presentation, laboratory investigation and exome sequencing result for 10 patients with undiagnosed cerebellar atrophy *(Continued)*

MRI									
Cerebellum:Hypoplasia/ Progressive or fixed Atrophy	Atrophy/ hypoplasia	Atrophy	Atrophy,hypoplasia, dilated cisterna magna	Atrophy	Atrophy	Atrophy + abnormal signal intensity	Atrophy	Atrophy	Atrophy
Brainstem	-	-	-	-	-	Abnormal signal intensity as well as in BG	-	-	-
Cerebral cortex	Mild cortical atrophy	-	-	Right frontal arachnoid cyst, mild frontal lobe atrophy	Mild cortical atrophy/-	-	Atrophy	-	-
Ventricular system	-	-	Dilated	-	Moderate dilatation	-	Mild dilatation	-	-
Facial dysmorphism	-	Squint	-	Mild dysmorphism	-	-	-	-	-
Ophtalmologic finding	Fundus exam: Macular lesion	-	-	-	-	-	-	-	-
Relevant metabolic result				High Plasma S-Sulphocysteine level and high plamsa Xhantine level (see text)		Plasma lactate in the normal range	Blood ammonia: 62.2 µmol/L (normal 15–45); blood lactate: 20.6 mmol/L (normal = 0.5-2.2)		

Abbreviations: GTC generalized tonic-clonic, *PCH* pontocerebellar hypoplasia, *PLAN* PLA2G6-associated neurodegeneration, *INAD* infantile neuroaxonal dystrophy, *MoCo* Molybdenum cofactor, *CLN* Ceroid lipofuscinosis neuronal, *AD* autosomal dominant, *ID* intellectual disability, *BG* basal ganglia

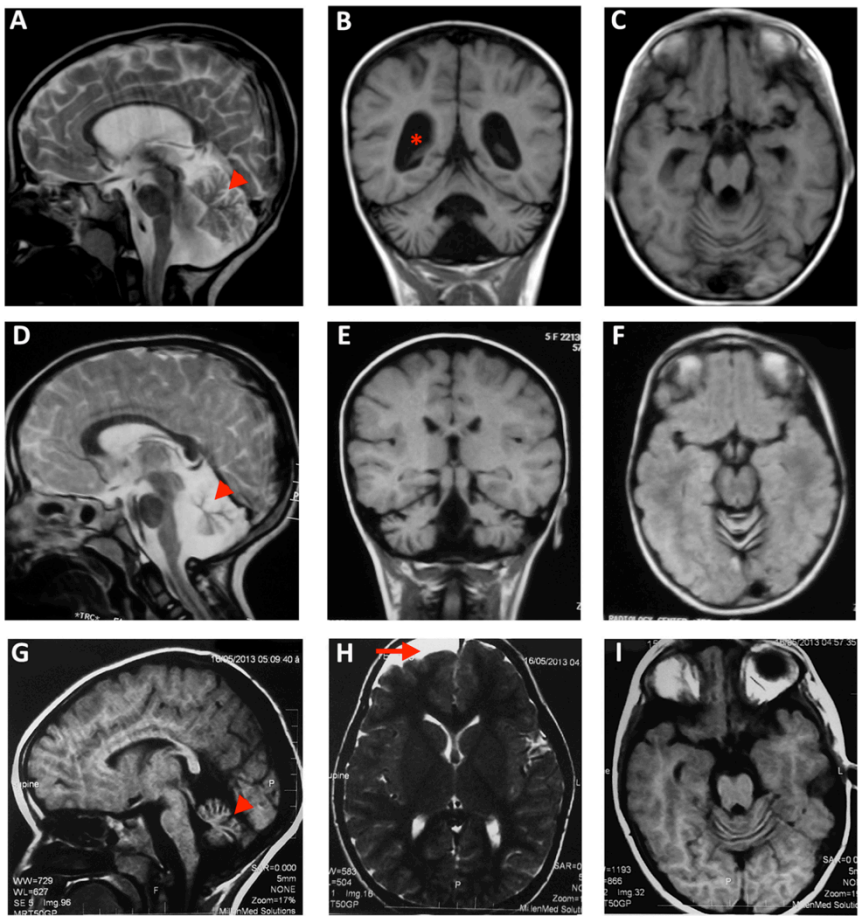

Fig. 2 Brain MRI scans from families CIE17, CIE21 and CIE12. **a**-**c** MRIs of case CIE17-A1 (*MFSD8* mutation) at 3 years. **a** Midline Sagittal T2-weighted image demonstrating enlarged cerebellar folia (*arrow head*) and thin corpus callosum. Ventricular system dilatation (*star*) is visible on coronal T1 image (**b**). **d**-**f** MRIs of patient CIE-21-A1 (*KIF1A* mutation) at 5 years showing cerebellar atrophy (*arrowhead*) on midline sagittal T2 (**d**), coronal T1 (**e**) and axial T1 (**f**) images. **g**-**i** MRIs of patient CIE12-A2 (*MOCS2* mutation) with evidence of cerebellar vermis atrophy (*arrowhead*) on sagittal T1 image (**g**) and Right frontal arachnoid cyst (*red arrow*) visible on axial T2 scan (**h**)

an uncomplicated pregnancy although she was exposed to X-Rays when she was one month pregnant. This patient has two unaffected siblings, one deceased brother and an older brother who suffered from global development delay since birth and mild cortical brain atrophy on MRI associated with abnormal EEG. At 6.0 years, patient CIE12-A2 appeared to improve gradually. Despite some residual unsteadiness, she can walk, read and memorize short sentences. Her initial investigations included CT and MRI, which revealed right frontal arachnoid cyst, mild right frontal lobe brain atrophy and cerebellar atrophy (Fig. 2g-i). A follow up CT two years latter indicated that the arachnoid cyst had slightly resolved. Her EEG revealed left fronto-temporal epileptogenic dysfunction. The follow up EEGs showed improvement in the epileptogenic bursts probably as a result of the antiepileptic therapy she is receiving. The molecular diagnosis was supported by the blood tests results, consistent with Molybdenum Cofactor deficiency. Plasma S-Sulphocysteine level was 309 micromol/mmol (Control value <10) and Plasma Xanthine 1291 micromol/mmol (Control value <40). She is currently receiving sodium valproate (30mh/kg), Levitiracetam (20 mg/kg), omega 3 supplements, and IM (intra-muscular) B complex.

Discussion

In this study, we explored sporadic and multiplex Egyptian families with early-onset cerebellar atrophy associated with developmental delay by using high-coverage whole exome sequencing. Our analysis included the investigation of recessive and dominant variants and we identified pathogenic mutations in 50 % of the 18 families studied. Previous reports that focused on sporadic and inherited cerebellar atrophies [11] or ataxias [12] and obtained

comparable success rates of 39.1 and 41 % respectively, in the identification of pathological mutations.

The absences of diagnosis for half of the cohort could be explain with the following reasons. Despite high depth of sequencing (mean depth of coverage > 160x), exome capture does not provide complete coverage of all coding regions of the genome, particularly those with GC-rich regions. Moreover, large genomic rearrangements and trinucleotide repeat sequences are not reliably detected from exome-capture data. It is also possible that some causal variants will reside within non-coding regulatory regions. Some of these issues will be resolved by whole genome sequencing, although not without substantial additional cost and bioinformatics analyses. However it is likely that mutation in yet unknown cerebellar atrophy genes contribute significantly to these diseases. In this study, half of the patients were explored by using trio WES and the other half by singletons WES. Trio WES did not improve the diagnosis rate but considerably decreased the number of Sanger cosegregation analyses. It impacted specially de novo mutations analysis but singleton WES did not prevent de novo mutation identification as illustrated with the *KIF1A* gene mutation. One of the clear advantages of trio WES is its ability to point to a limited number of variants located in novel candidate disease-causing genes when mutations located in known disease gene are absent. The identification of *KIF1A* de novo mutation highlights the importance of considering not only recessive inheritance patterns when analyzing consanguineous exomes despite the presence of extensive regions of homozygosity (data not shown). This finding identifies p.Ser58Leu as a recurrent *KIF1A* mutation [13] and indicates that cerebellar atrophy is the main MRI feature associated with this allele. Several typical symptoms of infantile-onset *PLA2G6*-associated neurodegeneration (PLAN) are not always observed before 4 years, such as optic atrophy, electroencephalogram fast rhythms and amyotrophy [4], making very early diagnosis more difficult. *PLA2G6* is the most frequently mutated gene in this cohort; 3 families were identified with the same homozygous mutation previously described as a founder mutation in Mediterranean countries [4]. This observation suggests that the p.Val691del allele is an especially common cause of PLAN in the Egyptian population. Among other clinical symptoms, patients with this mutation shared the association of development delay or regression with cerebellar atrophy, epilepsy and nystagmus. Mutations in the *MOCS2* genes cause MoCo deficiency type B, which is currently untreatable [14]. These mutations can occur in one of the two open-reading frames (i.e., MOCS2A and MOCS2B) of this bi-cistronic gene and are generally associated with untreatable seizures, multiple cystic cavities on MRI and death at early age [10]. Milder cases have been reported to be associated with a hypomorphic allele [15] or mutations involving a non-constitutively spliced exon [16]. Strikingly, the p.Met1? mutation identified in MOCS2A has been tested in vitro and shown to abolish translation [17]. This result highlights the existence of mild presentations of MoCo syndrome, potentially detectable with plasma sulfite and xanthine screening of patients with undiagnosed cerebellar atrophy, developmental delay and isolated arachnoid cyst.

Conclusions

Our study emphasizes the benefits of whole exome sequencing to efficiently diagnose early-onset cerebellar atrophy defects, to better delineate the clinical spectrum associated with these disorders and to open the way for the identification of new disease genes.

Ethics approval and consent to participate and for publication

Written informed consent was obtained from all families, and the study was approved by the ethics committee of the National Research Center in Cairo.

Additional file

Additional file 1: Figure S1. Modeling of the p.S58L mutation using the crystal structure of the motor domain of human KIF1A (PDB number 1VFV). The image was generated using PyMOL (http://www.pymol.org). The side-chain of Ser58 is involved in inferred hydrogen bonds (arrow) with other amino-acids located in the ATP-binding pocket (A). These interactions are predicted to be disrupted by the mutation (B) including the hydrogen bonds with the highly conserved Arginine 11 that interacts with ATP through a molecule of water. (JPG 499 kb)

Abbreviations

MoCo: molybdenum cofactor; PLAN: *PLA2G6*-associated neurodegeneration; WES: whole exome sequencing.

Competing interests

The authors declare that they have no competing interests.

Authors' contributions

HM ascertained all the Egyptian patients and participated in the WES analysis. MN coordinated samples preparation, analyzed and validated the data with the help of KSP and DMC; CBF coordinated the exome sequencing. CM and PN designed and adjusted the bioinformatics pipeline to analyze sequence data. GB, MR, ID, NBB and AM reviewed clinical data in regard of the WES results. NB reviewed brain imaging. VC analyzed the data, directed the study and wrote the manuscript with the help of LC. All authors read and approved the final manuscript.

Acknowledgments

This project was funded by grant ANR-12-PDOC-0026 that supported also VC and MN salary and by grant ANR-10-IAHU-01. We are grateful to Campus France that allowed the French-Egyptian collaboration and supported some travel and accommodation fees for HM. We acknowledge the assistance and expert advice from collaborators at the genomic and bioinformatics cores of the Imagine institute. We thank L. S. Nguyen and C. Gordon for critical reading of the manuscript.

Funding

The project was funded by grant ANR-12-PDOC-0026, ANR-10-IAHU-01 and Campus France.

Author details
[1]Clinical Genetics Department, Human Genetics and Genome Research Division, National Research Center, Cairo 12311, Egypt. [2]INSERM UMR 1163, Laboratory of Molecular and Pathophysiological Bases of Cognitive Disorders, Paris, France. [3]Paris Descartes – Sorbonne Paris Cité University, Imagine Institute, Paris, France. [4]Genomic Platform, INSERM UMR 1163, Paris Descartes – Sorbonne Paris Citée University, Imagine Institute, 75015 Paris, France. [5]Bioinformatic Platform, INSERM UMR 1163, Paris Descartes – Sorbonne Paris Citée University, Imagine Institute, 75015 Paris, France. [6]Imagine Institute, INSERM UMR 1163, Genetics of mitochondrial diseases, 75015 Paris, France. [7]Imagine Institute, INSERM UMR 1163, Embryology and genetics of human malformation, 75015 Paris, France. [8]Pediatric Neurology, Necker Enfants Malades University Hospital, APHP, 75015 Paris, France. [9]Department of Genetics, Necker Enfants Malades University Hospital, APHP, 75015 Paris, France. [10]Department of Pediatric Radiology, Necker Enfants Malades University Hospital, APHP, 75015 Paris, France.

Received: 16 December 2015 Accepted: 21 April 2016
Published online: 04 May 2016

References

1. Boddaert N, Desguerre I, Bahi-Buisson N, Romano S, Valayannopoulos V, Saillour Y, et al. Posterior fossa imaging in 158 children with ataxia. Journal of neuroradiology Journal de neuroradiologie. 2010;37(4):220–50.
2. Poretti A, Wolf NI, Boltshauser E. Differential diagnosis of cerebellar atrophy in childhood. Eur J Paediatr Neurol. 2008;12(3):155–67. doi:10.1016/j.ejpn.2007.07.010.
3. Al-Maawali A, Blaser S, Yoon G. Diagnostic approach to childhood-onset cerebellar atrophy: a 10-year retrospective study of 300 patients. J Child Neurol. 2012;27(9):1121–32. doi:10.1177/0883073812448680.
4. Romani M, Kraoua I, Micalizzi A, Klaa H, Benrhouma H, Drissi C, et al. Infantile and childhood onset PLA2G6-associated neurodegeneration in a large North African cohort. Eur J Neurol. 2015;22(1):178–86. doi:10.1111/ene.12552.
5. Gregory A, Westaway SK, Holm IE, Kotzbauer PT, Hogarth P, Sonek S, et al. Neurodegeneration associated with genetic defects in phospholipase A(2). Neurology. 2008;71(18):1402–9. doi:10.1212/01.wnl.0000327094.67726.28.
6. Deciphering Developmental Disorders S. Large-scale discovery of novel genetic causes of developmental disorders. Nature. 2015;519(7542):223–8. doi:10.1038/nature14135.
7. Dixon-Salazar TJ, Silhavy JL, Udpa N, Schroth J, Bielas S, Schaffer AE, et al. Exome sequencing can improve diagnosis and alter patient management. Sci Transl Med. 2012;4(138):138ra78. doi:10.1126/scitranslmed.3003544.
8. Li H, Durbin R. Fast and accurate short read alignment with Burrows-Wheeler transform. Bioinformatics. 2009;25(14):1754–60. doi:10.1093/bioinformatics/btp324.
9. Kousi M, Lehesjoki AE, Mole SE. Update of the mutation spectrum and clinical correlations of over 360 mutations in eight genes that underlie the neuronal ceroid lipofuscinoses. Hum Mutat. 2012;33(1):42–63. doi:10.1002/humu.21624.
10. Reiss J, Johnson JL. Mutations in the molybdenum cofactor biosynthetic genes MOCS1, MOCS2, and GEPH. Hum Mutat. 2003;21(6):569–76. doi:10.1002/humu.10223.
11. Ohba C, Osaka H, Iai M, Yamashita S, Suzuki Y, Aida N, et al. Diagnostic utility of whole exome sequencing in patients showing cerebellar and/or vermis atrophy in childhood. Neurogenetics. 2013;14(3–4):225–32. doi:10.1007/s10048-013-0375-8.
12. Pyle A, Smertenko T, Bargiela D, Griffin H, Duff J, Appleton M, et al. Exome sequencing in undiagnosed inherited and sporadic ataxias. Brain. 2015;138(Pt 2):276–83. doi:10.1093/brain/awu348.
13. Lee JR, Srour M, Kim D, Hamdan FF, Lim SH, Brunel-Guitton C, et al. De novo mutations in the motor domain of KIF1A cause cognitive impairment, spastic paraparesis, axonal neuropathy, and cerebellar atrophy. Hum Mutat. 2015;36(1):69–78. doi:10.1002/humu.22709.
14. Schwahn BC, Van Spronsen FJ, Belaidi AA, Bowhay S, Christodoulou J, Derks TG et al. Efficacy and safety of cyclic pyranopterin monophosphate substitution in severe molybdenum cofactor deficiency type A: a prospective cohort study. Lancet. 2015. doi:10.1016/S0140-6736(15)00124-5.
15. Leimkuhler S, Freuer A, Araujo JA, Rajagopalan KV, Mendel RR. Mechanistic studies of human molybdopterin synthase reaction and characterization of mutants identified in group B patients of molybdenum cofactor deficiency. J Biol Chem. 2003;278(28):26127–34. doi:10.1074/jbc.M303092200.
16. Arenas M, Fairbanks LD, Vijayakumar K, Carr L, Escuredo E, Marinaki AM. An unusual genetic variant in the MOCS1 gene leads to complete missplicing of an alternatively spliced exon in a patient with molybdenum cofactor deficiency. J Inherit Metab Dis. 2009;32(4):560–9. doi:10.1007/s10545-009-1151-7.
17. Stallmeyer B, Drugeon G, Reiss J, Haenni AL, Mendel RR. Human molybdopterin synthase gene: identification of a bicistronic transcript with overlapping reading frames. Am J Hum Genet. 1999;64(3):698–705. doi:10.1086/302295.

Submit your next manuscript to BioMed Central and we will help you at every step:

- We accept pre-submission inquiries
- Our selector tool helps you to find the most relevant journal
- We provide round the clock customer support
- Convenient online submission
- Thorough peer review
- Inclusion in PubMed and all major indexing services
- Maximum visibility for your research

Submit your manuscript at
www.biomedcentral.com/submit

BioMed Central

doi:10.1093/brain/awx218 BRAIN 2017: 140; 2597–2609 | 2597

BRAIN
A JOURNAL OF NEUROLOGY

WDR81 mutations cause extreme microcephaly and impair mitotic progression in human fibroblasts and *Drosophila* neural stem cells

Mara Cavallin,[1,2,3,*] Maria A. Rujano,[2,4,*] Nathalie Bednarek,[5] Daniel Medina-Cano,[2,6] Antoinette Bernabe Gelot,[7,8] Severine Drunat,[9] Camille Maillard,[1,2] Meriem Garfa-Traore,[10] Christine Bole,[11] Patrick Nitschké,[12] Claire Beneteau,[13] Thomas Besnard,[13] Benjamin Cogné,[13] Marion Eveillard,[14] Alice Kuster,[15] Karine Poirier,[16,17] Alain Verloes,[9,18] Jelena Martinovic,[19] Laurent Bidat,[20] Marlene Rio,[21] Stanislas Lyonnet,[1,2] M. Louise Reilly,[2,22,23] Nathalie Boddaert,[24,25] Melanie Jenneson-Liver,[5] Jacques Motte,[5] Martine Doco-Fenzy,[26] Jamel Chelly,[27,28] Tania Attie-Bitach,[1,2,21] Matias Simons,[2,4] Vincent Cantagrel,[2,6] Sandrine Passemard,[9,18] Alexandre Baffet,[29] Sophie Thomas[1,2,#] and Nadia Bahi-Buisson[1,2,3,#]

[*,#]These authors contributed equally to this work.

Microlissencephaly is a rare brain malformation characterized by congenital microcephaly and lissencephaly. Microlissencephaly is suspected to result from abnormalities in the proliferation or survival of neural progenitors. Despite the recent identification of six genes involved in microlissencephaly, the pathophysiological basis of this condition remains poorly understood. We performed trio-based whole exome sequencing in seven subjects from five non-consanguineous families who presented with either microcephaly or microlissencephaly. This led to the identification of compound heterozygous mutations in *WDR81*, a gene previously associated with cerebellar ataxia, intellectual disability and quadrupedal locomotion. Patient phenotypes ranged from severe microcephaly with extremely reduced gyration with pontocerebellar hypoplasia to moderate microcephaly with cerebellar atrophy. In patient fibroblast cells, *WDR81* mutations were associated with increased mitotic index and delayed prometaphase/metaphase transition. Similarly, *in vivo*, we showed that knockdown of the *WDR81* orthologue in *Drosophila* led to increased mitotic index of neural stem cells with delayed mitotic progression. In summary, we highlight the broad phenotypic spectrum of *WDR81*-related brain malformations, which include microcephaly with moderate to extremely reduced gyration and cerebellar anomalies. Our results suggest that WDR81 might have a role in mitosis that is conserved between *Drosophila* and humans.

1 Laboratory of Embryology and Genetics of Congenital Malformations, INSERM UMR 1163, Imagine Institute, Paris, France
2 Paris Descartes - Sorbonne Paris Cité University, Imagine Institute, Paris, France
3 Pediatric Neurology APHP- Necker Enfants Malades University Hospital, Paris, France
4 Laboratory of Epithelial biology and disease, INSERM UMR 1163, Imagine Institute, Paris, France
5 University of Reims Champagne Ardennes, UFR médecine, Reims, France
6 Laboratory of Molecular and Pathophysiological Bases of Cognitive Disorders, INSERM UMR 1163, Imagine Institute, Paris, France
7 AP-HP, Hôpital Armand Trousseau, Laboratoire d'Anatomie Pathologique, Neuropathologie, Paris, France
8 INMED, INSERM U 901 Campus de Luminy, Marseille, France
9 Department of Medical Genetics and INSERM UMR1141, APHP-Robert DEBRE Universitary Hospital, Paris, France
10 Cell Imaging platform, INSERM UMR 1163, Imagine Institute, Paris, France

Received February 27, 2017. Revised July 3, 2017. Accepted July 6, 2017. Advance Access publication September 13, 2017
© The Author (2017). Published by Oxford University Press on behalf of the Guarantors of Brain. All rights reserved.
For Permissions, please email: journals.permissions@oup.com

11 Genomic Core Facility, INSERM UMR 1163, Imagine Institute, Paris, France
12 Bioinformatics Core Facility, INSERM UMR 1163, Imagine Institute, Paris, France
13 CHU Nantes, Service de Génétique Médicale, 9 quai Moncousu, 44093 Nantes CEDEX 1, France
14 CHU Nantes, Service d'Hématologie Biologique, 9 quai Moncousu, 44093 Nantes CEDEX 1, France
15 CHU Nantes, Service de réanimation Pédiatrique, Centre de compétence des maladies héréditaires du métabolisme, 38 boulevard Jean Monet, 44093 Nantes, France
16 Inserm, U1016, Institut Cochin, Paris, France
17 CNRS, UMR8104, Paris, France
18 Sorbonne-Paris Cité University, Denis Diderot School of Medicine, Paris, France
19 Unit of Fetal Pathology Hospital Antoine Béclère, AP-HP, Clamart, France
20 Department of Prenatal Diagnosis, Department of Obstetrics and Gynecology, René Dubos Hospital, Pontoise, France
21 Service de Génétique, Necker Enfants Malades University Hospital, AP-HP, Paris, France
22 Laboratory of Inherited Kidney Disease, INSERM UMR 1163, Imagine Institute, Paris, France
23 Paris Diderot University, 75013 Paris, France
24 Pediatric Radiology, Necker Enfants Malades University Hospital, APHP, Paris, France
25 Image - Institut Imagine, INSERM UMR1163, Université Paris Descartes, Hôpital Necker Enfants Malades, Paris, France
26 Service de Génétique, Hôpital Maison Blanche, CHU Reims, Reims, France
27 IGBMC, INSERM U964 , CNRS UMR 7104, Université de Strasbourg. 67404 Illkirch Cedex, France
28 Pôle de biologie, Hôpitaux Universitaires de Strasbourg, Strasbourg, France
29 Institut Curie. CNRS UMR144, PSL Research University, Paris, France

Correspondence to: Nadia Bahi-Buisson
INSERM UMR 1163 - Embryology and Genetics of Congenital Malformations
Institut Imagine
24, Boulevard du Montparnasse
75015 Paris
France
E-mail: nadia.bahi-buisson@aphp.fr

Keywords: microcephaly; microlissencephaly; ponto-cerebellar hypoplasia; *WDR81*

Abbreviation: MCD = malformations of cortical development

Introduction

The development of the human cerebral cortex is an orchestrated process involving the birth of neural progenitors in the periventricular germinal zones, cell proliferation characterized by both symmetric and asymmetric mitoses and the subsequent migration of post-mitotic neurons to their final destinations in six highly ordered, functionally-specialized layers (Bystron *et al.*, 2008; Rakic, 2009). Understanding of the molecular mechanisms guiding these intricate processes is in its infancy, and substantially driven by the discovery of rare mutations that cause malformations of cortical development (MCD) (Barkovich *et al.*, 2012; Guerrini and Dobyns, 2014; Jamuar and Walsh, 2015). These mutations are a major cause of intellectual disability, epilepsy, and neurological deficits, often resulting in life-long support and treatments. MCD are classified based on the stage of development at which the developmental process was likely disturbed: neural progenitor proliferation or apoptosis, neuronal migration and cortical organization (Manzini and Walsh, 2011; Barkovich *et al.*, 2012).

Abnormal proliferation of neural progenitors and neuronal migration can result in a wide range of disease phenotypes such as microcephaly (MIC, MIM 251200) and lissencephaly (LIS, MIM 607432) (Gilmore and Walsh, 2013). Congenital microcephaly is classified as a disorder of neurogenesis suggesting either a decrease in the number of proliferative divisions or an increase in apoptotic cell death of neural progenitors. Underlying cellular mechanisms include abnormal mitotic spindle structure, structurally abnormal or extra centrosomes, altered cilia function, impaired DNA repair, DNA damage response signalling and DNA replication, along with attenuated cell cycle checkpoint proficiency (Thornton and Woods, 2009; Bilgüvar *et al.*, 2010; Kaindl *et al.*, 2010; Bettencourt-Dias *et al.*, 2011). In contrast to microcephaly, human lissencephaly manifests as a lack of normal cortical folding. The lack of folding reflects abnormal histological organization of the cortical layers and is most often due to disruption of neuronal migration (Bystron *et al.*, 2008). Microlissencephaly (MLIS, MIM 616212) is an extremely rare entity characterized by the combination of extreme primary microcephaly with disordered cortical lamination. Most cases of microlissencephaly are described in consanguineous families suggesting an autosomal recessive inheritance with only a few disease-causing genes identified thus far. These include biallelic mutations in *NDE1* (Alkuraya *et al.*, 2011), *KATNB1* (Hu *et al.*, 2014; Mishra-Gorur *et al.*, 2014), and *WDR62* (Bilgüvar *et al.*, 2010). *NDE1*

encodes a partner of dynein that localizes to the centrosome and mitotic spindle poles (Alkuraya *et al.*, 2011). *KATNB1* encodes a microtubule-severing enzyme that localizes to microtubules and centrosomes (Hu *et al.*, 2014; Mishra-Gorur *et al.*, 2014) and *WDR62* encodes another centrosomal protein (Chen *et al.*, 2014). Dominant mutations in tubulin genes, *TUBA1A*, *TUBB2B* and *TUBB3* (Bahi-Buisson *et al.*, 2014; Fallet-Bianco *et al.*, 2014) have also been identified in patients with microlissencephaly, underlining the critical role of the microtubule cytoskeleton in this condition. Remarkably, most of the genes involved in microlissencephaly can also cause microcephaly, suggesting both conditions belong to the same disease spectrum. Despite significant progress in understanding the genetic basis of these conditions, the causative genes and pathophysiological mechanisms underlying most cases of microcephaly/microlissencephaly remain unknown. This makes it challenging to provide families with a genetic diagnosis, prenatal testing and genetic counselling (Bahi-Buisson *et al.*, 2014).

In the present study, we report on seven novel compound heterozygous mutations in *WDR81* leading to microcephaly with moderate to extremely reduced gyration with or without cerebellar anomalies ranging to cerebellar hypoplasia to cerebellar atrophy. In addition, we show that in patient fibroblasts and in *Drosophila*, *WDR81* disruption is associated with an increased mitotic index and delayed prometaphase/metaphase transition.

Overall, our results expand the phenotypic spectrum of *WDR81* mutations and suggest a highly conserved role of this gene in mitotic progression.

Patients and methods

As part of our ongoing research program on cortical malformations, we performed whole exome sequencing in individuals in whom clinically available molecular genetic tests had failed to detect any mutation, and for whom the phenotype shows specific features that could allow the identification of additional cases for a replicative cohort if a novel gene is identified.

In all cases, metabolic work up and array comparative genomic hybridization were normal. Next-generation sequencing on a panel of genes involved in MCD, including *NDE1*, *WDR62* and tubulin genes did not demonstrate any mutations in 50 genes of MCD. The genetic analysis performed was subject to informed consent procedures and approved by the Institutional Review Boards at Necker Enfants Malades Hospital and Paris Descartes University.

Whole-exome sequencing

Whole exome sequencing of peripheral blood DNA from proband and both parents was performed using the Agilent SureSelect Human All Exon Kits v5, and sequence was generated on a HISeq2500 machine (Illumina). Sequences were aligned to hg19 by using BWA v.0.6.1, and single nucleotide variants (SNVs) and indels were called by using GATK v.1.3. Annotation of variants was performed with GATK Unified Genotyper. All calls with read coverage of $\leqslant 2\times$ or a Phred-scaled SNP quality score of $\leqslant 20$ were removed from consideration. The annotation process was based on the latest release of the Ensembl database. Variants were annotated and analysed using the Polyweb software interface designed by the Bioinformatics platform of University Paris Descartes and Imagine Institute.

Filters used for variant screening were as following: (i) all variants previously observed (in dbSNP138 and/or in in-house projects) were excluded; (ii) only variants leading to abnormal protein sequence (splicing, non-synonymous, frameshift, stop) were retained; (iii) we considered the PolyPhen-2 and SIFT prediction status as informative but not restrictive; and (iv) because most MCD are autosomal recessive, we searched for autosomal recessive events. Because all patients were sporadic cases from unrelated parents, the following models of inheritance in the variant screening were considered, by order of priority: autosomal recessive (in particular compound heterozygous but without excluding homozygous variants), X-linked and *de novo* SNVs.

Validation was achieved by standard bidirectional Sanger methods (primer sequences available on request).

Cell culture

Available fibroblast cells from Patients IM-MCD_606 and CerID-22 and from age-matched controls were grown in Opti-MEM® supplemented with 1% foetal bovine serum, 1% penicillin-streptomicin and 1% Fungizone at 37°C in humid air containing 5% CO_2. For cell proliferation studies, patient and control cells were plated at the same concentration and synchronized by serum starvation for 24 h after which serum was reintroduced for 24 h. For ciliogenesis studies, confluent fibroblasts were serum starved for 48 h.

Real-time reverse-transcription PCR

RNA was extracted from patient and control fibroblasts and *Drosophila* brain tissues using Qiagen RNA kit, including on-column DNase digestion. RNA was quantified using the spectrophotometer NanoDrop 2000 (Thermo Fisher Scientific). cDNA synthesis from total RNA was conducted using the GeneAmp RNA PCR Core Kit (Applied Biosystems) or Verso cDNA kit with random hexamers. *ACTB* was used as internal control gene. cDNA Sanger sequencing was performed as described above for genomic DNA. Real time RT-PCR was performed using the GoTaq® qPCR Master Mix (Promega) and the *WDR81* Forward/Reverse primer set. *HPRT* and *GUSB* genes were used as internal control for normalization in fibroblasts,

and *Gapdh1* for normalization in *Drosophila* tissues. (Sequences of primers are available upon request).

Immunocytochemistry

Fibroblast cells were fixed in 4% paraformaldehyde and treated in 50 mM NH4Cl, 0.5% Triton™ X-100 followed by 1 h in phosphate-buffered saline-bovine serum albumin (PBS-BSA) 3% Tween 0.1% blocking solution or treated in 0.5 M glycine pH 7.5, 0.2% saponin followed by 1 h in PBS-saponin 0.2% BSA 0.2% for endolysosomal membrane integrity and structural preservation. Cells were then incubated with mouse monoclonal acetylated α-tubulin (1:1000, Sigma clone 6-11B-1), rabbit polyclonal pericentrin (1:1000, Abcam ab4448), rabbit monoclonal Ki67 (1:200, Abcam ab16667), mouse monoclonal pH3 (1:200, Cell Signaling #9706), monoclonal Anti-phospho-Histone3 H2A.X (Ser139), clone JBW301 (1:200, Millipore 05-636), rabbit monoclonal EEA1 (1:1000, Cell Signaling #C45B10), mouse monoclonal anti-Lamp2 (1:500, Abcam ab25631) antibodies for 1 h at room temperature. After three washes, cells were incubated with Alexa Fluor® fluorescent dye coupled secondary antibodies: Alexa Fluor® 488 goat anti-rabbit IgG (1:200, Invitrogen), Alexa Fluor® 555 donkey anti-mouse IgG (1:200, Invitrogen). Images were taken using a Leica SP8 confocal microscope. At least 150 control and patient cells were analysed per experiment.

Drosophila stocks and genetics

Flies were raised on cornmeal medium at 25°C. The following stocks were used: wild-type *W1118*, *w;worniu-GAL4*, *w[1118]; y[1] w[*]; P{Act5C-GAL4-w}E1/CyO* (Bloomington stock centre), *cg6734* RNAi lines used were P{KK102429}VIE-260B (obtained from VDRC, stock number v106697), y1 v1; P{TRiP.HMJ22542}attP40/CyO (Bloomington stock center) and *hsflp*; tub-FRT-Gal80-FRT-Gal4, UAS–mCD8–mRFP (gift from F. Bosveld). The two independent *cg6734* RNAi lines showed similar results. Crosses were maintained at 25°C and laid eggs were then transferred to 29°C to achieve maximum efficacy of the UAS-Gal4 system. Neural stem cells clones were induced in second instar larvae by heat shock (1 h 37°C) and mid third instar larval brains were analysed.

Immunohistochemistry and tissue imaging

Immunohistochemistry was performed as described (Rujano *et al.*, 2013, 2015). Briefly, staged brains from third instar larvae were dissected in PBS, fixed for 20 min in 4% paraformaldehyde in PBS with 0.1% Triton™ X-100; washed once in PBS-T (PBS, 0.3% Triton™ X-100) and incubated overnight at 4°C with primary antibodies diluted in PBS-T. After washing in PBS-T, brains were incubated overnight at 4°C with secondary antibodies, Hoechst (0.5 µg/ml) to stain the nuclei and phalloidin to stain actin cortex (Rhodamine or 488, Molecular Probes) followed by three 10-min washes with PBS and mounted in mounting media (1.25% n-propyl gallate, 75% glycerol, 25% H_2O). Primary antibodies used: guinea pig anti-Deadpan (Dpn) (1:100, gift from R. Basto), mouse anti-α-tubulin (T6199) (1:1000, Sigma-Aldrich), mouse anti-phospho-Histone H3 (Ser10) (6G3) (1:200, Ab9706, Cell Signalling), rabbit anti-Rab7 (1:2000, gift from A. Nakamura), rat anti-RFP (1:1000, Chromotek 5f8-100). Secondary antibodies used: fluorescent conjugated Alexa Fluor® 488, Alexa Fluor® 555 and Alexa Fluor® 647 (Molecular probes). All images were acquired on a Leica Sp8 confocal microscope with a 60 × 1.4 NA objectives using NIS Element software. Images were processed with Fiji 63 and Adobe Photoshop.

Quantification of mitotic neuroblasts

Quantifications were performed manually using the cell counter tool in the Fiji software. Total number of neuroblasts and mitotic neuroblasts were always quantified on the ventral side of the brains at the plane were the maximum number of neuroblasts are present. Sixteen and 20 lobes from individual larvae were quantified for wild-type and *dWDR81* knockdown, respectively.

Statistical analysis

Data were analysed with Prism (GraphPad Software) or Excel (Microsoft Office) to generate bar graphics. Error bars represent ± standard error of the mean (SEM) as indicated in figure legends. The two-tailed unpaired t-test was used for statistical analysis of two groups of samples. Two-way ANOVA with a Bonferroni post-test was used to evaluate statistical significance of multiple groups of samples. $P < 0.05$ was considered significant.

Results

Identification of *WDR81* variations by whole exome sequencing

Trio based exome sequencing was performed in all cases with a mean depth of coverage for each sample of at least 136-fold and with at least 99% of the exome covered 15-fold or greater. *De novo*, autosomal-recessive, X-linked nonsynonymous SNVs and frameshift indels were identified with the publicly available SOLVE-Brain package (https://github.com/Paciorkowski-Lab/SOLVE-Brain.git). This was then used to annotate candidate genes with brain expression. Exome read-depth metrics are summarized in Supplementary Table 1, as well as other non-pathogenic variations identified in other genes. Exome sequencing revealed that all of these patients harbour rare predicted damaging nonsense or missense

mutations in the *WDR81* gene (Gene Bank Reference Sequence: NM_001163809.01) (Fig. 1B and Supplementary Table 1). Each mutation was confirmed by Sanger sequencing and segregated in the expected autosomal-recessive pattern in all available family members. None of the mutations were observed in the public databases including dbSNP, 1000 Genomes, the NHLBI Exome Variant Server (EVS) and the Exome Aggregation Consortium (ExAC) browser.

Further direct Sanger Sequencing of the 10 exons of *WDR81* in a replicative cohort of 17 patients and foetuses with unexplained sporadic microcephaly/microlissencephaly did not lead to the identification of additional mutations (Supplementary Table 2).

Phenotype of patients with *WDR81* mutations

WDR81 mutations were identified in seven individuals from non-consanguineous healthy parents including four sporadic cases (i.e. three unrelated children and one foetal case) and one family with one living boy and two twin sisters diagnosed prenatally with subsequent termination of pregnancy (Fig. 1).

The living Patients Im-MCD_606 (Family 1), CerID-22 (Family 3), Rdb-MIC_233 (Family 4) and Nan-MCD-001 (Family 5), carrying *WDR81* mutations were 3, 22, 13 and 17 years of age at their last evaluation and all presented with extreme microcephaly. All were born at term, after uneventful pregnancies and normal prenatal ultrasound at 30 weeks of

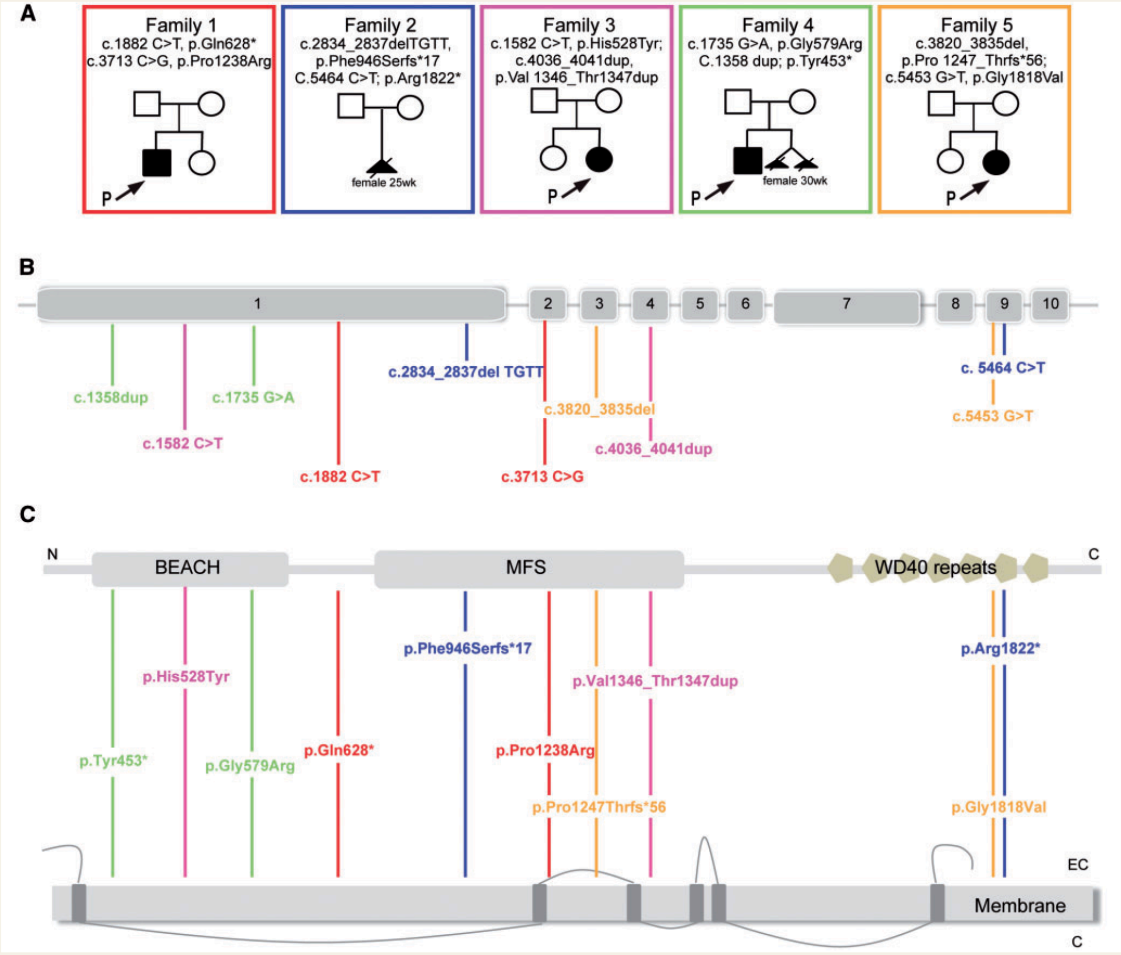

Figure 1 ***WDR81* mutations identified in five affected families.** (**A**) Pedigrees (P = proband); (**B**) schematic representation of *WDR81* gene and (**C**) predicted protein domain structure with the positions of the variations identified [red: Patient Im-MCD_606 (Family 1), blue: Patient Im-MCD_752 (Family 2), pink: Patient CerID-22 (Family 3), green: Patient Rdb-MIC_233 (Family 4), yellow: Patient Nan-MCD-001 (Family 5); RefSeq NM_001163809.01]. BEACH = Beige and Chediak-Higashi domain; C = cytosol; EC = extracellular; MFS = major facilitator superfamily domain; WD40 = WD40 beta-propeller domain.

gestation. All presented initially with a minor or mild microcephaly from −1 to −3 standard deviations (SD) without growth deficiency. In all cases, microcephaly proceeded to worsen with age reaching −5 to −10 SD at last evaluation. Neurological development was extremely impaired in all cases; none were able to hold their head, develop any voluntary hand use, visual contact or acquire any babbling. They developed early onset dyskinetic movement disorder and spastic tetraplegia from 2 months of age. Two developed drug resistant epilepsy (Patients Rdb-MIC_233 and Nan-MCD-001). Apart from microcephaly, they grew normally, were not dysmorphic and did not have any other congenital anomalies. Ophthalmological and auditory investigations were normal in all cases. There was no evidence of neurological decline or immune deficiency.

Brain MRI revealed extreme gyral simplification with abnormal gyral pattern comprising foci of extremely reduced sulcation and agyria, with increased subarachnoid spaces and deformed and enlarged ventricles, with mild cerebellar atrophy (Fig. 2). Detailed clinical data are provided in Table 1.

WDR81 mutations were also identified in three foetal cases (Families 2 and 4). The first (Patient Im-MCD_752) was a sporadic female case diagnosed by foetal ultrasound at 25 weeks of gestation with corpus callosum agenesis and pontocerebellar hypoplasia. The two remaining cases (Patients Rdb-MIC_234 and 235) were dizygotic twins, sisters of Patient Rdb-MIC_233 in whom foetal MRI at 30 weeks of gestation showed deceleration of head growth and delayed gyration. In accordance with the French law, these brain malformations lead to medical termination of pregnancy. Macroscopic examinations showed extreme microcephaly with absent to extremely delayed gyration pattern in all cases, corpus callosum agenesis (1/3) and pontocerebellar hypoplasia (2/3). The neuropathological classification would be within microcephaly with extremely reduced gyration with or without pontocerebellar hypoplasia and with or without corpus callosum agenesis and normal growth.

Expression of *WDR81* in patient fibroblasts

To study the functional consequences of the *WDR81* mutations at the cellular level, we used dermal fibroblast cultures established from skin biopsies of two patients (Patients Im-MCD_606 and CerID-22; Table 1) and age-matched controls. Expression of *WDR81* in Patient Im-MCD_606, harbouring a nonsense mutation (p.Gln628*), was reduced by almost 40%, indicating nonsense-mediated mRNA decay (Supplementary Fig. 1A).

Cellular consequences of *WDR81* variations in patient fibroblasts

In view of the cellular phenotypes associated with other microcephaly causing genes including multipolar spindle and supernumerary cilia, we next analysed mitotic spindle and centrosome structures and ciliogenesis in patient fibroblasts. Immunostaining experiments did not reveal any impact on mitotic spindle organization nor any abnormal primary cilia structure and number (Supplementary Fig. 1B and C). Microcephaly has also been associated with altered DNA damage response, yet no spontaneous accumulation of double-strand breaks was observed in patient fibroblasts compared to controls (Supplementary Fig. 2). Disruptions in cell cycle progression and decreased proliferation can also induce microcephaly, but no difference was observed in the percentage of cycling cells between patient and control cells (Fig. 3A). However, using a mitotic DNA specific marker (phospho-histone H3; PH3), we analysed the mitotic index and found that it was significantly increased in Patient Im-MCD_606 fibroblasts (carrying a stop mutation and subsequent nonsense-mediated decay), and also in fibroblasts from Patient CerID-22 (no nonsense-mediated decay) although not significant (Fig. 3A). To gain further insights into the mechanisms leading to this increase, we next analysed the proportion of cells in each mitotic phase and found a significant increase in the number of cells in prometaphase/metaphase in both patient fibroblasts as compared to control cells (Fig. 3B).

Knockdown of the *WRD81* orthologue in *Drosophila* neuroblasts results in mitotic delay

To investigate the consequences of *WDR81* disruption further, we extended our analyses to *Drosophila*, an *in vivo* model previously shown to be a valuable tool to assess the underlying mechanisms of MCDs (Rujano *et al.*, 2013; Mishra-Gorur *et al.*, 2014; Yamamoto *et al.*, 2014). The *Drosophila* larval brain contains proliferating neural stem cells that give rise to all neurons and glial cells present in the adult fly brain. We used an RNAi-mediated approach to downregulate *CG6734*, the fly orthologue of *WDR81* (hereafter referred to as *dWDR81*). Since no antibody against *dWDR81* was available, we used *Act5c-Gal4* to drive expression of *dWDR81* RNAi ubiquitously and determined the efficiency of the RNAi-mediated knockdown by quantitative PCR (qPCR) in brain RNA extracts. RNA levels were reduced by ~40% (Fig. 4B) in larval brains resulting in a partial decrease in *dWDR81* expression. We subsequently used *Worniu-Gal4* to drive expression of *dWDR81* RNAi exclusively in neural stem cells (neuroblasts) and analysed mitoses. Neuroblasts were identified by their large size (Fig. 4A) and Deadpan (Dpn, a marker for neuroblasts) expression. Defects in overall brain size or viability were not observed. However, at the cellular level we found that the partial knockdown of *dWDR81* resulted in an increased mitotic index in the neuroblasts from the central brain, with an increase in the proportion of mitotic cells in prometaphase/metaphase and a decrease in anaphase/telophase, indicating a delay in mitotic progression

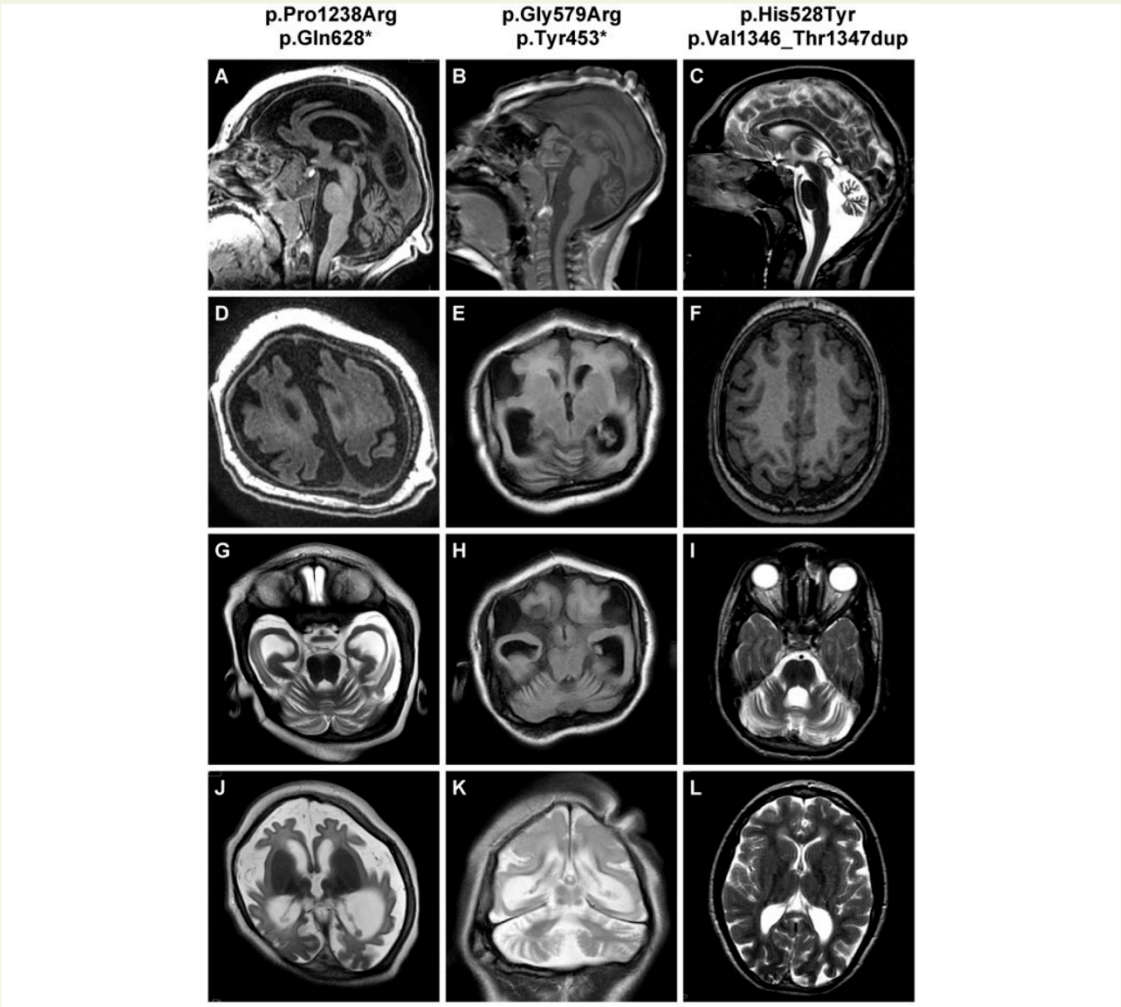

Figure 2 Representative brain MRI of patients with *WDR81* mutations. Patients Im-MCD_606 (p.Pro1238Arg; p.Gln628*), Rdb-MIC_233 (p.Gly579Arg; p.Tyr453*) and CerID-22 (p.His528Tyr; p.Val1346_Thr1347dup) respectively aged 22 months (**A**, **D**, **G** and **J**), 4 years (**B**, **E**, **H** and **K**), and 14.5 years (**C**, **F**, **I** and **L**) at the time of MRI. Sagittal sections T_1-weighted (**A** and **B**) or T_2-weighted (**C**) show moderate (**A**) to severe cerebellar atrophy (**C**), and thin corpus callosum in all cases. Axial weighted sections show extreme gyral simplification (**D** and **E**) or milder (**F**), with area of absence of gyri (agyria) without thickening of cortex. At the level of the cerebellar hemispheres, cerebellar atrophy with excess of visibility of hemisphere foliation (**G**, **H** and **I**); T_2-weighted sections also demonstrate delayed myelination at 22 months (**J**), hypomyelination at 9 years (**K**) or periventricular white matter hyperintensities (**L**).

(Fig. 4C, E and F). As with the patient fibroblasts, no defects in centrosome number or mitotic spindle organization were observed (Fig. 4D). Taken together, these results indicate that the *Drosophila* orthologue of *WDR81* plays an important function in brain development in the fly and, similarly to other previously described microcephaly-related proteins, *dWDR81* likely plays a role in mitotic progression of proliferating neural stem cells (Novorol *et al.*, 2013; Chen *et al.*, 2014; Mishra-Gorur *et al.*, 2014). Furthermore, our observations suggest a conserved mechanism in humans and *Drosophila* resulting from *WDR81* depletion.

Discussion

Our data demonstrate that compound heterozygous mutations in *WDR81* are responsible for microcephaly with extremely reduced gyration or agyria with or without cerebellar anomalies ranging from pontocerebellar

Table 1 Detailed clinical data

Family	Family 1	Family 2	Family 3	Family 4			Family 5	
Patient	**Im-MCD_606**	**Im-MCD_752**	**CerID-22**	**Rdb-MIC_233**	**Rdb-MIC_234**	**Rdb-MIC_235**	**Nan-MCD-001**	**Published case**
Gender	Male	Foetus female (25 GW)	Female	Male	Foetus female (30 GW)	Foetus female (30 GW)	Female	
Gene (RefSeq) WDR81 (NM_001163809.1)								
Nucleotide variation 1	c.1882 C>T	c.2834_2837delTGTT	c.1582 C>T	c.1735G>A	c.1735G>A	c.1735G>A	c.3820_3835del	c.2567C>T
Nucleotide variation 2	c.3713 C>G	c.5464 C>T	c.4036_4041dup	c.1358 dup	c.1358 dup	c.1358 dup	c.5453G>T	
Protein variation 1	p.Gln628*	p.Phe946Serfs*17	p.His528Tyr	p.Gly579Arg	p.Gly579Arg	p.Gly579Arg	p.Pro1274Thrfs*56	p.Pro856Leu
Protein variation 2	p.Pro1238Arg	p.Arg1822*	p.Val1346_Thr1347dup	p.Tyr453*	p.Tyr453*	p.Tyr453*	p.Gly1818Val	
	Sporadic case	Sporadic case	Sporadic case	Familial case	Familial case	Familial case	Sporadic case	Familial cases (n = 5)
Ethnicity	European	European	European	European	European	European	European	Turkish
Transmission	AR	AR	AR	AR	AR	AR	AR	AR
References	This series	This series	This series	This series	This series	This series	This series	Gulsuner, 2011
Clinic								
Head circumference at birth, cm	30.5 (−2.7 SD)	NA	32 (−1.8 SD)	30 (−3 SD)	N/A	N/A	33 (−1 SD)	N/K
Birth weight, g	3620 (+0.5 SD)	NA	3180 (−0.4 SD)	3320 (−0.1 SD)	N/A	N/A	3700 (+1 SD)	N/K
Birth length, cm	48 (−1.4 SD)		50.5 (−0.3 SD)	49 (−1 SD)			51.5 (+1.5 SD)	N/K
Age at last evaluation	27 months	25 GW	22 years	13 years	33 GW	33 GW	17 years	28 years
Head circumference, cm	37.5 (−9 SD)	23 (−1 SD)	44 (−7 SD)	41 (<−8 SD)	25.7 (<−8 SD)	27.4 (−4 SD)	42 (−10 SD)	Disproportionate short stature (150 cm)
Growth parameter (weight)	9300 g (−1 SD)	970 g (+1 SD)	30 kg (−5 SD)	32 kg (−1.5 SD)	1561 g (−2 SD)	2056 g (+0.1 SD)	50 kg (−1 SD)	Normal
Growth parameter (height), cm	71	34.5 (+1 SD)	N/K	121 (−5 SD)	41.5 (−1.5 SD)	42.2 (−1 SD)	158 (−1 SD)	N/K
Level of neurological development	Virtually no development	N/A	Virtually no development	Virtually no development	N/A	N/A	Virtually no development	Intellectual disability
Neurological examination	Spastic tetraplegia	N/A	Spastic tetraplegia	Spastic tetraplegia	N/A	N/A	Spastic tetraplegia	No spasticity
Epilepsy	Absent	N/A	Absent	Infantile spasms (2.5 years)	N/A	N/A	Drug resistant > 1 seizures/day	Absent
Movement disorder	Generalized dyskinesia	N/A	Generalized dyskinesia	Dystonia	N/A	N/A	Absent	Cerebellar ataxia
Other signs	Nystagmus (neonatal period)	N/A	Nystagmus	Nystagmus (neonatal period)	N/A	N/A	Scoliosis, precocious puberty	Bilateral external ophthalmoplegia
MRI								
Age at MRI	22 months	25 GW (US)	14.5 years	4 years	30 GW (foetal MRI)	30 GW (foetal MRI)	6 years	
Cortex	LIS/extremely reduced gyration	Delayed primary gyration	Gyral simplification	LIS/extremely reduced gyration	Delayed primary gyration	Delayed primary gyration	Cortical atrophy	Normal/brain atrophy
Basal ganglia	Normal	Normal	Normal	Normal	Normal	Normal	Normal	Normal

(continued)

Table 1 Continued

Family	Family 1	Family 2	Family 3	Family 4			Family 5	
Patient	Im-MCD_606	Im-MCD_752	CerID-22	Rdb-MIC_233	Rdb-MIC_234	Rdb-MIC_235	Nan-MCD-001	Published case
Corpus callosum	Thin	Corpus callosum agenesis	Thin	Thin	Thin	Thin	Thin	Thin
Brainstem	Normal	Severe hypoplasia	Normal	Normal	Normal	Normal	Normal	Normal
Cerebellum	Normal	Severe hypoplasia	Cerebellar atrophy	Normal	Normal	Normal	Cerebellar atrophy	Cerebellar atrophy + vermis midline cleft
Myelination	Immature/dysmyelination Enlarged ventricles and subarachnoid space	N/A	Gliosis (periventricular)	Immature/dysmyelination Enlarged ventricles and subarachnoid space	N/A	N/A	Immature/dysmyelination	N/A

AR = autosomal recessive; GW = weeks of gestation; LIS = lissencephaly; N/A = non-applicable; NK = not known; US = ultrasound.

hypoplasia to cerebellar atrophy expanding the phenotypic spectrum associated with *WDR81* mutations. Our results suggest that WDR81 has a role in normal cell proliferation. Patient fibroblasts exhibit increased mitotic index associated with prolonged prometaphase/metaphase suggestive of chromosome congression and/or separation defects (Nasmyth, 2002; Lara-Gonzalez *et al.*, 2012). These mitotic defects may lead to reduced neurogenic cell divisions, alterations of neural cell fates or to a failure to maintain the progenitor cell population. As previously demonstrated, with mutations in other microcephaly/microlissencephaly-causing genes, these defects would lead to a greatly reduced cerebral cortex (Nicholas *et al.*, 2010; Alkuraya *et al.*, 2011; Hu *et al.*, 2014; Mishra-Gorur *et al.*, 2014).

In 2011, the *WDR81* homozygous missense mutation p.Pro856Leu was reported in one large Turkish family suffering from cerebellar hypoplasia and quadrupedal locomotion (CAMRQ2, MIM 610185) (Gulsuner *et al.*, 2011), a brain disorder that falls into the category of autosomal recessive cerebellar ataxia (Tan, 2006). A subsequent study performed on an ENU-induced mouse line carrying a distinct missense *WDR81* mutation (p.Leu1349Pro) suggested that the *WDR81* mutation resulted in the formation of abnormal spheroid-like mitochondria and the progressive death of Purkinje cells and photoreceptor cells (Traka *et al.*, 2013). This finding was consistent with the phenotype of slowly progressing degenerative process of cerebellar atrophy that may represent the less severe end of the spectrum of the disorder described here. Remarkably, in our series, the mildest phenotype was associated with missense and in-frame deletion, while the most severe case carried nonsense and frameshift variants suggesting putative phenotype-genotype correlations. Of note, none of these cases demonstrated retinal anomalies or photoreceptor degeneration as described in the initial report (Gulsuner *et al.*, 2011).

WDR81 encodes WD repeat-containing protein 81, [UniProt Knowledgebase (UniProtKB), see 'Web resources' section], a large protein (1941 amino acids) of unclear function. *WDR81* is a poorly characterized gene that encodes nine protein isoforms (Traka *et al.*, 2013). The longest human isoform is predicted to be a transmembrane protein, composed of an N-terminal BEACH (Beige and Chediak-Higashi) domain and belonging to the major facilitator superfamily (MFS) consisting of solute carrier proteins (Pao *et al.*, 1998). Additionally, this isoform contains a C-terminal WD40 beta-propeller domain (Stirnimann *et al.*, 2010; Xu and Min, 2011), which is shared with common to other previously identified microcephaly genes, *WDR62* (Bilgüvar *et al.*, 2010; Nicholas *et al.*, 2010; Chen *et al.*, 2014), *KATNB1* (Hu *et al.*, 2014; Mishra-Gorur *et al.*, 2014) and *LIS1* (Reiner *et al.*, 1993; Hattori *et al.*, 1994). Importantly, the mutations are distributed along the entire length of the gene and predicted to affect the

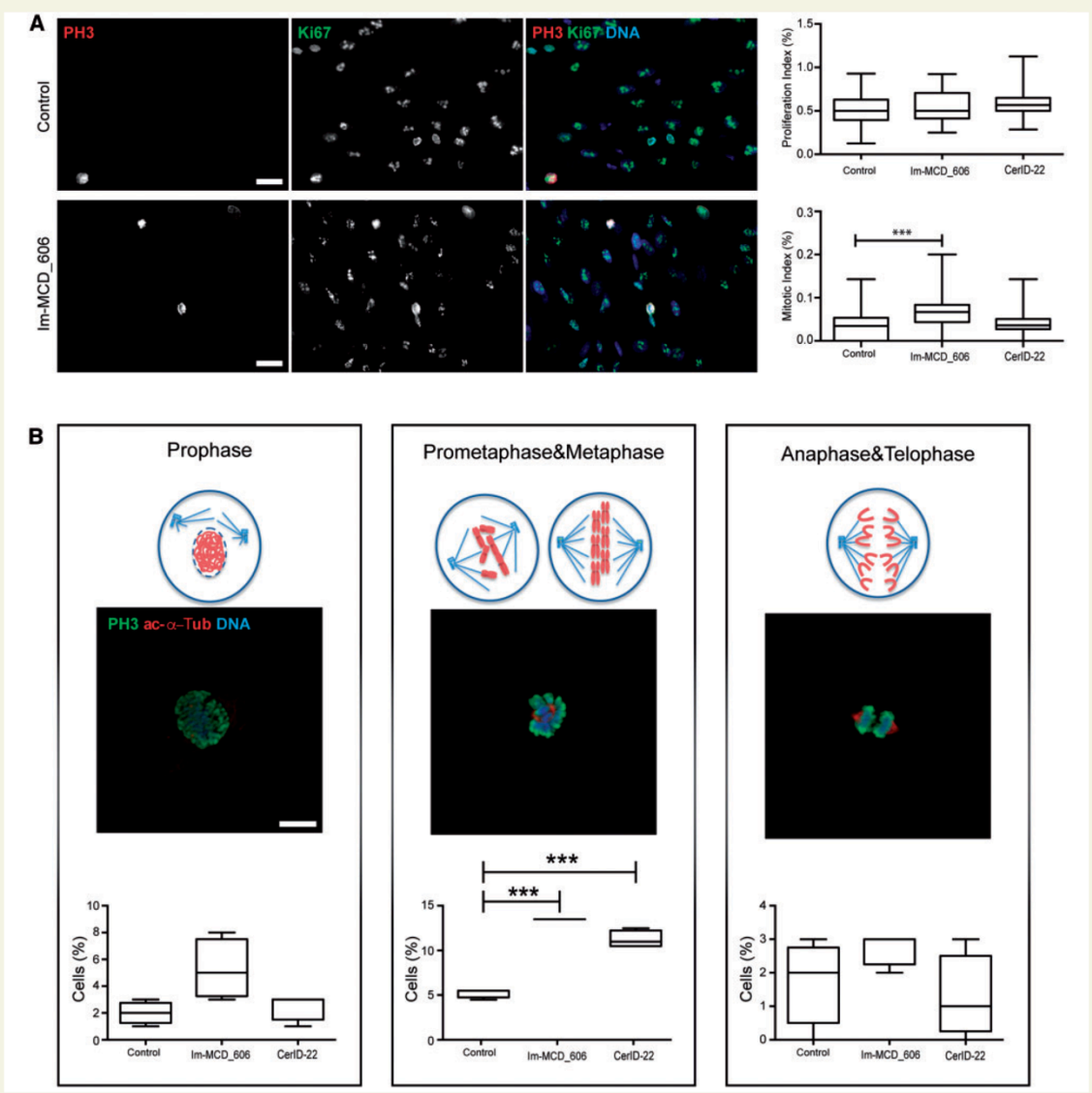

Figure 3 ***WDR81*** **mutant cells exhibit an increased mitotic index associated with delayed mitotic progression.** (**A**) Immunostaining with a static marker of proliferative activity (Ki67; AbCam Ab16667) and DAPI revealed no difference in proliferative index in patient cells as compared to control cells (control: 0.5192% ± 0.01974%, Patient Im-MCD_606: 0.5478 ± 0.02149 (not significant) and Patient CerID-22: 0.5825% ± 0.01782% (not significant). Staining with a mitosis specific marker (phospho-histone H3; PH3; Cell Signaling #9706) showed increased mitotic index in patient cells as compared to controls (0.038% ± 0.0038% for the control, 0.069% ± 0.005% for Patient Im-MCD_606 ($P < 0.0001$) and 0.041% ± 0.0037% for Patient CerID-22 (not significant); $n > 400$ mutant and control cells in four independent experiments. Scale bar = 10 μm. (**B**) Percentage of cells at each mitosis stage measured after staining using PH3 and acetylated alpha-tubulin (Sigma clone 6-11B-1; mitotic spindle) antibodies. *WDR81* mutant cells showed a significant increase in the number of mutant cells in prometaphase/metaphase as compared to control cells (control = 4.75% ± 0.25%, Patient Im-MCD_606 = 13% ± 0% ($P < 0.0001$) and CerID-22 = 10.75% ± 0.48% ($P < 0.0001$); $n > 400$ cells in three independent experiments) indicating mitotic progression delay in *WDR81* mutant cells. Numbers represent the average ± SEM. The *P*-values were calculated with the two-tailed unpaired *t*-test (***$P < 0.001$). Scale bar = 5 μm.

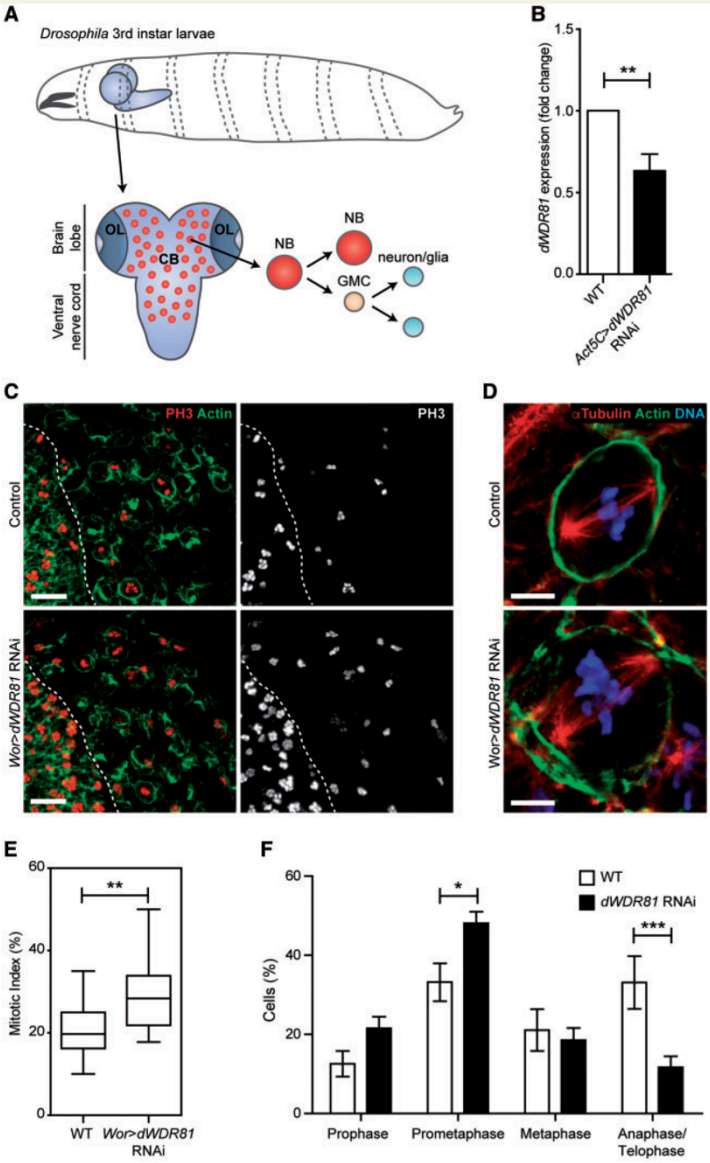

Figure 4 Knockdown of *WDR81* orthologue in *Drosophila* results in increased mitotic index and a delay in mitotic progression. (**A**) Schematic representation of the *Drosophila* third instar larval brain depicting the central brain (CB) and optic lobes (OL). Neural stem cells (neuroblasts, NB) in the central brain divide asymmetrically to produce a self-renewed neural stem cell and a ganglion mother cell (GMC) that divides once more to give rise to two neurons or glial cells. (**B**) *dWDR81* mRNA levels measured by qPCR in brain tissue of wild-type larvae and larvae expressing *dWDR81* RNAi under *Act5C*-Gal4. (**C**) Expression of *dWDR81* RNAi in neural stem cells with *Worniu*-Gal4 (*Wor* > *WDR81* RNAi) results in an increase in the number of mitotic cells in the central brain (right side of the dashed line) as seen with PH3. Actin was used to visualize cell contours. Scale bar 20 = μm. (**D**) No alteration in mitotic spindle organization (visualized with α-tubulin) was observed in *dWDR81* depleted neural stem cells. Scale bar = 5 μm. (**E**) Quantification of the mitotic index showed a significant increase in the amount of neural stem cells in mitosis when *dWDR81* is depleted (29% ± 8.6%) as compared to controls (21% ± 6.8%) ($P = 0.0026$); $n = 694$ *dWDR81 RNAi* cells from three independent experiments and $n = 552$ wild-type cells from five independent experiments. Numbers represent the average ± SD. Statistical significance was assessed by a two-tailed unpaired *t*-test. (**F**) Quantification of the number of mitotic cells in prophase, prometaphase, metaphase and anaphase/telophase in wild-type and *dWDR81* depleted neural stem cells, shows an increase in prometaphase state (33% in wild-type versus 48% in *dWDR81* RNAi ($P < 0.05$) and a decrease in the number of cells in anaphase/telophase (33% in wild-type versus 12% in *dWDR81* RNAi ($P < 0.001$), indicative of a delay in mitotic progression. Bars represent the mean and lines SEM. Statistical significance was assessed by a two-way ANOVA followed by a Bonferroni post-test.

different crucial domains of the protein. In Patient IM-MCD_606, harbouring the nonsense mutation p.Gln628*, we demonstrated the existence of nonsense-mediated decay. We would therefore anticipate that all the nonsense mutations identified would also result in nonsense-mediated decay, although this could not be tested as no patient material was available.

WDR81 is stably expressed in neural progenitor cells and post-mitotic neurons in the developing human brain (http://www.mitocheck.org). *WDR81* expression remains detectable during infancy and in the adult brain particularly in neocortex, hippocampus and striatum. This expression pattern suggests a continuing role of WDR81 in the proliferation of neural progenitors, neuronal migration and laminar organization of the human cortex (Neumann *et al.*, 2010). To understand the cellular role of WDR81 in the proliferation of neural progenitors, we used *Drosophila* as a model system. The larval brain of *Drosophila* has already been used to investigate the function of microcephaly-related genes (Rujano *et al.*, 2013; Mishra-Gorur *et al.*, 2014; Yamamoto *et al.*, 2014). Our studies show that partial loss of *WDR81* orthologue in the fly leads to an increased mitotic index of neural stem cells. In human, we found that *WDR81* patient fibroblasts also exhibit increased mitotic index associated with delayed prometaphase/metaphase transition. These data are in accordance with a previous high-throughput siRNA screen in HeLa cells, which showed that *WDR81* is a cell division gene whose inactivation leads to mitotic delays (Neumann *et al.*, 2010). Increased mitotic index was also shown in *WDR62*-depleted cells (Nicholas *et al.*, 2010) suggesting common pathophysiological mechanisms. However, in contrast to the cellular phenotypes associated to *WDR62* and *KATNB1* depletion, we found that centrosomes, mitotic spindle structure, and primary cilia number and structure remain normal in *WDR81* patient fibroblasts and *Drosophila* neuroblasts.

Recently, the orthologue of WDR81 in *C. elegans*, SORF-1, together with SORF-2 (WDR91 orthologue) was found to have a critical role in facilitating endosomal maturation and delivery of cargo to late endo-lysosomes. In *C. elegans* as well as mammalian Hela cells, WDR81 acts in a complex with WDR91 and Beclin1 to regulate endosomal phosphatidyl inositol phosphate 3 (PtdIns3) levels by suppressing phosphatidylinositol 3-kinase activity. Loss of function of WDR81 leads to the elevation and prolonged existence of endosomal PtdIns3P, which induces excessive fusion of early endosomes and delays early to late endosome conversion (Liu *et al.*, 2016; Rapiteanu *et al.*, 2016). We have analysed early and late endosomes in our patient's fibroblasts and *Drosophila* neural stem cells knockdown for WDR81, and neither model showed defects in the morphology of these compartments. The differences with the previous studies (Liu *et al.*, 2016; Rapiteanu *et al.*, 2016), might be due to residual activity of WDR81 in patient fibroblasts and *Drosophila* neural stem or due to cell type related differences. Future research using neuronal cell lines may shed light on the link between delayed mitotic progression observed in our patients and models and altered early to late endosome conversion.

Overall, our study reports ten *WDR81* mutations in seven cases from five families with microcephaly with extremely reduced gyration including agyria, thus expanding the phenotypic spectrum of *WDR81* mutations with potential phenotype–genotype correlations. These findings will contribute to improving the diagnosis of such extremely rare disorders. Taken together, our functional data in both *Drosophila* and patient cells provide new clues as to the role of WDR81 and sheds light onto its highly conserved function.

Web resources

The URLs for data presented herein are as follows:
1000 Genomes, http://browser.1000genomes.org
World Health Organization Align GVGD, http://agvgd.iarc.fr/agvgd_input.php/
dbSNP, http://www.ncbi.nlm.nih.gov.gate2.inist.fr/projects/SNP/
NHLBI Exome Sequencing Project (ESP) Exome Variant Server, http://evs.gs.washington.edu/EVS/
Online Mendelian Inheritance in Man (OMIM), http://www.omim.org/
PolyPhen-2, http://www.genetics.bwh.harvard.edu/pph2/
Uniprot, http://www.uniprot.org/uniprot/
SIFT, http://sift.bii.a-star.edu.sg/
ExAC, http://exac.broadinstitute.org/
MitoChek database: http://www.mitocheck.org/

Acknowledgements

The authors would like to thank the affected individuals and their families for participation in this study as well as the clinicians in charge of these patients who may not be cited. We would also like to thank Brian Popko for providing WDR81 antibodies. We thank Renata Basto for the Dpn antibody and the Vienna Drosophila Resource Center for the RNAi lines. The Imaging platform in the Imagine Institute for help and advice with image acquisition. We thank Mr Michaël Nicouleau for technical assistance.

Funding

Research reported in this publication was supported by the Agence Nationale de la Recherche (ANR-10-IAHU-01) (M.C., M.R., C.M., S.L., S.T., N.B.B.), The Agence Nationale de la Recherche (ANR 16-CE16-0011; R16198KK) (M.C., C.M., N.B.B.), the Fondation Maladies Rares, the Fondation pour la Recherche Médicale (FRM funding within the frame of the programme Equipe FRM; J.C–DEQ20130326477), the

Fondation Maladies Rares, Fondation NRJ – Institut de France, Agence Nationale de Recherche (ANR Blanc 1103 01, project R11039KK; ANR E-Rare-012-01, project E10107KP; ANR-13-BSV-0009-01), the EU-FP7 project GENECODYS (grant number 241995) and DESIRE (grant agreement 602531) and Agence Nationale de Recherche (ANR Blanc-SVSE1-2013; ANR-13-BSV1-0027) (ST,TAB), M.S. has been supported by the ATIP-Avenir program, the Fondation Bettencourt-Schueller (Liliane Bettencourt Chair of Developmental Biology) as well as State funding by the Agence Nationale de la Recherche (ANR) under the "Investissements d'avenir" program (ANR-10-IAHU-01) and the NEPHROFLY (ANR-14-ACHN-0013) grant.

Supplementary material

Supplementary material is available at *Brain* online.

References

Alkuraya FS, Cai X, Emery C, Mochida GH, Al-Dosari MS, Felie JM, et al. Human mutations in NDE1 cause extreme microcephaly with lissencephaly [corrected]. Am J Hum Genet 2011; 88: 536–47.

Bahi-Buisson N, Poirier K, Fourniol F, Saillour Y, Valence S, Lebrun N, et al. The wide spectrum of tubulinopathies: what are the key features for the diagnosis? Brain J Neurol 2014; 137: 1676–700.

Barkovich AJ, Guerrini R, Kuzniecky RI, Jackson GD, Dobyns WB. A developmental and genetic classification for malformations of cortical development: update 2012. Brain J Neurol 2012; 135: 1348–69.

Bettencourt-Dias M, Hildebrandt F, Pellman D, Woods G, Godinho SA. Centrosomes and cilia in human disease. Trends Genet 2011; 27: 307–15.

Bilgüvar K, Oztürk AK, Louvi A, Kwan KY, Choi M, Tatli B, et al. Whole-exome sequencing identifies recessive WDR62 mutations in severe brain malformations. Nature 2010; 467: 207–10.

Bystron I, Blakemore C, Rakic P. Development of the human cerebral cortex: Boulder Committee revisited. Nat Rev Neurosci 2008; 9: 110–22.

Chen JF, Zhang Y, Wilde J, Hansen KC, Lai F, Niswander L. Microcephaly disease gene Wdr62 regulates mitotic progression of embryonic neural stem cells and brain size. Nat Commun 2014; 5: 3885.

Fallet-Bianco C, Laquerrière A, Poirier K, Razavi F, Guimiot F, Dias P, et al. Mutations in tubulin genes are frequent causes of various foetal malformations of cortical development including microlissencephaly. Acta Neuropathol Commun 2014; 2: 69.

Gilmore EC, Walsh CA. Genetic causes of microcephaly and lessons for neuronal development. Wiley Interdiscip Rev Dev Biol 2013; 2: 461–78.

Guerrini R, Dobyns WB. Malformations of cortical development: clinical features and genetic causes. Lancet Neurol 2014; 13: 710–26.

Gulsuner S, Tekinay AB, Doerschner K, Boyaci H, Bilguvar K, Unal H, et al. Homozygosity mapping and targeted genomic sequencing reveal the gene responsible for cerebellar hypoplasia and quadrupedal locomotion in a consanguineous kindred. Genome Res 2011; 21: 1995–2003.

Hattori M, Adachi H, Tsujimoto M, Arai H, Inoue K. Miller-Dieker lissencephaly gene encodes a subunit of brain platelet-activating factor acetylhydrolase [corrected]. Nature 1994; 370: 216–18.

Hu WF, Pomp O, Ben-Omran T, Kodani A, Henke K, Mochida GH, et al. Katanin p80 regulates human cortical development by limiting centriole and cilia number. Neuron 2014; 84: 1240–57.

Jamuar SS, Walsh CA. Genomic variants and variations in malformations of cortical development. Pediatr Clin North Am 2015; 62: 571–85.

Kaindl AM, Passemard S, Kumar P, Kraemer N, Issa L, Zwirner A, et al. Many roads lead to primary autosomal recessive microcephaly. Prog Neurobiol 2010; 90: 363–83.

Lara-Gonzalez P, Westhorpe FG, Taylor SS. The spindle assembly checkpoint. Curr Biol 2012; 22: R966–80.

Liu K, Jian Y, Sun X, Yang C, Gao Z, Zhang Z, et al. Negative regulation of phosphatidylinositol 3-phosphate levels in early-to-late endosome conversion. J Cell Biol 2016; 212: 181–98.

Manzini MC, Walsh CA. What disorders of cortical development tell us about the cortex: one plus one does not always make two. Curr Opin Genet Dev 2011; 21: 333–9.

Mishra-Gorur K, Çağlayan AO, Schaffer AE, Chabu C, Henegariu O, Vonhoff F, et al. Mutations in KATNB1 cause complex cerebral malformations by disrupting asymmetrically dividing neural progenitors. Neuron 2014; 84: 1226–39.

Nasmyth K. Segregating sister genomes: the molecular biology of chromosome separation. Science 2002; 297: 559–65.

Neumann B, Walter T, Hériché JK, Bulkescher J, Erfle H, Conrad C, et al. Phenotypic profiling of the human genome by time-lapse microscopy reveals cell division genes. Nature 2010; 464: 721–7.

Nicholas AK, Khurshid M, Désir J, Carvalho OP, Cox JJ, Thornton G, et al. WDR62 is associated with the spindle pole and is mutated in human microcephaly. Nat Genet 2010; 42: 1010–14.

Novorol C, Burkhardt J, Wood KJ, Iqbal A, Roque C, Coutts N, et al. Microcephaly models in the developing zebrafish retinal neuroepithelium point to an underlying defect in metaphase progression. Open Biol 2013; 3: 130065.

Pao SS, Paulsen IT, Saier MH. Major facilitator superfamily. Microbiol Mol Biol Rev 1998; 62: 1–34.

Rakic P. Evolution of the neocortex: a perspective from developmental biology. Nat Rev Neurosci 2009; 10: 724–35.

Rapiteanu R, Davis LJ, Williamson JC, Timms RT, Paul Luzio J, Lehner PJ. A genetic screen identifies a critical role for the WDR81-WDR91 complex in the trafficking and degradation of tetherin. Traffic 2016; 17: 940–58.

Reiner O, Carrozzo R, Shen Y, Wehnert M, Faustinella F, Dobyns WB, et al. Isolation of a Miller-Dieker lissencephaly gene containing G protein beta-subunit-like repeats. Nature 1993; 364: 717–21.

Rujano MA, Sanchez-Pulido L, Pennetier C, le Dez G, Basto R. The microcephaly protein Asp regulates neuroepithelium morphogenesis by controlling the spatial distribution of myosin II. Nat Cell Biol 2013; 15: 1294–306.

Rujano MA, Basto R, Marthiens V. New insights into centrosome imaging in drosophila and mouse neuroepithelial tissues. Methods Cell Biol 2015; 129: 211–27.

Stirnimann CU, Petsalaki E, Russell RB, Müller CW. WD40 proteins propel cellular networks. Trends Biochem Sci 2010; 35: 565–74.

Tan U. A new syndrome with quadrupedal gait, primitive speech, and severe mental retardation as a live model for human evolution. Int J Neurosci 2006; 116: 361–9.

Thornton GK, Woods CG. Primary microcephaly: do all roads lead to Rome? Trends Genet 2009; 25: 501–10.

Traka M, Millen KJ, Collins D, Elbaz B, Kidd GJ, Gomez CM, et al. WDR81 is necessary for purkinje and photoreceptor cell survival. J Neurosci 2013; 33: 6834–44.

Xu C, Min J. Structure and function of WD40 domain proteins. Protein Cell 2011; 2: 202–14.

Yamamoto S, Jaiswal M, Charng WL, Gambin T, Karaca E, Mirzaa G, et al. A drosophila genetic resource of mutants to study mechanisms underlying human genetic diseases. Cell 2014; 159: 200–14.

De novo mutation screening in childhood-onset cerebellar atrophy identifies gain of function mutations in the calcium channel *CACNA1G*

Jean Chemin[1,2] *, Karine Siquier-Pernet[3,4] *, Michaël Nicouleau[3,4], Giulia Barcia[3,4], Ali Ahmad[1,2], Daniel Medina-Cano[3,4], Sylvain Hanein[5], Nami Altin[3,4], Laurence Hubert[5], Christine Bole-Feysot[6], Cécile Fourage[7], Patrick Nitschké[7], Julien Thevenon[8], Marlène Rio[4,9], Pierre Blanc[4,9], Céline vidal[5], Nadia Bahi-Buisson[3,10,11], Isabelle Desguerre[3,11], Arnold Munnich[3,9], Stanislas Lyonnet[3,9,10], Nathalie Boddaert[3, 12,13], Emily Fassi[14], Marwan Shinawi[14], Holly Zimmerman[15], Jeanne Amiel[3,9,10], Laurence Faivre[8], Laurence Colleaux[3,4], Philippe Lory[1,2] *, Vincent Cantagrel[3,4] *

* These authors contributed equally to this work

Affiliations

1. IGF, CNRS, INSERM, University of Montpellier, Montpellier, France.
2. LabEx 'Ion Channel Science and Therapeutics', Montpellier, France.
3. Paris Descartes - Sorbonne Paris Cité University, Imagine Institute, Paris, France.
4. Laboratory of developmental brain disorders, INSERM UMR 1163, Paris, France.
5. Translational Genetics, INSERM UMR 1163, Imagine Institute, Paris, France.
6. Paris Descartes-Sorbonne Paris Cité University, Imagine Institute, Genomic Core Facility, 75015 Paris, France.
7. Paris-Descartes Sorbonne Paris-Cité University, Imagine Institute, Bioinformatics Core Facility, 75015 Paris, France.
8. Centre de Génétique et Centre de Référence “Anomalies du Développement et Syndromes Malformatifs”, Hôpital d’Enfants, CHU Dijon, Dijon, France.
9. Service de Génétique, Necker Enfants Malades University Hospital, APHP, Paris.
10. Laboratory of embryology and genetics of congenital malformations, INSERM UMR1163, Paris, France.
11. Service de neurologie pédiatrique, Necker Enfants Malades University Hospital, APHP, Paris.

12. Pediatric Radiology Department, Necker Enfants Malades University Hospital, APHP, Paris, France.
13. Image - Institut Imagine, INSERM UMR1163, Université Paris Descartes, Hôpital Necker Enfants Malades, Paris, France
14. Division of Genetics and Genomic Medicine, Department of Pediatrics, Washington University School of Medicine, St. Louis, Missouri, USA.
15. Division of Genetics, Department of Pediatrics, University of Mississippi Medical Center, 2500N State St, Jackson, MS, 39216, USA.

Corresponding authors:

- Vincent Cantagrel vincent.cantagrel@inserm.fr
  Institut IMAGINE, Lab 323- B3
  24, Bd du Montparnasse
  75015 Paris, FRANCE
- Philippe Lory philippe.lory@igf.cnrs.fr
  Institut de Génomique Fonctionnelle, Université de Montpellier
  141, rue de la Cardonille
  34094 Montpellier, FRANCE

Running title

De novo mutations in *CACNA1G* cause early onset cerebellar atrophy

Abstract

Cerebellar atrophy is a key neuroradiological finding usually associated with cerebellar ataxia and cognitive development defect in children. Unlike the adult forms, early onset cerebellar atrophies are classically described as mostly autosomal recessive conditions and the exact contribution of de novo mutations to this phenotype has not been assessed. In contrast, recent studies pinpoint the high prevalence of pathogenic de novo mutations in other developmental disorders such as intellectual disability, autism spectrum disorders and epilepsy. Here, we investigated a cohort of 47 patients with early onset cerebellar atrophy and/or hypoplasia using a custom gene panel as well as whole exome sequencing. De novo mutations were identified in 35% of patients while 27% had mutations inherited in an autosomal recessive

manner. Understanding if these de novo events act through a loss or a gain of function effect is critical for treatment considerations. To gain a better insight into the disease mechanisms causing these cerebellar defects, we focused on *CACNA1G*, a gene not yet associated with the early-onset form. This gene encodes the Cav3.1 subunit of T-type calcium channels highly expressed in Purkinje neurons and deep cerebellar nuclei. In total, we identified four patients with de novo *CACNA1G* mutations. They all display severe motor and cognitive impairment, cerebellar atrophy as well as variable features such as facial dysmorphisms, digital anomalies, microcephaly and epilepsy. Three subjects share a recurrent c.2881G>A/p.Ala961Thr variant while the fourth patient has the c.4591A>G/p.Met1531Val variant. Both mutations drastically impaired channel inactivation properties with significantly slower kinetics (~5 times) and negatively shifted potential for half-inactivation (> 10 mV). In addition, these two mutations increase neuronal firing in a cerebellar nuclear neuron model and promote a larger window current fully inhibited by TTA-P2, a selective T-type channel blocker. This study highlights the prevalence of de novo mutations in early-onset cerebellar atrophy and demonstrates that Ala961Thr and Met1531Val are gain of function mutations. Moreover, it reveals that aberrant activity of Cav3.1 channels can markedly alter brain development and suggests that this condition could be amenable to treatment.

Keywords

CACNA1G, Cav3.1, voltage-gated calcium channel, de novo mutation, cerebellar atrophy,

Abbreviations

ChCA	Childhood-onset cerebellar atrophy
WES	Whole exome sequencing
CGH	Comparative genomic hybridization
TNGS	Targeted next generation sequencing
EEG	Electroencephalogram
DD	Developmental delay
MRI	Magnetic resonance imaging
WT	Wild-type

Introduction

Cerebellar atrophy is commonly identified in pediatric forms of cerebellar ataxias. This neuroradiological finding defines the childhood-onset cerebellar atrophy (ChCA) group and is generally associated with imbalance, poor coordination, developmental delay, and intellectual disability (Tavano *et al.*, 2007) (Al-Maawali *et al.*, 2012). This ChCA group includes a large number of clinically heterogeneous genetic diseases frequently comprising epilepsy. Molecular diagnosis is challenging, as an ever-increasing number of very rare conditions are associated with ChCA. Importantly, such cerebellar atrophies are present in a group of progressive, very severe diseases with key diagnostic features that can appear several years after initial patient assessment (Gregory *et al.*, 2008; Romani *et al.*, 2015) (Fusco *et al.*, 2013) and with a critical need of early diagnosis. Next generation sequencing including whole exome sequencing (WES) has accelerated molecular diagnosis and improved patient management (Deciphering Developmental Disorders, 2015) (Megahed *et al.*, 2016) (Sawyer *et al.*, 2014). These approaches have identified a high prevalence of damaging de novo mutations with dominant effect in common developmental disorders such as intellectual disability, autism spectrum disorders and epilepsy (Deciphering Developmental Disorders, 2017). A mean prevalence of 1 in 295 births (42% of the affected individuals) was estimated for monoallelic developmental disorders caused by de novo mutations. Understanding if these de novo events act through loss or gain of function effect can be important for treatment consideration (Boycott *et al.*, 2013). About half of de novo mutations alter protein function through gain of function or dominant negative effects (Deciphering Developmental Disorders, 2017). Gain of function mutations that are associated with the ectopic or increased activation of specific protein or pathway allow the identification of define targets used for the drug design (Segalat, 2007). In contrast small molecule drug development for loss-of-function mutations is especially challenging (Yue, 2016). Consequently, the identification of de novo, gain of function mutations could benefit both molecular diagnosis and treatment development. The prevalence of de novo mutations has been documented in large cohorts (Deciphering Developmental Disorders, 2017) but such studies often include a very wide range of heterogeneous conditions with limited clinical data. Among these conditions, brain structural defects including microcephaly, diffuse cortical brain malformations or ChCA are classically associated with recessive inheritance (Desikan and Barkovich, 2016) (Cavallin *et al.*, 2017) (Al-Maawali *et al.*, 2012) (Sawyer *et al.*, 2014). More recently, de novo mutations in several genes have been reported in ChCA (Travaglini *et al.*, 2017) (Gerber *et al.*, 2016) (Watson *et*

al., 2017) (Kurihara *et al.*, 2017). However the extend of the contribution of these rare de novo events to the genetic basis of ChCA is not known.

In order to estimate the prevalence of de novo versus inherited mutations in ChCA, we investigated a cohort of 47 patients with ChCA and/or hypoplasia using a custom targeted next generation sequencing gene panel (TNGS) and whole exome sequencing (WES). This investigation led us to identify pathogenic de novo events as the major cause of ChCA. Additional exploration of candidate de novo mutations identified *CACNA1G* as a new ChCA gene with a gain of function effect as the disease mechanism.

Materials and Methods

Subject information

The 47 patients included in this study are from the 37 families and were referred to the departments of pediatric neurology, genetics, metabolism or ophthalmology of the Necker Enfants Malades Hospital. This cohort includes 25 female and 22 male subjects. Consanguinity of the parents was documented for 6 families (16.2%) and 10 families (27%) include two affected siblings. Patients were recruited upon the clinical findings of cognitive and motor impairment during pediatric age including cerebellar signs such as oculomotor abnormalities, truncal ataxia and head movements and the presence of cerebellar atrophy and/or hypoplasia on MRI. Patients with both atrophy and hypoplasia are included as these conditions are not always distinguishable (Poretti *et al.*, 2008). Both static and progressive conditions were included. This cohort includes 15 families with pons involvement (40.5%). The MRI examination consisted of sagittal spin echo (SE) T1, axial fast SE T2 and coronal fluid-attenuated inversion recovery (FLAIR) images. In the absence of sequential scans, cerebellar atrophy was diagnosed with the identification on MRI of shrunken folia and large cerebellar fissures. High-resolution karyotype, array-CGH (400kb resolution) was performed. Informed consents have been obtained both from the participants and the legal representatives of the children.

Targeted gene panel and whole exome sequencing

TNGS was prioritized unless the clinical presentation suggested a new syndromic entity that was directly explored through WES. Patients negative with TNGS were explored with WES to identify new disease gene. Patients primarily tested negative with WES were also analyzed with TNGS in order to rule out mosaic mutations or small copy number variations (Hayashi *et al.*, 2017) (de Ligt *et al.*, 2013).

A custom gene panel including 72 ChCA genes (Supplementary Table 1) was set up for this study. Cerebellar hypoplasia genes were included as this phenotype often overlaps with cerebellar atrophy at the pediatric age (Poretti *et al.*, 2014). Genes such as *CASK*, *EXOSC3* or *WDR81* can be involved in cerebellar atrophy/hypoplasia without or with pons hypoplasia (i.e. pontocerebellar hypoplasia (PCH)) and consequently PCH genes are also included. Genomic DNA libraries were generated from 2 µg DNA sheared with a Covaris S2 Ultrasonicator using SureSelectXT Library PrepKit (Agilent, Garches, France) and the Ovation® Ultralow System V2 (NuGen) according to the suppliers' recommendations. 1459 regions of interest encompassing all exons and 25 base pairs intronic flanking sequences of the 72 selected genes were captured by hybridation with biotinylated complementary 120-pb RNA baits designed with SureSelect SureDesign software (hg19, GRCh37, February 2009). The 309.16 Kb targeted DNA region was pulled out with magnetic streptavidin beads, PCR-amplified using indexing primers and sequenced on an Illumina HiSeq2500 HT system. NGS data analysis was performed with Paris Descartes University / Institut IMAGINE's Bioinformatics core facilities. Paired-end sequences were mapped on the human genome reference (NCBI build37/hg19 version) using the Burrows-Wheeler Aligner. Downstream processing was carried out with the Genome Analysis Toolkit (GATK), SAMtools, and Picard, according to documented best practices (http://www.broadinstitute.org/gatk/guide/topic?name=best-practices).

WES was performed with DNA extracted from blood and processed at the Genomic core facility in the Imagine Institute as previously described (Megahed *et al.*, 2016). A WES trio approach (i.e. Sequencing of DNA from the mother, father and the affected child) was performed for 24 families. Briefly, exome capture was performed with the SureSelect Human All Exon kit (Agilent technologies) and sequencing was carried out on a HiSeq2500 (Illumina). The mean depth of coverage obtained for each sample was > 150x with >97 % of the exome covered at least 30x.
All identified variants were validated using Sanger sequencing or multiplex ligation-dependent probe amplification (MLPA) for duplications or deletions.
Identification of additional patients with neurodevelopmental disorders and de novo *CACNA1G* mutations was possible through collaborations. Subject 2 (S.2) was identified at the Children's Hospital CHU of Dijon that sequenced ~ 650 clinical exomes from patients with neurodevelopmental defects (Bourchany *et al.*, 2017). S.3 and S.4 were identified through GeneMatcher web site (Sobreira *et al.*, 2015) and sequenced by the GeneDx laboratory (Kury *et al.*, 2017).

Variant analysis, databases and bioinformatic tools

A variant filtering pipeline was systematically applied to narrow down the number of putative causative variants. All the possible inheritance patterns were tested. Briefly, variant calling was performed with the GATK Unified Genotyper (https://www.broadinstitute.org/ gatk/) based on the 72 version of ENSEMBL database. Common variants (i.e. minor allele frequency >1 %) were filtered out by using dbSNP, 1000 genomes databases and our In-house exome collection, which includes more than 10,000 exomes. Further, functional (protein-altering) alleles were prioritized versus non-functional. Potentially pathogenic variants in known disease genes were identified if flagged as damaging by polyphen2 (http://genetics.bwh. harvard.edu/pph2/), Sift (http://sift.jcvi.org/) or mutation taster (http://www.mutationtaster.org/). Remaining variants were compared with those in the public databases ExAC (http://exac.broadinstitute.org/) and EVS (http://evs.gs.washington.edu/EVS/) exome database. The presence of candidate recessive variants in homozygous intervals was checked by identifying predicted regions of SNP homozygosity from exome data with the UnifiedGenotyper tool from GATK (https://www.broadinstitute.org/ gatk/). Additional filtering of de novo variants was done using the following criteria. Candidate de novo mutations were excluded if already reported in the ExAC database, if present more than 5 times in our In-house exome and genome database or if located in a gene already involved in a distinct developmental defect without neurological involvement. New genes (Supplementary table 2 and 3) include genes with variants identified in at least two unrelated families with similar clinical phenotype but not previously reported. Cav3.1 protein structure modeling was performed using the RaptorX web server (Kallberg *et al.*, 2012), based on Cav1.1 structure (Wu *et al.*, 2015).

Site directed mutagenesis, cell culture and transfection protocols

Site-directed mutagenesis of the human wild-type (WT) Cav3.1 encoding plasmid (canonical transcript NM_018896.4 cloned into pcDNA3.1) was performed using the QuikChange site-directed mutagenesis kit (Agilent Technologies) to introduce the A961T and M1531V *CACNA1G* mutations. Mutations were verified by Sanger sequencing of the full coding sequence. HEK-293T cells (Human Embryonic Kidney cells transformed with large T antigen) were cultured in DMEM supplemented with GlutaMax, 10 % fetal bovine serum and 1% penicillin / streptomycin (Invitrogen). Transfections were performed using jet-PEI (QBiogen) with a DNA mix (1.5 µg total) containing 0.5 % of a GFP-encoding plasmid and 99.5 % of either of the plasmids that code for the human Cav3.1 WT, Cav3.1 A961T and Cav3.1 M1531V constructs. Two days after transfection, HEK-293T cells were split using Versene (Invitrogen) and plated at a density of ~35×10^3 cells per 35 mm Petri dish for electrophysiological recordings, which were performed the following day.

Electrophysiological recordings

Macroscopic T-type Ca^{2+} currents were recorded at room temperature using an Axopatch 200B amplifier (Molecular Devices). Borosilicate glass pipettes had a resistance of 1.5–2.5 MOhm when filled with an internal

solution containing (in mM): 140 CsCl, 10 EGTA, 10 HEPES, 3 Mg-ATP, 0.6 Na-GTP, and 3 $CaCl_2$ (pH adjusted to 7.25 with KOH, ~315 mOsm). The extracellular solution contained (in mM): 135 NaCl, 20 TEACl, 2 $CaCl_2$, 1 $MgCl_2$, and 10 HEPES (pH adjusted to 7.25 with KOH, ~330 mOsm). Recordings were filtered at 2 kHz. In some experiments, TTA-P2 (Alomone) was applied using a gravity-driven homemade perfusion device (100 µl/min) and control experiments were performed similarly using the vehicle alone. Data were analyzed using pCLAMP9 (Molecular Devices) and GraphPad Prism (GraphPad) softwares. Results are presented as the mean ± SEM, and n is the number of cells. Statistical analysis were performed with the Student *t*-test or with one-way ANOVA combined with a Tukey post-test for multiple comparisons (* $p<0.05$, ** $p<0.01$, *** $p<0.001$).

Cerebellar nuclear neuron modeling

Modeling was performed using the NEURON simulation environment (Hines and Carnevale, 1997). The model of cerebellar nuclear neuron is based on a previously published model ((Sudhakar *et al.*, 2015), downloaded from the model database at Yale University (https://senselab.med.yale.edu/modeldb/)). We generated neuronal activities using medium value of input gain, as described in Fig.1B in Sudhakar et al., 2015. The electrophysiological properties of the Cav3.1 channels were modeled using Hodgkin-Huxley equations as described previously (Huguenard and Prince, 1992; Destexhe *et al.*, 1996). The values obtained for the Cav3.1 WT, A961T and M1531V mutants were substituted for the corresponding values of native T-channels in cerebellar nuclear neurons. The membrane voltage values were corrected for liquid junction potential, which was 4.5 mV in our recording conditions. The equations to model the Cav3.1 WT current properties were: m_inf = 1 / (1+exp((v+50.78)/-5.05)) ; h_inf = 1 / (1+exp((v+78.2)/5.12)) ; tau m = 0.333 / (exp((v + 133.9) / -19.75) + exp((v + 21.53) / 7.968)) + 1.267 ; tau h = 0.333 * exp((v + 21.01) / -8.385) + 18.75. The equations to model the Cav3.1 A961T current properties were: minf = 1 / (1 + exp((v + 56.85) / -4.842)) ; hinf = 1 / (1 + exp((v + 90.93) / 8.719)) ; taum = 0.333 / (exp((v + 154.7) / -15.84) + exp((v + 21.53) / 8.479)) + 1.638 ; tauh = 0.333 * exp((v + 5.692) / -11.66) + 106.6. The equations to model the Cav3.1 M1531V current properties were: minf = 1 / (1 + exp((v + 61.9) / -5.93)) ; hinf = 1 / (1 + exp((v + 90.19) / 6.35)) ; taum = 0.333 / (exp((v + 176) / -22.66) + exp((v + 28.78) / 8.13)) + 1.32 ; tauh = 0.333 * exp((v + 29.01) / -8.532) + 65.01.

Results

Combined custom gene panel and exome sequencing identify de novo mutations as a prevalent cause of ChCA

In order to identify the molecular causes of ChCA, we investigated a cohort of 47 patients with ChCA and/or hypoplasia using a combination of custom TNGS and whole exome sequencing (WES). With mean target coverage of 430X (99.9% of targeted DNA covered more than 30X), the TNGS was used as a primary test for most of the families and identified likely diagnosis for 7 out of 25 families sequenced (28%; Supplementary tables 1 and 2) including heterozygous insertions and deletions (n=4) poorly or not detected by WES and CGH array analysis. WES identified likely causative variants in known ChCA genes for 6 out of 32 families tested and the combination of these approaches was able to identify confident causative variants for 35% of families (Fig. 1A). All these variants are located in genes

previously associated with comparable clinical phenotypes. They are inherited through an autosomal recessive mode (13% of the families; n=5) or arise de novo (22% of the families; n=8) as either X-linked or autosomal dominant. Most of the cases of de novo mutations involve the *CASK* (Calcium/Calmodulin Dependent Serine Protein Kinase) gene, including a male patient with a truncating germ line de novo mutation and spared pontine bulging on MRI (Fig. 1B). A recurrent de novo variant was also identified in the recently reported *CTBP1* (C-terminal-binding protein 1) gene (Beck *et al.*, 2016) in a patient with non-progressive cerebellar atrophy (Fig. 1C) but without the previously described tooth enamel defects. In order to assess the prevalence of de novo events in the remaining undiagnosed patients, we explored the WES data for de novo and recessive variants located in genes not previously associated with ChCA. Using strict variant frequency criteria (see methods), we identified five index cases with de novo variants and five others with recessive variants (Fig. 1A). Four of the de novo variants are located in highly constrained genes (P_{LI}=1; Supplementary table 3) as expected for causative de novo mutations (Samocha *et al.*, 2014). In total, 10 females and 3 males carry validated and probably causative de novo variants. A probably causative variant was identified for 62% of the families (n=23) with a molecular finding, which supports the idea that de novo mutations are prevalent in ChCA. To unravel how these de novo mutations can affect the developing cerebellum integrity, we focused on a variant located in the *CACNA1G* gene, the gene encoding the Cav3.1 T-type calcium channel. Cav3.1 channel is highly expressed in Purkinje neurons and deep cerebellar nuclei where it plays an important role in signal processing and synaptic plasticity (Isope *et al.*, 2012) (Ly *et al.*, 2013). However, evidences supporting its involvement in human cerebral development are lacking.

De novo variants in CACNA1G gene are associated with severe congenital encephalopathy

WES analysis on subject 1 (S.1) and her parents (family CerID08) did not identify recessive variant that could have explained the cerebellar syndrome but identified a Sanger-validated de novo variant in the *CACNA1G* gene predicting a p.Ala961Thr alteration as the only disease-causing variant. By using a collaborative network and the GeneMatcher platform, we followed a genotype-first approach and identified three additional cases with confirmed de novo mutation in the *CACNA1G* gene. These cases were subsequently included in this study for clinical comparison and functional investigation. WES analysis performed in these additional cases identified the same p.Ala961Thr missense change in subjects 3 and 4,

suggesting a hotspot mutation, while the subject 2 harbors a p.Met1531Val alteration (see Supplementary case reports). These four patients were born after a full term pregnancy. Epileptic encephalopathy was first detected for subjects 2 and 3 in the first 2 weeks of life but seizures were not present in the two others. All the subjects presented between birth and 1 year of age with global developmental delay, axial hypotonia, and peripheral hypertonia. As early as 8 months of age, cerebellar symptoms were detected and associated with global cerebellar atrophy seen on MRI (Fig. 2A-J). Motor and cognitive developments were very limited as patients could not stand or walk without aid and patients were described as either non-verbal or with very limited language development. Microcephaly was detected in two patients. Facial dysmorphisms and digital anomalies were present including abnormal hairline, short hands and feet, broad thumbs and great toes (see Fig.2K-O, Table 1 and Supplementary case reports). The identified de novo variants involve two amino-acids fully conserved at the protein level (Fig. 2P). In addition, these variants are absent from ExAC database and predicted to be deleterious by polyphen, SIFT, and Mutation Taster. The four subjects have comparable clinical signs including cognitive developmental defects and cerebellar ataxia. Based on this observation, in combination with the predicted deleterious impact of the variants, we hypothesized that p.Ala961Thr and p.Met1531Val alterations are responsible for the congenital encephalopathy present in these patients.

The A961T and the M1531V Cav3.1 mutants display currents with very slow kinetics that activate and inactivate at more negative membrane potentials.

Both Ala961 and Met1531 amino-acids are located at the inner part of the S6 segments of the domains II and III of the Cav3.1 protein, respectively, the S6 segments contributing to the pore lining of the channel (Fig.2 Q-S). We therefore investigated the electrophysiological impact of the A961T and M1531V mutations. It is worth to note that these mutations were introduced in the Cav3.1a channel isoform, which is highly expressed in the human cerebellum (Monteil *et al.*, 2000). The Cav3.1 channels, WT and mutants (A961T and M1531V) were expressed in HEK-293T cells and the T-type Ca^{2+} current was measured in the whole-cell configuration of the patch-clamp technique. As presented in Figure 3, all the Cav3.1 constructs generated robust low-voltage-activated currents with a peak current near -35 / -40 mV (Fig. 3A). The current density was unchanged in cells expressing A961T and M1531V mutant channels, compared to cells expressing WT channels (Table 2). The A961T

and the M1531V currents activated at more negative potentials as compared to the WT Cav3.1 current (Fig. 3A, B). We found that the potential for half-activation ($V_{1/2}$) was significantly shifted by ~ -6 mV and by ~ -11 mV for the A961T and the M1531V mutants, respectively (see Table 2). Importantly, both mutants displayed currents with markedly slow inactivation kinetics at all test pulse potentials (Fig. 3A, C). As shown in the Table 2, the A961T mutant exhibited in average ~5 times slower inactivation kinetics than the WT channel whereas the inactivation kinetics of the M1531V mutant was ~3 times slower. Similarly, the deactivation kinetics of both mutants was ~ 3 /5 times slower than those of WT channels (Fig. 3D, Table 2). We next investigated the steady-state inactivation properties of the Cav3.1 mutants by stepping holding potentials from -130 mV to -40 mV (Fig. 4A). Both A961T and M1531V currents showed a potential for half-inactivation ($V_{1/2}$) that was shifted by about 12 mV toward negative potentials (Fig. 4A, B and Table 2). In addition, the recovery from inactivation of the A961T current, but not of the M1531V current, was markedly slower than the recovery from inactivation of the WT channels (Fig. 4C, D). Notably, the A961T current did not entirely recover after an interpulse as long as 15 seconds (Fig.4D). Overall, these experiments have revealed striking changes in the electrophysiological properties for A961T and M1531V mutant channels likely supporting gain of channel activity.

The A961T and the M1531V Cav3.1 mutants increase neuronal firing in a model of deep cerebellar nucleus neuron

In order to elucidate whether the A961T and M1531V mutants would correspond to gain of function mutations and promote increased excitability in cerebellar neurons, we performed simulation experiments. These experiments were carried out using an established computational model of the neuronal activities in deep cerebellar nucleus neuron (Steuber *et al.*, 2011) (Sudhakar *et al.*, 2015), in which the electrophysiological parameters of A961T and M1531V mutants were computed and compared to the WT Cav3.1 channel condition for their ability to modulate firing activity (Fig. 5). Turning off the T-type channel conductance in this model resulted in a decrease in spike frequency (Fig. 5A and 5B). Importantly, substituting the WT Cav3.1 channel parameters with those of the two mutants, especially A961T, markedly increased the spike frequency. The spike frequency was 44 Hz with the WT (Fig. 5A and 5E) channel whereas it reached 54 Hz (> 22%) with the M1531V mutant (Fig. 5D and 5E) and 88 Hz (> 100%) with the A961T mutant (Fig. 5C and 5E). These data support that the

A961T and M1531V are gain of function mutations, promoting increased firing activity in deep cerebellar nucleus neurons.

The A961T and the M1531V Cav3.1 mutants generate a large window current fully blocked by TTA-P2

Collectively, the changes in T-type channel gating for the A961T and M1531V mutants are expected to support larger Ca^{2+} influx at membrane potentials close to the cell's resting potential. In addition, these mutant channels that remain open longer upon depolarization would allow further increase in the Ca^{2+} entry. Our electrophysiological data are predictive of a T-type window current (a persistent background calcium current) that would be larger for the A961T and M1531V mutants than the one generated by WT channels. To test this hypothesis, we first performed long-lasting recordings at -70 mV (Fig. 6A-D). We found that the WT channel displayed a fast inactivating current with no detectable current measured after 5 seconds (Fig. 6A). In contrast, a significant fraction of the calcium current was persistent for the A961T (Fig. 6B) and M1531V mutants (Fig. 6C). In average, this persistent current represented only ~0.33 % of the maximal current for the WT channel (n=5) whereas it reached ~2.5 % of the maximal current for the A961T mutant ($p<0.05$; n=8), and ~3.8 % of the maximal current for the M1531V mutant ($p<0.01$; n=10; Fig. 6D). We next performed ultra-slow depolarizing voltage ramps (10 seconds duration) to record directly the window current over a large range of membrane potentials (Fig. 6E-G). The Cav3.1 WT generated a window current of small amplitude, whereas both the A961T and the M1531V mutants produced a window current of significantly much larger amplitude (Fig. 6E-G, left panels). To better analyze the window current, the ratio of the window current amplitude over the maximal current obtained in the same cell using a standard pulse protocol was quantified (Fig. 6H). In average we found that the window current represented about 1 % of the total current for the WT channel (n=6), while it was significantly larger for the A961T mutant (~11 %; $p<0.01$, n=6) and the M1531V mutant (~8%; $p<0.01$, n=6). In addition, in the presence of TTA-P2 (5 μM), a selective T-type channel blocker that penetrates well the CNS (Shipe *et al.*, 2008) and blocks the native T-type currents in deep cerebellar nuclear neurons (Boehme *et al.*, 2011), the window current was completely abolished both for WT and mutant Cav3.1 channels (Fig. 6H). Furthermore, concentration-response curves for TTA-P2 (Fig. 6I) indicated similar inhibition of WT (IC_{50}=0.16 ± 0.02 μM, n=7), A961T (IC_{50}=0.14 ± 0.03

μM, n=5) and M1531V Cav3.1 channels (IC_{50}=0.24 ± 0.05 μM, n=6). Importantly, TTA-P2 used at micromolar concentration is known to have no inhibitory effect on sodium and HVA calcium channels, including Cav2.3 (Choe *et al.*, 2011).

Discussion

Based on the exploration of a cohort of 47 children, our study provides several novel and important findings documenting the etiology of ChCA. First, using a combination of a gene panel and whole exome sequencing, we identified causative and likely causative variants in previously reported genes as well as novel candidate genes. Overall, de novo mutations appear to be more prevalent than recessive mutations in ChCA. Second, further investigation of a de novo variant in the *CACNA1G* gene, in collaboration with other groups, led to the discovery of 3 additional cases with recurrent or clustered de novo variants and comparable clinical phenotype. Third, our electrophysiological study of these *CACNA1G* mutations provided evidences for a gain of activity of the mutant Cav3.1 channels causing hyperexcitability in deep cerebellar neurons.

Here we describe a comparable incidence of likely causative de novo mutations in our cohort of ChCA cases compared to the whole group of developmental disorders, 35% versus 42% respectively (Deciphering Developmental Disorders, 2017). As previously reported in studies of cohorts with de novo mutations, we also observed an unexplained higher incidence in females versus males, a variable expression of epilepsy phenotype seen in patients with mutations in epilepsy/seizures-associated genes and the clustering of characterized gain of function mutations (Deciphering Developmental Disorders, 2017) (Geisheker *et al.*, 2017). Alteration of calcium homeostasis and signaling is one of the recurrent causes of ataxia and neurodegeneration (Matilla-Duenas *et al.*, 2014) (Tomlinson *et al.*, 2009) (Coutelier *et al.*, 2017). In addition to *CACNA1G*, mutations in other genes involved in intracellular calcium signaling (*ITPR1)*(Tada *et al.*, 2016) or regulated by intracellular calcium (*CASK)* (Lu *et al.*, 2003) were also identified in our screen, further supporting the relevance of calcium homeostasis alteration in the context of ChCA.

This study is the first report characterizing de novo gain of function mutations in *CACNA1G* associated with a congenital disorder. Based on the phenotype in four children with mutations exhibiting strong Cav3.1 dysfunction, we could delineate a novel calcium channelopathy condition that includes severe psychomotor retardation, cerebellar ataxia, digital anomalies

and variable facial dysmorphisms, as well as features with incomplete penetrance such as microcephaly and epilepsy.

Our study adds to previous genetic and functional investigations of de novo gain of function mutations in other voltage-gated calcium channel genes. The Timothy syndrome is a multi-systemic disorder with developmental delay, autism spectrum disorder, facial dysmorphism, cardiac arrhythmia (long QT syndrome) and syndactyly as the core features (Splawski *et al.*, 2004) (Splawski *et al.*, 2005). It results from gain of function mutations in the *CACNA1C* gene that codes for the L-type Cav1.2 calcium channel. Recently, investigation of patients with primary aldosteronism led to the identification of de novo mutations in the *CACNA1H* (Scholl *et al.*, 2015) (Daniil *et al.*, 2016) and *CACNA1D* (Scholl *et al.*, 2013) genes coding respectively for the T-type Cav3.2 and the L-type Cav1.3 calcium channels. Other *CACNA1D* mutations with consequences on the cognitive development were also reported (Pinggera *et al.*, 2015). Collectively, these studies highlight the broad role of calcium and voltage-gated calcium channels in the development and/or function of the heart, adrenal cortex and brain, among others, and that altered calcium signaling can give rise to a variety of cellular and organ defects exemplified in the human calcium channelopathies previously described.

It is likely that the full clinical spectrum associated with *CACNA1G* mutations is incomplete. Monoallelic deletions of the *CACNA1G* gene have been associated with mild intellectual disability without cerebellum atrophy (Preiksaitiene *et al.*, 2012; Bardai *et al.*, 2016; Jewell *et al.*, 2017). The significant difference with the neurological phenotype associated with A961T and M1531V *CACNA1G* variants is consistent with a gain of function effect for these mutations. A *CACNA1G de novo* variant of unknown pathogenicity and associated with autism, mild intellectual disability and dyspraxia was previously reported (Deciphering Developmental Disorders, 2015). Interestingly, a recurrent and inherited mutation in *CACNA1G* was described in patients with late-onset cerebellar ataxia (Coutelier *et al.*, 2015; Morino *et al.*, 2015). This R1715H mutation is located in the S4 of domain IV and exhibits a modest but significant effect on the electrophysiological properties (Coutelier *et al.*, 2015). In this context, the cognitive function of the patients was generally described as normal contrasting with the severely impaired cognitive development of the patients with de novo *CACNA1G* mutations. The role of the cerebellum in the cognitive function and especially in children's learning is recognized although not well understood (Tavano *et al.*, 2007) (Steinlin, 2008). Considering the prevalent expression of *CACNA1G* in the cerebellum, it is tempting to

speculate that a disrupted cerebellar development caused by severe *CACNA1G* mutations could be mainly responsible for cognitive impairment, supporting a critical role of the cerebellum in cognitive development.

Our patch-clamp experiments clearly document that A961T and M1531V *CACNA1G* mutations strikingly alter the electrophysiological behavior of Cav3.1 channels, especially the fast inactivation property, which is one of the most distinctive features of these channels. Both inactivation and deactivation kinetics were significantly slowed for the mutated channels. Both steady-state activation and inactivation properties were affected with the potentials for half-inactivation and for half-activation significantly shifted toward negative potentials. On the one hand, slowing of inactivation and deactivation kinetics would correspond to a gain of channel activity, allowing larger entry of calcium into the cell. On the other hand, a negative shift in the steady-state inactivation would be consistent with a loss of channel activity as a smaller fraction of Cav3.1 channels would activate in the physiological range of the membrane potential. Modeling experiments were therefore instrumental to demonstrate that both A961T and M1531V could enhance firing activity in deep cerebellar nucleus neurons and, consequently, to validate that these two mutations are gain of function mutations.

A961 and M1531 amino-acids are located in the intracellular part of the S6 segment in domains II and III, respectively. In good agreement with the hypothesis that clustering of de novo missense variants help identify functional protein domains (Geisheker *et al.*, 2017), we show here the close 3D proximity of the Ala961 and Met1531 residues in the Cav3.1 protein. The M1531 residue is part of a Met-Phe-Val (MFV) sequence of the IIIS6 segment, which was implicated in Cav3.1 channel inactivation in early structure-function studies (Marksteiner *et al.*, 2001) (Talavera and Nilius, 2006). The study by Marksteiner et al. (2001), in which M1531 corresponds to M1501 in the rat cDNA, described that the mutants showing a delayed inactivation also showed a slower recovery from inactivation. Interestingly, the recurrent mutation in *CACNA1H* (Cav3.2) described at position M1549 with two distinct substitutions, M1549V (Scholl *et al.*, 2015) and M1549I (Daniil *et al.*, 2016) is also part of the highly conserved MFV sequence in IIIS6 segment of Cav3 channels. Similar to the M1531V-Cav3.1 described here, M1549V and M1549I mutations profoundly alter the electrophysiological properties of the Cav3.2 current, exhibiting a significant hyperpolarization shift in activation and inactivation properties, a significant slowing of the activation, inactivation and deactivation kinetics with an expected increase in calcium entry and aldosterone production

(Daniil *et al.*, 2016). Combined together, these studies establish this conserved methionine residue in IIIS6 as a major determinant for T-type channel inactivation.

By describing marked effects of the A961T mutation on the inactivation properties, our study demonstrates that both the S6 segments of domains II and III contribute to the inactivation gate of the Cav3.1 channel pore. To the best of our knowledge, a role in inactivation of this conserved Alanine residue in IIS6 is not yet documented, but surrounding residues, especially Valine 960 and Isoleucine 962, were reported for their implication in Cav3.2 inactivation (Demers-Giroux et al 2013). When expressed in Xenopus oocytes, the Cav3.2 mutants V1011G and I1013G, but not A1012G, showed significantly slower activation, deactivation and inactivation kinetics (Demers-Giroux et al 2013). This VAI sequence in IIS6 segment, highly conserved in Cav3 channels, may correspond to the MFV locus in IIIS6, being also a critical determinant in T-type channel inactivation.

Remarkably, other de novo mutations in voltage-gated calcium channels α1 paralogs share similitudes in their location and functional consequences. The two original mutations identified in Timothy syndrome, G406R and G402S are located at the boundary between the S6 segment of domain I (IS6) and the I-II loop in the Cav1.2 protein. These mutations markedly slow inactivation kinetics of the L-type current leading to a net increase in calcium influx and a prolonged cardiac action potential (Splawski *et al.*, 2004) (Splawski *et al.*, 2005) (Bidaud and Lory, 2011). A similarly localized de novo mutation (G407R) was recently found in *CACNA1D*, the gene encoding the L-type Cav1.3 calcium channel. It was associated with pronounced slowing of current inactivation as well as a negative shift in the steady-state activation and inactivation (Pinggera *et al.*, 2015). All together, these data highlight the physiological importance of the intracellular part of the S6 segments as a hot-spot for de novo gain of function mutations in Cav channel family. These cross-paralog similarities should stimulate further investigations of *de novo* variants in other protein families and facilitate the identification of gain of function mutations.

Identifying a gain of channel activity for ChCA mutants of the T-type Cav3.1 channel may represent a clue to design a therapeutic strategy as T-type channel blockers exist. Interestingly, both A961T and M1531V mutant channels generate an aberrantly elevated window current. The T-type window current allows a permanent entry of calcium ions at physiological cell's resting membrane potentials and any elevated window current would

disrupt intracellular calcium homeostasis, thus contributing to the pathological effects. Expectedly, we found that the window current was fully inhibited by TTA-P2, a selective T-type channel blocker (Shipe *et al.*, 2008) (Dreyfus *et al.*, 2010). It is tempting to speculate that TTA-P2 could be a useful drug to treat T-type dependent cerebellar atrophy. Preclinical studies in dogs and rats have shown that an oral dose of 10 mg/kg TTA-P2 could lead to micromolar plasma concentration. TTA-P2 penetrates well the central nervous system as it blocks tremor activity induced by harmaline without cardiac and renal deleterious side effects (Shipe *et al.*, 2008). Compounds selective on T-type channels are expected to have therapeutic utility to treat neurological disorders in which Cav3 channels are up‑regulated, including neuropathic pain and epilepsy (Zamponi, 2016). Further studies are now necessary to establish the precise therapeutic potential of T-type calcium channel blockers in ChCA.

Acknowledgements and funding

We thank the families for their participation. This work was supported by the MSDAvenir fund, la Fondation pour la Recherche Médicale (FRM) DEQ20160334938 (to Laurence Colleaux), l'Agence Nationale de la Recherche ANR-16-CE12-0005-01 (to Vincent Cantagrel), and ANR-11-LABX-0015 (to Philippe Lory). We thank Giovanni Stevanin, Arnaud Monteil, LamSon Nguyen, Karthyayani Radjamani for helpful discussions.

References

Al-Maawali A, Blaser S, Yoon G. Diagnostic approach to childhood-onset cerebellar atrophy: a 10-year retrospective study of 300 patients. J Child Neurol 2012; 27(9): 1121-32.

Bardai G, Lemyre E, Moffatt P, Palomo T, Glorieux FH, Tung J, *et al.* Osteogenesis Imperfecta Type I Caused by COL1A1 Deletions. Calcif Tissue Int 2016; 98(1): 76-84.

Beck DB, Cho MT, Millan F, Yates C, Hannibal M, O'Connor B, *et al.* A recurrent de novo CTBP1 mutation is associated with developmental delay, hypotonia, ataxia, and tooth enamel defects. Neurogenetics 2016; 17(3): 173-8.

Bidaud I, Lory P. Hallmarks of the channelopathies associated with L-type calcium channels: a focus on the Timothy mutations in Ca(v)1.2 channels. Biochimie 2011; 93(12): 2080-6.

Boehme R, Uebele VN, Renger JJ, Pedroarena C. Rebound excitation triggered by synaptic inhibition in cerebellar nuclear neurons is suppressed by selective T-type calcium channel block. J Neurophysiol 2011; 106(5): 2653-61.

Bourchany A, Thauvin-Robinet C, Lehalle D, Bruel AL, Masurel-Paulet A, Jean N, *et al.* Reducing diagnostic turnaround times of exome sequencing for families requiring timely diagnoses. Eur J Med Genet 2017; 60(11): 595-604.

Boycott KM, Vanstone MR, Bulman DE, MacKenzie AE. Rare-disease genetics in the era of next-generation sequencing: discovery to translation. Nat Rev Genet 2013; 14(10): 681-91.

Cavallin M, Rujano MA, Bednarek N, Medina-Cano D, Bernabe Gelot A, Drunat S, *et al.* WDR81 mutations cause extreme microcephaly and impair mitotic progression in human fibroblasts and Drosophila neural stem cells. Brain 2017; 140(10): 2597-609.

Choe W, Messinger RB, Leach E, Eckle VS, Obradovic A, Salajegheh R, *et al.* TTA-P2 is a potent and selective blocker of T-type calcium channels in rat sensory neurons and a novel antinociceptive agent. Mol Pharmacol 2011; 80(5): 900-10.

Coutelier M, Blesneac I, Monteil A, Monin ML, Ando K, Mundwiller E*, et al.* A Recurrent Mutation in CACNA1G Alters Cav3.1 T-Type Calcium-Channel Conduction and Causes Autosomal-Dominant Cerebellar Ataxia. Am J Hum Genet 2015; 97(5): 726-37.
Coutelier M, Coarelli G, Monin ML, Konop J, Davoine CS, Tesson C*, et al.* A panel study on patients with dominant cerebellar ataxia highlights the frequency of channelopathies. Brain 2017; 140(6): 1579-94.
Daniil G, Fernandes-Rosa FL, Chemin J, Blesneac I, Beltrand J, Polak M*, et al.* CACNA1H Mutations Are Associated With Different Forms of Primary Aldosteronism. EBioMedicine 2016; 13: 225-36.
de Ligt J, Boone PM, Pfundt R, Vissers LE, Richmond T, Geoghegan J*, et al.* Detection of clinically relevant copy number variants with whole-exome sequencing. Hum Mutat 2013; 34(10): 1439-48.
Deciphering Developmental Disorders S. Large-scale discovery of novel genetic causes of developmental disorders. Nature 2015; 519(7542): 223-8.
Deciphering Developmental Disorders S. Prevalence and architecture of de novo mutations in developmental disorders. Nature 2017; 542(7642): 433-8.
Desikan RS, Barkovich AJ. Malformations of cortical development. Annals of neurology 2016; 80(6): 797-810.
Destexhe A, Contreras D, Steriade M, Sejnowski TJ, Huguenard JR. In vivo, in vitro, and computational analysis of dendritic calcium currents in thalamic reticular neurons. J Neurosci 1996; 16(1): 169-85.
Dreyfus FM, Tscherter A, Errington AC, Renger JJ, Shin HS, Uebele VN*, et al.* Selective T-type calcium channel block in thalamic neurons reveals channel redundancy and physiological impact of I(T)window. The Journal of neuroscience : the official journal of the Society for Neuroscience 2010; 30(1): 99-109.
Fusco C, Russo A, Galla D, Hladnik U, Frattini D, Giustina ED. New Niemann-Pick type C1 gene mutation associated with very severe disease course and marked early cerebellar vermis atrophy. J Child Neurol 2013; 28(12): 1694-7.
Geisheker MR, Heymann G, Wang T, Coe BP, Turner TN, Stessman HAF*, et al.* Hotspots of missense mutation identify neurodevelopmental disorder genes and functional domains. Nat Neurosci 2017; 20(8): 1043-51.
Gerber S, Alzayady KJ, Burglen L, Bremond-Gignac D, Marchesin V, Roche O*, et al.* Recessive and Dominant De Novo ITPR1 Mutations Cause Gillespie Syndrome. Am J Hum Genet 2016; 98(5): 971-80.
Gregory A, Westaway SK, Holm IE, Kotzbauer PT, Hogarth P, Sonek S*, et al.* Neurodegeneration associated with genetic defects in phospholipase A(2). Neurology 2008; 71(18): 1402-9.
Hayashi S, Uehara DT, Tanimoto K, Mizuno S, Chinen Y, Fukumura S*, et al.* Comprehensive investigation of CASK mutations and other genetic etiologies in 41 patients with intellectual disability and microcephaly with pontine and cerebellar hypoplasia (MICPCH). PloS one 2017; 12(8): e0181791.
Hines ML, Carnevale NT. The NEURON simulation environment. Neural Comput 1997; 9(6): 1179-209.
Huguenard JR, Prince DA. A novel T-type current underlies prolonged Ca(2+)-dependent burst firing in GABAergic neurons of rat thalamic reticular nucleus. The Journal of neuroscience : the official journal of the Society for Neuroscience 1992; 12(10): 3804-17.
Isope P, Hildebrand ME, Snutch TP. Contributions of T-type voltage-gated calcium channels to postsynaptic calcium signaling within Purkinje neurons. Cerebellum 2012; 11(3): 651-65.
Jewell R, Sarkar A, Jones R, Wilkinson A, Martin K, Arundel P*, et al.* Atypical osteogenesis imperfecta caused by a 17q21.33 deletion involving COL1A1. Clin Dysmorphol 2017; 26(4): 228-30.
Kallberg M, Wang H, Wang S, Peng J, Wang Z, Lu H*, et al.* Template-based protein structure modeling using the RaptorX web server. Nat Protoc 2012; 7(8): 1511-22.
Kurihara M, Ishiura H, Sasaki T, Otsuka J, Hayashi T, Terao Y*, et al.* Novel De Novo KCND3 Mutation in a Japanese Patient with Intellectual Disability, Cerebellar Ataxia, Myoclonus, and Dystonia. Cerebellum 2017.
Kury S, van Woerden GM, Besnard T, Proietti Onori M, Latypova X, Towne MC*, et al.* De Novo Mutations in Protein Kinase Genes CAMK2A and CAMK2B Cause Intellectual Disability. Am J Hum Genet 2017; 101(5): 768-88.
Lu CS, Hodge JJ, Mehren J, Sun XX, Griffith LC. Regulation of the Ca2+/CaM-responsive pool of CaMKII by scaffold-dependent autophosphorylation. Neuron 2003; 40(6): 1185-97.
Ly R, Bouvier G, Schonewille M, Arabo A, Rondi-Reig L, Lena C*, et al.* T-type channel blockade impairs long-term potentiation at the parallel fiber-Purkinje cell synapse and cerebellar learning. Proceedings of the National Academy of Sciences of the United States of America 2013; 110(50): 20302-7.
Marksteiner R, Schurr P, Berjukow S, Margreiter E, Perez-Reyes E, Hering S. Inactivation determinants in segment IIIS6 of Ca(v)3.1. J Physiol 2001; 537(Pt 1): 27-34.
Matilla-Duenas A, Ashizawa T, Brice A, Magri S, McFarland KN, Pandolfo M*, et al.* Consensus paper: pathological mechanisms underlying neurodegeneration in spinocerebellar ataxias. Cerebellum 2014; 13(2): 269-302.

Megahed H, Nicouleau M, Barcia G, Medina-Cano D, Siquier-Pernet K, Bole-Feysot C, *et al.* Utility of whole exome sequencing for the early diagnosis of pediatric-onset cerebellar atrophy associated with developmental delay in an inbred population. Orphanet J Rare Dis 2016; 11(1): 57.
Monteil A, Chemin J, Bourinet E, Mennessier G, Lory P, Nargeot J. Molecular and functional properties of the human alpha(1G) subunit that forms T-type calcium channels. The Journal of biological chemistry 2000; 275(9): 6090-100.
Morino H, Matsuda Y, Muguruma K, Miyamoto R, Ohsawa R, Ohtake T, *et al.* A mutation in the low voltage-gated calcium channel CACNA1G alters the physiological properties of the channel, causing spinocerebellar ataxia. Mol Brain 2015; 8: 89.
Pinggera A, Lieb A, Benedetti B, Lampert M, Monteleone S, Liedl KR, *et al.* CACNA1D de novo mutations in autism spectrum disorders activate Cav1.3 L-type calcium channels. Biol Psychiatry 2015; 77(9): 816-22.
Poretti A, Boltshauser E, Doherty D. Cerebellar hypoplasia: differential diagnosis and diagnostic approach. Am J Med Genet C Semin Med Genet 2014; 166C(2): 211-26.
Poretti A, Wolf NI, Boltshauser E. Differential diagnosis of cerebellar atrophy in childhood. Eur J Paediatr Neurol 2008; 12(3): 155-67.
Preiksaitiene E, Mannik K, Dirse V, Utkus A, Ciuladaite Z, Kasnauskiene J, *et al.* A novel de novo 1.8 Mb microdeletion of 17q21.33 associated with intellectual disability and dysmorphic features. Eur J Med Genet 2012; 55(11): 656-9.
Romani M, Kraoua I, Micalizzi A, Klaa H, Benrhouma H, Drissi C, *et al.* Infantile and childhood onset PLA2G6-associated neurodegeneration in a large North African cohort. Eur J Neurol 2015; 22(1): 178-86.
Samocha KE, Robinson EB, Sanders SJ, Stevens C, Sabo A, McGrath LM, *et al.* A framework for the interpretation of de novo mutation in human disease. Nature genetics 2014; 46(9): 944-50.
Sawyer SL, Schwartzentruber J, Beaulieu CL, Dyment D, Smith A, Warman Chardon J, *et al.* Exome sequencing as a diagnostic tool for pediatric-onset ataxia. Hum Mutat 2014; 35(1): 45-9.
Scholl UI, Goh G, Stolting G, de Oliveira RC, Choi M, Overton JD, *et al.* Somatic and germline CACNA1D calcium channel mutations in aldosterone-producing adenomas and primary aldosteronism. Nature genetics 2013; 45(9): 1050-4.
Scholl UI, Stolting G, Nelson-Williams C, Vichot AA, Choi M, Loring E, *et al.* Recurrent gain of function mutation in calcium channel CACNA1H causes early-onset hypertension with primary aldosteronism. Elife 2015; 4: e06315.
Segalat L. Loss-of-function genetic diseases and the concept of pharmaceutical targets. Orphanet J Rare Dis 2007; 2: 30.
Shipe WD, Barrow JC, Yang ZQ, Lindsley CW, Yang FV, Schlegel KA, *et al.* Design, synthesis, and evaluation of a novel 4-aminomethyl-4-fluoropiperidine as a T-type Ca2+ channel antagonist. J Med Chem 2008; 51(13): 3692-5.
Sobreira N, Schiettecatte F, Valle D, Hamosh A. GeneMatcher: a matching tool for connecting investigators with an interest in the same gene. Hum Mutat 2015; 36(10): 928-30.
Splawski I, Timothy KW, Decher N, Kumar P, Sachse FB, Beggs AH, *et al.* Severe arrhythmia disorder caused by cardiac L-type calcium channel mutations. Proceedings of the National Academy of Sciences of the United States of America 2005; 102(23): 8089-96; discussion 6-8.
Splawski I, Timothy KW, Sharpe LM, Decher N, Kumar P, Bloise R, *et al.* Ca(V)1.2 calcium channel dysfunction causes a multisystem disorder including arrhythmia and autism. Cell 2004; 119(1): 19-31.
Steinlin M. Cerebellar disorders in childhood: cognitive problems. Cerebellum (London, England) 2008; 7(617b2600-bce9-f736-c7ef-536dfb003939): 607-17.
Steuber V, Schultheiss NW, Silver RA, De Schutter E, Jaeger D. Determinants of synaptic integration and heterogeneity in rebound firing explored with data-driven models of deep cerebellar nucleus cells. J Comput Neurosci 2011; 30(3): 633-58.
Sudhakar SK, Torben-Nielsen B, De Schutter E. Cerebellar Nuclear Neurons Use Time and Rate Coding to Transmit Purkinje Neuron Pauses. PLoS Comput Biol 2015; 11(12): e1004641.
Tada M, Nishizawa M, Onodera O. Roles of inositol 1,4,5-trisphosphate receptors in spinocerebellar ataxias. Neurochem Int 2016; 94: 1-8.
Talavera K, Nilius B. Evidence for common structural determinants of activation and inactivation in T-type Ca2+ channels. Pflugers Arch 2006; 453(2): 189-201.
Tavano A, Grasso R, Gagliardi C, Triulzi F, Bresolin N, Fabbro F, *et al.* Disorders of cognitive and affective development in cerebellar malformations. Brain : a journal of neurology 2007; 130(Pt 10): 2646-706.
Tomlinson SE, Hanna MG, Kullmann DM, Tan SV, Burke D. Clinical neurophysiology of the episodic ataxias: insights into ion channel dysfunction in vivo. Clin Neurophysiol 2009; 120(10): 1768-76.

Travaglini L, Nardella M, Bellacchio E, D'Amico A, Capuano A, Frusciante R, *et al.* Missense mutations of CACNA1A are a frequent cause of autosomal dominant nonprogressive congenital ataxia. Eur J Paediatr Neurol 2017; 21(3): 450-6.
Watson LM, Bamber E, Schnekenberg RP, Williams J, Bettencourt C, Lickiss J, *et al.* Dominant Mutations in GRM1 Cause Spinocerebellar Ataxia Type 44. Am J Hum Genet 2017; 101(3): 451-8.
Wu J, Yan Z, Li Z, Yan C, Lu S, Dong M, *et al.* Structure of the voltage-gated calcium channel Cav1.1 complex. Science 2015; 350(6267): aad2395.
Yue WW. From structural biology to designing therapy for inborn errors of metabolism. J Inherit Metab Dis 2016; 39(4): 489-98.
Zamponi GW. Targeting voltage-gated calcium channels in neurological and psychiatric diseases. Nat Rev Drug Discov 2016; 15(1): 19-34.

Figures

Figure 1

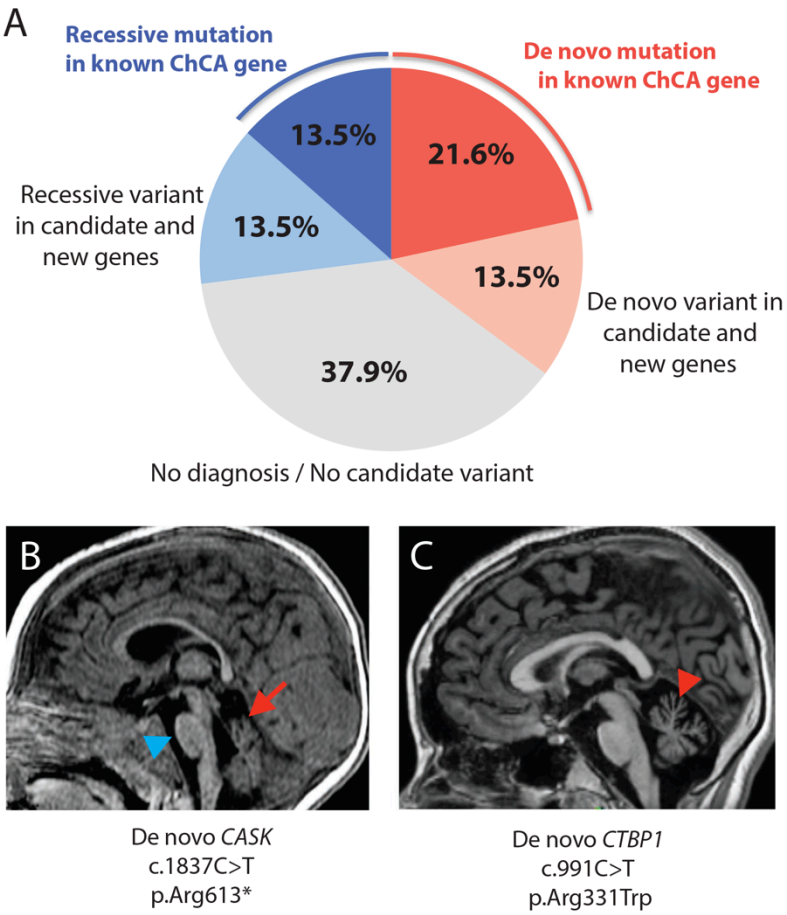

Figure 1. Modes of inheritance and MRI findings across a cohort of 47 patients with Childhood-onset cerebellar atrophy.

(A) Distribution of modes of inheritance across our ChCA cohort. De novo dominant events were identified in 35 % of the families versus 27% for recessive inheritance.

(B, C) Sagittal MRIs of patients with de novo mutations in *CTBP1* gene (**B**; 11 years old), and *CASK* gene (**C**; 6 months old) indicating cerebellar atrophy (red arrow), intact pons (blue arrowhead) and cerebellar hypoplasia (red arrowhead).

Figure 2

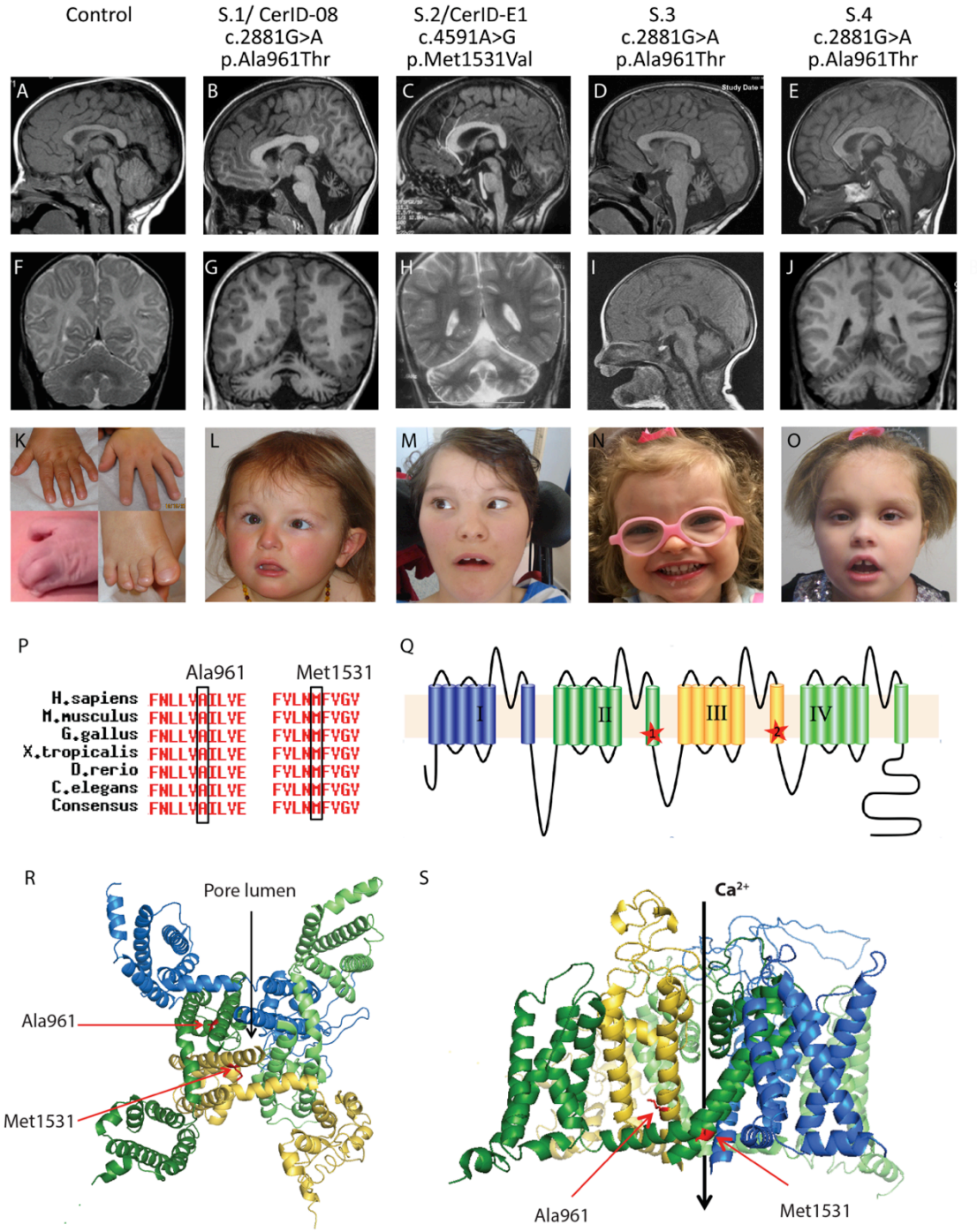

Figure 2. *CACNA1G* de novo mutations are associated with a syndromic form of cerebellar atrophy.

(A-J) Sagittal and coronal brain MRI (when available) of control (**A, F**) and patients S.1 at 8 months (**B, G**), S.2 at 2 years (**C, H**), S.3 at 2 years (**D**) and 9 days (**I**) and S.4 at 9 years (**E, J**). Images show atrophic cerebellar vermis and hemisphere in all patients but not visible at 9 days for subject 3. (**K**) Hands and feet anomalies include large 1st finger, persistent fetal pads and clinodactyly (upper panels for S.1, S.4), syndactyly (bottom left for S.3) and large 1st toes (Bottom right for S.4). (**L-O**) Facies show abnormal hair lines, hirsutsim and strabismus. (**P**) Mutated amino-acids alanine 961 and methionine 1531 are fully conserved among species. (**Q**) Schematic representation of the Cav3.1 membrane topology with alanine 961 (1) and methionine 1531 (2) localization at the bottom of the S6 segments in domains II and III, respectively.

(**R, S**) Homology 3D modeling of the Cav3.1 protein based on the crystal structure of rabbit voltage-gated calcium channel Cav1.1 as a template with a view from the top (**R**) and from the side (**S**). Repeat domains I to IV (blue, dark green, yellow and green in ascending order) are indicated as well as mutated amino-acids (in red) that cluster in the pore of the channel.

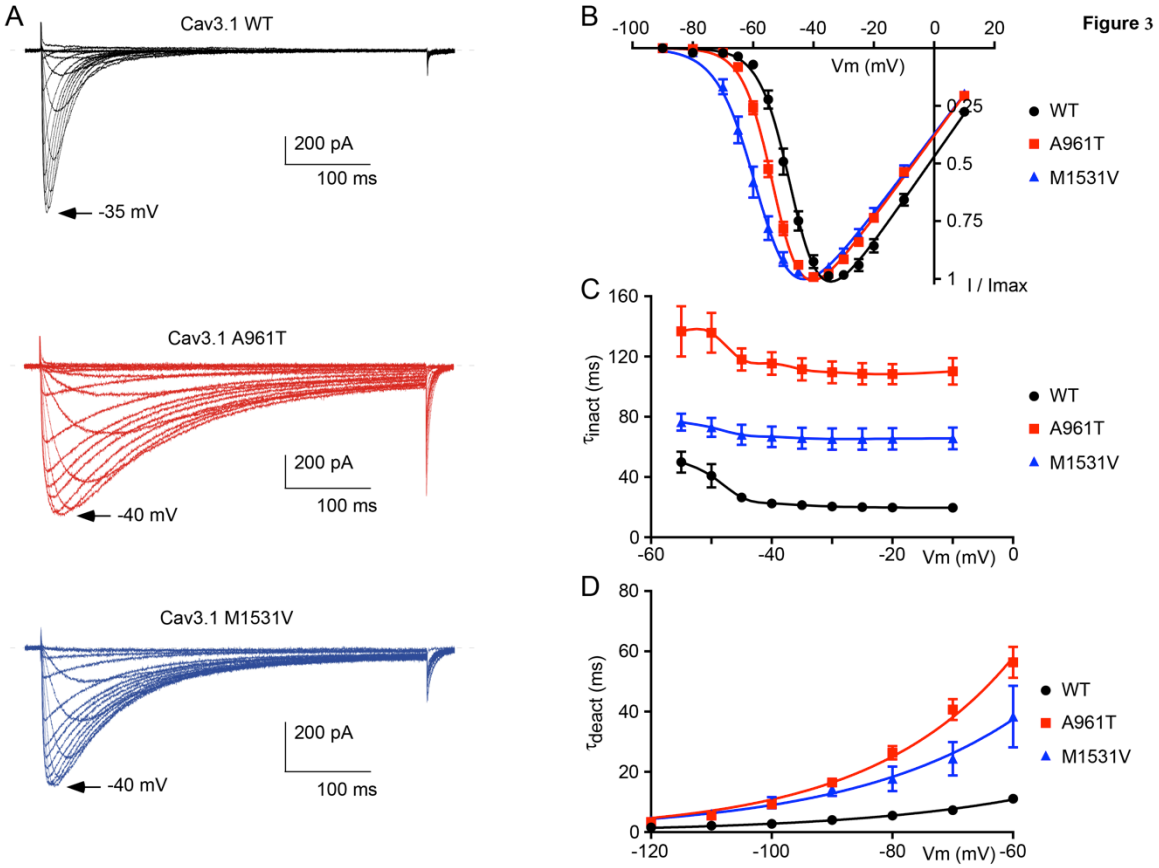

Figure 3. The ChCA mutants of Cav3.1 channels exhibit a hyperpolarized shift in activation properties and slower inactivation and deactivation kinetics.

(A) Typical recordings in HEK-293T cells expressing either Cav3.1 WT (black traces), Cav3.1 A961T (red traces), or Cav3.1 M1531V (blue traces) channels. Current were elicited by a 450 ms test pulse ranging from -90 mV to +10 mV applied from a holding potential of -100 mV. **(B)** Current-voltage (I-V) curves for the Cav3.1 WT (n=7), Cav3.1 A961T (n=10) and Cav3.1 M1531V (n=8) currents extracted from experiments presented in (A). **(C)** Inactivation kinetics (τ) (n=8-13) extracted from monoexponential fit of traces presented in

(A). **(D)** Deactivation kinetics (τ) obtained by monoexponential fit of Cav3.1 WT (n=4), Cav3.1 A961T (n=10) and Cav3.1 M1531V (n=6) currents. Deactivation (Tail) current were generated by a short (4 ms) test pulse at -30 mV followed by repolarization potentials ranging from -120 mV to -60 mV. Average values and statistical analysis can be found in Table 2.

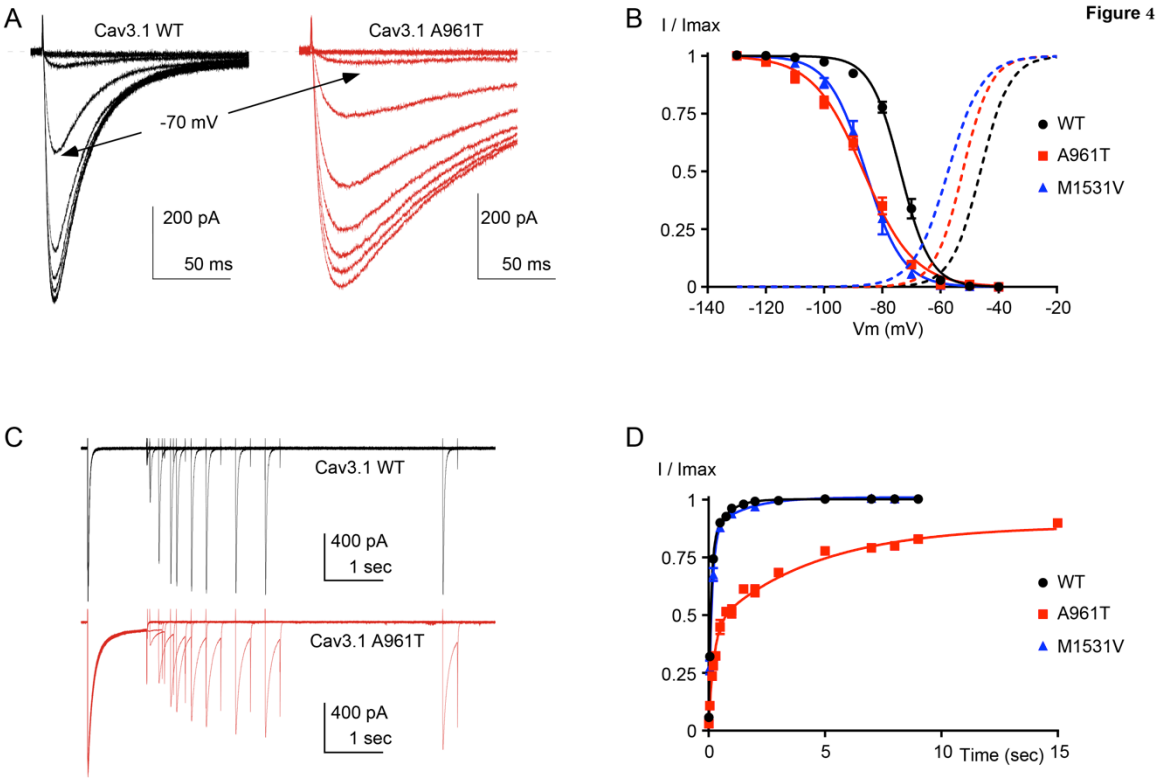

Figure 4. The Cav3.1 A961T mutant exhibits a hyperpolarized shift in the steady-state inactivation and slower recovery from inactivation.

(A-B) Steady-state inactivation of Cav3.1 currents. **(A)** Typical Cav3.1 WT (black trace) and Cav3.1 A961T (red trace) currents obtained at -30 mV from holding potentials ranging from -130 to -40 mV (5 second duration). **(B)** Steady-state inactivation curves obtained from experiments presented in (A) and activation curves (dashed line) for Cav3.1 WT (n=5), Cav3.1 A961T (n=10) and M1531V currents (n=10). **(C-D)** Recovery from inactivation of WT and mutant Cav3.1 channels. **(C)** Example of recordings from a cell expressing Cav3.1 WT (top, black traces) and a cell expressing Cav3.1 A961T (bottom, red traces). Recovery from inactivation was measured using a two-pulse protocol at -30 mV separated by an interpulse at -100 mV whose duration ranged from 10 ms to 15 seconds. **(D)** Recovery from inactivation of Cav3.1 WT (black, n=7), Cav3.1 A961T (red, n=7) and M1531V currents (blue, n=6). Note that recovery from inactivation of Cav3.1 A961T mutant channels was best fitted with a two exponential function, contrary to the recovery from inactivation of WT and M1531V channels (see Table 2).

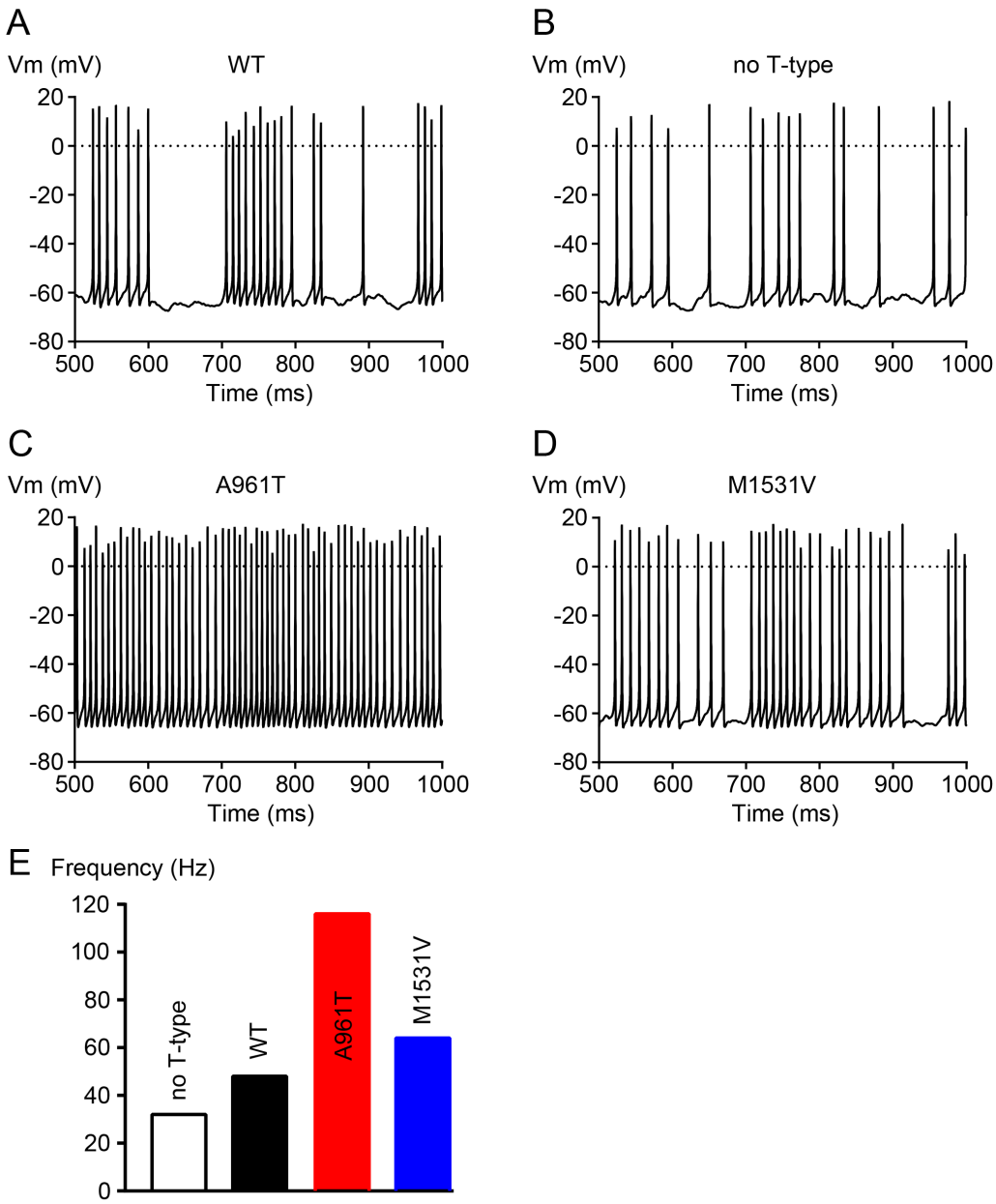

Figure 5. Computational modeling reveals that ChCA mutations of the Cav3.1 channel markedly increase the firing of cerebellar nuclear neurons.

(A-D) Simulation of cerebellar nuclear neuron activities expressing the WT Cav3.1 channel **(A)**, no T-type Cav3.1 channel **(B)**, the Cav3.1 A961T mutant **(C)** and the Cav3.1 M1531V mutant **(D)**. **(E)** Frequency of action potentials measured during 500 ms of simulation in the 4 conditions.

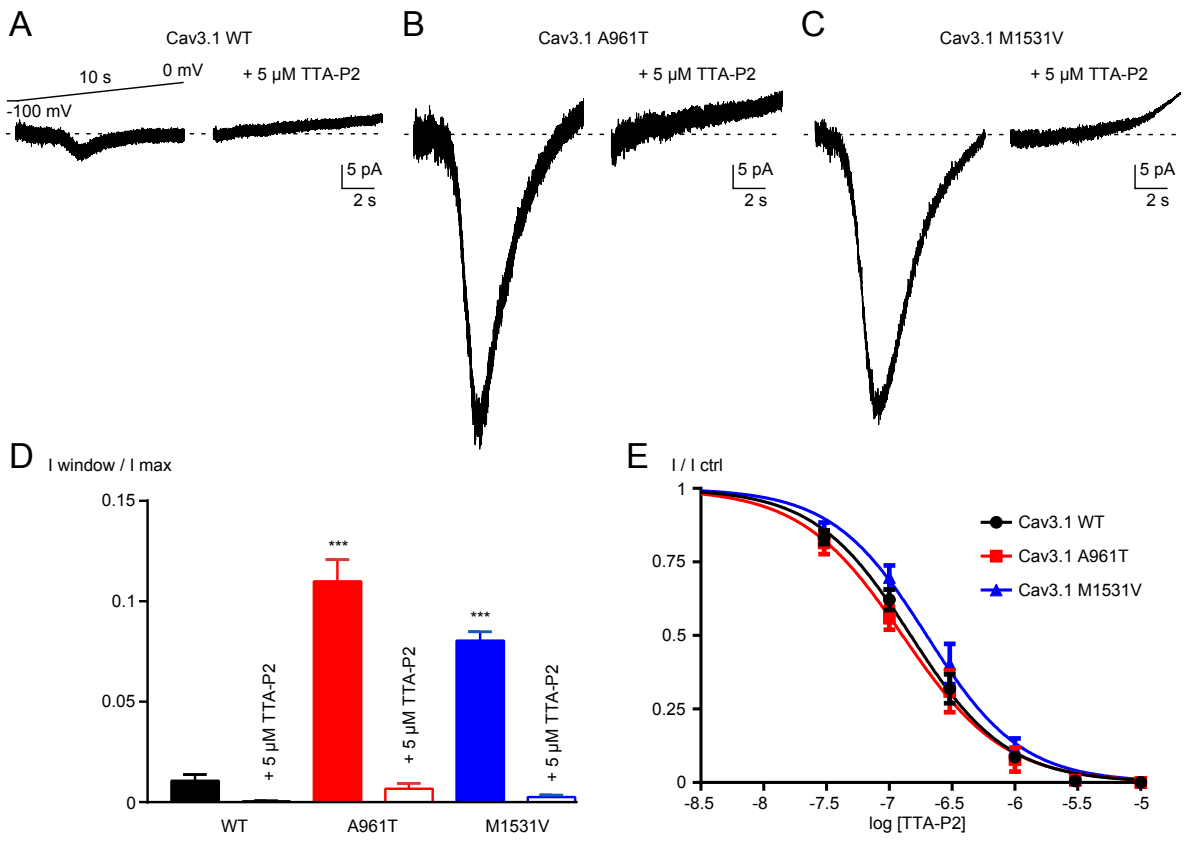

Figure 6. The ChCA Cav3.1 mutants display a persistent window current near the cell membrane resting potential.

(A-C) Typical calcium current recorded during a 5 seconds duration test pulse at -70 mV (dark traces), for Cav3.1 WT **(A),** A961T **(B)** and M1531V **(C)** channels. The light traces correspond to 5 seconds duration test pulse at -100 mV. **(D)** Average normalized persistent current amplitude. For each cell, the current was measured after 5 seconds at -70 mV and was normalized to the maximal current recorded using standard I-V curve protocol (Cav3.1 WT (n=5), Cav3.1 A961T (n=8) and Cav3.1 M1531V (n=10) channels). **(E-G)** Window currents were elicited using very slow (10 seconds) voltage-ramps from -100 mV to 0 mV in the absence (left panels) and in the presence of 5 µM TTA-P2 (right panels) for Cav3.1 WT **(E),** A961T **(F)** and M1531V **(G)** channels. **(H)** Average normalized window current amplitude. For each cell, the window current was normalized to the maximal current recorded using standard I-V curve protocol and averaged for each condition (Cav3.1 WT (n=6), Cav3.1 A961T (n=6) and Cav3.1 M1531V (n=6) channels) before (filled bars) and after application of 5 µM TTA-P2 (open bars), a selective T-type calcium channel blocker. **(I)** Concentration-response curves of TTA-P2 for WT (n=7), A961T (n=5) and M1531V (n=6) Cav3.1 channels. The dose dependence of the current inhibition by TTA-P2 was fitted with the sigmoidal Hill equation. Currents were elicited at -30 mV from a holding potential of -90 mV at a frequency of 0.1 Hz.

# Subject	Subject 1 (S.1/CerID-08)	Subject 2 (S.2/CerID-E1)	Subject 3 (S.3)	Subject 4 (S.4)
Mutation gDNA Chr17(GRCh38)	g.50592063G>A	g.48685266A>G	g.50592063G>A	g.50592063G>A
Mutation cDNA (NM_018896.4) ; protein	c.2881G>A ; p.Ala961Thr	c.4591A>G ; p.Met1531Val	c.2881G>A ; p.Ala961Thr	c.2881G>A ; p.Ala961Thr
Inheritance	De Novo	De Novo	De Novo	De Novo
Age at last follow-up	11,5 y	13 y	3 Y	8 y
Gender	Female	Female	Female	Female
Ethnic origin	Caucasian	Caucasian	Caucasian	Caucasian
Weight at birth	2.4 kg (-2SD)	2.8 kg (-1SD)	2,9 kg (-1SD)	2.9 kg (-1SD)
Length at birth	43 cm (-2SD)	49 cm	49,5cm	49,5 cm
HC at birth	32 cm (-2SD)	N/A	35cm	N/A
HC at last examination	50,5 cm (-2SD)	50,3 cm (-2,5 SD)	48,3 cm	52 cm
Age at initial symptoms	3 months	8 days	7 days	4 months
ID/DD/ASD	severe ID	profound ID	severe DD	profound ID, autistic behavior
Psychomotor development				
Gross motor	Delayed (Can stand hand supported)	Delayed (cannot hold her head)	Delayed (sat in tripod at 2y 7mo)	Delayed with regression (Does not walk)
Fine motor	Delayed (Can use the fork)	Delayed	Delayed	Delayed (cannot use utensils)
Language	Delayed (Speaks few words)	Delayed	Delayed (non verbal)	Delayed (non verbal)
Social	Delayed (Understands simple orders)	Delayed	Delayed	Delayed (behavior issues)
Seizures				
Seizures	-	Yes	Yes	-
Onset	-	8 days (Epileptic encephalopathy)	7 days (Epileptic encephalopathy)	-
Neurological Findings				
Distal hypertonia	-	+	+	+
Axial hypotonia	+	+	+	+
Deep tendon reflexes	+	+	+	+
Nystagmus	-	-	-	-
Dysmetria	+	NA	NA	+
Cerebellar ataxia	+	+	+	+
Ophthalmological findings	Oculomotor apraxia, strabismus	Oculomotor apraxia, strabismus	hyperopia	Oculomotor apraxia, strabismus
Investigations				
Metabolic	Normal	Normal	Normal	Normal
EEG	Normal	Normal	Multifocal epileptic discharges	Slow background activity
MRI				
Cerebellum	Global atrophy	Vermis atrophy	Global atrophy	Global atrophy and hypoplasia
Pons	Normal	Normal	Normal	Normal
Cerebral cortex	Normal	Normal	Normal	Normal
Other systemic findings				
Hypothyroidism	-	+	-	-
Cardiovascular	-	-	-	Prolonged QT on ECG
Dysmorphic features				
Hands and feet	Short hands and feet, thin digits, clinodactyly	Short hand and feet, clinodactyly	Syndactyly of hands and toes	Broad thumbs and great toes, persistent fetal pads on fingers
Hair	Hypotrichosis and sparse hair	Hirsutism, low posterior hairline		Hypertrichosis on back and proximal extremities, thick hair
Face	Small palpebral fissures, anteverted ears	Prognathism, synophrys	Mild hypertelorism	Missing upper incisors

Table 1. Summary of clinical, EEG and brain MRI data. Abbreviations. ASD Autism spectrum disorder, ID Intellectual disability, EEG Electroencephalogram, DD Developmental

delay, MRI Magnetic resonance imaging, N/A Not available, SD Standard deviation, ECG Electrocardiogram.

	Cav3.1 - WT	Cav3.1 - A961T	Cav3.1 - M1531V
Current density (pA/pF)	41.20 ± 7.06 (9)	38.47 ± 4.00 (13)	52.24 ± 7.40 (12)
Activation $V_{1/2}$ (mV)	-46.28 ± 0.52 (7)	-52.35 ± 0.14 (10) **	-57.41 ± 1.45 (8) ***
Activation slope (k, mV)	5.04 ± 0.17 (7)	4.84 ± 0.15 (10)	5.93 ± 0.31 (9)
Inactivation $V_{1/2}$ (mV)	-73.72 ± 0.29 (5)	-86.43 ± 0.45 (10) ***	-85.69 ± 0.53 (10) ***
Inactivation slope (k, mV)	5.13 ± 0.25 (5)	8.72 ± 0.4 (10) **	6.35 ± 0.46 (10)
Activation kinetics @ -40 mV (Tau act, ms)	6.22 ± 0.73 (8)	6.68 ± 0.76 (9)	3.91 ± 0.34 (13) ***
Inactivation kinetics @ -40 mV (Tau inact, ms)	22.51 ± 1.53 (8)	115.46 ± 7.55 (13) ***	66.79 ± 62.85 (12) ***
Recovery (Tau fast, ms)	142.01 ± 7.43 (7)	241.41 ± 20.77 (7) ***	181.30 ± 17.14 (6)
Recovery (Tau slow, ms)	NA	10469.71 ± 2773.98 (7)	NA
Deactivation kinetics @-80 mV (Tau deact, ms)	5.50 ± 0.62 (4)	26.38 ± 2.22 (10) ***	17.72 ± 4.08 (6) ***

* $P < 0.05$ compared with WT channels ; ** $P < 0.01$ compared with WT channels ; *** $P < 0.001$ compared with WT channels, using one way ANOVA for multiple comparisons.

Table 2. Electrophysiological properties of the A961T and M1531V mutants of Cav3.1 channels.

High N-glycan multiplicity is critical for neuronal adhesion and sensitizes the developing cerebellum to N-glycosylation defect

Daniel Medina-Cano[1,2], Ekin Ucuncu[1,2], Michael Nicouleau[1,2], Joanna Lipecka[3], Jean-Charles Bizot[4], Christian Thiel[5], François Foulquier[6], Nathalie Lefort[7], Ida Chiara Guerrera[3], Laurence Colleaux[1,2], Vincent Cantagrel[1,2*]

Affiliations

1. Paris Descartes-Sorbonne Paris Cité University, Imagine Institute, Paris, France.
2. Laboratory of developmental brain disorders, INSERM UMR 1163, Paris, France.
3. Proteomics Platform 3P5-Necker, Université Paris Descartes-Structure Fédérative de Recherche Necker, Inserm US24/CNRS UMS3633, Paris, France
4. Key-Obs SAS, Orléans, France
5. Center for Child and Adolescent Medicine, Kinderheilkunde I, University of Heidelberg, Germany
6. Université Lille, Centre National de la Recherche Française, UMR 8576-Unité de Glycobiologie Structurale et Fonctionnelle-Unité de Glycobiologie Structurale et Fonctionnelle, Lille, France
7. Paris Descartes-Sorbonne Paris Cité University, Imagine Institute, iPS Core Facility, Paris, France.

Corresponding authors:

Vincent Cantagrel vincent.cantagrel@inserm.fr
Institut IMAGINE, Lab 323- B3
24, Bd du Montparnasse
75015 Paris, FRANCE

Abstract

Proper brain development relies highly on protein N-glycosylation to sustain neuronal migration, axon guidance and synaptic physiology. Impairing the N-glycosylation pathway at early steps produces broad neurological symptoms identified in congenital disorders of glycosylation. However, little is known about the molecular mechanisms underlying these defects. We generated a cerebellum specific knockout mouse for *Srd5a3*, a gene involved in the initiation of N-glycosylation. In addition to motor coordination defects and abnormal granule cell development, *Srd5a3* deletion causes mild N-glycosylation impairment without significantly altering ER homeostasis. Using proteomic approaches, we identified that *Srd5a3* loss affects a subset of glycoproteins with high N-glycans multiplicity per protein and decreased protein abundance or N-glycosylation level. As IgSF-CAM adhesion proteins are critical for neuron adhesion and highly N-glycosylated, we observed impaired IgSF-CAM-mediated neurite outgrowth and axon guidance in *Srd5a3* mutant cerebellum. Our results link high N-glycan multiplicity to fine-tuned neural cell adhesion during mammalian brain development.

Introduction

Protein N-glycosylation, one of the most abundant post-translational modification, helps direct various cellular functions, such as protein folding, stability, trafficking and localization(Cherepanova & Gilmore, 2016) (Freeze, Chong, Bamshad, & Ng, 2014). Nearly all proteins transported through the secretory pathway undergo N-glycosylation, particularly to regulate cell surface abundance and cellular interactions(Dennis, Nabi, & Demetriou, 2009). This template-independent process shows distinct glycosylation patterns that varies by protein and physiological context(Dennis et al., 2009). Protein N-glycosylation begins in the endoplasmic reticulum (ER), where a tightly controlled and conserved biosynthetic pathway synthesizes a precursor named the lipid-linked oligosaccharide (LLO). This LLO comprises a sequential assembly of 14 monosaccharides ($Glc_3Man_9GlcNAc_2$) on top of the phosphorylated lipid carrier dolichol. Then, the oligosaccharyltransferase (OST) complex transfers *en bloc* the oligosaccharide part of the LLO to Asn residues on specific sites (Asn-X-Ser/Thr, X≠Pro) in nascent glycoproteins(Chavan & Lennarz, 2006). N-linked glycan undergoes final modifications in the ER and Golgi compartments.

Disrupting the N-glycosylation process in humans causes congenital disorders of glycosylation (CDG), a wide and highly heterogeneous group of inherited metabolic disorders (Ng & Freeze, 2018) (Freeze et al., 2014) (Jaeken & Peanne, 2017). The analysis of the clinical and metabolic consequences of each defect is challenging as the underlying mutated enzymes or transporters are often involved in multiple and intricate pathways(Freeze et al., 2014). Among them, disrupted synthesis or transfer of LLO underlies the most prevalent disorder, CDG type I (CDG-I)(Jaeken & Peanne, 2017). CDG-I diagnosis is based on the detection of hypoglycosylation of the patients' serum transferrin that exhibits unoccupied N-glycosylation site(s). Clinically, CDG-I disorders present psychomotor retardation (the most common feature) associated with cerebellar ataxia, seizures, retinopathy, liver fibrosis, coagulopathies, abnormal fat distribution and failure to thrive. Cerebellar ataxia is the primary diagnostic indicator in patients with *PMM2* mutations (PMM2-CDG, also known as CDG-Ia disorder), which is the most frequent CDG (Schiff et al., 2017). These phenotypic defects may arise from unoccupied glycosylation sites (i.e. protein hypoglycosylation) in numerous and mostly unidentified proteins.

The efficacy of protein glycosylation relies on the primary sequence at the glycosylation site (i.e. the sequon), the neighboring amino acids and the local structure (Poljak et al., 2017) (Murray et al., 2015). In CDG, the limited amount of LLO, the OST complex substrate, can also impact glycosylation site occupancy to cause hypoglycosylation (Burda & Aebi, 1999) (Freeze, Schachter, & Kinoshita, 2015). Initial studies investigated the consequences of this metabolic defect mainly in serum (Hulsmeier, Paesold-Burda, & Hennet, 2007) (Richard et al., 2009). However, tissue accessibility and technical limitations precluded examining defects in organs, specifically the developing brain (Freeze, Eklund, Ng, & Patterson, 2015). The lack of data related to the consequence of the defect at the proteomic level contrasts with the well-known importance of N-glycans in specific phases of neural development (Scott & Panin, 2014b).

While several CDG models showing neural developmental defects exist, the mis-glycosylated targets remain unidentified (Chan et al., 2016; Cline et al., 2012; Scott & Panin, 2014a). We still do not know whether some specific proteins show a predisposition for these alterations, which contribute to disease pathogenesis. We predict that some glycoproteins possess a proclivity for hypoglycosylation based on their intrinsic properties (Poljak et al., 2017) (Hulsmeier et al., 2007). Previous studies identified SRD5A3, an enzyme involved in LLO

synthesis, as mutated in CDG type I patients (SRD5A3-CDG) (Cantagrel et al., 2010) (Morava et al., 2010). SRD5A3 is a steroid-reductase-like enzyme involved in the last step of *de novo* synthesis of dolichol, the lipid used to build the LLO precursor. The broad clinical spectrum observed in patients with *SRD5A3* mutations shows many similarities with other ER-related glycosylation defects including psychomotor retardation and cerebellar ataxia. These symptoms result from likely null *SRD5A3* alleles (Kara, Ayhan, Gokcay, Basbogaoglu, & Tolun, 2014; Tuysuz et al., 2016) (Wheeler et al., 2016) (Cantagrel et al., 2010) (Grundahl et al., 2012) and reflect impaired protein N-glycosylation, as previously described in yeast and mouse embryos mutated for the corresponding *SRD5A3* ortholog (Cantagrel et al., 2010). Here, we sought to gain mechanistic and functional insight into protein N-glycosylation during neural development, so we used conditional disruption of the *Srd5a3* gene in the mouse cerebellum, a tissue often affected in CDG.

Results

Conditional deletion of Srd5a3 in the whole developing cerebellum

Since we sought to examine the function of *SRD5A3* in brain disease pathogenesis, we generated targeted conditional and null alleles of mouse *Srd5a3*, flanking exons 2-4 with loxP sequences (Fig.S1a, b). Homozygous germline mutants (*Srd5a3*$^{-/-}$) are embryonic lethal (data not shown) consistent with results from the *Srd5a3* gene-trap mutant (Cantagrel et al., 2010). So, we used the Engrailed1-cre (En1-Cre) transgenic line to produce conditional knockouts En1-Cre; *Srd5a3*$^{fl/-}$ in the developing hindbrain (Sgaier et al., 2007) and confirmed the gene deletion at the transcript level (Fig.S1c,d,e). En1-Cre; *Srd5a3*$^{fl/-}$ mice were fertile and showed nearly Mendelian ratios at weaning age (data not shown). We used far-western blotting with biotinylated Sambucus Nigra lectin (SNA) to investigate the abundance of complex sialylated N-glycans (Cao, Guo, Arai, Lo, & Ning, 2013). Total protein extracts from mutant cerebellums showed a non-significant 12% decrease in normalized signal intensity (Fig.1a,b). We obtained similar results with Concanavalin A (ConA) lectin that binds to core and immature mannosylated N-glycans (Fig.S1f,g). These results indicate that cerebellar *Srd5a3* deletion does not cause a severe general glycosylation defect. However, Lamp1, a broadly used marker for N-glycosylation defects (Rujano et al., 2017) (Kretzer et al., 2016), indicated a severe decrease in protein levels across different tissues (Fig 1c, d, e). The remaining

proteins showed a shift toward a lower molecular weight before PNGase treatment, which indicated impaired glycosylation (Fig.1d, f).

Next, we investigated the functional consequences of this cerebellar glycosylation defect on learning ability and motor behavior (Koziol et al., 2014) in a cohort of control and mutant mice (n=30). In the Morris Water Maze (MWM), we exposed mice twice to the same hidden platform to test working memory. We found no significant difference on swimming speed between En1-Cre; *Srd5a3*$^{fl/-}$ and control mice (Fig.S1h). The latency to reach the platform was significantly lower on the second trial than on the first one for control mice, but not for En1-Cre; *Srd5a3*$^{fl/-}$ mice (Fig.S1i). This result suggests a mild impairment of working memory in the mutant mice. In contrast, En1-Cre; *Srd5a3*$^{fl/-}$ mice showed a severe and highly significant (p=0.0007) motor coordination defect assessed with the rotarod test (Fig. 1g). These results suggest that in the absence of *Srd5a3,* the impaired cerebellum function arises from a mild and potentially selective hypoglycosylation of glycoproteins.

Conditional deletion of Srd5a3 disrupts cerebellum granule cell development

Then, we wanted to examine cerebellar development after deletion of *Srd5a*3 by conducting a morphological and histological survey at P14, P21, 2 and 6 months. We observed a significant hypoplasia in the En1-Cre; *Srd5a3*$^{fl/-}$ mice (Fig. 2a-d). Examining the mutant cerebellum cytoarchitecture revealed an accumulation of scattered ectopic cell clusters in the external part of the molecular layer (ML; Fig. 2e). These clusters were NeuN-positive, post-mitotic granule cells (GCs) (Fig. 2f) that failed to migrate to the internal granule cell layer (IGL). These cells remained in the external granule cell layer (EGL), a transient germinal zone. We observed this pattern at all our investigated latter timepoints. Our examination of the two other major cerebellar cell populations, Purkinje cells (PCs) and Bergman glia (BG), did not reveal major cellular defects (Fig. S2a, b). Cerebellar development relies on key glycosylated proteins expressed and secreted by PC or BG cells, such as Shh (Dahmane & Ruiz i Altaba, 1999) or dystroglycan (Nguyen et al., 2013). So, we investigated the origin of the identified GCs ectopia. We deleted *Srd5a3* using a GC-specific cre line (Atoh1-Cre)(Matei et al., 2005) (Fig. S2c). Atoh1-Cre; *Srd5a3*$^{fl/fl}$ mice exhibit similar GC ectopia, which indicates that a GC-autonomous defect underlies the formation of these ectopic cell clusters (Fig. 2g). Taken together, our results support a critical role for *Srd5a3* during cerebellar granule cells

development likely through a GC-autonomous glycosylation impairment of specific, but undetermined, proteins.

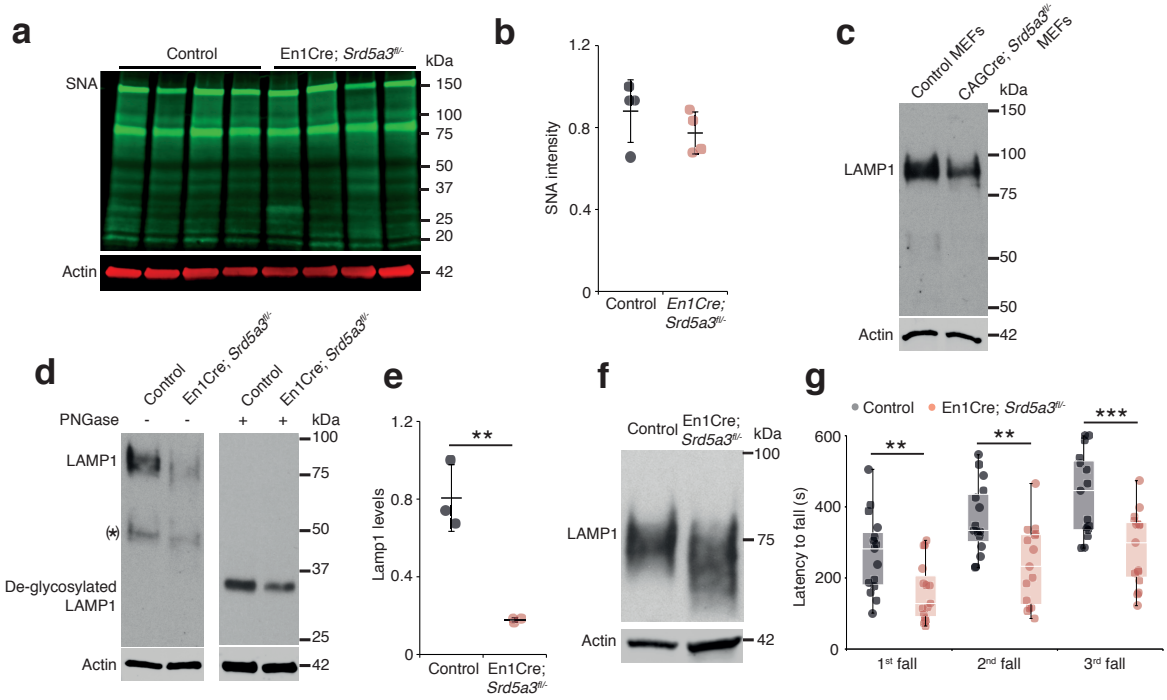

Figure 1. Deletion of *Srd5a3* in the cerebellum impairs protein N-glycosylation and motor function. (a) Far-western blot with SNA lectin in P7 cerebellum and (b) quantification (n=4) for each genotype, p-value=0.29 (c) WB analysis of LAMP1 expression in mouse embryonic fibroblasts (MEFs). (d) WB analysis of LAMP1 level from P7 cerebellum and quantification (e). * indicates a PNGase sensitive LAMP1 isoform; ** p-value=0.0032. (f) WB analysis as described in (d) but with increased electrophoretic migration and adjusted protein amounts to highlight LAMP1 hypoglycosylation in the mutant sample. (g) Box plot of the latency to fall during rotarod testing (n=15 for each condition). One-way ANOVA was used for rotarod statistics. For all others, two-tailed student t-test was used. ** $p<0.01$; *** $p<0.001$. Results are presented as mean ± s.d.

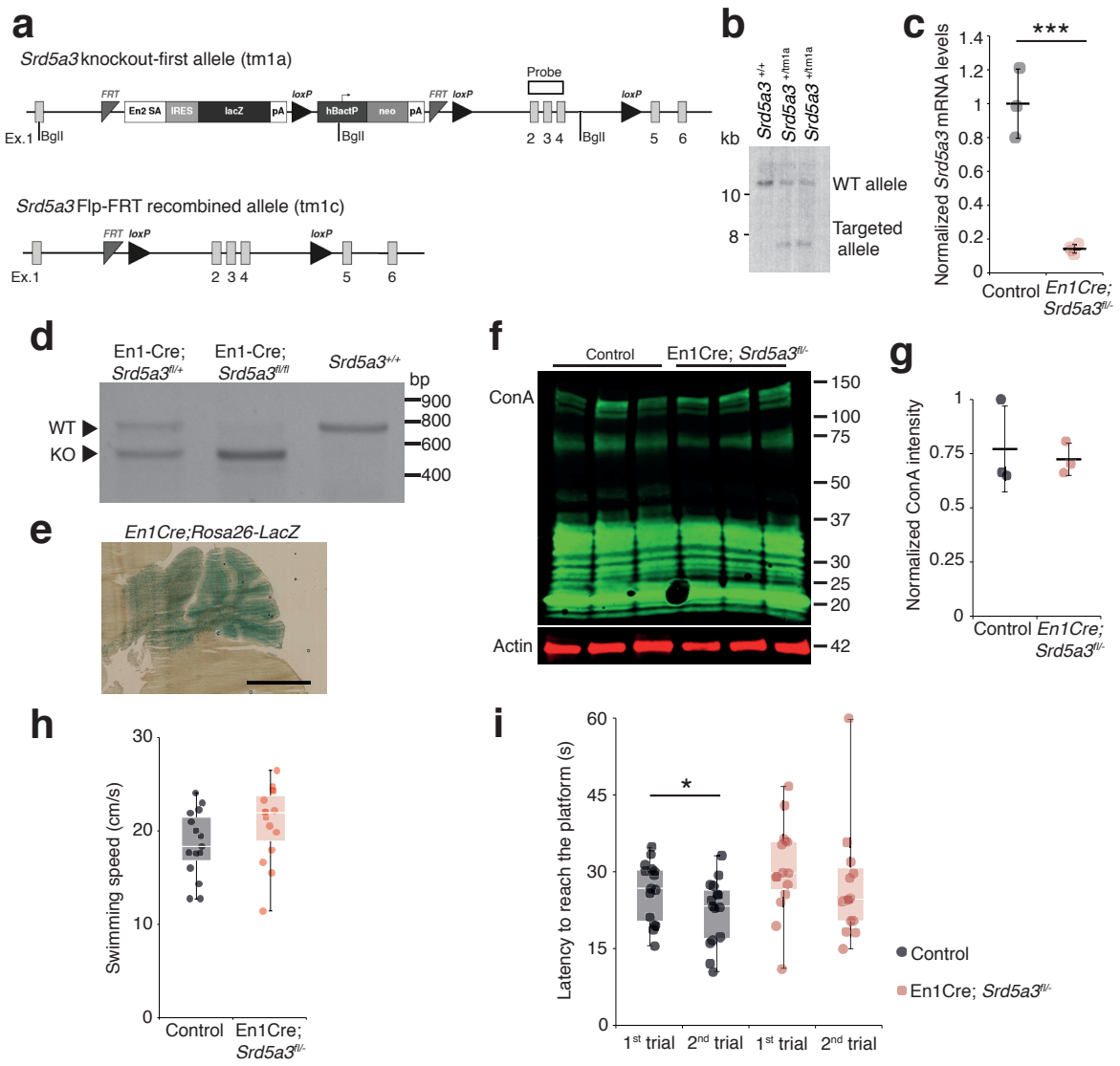

Figure S1. Generation of conditional *Srd5a3* knockout mice and extended biochemical and behavioral analyses. (a) Schematic of the *Srd5a3* knockout-first allele (tm1a), the same allele after Flp-mediated recombination (tm1c) and (b) validation of the tm1a allele insertion by southern blot. (c) RT-qPCR analysis of *Srd5a3* expression levels in the P7 cerebellum (Control, n=3; En1-Cre; $Srd5a3^{fl/-}$, n=4) (d) RT-PCR analysis of the recombined (KO) and wild-type (WT) *Srd5a3* transcripts in the cerebellum. (e) LacZ staining image of the En1Cre; Rosa26 mouse showing Cre expression within the entire cerebellum. Scale bar 2mm. (f) ConA far-WB and (g) quantification (t-test, p-value=0.7190; n=3 for each genotype). (h) Average swimming speed during the Morris water maze test (MWM; n=15 for each genotype). (i) MWM results. After two trials to find the same hidden platform (average of a total of eight sessions), only control mice significantly reduced the time to find the platform on the second trial (t-test, type I, p=0.0329). Unless indicated, two-tailed t-test was used for statistics. * $p<0.05$; *** $p<0.001$.

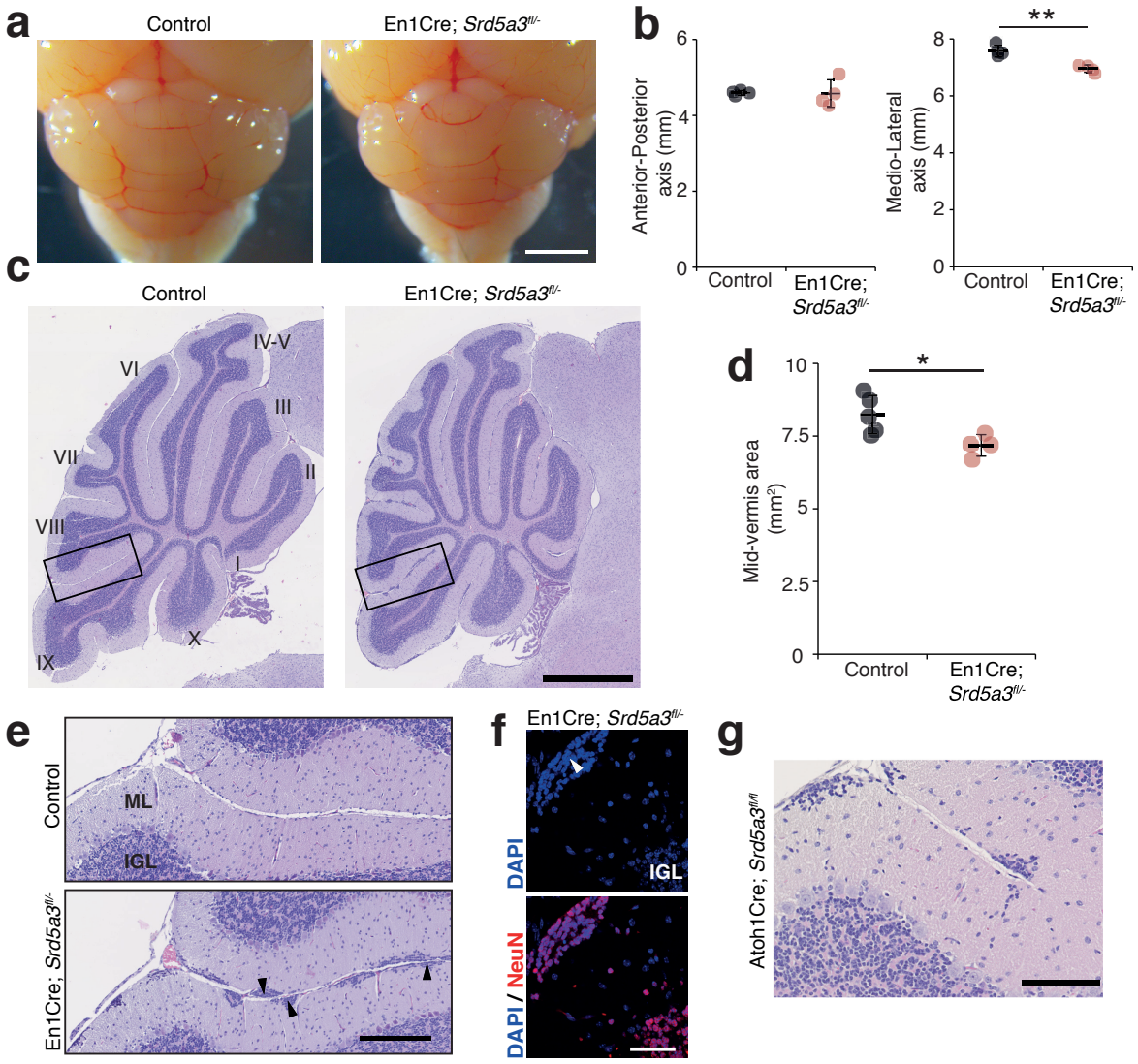

Figure 2. Reduced cerebellum size and ectopic granule neurons in the *Srd5a3* mutant. (a) Dorsal view of P21 posterior brains, scale bar 2mm. (b) Quantification of the cerebellar anterior-posterior and medio-lateral axes (n=4 for each genotype), ** p-value=0.0018. (c) Representative images of hematoxylin-eosin (HE) stained P21 sagittal slices of control and mutant cerebella, scale bar 1mm. Lobule numbers are indicated. (d) Quantification of the mid-vermis area in sagittal slices (Control, n=5; En1-Cre; *Srd5a3*$^{fl/-}$, n=4); *p-value=0.0245. (e) Magnification of HE-stained cerebellar cortex, scale bar 200µm. All examined mutants show ectopic cell clusters (arrow-head) in the outer part of the molecular layer (ML). (f) DAPI (blue) and NeuN (red) staining of P21 En1-Cre; *Srd5a3*$^{fl/-}$ cerebellum. Ectopic cells (arrow-head) are positive for the post-mitotic GCs marker NeuN, scale bar 50µm. (g) Representative image of an HE-stained sagittal slice of Atoh1-Cre; *Srd5a3*$^{fl/fl}$ cerebellum showing similar ectopic cells in the outer ML under GC-specific Srd5a3 deletion, scale bar 100µm (n=2). Two-tailed student t-test was used for statistics. * p<0.05; ** p<0.01. Results are presented as mean ± s.d.

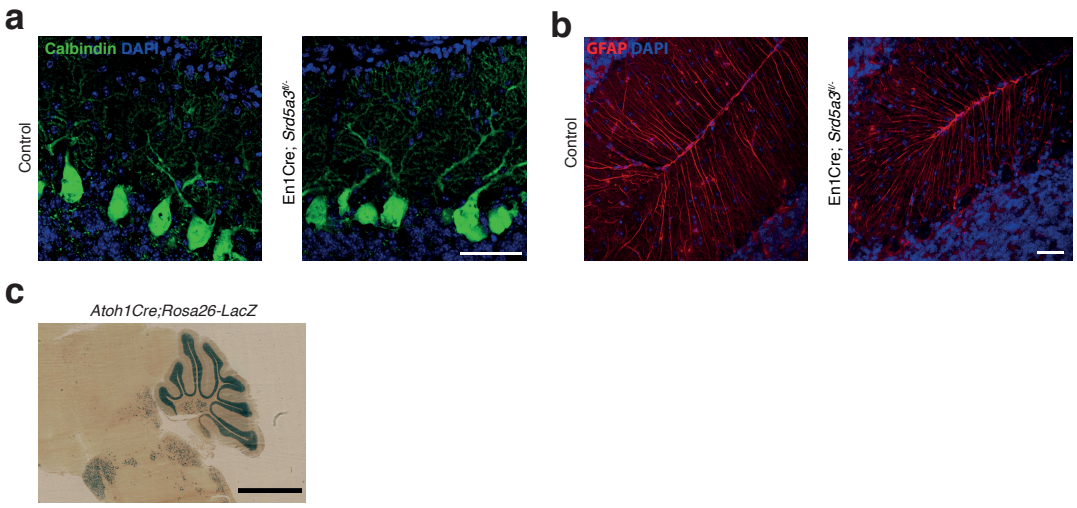

Figure S2. Histological analysis of Purkinje cells (PCs) and Bergmann glia (BG). (a) Representative immunohistochemical staining of control and mutant PCs (Calbindin, P14) and (b) BG (GFAP, P21). Scale bar 50µm. (c) LacZ staining image of the Atoh1Cre; Rosa26-LacZ. Scale bar 2mm.

Cerebellum-specific Srd5a3 deletion decreases the levels of highly glycosylated proteins

Next, we evaluated the molecular mechanisms underlying our observed cerebellar defect by conducting a total proteomic analysis on the developing P7 mouse cerebellum (Lipecka et al., 2016; Wisniewski, Zougman, Nagaraj, & Mann, 2009, dataset publicly available at EBI PRIDE, temporary accession no. #276347). This approach quantified 1982 proteins, whose abundance profiles can cluster each sample by genotype (Fig. S3a, Table S1). Our statistical analysis identified 97 differentially abundant proteins (DAP) (≈ 5% of the total; q-value < 0,05) in the En1-Cre; *Srd5a3*$^{fl/-}$ mice (Fig. 3a). To determine the deregulated pathways among the highly active, neural development pathways at this stage, we performed an over-representation analysis of the 97 DAP using ConsensusPathDB. Our analysis indicated that different pathways involved in ion and amino acid transport, synapse function, cell adhesion-related signaling and cholesterol biosynthesis interplay to generate the mouse phenotype (Fig. 3b). Aside from changes in cholesterol metabolism, all enriched pathways contained at least one deregulated N-glycoprotein. Protein N-glycosylation is critical for ER-protein folding, however we did not find any enrichment in the ER stress pathway. Manual inspection of the 97 DAP revealed increased levels of only two ER-stress-related proteins, SDF2L1 (Fujimori et al., 2017) and HYOU1 (Zhao, Rosales, Seburn, Ron, & Ackerman, 2010), while BiP, the classical ER-stress marker(Ron & Walter, 2007), showed a 1.3 fold non-significant (q=0.08)

increase (Table S1). We then performed a transcriptomic study on additional samples at the same stage, which confirmed the absence of any significant deregulation of the most widely used UPR markers (Fig. S3b). In addition, we did not observe any change in BIP levels restricted to ectopic GC clusters (Fig. S3c,d). Surprisingly, our results exclude a main effect of deregulated N-glycosylation processes on ER stress.

One possible consequence of defective protein N-glycosylation is decreased stability of hypoglycosylated proteins. We observed a significant, 4-fold enrichment of N-glycoproteins among the DAP with decreased levels (simplified as decreased N-glycoproteins; p=0.0012, Fig. 3a). Examining this group of decreased N-glycoproteins revealed that they have more N-glycosylation sites (i.e. higher site multiplicity) with an average of 5.57 sites versus 3.24 in unchanged N-glycoproteins (Fig. 3c). Indeed, N-glycoproteins with 4 or more N-glycosylation sites within the decreased N-glycoproteins show significant enrichment (Fig. 3d).

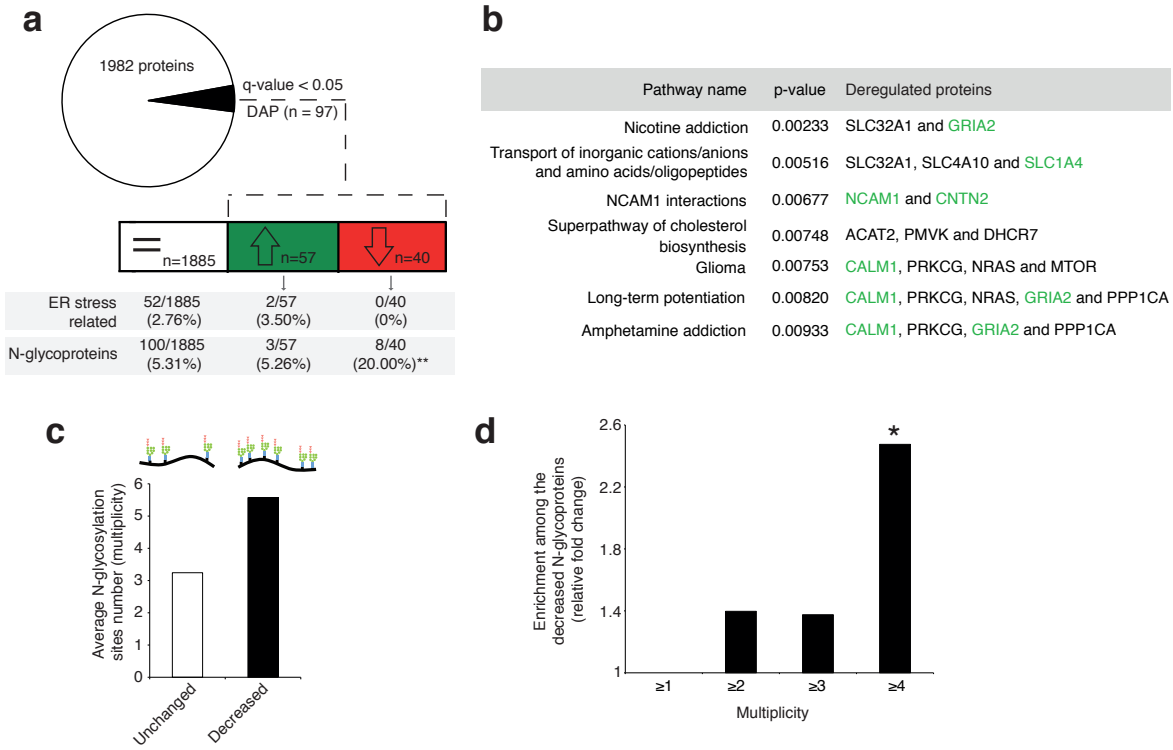

Figure 3. Disrupted neural pathways in the *Srd5a3* mutant developing cerebellum. (a, upper panel) Pie chart representing the total proteomics analysis in P7 cerebellum (n=4 for each genotype). 97 proteins were detected as differentially abundant proteins (DAP) in the mutant samples (q-value<0.05). (a, lower panel) Distribution of unchanged proteins (white box), increased DAP (green box) and decreased DAP (red box) into ER stress-related (GO:0034976) or N-glycoproteins (Reference glycoproteomic database, see method) categories. A significant enrichment was detected within the decreased DAP for N-glycoproteins (n=8, Fisher

exact test, p-value=0.0012). (b) Over-representation analysis on DAP performed with ConsensusPathDB using the 1982 detected proteins as background. All pathways with p-value<0.01 are represented. N-glycoproteins are indicated in green. (c) Average multiplicity in the unchanged and the decreased N-glycoproteins groups. (d) Enrichment for different glycoprotein categories among the decreased N-glycoproteins. Multiplicity represents groups of proteins with more than one (≥2), two (≥3) or three (≥4) N-glycosylation sites. Multiplicity of ≥1 represents all of the decreased N-glycoproteins and is set to one (no enrichment). There is a significant 2.4 fold-change enrichment for glycoproteins with 4 or more N-glycans among the decreased N-glycoproteins (Fischer exact test, p-value=0.0378).

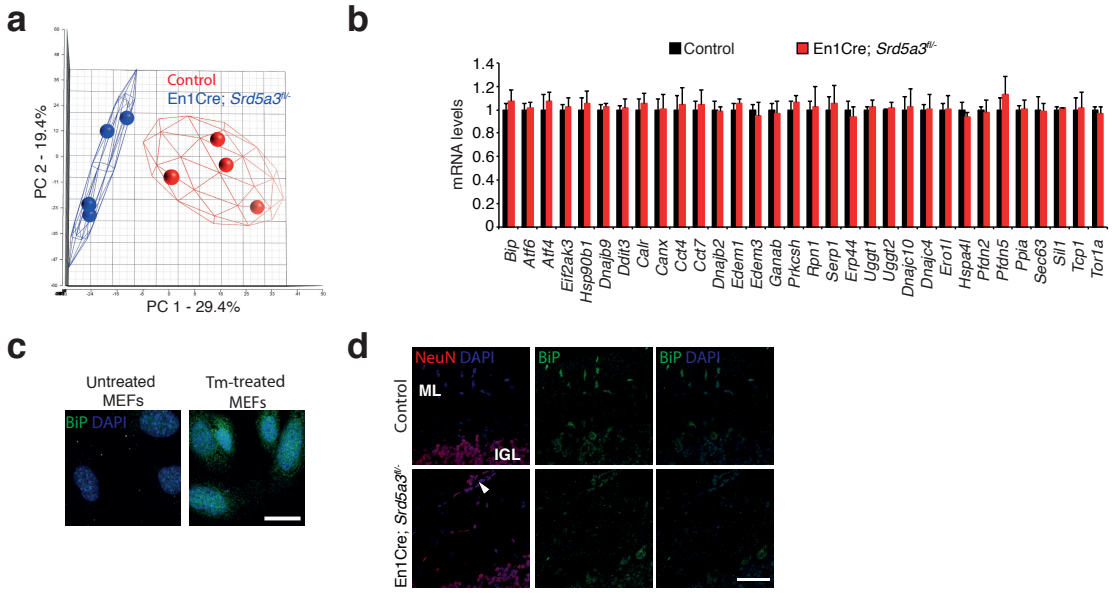

Figure S3. Extended total proteomic analysis of the unfolded protein response (UPR). (a) Principal component analysis (PCA) based on the abundance profiles of the 1982 detected proteins. (b) Transcriptomic analysis of UPR-related mRNAs in the control (n=4) and mutant (n=4) cerebellum. (c) Immunocytochemistry against BiP in MEFs treated with tunicamycin (Tm) for 24h to induce UPR activation and BiP over-expression (positive control) in mouse cells. Scale bar 25µm. (d) Immunohistochemistry against BiP and NeuN in the P21 mouse cerebellum. The arrowhead points to ectopic GCs. Scale bar 50µm. Student t-test was used for statistics. Results are presented as mean ± s.d.

These data demonstrate that the mild glycosylation defect detected in the *Srd5a3* mutant cerebellum disrupts the levels of highly glycosylated proteins, but does not disrupt ER homeostasis.

N-glycosylation site multiplicity and primary sequence underlies the selective protein glycosylation defect

To further elucidate the N-glycosylation deficiency, we included a lectin-affinity based (ConA, WGA, RCA_{120}) enrichment step at the peptide level, followed by deglycosylation (Zielinska, Gnad, Wisniewski, & Mann, 2010), prior proteomic analysis (Fig. S4a, dataset publicly available at EBI PRIDE, PXD009906). This enrichment can identify N-glycosylation sites and quantify the abundance of each site when they are glycosylated. Using this dataset, we identified 140 likely new glycosylation sites (≈8% of the total, see method, Table S2) with high recurrence of non-canonical sequons (≈40% of the new sites, Table S2). Most proteins carrying these sites are intrinsic to membrane as observed for proteins with previously identified glycosylation sites (Gene Ontology analysis in Table S2). In total, we identified 1404 glycopeptides detected in at least 3 out of 4 control samples (Fig. 4a, Table S2). As we observed for the total proteome, we could cluster the expression levels of all the glycopeptides according to the genotype (see method, Fig. S4b). Total proteomics and glycoproteomic analysis yielded complementary information. Total proteomics provides information of the protein abundance level but can only detect peptides containing an unoccupied N-glycosylation site. Glycoproteomics only allows detection of glycopeptides if the site is occupied. For 15% of the N-glycopeptides detected in glycoproteomics (n=206), we found decreased levels in the mutant samples. Of these, we only detected 24 N-glycopeptides in the previous total proteomic experimental settings, consistent with the high enrichment observed with the glycoproteomics analysis (Fig. S4c, Table S3). Among these peptides, 13 were never detected in control but only in mutant samples in total proteomics. These data indicate that these 13 peptides were not glycosylated in the mutant. We conclude that most differences we detected in the glycoproteomic experiment reflect reduced glycosylation site occupancy.

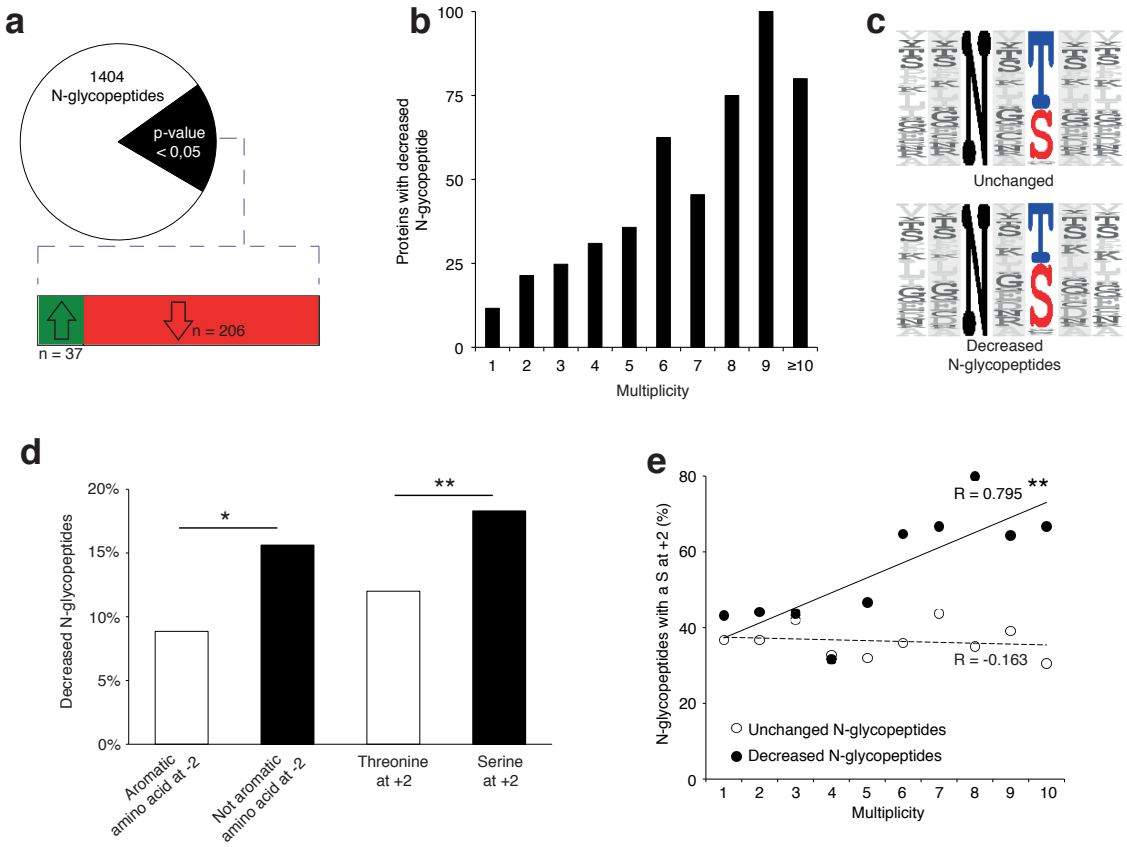

Figure 4. *Srd5a3* deletion impairs protein N-glycosylation in a sequon and multiplicity-dependent manner. (a) Pie chart representation of the glycoproteomic analysis in P7 cerebellum (n=4 for each genotype). The vast majority of the differentially abundant N-glycopeptides was decreased in the mutant samples (206/241, 85%). (b) Percentage of proteins with decreased N-glycopeptide according to their multiplicity (Mann-Whitney test, p-value<0.0001). Proteins with higher multiplicity are more likely to have decreased N-glycopeptide levels. (c) Motif analyses of the N-glycopeptides unchanged or decreased in the mutant. (d) Significant enrichment within the decreased N-glycopeptides for a non-aromatic amino acid (other than Phe, Tyr, His or Trp) in position -2 and a Ser in position +2 (NxS motif). (e) Correlation between protein multiplicity and their percentages of decreased (black) or unchanged (dashed line) glycopeptides with NxS sequon in the mutant samples. A significant positive correlation was found between the NxS-containing glycopeptides decreased occupancy in the mutant and their N-glycoprotein multiplicity (Pearson's coefficient, p-value=0.0062). NxS-containing N-glycopeptides are more likely to have decreased level when located in a highly glycosylated protein. Unless indicated, two-tailed T student was used for statistics. * p<0.05; ** p<0.01.

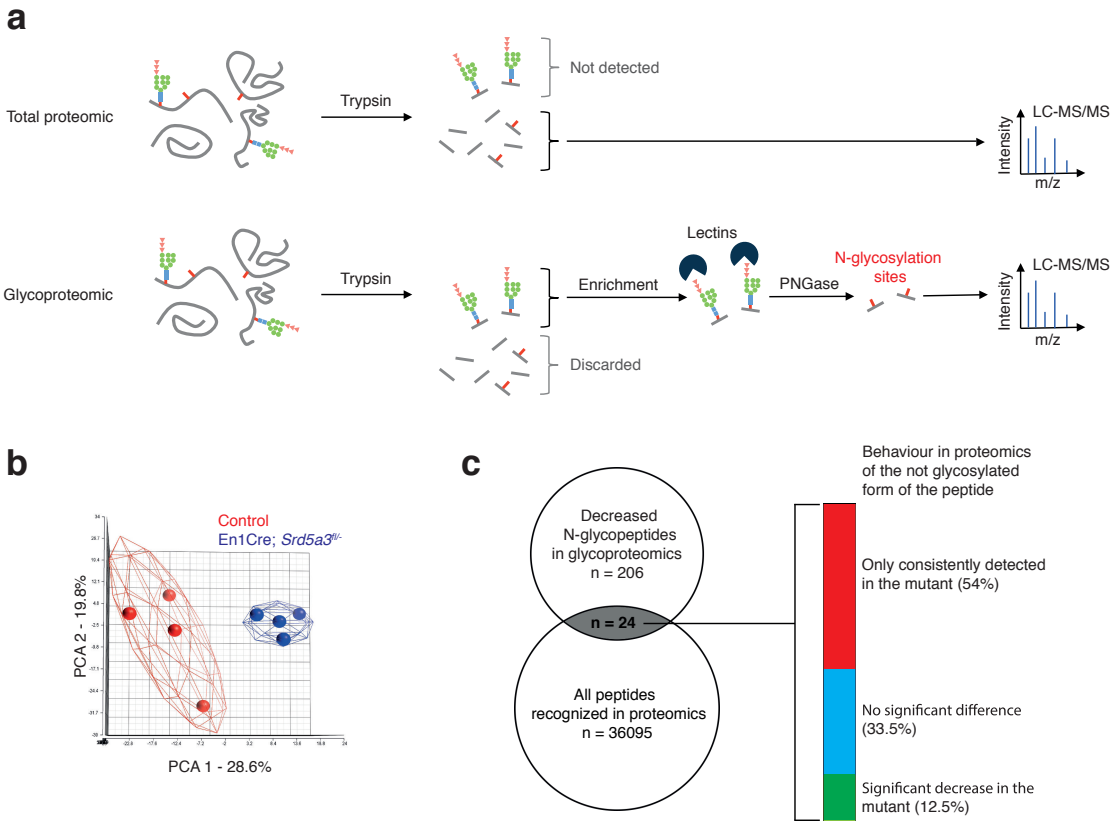

Figure S4. Extended glycoproteomic analysis results and validation. (a) Outline of the total proteomic and glycoproteomic techniques. In regular total proteomics, the proteins are digested into peptides by trypsin. Peptides containing an N-glycan chain cannot be recognized by LC-MS/MS due consequent changes in ion charge and mass. Only the not glycosylated form of the peptide is recognized, if it exists. In glycoproteomics, only the N-glycosylated peptides will be retained (lectin enrichment). After the glycopeptide is released by PNGase treatment, the resulting peptides are then analyzed by LC-MS/MS. (b) PCA based on the MS intensities of the 1404 N-glycopeptides consistently detected in control samples. (c) Qualitative behavior of N-glycopeptides with lower abundance in mutant samples (glycoproteomics analysis) and also detected in the total proteomics analysis. Total proteomics analysis detected most of the peptides (54%) only in the mutant samples, a result consistent with constant glycosylation site occupancy in controls and hypoglycosylation in mutants.

We also detected an extremely significant correlation between N-glycan multiplicity and N-glycopeptide levels (Fig. 4b, Mann-Whitney test, p-value<0.0001). This result is consistent with our larger glycoprotein dataset. To delineate the origin of reduced occupancy of individual N-glycosylation sites, we analyzed their primary sequences (Fig. 4c). We identified a mild effect of the presence of a non-aromatic amino-acid (other than Phe, Tyr, His or Trp) at position -2 and a more significant effect of the Serine at position +2 (Fig. 4d), as previously described(Gavel & von Heijne, 1990; Murray et al., 2015), with an increased impact in highly glycosylated proteins (Fig. 4e). These findings demonstrate that N-glycan multiplicity combined with sequon efficiency is a major parameter driving protein sensitivity to N-glycosylation defects.

Impaired protein N-glycosylation targets IgSF-CAMs

We next wanted to delineate the affected pathways based on our glycoproteomic results. We performed an over-representation analysis using proteins carrying at least one N-glycopeptide significantly decreased in mutant samples (145 N-glycoproteins, 206 N-glycopeptides). This analysis revealed that the most significantly affected proteins (4 out of the top 10 deregulated pathways) derive directly from cell adhesion and axon guidance-related pathways involving adhesion proteins from the L1CAM family (Fig. 5a, red circles). L1CAMs and the previously identified NCAM1 and CNTN2 (Fig. 3b) belong to the immuno-globulin superfamily of cell adhesion molecules (IgSF-CAMs) with critical roles in brain development (Maness & Schachner, 2007; Pollerberg, Thelen, Theiss, & Hochlehnert, 2013; Stoeckli, 2010). We speculate that this particular sensitivity of IgSF-CAMs to a N-glycosylation defect arises from their higher N-glycosylation site multiplicity with an average of 3.3 sites versus 2.3 in non IgSF-CAM proteins (Calculated based on the reference glycoproteomic dataset, Table S2, Mann Whitney test, p-value < 0.0001).

So, we next hypothesized that impaired IgSF-CAMs function derived from sub-optimal N-glycosylation and that defective IgSF-CAMs contributed to our observed histological defect.
We confirmed our observed enrichment for IgSF-CAMs found in our over-representation analysis at the N-glycopeptide level (18.4% of the decreased N-glycopeptides belong to an IgSF-CAM protein, Fisher exact test, p-value=0.0058, Fig 5b).

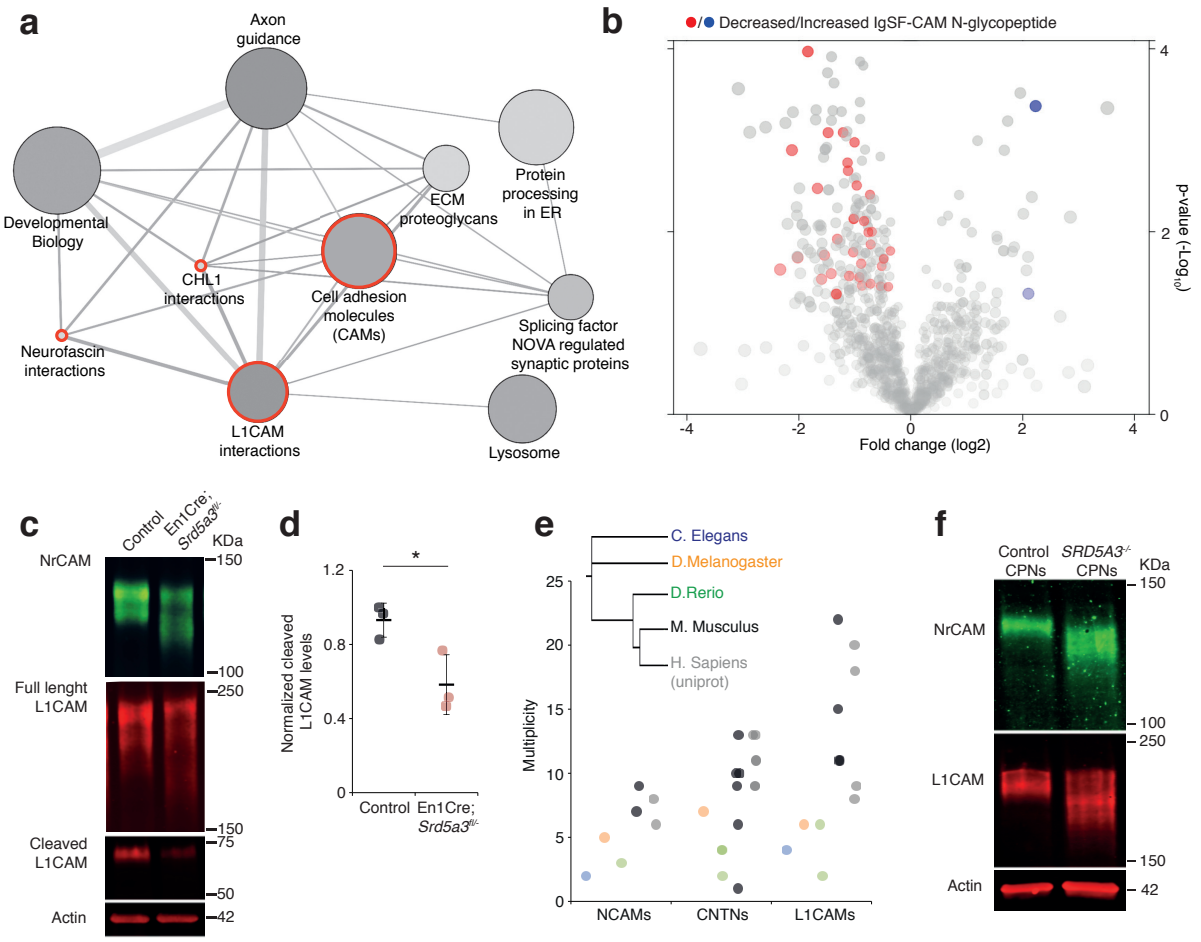

Figure 5. IgSF-CAMs are especially sensitive to a mild N-glycosylation impairment. (a) Graphical representation of enriched pathways and their interactions within proteins with reduced N-glycopeptide in the mutant (ConsensusPathDB). The nodes size indicates the number of proteins within the pathway, and their colour notes the significance (the darkest, the more significantly enriched). Red circles enclose the L1CAM family-related pathways. (b) Volcano plot against all N-glycopeptides. The decreased (red) or increased (blue) N-glycopeptides belonging to an IgSF-CAM protein are highlighted. There is enrichment for IgSF-CAMs glycopeptides within the decreased ones (Fisher exact test, p-value=0.0058). (c) WB against L1CAM and NrCAM in the P7 mouse cerebellum and (d) quantification of the 70kDa cleaved isoform of L1CAM (n=3 for each genotype, p-value=0.0312). (e) Multiplicity per protein of three IgSF-CAMs subfamilies (L1CAMs, CNTNs and NCAMs) in different species. Multiplicity information was collected from experimental datasets (Zielinska et al, 2010 and Zielinska et al, 2012) except for human information extracted from uniprot database(e) WB analysis of L1CAM and NrCAM levels in CPNs. Unless indicated, two-tailed T student was used for statistics. Results are presented as mean ± s.d. * $p<0.05$.

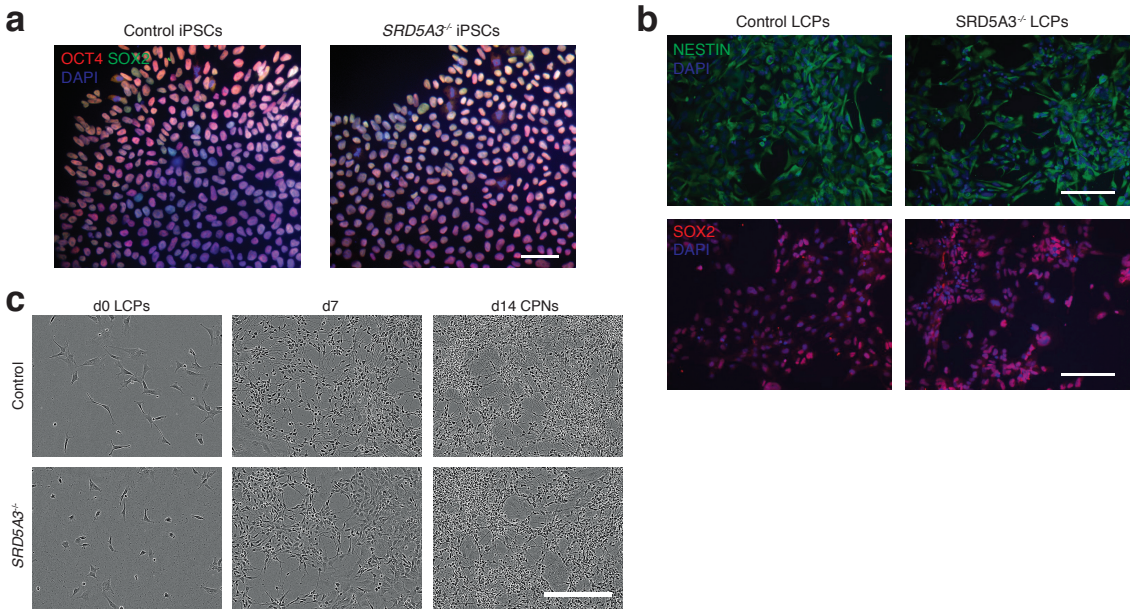

Figure S5. hiPSCs differentiation towards human cortical projection neurons (CPNs). (a) hiPSCs stained for the undifferentiation/pluripotency markers SOX2 and OCT4. (b) hiPSCs differentiated towards late cortical progenitors (LCPs, see method) and stained against Nestin and SOX2. Scale bar 100µm. (c) Representative images of control and *SRD5A3*$^{-/-}$ LCPs differentiation towards cortical projection neurons (CPNs, see method). Scale bar 300µm.

We selected two highly N-glycosylated IgSF-CAMs relevant for the granule cell histological phenotype for validation by western-blotting. We did observe a clear hypoglycosylation defect for L1CAM and NrCAM with a detected shift to lower molecular weights and a significant decrease in the glycosylation-dependent cleavage of L1CAM (Lutz et al., 2014) (Fig. 5c,d).

A major role for IgSF-CAMs in mammalian development is illustrated by the increased number of their encoding genes across evolution (Hortsch, 2000). We also observed an increased in the N-glycan multiplicity for three IgSF-CAM families with critical roles in brain development (Fig.5e). To test if the IgSF-CAM sensitivity for glycosylation impairment is conserved, we generated *SRD5A3* knockout (KO) human induced pluripotent stem cells (hiPSCs). We then differentiated them toward cortical projection neurons (CPNs, Fig S5). As previously observed in mouse, human L1CAM and NrCAM immuno-blotting profiles exhibit clear shifts in *SRD5A3*$^{-/-}$ CPNs (Fig 5f). These data demonstrated a similar exacerbated sensitivity of IgSF-CAMs to SRD5A3 loss in human neurons. Our data suggest that the high multiplicity of N-glycosylation sites in IgSF-CAMs play a conserved and critical role for proper function during mammalian brain development.

Srd5a3 is necessary for IgSF-CAM-dependent cerebellar granule cells adhesion and axon guidance

IgSF-CAMs rely on their glycan charge to interact with each other (Wei & Ryu, 2012) (Horstkorte, Schachner, Magyar, Vorherr, & Schmitz, 1993). Proper IgSF-CAMs trans-interaction is essential for adequate nervous system connectivity for fasciculation and axonal guidance(Pollerberg et al., 2013). To demonstrate that IgSF-CAMs hypoglycosylation is directly involved in En1-Cre; *Srd5a3*$^{fl/-}$ mouse phenotype, we examined the neurite dynamics of GC re-aggregates on a coating with IgSF-CAM substrate (CNTN2, see method). We found a major defect in both neurite extension and number (Fig. 6a). To quantify this defect, we used live cell imaging with isolated GCs cultured under different surface coating conditions. *En1-Cre; Srd5a3*$^{fl/-}$ GCs did not show any significant alterations that suggested differences in proliferation or cell death under any coating (Fig. S6). In contrast, GCs showed defective neurite sprouting with a 20% decrease using regular coating conditions (i.e. laminin with D-lysine) (Fig 6b,c). This phenotype is exacerbated in the presence of coatings that enhance homophilic interactions in IgSF-CAMs (i.e. human recombinant L1CAM or NrCAM proteins) (Dequidt et al., 2007). These results show a 37 and 52% decrease in neurite number compared to control GCs, respectively (Fig 6d). These results support our premise that IgSF-CAMs hypoglycosylation regulates cell adhesion. Given the prominent role of many IgSF-CAMs in axon guidance and the granule cells adhesion defect, we examined axon orientation in GCs. We analyzed the parallel fibers (PFs) organization in the cerebellar ML using electronic microscopy. In control samples, PFs are consistently oriented perpendicular to PCs branches. However, *Srd5a3* mutant mice exhibit an aberrant orientation of groups of PFs in the outer ML, likely due to defective axonal guidance (Fig.6e). Taken together, our data suggest that IgSF-CAMs hypoglycosylation may underlie many neurological defects in CDGs.

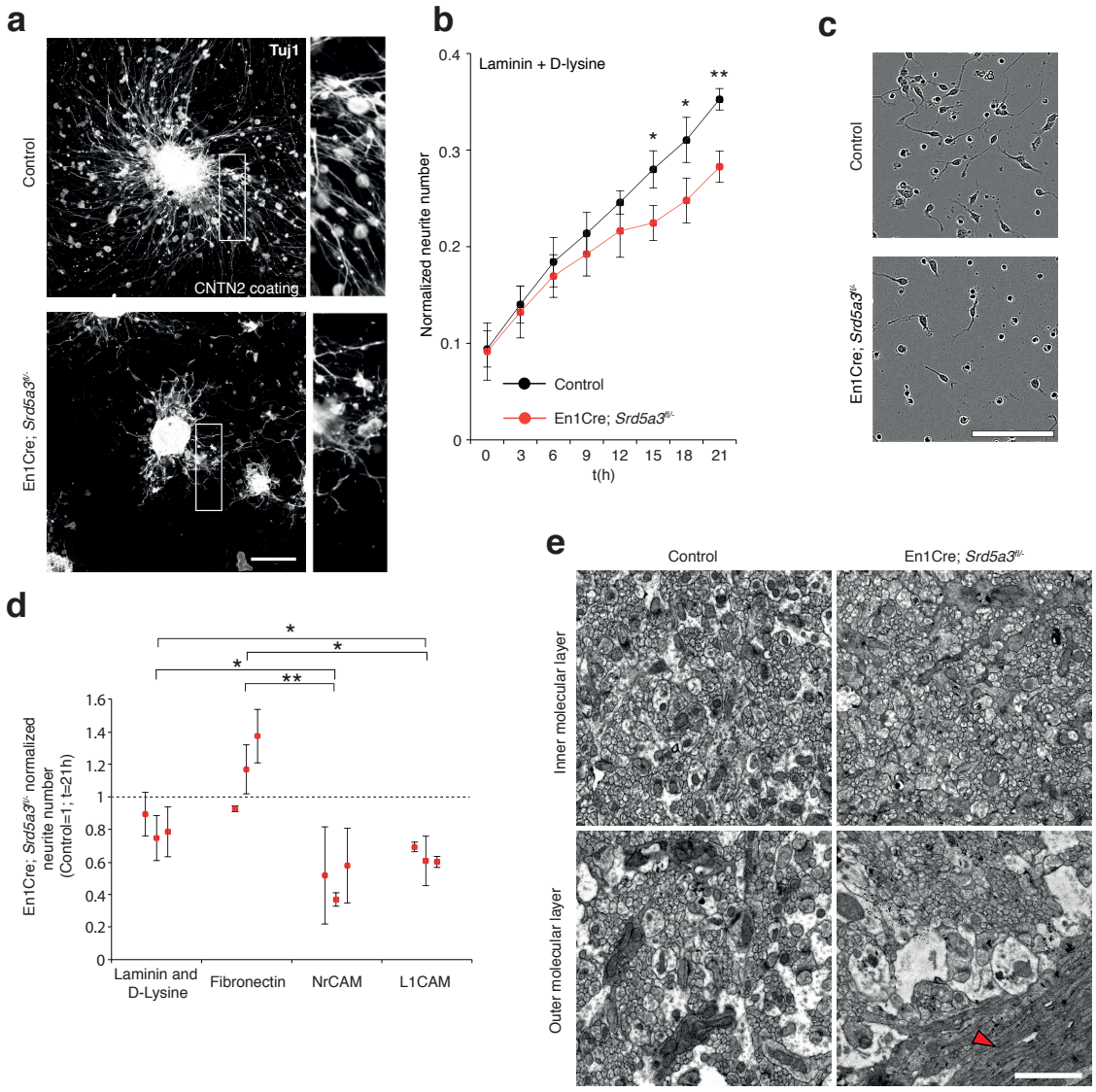

Figure 6. IgSF-CAM-dependent neurite dynamic and axon orientation defects in *Srd5a3* mutant cerebellum. (a) Representative images of GC re-aggregates seeded for 36h on an IgSF-CAM-coated surface (CNTN2) and stained for Tuj1 in control (n=2) and mutant (n=2). Scale bar 200µm. (b) Neurite number per GC body cluster across 21h in laminin and D-lysine coated wells as measured with Incucyte live cell imaging system (Control, n=3; En1-Cre; *Srd5a3*$^{fl/-}$, n=3). (c) Representative image of control and En1-Cre; *Srd5a3*$^{fl/-}$ GCs after 21h in laminin and D-lysine-coated wells. Scale bar 100µm. (d) Neurite number normalized to GC body clusters after 21h with laminin/D-lysine coatings, fibronectin or IgSF-CAMs-coated wells (NrCAM and L1CAM). Each dot per coating represents results a single mutant mouse. All GC cultures were performed in technical triplicates (Control, n=3; En1-Cre; *Srd5a3*$^{fl/-}$, n=3). (e) Representative electron microscopy images of cerebellar ML Sagittal view at P21 taken from control (n=3) and *Srd5a3* mutant (En1-Cre; *Srd5a3*$^{fl/-}$ n=1; Atoh1-Cre; *Srd5a3*$^{fl/-}$ n=2) mice. Scale bar 2µm. Parallel fibers show a single orientation in control ML, whereas some exhibit an abnormal perpendicular orientation in the most outer ML in the mutant mice (red arrow-head). Two-tailed student t-test was used for statistics. * $p<0.05$; ** $p<0.01$. Results are presented as mean ± s.d.

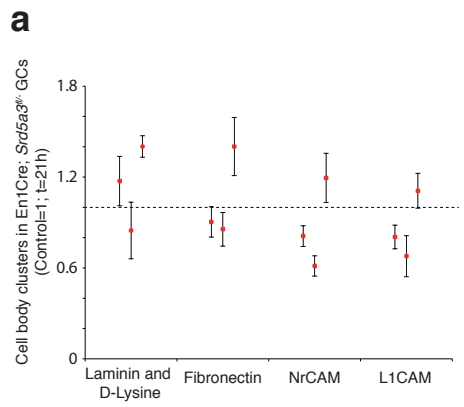

Figure S6. Changes in granule cell (GC) number under different coating conditions. (a) GC body cluster number after 21h using different coatings and normalized to control littermates. Each dot per coating represents results from a single mutant mouse. All GC cultures were performed in technical triplicates (n=3 for each genotype). Student t-test was used for statistics. Results are presented as mean ± s.d.

Discussion

We sought to delineate the impact of *Srd5a3*-driven hypoglycosylation of N-glycoproteins during development, a biochemical defect likely shared between multiple CDG. Here, we generated a conditional KO mouse that recapitulates some neurological symptoms induced by this ER glycosylation defect. We hypothesized that patients with *SRD5A3*-related and other types of CDG exhibit protein hypoglycosylation leading to cerebellar dysfunction. From a physiological perspective, we hypothesized that the characterization of the affected glycoproteins and glycosylation sites would identify new roles for protein N-glycosylation during central nervous system development. So, we combined total proteomic and glycoproteomic approaches to identify the molecular mechanisms underlying the observed cerebellar dysfunction and GC histological defects. Our strategy assessed the relative occupancy at each N-glycosylation site regardless of the N-glycan nature. The pleiotropic roles of glycans on development and synaptic transmission suggest that genetic defects in the synthesis of the N-glycan core structure would have multiple distinct and integrated consequences. We unexpectedly found that partial inhibition in N-glycosylation during cerebellar development has persistent consequences on a specific set of glycoproteins and pathways. Among them, we found that IgSF-CAMs-mediated cell adhesion is the most consistently affected. Our further investigations revealed impaired GC adhesion and axon guidance, which supports IgSF-CAM hypoglycosylation as the primary underlying defect.

Our glycoproteomic and total proteomic analyses strongly suggest an intuitive mechanism where N-glycan multiplicity is a critical factor driving the molecular defects.

SRD5A3 acts at the last step of dolichol synthesis and facilitates also the synthesis of O-mannose-linked glycans, C-mannosylation, and glycophosphatidylinositol (GPI) anchored proteins. However, N-glycosylation is the most demanding cellular process with eight dolichol molecules needed for each N-linked glycan(Cantagrel & Lefeber, 2011). Defects in SRD5A3 alter lipid membrane composition that subsequently impairs protein N-glycosylation. Consistently with previous results using *Srd5a3* gene-trapped embryos(Cantagrel et al., 2010), several enzymes from the cholesterol/mevalonate pathway were deregulated (Fig. 3b). These observations indicate a regulatory mechanism that could alleviate these glycosylation defects by stimulating the mevalonate pathway (Haeuptle et al., 2011) (Welti, 2013). While we cannot exclude defects in other glycosylation pathways, our results demonstrate that changes in N-glycosylated proteins and correlations between the N-glycan number and peptides abundance in both proteomic analyses strongly implicate the N-glycosylation pathway as the major metabolic defect underlying the phenotype and neurological symptoms in SRD5A3-CDG.

Our work shows that proteins with high N-glycan multiplicity, estimated to average four or more sites, show an increased risk for hypoglycosylation to induce protein degradation or dysfunction. Moreover, differences in the sequon can have an additive effect to this increased risk. Although several highly-glycosylated proteins are frequently used as sensitive biomarker for N-glycosylation defects(He, Ng, Losfeld, Zhu, & Freeze, 2012) (Park et al., 2014), we provide initial evidence that the total number of glycosites per protein is a major parameter that influences N-glycoproteins sensitivity. Our total proteomic analysis clearly indicates that decreased glycoprotein abundance is a direct consequence of incomplete glycosylation of highly glycosylated proteins. Yet, examining individual proteins, such as the IgSF-CAM member L1CAM, did not reveal significant differences in full-length isoform abundance by western blot but showed altered cleavage as a consequence of its hypoglycosylation. The cleaved L1CAM isoform (70kDa) enhances cerebellar GC neurite outgrowth(Lutz et al., 2014), which indicates that hypoglycosylation of some proteins can impair their processing, trafficking and/or function without necessarily causing significant changes in their cellular abundance.

The number of N-glycans, in conjunction with their degree of branching, regulates cell proliferation and differentiation. Highly glycosylated growth factor receptors show increased cell-surface expression by forming galectin-mediated molecular lattices(Lau et al., 2007). We cannot exclude that some cell adhesion proteins utilizing a similar mechanism also show alterations in the *Srd5a3* mutant cerebellum. To our knowledge, neuronal galectin-IgSF-CAM interactions remain unreported. The pivotal role of IgSF-CAMs in cell migration, axonal guidance and synaptogenesis has been widely studied in mouse (Sakurai et al., 2001) (Fransen et al., 1998) (Berglund et al., 1999) (Colakoglu, Bergstrom-Tyrberg, Berglund, & Ranscht, 2014) (Sytnyk, Leshchyns'ka, & Schachner, 2017). However, we still understand very poorly how N-glycans contribute to these functions with the exception of the established role for the polysialic acid modification of NCAM1 N-glycan chains(Weinhold et al., 2005).

Among proteins identified in our proteomic approaches, NrCAM and L1CAM show redundant functions in cerebellar GC development, in addition to their roles in axonal growth (Sakurai et al., 2001) (Demyanenko, Tsai, & Maness, 1999) (Demyanenko et al., 2011). CNTN2/TAG-1 contributes to neuronal polarization and axonal organization. Interestingly, the corresponding KO mouse shows ectopic GC clusters at the pial surface of the cerebellum (Xenaki et al., 2011), as observed in the *Srd5a3* mutant cerebellum. Mice lacking *Cntn1* show aberrant parallel fibers distribution and motor coordination defects (Berglund et al., 1999). Since neural IgSF-CAMs largely bind to each other homophilically and heterophilically (Pollerberg et al., 2013), we suspect that the observed neuronal adhesion defects arise from a cumulative effect of partial hypoglycosylation of multiple interacting partners (Schwarz, Pan, Voltmer-Irsch, & Hutter, 2009) (Stoeckli, Sonderegger, Pollerberg, & Landmesser, 1997). IgSF-CAMs show increased complexity and members in vertebrates (Vogel & Chothia, 2006). The increased diversity in some IgSF-CAM proteins correlates with the presence of homologs with higher multiplicity in mammals (Fig.5e). We speculate that a positive selection of adhesion proteins with high N-glycosylation site multiplicity can support the increased complexity of mammalian neuronal organization and connectivity.

In addition to the central nervous system, highly glycosylated IgSF-CAM members also play critical roles in other systems affected in CDG patients, such as the developing eyes (Morava et al., 2009) and immune system with ICAM1 (Blank et al., 2006; He, Srikrishna, & Freeze, 2014), or in other diseases like cancer, where L1CAM plays a critical role in tumor metastasis (Kiefel et al., 2012) (Agrawal et al., 2017). Further investigations will determine how IgSF-

CAM hypoglycosylation regulates or alters the clinical outcomes and responsivity to therapeutic strategies. In conclusion, our study demonstrates that suboptimal function of the ER-glycosylation machinery impairs primarily highly glycosylated N-glycoproteins with mild or no effect on ER homeostasis. We propose that the prevalent neurological symptoms observed in SRD5A3-CDG patients and likely other types of CDG type I result from defective neural cell adhesion, caused by IgSF-CAM hypoglycosylation. Deciphering how multiple N-glycans can influence differential IgSF-CAM adhesion properties will address important unresolved neurobiological questions regarding neuronal migration, axonal outgrowth and synaptogenesis.

Methods

Animal care

Animals were used in compliance with the French Animal Care and Use Committee from the Paris Descartes University (APAFIS#961-201506231137361). All behavioural analysis were performed in compliance with the guidelines of the French Ministry of Agriculture for experiments with laboratory animals. The experimental protocol and euthanasia have been approved by the Ethical Committee 27, registered at the French ministry of research.

Generation of the *Srd5a3* conditional KO mouse

Embryonic stem (ES) cell clone EPD0575_2_F01 carrying the *Srd5a3*$^{tm1a(EUCOMM)Wtsi}$ allele was acquired from the International Mouse Phenotyping Consortium (IMPC; http://www.mousephenotype.org/). After additional QC validation based on Southern-blot, ES cells were injected into C57BL/6 at the University of California, San Diego Transgenic and Gene targeting Core yielding chimeric mice. Chimera were bred to C57Bl/6 until germline transmission was successful to produce knockout first allele. Then, the *Srd5a3*tm1a mice were bred with ACTB:FLPe B6J (JAX stock #005703) Flp recombinase expressing transgenic mice to produce mice expressing a functional *Srd5a3* allele that retained flox sites surrounding exon 2 to 4 (out of the 6 exons) and including part of the enzymatic domain (PFAM, *Steroid_dh*). After outbreeding the Flp recombinase transgene, *Srd5a3* floxed mice were crossed with hemizygous CMV-Cre line transgenic mice (Metzger, Clifford, Chiba, & Chambon, 1995) to generate *Srd5a3* KO allele. *Srd5a3* floxed mice were bred with hemizygous *En1*$^{tm2(cre)Wrst}$ transgenic mice (JAX stock #007916) expressing Engrailed1 promoter driven Cre to produce cerebellum-specific deletion (En1Cre; *Srd5a3*$^{fl/-}$) or with hemizygous Tg(Atoh1-cre)1Bfri (JAX stock #011104) expressing Atoh1 promoter driven Cre to produce cerebellum granule cell-specific deletion (Atoh1Cre; *Srd5a3*$^{fl/-}$). Specific Cre expression was confirmed by breeding with a LacZ reporter-carrier mouse line (R26R^{LacZ} mouse). Efficient *Srd5a3* recombination was assessed by RT-PCR and RT-qPCR in the absence of any specific antibody.

Mouse embryonic fibroblasts (MEFs) generation

For MEFs generation, *Srd5a3*$^{fl/-}$ mice were bred with CAGCre mice (B6.Cg-Tg(CAG-cre/Esr1*)5Amc/J; CAGCre; *Srd5a3*$^{fl/-}$). *CAGCre;Srd5a3*$^{fl/-}$ embryos fibroblasts were isolated at E14.5 and immortalized by serial passaging as described by Xu(Xu, 2005). For *Srd5a3* recombination primary MEFs were treated for 4 days with tamoxifen (1μM, H6278, Sigma) prior to immortalization. Efficient *Srd5a3* recombination was assessed by RT-qPCR after immortalization.

Behavioral studies

For behavioral analysis, 15 *En1Cre; Srd5a3*$^{fl/-}$ and 15 control littermates, gender-matched, 2-3 months old were used. The number of animals per group was chosen as the optimal number likely required for conclusion of statistical significance, established from prior experience using the same behavioral tests (Pereira et al., 2009). Morris water maze (MWM) test was used to assess working memory. Prior to the test, the mouse swimming speed was analyzed. No differences in the swimming speed were detected. For MWM, mice were exposed twice to the same hidden platform for a total of eight sessions. The improvement to find the platform on the second trial was evaluated. For motor coordination, classic accelerating rotarod testing was done for 10 minutes and for a total of three sessions, 24h apart. The first three falls from the rod during each session were annotated.

Histological analysis

Gross anatomical analyses and HE staining was performed as previously described (Akizu et al., 2013). The resulting slices were scanned with NanoZoomer-XR (Hamamatsu Photonics, Japan). For IHC, the cerebellum was embedded in OCT. 12μm-thick slices were generated with cryostat. The following antibodies were used for IHC: NeuN (1:200, MAB377; Millipore), Calbindin (1:10.000; CB-38A, Swant), GFAP (1:1.000; AB5804, Millipore) and BiP (1:50, ADI-SPA-826, Enzo). All samples were mounted with ProLong Gold Antifade Mountant with DAPI (Life Tech). Images were taken with confocal Leica SP8 STED and analyzed with ImageJ.

Protein extraction and western blotting

P7 mouse cerebellum samples and MEFs were isolated in RIPA buffer (1% SDS; 0,1% for cell extracts) supplemented with EDTA-free protease inhibitor (11836170001, Sigma) and phosphatase inhibitor cocktail (4906845001, Sigma), homogenized by sonication (Bioruptor Pico sonication device – 8 cycles 30''ON/30''OFF) and centrifuged at 12.000g at 4ºC for 20min. The supernatant was recovered and quantified with BCA (Life technologies). For cell extracts, RIPA was added directly to the flask and the cells were recovered with a cell scrapper followed by the same protocol. Equal amounts of protein were loaded from each sample in polyacrylamide gels. Gel transfer to nitrocellulose membranes was performed with the Trans-Blot Turbo Transfer System for 10min at 1.3A and 25V. Membranes were blocked with 5% dry milk and incubated O/N at 4ºC with the following antibodies: LAMP1 (1:2.000; AB24170, Abcam), L1CAM (1:2.000; AB24345, Abcam), NrCAM (1:2.000; AB24344, Abcam) and β-actin (1:20.000; AM4302, Thermo Fisher). Depending on the antibody suitability, the membrane was developed by HRP system (LAMP1, ChemiDoc XRS+ System) or with fluorescent secondary antibodies (Odyssey CLx imaging system). All secondary antibodies were used at 1:10000. For far-western blotting, no blocking step was performed, and the membrane was directly incubated for 1h with biotinylated SNA (1:2.000; B-1305, Vector laboratories) or ConA (1:2000; C2272, Sigma) and

posteriorly with IRDye 800CW-streptavidin for 1 extra hour (1:10.000; 926-32230, LI-COR). All WB results were replicated at least twice.

RNA extraction, RT-PCR, RT-qPCR and transcriptomic analysis

RNA was extracted with Trizol reagent (15596-026, Thermo Fisher) according to manufacturer's instructions. For transcriptomic studies, 4 *En1Cre;Srda5a3*$^{fl/-}$ P7 mice and 4 control littermates were used. RNA quality was validated with Bioanalyzer 2100 (using Agilent RNA6000 nano chip kit) and 180 ng of total RNA were reverse transcribed using the GeneChip WT Plus Reagent Kit (Affymetrix). The resulting double strand cDNA was used for *in vitro* transcription with T7 RNA polymerase (WT cDNA synthesis and amplification kit, Affymetrix). After purification according to Affymetrix protocol, 5.5 ug of the cDNA obtained were fragmented and biotin-labelled using Terminal Transferase (WT terminal labelling kit, Affymetrix). cDNA was then hybridized to GeneChip Mouse Transcriptome Array 1.0 (MTA 1.0., Affymetrix) at 45°C for 17 hours. After O/N hybridization, chips were washed on the fluidic station FS450 following specific protocols (Affymetrix) and scanned using the GCS3000 7G. The scanned images were then analyzed with Expression Console software (Affymetrix) to obtain raw data (cel files) and metrics for Quality Controls. The observations of these metrics and the study of the distribution of raw data showed no outlier experiment. Robust multi-array average (RMA) normalization was obtained using R, and normalized data were subjected to statistical tests. For RT-PCR/RT-qPCR 1µg of RNA was retrotranscribed into cDNA with SuperScript II reverse transcriptase (18064014, Thermo Fisher). qPCR was performed with PowerUp SYBR Green Master Mix (A25777, Thermo Fisher). The following primers were used: m*βActin* (F 5'-TACAGCTTCACCACCACAGC-3'; R 5'-AAGGAAGGCTGGAAAAGAGC-3') and m*Srd5a3* (F 5'-CCGGGCTATGGCTGGGTGG-3' and R 5'-CTGTCTCAGTGCCTCTAGGAATGG-3').

Total proteomics and Glycoproteomics

Four P7 *En1Cre;Srd5a3*$^{fl/-}$ and four control littermates were used for cerebellar protein extraction as previously described. Two different batches, each from at least two different litters, were used for total proteomics and another for glycoproteomics. For total proteomics, 100µg of protein were processed by filter-aided sample preparation (FASP) protocol, as described previously (Lipecka et al., 2016). Briefly, samples were applied to 30KDa MWCO centrifugal filter units (UFC503024, Amicon Ultra, Millipore) mixed with 200uL of urea (UA) buffer (8M urea, 100mM Tris-HCl pH 8.8) and centrifuged twice. The samples were incubated for 20min in the dark with UA buffer containing 50mM iodocetamide for alkylation. The filter units were subsequently washed twice with UA buffer and twice more with ABC buffer (50mM ammonium bicarbonate). Peptide digestion was carried by incubation with trypsin (1:50) O/N at 37ºC. The resulting peptides were collected by two washes with ABC buffer, vacuum dried and dissolved in 0.1% (v/v) trifluoroacetic acid with 10% acetonitrile.

Glycoproteome analysis was performed by FASP with an additional step of enrichment in N-glycopeptides by lectins, as described by M. Mann and colleagues (Zielinska et al, 2010). Briefly, 100ug of trypsinized peptides were recovered in binding buffer (20mM Tris/HCl pH 7.6, 1mM $MnCl_2$, 1mM $CaCl_2$, 0.5; NaCl) and incubated with a lectin mixture (90ug ConA, 90ug WGA and 71.5 ug RCA_{120}) for 1h. To elute the non-glycosylated peptides, not attached to the lectins, the filter units were washed four times with binding buffer and after with ABC solution in H_2O_{18} (O188P, Eurositop). To release the N-glycopeptides from the lectins, the samples were

incubated with PNGase diluted in H_2O_{18} (P0704L, New England BioLabs) for 3h at 37ºC. The N-glycopeptides were recovered by washing twice with ABC. All centrifugation steps were performed at 14.000g at RT.

LC-MS/MS analysis

For each run, estimated 0.5 µg were injected in a nanoRSLC-Q Exactive PLUS (Dionex RSLC Ultimate 3000, Thermo Scientific, Waltham, MA, USA). Peptides were separated on a 50cm reversed-phase liquid chromatographic column (Pepmap C18, Dionex). Chromatography solvents were (A) 0.1% formic acid in water and (B) 80% acetonitrile, 0.08% formic acid. Peptides were eluted from the column with a linear gradient of 120 minutes from 5% A to 80% B followed by 27 minutes of column re-equilibration in 5% A. Two blanks, each with two 25 min-linear gradient, were run between samples to prevent carryover. Peptides eluting from the column were analyzed by data dependent MS/MS, using top-10 acquisition method. Briefly, the instrument settings were as follows: resolution was set to 70,000 for MS scans and 17,500 for the data dependent MS/MS scans in order to increase speed. The MS AGC target was set to 3.10^6counts with 200ms for the injection time, while MS/MS AGC target was set to 1.10^5 with 120ms for the injection time. The MS scan range was from 400 to 2000 m/z. Dynamic exclusion was set to 30 sec. All analyses were performed in four biological replicates.

Total proteomics and glycoproteomics data analysis

The MS files were processed with MaxQuant software version 1.5.8.3 and searched with Andromeda search engine against the mouse subset from the UniProtKB/Swiss-Prot complete proteome database (release 2016_06). Statistical analysis and logo extractions were performed using Perseus version 1.5.5.3. Different thresholds were applied to total proteomics and glycoproteomics analysis given that the intensity of several peptides in total proteomics is used for determining protein intensity, while a single peptide in glycoproteomics is analysed at the time. For total proteomics, only proteins detected in all 8 samples (4 controls and 4 mutants) were retained for statistical analysis, avoiding all data imputation. For comparative glycoproteomics, we retained glycosites detected in at least 3 out of 4 control samples. Additionally, we selected proteins that were specifically detected in control or mutant samples by retaining proteins detected solely in at least 3 samples of one group. Both FDR and p-value (q-value < 0,05, paired student t-test) was used for total proteomics, whereas the p-value (< 0,05, unpaired student t-test) was used for N-glycopeptides. As a database for N-glycoproteins and number of N-glycosylation sites per protein (qualitative dataset, reference glycoproteomic dataset), the data obtained by glycoproteomics was used: any glycopeptide detected in at least 2 control samples was considered as potentially N-glycosylated (Table S2). Sites that were not previously described in Zielinska et al. or not predicted by uniprot were classified as likely novel N-glycosylation sites. Volcano plots were generated using the VolcanoShiny app (https://hardingnj.shinyapps.io/volcanoshiny/). PCA and variance analysis were done with the Partek Genomics Suite software. For homologous IgSF-CAM proteins (CNTNs, L1CAMs and NCAMs), HomoloGene and the study from Chen et al. (Chen & Zhou, 2010) were used.

Granule cells culture

Cerebellar granule cells were extracted from P7 cerebellum following the Manzini and colleagues protocol(Lee, Greene, Mason, & Manzini, 2009). Cells were kept at 37ºC in 48-well plates for at least 24h. For surface coating, 48-well plates were incubated at 4ºC O/N with the coating solution, followed by 3 PBS washes, blocking for 30

min with BSA to inhibit non-specific binding (10mg/mL) and three more PBS washes. The coatings used were: human recombinant L1CAM (10µg/mL; 777-NC, R&D), human recombinant NrCAM (5µg/mL; 2034-NR, R&D) human recombinant CNTN2 (10µg/mL; 1714-CN-025, R&D), fibronectin (50µg/mL; F2006, Sigma) and Laminin D-Lysine (2µg/mL and 30µg/mL; 11243217001 and P6407, respectively, Sigma). Cell and neurite dynamics were measured every 3h by live cell imaging (Incucyte ZOOM with Neurotracker module). As long as GCs do not arborize, the neurite branching points parameter provided by the Incucyte software was translated as neurite number. For GCs re-aggregates, cells were isolated and seeded for 24h in un-coated surfaces ($1x10^6$ cells/cm^2) to promote aggregation. The aggregates were then collected and seeded in the coated surface for 36h.

Human induced pluripotent stem cells (hiPSCs) *SRD5A3*$^{-/-}$ generation and culture

iPSCs were derived from hPBMCs from a control male donor via Cyto-Tune Sendai virus reprogramming. Cells were cultured at 37ºC on vitronectin-coated (10µg/mL; 07180, Stem Cell) dishes with mTeSR media (Stem Cell). *SRD5A3* KO hiPSCs clones were generated by CRISPR/Cas9. sgRNA (inserted into a GFP-containing PX458 plasmid, Addgene) targeting the first exon of the gene were generated via the CRISPOR website and validated in T293 HEK cells by Sanger sequencing combined with tides analysis (https://tide-calculator.nki.nl/; data not shown). hiPSCs were transfected by nucleofection (Amaxa 4D, Lonza) and transfected cells (GFP+) were isolated by FACs (BD FACSAria II SORP, BD Biosciences) to generate single-cell-of-origin colonies. DNA was extracted from a piece of each colony by ZR-Duet DNA MiniPrep (D7003, Zymo) and sequenced. After selection, SOX2 (1:2000; AB5603, Millipore) and OCT4 (1:100; SC5279, Santa Cruz) immunostaining was used to confirm pluripotency (Fig. S5). No major chromosomal abnormalities were detected by CGH array (60K, data not shown).

hiPSCs differentiation towards late cortical progenitors (LCPs)

Differentiation of hiPSCs towards LCPs and cortical projection neurons (CPNs) was carried as described by Benchoua and colleagues (Boissart et al., 2013). Briefly, iPSCs colonies were transferred to a non-coated dish with neural induction media (N2B27 with FGF2 and double SMAD inhibition by SB431542 and LDN193189, Stem Cell) for 6h and were afterwards transferred onto poly-ornithine and laminin coated dishes. Following neural rosette formation (12-15 days), the cells were passaged onto a geltrex-coated (A1413301, Life Tech) flask (LCPs P1) and were further cultured with N2B27 supplemented with FGF2, EGF and BDNF (Stem Cell). SOX2 and Nestin (1:250; N5413, Sigma) staining confirmed LCPs multipotency. Neuroectodermal origin of the emerging neural progenitor-like cells was assessed by HNK1/P75 FACs staining (data not shown). LCPs were further differentiated towards CPNs by growth factor withdrawal for 15 days. Neuronal identity was assessed with Tuj1 (1:2000; T2200, Sigma) staining (data not shown). WB results were replicated with two different clones of control and *SRD5A3* mutant hiPSCs.

Electronic microscopy experiments

P21 *En1Cre; Srd5a3*$^{fl/-}$ (n=1), *Atoh1Cre; Srd5a3*$^{fl/-}$ (n=2) and control littermates (n=3) were perfused with 4% PFA / 2% glutaraldehyde. The cerebellum was kept in the same solution for at least one week. Sagittal slices, less than 1mm thick, were post-fixed with 1% osmium tetroxide in 0.1 M phosphate buffer and then dehydrated in ethanol. After 10 min in a 1:2 mixture of epoxy propane and epoxy resin and 10 min in epon, samples were

covered by upside down gelatin capsules filled with freshly prepared epoxy resin and polymerized at 60°C for 24 h. After heat separation, ultrathin sections of 90nm were cut with an ultra-microtome (Reichert ultracut S), stained with uranyl acetate and Reynold's lead and observed with a transmission electron microscope (JEOL 1011). Acquisition was performed with a Gatan Orius 1000 CCD camera.

Statistics

For mouse experiments, no statistical methods were used to predetermine sample size. No animals or samples were excluded from the analysis. All mouse experiments included at least two different litters. For mouse behavioral analysis, one way ANOVA was used. Regular enrichment analyses were performed by Fisher exact test (significance 0.05). For multiplicity and NxS motif correlation, the Pearson coefficient was used. For enrichment in highly N-glycosylated proteins, two-tailed Mann-Whitney test was performed. Statistical differences between groups were assessed by two-tailed student t-test. For all statistical tests, confidence intervals were set at 95%. All results are presented in mean value and standard deviation was used to calculate the error bars.

Data availability

Full transcriptomic data is publicly available at ArrayExpress (accession no. E-MTAB-6861). Total proteomics and glycoproteomics data are publicly available at EDI PRIDE (PXD009906).

Acknowledgements

We thank J.G. Gleeson for the support to generate *Srd5a3* conditional mouse and helpful advices. We are grateful to L. Goutebroze, F. Francis, S. Nguyen, K. Radjamani for valuable discussions. The project is funded by the French National Research Agency ANR-16-CE12-0005-01 (V.C.), la Fondation pour la Recherche Médicale FRM-DEQ20160334938 (L.C), the association Connaître les Syndromes Cérébelleux CSC (V.C.), the program ERA-NET 643578-EURO-CDG2 and E-Rare-3 (F.F. and C.T.), Paris Descartes University BioSPC program (D.M-C), Imagine Foundation (D.M-C), Imagine International PhD program with Bettencourt-Schueller-foundation (E.U.). We thank Cochin genomic (GENOM'IC), electron microscopy core facilities and the Imagine animal facilities (LEAT) for services and support. We also thank the Animal Histology and Morphology Core Facility of SFR Necker (Inserm US24). We also thank L. Legeai-Mallet and C. Colnot for providing the CMV-Cre and the Rosa26-LacZ mouse, respectively and Nicolas Cagnard for statistical advice.

Competing interests

The authors declare no competing interests.

References

Agrawal, P., Fontanals-Cirera, B., Sokolova, E., Jacob, S., Vaiana, C. A., Argibay, D., . . . Hernando, E. (2017). A Systems Biology Approach Identifies FUT8 as a Driver of Melanoma Metastasis. *Cancer Cell, 31*(6), 804-819 e807. doi:10.1016/j.ccell.2017.05.007

Akizu, N., Cantagrel, V., Schroth, J., Cai, N., Vaux, K., McCloskey, D., . . . Gleeson, J. G. (2013). AMPD2 regulates GTP synthesis and is mutated in a potentially treatable neurodegenerative brainstem disorder. *Cell, 154*(3), 505-517. doi:10.1016/j.cell.2013.07.005

Berglund, E. O., Murai, K. K., Fredette, B., Sekerkova, G., Marturano, B., Weber, L., . . . Ranscht, B. (1999). Ataxia and abnormal cerebellar microorganization in mice with ablated contactin gene expression. *Neuron, 24*(3), 739-750.
Blank, C., Smith, L. A., Hammer, D. A., Fehrenbach, M., Delisser, H. M., Perez, E., & Sullivan, K. E. (2006). Recurrent infections and immunological dysfunction in congenital disorder of glycosylation Ia (CDG Ia). *J Inherit Metab Dis, 29*(4), 592. doi:10.1007/s10545-006-0275-2
Boissart, C., Poulet, A., Georges, P., Darville, H., Julita, E., Delorme, R., . . . Benchoua, A. (2013). Differentiation from human pluripotent stem cells of cortical neurons of the superficial layers amenable to psychiatric disease modeling and high-throughput drug screening. *Transl Psychiatry, 3*, e294. doi:10.1038/tp.2013.71
Burda, P., & Aebi, M. (1999). The dolichol pathway of N-linked glycosylation. *Biochim Biophys Acta, 1426*(2), 239-257.
Cantagrel, V., & Lefeber, D. J. (2011). From glycosylation disorders to dolichol biosynthesis defects: a new class of metabolic diseases. *J Inherit Metab Dis, 34*(4), 859-867. doi:10.1007/s10545-011-9301-0
Cantagrel, V., Lefeber, D. J., Ng, B. G., Guan, Z., Silhavy, J. L., Bielas, S. L., . . . Gleeson, J. G. (2010). SRD5A3 is required for converting polyprenol to dolichol and is mutated in a congenital glycosylation disorder. *Cell, 142*(2), 203-217. doi:10.1016/j.cell.2010.06.001
Cao, J., Guo, S., Arai, K., Lo, E. H., & Ning, M. (2013). Studying extracellular signaling utilizing a glycoproteomic approach: lectin blot surveys, a first and important step. *Methods Mol Biol, 1013*, 227-233. doi:10.1007/978-1-62703-426-5_15
Chan, B., Clasquin, M., Smolen, G. A., Histen, G., Powe, J., Chen, Y., . . . Jin, S. (2016). A mouse model of a human congenital disorder of glycosylation caused by loss of PMM2. *Hum Mol Genet, 25*(11), 2182-2193. doi:10.1093/hmg/ddw085
Chavan, M., & Lennarz, W. (2006). The molecular basis of coupling of translocation and N-glycosylation. *Trends Biochem Sci, 31*(1), 17-20. doi:S0968-0004(05)00338-5 [pii]
10.1016/j.tibs.2005.11.010
Chen, L., & Zhou, S. (2010). "CRASH"ing with the worm: insights into L1CAM functions and mechanisms. *Dev Dyn, 239*(5), 1490-1501. doi:10.1002/dvdy.22269
Cherepanova, N. A., & Gilmore, R. (2016). Mammalian cells lacking either the cotranslational or posttranslocational oligosaccharyltransferase complex display substrate-dependent defects in asparagine linked glycosylation. *Sci Rep, 6*, 20946. doi:10.1038/srep20946
Cline, A., Gao, N., Flanagan-Steet, H., Sharma, V., Rosa, S., Sonon, R., . . . Steet, R. (2012). A zebrafish model of PMM2-CDG reveals altered neurogenesis and a substrate-accumulation mechanism for N-linked glycosylation deficiency. *Mol Biol Cell, 23*(21), 4175-4187. doi:10.1091/mbc.E12-05-0411
Colakoglu, G., Bergstrom-Tyrberg, U., Berglund, E. O., & Ranscht, B. (2014). Contactin-1 regulates myelination and nodal/paranodal domain organization in the central nervous system. *Proc Natl Acad Sci U S A, 111*(3), E394-403. doi:10.1073/pnas.1313769110
Dahmane, N., & Ruiz i Altaba, A. (1999). Sonic hedgehog regulates the growth and patterning of the cerebellum. *Development, 126*(14), 3089-3100.
Demyanenko, G. P., Riday, T. T., Tran, T. S., Dalal, J., Darnell, E. P., Brennaman, L. H., . . . Maness, P. F. (2011). NrCAM deletion causes topographic mistargeting of thalamocortical axons to the visual cortex and disrupts visual acuity. *J Neurosci, 31*(4), 1545-1558. doi:10.1523/JNEUROSCI.4467-10.2011
Demyanenko, G. P., Tsai, A. Y., & Maness, P. F. (1999). Abnormalities in neuronal process extension, hippocampal development, and the ventricular system of L1 knockout mice. *J Neurosci, 19*(12), 4907-4920.
Dennis, J. W., Nabi, I. R., & Demetriou, M. (2009). Metabolism, cell surface organization, and disease. *Cell, 139*(7), 1229-1241. doi:10.1016/j.cell.2009.12.008
Dequidt, C., Danglot, L., Alberts, P., Galli, T., Choquet, D., & Thoumine, O. (2007). Fast turnover of L1 adhesions in neuronal growth cones involving both surface diffusion and exo/endocytosis of L1 molecules. *Mol Biol Cell, 18*(8), 3131-3143. doi:10.1091/mbc.E06-12-1101
Fransen, E., D'Hooge, R., Van Camp, G., Verhoye, M., Sijbers, J., Reyniers, E., . . . Willems, P. J. (1998). L1 knockout mice show dilated ventricles, vermis hypoplasia and impaired exploration patterns. *Hum Mol Genet, 7*(6), 999-1009.
Freeze, H. H., Chong, J. X., Bamshad, M. J., & Ng, B. G. (2014). Solving glycosylation disorders: fundamental approaches reveal complicated pathways. *Am J Hum Genet, 94*(2), 161-175. doi:10.1016/j.ajhg.2013.10.024
Freeze, H. H., Eklund, E. A., Ng, B. G., & Patterson, M. C. (2015). Neurological aspects of human glycosylation disorders. *Annu Rev Neurosci, 38*, 105-125. doi:10.1146/annurev-neuro-071714-034019
Freeze, H. H., Schachter, H., & Kinoshita, T. (2015). Genetic Disorders of Glycosylation. In rd, A. Varki, R. D. Cummings, J. D. Esko, P. Stanley, G. W. Hart, M. Aebi, A. G. Darvill, T. Kinoshita, N. H. Packer, J. H. Prestegard, R. L. Schnaar, & P. H. Seeberger (Eds.), *Essentials of Glycobiology* (pp. 569-582). Cold Spring Harbor (NY).
Fujimori, T., Suno, R., Iemura, S. I., Natsume, T., Wada, I., & Hosokawa, N. (2017). Endoplasmic reticulum proteins SDF2 and SDF2L1 act as components of the BiP chaperone cycle to prevent protein aggregation. *Genes Cells, 22*(8), 684-698. doi:10.1111/gtc.12506
Gavel, Y., & von Heijne, G. (1990). Sequence differences between glycosylated and non-glycosylated Asn-X-Thr/Ser acceptor sites: implications for protein engineering. *Protein Eng, 3*(5), 433-442.
Grundahl, J. E., Guan, Z., Rust, S., Reunert, J., Muller, B., Du Chesne, I., . . . Marquardt, T. (2012). Life with too much polyprenol: polyprenol reductase deficiency. *Mol Genet Metab, 105*(4), 642-651. doi:10.1016/j.ymgme.2011.12.017
Haeuptle, M. A., Welti, M., Troxler, H., Hulsmeier, A. J., Imbach, T., & Hennet, T. (2011). Improvement of dolichol-linked oligosaccharide biosynthesis by the squalene synthase inhibitor zaragozic acid. *J Biol Chem, 286*(8), 6085-6091. doi:10.1074/jbc.M110.165795
He, P., Ng, B. G., Losfeld, M. E., Zhu, W., & Freeze, H. H. (2012). Identification of intercellular cell adhesion molecule 1 (ICAM-1) as a hypoglycosylation marker in congenital disorders of glycosylation cells. *J Biol Chem, 287*(22), 18210-18217. doi:10.1074/jbc.M112.355677
He, P., Srikrishna, G., & Freeze, H. H. (2014). N-glycosylation deficiency reduces ICAM-1 induction and impairs inflammatory response. *Glycobiology, 24*(4), 392-398. doi:10.1093/glycob/cwu006
Horstkorte, R., Schachner, M., Magyar, J. P., Vorherr, T., & Schmitz, B. (1993). The fourth immunoglobulin-like domain of NCAM contains a carbohydrate recognition domain for oligomannosidic glycans implicated in association with L1 and neurite outgrowth. *J Cell Biol, 121*(6), 1409-1421.
Hortsch, M. (2000). Structural and functional evolution of the L1 family: are four adhesion molecules better than one? *Mol Cell Neurosci, 15*(1), 1-10. doi:10.1006/mcne.1999.0809

Hulsmeier, A. J., Paesold-Burda, P., & Hennet, T. (2007). N-glycosylation site occupancy in serum glycoproteins using multiple reaction monitoring liquid chromatography-mass spectrometry. *Mol Cell Proteomics, 6*(12), 2132-2138. doi:10.1074/mcp.M700361-MCP200
Jaeken, J., & Peanne, R. (2017). What is new in CDG? *J Inherit Metab Dis, 40*(4), 569-586. doi:10.1007/s10545-017-0050-6
Kara, B., Ayhan, O., Gokcay, G., Basbogaoglu, N., & Tolun, A. (2014). Adult phenotype and further phenotypic variability in SRD5A3-CDG. *BMC Med Genet, 15*, 10. doi:10.1186/1471-2350-15-10
Kiefel, H., Bondong, S., Hazin, J., Ridinger, J., Schirmer, U., Riedle, S., & Altevogt, P. (2012). L1CAM: a major driver for tumor cell invasion and motility. *Cell Adh Migr, 6*(4), 374-384. doi:10.4161/cam.20832
Koziol, L. F., Budding, D., Andreasen, N., D'Arrigo, S., Bulgheroni, S., Imamizu, H., . . . Yamazaki, T. (2014). Consensus paper: the cerebellum's role in movement and cognition. *Cerebellum, 13*(1), 151-177. doi:10.1007/s12311-013-0511-x
Kretzer, N. M., Theisen, D. J., Tussiwand, R., Briseno, C. G., Grajales-Reyes, G. E., Wu, X., . . . Murphy, K. M. (2016). RAB43 facilitates cross-presentation of cell-associated antigens by CD8alpha+ dendritic cells. *J Exp Med, 213*(13), 2871-2883. doi:10.1084/jem.20160597
Lau, K. S., Partridge, E. A., Grigorian, A., Silvescu, C. I., Reinhold, V. N., Demetriou, M., & Dennis, J. W. (2007). Complex N-glycan number and degree of branching cooperate to regulate cell proliferation and differentiation. *Cell, 129*(1), 123-134. doi:S0092-8674(07)00315-7 [pii]
10.1016/j.cell.2007.01.049
Lee, H. Y., Greene, L. A., Mason, C. A., & Manzini, M. C. (2009). Isolation and culture of post-natal mouse cerebellar granule neuron progenitor cells and neurons. *J Vis Exp*(23). doi:10.3791/990
Lipecka, J., Chhuon, C., Bourderioux, M., Bessard, M. A., van Endert, P., Edelman, A., & Guerrera, I. C. (2016). Sensitivity of mass spectrometry analysis depends on the shape of the filtration unit used for filter aided sample preparation (FASP). *Proteomics, 16*(13), 1852-1857. doi:10.1002/pmic.201600103
Lutz, D., Loers, G., Kleene, R., Oezen, I., Kataria, H., Katagihallimath, N., . . . Schachner, M. (2014). Myelin basic protein cleaves cell adhesion molecule L1 and promotes neuritogenesis and cell survival. *J Biol Chem, 289*(19), 13503-13518. doi:10.1074/jbc.M113.530238
Maness, P. F., & Schachner, M. (2007). Neural recognition molecules of the immunoglobulin superfamily: signaling transducers of axon guidance and neuronal migration. *Nat Neurosci, 10*(1), 19-26. doi:10.1038/nn1827
Matei, V., Pauley, S., Kaing, S., Rowitch, D., Beisel, K. W., Morris, K., . . . Fritzsch, B. (2005). Smaller inner ear sensory epithelia in Neurog 1 null mice are related to earlier hair cell cycle exit. *Dev Dyn, 234*(3), 633-650. doi:10.1002/dvdy.20551
Metzger, D., Clifford, J., Chiba, H., & Chambon, P. (1995). Conditional site-specific recombination in mammalian cells using a ligand-dependent chimeric Cre recombinase. *Proc Natl Acad Sci U S A, 92*(15), 6991-6995.
Morava, E., Wevers, R. A., Cantagrel, V., Hoefsloot, L. H., Al-Gazali, L., Schoots, J., . . . Lefeber, D. J. (2010). A novel cerebello-ocular syndrome with abnormal glycosylation due to abnormalities in dolichol metabolism. *Brain, 133*(11), 3210-3220. doi:10.1093/brain/awq261
Morava, E., Wosik, H. N., Sykut-Cegielska, J., Adamowicz, M., Guillard, M., Wevers, R. A., . . . Cruysberg, J. R. (2009). Ophthalmological abnormalities in children with congenital disorders of glycosylation type I. *Br J Ophthalmol, 93*(3), 350-354. doi:bjo.2008.145359 [pii]
10.1136/bjo.2008.145359
Murray, A. N., Chen, W., Antonopoulos, A., Hanson, S. R., Wiseman, R. L., Dell, A., . . . Kelly, J. W. (2015). Enhanced Aromatic Sequons Increase Oligosaccharyltransferase Glycosylation Efficiency and Glycan Homogeneity. *Chem Biol, 22*(8), 1052-1062. doi:10.1016/j.chembiol.2015.06.017
Ng, B. G., & Freeze, H. H. (2018). Perspectives on Glycosylation and Its Congenital Disorders. *Trends Genet*. doi:10.1016/j.tig.2018.03.002
Nguyen, H., Ostendorf, A. P., Satz, J. S., Westra, S., Ross-Barta, S. E., Campbell, K. P., & Moore, S. A. (2013). Glial scaffold required for cerebellar granule cell migration is dependent on dystroglycan function as a receptor for basement membrane proteins. *Acta Neuropathol Commun, 1*, 58. doi:10.1186/2051-5960-1-58
Park, E. J., Grabinska, K. A., Guan, Z., Stranecky, V., Hartmannova, H., Hodanova, K., . . . Sessa, W. C. (2014). Mutation of Nogo-B receptor, a subunit of cis-prenyltransferase, causes a congenital disorder of glycosylation. *Cell Metab, 20*(3), 448-457. doi:10.1016/j.cmet.2014.06.016
Pereira, P. L., Magnol, L., Sahun, I., Brault, V., Duchon, A., Prandini, P., . . . Herault, Y. (2009). A new mouse model for the trisomy of the Abcg1-U2af1 region reveals the complexity of the combinatorial genetic code of down syndrome. *Hum Mol Genet, 18*(24), 4756-4769. doi:10.1093/hmg/ddp438
Poljak, K., Selevsek, N., Ngwa, E., Grossmann, J., Losfeld, M. E., & Aebi, M. (2017). Quantitative Profiling of N-linked Glycosylation Machinery in Yeast Saccharomyces cerevisiae. *Mol Cell Proteomics*. doi:10.1074/mcp.RA117.000096
Pollerberg, G. E., Thelen, K., Theiss, M. O., & Hochlehnert, B. C. (2013). The role of cell adhesion molecules for navigating axons: density matters. *Mech Dev, 130*(6-8), 359-372. doi:10.1016/j.mod.2012.11.002
Richard, E., Vega, A. I., Perez, B., Roche, C., Velazquez, R., Ugarte, M., & Perez-Cerda, C. (2009). Congenital disorder of glycosylation Ia: new differentially expressed proteins identified by 2-DE. *Biochem Biophys Res Commun, 379*(2), 267-271. doi:10.1016/j.bbrc.2008.12.036
Ron, D., & Walter, P. (2007). Signal integration in the endoplasmic reticulum unfolded protein response. *Nat Rev Mol Cell Biol, 8*(7), 519-529. doi:10.1038/nrm2199
Rujano, M. A., Cannata Serio, M., Panasyuk, G., Peanne, R., Reunert, J., Rymen, D., . . . Simons, M. (2017). Mutations in the X-linked ATP6AP2 cause a glycosylation disorder with autophagic defects. *J Exp Med, 214*(12), 3707-3729. doi:10.1084/jem.20170453
Sakurai, T., Lustig, M., Babiarz, J., Furley, A. J., Tait, S., Brophy, P. J., . . . Grumet, M. (2001). Overlapping functions of the cell adhesion molecules Nr-CAM and L1 in cerebellar granule cell development. *J Cell Biol, 154*(6), 1259-1273. doi:10.1083/jcb.200104122
Schiff, M., Roda, C., Monin, M. L., Arion, A., Barth, M., Bednarek, N., . . . De Lonlay, P. (2017). Clinical, laboratory and molecular findings and long-term follow-up data in 96 French patients with PMM2-CDG (phosphomannomutase 2-congenital disorder of glycosylation) and review of the literature. *J Med Genet, 54*(12), 843-851. doi:10.1136/jmedgenet-2017-104903
Schwarz, V., Pan, J., Voltmer-Irsch, S., & Hutter, H. (2009). IgCAMs redundantly control axon navigation in Caenorhabditis elegans. *Neural Dev, 4*, 13. doi:10.1186/1749-8104-4-13
Scott, H., & Panin, V. M. (2014a). N-glycosylation in regulation of the nervous system. *Adv Neurobiol, 9*, 367-394. doi:10.1007/978-1-4939-1154-7_17

Scott, H., & Panin, V. M. (2014b). The role of protein N-glycosylation in neural transmission. *Glycobiology, 24*(5), 407-417. doi:10.1093/glycob/cwu015
Sgaier, S. K., Lao, Z., Villanueva, M. P., Berenshteyn, F., Stephen, D., Turnbull, R. K., & Joyner, A. L. (2007). Genetic subdivision of the tectum and cerebellum into functionally related regions based on differential sensitivity to engrailed proteins. *Development, 134*(12), 2325-2335. doi:10.1242/dev.000620
Stoeckli, E. T. (2010). Neural circuit formation in the cerebellum is controlled by cell adhesion molecules of the Contactin family. *Cell Adh Migr, 4*(4), 523-526. doi:10.4161/cam.4.4.12733
Stoeckli, E. T., Sonderegger, P., Pollerberg, G. E., & Landmesser, L. T. (1997). Interference with axonin-1 and NrCAM interactions unmasks a floor-plate activity inhibitory for commissural axons. *Neuron, 18*(2), 209-221.
Sytnyk, V., Leshchyns'ka, I., & Schachner, M. (2017). Neural Cell Adhesion Molecules of the Immunoglobulin Superfamily Regulate Synapse Formation, Maintenance, and Function. *Trends Neurosci, 40*(5), 295-308. doi:10.1016/j.tins.2017.03.003
Tuysuz, B., Pehlivan, D., Ozkok, A., Jhangiani, S., Yalcinkaya, C., Zeybek, C. A., . . . Jaeken, J. (2016). Phenotypic Expansion of Congenital Disorder of Glycosylation Due to SRD5A3 Null Mutation. *JIMD Rep, 26*, 7-12. doi:10.1007/8904_2015_478
Vogel, C., & Chothia, C. (2006). Protein family expansions and biological complexity. *PLoS Comput Biol, 2*(5), e48. doi:10.1371/journal.pcbi.0020048
Wei, C. H., & Ryu, S. E. (2012). Homophilic interaction of the L1 family of cell adhesion molecules. *Exp Mol Med, 44*(7), 413-423. doi:10.3858/emm.2012.44.7.050
Weinhold, B., Seidenfaden, R., Rockle, I., Muhlenhoff, M., Schertzinger, F., Conzelmann, S., . . . Hildebrandt, H. (2005). Genetic ablation of polysialic acid causes severe neurodevelopmental defects rescued by deletion of the neural cell adhesion molecule. *J Biol Chem, 280*(52), 42971-42977. doi:10.1074/jbc.M511097200
Welti, M. (2013). Regulation of dolichol-linked glycosylation. *Glycoconj J, 30*(1), 51-56. doi:10.1007/s10719-012-9417-y
Wheeler, P. G., Ng, B. G., Sanford, L., Sutton, V. R., Bartholomew, D. W., Pastore, M. T., . . . Freeze, H. H. (2016). SRD5A3-CDG: Expanding the phenotype of a congenital disorder of glycosylation with emphasis on adult onset features. *Am J Med Genet A, 170*(12), 3165-3171. doi:10.1002/ajmg.a.37875
Wisniewski, J. R., Zougman, A., Nagaraj, N., & Mann, M. (2009). Universal sample preparation method for proteome analysis. *Nat Methods, 6*(5), 359-362. doi:10.1038/nmeth.1322
Xenaki, D., Martin, I. B., Yoshida, L., Ohyama, K., Gennarini, G., Grumet, M., . . . Furley, A. J. (2011). F3/contactin and TAG1 play antagonistic roles in the regulation of sonic hedgehog-induced cerebellar granule neuron progenitor proliferation. *Development, 138*(3), 519-529. doi:10.1242/dev.051912
Xu, J. (2005). Preparation, culture, and immortalization of mouse embryonic fibroblasts. *Curr Protoc Mol Biol, Chapter 28*, Unit 28 21. doi:10.1002/0471142727.mb2801s70
Zhao, L., Rosales, C., Seburn, K., Ron, D., & Ackerman, S. L. (2010). Alteration of the unfolded protein response modifies neurodegeneration in a mouse model of Marinesco-Sjogren syndrome. *Hum Mol Genet, 19*(1), 25-35. doi:10.1093/hmg/ddp464
Zielinska, D. F., Gnad, F., Wisniewski, J. R., & Mann, M. (2010). Precision mapping of an in vivo N-glycoproteome reveals rigid topological and sequence constraints. *Cell, 141*(5), 897-907. doi:10.1016/j.cell.2010.04.012